CCD Photometry and Spectroscopy of Small Main-Belt Asteroids

by

Shui Xu

Submitted to the Department of Earth, Atmospheric and Planetary Sciences
in Partial Fulfillment of the Requirements for the Degree of
Doctor of Philosophy

at the

Massachusetts Institute of Technology

April 1994

© Massachusetts Institute of Technology 1994

Signature of Author _____
Department of Earth, Atmospheric and Planetary Sciences
April 19, 1994

Certified by ___ _____
Richard P. Binzel
Associate Professor, Planetary Science
Thesis Supervisor

Accepted by _____
Thomas H. Jordan
Department Chairman

ARCHIVES

MASSACHUSETTS INSTITUTE
OF TECHNOLOGY

MAY 18 1994

LIBRARIES

CCD Photometry and Spectroscopy of Small Main-Belt Asteroids

by

Shui Xu

Submitted to the Department of Earth, Atmospheric and Planetary Sciences on April 19, 1994
in Partial Fulfillment of the Requirements for the Degree of
Doctor of Philosophy

ABSTRACT

Dedicated CCD photometric and spectroscopic surveys of small main-belt asteroids have been conducted to investigate their physical and possible mineralogical properties. Investigations of asteroids at small sizes are critical for understanding the origins of near-Earth asteroids; for placing important constraints on models of asteroid collisional and chemical evolution; for finding solutions to the ordinary chondrite paradox and the missing olivine problem. Rotational rates and shapes have been measured for 33 asteroids with a mean diameter less than 5 km. Three of these objects were new discoveries made during the course of the photometric survey. Low resolution spectra of 316 asteroids were obtained, with wavelength coverage ranging from 4000- to 10000-Å. More than half of the objects in the spectroscopic survey have diameters less than 20 km.

The photometric results show that small asteroids have a mean rotational frequency faster than that of larger main-belt asteroids. Their lightcurve amplitudes are similar, which implies that there is no significant size dependence on the shapes of collisional fragments over the range of 1 to 50 km. We detected the second shortest rotational period currently known, 2.35 hr, suggesting a density of ≥ 2 g cm^{-3} for an unstressed interior. The lack of substantially faster rotational periods could indicate that small asteroids have weak or fractured interiors. No conclusive detection of free precession was made although such motion could not be ruled out in all cases. Our statistical study shows that near-Earth asteroids have

comparable properties with their similar-sized main-belt counterparts. This result is fully consistent with a main-belt origin for the majority of the near-Earth asteroids.

The spectroscopic survey discovered an object resembling ordinary chondrite meteorites for the first time among the main-belt asteroids. The discovery apparently demonstrates that ordinary chondrite materials do exist in the main belt and can be detected with current instrumentation. But the paucity of ordinary chondrites in the main belt remains an unresolved problem. We also found more than 20 asteroids showing basaltic achondrite spectral properties. Among them, 13 have orbits that are similar to Vesta's and were previously predicated to be dynamically associated with Vesta. Eight bridge the orbital space between Vesta and the 3:1 Jovian resonance, a proposed source region for meteorites. These asteroids are probably multikilometer-sized fragments excavated from Vesta through one or more impacts. Our investigation appears to establish that Vesta is the parent body for the basaltic achondrite meteorites.

Principal component analysis was used to classify the observed small asteroid population. Our statistical analysis shows that the majority of the small main-belt asteroids belong to C and S classes. However, the small asteroids show much more diverse spectral features than the larger ones, which may indicate that small asteroids have a greater variety of compositions. A compositional gradient or inhomogeneity was found in a few asteroid families. Olivine-rich dunite asteroids continue to be rare in our observed size range. Such material could exist among some of the S asteroids showing olivine-rich spectral features. Our spectroscopic survey has begun to reveal a more complete picture of asteroid compositions down to small sizes.

Thesis Supervisor: Dr. Richard P. Binzel.
Title: Associate Professor of Planetary Science.

This thesis is dedicated to Prof. **Roger G. Burns** (1937-1994).

Acknowledgments

First and foremost, I would like to thank Rick Binzel for his guidance, advice, financial and travel support. He taught me how to approach and solve scientific problems. I am grateful to him for involving me in this project, and for allowing me to share his precious telescope time. His wisdom, encouragement and patience will help me become another outstanding advisor in the future.

I would also like to thank Edwin Barker, Ted Bowell, Tom Burbine, Bobby Bus, Pat Knezek, Mike Meyer, and Mike Skrutskie. They have contributed a lot to this big project. Especially, I thank Tom and Bobby for their invaluable help and innumerable useful discussions.

I learned a lot from Roger Burns, Maren Cooke, Tim Dowling, Ted Dunham, Mike Gaffey, Jim Elliot, Heidi Hammel, and Jack Wisdom through classroom teaching or discussions. Thanks to Joe Harrington, Jim Klavetter, Steve Mcdonald, and Rich Meserole for answering many questions about IRAF, Mac, and UNIX. Not all of them were dumb questions. I benefited a lot from discussions with former classmates or officemates, especially, Amanda Bosh, Jeff Foust, Matt Holman, Ray LeBeau, Anand Mehta, Cathy Olkin, Steve Slivan, Eliot Young, and Leslie Young. Ginny Siggia provided valuable advice and help during my stay in the Green Building. I am also indebted to Bob Barr, Larry Breuer, and Peter Mack at MDM Observatory for helping me catch the asteroids and stars through difficult instrumental and weather conditions. I would like to express my thanks to many people for supplying their data or other information, especially Mike Gaffey, Dave Jewitt, Jane Luu, David Tholen, and Jim Williams.

I acknowledge the Department of Earth, Atmospheric, and Planetary Sciences at MIT for more than five years financial support. Thanks also go to the Student Research Fund for generously providing research and travel support.

Finally, I thank my parents for their both short and long distance encouragement and support. And most of all, I thank my wife Yue and daughter Helen for their love, inspiration, and joy.

Table of Contents

Abstract 2
Acknowledgments 5
List of Tables 7
List of Figures 8

1. Introduction 11
   1.1. Background and Outstanding Problems 11
   1.2. Motivation for a New Observational Survey 17

2. The CCD Photometric Survey 18
   2.1 Survey Description and Data Reduction 18
   2.2 Observational Results 25
   2.3 Analysis and Discussion 32
   2.4 Origins for the Near-Earth Asteroids 35

3. The CCD Spectroscopic Survey 42
   3.1 Survey Description and Data Reduction 42
   3.2 Origins of the Spectral Features 58
   3.3 Taxonomy and Observational Results 71
   3.4 Analysis and Discussion 117
   3.5 Observational Results for Several Asteroid Families 132
   3.6 Chips Off of Vesta: Evidence for the Parent Body of Basaltic Achondrites . 146
   3.7 Evidence for the Existence of a Main-Belt Ordinary Chondrite Asteroid 159

4. Summary and Future Work 166
   4.1 Summary 166
   4.2 Future Work 169

References 171
Appendix: Composite Lightcurves and Spectra 183

List of Tables

1.1 Classification of Meteorites 14
2.1 Photometric Observational Circumstances 22
2.2 Photometric Observational Results 27
2.3 Statistical Summary I 33
2.4 Statistical Summary II 36
3.1 Spectroscopic Observational Circumstances 45
3.2 Assumed Mean Geometric Albedos for Different Types 54
3.3 Crystal System 61
3.4 Asteroid Classes, Albedos, and Spectrum 73
3.5 General Mineralogy and Possible Meteorite Analogues of the Asteroid Taxonomic Types 74
3.6 Compositional Interpretations of Asteroid Taxonomic Classes 75
3.7 Names and Types of 80 Meteorites Used in the PCA 79
3.8a Summary of the Sub-Classification of S-Type Asteroids 81
3.8b General Mineralogy and Possible Meteorite Analogues of the S-Asteroid Subtypes 82
3.9 Variance Distribution among the Components 83
3.10 Correlation Matrix from PCA 83
3.11 Scores on Principal Component Axes for Asteroids, Meteorites, and Sub S-classes and Assigned Classes for Asteroids 84
3.12 List of Pyroxene- and Olivine-Rich Asteroids in SMASS 105
3.13 Observational Results for 12 Asteroid Families 132
3.14 Summary of Vesta-Family Observations 148
3.15 Summary of Dynamical and Physical Properties for Observed Vesta Family Members and Near-Resonance Asteroids 156
3.16 Visible and Near-Infrared Observations of Asteroid 3628 Boznemcová ... 160
3.17 Results for Simultaneous Visible and Near-Infrared Observations of Asteroid 3628 161

List of Figures

1.1 Heliocentric Distribution of Nearly 4,000 Numbered Asteroids 12
2.1 A Composite CCD Image of Asteroid 1981 ER27 21
2.2 Histograms of Rotational Frequency Distributions for Near-Earth Asteroids, Main-Belt Asteroids, and Cometary Nuclei 38
2.3 Histograms of Lightcurve Amplitude Distributions for Near-Earth Asteroids, Main-Belt Asteroids, and Cometary Nuclei 39
3.0 Absorption Bands of Water and Oxygen Molecules in the Earth's Atmosphere 44
3.1a Heliocentric and Size Distributions of SMASS New Objects 55
3.1b Size Limits of SMASS and ECAS Samples 56
3.2 Comparison between Measurements by SMASS and the Eight-Color Asteroid Survey 57
3.3 Crystallographic Axes and Angles 61
3.4 Orthopyroxene Crystal Structure 62
3.5 Relative Energies of 3-*d* Orbitals of a Transition Metal Ion in Different Coordination Environments 63
3.6 Energy Level Diagrams for Fe^{2+} Ions in the Orthopyroxene Structure 64
3.7a Absorption Spectra (polarized) of Bronzite Orthopyroxenes 65
3.7b Absorption Spectra (polarized) of Orthoferrosilite Orthopyroxenes 66
3.8 Olivine Crystal Structure 67
3.9 Energy Level Diagrams for Fe^{2+} Ions in the Olivine Structure 68
3.10a Absorption Spectra (polarized) of Forsterite Olivines 69
3.10b Absorption Spectra (polarized) of Fayalite Olivines 70
3.11 Mean Reflectance Spectra for the Asteroid Classes 72
3.12 Distributions of Asteroid Taxonomic Classes and Superclasses 76
3.13a Domains of Various Asteroid Taxonomic Classes in the Principal Component Space for SMASS Objects (50 Wavelength Band) 94
3.13b Domains of Various Asteroid Taxonomic Classes in the Principal Component Space for SMASS Objects (28 Wavelength Band) 95
3.13c Domains of Asteroid Classes from the Eight-Color Asteroid Survey 96
3.14a Domains of SMASS and Meteorites Classes in the Principal Component Space (50 Wavelength Band) 97
3.14b Domains of SMASS and Meteorites Classes in the Principal Component Space (28 Wavelength Band) 98

3.15a Domains of SMASS S-Classes and Gaffey *et al*'s Sub S-classes in the Principal Component Space 99
3.15b Domains of SMASS S-Classes and Howell *et al*'s Sub S-classes in the Principal Component Space 100
3.15c Comparison between Tholen Principal Components and SMASS Principal Components..... 101
3.16a Band I Position vs Depth Plot for Meteorites and SMASS Objects 103
3.16b Band I Position vs Depth Plot for SMASS Objects 104
3.16c The Locations of Identified Pyroxene-Rich Asteroids in the Principal Component Space 107
3.17a Spectra of 8 Olivine-Rich Objects and an A-Type Asteroid 108
3.17b The Locations of Identified Olivine-Rich Asteroids in the Principal Component Space 109
3.18a PC1 vs PC2 Plots for Large and Small SMASS S-Asteroids 111
3.18b Diameter vs PC1 Running Box Plots for SMASS S-Asteroids 112
3.18c Diameter vs PC2 Running Box Plots for SMASS S-Asteroids 113
3.19 Band I Position vs Depth Plots for Large and Small Asteroids 114
3.20 Featureless Red to Near-Infrared Spectra for 5 Asteroids 115
3.21 Spectra of Asteroids 44, 1279, and 1653 116
3.22 Distributions of SMASS and ECAS Asteroids 120
3.23a Heliocentric Distributions of the Taxonomic Classes of SMASS and ECAS Objects 121
3.23b Size Distributions of the Taxonomic Classes of SMASS and ECAS objects 122
3.24a Heliocentric Distribution of the Taxonomic Classes of 800 Asteroids Surveyed by SMASS and ECAS 123
3.24b Size Distribution of the Taxonomic Classes of 800 Asteroids Surveyed by SMASS and ECAS 124
3.25 Type Distribution for 3 Different Size Groups in the Inner Belt 125
3.26 Type Distribution for 3 Different Size Groups in the Outer Belt 126
3.27 Histogram of Asteroid Type Distribution before (top) and after (bottom) Albedo Bias Correction 127
3.28 An Example of Diverse Spectral Features Observed in SMASS 128
3.29 Reflectance Spectra of Mixed-Mineral Assemblages 129
3.30a a vs e Plot for SMASS New Objects 130

3.30b a vs sin i Plot for SMASS New Objects 131
3.31 Spectra of 9 Members in the Koronis Family 135
3.32 Heliocentric Distribution of 9 Observed Asteroids in the Koronis Family .. 136
3.33 Spectra of 10 Members in the Phocaea Group 137
3.34 Heliocentric Distribution of 9 Observed Asteroids in the Phocaea Group . 138
3.35 Spectra of 6 Members in the Eos Family 139
3.36 Heliocentric Distribution of 6 Observed Asteroids in the Eos Family 140
3.37 Spectra of 6 Members in the Maria Family 141
3.38 Heliocentric Distribution of 6 Observed Asteroids in the Maria Family 142
3.39 Spectra of 5 Members in the Nysa Family 143
3.40 Spectra of 9 Near-Earth Asteroids 144
3.41 The Locations of 9 Near-Earth Asteroids in the Principal Component Space 145
3.42 Heliocentric Distributions of Asteroids in the Vicinity of Vesta 149
3.43 Spectra of 15 Basaltic Achondrite-Like Asteroids 150
3.44 Spectra of 6 Additional Basaltic Achondrite-Like Asteroids 151
3.45 Distributions of Collisional Probabilities and Encounter Velocities 155
3.46 Spectrum of Asteroid 3628 Boznemcová 164
3.47 Distributions of Asteroid Orbital Eccentricities and Diameters vs Heliocentric Distance in the Vicinity of 3:1 Resonance Region 165

1. Introduction

1.1 Background and Outstanding Problems

Asteroids are small natural bodies orbiting around the Sun. We believe they are remnant representatives of the population of planetesimals that filled the early solar system after the collapse of the solar nebula. The asteroids occupy the transition region between the rocky terrestrial planets and the outer gas giants. It is believed that Jovian perturbations led to the failure of planet formation in that region (e.g., Binzel 1989, Wetherill 1989). Most of the asteroids reside between the orbits of Mars and Jupiter in a region commonly called the "main belt" (Fig. 1.1). More than 15,000 asteroids have been discovered with diameters ranging from hundreds of meters to hundreds of kilometers. There are asteroid families (clumps) as well as gaps (depletions) found in the solar system. The history of asteroid study was reviewed in detail by Cunningham (1985). Asteroids have undergone various physical evolution such as collisions and erosion. Some of them have been chemically reprocessed by various geological processes such as differentiation, metamorphism, and remelting. Some of them have preserved their original physical and chemical conditions. Thus, asteroids can not only help us study the interiors of planets or other differentiated bodies, but also provide us a clear view of the conditions and processes of the early solar system. In addition, the study of asteroids is the only way to identify the parent bodies of the meteorites in order to obtain the information about the compositional distribution and temperature gradients of the solar nebula (Gaffey *et al.* 1993a).

Investigations of asteroid physical and chemical properties have been advanced substantially during the past two decades, by ground and space observations and by theoretical and experimental studies as well. Comprehensive research results appeared in two classic books: *Asteroids* edited by Gehrels (1979) and *Asteroids II* edited by Binzel *et al.* (1989a). However, our knowledge of the asteroids has come only from observations of the largest asteroids. The most notable groundbased observational investigations are the Asteroid Photoelectric Survey carried out by Binzel (1986, and 1987) and the Eight-Color Asteroid Survey by Zellner *et al.* (1985). Due to the apparent faintness of the small main-belt asteroids and instrumental limits, very few small asteroids have been investigated.

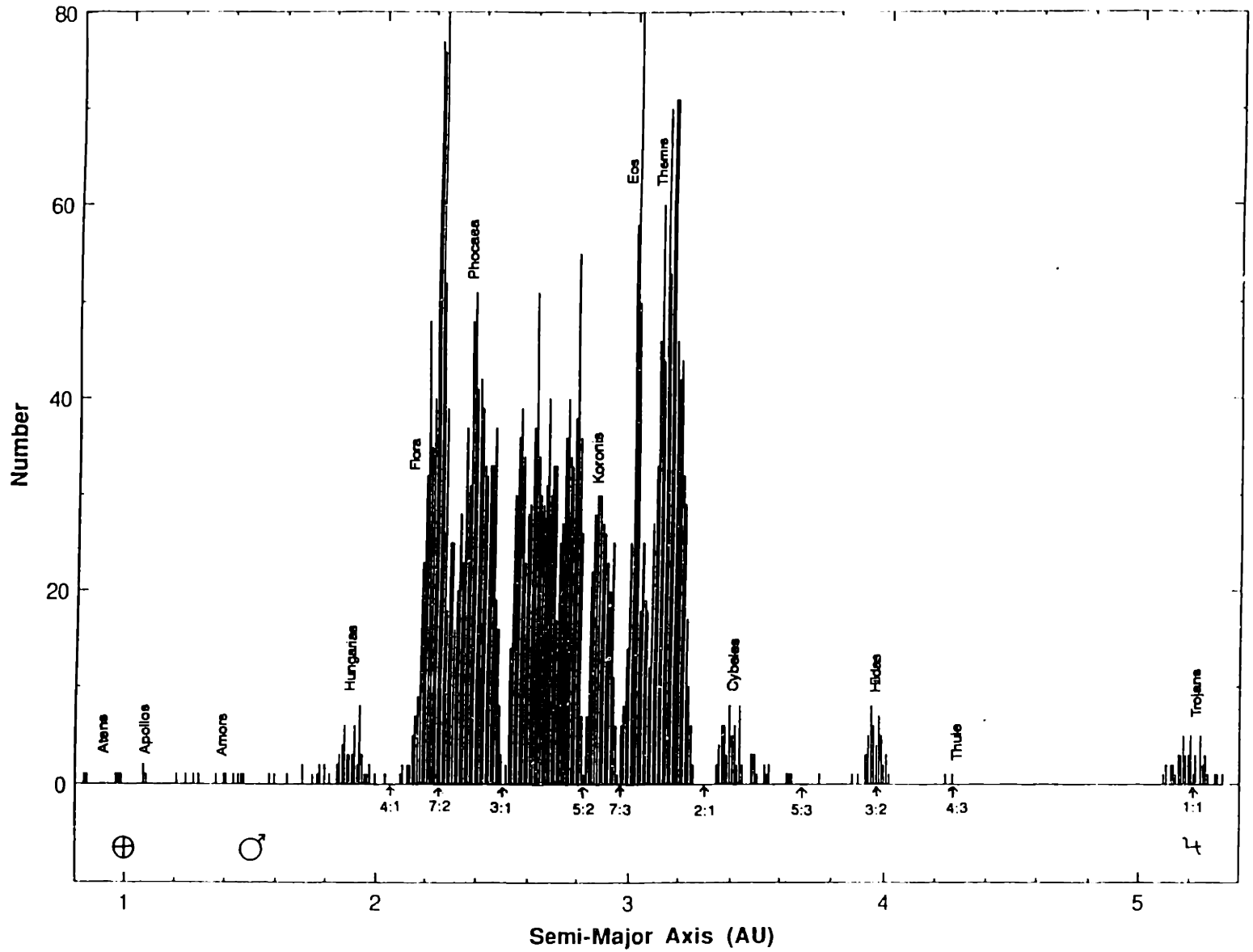

Fig. 1.1. Heliocentric distribution of orbital semi-major axes for nearly 4,000 numbered asteroids. Commonly referred to regions and the major Jovian resonances are labeled. (From Binzel 1989.)

Many planetary scientists believe that our poor understanding of the small asteroids impedes us from solving the following fundamental problems:

The Ordinary Chondrite Paradox and the Great Dunite Shortage

One of the most puzzling questions of current asteroid study is the absence of ordinary chondrite objects among the larger main-belt asteroids. Ordinary chondrites are the most common meteorite type and consist of 81% of the Earth's meteorite flux (Table 1.1). Dynamical models and meteoritic investigations suggest that these meteorites should derive from the main belt, probably in the 3:1 resonance region (Wisdom 1985, Wetherill 1988). However, until now, no observational surveys, including the Eight-Color Asteroid Survey (Zellner *et al.* 1985), have found any ordinary chondrite object among more than 600 large main-belt asteroids. There are two different and intensely debated theories for the mismatch: One hypothesis is that the physical interpretations of the obtained asteroid spectra are wrong and some "space weathering" processes have altered the surface of ordinary chondrite asteroids (e.g., Wetherill and Chapman 1988); the second is that ordinary chondrites do exist, but at smaller sizes that escape electromagnetic induction heating (Scott *et al.* 1989). Such small objects are just below the limits of previous observational surveys (Bell *et al.* 1989). Additional models have also been proposed to address this problem (Gaffey 1984, Gaffey *et al.* 1989, Lipschutz *et al.* 1989, Gaffey *et al.* 1993b). However, none of these theories has been generally accepted so far due to the lack of observational support, especially the observations of small objects.

A second paradox in our understanding of asteroid evolution is the olivine problem. Olivine is by far the most common mineral in chondritic meteorites. Since the solar system formation, asteroids have been affected by collisions and thermal processing. Differentiation of an ordinary chondrite or carbonaceous chondrite parent body would result in a small Ni-Fe metal core, a thick olivine mantle, and a thin pyroxene/plagioclase crust. We believe that we have observed many objects which represent such differentiated cores and crusts, but there is a significant absence of olivine-dominated mantle materials (dunites). Until now, only a few dunite-like asteroids (246 Asporina, 289 Nenetta, 446 Aeternitas, 863 Benkoela) have been found (Zellner *et al.* 1985, Tholen 1984). Either the olivine mantles that have been collisionally stripped away only remain among small bodies (D < 25 km)

(Bell *et al.* 1989), or our understanding of asteroid evolution is not complete or correct. The observation of small main-belt asteroids may help us understand this fundamental problem (Bell *et al.* 1989).

Table 1.1
Classification of Meteorites*

Broad classification			Group name assigned by Wasson[a]	Mineralogical-structural name	Percentage of falls[b]
Primitive Bodies ↑	Stones 95%	Chondrites 86%	Carbonaceous chondrites 5%	CI = C1 = CI	0.7
				CM = C2 = CII	2.0
				CO, CV = C3 = CIII	2.0
			Ordinary chondrites 81%	E = Enstatite	1.5
				H[c] = Bronzite	32.3
				L[d] = Hypersthene	39.3
				LL[e] = Amphoterite	7.2
				Others —	0.3
Increasing Differentiation ↓		Achondrites 9%		Ureilites = Olivine-pigeonite	0.4
				Aubrites = Enstatite	1.1
				Diogenites = Hypersthene	1.1
				Howardites and eucrites = Pyroxene-plagioclase	5.3
				Others = Other differentiated stones	1.0
	Stony irons 1%			Mesosiderites = Mesosiderites	0.9
				Pallasites = Pallasites	0.3
	Irons 4%			IA = Medium and coarse octahedrites	0.8
				IIA = Hexahedrites	0.5
				IIIA = Medium octahedrites	1.5
				IVA = Fine octahedrites	0.4
				Others = Ataxites, etc.	1.3
					99.9%

* From Hartmann (1993, pp. 165).

Physical Parameters for the Collisional Models

Collisional models and laboratory experiments (e.g., Davis *et al.* 1985 and 1989) predicted that small main-belt asteroids would have different physical properties than the larger asteroids because these small objects have been affected more significantly by collisions. The computed rotational rates in these models for the small asteroids are extremely sensitive to model parameters such as the impact strength of the asteroid, the partitioning of the impact energy and the projectile distribution. Actual distributions of rotational rates and shapes are necessary to establish reliable parameters and boundary conditions. Therefore, complete statistical studies of the rotational rates and shapes from the observations are urgently needed to increase our understanding of asteroid collisional history.

Origins for the Near-Earth Asteroids

The origin and re-supply sources of the near-Earth asteroids (Aten-Apollo-Amor objects) have been perplexing astronomers for most of this century. The near-Earth asteroids (also called Earth-approaching asteroids) are astronomically observed objects with perihelia close to the Earth's semi-major axis. Over 200 such objects have been found and the majority of them are kilometer-sized objects. Due to their close approaches to the Earth, these small objects appear sufficiently bright so their physical properties can be investigated comprehensively (McFadden *et al.* 1989). The collisional and dynamical lifetime of the near-Earth asteroids (10^7 to 10^8 yr) is much less than the age of the solar system (Wetherill 1975, Shoemaker *et al.* 1979, Shoemaker 1983). Any primordial population of these objects should have been diminished either by colliding with the terrestrial planets, or by being ejected from the solar system. But observations and analyses suggest that their current population exists at a steady state value (Shoemaker and Wolfe 1986, Wetherill 1988). After studying the 3:1 resonance region in the main belt and its connection with the origin of the near-Earth asteroids, Wisdom (1982, 1983 and 1985) and Wetherill (1987, 1988) proposed that the near-Earth asteroids come from the main belt through a chaotic route. Chaotic orbits caused by resonance lead to increased eccentricities, allowing asteroids to cross the orbit of Mars and Earth. Because such conveyance is a purely dynamical process, it can be hypothesized that these near-Earth objects will show similar properties as compared with the small main-belt asteroids. After studying the rotational rates and

lightcurve amplitudes (indicators of shapes), we can compare the physical properties of these two kinds of asteroids. This comparison can be used to determine whether or not the source of the near-Earth asteroids is consistent with their being dynamically derived from the main belt. A fraction of the near-Earth asteroids may be extinct cometary nuclei (Weissman *et al.* 1989, Jewitt and Meech 1988, and Jewitt 1990). Comparison of the small asteroids with the cometary nuclei can also be performed.

Genetic Links between Asteroids and Meteorites

Meteorites are small naturally-delivered fragments of a portion of the asteroid (and perhaps comet) population. Meteorite study has provided detailed insights into the conditions and time scales of the events during the formation of the solar system (Gaffey *et al.* 1993a). However, meteorites provide no direct information on their formation locations in the solar system. In contrast, most of the main-belt asteroids likely remain near their original formation locations. In order to obtain a spatial context for the detailed chemical and chronological data derived from the meteorite studies, we need to identify the parent bodies of the meteorites in the main belt. There has been no observational evidence of a direct link between the major meteorite classes and the main-belt source bodies.

1.2 Motivation for a New Observational Survey

A complete understanding of the physical properties of the small main-belt asteroids may provide solutions to the above questions. With the advent of Charge-Coupled Device (CCD) detectors, now it becomes technologically possible to carry out large scale photometric and spectroscopic studies of these small main-belt asteroids (diameter down to 1 km) with moderate-sized telescopes. High-quantum-efficiency CCDs can make precise photometric measurements ($\sigma = \pm 2\%$) of these faint objects in just several minutes' exposure time. Lightcurve variations from time-resolved CCD photometry can help us to determine some fundamental parameters such as spin rates and shapes. By using a CCD and spectrograph with appropriate blocking filters, we can obtain an asteroid spectrum over the wavelength range from 4000- to 10000-Å (0.4- to 1-μm) with a resolution of about 10 Å/pixel. Such wavelength range and resolution are sufficient for determining the asteroid compositional types. A convincing solution to the above fundamental problems can be achieved if the physical and compositional properties of a sufficient number of small asteroids can be obtained through a new photometric and spectroscopic survey. Our goals are

(a) to obtain the rotational periods and lightcurve amplitudes for more than 30 kilometer-sized asteroids for comparison with those of larger main-belt asteroids, near-Earth asteroids, and comets.

(b) to obtain visual spectra for more than 200 asteroids with diameters down to 1 km; to classify the newly observed asteroids and compare their type distribution with that of larger asteroids; to investigate the ordinary chondrite paradox, the missing-olivine problem, and the link between asteroid families and particular meteorites.

2. The CCD Photometric Survey

2.1 Survey Description and Data Reduction

Infrequent access to large telescopes, instrumental limits, and faint apparent magnitudes have allowed very few physical measurements of main-belt asteroids smaller than 15 km (Binzel and Mulholland 1983; Wisniewski 1991). No previous physical studies have been achieved for main-belt asteroids smaller than 5 km. Physical observations of asteroids in this size range are critically important for at least two lines of current research: determining the source of the similar diameter near-Earth asteroid population and using the small end members as constraints for models of asteroid collisional evolution.

A program called the Small Main-belt Asteroid Lightcurve Survey (SMALS, Binzel *et al.* 1992a) was initiated to make the first systematic physical observations of main-belt asteroids in the $D \leq 5$ km size range. The SMALS was carried out on 50 nights between November 1987 and May 1991 at the Anderson Mesa, AZ station of Lowell Observatory and at the Michigan-Dartmouth-MIT Observatory (MDM) located on Kitt Peak, AZ. At Lowell Observatory, the Perkins 1.8-m telescope was equipped with an RCA SID501EX CCD (320x512 pixels), giving an image scale of 0.8 arcseconds per pixel. The 1.3-m McGraw-Hill and 2.4-m Hiltner telescopes were used at MDM Observatory with either a Thomson (400x576 pixels) CCD or a TI 4849 (398x598 pixels) CCD. The optional use of different reducing lenses allowed image scales of 0.5 to 1.5 arcseconds per pixel to be utilized.

SMALS target asteroids were selected primarily from the United Kingdom Caltech Asteroid Survey (UCAS) (Bus *et al.* 1986) which provided accurate orbits for over 200 main-belt objects with estimated diameters of less than 5 km. Typical astrometric uncertainties of ± 2 arcminutes for the UCAS objects usually allowed them to be located within an image frame centered on the predicted position. Objects from the Palomar-Leiden survey as well as some recently numbered asteroids provided additional targets. The asteroid's identity was certified through detection and measurement of its motion vector. Through the course of searching for, identifying, and observing the intended target objects, three new asteroids were serendipitously discovered: 1987 WJ1, 1989 TY, and 1990 YY, the latter being a Trojan orbiting near the L5 point of Jupiter. All such discoveries remained in the

same CCD field as the planned target for at least one complete night, allowing their simultaneous lightcurve measurement.

Target asteroids typically fell in the V magnitude range of 17 to 19. Depending on the target's magnitude and the telescope aperture, an exposure of either 300 or 600 seconds was used with the goal of obtaining a signal-to-noise ratio of at least 50 for the asteroid. Typical trail rates for asteroid motion were about 0.5 arcseconds per minute, causing elongated images for the longer exposures. The observing technique we found optimal was to track at the asteroid rate, rather than the sidereal rate. The benefits for the data reduction of round asteroid images with trailed stars, as opposed to the converse, are discussed below.

Because of the red sensitivity of the CCDs, we chose to make all lightcurve measurements using an R filter. Upon reaching an airmass value near 1.2, a set of alternating V and R filter exposures were made. Exposures in V and R filters were then obtained for standard stars from Landolt (1983) located near the meridian where they transited with an airmass value near 1.2. Standard stars were chosen having Landolt V-R indices of 0.4 to 0.5, similar to the expected values for the asteroids. By working at the telescope to minimize differences in airmass and color indices, errors due to uncertainties associated with extinction coefficients and color correction terms could be reduced to below 0.01-0.02 magnitudes. Note that these V-R colors as measured on the Landolt (1983) system correspond to R magnitudes in the Kron-Cousins system. Landolt (1983, p. 452) gives the transformation to V-R in the Johnson system, which is more traditionally used for planetary applications. All SMALS V-R measurements in the Landolt system have been transformed to the Johnson system in this work. This transformation adds an additional ~0.01 magnitudes uncertainty to each color index.

Flat fields for the CCD frames were obtained using a white screen illuminated with color-balanced lamps at Lowell and using the twilight sky at MDM. Ten or more bias frames were obtained through the course of each night to monitor the noise level of the CCD. All image processing, including bias subtraction and flat field corrections, were performed using the Image Reduction and Analysis Facility (IRAF) software package developed by the National Optical Astronomical Observatories. Magnitudes for the asteroid and at least two comparison stars were extracted from each image using aperture photometry. Specifically, this consisted

of using a central circular aperture for measuring an object's intensity surrounded by a circular annulus for measurement of the background. Aperture sizes were chosen on the basis of measurements of the full widths of image profiles and annulus sizes were chosen to have an area at least as large as the central aperture.

Tracking the telescope at the sidereal rate during an exposure produced round comparison star images and trailed asteroid images. We found it advantageous for exposures to be tracked at the asteroid rate as this provided the smallest possible image profiles for the fainter asteroid. Smaller image profiles helped reduce the aperture size necessary for extracting asteroid magnitude information. In this way, background noise in the asteroid aperture was minimized. Although larger aperture sizes were consequently required for the photometry of the comparison stars, they were substantially brighter than the asteroid and less adversely affected by the added noise. Once aperture sizes were chosen, they remained fixed for all reductions of a given night's data.

The CCD was oriented with its long axis east-west in the image plane corresponding to the principal direction of the asteroid's motion. Each asteroid was imaged repeatedly for as long an interval as possible during a night while remaining above an airmass of 2. Comparison stars that were initially located ahead of the asteroid could often be used during the entire observing interval. If not, new ones were acquired and calibrated with respect to older ones before the latter fell beyond the bounds of the image frame. A typical night yielded around 100 separate images.

Fig. 2.1 shows a composite image of an asteroid on a CCD frame. Table 2.1 lists the observational circumstances for the 33 asteroids observed in this survey. For each night of observation, the table gives the geocentric equatorial and ecliptic coordinates (RA, Dec, λ, β), the phase angle (α), the magnitudes of the heliocentric and geocentric vectors (r, Δ), and the telescope aperture (m) used.

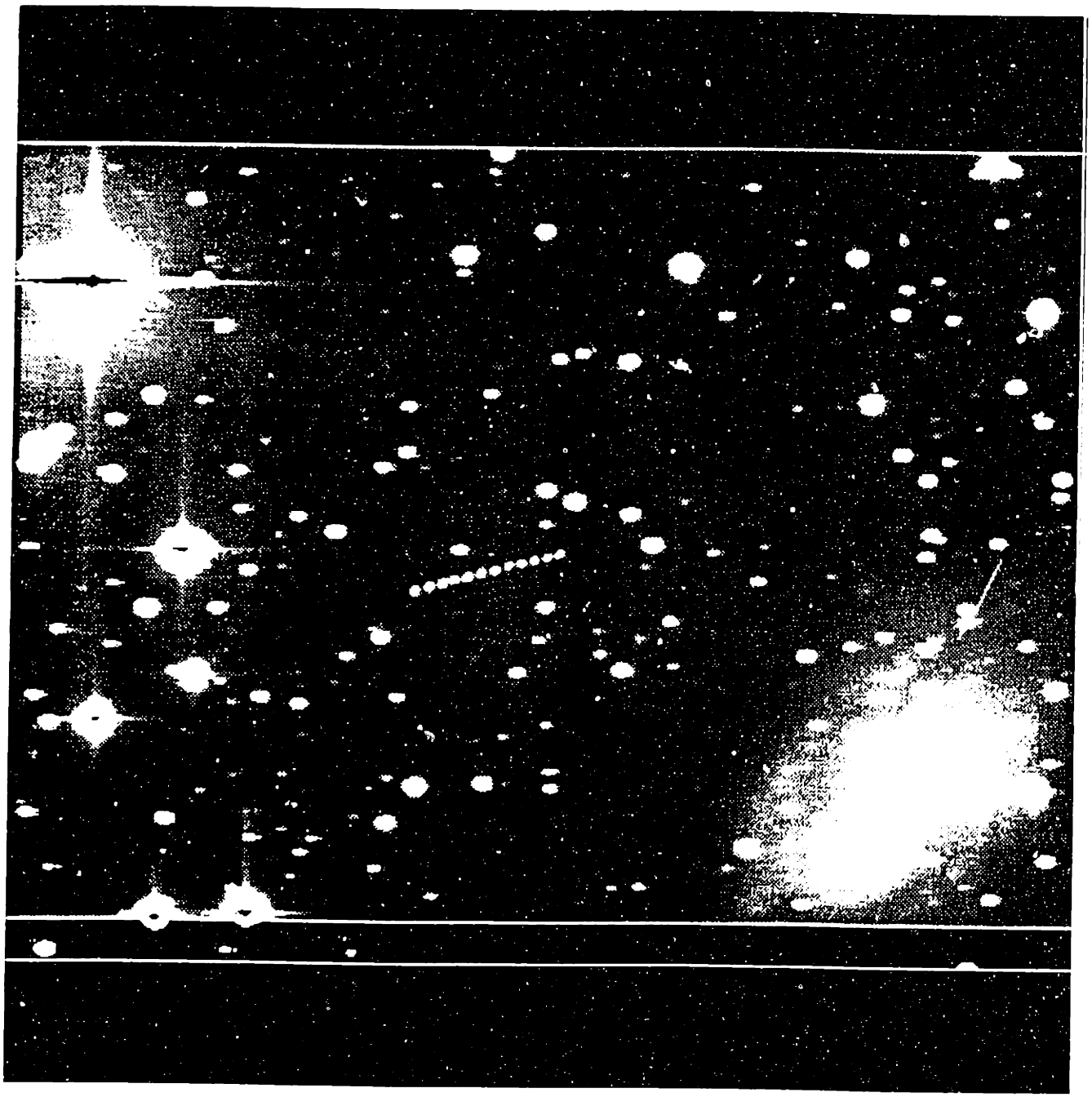

Fig. 2.1. A composite image of 12 separate CCD frames obtained on 11 January 1991 UT containing the 2-km diameter main-belt asteroid 1981 ER27 (V mag. = 18.5). Each frame consisted of a 300-s exposure using a TI 4849 CCD attached to the 1.3-m McGraw-Hill telescope at the Michigan Dartmouth MIT Observatory located on Kitt Peak, Arizona. The field size is 3 by 4.6 arc min. North is to the top and west is to the left. The asteroid's motion was from northeast to southwest. The diffuse object in the southeast corner of the field is the galaxy UGC 03390. (Figure from Binzel *et al.* 1992b.)

Table 2.1

Photometric Observational Circumstances

UT Date	R A (1950) h	m	Dec °	'	α °	r (AU)	Δ (AU)	λ °	β °	Tel*
2952 Lilliputia										
1991 Jan 12	07	7	26	9	3.2	2.104	1.124	105.0	3.6	1.8
Jan 14	07	5	26	8	4.3	2.108	1.131	104.6	3.5	1.8
3536 Schleicher										
1990 Nov 13	03	49	31	30	7.0	2.251	1.285	62.0	11.2	1.8
Nov 14	03	48	31	29	6.8	2.251	1.282	61.8	11.2	1.8
3651 Friedman										
1991 May 19	14	1	-5	36	12.7	2.138	1.191	210.1	6.3	1.8
May 20	14	0	-5	38	13.2	2.139	1.196	209.9	6.2	1.8
4432 McGraw-Hill										
1990 Dec 19	03	27	18	12	14.5	2.110	1.213	54.0	-0.6	1.3
Dec 23	03	25	18	8	16.2	2.119	1.249	53.5	-0.5	1.3
4659 Roddenberry										
1990 Nov 14	01	34	11	41	13.0	1.851	0.905	26.0	1.7	1.8
Nov 15	01	34	11	40	13.7	1.852	0.913	26.0	1.8	1.8
4924 Hiltner										
1990 Jan 28	08	53	15	18	1.7	2.582	1.599	131.4	-2.1	1.8
1981 EA7										
1989 Sep 1	01	1	18	37	23.3	1.773	0.903	21.2	11.2	1.3
Sep 4	01	1	18	51	22.1	1.772	0.886	21.3	11.4	1.3
Sep 5	01	1	18	55	22.1	1.772	0.881	21.3	11.5	1.3
1981 EV8										
1989 Aug 28	22	2	-1	4	5.7	1.853	0.851	332.2	10.3	1.8
Aug 29	22	1	-1	11	5.9	1.852	0.851	331.9	10.3	1.8
Aug 30	22	1	-1	19	6.1	1.852	0.851	331.8	10.2	1.8
1981 EJ9										
1989 Mar 7	9	28	12	40	11.0	2.280	1.346	140.3	-2.2	2.4
Mar 8	9	27	12	41	11.4	2.280	1.351	140.1	-2.2	2.4
1981 EV9										
1989 Oct 1	02	33	22	27	15.4	2.225	1.337	43.0	7.0	2.4
Oct 2	02	32	22	26	14.9	2.224	1.329	42.8	7.1	2.4
1981 EA12										
1989 Sep 29	23	37	00	21	4.7	2.272	1.281	354.9	2.6	2.4
Sep 30	23	36	00	14	5.2	2.271	1.282	354.5	2.6	2.4

Table 2.1 (continued)

UT Date	R A (1950) h m	Dec ° '	α °	r (AU)	Δ (AU)	λ °	β °	Tel*
1981 EE12								
1991 Jan 13	07 15	20 53	2.2	2.121	1.139	107.5	-1.4	1.3
Jan 14	07 14	20 52	2.7	1.122	1.141	107.3	-1.5	1.3
1981 EF12								
1989 Oct 2	00 35	12 44	3.8	2.482	1.489	13.0	8.3	2.4
Oct 3	00 34	12 37	3.6	2.482	1.489	12.8	8.2	2.4
1981 EP13								
1990 Feb 28	08 7	19 23	15.0	2.394	1.541	119.8	-0.8	1.3
Mar 1	08 7	19 23	15.4	2.395	1.550	119.8	-0.8	1.3
1981 EY14								
1991 Jan 13	07 8	21 7	2.9	2.042	1.061	105.8	-1.3	1.3
Jan 14	07 7	21 6	3.5	2.042	1.062	105.6	-1.4	1.3
1981 EC15								
1989 Mar 7	08 49	19 51	16.3	2.113	1.233	129.3	2.0	2.4
Mar 8	08 48	19 49	16.8	2.112	1.239	129.2	1.9	2.4
Mar 9	08 48	19 46	17.2	2.112	1.245	129.1	1.8	2.4
1981 EP15								
1990 Dec 18	04 45	26 47	6.2	2.008	1.037	73.2	4.4	1.3
Dec 19	04 44	26 41	6.8	2.009	1.040	73.0	4.3	1.3
1981 EU15								
1991 Jan 15	07 6	14 55	5.2	2.035	1.060	106.1	-7.6	1.3
1981 ER18								
1989 Mar 8	09 26	17 15	12.5	2.199	1.276	138.4	2.1	2.4
Mar 9	09 25	17 15	12.9	2.200	1.281	138.2	2.0	2.4
1981 ET20								
1988 Dec 31	06 59	36 53	5.5	2.552	1.588	102.1	14.1	1.3
1981 ED21								
1990 Feb 28	11 30	02 59	5.6	2.307	1.331	171.9	-0.2	1.3
Mar 1	11 29	03 1	5.1	2.311	1.332	171.7	-0.2	1.3
1981 EH23								
1987 Dec 21	05 54	23 37	0.1	2.138	1.154	88.6	0.2	1.8
Dec 22	05 53	23 36	0.5	2.139	1.155	88.4	0.2	1.8
1981 ER27								
1991 Jan 11	05 58	36 7	10.3	2.194	1.258	89.6	12.7	1.3

Table 2.1 (continued)

UT Date	R A (1950) h m	Dec ° '	α °	r (AU)	Δ (AU)	λ °	β °	Tel*
1981 EX28								
1989 Aug 29	21 58	-5 27	3.9	2.252	1.248	329.7	6.5	1.8
Sep 5	21 51	-5 47	6.8	2.259	1.271	327.9	6.8	1.3
1981 ED35								
1987 Nov 17	02 23	16 32	7.5	2.002	1.031	38.9	2.2	1.8
Nov 18	02 22	16 27	8.0	1.999	1.033	38.6	2.2	1.8
Nov 21	02 19	16 17	9.6	1.996	1.039	37.9	2.2	1.8
1981 EO35								
1989 Sep 29	02 34	23 26	18.0	2.027	1.145	43.5	7.9	2.4
Sep 30	02 33	23 25	17.6	2.027	1.140	43.3	8.0	2.4
Oct 1	02 32	23 23	17.2	2.028	1.135	43.1	8.0	2.4
1981 ES42								
1988 Dec 13	05 00	25 48	2.3	2.228	1.246	76.5	3.1	1.8
Dec 14	04 59	25 47	2.8	2.228	1.247	76.3	3.1	1.8
Dec 15	04 58	25 46	3.2	2.227	1.248	76.1	3.1	1.8
1987 WJ1								
1987 Nov 17	02 22	16 32	5.6	2.699	1.733	38.6	2.3	1.8
Nov 20	02 20	16 29	6.8	2.700	1.746	38.2	2.3	1.8
1989 TY								
1989 Oct 2	00 35	12 43	2.9	3.214	2.223	13.0	8.3	2.4
1990 YY								
1990 Dec 19	03 26	18 11	6.0	5.051	4.195	53.7	-0.6	1.3
Dec 23	03 25	18 8	6.7	5.050	4.229	53.5	-0.5	1.3
4068 P-L								
1991 Jan 12	06 59	27 27	4.2	2.155	1.179	103.2	4.7	1.8
Jan 13	06 58	27 26	4.6	2.156	1.181	102.9	4.6	1.8
4081 P-L								
1987 Nov 19	03 53	11 31	4.3	2.025	1.044	58.6	-8.5	1.8
Nov 20	03 52	11 24	4.2	2.026	1.044	58.5	-8.6	1.8
6608 P-L								
1991 Jan 11	07 23	33 58	5.9	1.992	1.019	107.5	11.8	1.3
Jan 12	07 22	33 58	6.0	1.993	1.021	107.3	11.8	1.3

* Key to Telescopes:
1.3: MDM 1.3-m; 2.4: MDM 2.4-m; 1.8: Lowell 1.8-m.

2.2 Observational Results

Observational results are summarized in Table 2.2. The first two columns give the asteroid's designation and its orbital semi-major axis in AU. Values for the absolute magnitude H were computed using the IAU standard system as described in Bowell *et al.* (1989), where the tabulated V-R value (in the Johnson system) was used for the magnitude transformation. Because asteroids in this survey were not observed over sufficiently large phase angles to precisely derive values for the slope parameter, values for G were assumed based on an asteroid's color and its correspondingly estimated compositional class. The v-w filters of the Eight-Color Asteroid Survey (ECAS, Zellner *et al.* 1985) approximate Johnson V-R. For Johnson V-R of the Sun equal to 0.52, the mean color indices from Zellner *et al.* for C-type and S-type asteroids are near 0.52 and 0.68, respectively. For SMALS objects which had color indices consistent with C-types, values of 0.09 and 0.048 were assumed for G and the albedo, respectively. For potential S-types, respective values of 0.23 and 0.186 were used. For all but one of the measured asteroids, every color index suggested an S-type classification. This is consistent with the dominance of S-types seen among the larger asteroids in this same inner-belt region. For cases where no color information was obtained, we assumed V-R = 0.70, G = 0.23, and an albedo of 0.186, based on the sampled colors and apparent predominance of S-types. For the Trojan asteroid, 1990 YY, the respective values 0.67, 0.09 and 0.048 were assumed based on its likely D-type composition.

A technique called Phase Dispersion Minimization (PDM, Stellingwerf 1978) in IRAF was used to search for the rotational period within the photometric data, where we assumed that two maxima and minima occurred per rotation. Based on a trial period, the PDM technique bins data according to the rotational phase, and the average variance of these subsets are compared to the overall variance of the full set of the observations. The best period is that for which the ratio of the average variance within a bin reaches a minimum. For each asteroid, a composite plot was made for each period solution as well as for often occurring alias periods. Thus all PDM period solutions were critically examined manually before being accepted. In all cases where viable alias periods arose, these were due to uncertainties in counting the number of integer (or half integer) cycles elapsed between two epochs. None of the alias periods found are believed to be due to multiply periodic

motion. In resolving alias periods, subjective choices for solutions based on manually matching lightcurve features were occasionally necessary. Notations for all such cases are included in the individual descriptions below. In general, the night providing the single longest lightcurve usually provided the best estimate for the period. For each rotational period solution, we list a quality code Q in Table 2.2 which follows the recommendations of an ad hoc committee of IAU Commission 15: 1 - tentative result that could be completely wrong; 2 - reasonably secure result; 3 - secure result with full lightcurve coverage and no ambiguity of period. The lightcurve amplitudes given in the table are the standard peak-to-peak values reported by asteroid observers.

The composite lightcurves for 33 asteroids are presented in the Appendix, and a brief description of each data set and its solution is given below:

2952 Lilliputia Observations on Jan. 12 suggested a short period near 3 hours. Measurements of several cycles on Jan. 14 allowed a period solution of 3.25 ± 0.05 hours to be derived.

3536 Schleicher Two consecutive nights of observations revealed a complete cycle and a relatively large amplitude of 0.94 magnitude. A unique period of 5.79 ± 0.02 hours was obtained using PDM.

3651 Friedman Complete rotational cycles were observed on each of two consecutive nights. A unique period of 2.81 ± 0.05 hours was derived. An unusual third maximum evident in the Figure near 6 hours UT was detected on both nights.

4432 McGraw-Hill Two nights of observations revealed an amplitude of about 0.10 magnitude. The data suggest a short period, but no consistent solution could be found, possibly due to the low amplitude relative to the data noise. Alternatively, our data do not rule out free precession for this object.

4659 Roddenberry Observations over four hours on Nov. 14 revealed one complete minimum and part of a maximum. If this represents slightly more than one quarter of a complete cycle, then our best guess is a period of about 12 hours.

4924 Hiltner This asteroid displayed a low amplitude lightcurve and measurements on Jan. 28 appear to reveal a period near 5 hours. The PDM method provides a value of 4.9 ± 0.1 hours. Data prior to 7 hours UT are replotted to show the quality of this period solution.

1981 EA7 Each of the three nights of observations covered one or two cycles with an amplitude of 0.17 magnitude, allowing an accurate period of 2.864 ± 0.005 hours to be determined.

Table 2.2
Photometric Observational Results

Asteroid	a (AU)	H (mag)	V - R[a] (mag)	Diam. (km)	Period (hours)	Uncer-tainty	Q	Amp. (mag)	Uncer-tainty
2952 Lilliputia	2.11	14.65	0.70*	4	3.26	0.05	2	0.12	0.02
3536 Schleicher	2.25	14.49	0.70*	4	5.79	0.02	3	0.94	0.03
3651 Friedman	2.14	13.95	0.70*	5	2.81	0.05	2	0.12	0.02
4432 McGraw-Hill	2.11	14.85	0.70*	3	?			0.10	0.02
4659 Roddenberry	1.85	14.78	0.70*	4	12 (?)		1	0.14	0.02
4924 Hiltner	2.58	15.55	0.70*	2	4.9	0.1	1	0.15	0.03
1981 EA7	1.77	15.10	0.70	3	2.864	0.005	3	0.17	0.01
1981 EV8	1.85	14.79	0.70*	3	3.14	0.02	2	0.32	0.02
1981 EJ9	2.28	16.19	0.77	2	?			0.14	0.03
1981 EV9	2.23	16.47	0.76	2	5.67	0.02	2	0.79	0.02
1981 EA12	2.27	15.71	0.67	2	5.20	0.05	1	0.41	0.02
1981 EE12	2.12	15.58	0.70*	2	7.4	0.1	1	0.07	0.02
1981 EF12	2.48	16.33	0.84	2	9.18	0.05	1	0.26	0.03
1981 EP13	2.39	15.09	0.76	3	12.40	0.03	2	1.11	0.02
1981 EY14	2.04	15.27	0.70*	3	14.15	0.05	2	0.14	0.02
1981 EC15	2.11	16.31	0.71	2	15.67	0.09	2	0.27	0.02
1981 EP15	2.01	16.40	0.70*	2	10.07	0.07	1	0.15	0.02
1981 EU15	2.04	15.90	0.70*	2	3.9	0.2	1	0.15	0.02
1981 ER18	2.20	15.53	0.64	2	2.35	0.05	2	0.13	0.01
1981 ET20	2.55	15.89	0.56	4	>24		1	0.36	0.03
1981 ED21	2.31	14.47	0.83	4	11.68	0.05	2	0.82	0.03
1981 EH23	2.14	15.89	0.70*	2	9.05	0.05	1	0.20	0.02
1981 ER27	2.19	15.68	0.78	2	4.9	0.1	2	0.46	0.02
1981 EX28	2.25	15.55	0.70*	2	3.1	0.1	1	0.20	0.03
1981 ED35	2.00	15.44	0.70*	3	3.86	0.02	2	0.20	0.02
1981 EO35	2.21	16.45	0.90	2	6.15	0.05	1	0.12	0.03
1981 ES42	2.23	15.06	0.70*	3	16.4	0.2	2	0.24	0.02
1987 WJ1	2.70	13.60	0.70*	6	7.62	0.05	1	0.21	0.02
1989 TY	3.21	14.62	0.81	4	24 (?)		1	0.29	0.03
1990 YY[b]	5.05	12.19	0.67*	22	long			0.38	0.03
4068 P-L	2.16	15.29	0.70*	3	5.37	0.05	3	0.70	0.02
4081 P-L	2.03	14.81	0.70*	3	4.30	0.05	1	0.11	0.03
6608 P-L	1.99	16.68	0.67	1	7.03	0.05	2	0.27	0.02

[a] Assumed values are indicated by *.
[b] 1990 YY is an L5 Trojan asteroid.

1981 EV8 Two complete rotations were observed during each of the first two nights of observation. Possible periods included 2.95 and 3.14 hours, with the PDM method indicating a better fit to the longer value. Composites were made for both possibilities. Overlaying the composites with their respective period shifts clearly indicated 3.14 ± 0.02 hours as the best solution.

1981 EJ9 Data obtained on Mar. 7 and 8 both show only apparent noise with no obvious periodic or secular variations. The PDM method failed to provide a satisfactory solution. Either this asteroid displayed a low amplitude lightcurve, not resolved by our measurement precision at V19.3, or it is a fast rotator not resolved by our 5 minute time resolution. The lightcurve for Mar. 7 is presented (see the appendix). The Mar. 8 data are similar and at the same magnitude level.

1981 EV9 Two consecutive nights of observation allowed a conclusive 5.67 ± 0.02 hour period to be determined. An appulse near 8^h UT on Oct. 1 prevented the definition of the first minimum. In the figure, nine points of the second night data were shifted by the period and replotted using a different symbol to show the quality of the fit to the derived period.

1981 EA12 Although nearly two maxima and minima were observed on each of two consecutive nights, none of them could be satisfactorily matched. A period of 5.20 ± 0.05 hours derived from PDM seems to be consistent with the data assuming the lightcurve has two minima and maxima. We believe the mismatched heights of the maxima at 4.5 and 9.7 UT are due to calibration uncertainties with respect to the standard stars. However, the problem could also be caused by free precession, or triple extrema.

1981 EE12 One maximum and three minima were revealed from two nights of observations. The amplitude is only 0.07 magnitude. PDM gave two possible periods: 7.4 ± 0.1 and 8.4 ± 0.1 hours. By shifting the data with these two periods and replotting, we found the first value gave the best fit for a composite lightcurve.

1981 EF12 Observations on two consecutive nights showed two maxima and one minimum. The separation of the two maxima observed on Oct. 2 suggests a period in the vicinity of 9 hours. A period value of 9.18 ± 0.05 hours was derived from PDM.

1981 EP13 Two consecutive nights of observations yielded two complete minima separated by 24.8 hours. The amplitude of 1.11 magnitude is the largest observed during this survey. PDM gave three possible periods: 8.25, 9.99 and 12.40 hours corresponding to 3, 2.5, or 2 elapsed cycles. Because the lightcurve

appears to need at least 5 hours to complete its half cycle, we think the latter value is the best choice.

1981 EY14 Two minima were detected on two consecutive nights with an elapsed interval of about 28 hours. A period of 14.15 ± 0.05 hours was obtained assuming that these two minima overlap and two cycles elapsed.

1981 EC15 This asteroid was observed for 6 hours on each of the three consecutive nights. A period of 15.67 ± 0.09 hours was uniquely determined.

1981 EP15 Two consecutive nights of observations revealed two maxima and one minimum. Although the data are noisy, a period of 10.07 ± 0.07 hours was uniquely determined from both PDM and manual matching of the lightcurve features.

1981 EU15 More than six hours of coverage on only one night revealed a complete cycle. A period of 3.9 ± 0.2 hours was determined by PDM after deleting several noisy points in the data. The data obtained after 9 hours UT are replotted to show the fit of the period.

1981 ER18 Observations on two consecutive nights showed evidence for a very fast rotation and relatively low amplitude. PDM yielded a 2.35 ± 0.05 hour period which is the shortest one yet discovered for a main-belt asteroid. In the final composite plot, data prior to 6 hours UT on Mar. 9 have been shifted by 2.35 hours and replotted with a different symbol to show the quality of the fit.

1981 ET20 About six hours of coverage on a single light yielded noisy measurements due to the object's faint apparent magnitude (V19.4) with the 1.3-m telescope. A minimum with a slow rise is suggested over six hours, perhaps indicating a long period > 24 hours.

1981 ED21 Observations from two nights yielded almost identical minima with an elapsed interval of 23.37 hours. PDM gave two possible periods: 9.3 and 11.68 hours corresponding to 2.5 and 2 elapsed cycles, respectively. The two maxima on March 1 are spaced by more than 5 hours, so the 11.68 hour period is probably the best estimate.

1981 EH23 A total of ten hours of lightcurve coverage on two consecutive nights revealed two complete maxima and one complete minimum. A period of 9.05 ± 0.05 hours is estimated.

1981 ER27 Observations over seven hours on a single night displayed three maxima and two minima. A unique period of 4.9 ± 0.1 hours was obtained using PDM. The data obtained after 7.5 hours UT are replotted to show the quality of the period solution.

1981 EX28 A period of about 3 hours seems to be consistent with the results from two separate nights of observation. Data on Sep. 5 covered 1.5 hours and appear to reveal one-half of a cycle. Six hours of observations on Aug. 29 revealed almost two complete cycles. A PDM solution using the Aug. 29 data gave a period of 3.1 ± 0.1 hours. The composite lightcurve was constructed by assuming a period of 3.11 hours, corresponding to 53 cycles elapsed between Aug. 29 and Sep. 5.

1981 ED35 Complete rotational cycles were observed on three nights. Two periods 3.62 ± 0.02 and 3.86 ± 0.02 hours were obtained using both PDM and the manual matching of lightcurve features. Composite lightcurves were constructed for both periods, and overlaying the plots upon themselves with their respective period offsets clearly led us to favor the longer period.

1981 EO35 The data for this asteroid are noisy and the amplitude is low. Two minima were detected on Sep. 30, spaced about three hours apart. Overlapping the minima observed on Sep. 29 and 30 gives a plausible period solution of 6.15 ± 0.05 hours.

1981 ES42 Measurements of this asteroid showed the structure of a long period lightcurve as each of the three consecutive nights revealed a single minimum separated by an interval of 24.6 hours. A period of 16.4 ± 0.2 hours was uniquely determined corresponding to 1.5 elapsed cycles. Observations on Dec. 15 were made through thin clouds, causing their higher noise level.

1987 WJ1 This asteroid was discovered in the same field as 1981 ED35. Observations on two nonconsecutive nights each showed two maxima separated by 3.5 to 4 hours. A unique period of 7.62 ± 0.05 hours was determined using PDM.

1989 TY This asteroid was discovered in the same field as 1981 EF12. During six hours of coverage on a single night, one minimum and part of one maximum separated by about six hours were detected. If this represents one quarter of the total lightcurve, then a period of ~24 hours is suggested.

1990 YY This asteroid, a Trojan near the L5 Lagrange point of Jupiter, was discovered in the same field as asteroid 4432. Two nights of well calibrated observations show very different lightcurve structures. Measurements on Dec. 19 show a flat structure while those on Dec. 23 show a continuous increase. A long period is suggested.

4068 P-L This asteroid was observed on two consecutive nights. Observations on the second night revealed a complete cycle, indicating a period

around 5 hours. A more precise solution of 5.37 ± 0.05 hours was obtained using PDM.

4081 P-L Two consecutive nights of observations showed a low lightcurve amplitude. The PDM method yielded possible periods of 2.72 and 4.30 hours. For the former period, a maximum would have had to occur during the data gap near 10 hours UT. Composites for both periods were constructed and offsetting these by their respective values indicated that the longer period is the best estimate.

6608 P-L Observations on Jan. 12 revealed a complete cycle with unequal maxima, suggesting a 7 hour period. Data from Jan. 11 allowed this value to be refined to 7.03 ± 0.05 hours.

2.3 Analysis and Discussion

We now offer an analysis of the survey results in terms of asteroid collisional evolution. A comparison of SMALS results with those for similar diameter near-Earth asteroids and cometary nuclei, and the implications for the origins of the near-Earth asteroids, are presented in the next section. As summarized in Table 2.3, we have derived lightcurve amplitude information for 32 small main-belt asteroids while rotational period estimates have been made for 30. The mean diameter for our newly sampled objects is 3 km. The only uniform sample of rotational properties for small asteroids previously available was obtained by Binzel and Mulholland (1983), where in a sample of 17 asteroids they achieved a mean diameter of 13 km through standard photoelectric techniques. Thus the results of the new CCD photometry survey reported here extend our knowledge of asteroid lightcurve parameters downward by a factor of ~4 in diameter and a factor of about ~64 in mass.

We first compare the mean lightcurve amplitudes between our SMALS sample and larger main-belt asteroids, where the mean from Table 2.3 is found to be 0.31 ± 0.05 magnitude. This value is quite consistent with a nearly constant mean of 0.30 ± 0.04 magnitude found for main-belt asteroids up to 50 km in diameter (Binzel *et al.* 1989b, Fig. 7), and the average amplitude of 0.29 ± 0.01 magnitude for all D > 10 km asteroids (Table 2.3). The lack of a sharp upturn in lightcurve amplitudes over an order of magnitude in size (three orders of magnitude in mass) from 50 km down to 3 km suggests that a single process is determining their shapes, specifically collisional fragmentation. Collisional models (e.g. Davis *et al.* 1985, 1989) suggest that all asteroids in this size range should be collisional fragments. Interestingly, the observational finding of nearly constant mean shapes for a wide range of sizes of asteroid fragments is consistent with results from laboratory impact experiments. As summarized by Fujiwara *et al.* (1989), laboratory fragments appear to maintain nearly constant mean shapes over a wide range sizes, impact energies, and target strengths. Further, mean axial ratios for laboratory fragment shapes are consistent with those inferred for asteroids five orders of magnitude larger. Whether this is purely coincidental or is fundamentally related to the structural properties of fracture mechanics is an important area for future investigation.

The mean rotational frequency for the SMALS sample, as derived from rotational periods in Table 2.3, is 4.30 ± 0.46 revolutions per day. This mean rotational rate for 3 km asteroids is substantially higher than the value 3.12 ± 0.53 rev/day found for 13 km asteroids (Binzel 1984), 2.40 ± 0.40 rev/day found for 50 km asteroids (Binzel *et al.* 1989b, Fig. 2), and 2.69 ± 0.07 rev/day for all D > 10 km asteroids (Table 2.3). Thus there is an apparent steep upturn toward increasing rotational rates with decreasing diameters, a factor consistent with decreasing moments of inertia with decreasing size (mass). However, collisional evolution models (e.g. Davis *et al.* 1989) suggest that small main-belt asteroids might be expected to spin even faster, if they have modest tensile strengths. Although our sampling rate could have reliably detected a rotational period shorter than about one hour, the shortest period detected here was 2.35 hours. Assuming that the interior of this asteroid (1981 ER18) is not in tension, then its limiting spin period (in hour) may be given as $P_{lim} = 3.3\ \rho^{1/2}$, where ρ is the density in g cm^{-3} (Weidenschilling 1981). If 1981 ER18 is at this limit, it implies a density near 2 g cm^{-3}. Taken at face value, the non-detection of substantially shorter periods by this survey suggests weak (highly fractured?) interiors for small asteroids.

Table 2.3
Statistical Summary I

Sample	Number	Diameter (km)	Mean Frequency (rev/day)	Mean Amplitude (mag.)
Small Main-Belt Asteroids	32	1-6 (mean = 3)	4.30 ± 0.46	0.31 ± 0.05
Larger Main-Belt Asteroids*	~400	> 10 (mean = 84)	2.69 ± 0.07	0.29 ± 0.01

* From Binzel *et al.* (1989b).

Although our survey was optimally designed to determine the statistical properties of small main-belt asteroid lightcurves having nominal characteristics, particular attention was also paid to identifying potential cases of free precession. This effect could result from an asteroid suffering a recent off-center collision so that its principal body axis is misaligned from its rotational axis. Work by Burns (1971),

Burns and Safronov (1973), and Harris (1993) has shown that damping from internal stresses will tend to re-align the principal axis and rotational axis in a timescale ranging from 10^5 years to the age of the solar system. This timescale is inversely proportional to diameter. Thus the smallest asteroids, which are also subject to the most frequent substantial collisions, have the greatest prospect for displaying incoherent or multiply-periodic lightcurves. Measurement of free precession would place important constraints on asteroid collision frequencies and internal properties.

In light of the above physical discussion, we conclude by restating that we cannot rule out a very short rotational period for 1981 EJ9 and cannot absolutely rule out free precession (with small nutation angles) for nearly all of the objects surveyed. Particular objects that offer some suspicion of non-periodic behavior (with perhaps modest nutation angles) are 4432 and 1981 EA12. However we should emphasize that no conclusive detection of free precession has been made for any object in this sample and it is entirely likely that all of these ambiguities are simply a consequence of our own limited data sets. We hope to perform some follow-up observations in the future which will concentrate on a single suspect object during an entire run with high time resolution measurements on five or more consecutive nights. In this way we might be able to impose even stricter limits on the inferred physical properties and collisional evolution of small main-belt asteroids.

2.4 Origins for the Near-Earth Asteroids

A comparison of physical properties between main-belt and near-Earth asteroids has been problematic because of the size difference between the near-Earth objects and the previously surveyed main-belt asteroids. A few dedicated surveys and analyses of physical properties have been made for asteroids below 30 km (Binzel and Mulholland 1983, Binzel 1984, and Wisniewski 1991), but the mean diameters of these main-belt samples are a factor of four or more larger than the near-Earth asteroid sample, corresponding to a difference in mass of nearly two orders of magnitude. With the results from the SMALS, now we can compare these two group asteroids, as well as with the cometary nuclei (Binzel *et al.* 1992b).

Periodic variations in an asteroid's intensity reveal its synodic rotational period and the amplitude (measured from minimum to maximum) is diagnostic of its shape. For a triaxial ellipsoid with axes $a<b<c$ rotating about its principal axis c, an observer orthogonal to the spin vector would measure two maxima and minima per complete rotation, where the ratio of the intensities for a body with a uniformly scattering surface is a simple measure of a/b. In reality, however, asteroids are not perfect ellipsoids with uniform scattering and the orientation of the spin vectors are generally unknown. Thus careful correction factors must be applied when comparing samples of asteroid rotational properties to achieve a meaningful physical analysis.

The samples compared here are summarized in Table 2.4, where the main-belt asteroid data are from the survey discussed above and the near-Earth asteroid and comet data are from *Asteroids II*, Jewitt (1991) and Belton (1991). Only 5 cometary nuclei have reliable rotational periods and lightcurve amplitudes. Near-Earth asteroids, 433 Eros and 1036 Ganymed are excluded from this study as they are substantially larger than the remainder of the population. The tabulated mean rotational frequency assumes that each object displays two maxima and minima per rotation and is measured in revolutions per day. The mean amplitude (in magnitudes) listed first is the value derived from the basic data with no correction for aspect or surface scattering. The corrected mean amplitude, whose derivation is described below, is given in a subsequent column. In all cases, the value given for sigma is the formal standard deviation of the mean for the respective sample.

Table 2.4

Statistical Summary II

Sample	Number	Mean Diameter (km)	Mean Frequency (rev/day)	Mean Amplitude (mag.)	Corrected Mean Amplitude (mag.)
Small Main-Belt Asteroids	32	3	4.30 ± 0.46	0.31 ± 0.05	0.27 ± 0.04
Near-Earth Asteroids	32	3	4.94 ± 0.54	0.48 ± 0.08	0.22 ± 0.03
Cometary Nuclei	5	11	1.64 ± 0.39	0.67 ± 0.08	0.60 ± 0.08

A key factor which must first be accounted for when comparing lightcurve amplitude measurements between main-belt and near-Earth asteroids is the effect caused by differences in the Earth-asteroid-Sun (phase) angle for the observations. Because of their proximity, near-Earth asteroids are observable at large phase angles (often exceeding 50 degrees). Main-belt asteroids are observable over a much narrower range with most observations performed at phase angles less than 15 degrees. To account for the effects of increasing lightcurve amplitude with increasing phase angle, we use the empirical relations developed by Zappalà *et al.* (1990) to correct amplitude measurements to zero degrees phase angle. These corrections were applied to all original data for the samples listed in Table 2.4.

A second factor that can affect the observed amplitude for a near-Earth asteroid is a change in aspect angle, since the object can traverse a large angular distance across the sky during a single apparition. Under the assumption that the spin vectors of the sampled asteroids are all randomly oriented, the observed aspect angles are randomly distributed about a mean of 60 degrees (measured from the asteroid's pole to the observer's line of sight). This assumed mean aspect angle is valid for the main-belt asteroid and comet samples as each object was observed at a single geometry. For cases of near-Earth asteroids observed over several aspects (often involving more than one apparition), the correction

procedure developed by Binzel and Sauter (1991) was applied to estimate the lightcurve amplitude that would be observed at an aspect angle of 60 degrees.

Figures 2.2 and 2.3 compare the distributions of rotational rates and corrected lightcurve amplitudes between small main-belt asteroids, near-Earth asteroids, and cometary nuclei. The dispersion in rotational rates shown in Figure 2.2 is quite similar for the small main-belt and near-Earth asteroid samples. Table 2.4 also shows that the mean rotational frequencies for these two samples are statistically indistinguishable. A corresponding similarity is shown in Figure 2.3 where comparable dispersions in the corrected lightcurve amplitude distributions are seen for the small main-belt and near-Earth asteroid samples. Table 2.4 also shows no statistical distinction between the mean corrected amplitudes for these two samples.

These comparable distributions provide the first physical evidence that near-Earth asteroids are similar to their equal diameter counterparts in the main belt. Formal hypothesis testing shows that we cannot reject the null hypothesis that these two samples are drawn from the same population. Thus we find that our observational results are fully consistent with the proposition that the main asteroid belt serves as the source of resupply for the near-Earth asteroid population.

A full evaluation of the relative contribution of cometary nuclei to the near-Earth asteroid population based on a comparison of physical properties is difficult due to the paucity of comet measurements. Those values that are available for cometary nuclei show distributions of rotational rates and lightcurves that are dissimilar to the asteroid samples, as evidenced in Figs. 2.2 and 2.3. Although the cometary nuclei measurements fall within the range of the dispersion for asteroid values, Table 2.4 shows that the mean values for rotational frequency and corrected amplitude are substantially different. A formal comparison of the means for the small sample size requires the use of a non-parametric such as Mann-Whitney U-test (e.g., Siegel 1956, Walsh 1965, Gibbons 1985, Gravetter and Wallnau 1988). This confirms that the mean values for the comet samples are significantly different from the asteroid samples at greater than 99% confidence level.

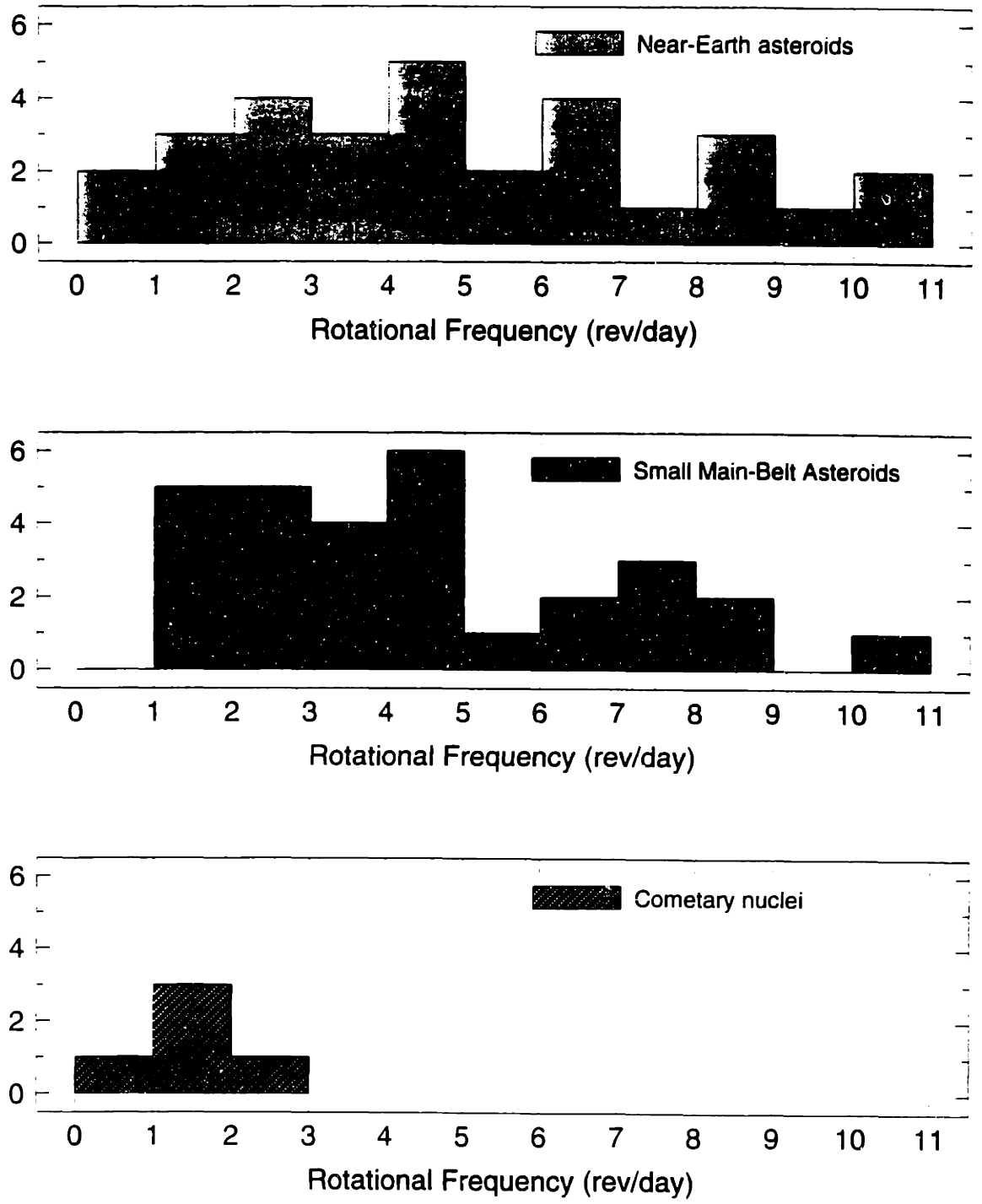

Fig. 2.2. Histograms showing the rotational frequency distributions for samples of (**top**) near-Earth asteroids, (**middle**) similar-sized (D < 5 km) small main-belt asteroids, and (**bottom**) cometary nuclei. Both asteroid samples show similar dispersions and have similar means. Although rotational rates of cometary nuclei fall within the observed range for asteroids, their mean rotational frequency is significantly lower.

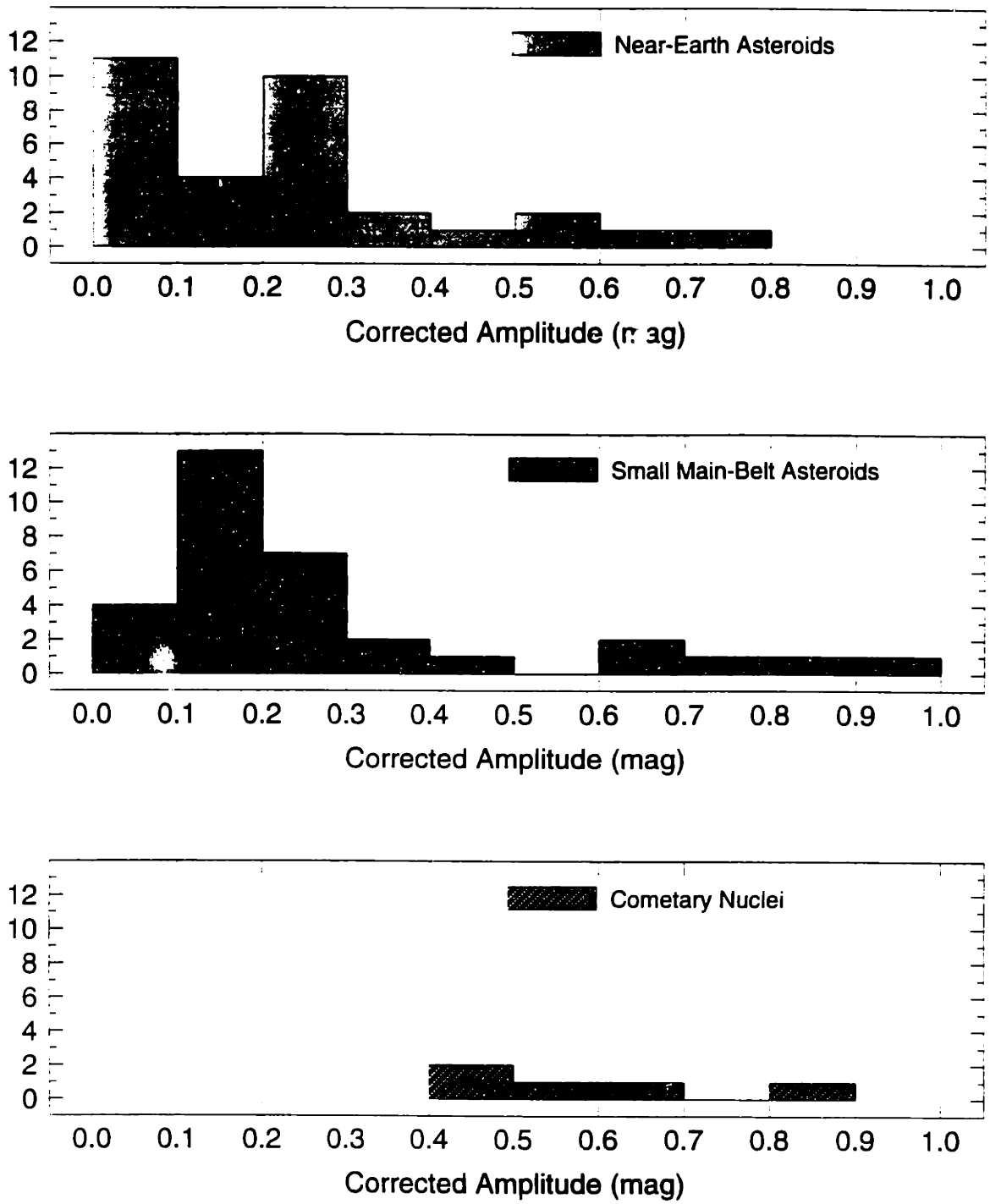

Fig. 2.3. Histograms showing the lightcurve amplitude distributions for samples of (**top**) near-Earth asteroids, (**middle**) similar-sized (D < 5 km) small main-belt asteroids, and (**bottom**) cometary nuclei. All samples have been corrected for phase angle and aspect angle effects. Both asteroid samples show similar dispersions and have similar means. Although cometary nuclei measurements fall within the observed range for asteroids, their mean corrected amplitude is significantly higher.

Systematic effects could be a strong factor in the apparent differences in lightcurve properties between small asteroids and cometary nuclei. Because rotational parameters for cometary nuclei are often derived when comae are present, or when the objects are at large distances with faint apparent magnitudes, the available results could have a selection effect toward objects having large amplitudes and modest rotational periods. Although comet researchers are careful to guard against such selection effects, the statistics of the small sample size for cometary nuclei are quite sensitive to such factors. The situation will improve with additional measurements of the rotational properties of cometary nuclei.

We now attempt to use the available physical data derived from rotational lightcurves to quantitatively evaluate the proportion of comets that could be contained in the near-Earth asteroid sample. Although we have found that the rotational lightcurve properties of the near-Earth asteroid population are consistent with their being entirely derived from the main belt, there is other physical and dynamical evidence that suggests cometary nuclei are indeed included in the near-Earth asteroid population (Weissman *et al.* 1989). As cometary nuclei have rotational properties that fall within the range observed for asteroids, these measurements do not rule out the presence of cometary nuclei within the near-Earth asteroid population.

To quantify the problem, we postulate that a fraction f of the near-Earth asteroid population is comprised by cometary nuclei and the remaining proportion $(1-f)$ is derived from the main belt. For the sake of this analysis, we assume that the available sample of cometary nuclei is a reasonable representation of its population. Similarly, our small main-belt sample is assumed to represent its population. We perform our analysis by comparing the observed near-Earth asteroid samples for rotational frequency and corrected amplitude with constructed samples comprised of f comet observations plus $(1-f)$ small main-belt observations, where f is allowed to vary.

For each chosen value of f, we use Student's t statistic to test the null hypothesis that the observed near-Earth asteroid sample mean is the same as that for our constructed sample. With a two-tailed (nondirectional) rejection criterion set at the 95% confidence level, we find the null hypothesis is acceptable for f in the range of 0 to 25 percent. To be conservative, we demand rejection of the null

hypothesis at the 99% confidence level. This stricter criterion allows acceptable values for *f* in the range of 0 to 40 percent. Stated in other words, our observed distributions are consistent with 0 to 40 percent of the near-Earth asteroid population being derived from dormant or extinct cometary nuclei. Our observations are also consistent with the largest proportion, 60 to 100 percent, of the near-Earth asteroid population being derived from the main belt. Thus our observationally based results favor a main-belt asteroid source for the majority of near-Earth asteroids, with comets contributing a percentage smaller than the equal share suggested by Monte Carlo calculations (Wetherill 1988).

3. The CCD Spectroscopic Survey

3.1 Survey Description and Data Reduction

Our Small Main-belt Asteroid Spectroscopic Survey (SMASS, Xu *et al.* 1993, Binzel *et al.* 1994) was conducted primarily using the MDM 2.4-m telescope, equipped with a TI 4849 CCD and Mark III spectrograph. A low resolution grating (150 line/mm, blazed at 7300 Å) was used to obtain a broad spectrum from 4000- to 10000-Å. In order to overcome the second order overlap problem, a piece of blocking filter (Wratten 12, cutoff < 6000 Å) was placed on the region of the CCD which receives photons beyond 6000 Å. This technique allows us to obtain a spectrum covering 4000- to 10000-Å (resolution ~10 Å/pix) in just a single exposure. Therefore this avoids a connection problem (Binzel and Xu 1990) if the spectral coverage is done in two pieces (one covering 4000- to 7500-Å, the other 7000- to 10000-Å) taken separately. For calibration, the spectra of Hg-Ar-Xe lamps and extinction stars were observed. One or two solar-analog stars were also observed (current candidates are 16 Cyg B and Hyades 64) for obtaining the asteroid's relative reflectance spectrum. Usually, each asteroid was observed at least twice to verify its spectrum. For comparison and monitoring of possible systematic errors, brighter asteroids with known spectral properties were observed. Target asteroid brightnesses were typically in the range V = 17 to 19. Exposure times were 15 to 30 minutes. Longer exposures were not used to minimize cosmic ray effects. The telescope was tracked at the asteroid rate, so the asteroid's identity was certified by checking the motion vector with respect to nearby stars. Up to 15 asteroids can be observed in a clear night. A total of 316 asteroids have been observed since the SMASS was initiated in 1990. Among them, 215 are new objects with previously unknown spectral properties (median diameter = 12 km).

The spectral data reduction was performed using IRAF software. Bias subtraction and flatfield correction were performed for each frame. Cosmic rays were identified and removed from each spectrum by averaging over the neighboring pixels. Within each CCD frame, spectra were dispersed along the CCD columns. By setting an upper and lower aperture limit (usually ± 5 pixels) relative to the center of the dispersed spectrum and by choosing a background region away from the dispersion area, the IRAF *apsum* package was used to sum the pixel values within the aperture at each point along the dispersion axis

(column), to subtract the background noise, and to give the pixel intensity (flux) along the column. Calibrations of wavelength and flux of the asteroid's spectrum were performed using the spectra of the lamps and standard stars obtained on the same night. We found there were no significant time-dependent dispersion variations for the spectra of the lamps. Flux calibration errors were minimized because we used a relatively large slit (4.7 arcseconds) to avoid photon losses from variable seeing (Luu and Jewitt 1990). The errors due to atmospheric extinction were also minimized since the standard stars were observed at air masses similar to those of asteroids (airmass difference ≤ 0.1, Luu and Jewitt 1990). For faint objects, the spectra are noisy at both extreme blue and near infrared end due to CCD's poor sensitivity in these spectral ranges. Dividing by the spectrum of the solar-type star which was observed at the same night, we can obtain the relative reflectance spectra of the asteroids. The systematic errors introduced by the use of two different solar analogs (16 Cyg B and Hya 64) are low. The ratio between their slopes is on the order of $1\%/10^3$ Å (Luu and Jewitt 1990).

The spectrum for an asteroid was the averaged result from all frames obtained during the same observing run. By convention, all asteroid spectra were normalized to unity at 5500 Å. Some strong absorption bands in the asteroid spectra are caused by the absorption of water and oxygen molecules in the Earth's atmosphere (Fig. 3.0). These telluric features were removed as well as possible in the final plots. Table 3.1 lists the observational circumstances for the 316 asteroids observed in the survey. For each night of observation, the table gives the asteroid number, name, absolute magnitude (H), semi-major axis (a), diameter (D), family group (Williams 1992), date in universal time, and the number of exposures. The diameter is calculated using the following equation (Bowell *et al.* 1989):

$$D = 10^{\left(\frac{6.259-0.4H-\log p}{2}\right)} \qquad (3.1.1)$$

where D is the diameter in km, H is the absolute magnitude, and p is the geometric albedo. Average geometric albedos assumed for different types in the diameter calculations are shown in Table 3.2 (Determinations of the types are presented in Table 3.11). The albedo uncertainty ($\Delta p/p$) is less than 50%. From Eq. (3.1.1), we obtained the diameter uncertainty ($\Delta D/D$) less than 25%. Fig. 3.1a shows the heliocentric and size distributions of the SMASS objects which have no previous spectroscopic measurements. Fig. 3.1b. shows the size limits of SMASS and

Eight-Color Asteroid Survey (ECAS, Zellner *et al.* 1985) samples. Fig. 3.2 shows our spectra match well with the results from the ECAS. The final asteroid spectral plots are presented in the Appendix.

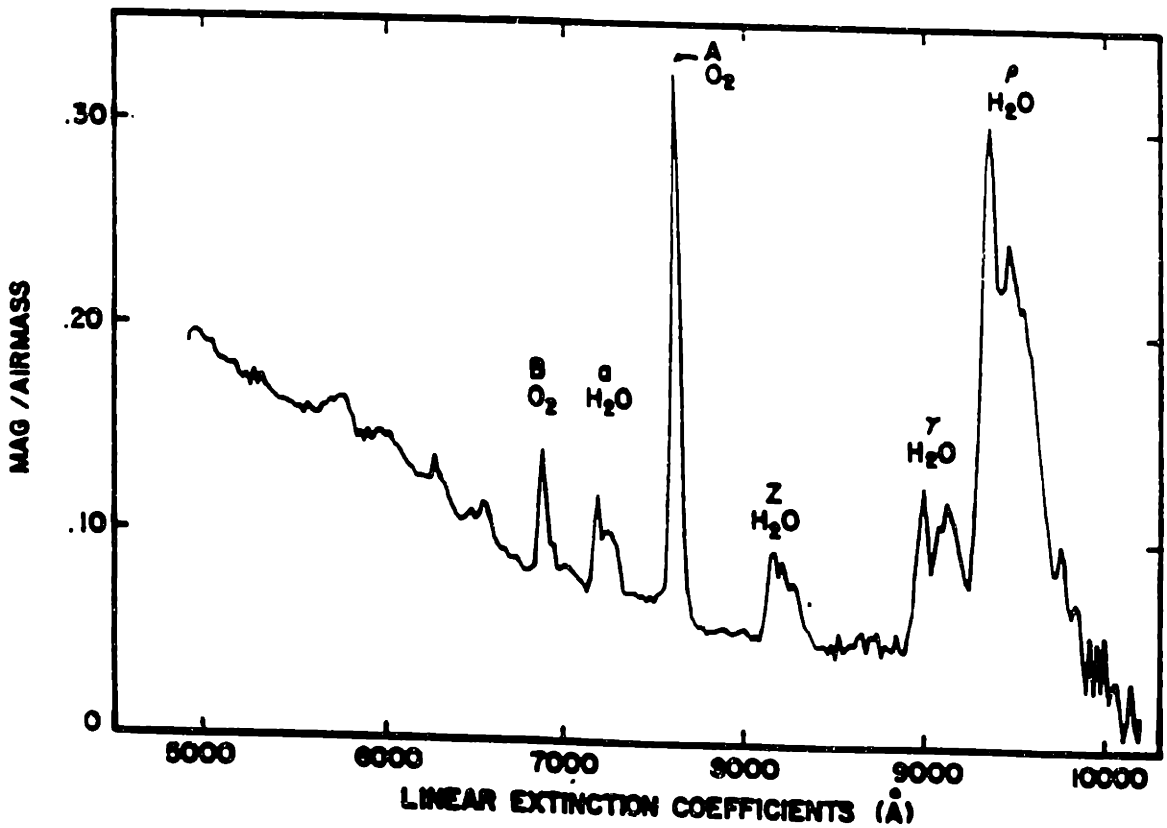

Fig. 3.0. Absorption bands of water and oxygen molecules in the Earth's atmosphere. (From Cochran *et al.* 1981.)

Table 3.1

Spectroscopic Observational Circumstances

Ast.	Name	*H*	*a*	*D*	Group	UT Date	#Exp.
3	Juno	5.33	2.669	266		92/11/27	2
	Juno	5.33	2.669	266		92/11/28	2
4	Vesta	3.20	2.362	501	169	91/10/31	3
	Vesta	3.20	2.362	501	169	91/12/07	1
	Vesta	3.20	2.362	501	169	92/03/14	1
6	Hebe	5.71	2.425	223		92/11/27	2
	Hebe	5.71	2.425	223		92/12/02	2
7	Iris	5.51	2.386	244		91/10/27	1
	Iris	5.51	2.386	244		92/01/14	2
	Iris	5.51	2.386	244		92/12/01	2
8	Flora	6.49	2.201	156	189	91/12/14	1
	Flora	6.49	2.201	156	189	92/01/17	3
10	Hygiea	5.43	3.135	494	110	91/11/01	2
14	Irene	6.30	2.587	170	150	92/01/15	3
	Irene	6.30	2.587	170	150	92/03/14	2
18	Melpomene	6.51	2.295	154		92/11/28	2
22	Kalliope	6.45	2.910	178		91/10/27	2
	Kalliope	6.45	2.910	178		93/01/20	1
25	Phocaea	7.83	2.400	84	PHO	93/01/04	1
28	Bellona	7.09	2.778	118		91/10/27	2
	Bellona	7.09	2.778	118		92/01/16	3
29	Amphitrite	5.85	2.554	209		91/12/07	3
	Amphitrite	5.85	2.554	209		92/01/17	3
	Amphitrite	5.85	2.554	209		92/03/11	3
32	Pomona	6.74	2.586	139		91/10/25	1
	Pomona	6.74	2.586	139		91/10/28	2
	Pomona	6.74	2.586	139		91/11/01	2
	Pomona	6.74	2.586	139		92/01/15	2
	Pomona	6.74	2.586	139		92/11/30	1
36	Atalante	8.46	2.747	122		93/01/21	1
38	Leda	8.32	2.741	131		91/12/07	1
39	Laetitia	6.10	2.768	186	67	92/12/01	1
42	Isis	7.53	2.441	96	157	92/01/17	3
43	Ariadne	7.93	2.204	80	185	92/09/06	2
	Ariadne	7.93	2.204	80	185	92/11/27	1
53	Kalypso	8.81	2.621	104		92/11/28	1
54	Alexandra	7.66	2.709	177	138	92/09/06	2
55	Pandora	7.80	2.759	96		91/10/30	2
61	Danae	7.68	2.992	90		92/01/14	3
	Danae	7.68	2.992	90		92/01/17	2
68	Leto	6.78	2.781	136	126	92/11/26	2
71	Niobe	7.30	2.755	107		91/12/08	1
	Niobe	7.30	2.755	107		92/01/14	3
72	Feronia	8.94	2.266	50	174	93/01/04	1

Table 3.1 (continued)

Ast.	Name	*H*	*a*	*D*	Group	UT Date	#Exp.
73	Klytia	9.00	2.665	49		92/01/17	3
82	Alkmene	8.40	2.764	65		92/11/29	1
86	Semele	8.54	3.111	118		91/10/26	1
88	Thisbe	7.04	2.767	236		92/01/13	2
111	Ate	8.02	2.595	150		93/01/21	1
116	Sirona	7.82	2.769	84		91/10/29	1
	Sirona	7.82	2.769	84		92/01/18	2
	Sirona	7.82	2.769	84		92/12/01	1
	Sirona	7.82	2.769	84		93/01/01	2
	Sirona	7.82	2.769	84		93/01/04	2
	Sirona	7.82	2.769	84		93/01/21	2
	Sirona	7.82	2.769	84		93/01/22	2
124	Alkeste	8.11	2.630	74	141	92/09/08	1
126	Velleda	9.27	2.440	43		92/01/14	3
	Velleda	9.27	2.440	43		92/01/17	2
128	Nemesis	7.49	2.750	191	132	91/12/13	2
131	Vala	10.0	2.432	60	161	92/11/29	2
	Vala	10.0	2.432	60	161	92/11/30	1
134	Sophrosyne	8.76	2.564	107		92/11/26	2
137	Meliboea	8.05	3.112	148	113	91/10/27	1
	Meliboea	8.05	3.112	148	113	93/01/22	1
138	Tolosa	8.75	2.450	55	158	92/01/13	3
	Tolosa	8.75	2.450	55	158	92/01/17	2
149	Medusa	10.8	2.175	21		91/12/14	2
	Medusa	10.8	2.175	21		92/01/14	3
157	Dejanira	10.6	2.580	46		92/01/14	3
158	Koronis	9.27	2.869	43	3	91/10/27	2
	Koronis	9.27	2.869	43	3	92/01/18	2
167	Urda	9.24	2.854	44	3	92/09/07	2
169	Zelia	9.56	2.358	38		93/01/04	1
185	Eunike	7.62	2.737	180		92/03/12	1
186	Celuta	8.91	2.362	51		93/01/21	1
196	Philomela	6.54	3.113	152		92/11/29	1
204	Kallisto	8.89	2.672	52		92/09/09	2
211	Isolda	7.89	3.046	159		91/12/16	2
218	Bianca	8.60	2.668	59	137	92/03/13	5
221	Eos	7.67	3.019	90	2	92/03/11	1
230	Athamantis	7.35	2.382	105		92/09/06	2
231	Vindobona	9.20	2.920	50		92/09/10	2
234	Barbara	9.02	2.386	49		92/01/15	3
	Barbara	9.02	2.386	49		92/01/17	2
235	Carolina	8.82	2.880	53		91/12/13	2
	Carolina	8.82	2.880	53		92/01/15	2
237	Coelestina	9.24	2.762	44		91/12/15	2
	Coelestina	9.24	2.762	44		92/01/15	2

Table 3.1 (continued)

Ast.	Name	*H*	*a*	*D*	Group	UT Date	#Exp.
239	Adrastea	10.3	2.969	27		92/09/11	2
	Adrastea	10.3	2.969	27		93/01/04	2
243	Ida	9.94	2.861	32	3	91/12/08	3
245	Vera	7.82	3.089	84		92/11/30	1
248	Lameia	10.2	2.471	32	156	91/12/16	2
	Lameia	10.2	2.471	32	156	92/11/28	1
	Lameia	10.2	2.471	32	156	93/01/04	2
256	Walpurga	9.80	3.001	38	120	92/12/02	1
287	Nephthys	8.30	2.353	68		92/01/17	2
	Nephthys	8.30	2.353	68		92/03/13	6
289	Nenetta	9.51	2.875	27		91/12/07	2
	Nenetta	9.51	2.875	27		92/03/12	1
290	Bruna	11.5	2.337	15	PHO	92/12/02	1
291	Alice	11.4	2.222	16	187	92/01/14	3
292	Ludovica	10.2	2.529	28		92/09/08	2
297	Caecilia	9.50	3.163	39		92/09/09	2
314	Rosalia	9.50	3.144	76		92/09/10	2
319	Leona	9.80	3.368	38	CYB	92/12/02	1
339	Dorothea	9.24	3.010	44	2	93/01/21	1
345	Tercidina	8.71	2.325	109		91/10/26	2
346	Hermentaria	7.13	2.798	116		91/12/15	2
	Hermentaria	7.13	2.798	116		92/01/13	2
	Hermentaria	7.13	2.798	116		92/03/12	1
349	Dembowska	5.93	2.925	151	124	92/11/27	3
350	Ornamenta	8.37	3.118	128		91/10/26	1
	Ornamenta	8.37	3.118	128		91/10/28	2
354	Eleonora	6.44	2.796	159		92/03/11	1
371	Bohemia	8.72	2.727	56		92/09/05	2
374	Burgundia	8.67	2.778	57	67	91/12/08	1
	Burgundia	8.67	2.778	57	67	92/01/16	3
	Burgundia	8.67	2.778	57	67	92/01/20	1
384	Burdigala	9.64	2.653	36		93/01/01	1
402	Chloe	9.02	2.557	49	148	93/01/01	1
416	Vaticana	7.89	2.786	82		91/12/14	2
	Vaticana	7.89	2.786	82		92/01/18	2
430	Hybris	10.3	2.843	52		92/09/09	1
441	Bathilde	8.51	2.807	69	67	92/11/28	1
	Bathilde	8.51	2.807	69	67	92/11/29	3
	Bathilde	8.51	2.807	69	67	92/11/30	1
446	Aeternitas	8.90	2.787	35	67	92/09/08	1
	Aeternitas	8.90	2.787	35	67	92/11/28	1
	Aeternitas	8.90	2.787	35	67	92/11/30	2
456	Abnoba	9.20	2.790	45		92/03/15	3
467	Laura	10.5	2.945	40		92/01/13	3
470	Kilia	10.1	2.405	30		92/12/01	1

Table 3.1 (continued)

Ast.	Name	*H*	*a*	*D*	Group	UT Date	#Exp.
471	Papagena	6.73	2.891	139		92/01/17	3
	Papagena	6.73	2.891	139		92/03/15	2
474	Prudentia	10.6	2.452	26		91/12/07	3
477	Italia	10.2	2.414	35	75	93/01/21	1
480	Hansa	8.38	2.644	65		92/09/08	2
481	Emita	8.60	2.741	115		93/01/20	1
495	Eulalia	10.8	2.488	42		92/09/10	2
509	Iolanda	8.40	3.065	65		91/10/31	2
	Iolanda	8.40	3.065	65		92/01/17	3
511	Davida	6.22	3.176	344		92/03/11	1
512	Taurinensis	10.7	2.189	22	MC	91/12/07	1
	Taurinensis	10.7	2.189	22	MC	92/01/13	3
518	Halawe	11.0	2.534	20	150	92/09/09	2
519	Sylvania	9.14	2.790	46		93/01/22	1
529	Preziosa	10.1	3.019	30	2	92/01/13	3
541	Deborah	10.1	2.817	58		92/03/15	3
550	Senta	9.37	2.590	41		91/10/26	2
	Senta	9.37	2.590	41		92/01/18	2
563	Suleika	8.50	2.713	62		92/09/07	1
	Suleika	8.50	2.713	62		92/11/29	1
582	Olympia	9.11	2.611	47		92/09/07	2
599	Luisa	8.71	2.772	56		92/01/14	3
	Luisa	8.71	2.772	56		92/01/17	2
631	Philippina	8.70	2.792	56		92/09/11	2
639	Latona	8.20	3.015	71	2	92/11/29	1
	Latona	8.20	3.015	71	2	93/01/01	1
653	Berenike	9.18	3.012	45	2	91/12/15	2
675	Ludmilla	7.91	2.771	81		91/10/25	1
	Ludmilla	7.91	2.771	81		92/01/13	2
	Ludmilla	7.91	2.771	81		92/12/01	1
683	Lanzia	8.72	3.119	109		92/09/08	2
702	Alauda	7.25	3.193	214		91/10/30	2
720	Bohlinia	9.71	2.889	35	3	92/01/13	3
	Bohlinia	9.71	2.889	35	3	92/01/17	2
722	Frieda	12.1	2.172	12		91/10/26	4
724	HAPAG	13.2	2.456	14		92/11/29	1
732	Tjilaki	10.7	2.456	49		92/03/14	3
737	Arequipa	8.81	2.592	53		91/10/28	2
	Arequipa	8.81	2.592	53		92/01/17	3
752	Sulamitis	10.1	2.463	33	156	92/11/29	1
774	Armor	8.60	3.047	59		92/09/08	2
787	Moskva	10.0	2.539	31	153	92/09/08	2
788	Hohensteina	8.30	3.134	132	113	92/09/09	2
803	Picka	9.60	3.201	61		92/09/11	2
808	Merxia	9.70	2.746	35	40	92/09/10	1
811	Nauheima	10.8	2.900	21	3	92/03/14	3

Table 3.1 (continued)

Ast.	Name	*H*	*a*	*D*	Group	UT Date	#Exp.
813	Baumeia	11.7	2.223	14		93/01/01	2
851	Zeissia	11.6	2.228	15	187	92/01/14	3
863	Benkoela	9.02	3.200	33		92/03/11	2
879	Ricarda	11.2	2.532	18	4	92/03/14	3
900	Rosalinde	11.7	2.474	14		92/09/08	2
	Rosalinde	11.7	2.474	14		92/09/09	2
	Rosalinde	11.7	2.474	14		92/11/27	1
	Rosalinde	11.7	2.474	14		92/11/28	2
915	Cosette	11.7	2.228	14	182	91/10/26	3
918	Itha	10.7	2.864	22		92/09/08	3
951	Gaspra	11.4	2.210	16	189	92/11/26	1
	Gaspra	11.4	2.210	16	189	92/11/30	1
1063	Aquilegia	11.4	2.314	18		93/01/04	2
1071	Brita	10.1	2.802	33		92/09/11	2
1084	Tamariwa	10.8	2.689	42		92/01/13	3
1110	Jaroslawa	11.8	2.218	13		91/10/26	3
	Jaroslawa	11.8	2.218	13		91/10/30	4
1143	Odysseus	7.93	5.251	175	TRO	92/03/13	1
1144	Oda	10.0	3.764	51	HIL	92/09/11	3
1145	Robelmonte	11.1	2.424	31		93/01/21	1
1165	Imprinetta	10.3	3.128	52	113	92/09/09	2
1166	Sakuntala	11.3	2.538	17		93/01/22	2
1198	Atlantis	14.6	2.250	4	MC	92/11/28	1
1257	Mora	12.2	2.488	22		91/10/27	3
1264	Letaba	9.10	2.863	91		92/09/09	3
1273	Helma	12.8	2.393	6	165	93/01/21	2
1279	Uganda	12.5	2.371	19		92/09/08	3
	Uganda	12.5	2.371	19		92/09/09	5
1289	Kutaissi	10.7	2.860	22	3	92/11/29	2
1302	Werra	10.6	3.122	46	1A	92/01/14	3
1325	Inanda	11.9	2.540	13		91/10/26	3
	Inanda	11.9	2.540	13		91/10/27	4
1358	Gaika	12.2	2.477	22		92/03/11	2
1375	Alfreda	11.6	2.448	15	156	92/09/06	3
1379	Lomonosowa	11.0	2.526	20		92/03/15	1
1393	Sofala	12.2	2.434	11		91/12/08	3
	Sofala	12.2	2.434	11		91/12/14	3
1451	Grano	12.1	2.203	12	189	93/01/22	2
1463	Nordenmarkia	10.6	3.148	26		93/01/04	1
1471	Tornio	10.7	2.717	49		93/01/01	1
1478	Vihuri	12.6	2.466	9		91/12/13	3
1480	Aunus	13.1	2.202	7		92/12/02	1
1501	Baade	12.1	2.545	12	43	91/12/07	2
1518	Rovaniemi	12.3	2.225	11	183	91/10/27	4
1534	Nasi	11.7	2.731	28		93/01/01	1
1577	Reiss	13.1	2.230	7	185	91/10/28	3

Table 3.1 (continued)

Ast.	Name	*H*	*a*	*D*	Group	UT Date	#Exp.
1584	Fuji	10.7	2.375	22	PHO	93/01/04	1
1607	Mavis	11.6	2.548	15		93/01/22	2
1626	Sadeya	10.5	2.363	25	PHO	91/10/25	2
	Sadeya	10.5	2.363	25	PHO	92/01/14	3
1628	Strobel	10.0	3.013	35		93/01/04	1
1646	Rosseland	11.8	2.360	26	169	92/11/26	2
	Rosseland	11.8	2.360	26	169	92/11/27	2
1651	Behrens	12.1	2.180	12	189	92/09/07	2
1653	Yakhontovia	11.4	2.608	32		92/09/11	2
1658	Innes	11.5	2.561	15	150	91/12/08	2
1679	Nevanlinna	10.6	3.127	26		92/09/11	3
1697	Koskenniemi	12.6	2.374	15	165	92/11/30	1
1712	Angola	9.80	3.186	38		92/09/08	3
1722	Goffin	12.3	2.514	11		92/12/01	2
1725	CrAO	10.9	2.908	20	3	92/03/14	3
1743	Schmidt	12.5	2.472	19		91/11/01	3
1749	Telamon	9.20	5.213	97	TRO	92/03/13	3
1772	Gagarin	12.8	2.529	9		92/03/11	3
1781	Van Biesbroeck	12.7	2.394	10		93/01/20	2
1807	Slovakia	12.1	2.226	12	6	91/10/26	3
	Slovakia	12.1	2.226	12	6	91/10/27	4
	Slovakia	12.1	2.226	12	6	91/10/29	4
1854	Skvortsov	12.3	2.540	11		92/11/28	1
	Skvortsov	12.3	2.540	11		92/11/29	2
1892	Lucienne	12.1	2.461	12		91/12/13	2
1906	Naef	12.7	2.374	6	VES	91/12/07	4
	Naef	12.7	2.374	6	VES	91/12/08	4
	Naef	12.7	2.374	6	VES	91/12/14	3
	Naef	12.7	2.374	6	VES	91/12/15	6
1907	Rudneva	11.8	2.546	13		92/09/07	2
1929	Kollaa	12.2	2.363	8	165	92/11/27	2
1933	Tinchen	12.9	2.353	6	196	92/09/06	2
	Tinchen	12.9	2.353	6	196	92/09/07	3
1934	Jeffers	12.8	2.391	9	PHO	92/03/11	2
1967	Menzel	12.3	2.233	11	6	92/12/02	1
1995	Hajek	12.8	2.528	10		91/10/30	4
	Hajek	12.8	2.528	10		91/10/31	3
2011	Veteraniya	12.9	2.387	6	165	92/11/29	1
	Veteraniya	12.9	2.387	6	165	92/11/30	1
	Veteraniya	12.9	2.387	6	165	92/12/01	1
2014	Vasilevskis	11.7	2.403	14	PHO	92/09/11	3
2017	Wesson	12.8	2.252	9	7	91/10/28	3
2024	McLaughlin	12.9	2.325	8	196	93/01/21	2
2060	Chiron	6.00	13.751	380		93/01/22	1
2070	Humason	13.9	2.250	5		91/11/01	4
2074	Shoemaker	14.0	1.800	5	MC	91/10/30	4

Table 3.1 (continued)

Ast.	Name	*H*	*a*	*D*	Group	UT Date	#Exp.
2078	Nanking	12.1	2.369	12	MC	92/09/08	3
	Nanking	12.1	2.369	12	MC	92/09/09	3
	Nanking	12.1	2.369	12	MC	92/11/29	1
	Nanking	12.1	2.369	12	MC	92/12/02	1
2091	Sampo	10.2	3.014	55	2	92/01/13	3
2098	Zyskin	12.5	2.423	16		93/01/21	1
2105	Gudy	10.7	2.390	22	PHO	92/09/10	3
	Gudy	10.7	2.390	22	PHO	92/09/11	1
2107	Ilmari	11.4	2.627	16		92/11/26	1
	Ilmari	11.4	2.627	16		92/11/27	1
2113	Ehrdni	13.2	2.473	5		93/01/21	3
2119	Schwall	12.8	2.251	9		91/10/31	4
2128	Wetherill	13.6	2.736	7		91/10/26	3
	Wetherill	13.6	2.736	7		91/10/30	3
2130	Evdokiya	13.5	2.252	6		91/10/31	4
2140	Kemerovo	10.9	2.988	23		93/01/01	2
2143	Jimarnold	11.2	2.282	18		91/12/16	3
2149	Schwambraniya	11.7	2.550	14		91/12/08	2
	Schwambraniya	11.7	2.550	14		93/01/20	2
2159	Kukkamaki	12.1	2.482	12		93/01/22	2
2174	Asmodeus	11.6	2.536	15		91/10/27	2
2204	Lyyli	11.6	2.595	17	MC	93/01/04	1
2215	Sichuan	11.9	2.792	13		93/01/01	1
2253	Espinette	12.9	2.283	8	MC	91/10/31	3
2259	Sofievka	12.6	2.294	18		92/09/08	3
2299	Hanko	13.3	2.586	7		91/10/31	4
2327	Gershberg	13.9	2.368	5		91/11/01	2
	Gershberg	13.9	2.368	5		91/12/14	3
2365	Interkosmos	11.7	2.544	14		92/12/02	1
2403	Sumava	12.5	2.547	10		93/01/21	2
2420	Ciurlionis	12.2	2.561	11	4	92/11/27	1
2440	Educatio	13.1	2.215	7		91/11/01	3
2442	Corbett	12.8	2.387	6		92/11/30	1
	Corbett	12.8	2.387	6		92/12/01	1
2444	Lederle	11.8	2.729	15		91/11/01	3
2503	Liaoning	13.9	2.192	10		91/10/28	3
2538	Vanderlinden	13.7	2.239	6		91/12/13	2
2558	Viv	13.3	2.216	7		91/10/28	3
	Viv	13.3	2.216	7		91/10/29	4
2590	Mourao	12.7	2.343	6	196	92/11/26	3
2599	Veseli	11.2	2.535	18		92/09/09	3
2645	Daphne Plane	12.3	2.391	12		93/01/22	2
2728	Yatskiv	12.4	2.456	20	24	91/12/08	2
2775	Odishaw	13.6	2.421	6	160	91/12/15	2
2790	Needham	12.8	2.653	9		91/10/31	3
2908	Shimoyama	11.5	2.979	30		91/10/26	3

Table 3.1 (continued)

Ast.	Name	*H*	*a*	*D*	Group	UT Date	#Exp.
2920	Automedon	8.80	5.158	117	TRO	92/03/13	2
2923	Schuyler	11.6	2.455	29	24	91/12/14	3
2946	Muchachos	13.0	2.454	15		91/12/16	3
2965	Surikov	13.6	2.392	6	PHO	92/11/28	1
2966	Korsunia	13.4	2.448	6		92/03/12	2
	Korsunia	13.4	2.448	6		92/03/13	8
3109	1974 DC	11.6	2.451	17		91/12/15	3
3153	Lincoln	13.3	2.423	5		92/11/28	1
	Lincoln	13.3	2.423	5		92/12/01	1
3155	Lee	12.6	2.343	7	196	91/10/28	4
	Lee	12.6	2.343	7	196	91/10/29	4
3158	Anga	12.5	2.549	10	4	92/09/06	3
3167	Babcock	11.4	2.541	16	4	93/01/21	2
3220	Murayama	13.3	2.225	7		91/12/16	3
3231	Mila	13.1	2.446	14		93/01/21	1
3268	De Sanctis	13.0	2.347	5	VES	92/03/11	2
3285	Ruth Wolfe	12.3	2.529	11		91/10/26	3
3321	Dasha	13.0	2.545	8		93/01/22	2
3332	Raksha	11.7	2.545	14	4	93/01/20	2
3354	McNair	13.1	2.325	7		92/09/06	4
3381	Mikkola	13.2	2.454	8		91/10/30	4
3431	Nakano	10.0	3.095	60		92/01/14	3
3494	1980 XW	12.9	2.349	6	VES	93/01/21	2
3501	1971 QU	11.6	2.922	32		93/01/21	2
3523	Arina	12.4	2.371	10		92/03/14	3
3528	1981 EW3	12.9	2.534	8		91/12/14	3
3559	Violaumayer	13.8	2.485	10		92/11/27	2
3578	1977 CC	8.10	3.202	145		92/01/16	2
	1977 CC	8.10	3.202	145		92/01/20	2
3586	1978 SW6	13.1	2.460	7		92/03/12	2
3628	1979 WD	12.6	2.537	9		91/12/08	2
	1979 WD	12.6	2.537	9		93/01/21	2
	1979 WD	12.6	2.537	9		93/01/22	2
3657	1978 ST6	12.6	2.313	7	196	92/09/06	2
	1978 ST6	12.6	2.313	7	196	92/09/07	4
3665	1979 FE	12.4	2.418	12		92/11/26	2
3674	Erbisbuhl	11.7	2.361	14	MC	92/09/11	2
3677	Magnusson	14.0	2.266	5		91/11/01	3
3740	1981 EM	14.0	2.465	6		91/12/15	3
3748	Tatum	12.8	2.531	9		91/12/15	3
3759	Piironen	11.9	2.720	25		93/01/04	1
3760	Poutanen	12.5	2.534	10		91/12/08	3
3792	Preston	13.3	2.292	7	PHO	92/03/11	2
	Preston	13.3	2.292	7	PHO	92/03/12	3
	Preston	13.3	2.292	7	PHO	92/03/14	2

Table 3.1 (continued)

Ast.	Name	*H*	*a*	*D*	Group	UT Date	#Exp.
3869	Norton	13.0	2.453	5		92/03/11	3
	Norton	13.0	2.453	5		92/03/12	3
3915	Fukushima	12.2	2.439	22		92/11/26	2
3935	Toatenmongakkai	12.1	2.541	12		93/01/21	1
3944	Halliday	13.1	2.368	5	165	92/11/28	1
	Halliday	13.1	2.368	5	165	92/11/29	2
	Halliday	13.1	2.368	5	165	92/12/01	1
3963	1969 TP2	13.6	2.440	6	24	92/12/02	1
3968	Koptelov	12.6	2.322	7	196	92/09/05	3
	Koptelov	12.6	2.322	7	196	92/09/06	3
3999	Aristarchus	12.4	2.458	20	24	92/11/26	1
4002	1950 JB	11.9	2.516	13		93/01/22	2
4005	1972 TC2	12.5	2.451	7		91/12/07	2
	1972 TC2	12.5	2.451	7		91/12/08	6
4006	1972 YR	12.6	2.517	11		92/11/26	2
4025	Ridley	14.0	2.252	5		91/11/01	3
4031	Mueller	13.3	1.934	8	HUN	92/11/27	2
4038	Kristina	13.5	2.366	4	VES	91/10/28	3
	Kristina	13.5	2.366	4	VES	91/10/29	4
4062	Schiaparelli	13.8	2.242	5		91/11/01	3
4085	Weir	12.0	2.604	12		91/10/31	3
4104	1979 SG10	12.6	3.421	9	CYB	91/12/07	4
4145	1981 SJ7	13.6	2.272	6		91/10/29	4
4147	Lennon	13.0	2.362	5	VES	92/09/05	3
	Lennon	13.0	2.362	5		92/09/06	3
4156	1988 BE	12.0	2.701	24		91/11/01	3
4159	1989 GK	10.8	2.550	21	4	92/01/13	3
4165	1976 GS3	13.3	2.453	8		92/09/07	2
4179	Toutatis	14.0	2.510	5	APO	92/09/05	2
	Toutatis	14.0	2.510	5	APO	93/01/01	4
	Toutatis	14.0	2.510	5	APO	93/01/04	3
	Toutatis	14.0	2.510	5	APO	93/01/21	3
	Toutatis	14.0	2.510	5	APO	93/01/22	3
4215	1987 VE1	11.7	2.417	10		93/01/21	2
4219	Nakamura	12.9	2.468	16	24	92/03/14	3
4282	Endate	13.0	2.391	15		91/12/15	3
4353	Onizaki	12.1	2.346	13		92/09/06	2
	Onizaki	12.1	2.346	13		92/09/07	3
4370	Dickens	14.6	2.196	4		92/11/28	1
4373	Crespo	13.8	2.232	5		92/12/02	1
4376	Shigemori	13.5	2.232	6		92/12/01	2
	Shigemori	13.5	2.232	6		92/12/02	1
4440	1984 YV	12.5	1.921	11	HUN	92/12/02	1
4510	Shawna	13.0	2.360	8		93/01/21	1
4546	Franck	13.7	2.356	4	196	92/11/28	2
4562	1979 UD2	13.0	2.471	15	24	91/12/07	3

Table 3.1 (continued)

Ast.	Name	*H*	*a*	*D*	Group	UT Date	#Exp.
4606	Saheki	12.7	2.252	9		91/12/16	3
4635	Rimbaud	12.5	2.472	19		91/12/07	3
	Rimbaud	12.5	2.472	19		92/03/12	2
4640	Hara	13.2	2.252	7		91/12/15	3
4673	Bortle	11.9	2.549	13		92/03/11	2
4761	1981 QC	13.5	2.340	6	PHO	92/11/30	1
	1981 QC	13.5	2.340	6	PHO	92/12/01	2
	1981 QC	13.5	2.340	6	PHO	92/12/02	1
4939	1986 QL1	13.2	2.527	7		91/12/13	3
	1986 QL1	13.2	2.527	7		91/12/14	4
4948	1988 VF1	13.9	2.169	5		91/10/31	4
4956	Noymer	13.4	2.446	7	PHO	92/03/12	3
5065	1990 FP1	13.3	2.514	13		93/01/22	2
5118	1988 RB	11.6	2.604	15		92/09/07	3
5145	1992 AD	7.30	2.661	15		92/03/12	4
	1991 VK	17.0	1.842	1	APO	91/12/14	3
	1991 VL	17.0	1.834	1	APO	91/12/14	3
	1991 WA	17.5	1.577	1	APO	91/12/14	3
	1991 XB	18.0	2.974	1	APO	91/12/15	4
	1992 CC1	15.0	1.360	4	APO	92/03/12	2
	1992 NA	16.5	2.390	2	AMO	92/09/09	2
	1992 TC	17.5	1.566	1	AMO	92/11/28	2
	1992 UB	16.0	3.066	2	AMO	92/11/27	2

Table 3.2

Assumed Mean Geometric Albedos for Different Types*

Type	C	S	X	D	A	T	V	R	Q
Albedo	0.05	0.19	0.15	0.04	0.40	0.07	0.38	0.34	0.19

* Estimated from Tedesco *et al.* (1989).

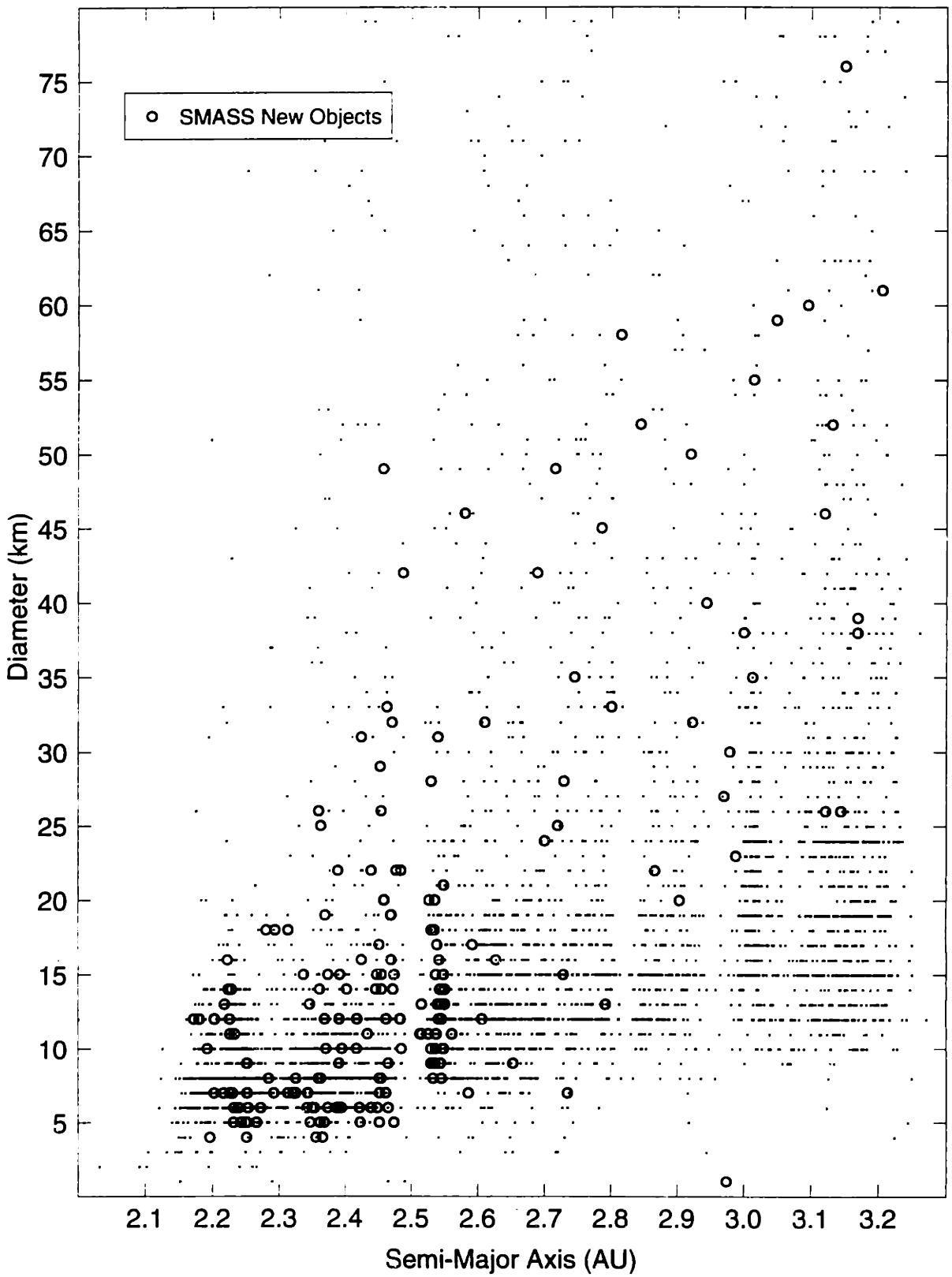

Fig. 3.1a. The heliocentric and size distributions of SMASS newly surveyed objects. This figure shows that SMASS concentrated on small inner main-belt asteroids (D ~10 km) which have no previous spectroscopic measurements.

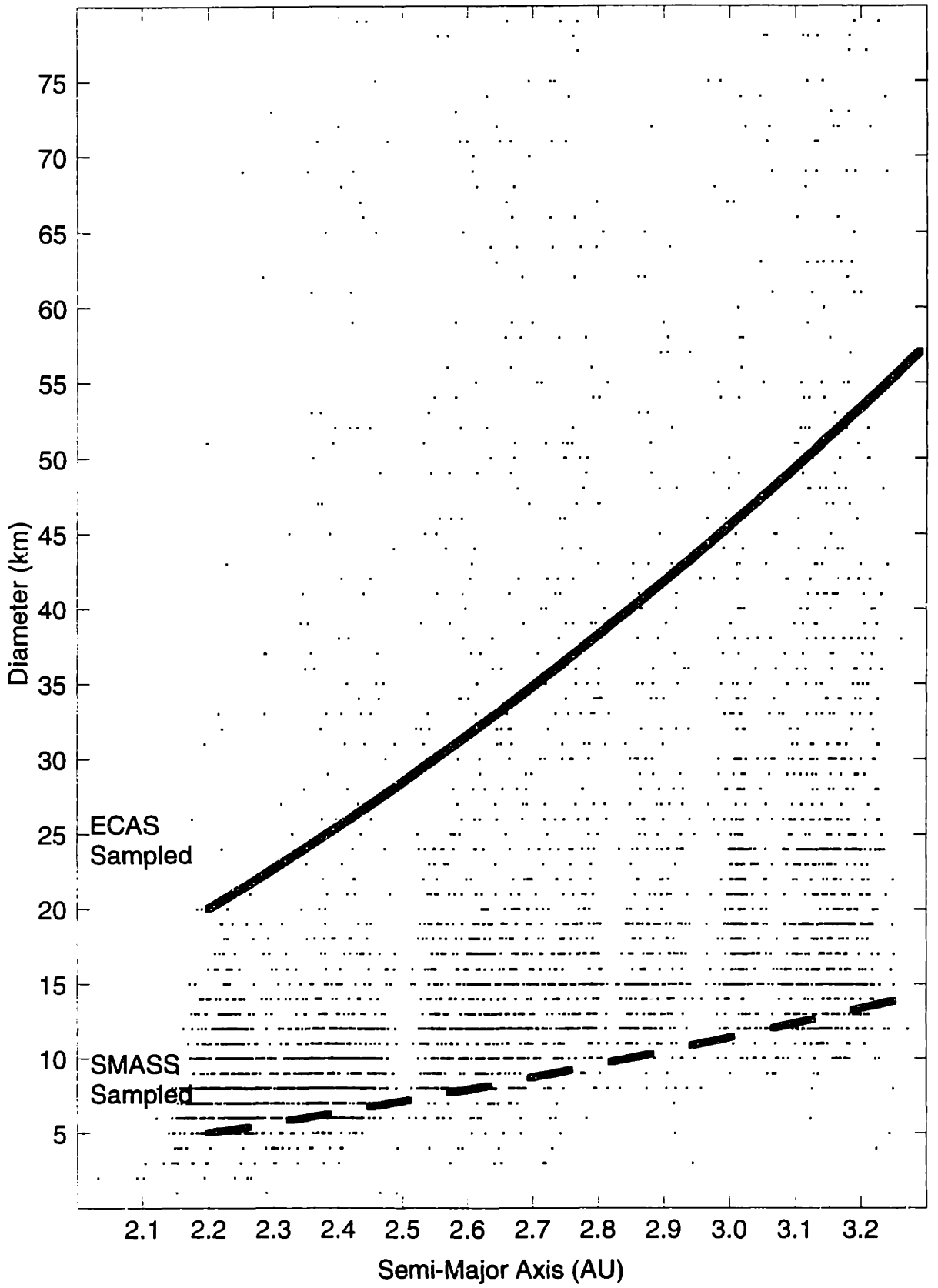

Fig. 3.1b. The size limits of SMASS and ECAS samples. This figure shows that SMASS has pushed the survey down to kilometer-sized main-belt objects.

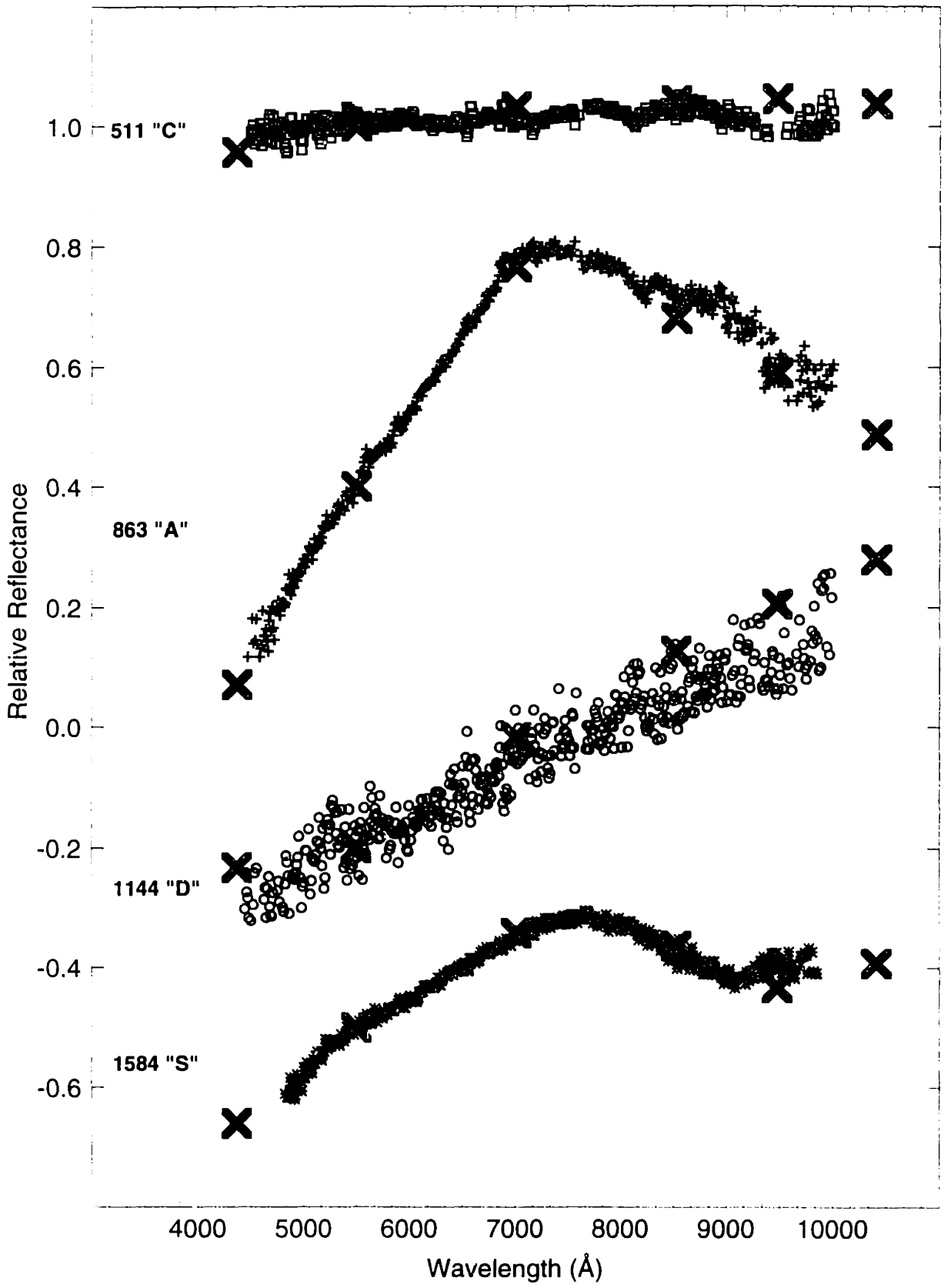

Fig. 3.2. Comparison between measurements by SMASS and by the Eight-Color Asteroid Survey (denoted by **X**, Zellner *et al.* 1985).

3.2 Origins of the Spectral Features

The absorption features in asteroid spectra are caused by the interaction between the solar electromagnetic radiation and the silicate minerals on the surface (Burns 1970, 1993, Gaffey *et al.* 1989, Adams 1974, 1975, Cloutis *et al* 1986, Pieters and McFadden 1993, Burbine 1991, and Sawyer 1991). The main factors that influence the spectra of silicate minerals are the presence of transition elements (e.g., Sc, Ti, V, Cr, Mn, Fe, Co, Ni, Cu). Fe is especially important because of its abundance, coordination and oxidation states. The slope in the ultraviolet and blue regions is mainly due to the charge transfer of O --> Fe^{2+} (band center at 3500 Å), the grain sizes, and the opacity of the silicate minerals (Burns 1993). There may be some other features, such as the band around 6900 Å caused by Fe^{2+} --> Fe^{3+} electron hopping. For minerals containing pyroxene and olivine, there are some strong absorption features in the near-infrared and infrared regions.

Pyroxenes are the most common and abundant ferromagnesian silicate minerals occurring in primary igneous rocks on the surfaces of terrestrial planets. Pyroxenes are also the main constituents of stony meteorites, and probably the principal minerals of the terrestrial planets' mantles and the asteroids (Burns 1993). Two strong absorption bands (1 μm and 2 μm) in pyroxene spectra are the most important diagnostic features for identification of the surface minerals and rocks of remote celestial objects. The chemical composition of pyroxenes can be expressed by a general formula as XYZ_2O_6, where X represents Na^+, Ca^{2+}, Mn^{2+}, Fe^{2+}, Mg^{2+}, and Li^+ in the *M2* crystallographic site; Y represents Mn^{2+}, Fe^{2+}, Mg^{2+}, Fe^{3+}, Al^{3+}, Cr^{3+}, Ti^{3+} and Ti^{4+} in the *M1* site; and Z represents Si^{4+}, Al^{3+}, Fe^{3+} in the tetrahedral sites of the chain (Klein and Hurlbut 1993). The commonest pyroxenes are Mg, Fe, and Ca silicates. In accordance with the cation size requirements of the sites *M2* and *M1*, the X cations in general are larger than the Y cations. Each SiO_4 tetrahedron shares two oxygens with adjacent tetrahedra to form infinite chains, giving a ratio of Si:O = 1:3. Pyroxenes are characterized by two cleavages which intersect almost at right-angles. There are two main groups of pyroxenes: the orthopyroxenes crystallize in the orthorhombic system and contain very little Ca (e.g., Enstatite $Mg_2Si_2O_6$, Ferrosilite $Fe_2Si_2O_6$); the clinopyroxenes are monoclinic and contain either Ca, or Na, Al, Fe^{3+}, or Li (e.g., Diopside

$CaMgSi_2O_6$, Hedenbergite $CaFeSi_2O_6$). Fig. 3.3 and Table 3.3 show the properties of various crystal systems.

Fig. 3.4 illustrates the structure of pyroxenes. The structure consists of infinite chains of SiO_3 groups linked by bands of cations extending along the *c* axis. Cations in the *M1* site are coordinated to 6 oxygen ions each linked to 1 silicon atom. The coordination closes to octahedral symmetry (octahedron is composed of 8 equilateral triangular faces, and each of which intersects all three of the crystallographic axes equally), and the cation lies almost at the center of symmetry of the site. Cations in the *M2* position are surrounded by 4 oxygen ions each linked to 1 silicon atom and 2 bridging oxygen atoms which are shared by 2 silicon atoms. The *M2* site is significantly distorted from octahedral symmetry, showing compression along the O_2-O_5 axis and elongation along the *b* axis, therefore, is non-centrosymmetric. Mossbauer measurements show that the distorted *M2* site contains the majority of the Fe^{2+} ions (Burns 1970, 1993).

Crystal field investigations (e.g., Burns 1970, 1993) show that the pyroxene absorption band around 1 μm is caused by the excitations of Fe electrons between energy levels of unfilled 3-*d* orbitals (electronic configuration of Fe is $1s^2 2s^2 2p^6 3s^2 3p^6 3d^6 4s^2$) induced by the crystal field of oxygen anions surrounding the transition metal cation in its coordination site. The *d*-orbitals have been classified into two groups, t_{2g} and e_g, on the basis of spatial configuration (Fyfe 1964, Burns 1970, 1993). The schematic energy level diagrams shown in Fig. 3.5 demonstrate that relative energies and separations of t_{2g} (three-fold degenerate) and e_g (two-fold degenerate) orbital groups are strongly influenced by the symmetry and distortion of the coordination environment about a transition metal ion. The *M1* site is almost a regular octahedron, but splittings of 3-*d* orbital energy levels for Fe^{2+} ions happen in the highly distorted pyroxene *M2* site. Enriched Fe^{2+} cations in the *M2* site produce two widely separated absorption bands in the vicinity of 1 and 2 μm (Fig. 3.6 and 3.7a, b). The infrared band can not be revealed in our CCD spectra. Fig. 3.7a and b show the spectral features of two orthopyroxenes. The α spectrum shows one intense band at 9100-9400 Å; the β spectrum shows two bands at 8900-9350 Å and 18500-21000 Å, and a shoulder at about 11500 Å which becomes increasingly prominent in Fe^{2+}-rich orthopyroxenes; and the γ spectrum consists of two weak bands around 9000 Å and 19000 Å (Burns 1970). Pyroxenes containing Fe^{3+} ions show a broad band at

5500-7000 Å which represents a charge transfer between neighboring Fe^{2+} and Fe^{3+} ions in the structure. Absorption bands move to longer wavelengths with increasing Fe and Ca contents (Burns 1970, 1993). Laboratory measurements of diffuse reflectance spectra of pyroxenes by Adams (1974) revealed similar results to the polarized spectra. The absorption features caused by Fe^{2+} in pyroxene *M2* positions dominate not only the spectra of the asteroids, but also the spectra of meteorites, rocks on the Moon, and the surface of terrestrial planets.

The compositions of the majority of olivines can be represented in the system CaO-MgO-FeO-SiO_2. Olivines of the forsterite-fayalite series, $(Mg, Fe)_2SiO_4$, are present in many lunar samples, stony meteorites, and asteroids. The olivine crystal structure contains Fe^{2+} in two distinct six-fold coordination sites having contrasting distortions from octahedral symmetry and centrosymmetric properties (Fig. 3.8). Differences between the two cation coordination environments of olivine produce characteristic spectral features in the near-infrared region (Burns 1993). Energy level diagrams for Fe^{2+} in the *M1* and *M2* sites are shown in Fig. 3.9. The polarized spectra of forsterite and fayalite are shown in Fig. 3.10a and b. The α and β spectra contain broad bands with absorption maxima between 8000 Å and 13000 Å (due to transitions of Fe^{2+} ions in the *M1* sites). The γ spectra consist of an intense band at 10400 to 10800 Å (due to Fe^{2+} ions in the non-centrosymmetric M_2 sites) with shoulders on both the short and long wavelength sides. Similar to pyroxene, absorption maxima of all bands show compositional variations and shift to longer wavelengths with increasing Fe content in olivine.

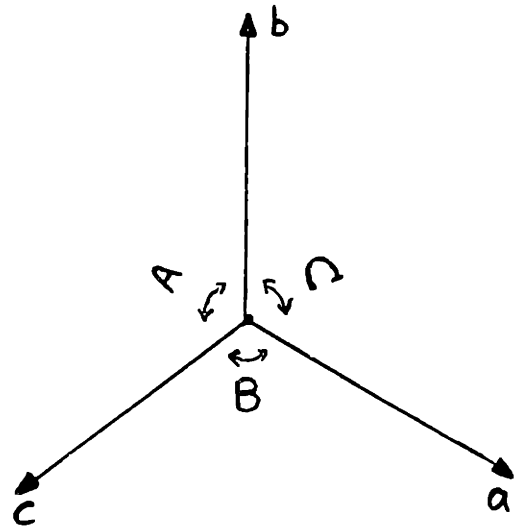

Fig. 3.3. Crystallographic axes and angles.

Table 3.3
Crystal System

System	Properties of crystallographic axes and angles
Triclinic	$a \neq b \neq c$, $A \neq B \neq C$
Monoclinic	$a \neq b \neq c$, $A = C = 90° \neq B$
Orthorhombic	$a \neq b \neq c$, $A = B = C = 90°$
Tetragonal	$a = b \neq c$, $A = B = C = 90°$
Cubic (Isometric)	$a = b = c$, $A = B = C = 90°$
Trigonal (Rhombohedral)	$a = b = c$, $A = B = C < 120°, \neq 90°$
Hexagonal	$a = b \neq c$, $A = B = 90°$, $C = 120°$

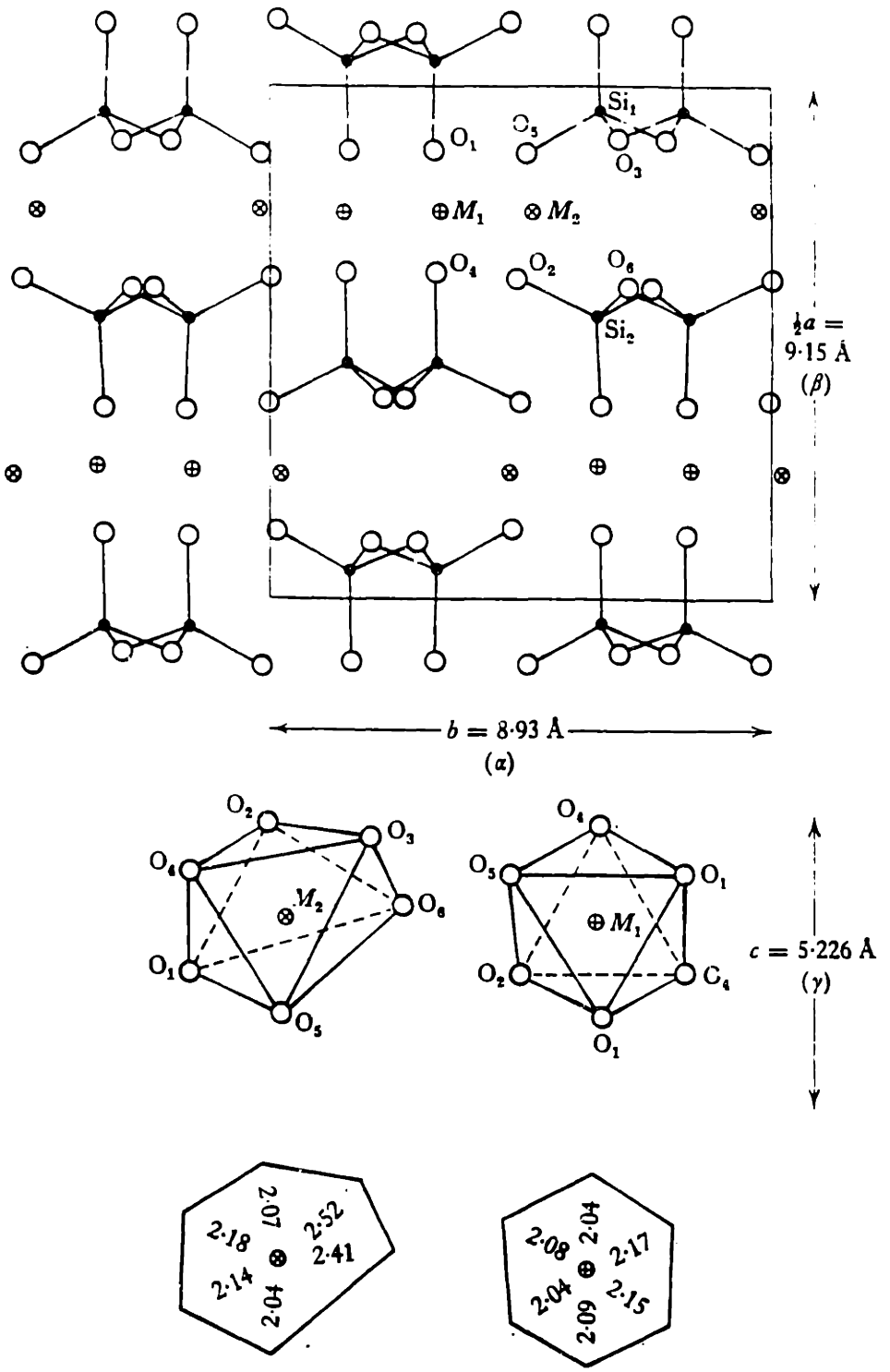

Fig. 3.4. The figure shows the orthopyxene crystal structure projected onto the plane parallel to the c axis. Oxygen coordination polyhedra projected onto the plane parallel to the a axis, and metal-oxygen distances in each site are indicated (Å). ⊕ *M1*; ⊗ *M2*; • silicon; O oxygen. (From Burns 1970.)

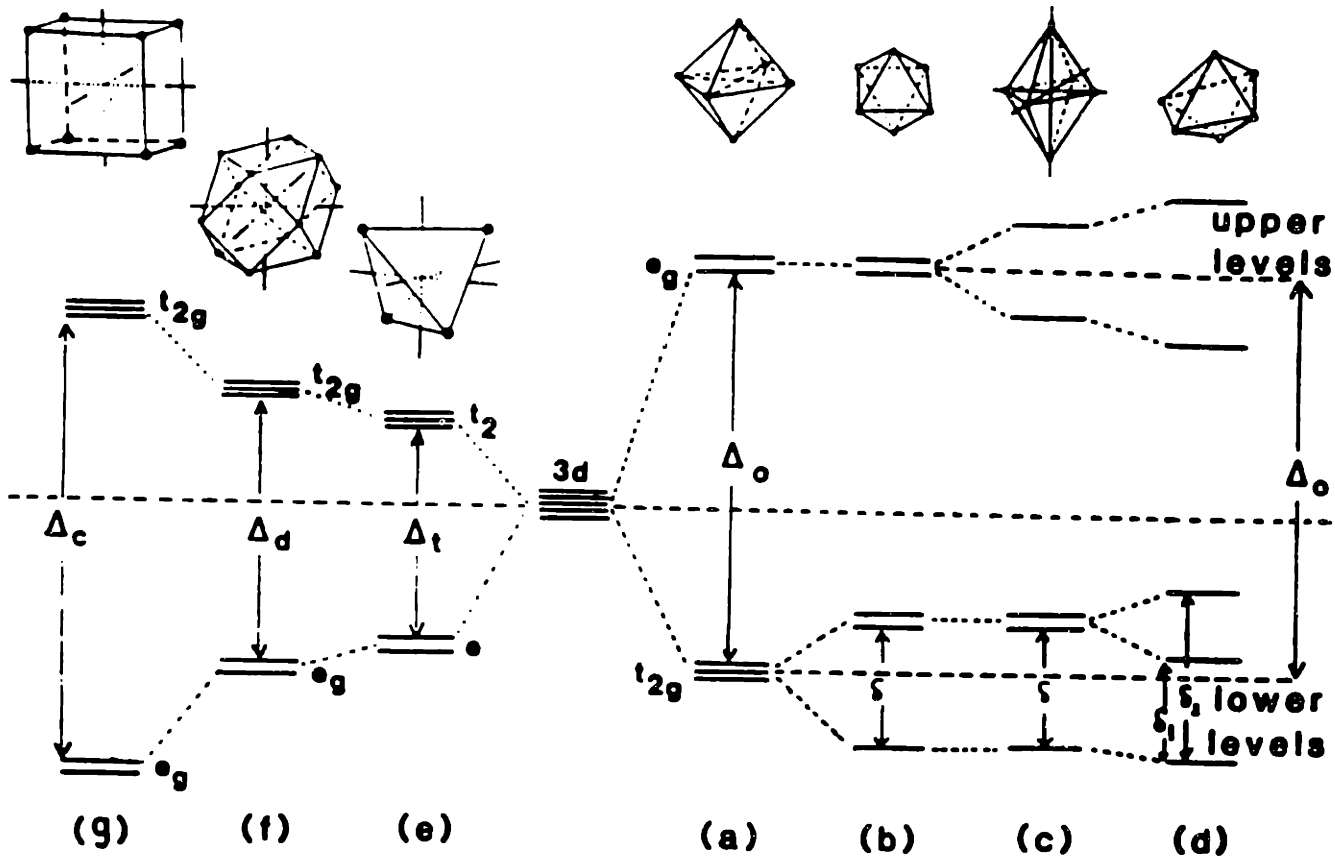

Fig. 3.5. Relative energies of 3-*d* orbitals of a transition metal ion in different coordination environments. (a) regular octahedron (e.g., ≈ pyroxene *M1* site); (b) trigonally distorted octahedron (e.g., ≈ olivine *M2* site); (c) tetragonally distorted octahedron (e.g., ≈ olivine *M1* site); (d) very distorted six-coordination site (e.g., pyroxene *M2* site); (e) tetrahedral site (e.g., spinel); (f) dodecahedral site (e.g., ≈ perovskite *A*-site); (g) cubic site (e.g., ≈ garnet). Δ and δ are the crystal field energy between different *d*-orbitals. Note that 3-*d* orbitals are separated into widely spaced energy levels in the pyroxene *M2* site, and these splittings are responsible for the 1 μm and 2 μm spectral features for Fe^{2+} ions. (From Burns 1989.)

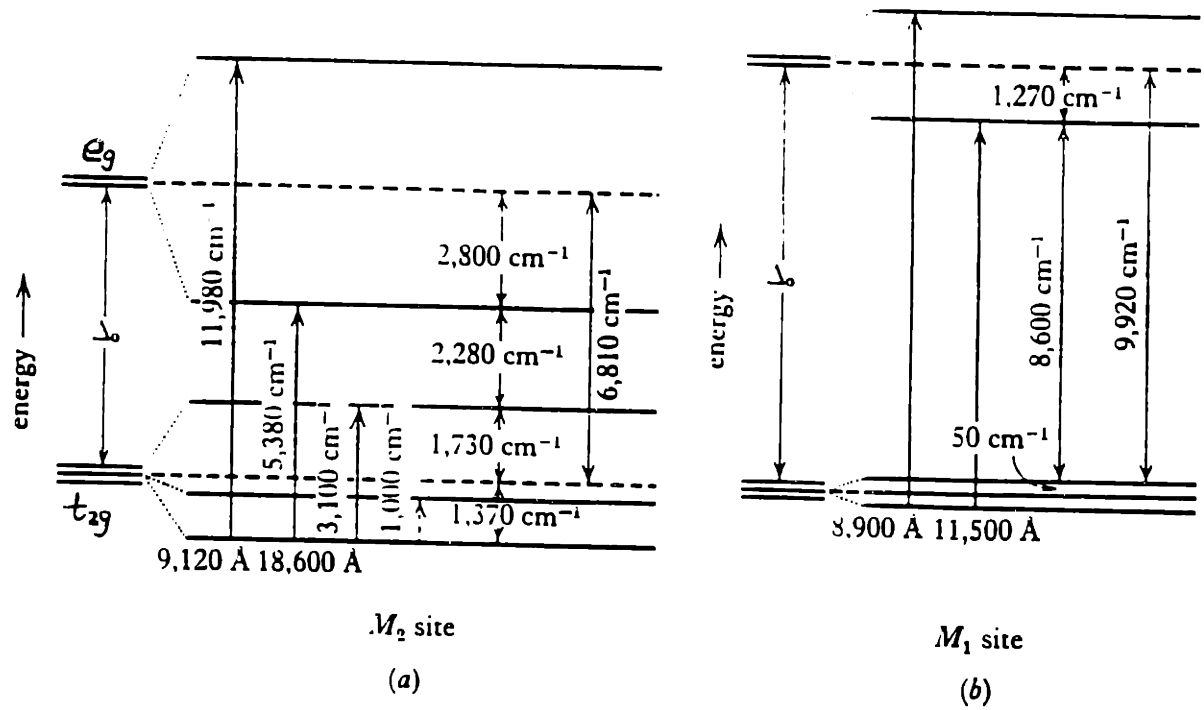

Fig. 3.6. Energy level diagrams for Fe^{2+} ions in the orthopyroxene structure. (a) *M2* site; (b) *M1* site. Δ_O is the crystal field energy between t_{2g} and e_g orbitals. Observed transitions in the spectra of bronzite (ferrosilite 14.5%, see Fig 3.7a) are indicated. (From Burns 1970.)

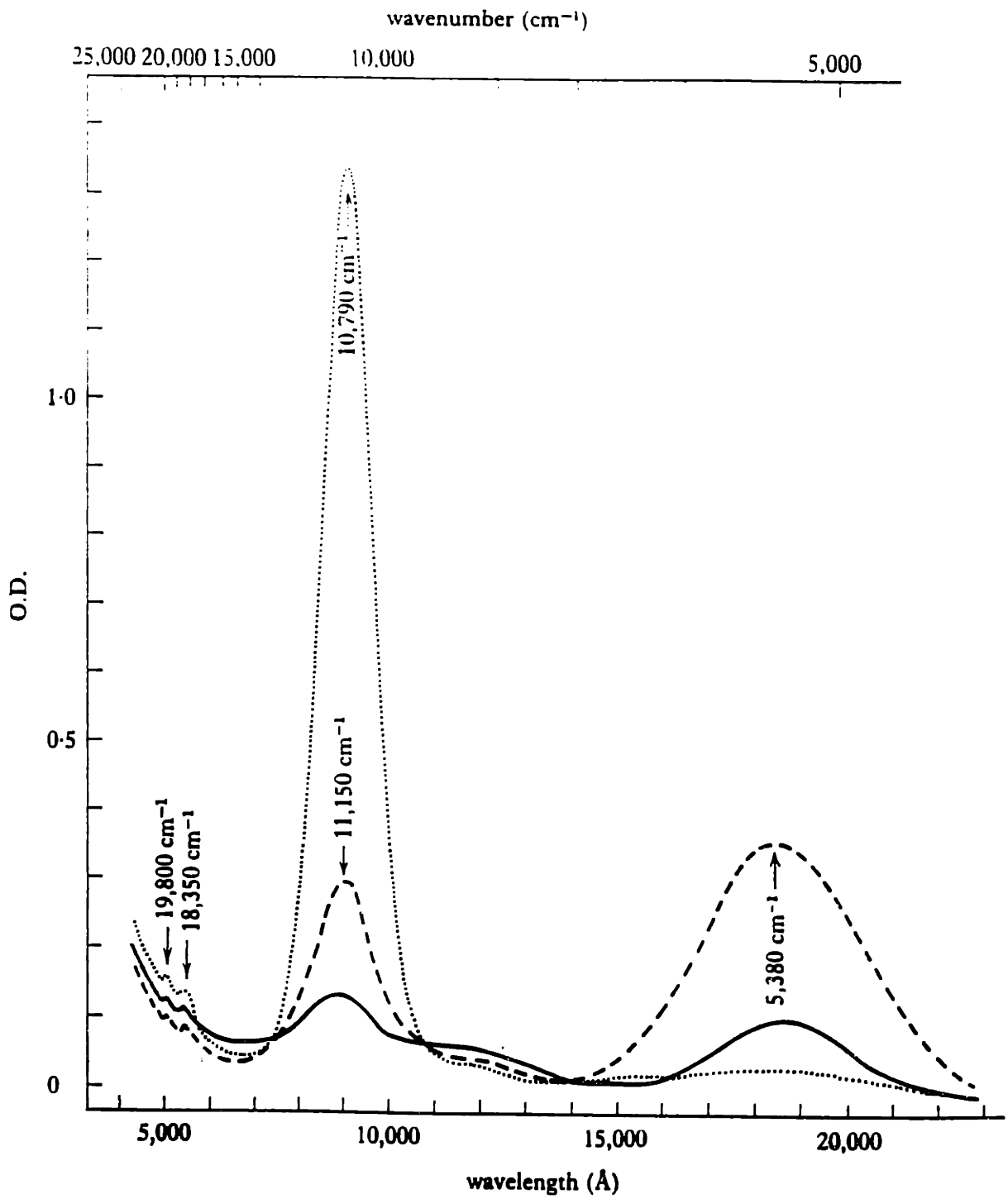

Fig. 3.7a. Absorption spectra (polarized) of orthopyroxenes.
... α spectra; --- β spectra; — γ spectra.
Mineral: bronzite (ferrosilite 14.5%), from Bamle, Norway.
Optic orientation: α = b; β = a; γ = c.
(From Burns 1970, 1993.)

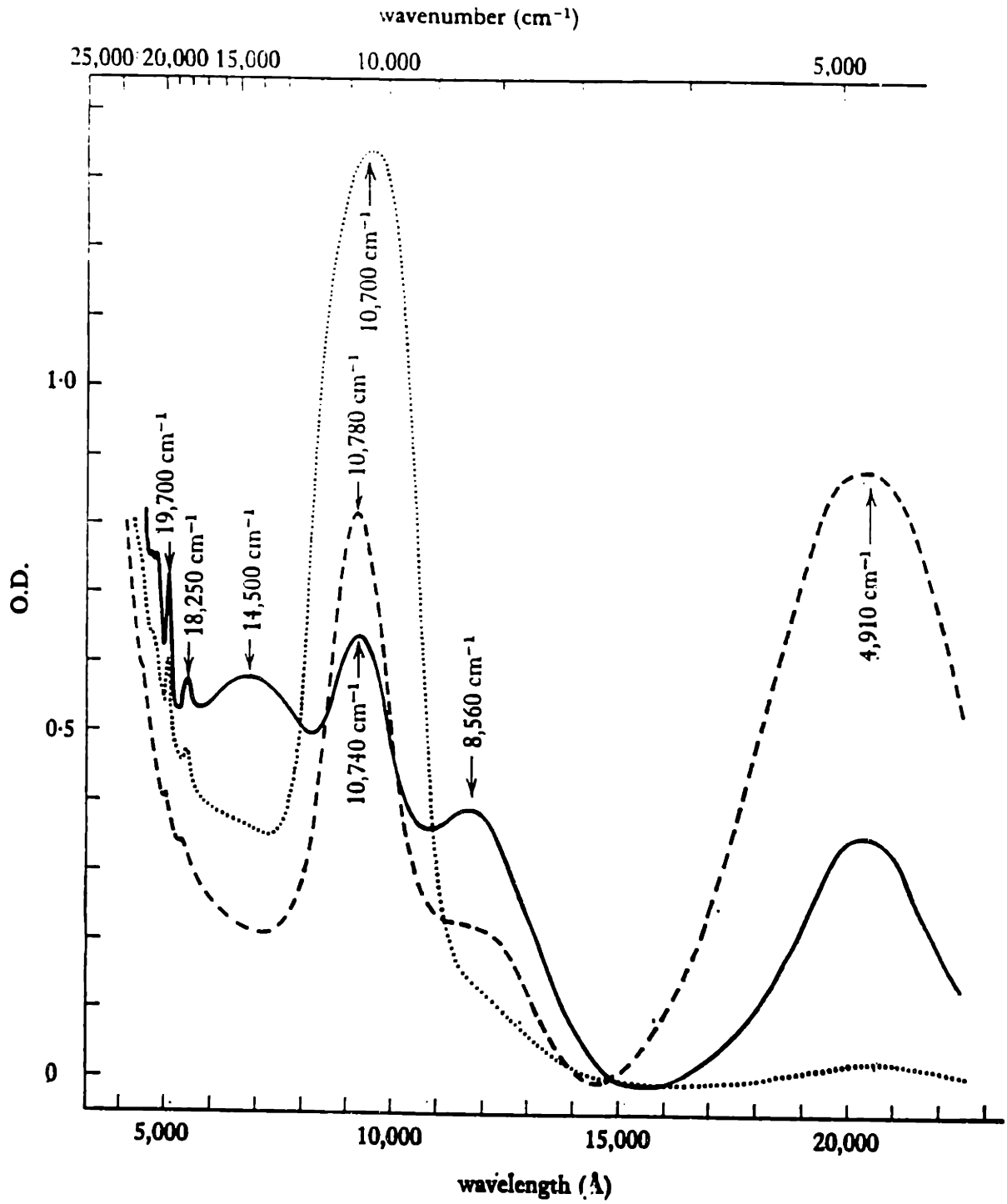

Fig. 3.7b. Absorption spectra (polarized) of orthopyroxenes.
... α spectra; --- β spectra; — γ spectra.
Mineral: orthoferrosilite (ferrosilite 86%), from northeast China.
Optic orientation: α = b; β = a; γ = c.
(From Burns 1970, 1993.)

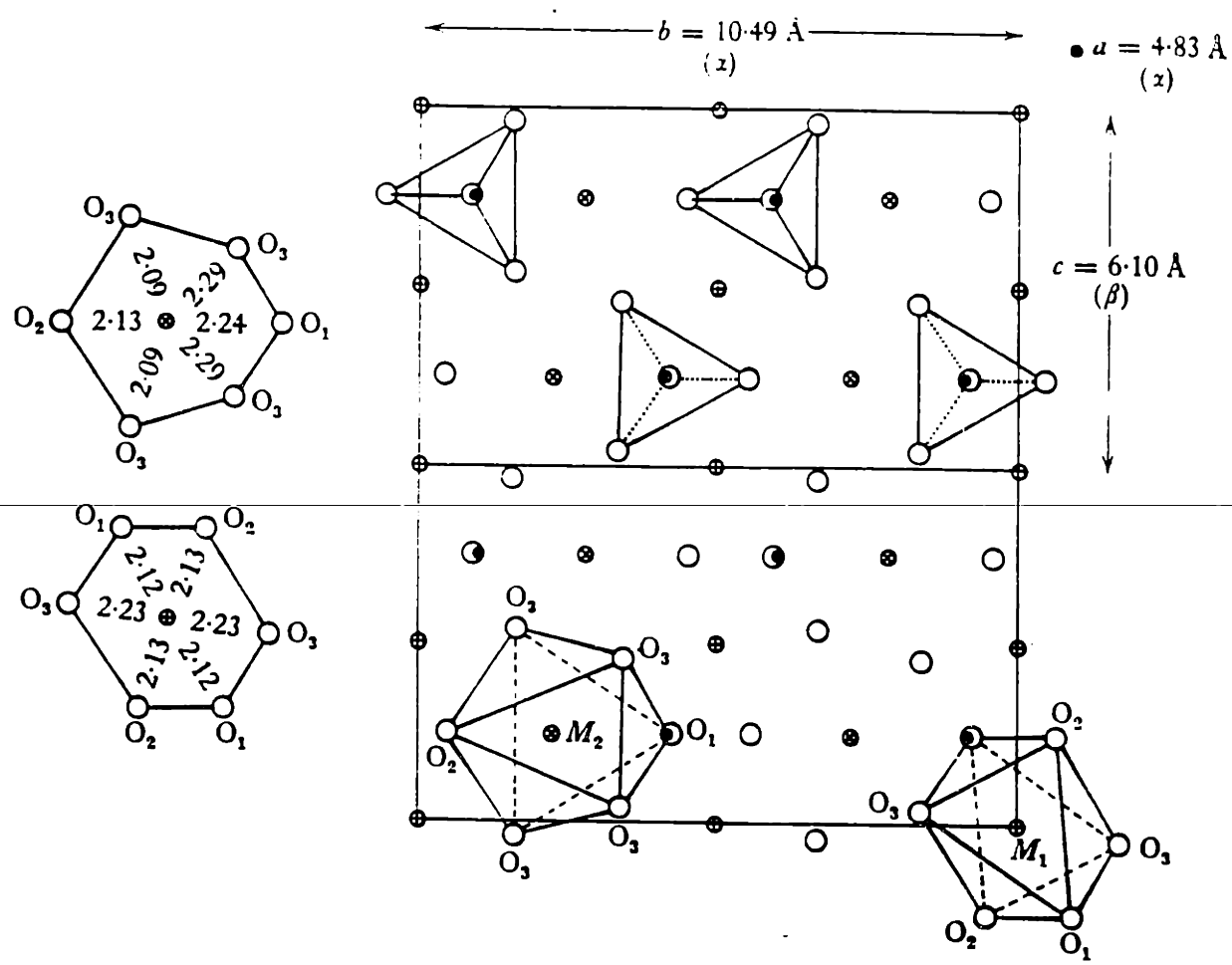

Fig. 3.8. The figure shows the olivine crystal structure projected onto the plane paralleling to the *a* axis and an oxygen coordination polyhedra about each metal position. The structure consists of independent SiO_4 tetrahedra linked by divalent cations in 6-fold co-ordination. There are two six-co-ordinate positions which are designated M_1 and M_2. Each co-ordination site is distorted from octahedral symmetry. M_1 is centrosymmetric, but M_2 is non-centrosymmetric. Metal-oxygen distances in each site are indicated (Å). ⊕ *M1*; ⊗ *M2*; • silicon; O oxygen. (From Burns 1970.)

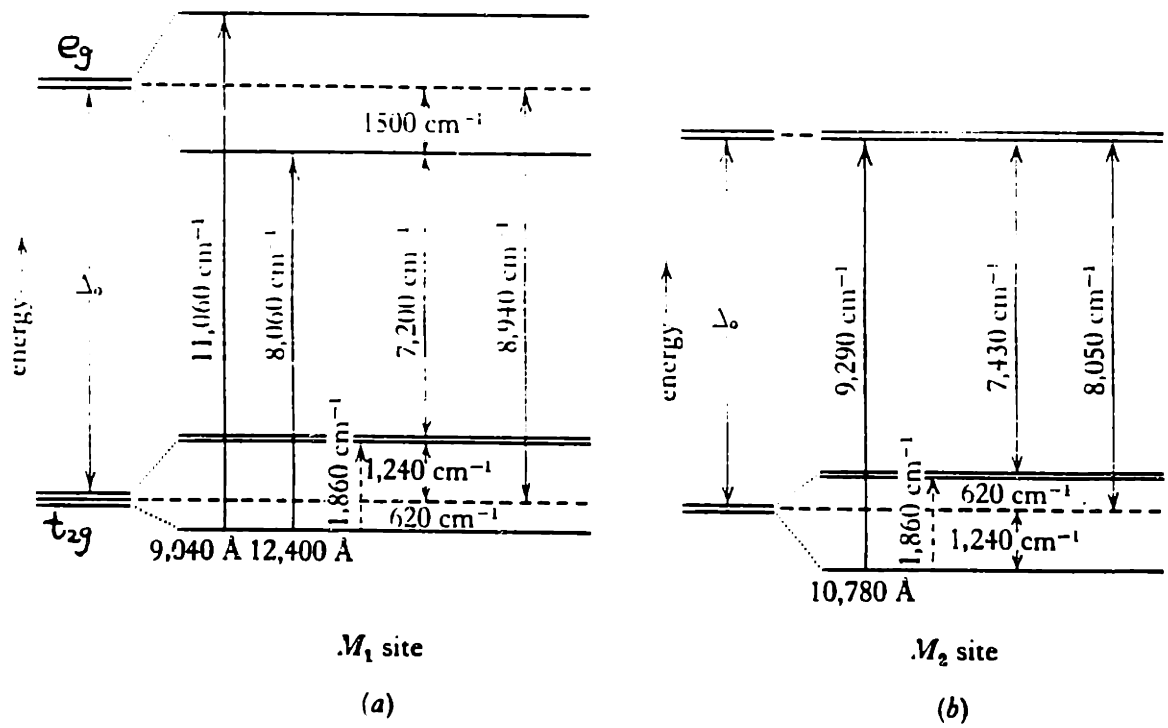

Fig. 3.9. Energy level diagrams for Fe^{2+} ions in the olivine structure. (a) *M1* site; (b) *M2* site. Observed transitions in the spectra of fayalite (see Fig 3.10b) are indicated (From Burns 1970.)

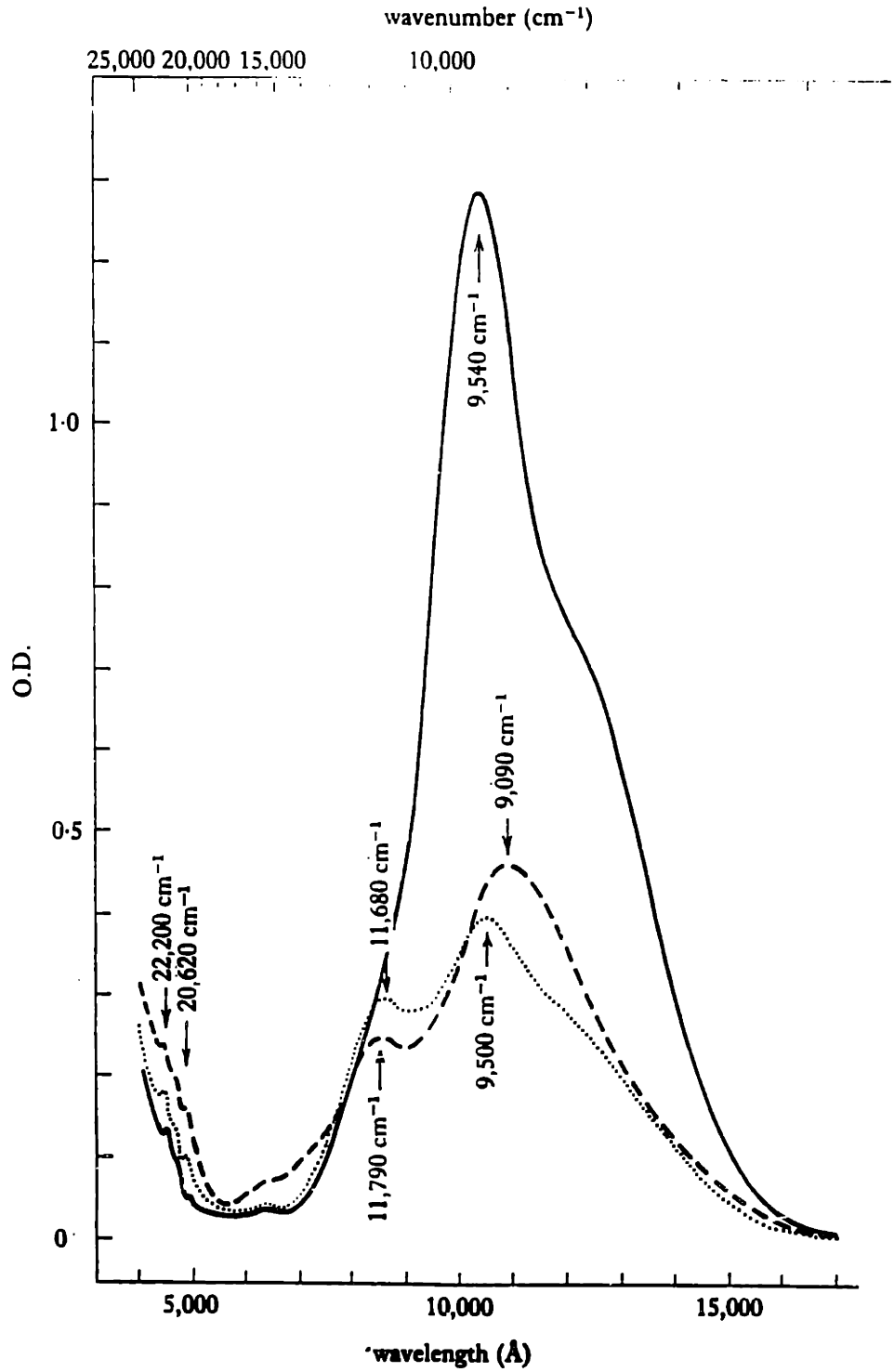

Fig. 3.10a. Absorption spectra (polarized) olivines.
... α spectra; --- β spectra; — γ spectra.
Mineral: forsterite with 12% fayalite, from Jan Mayan.
Optic orientation: α = b; β = c; γ = a.
(From Burns 1970.)

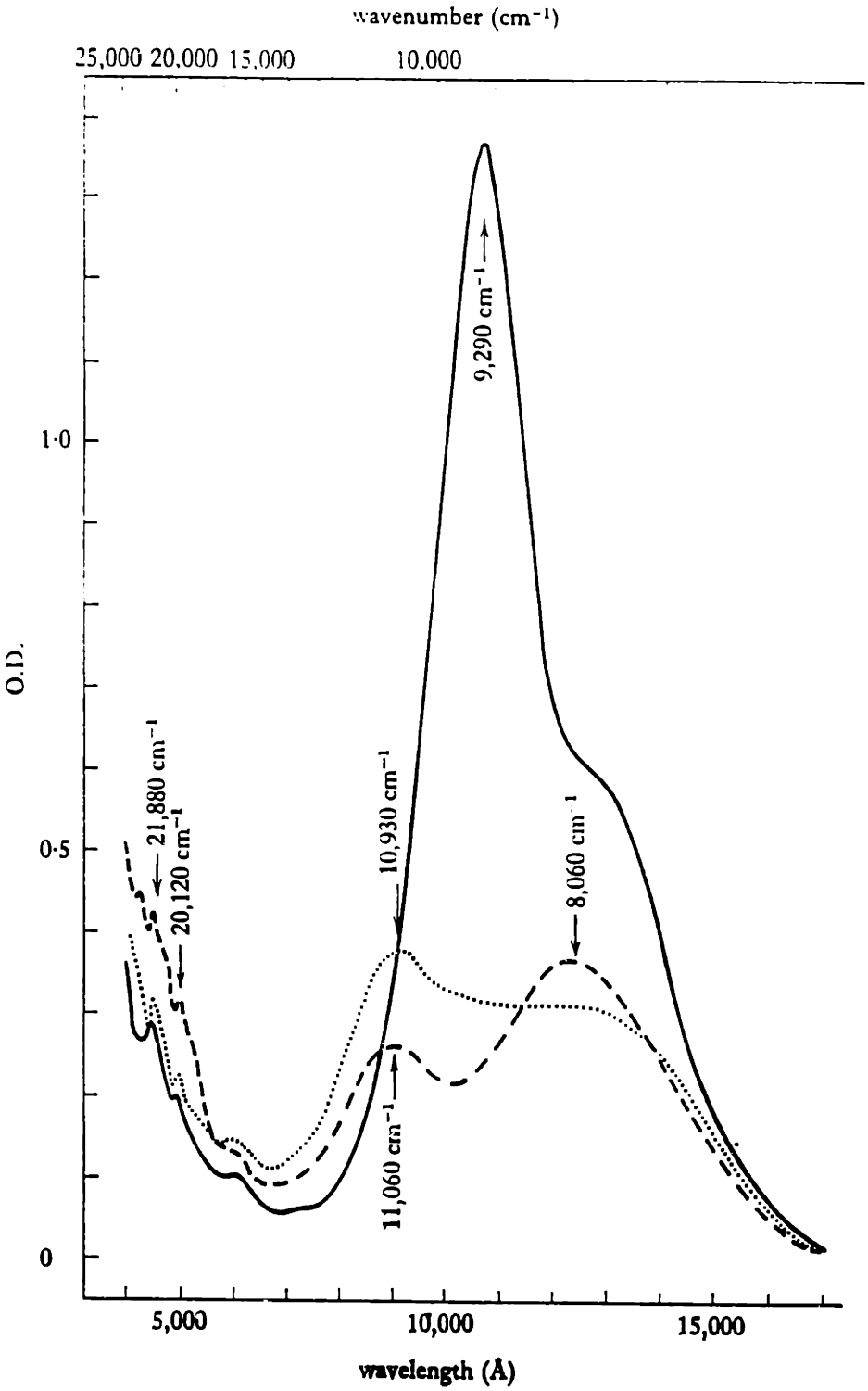

Fig. 3.10b. Absorption spectra (polarized) olivines.
... α spectra; --- β spectra; — γ spectra.
Mineral: fayalite (96%), from Rockport, Massachusetts.
Optic orientation: α = b; β = c; γ = a.
(From Burns 1970, 1993.)

3.3 Taxonomy and Observational Results

As a first step toward obtaining meaningful results from the spectroscopic observations, we need to classify the observed asteroids into different groups. Similar to stellar spectral classification, asteroid taxonomy is based on the spectral features, which are indicators of the asteroid mineralogical properties. Strictly speaking, the spectral features reflect only the surface compositions, especially in the cases for large asteroids. A recent review was given by Tholen *et al.* (1989). The most notable classification scheme was done by Tholen (1984). He applied the Minimal Tree method combined with Principal Component Analysis (PCA, Chatfield and Collins 1980) to nearly 600 asteroid spectra from the Eight-Color Asteroid Survey (Zellner *et al.* 1985). A total of 14 classes have been separated (see Fig. 3.11, Table 3.4). Another class, K, was proposed and defined by Bell (1988) and Tedesco *et al.* (1989) based on the observations of the Eos family and a number of other asteroids. Later taxonomic classifications derived by different techniques and applied to extended data sets (Barucci *et al.* 1987, Tedesco *et al.* 1989, Burbine 1991, and Howell *et al.* 1992) have confirmed the robustness of the Tholen classes. Although no specific mineralogical criteria were used in defining the classes, the same spectral and albedo information that is used in the classification can be interpreted to derive mineralogical characterizations for individual asteroids in each class (Gaffey *et al.* 1993a). Inferred surface mineralogy and possible meteorite analogs are summarized in Table 3.5. The distribution of asteroid classes shows a systematic trend (compositional gradients) with the heliocentric distance (Gradie *et al.* 1989). Based on the electromagnetic induction heating mechanism (Scott *et al.* 1989), Bell *et al.* (1989) proposed three superclasses to interpret the Tholen classes. They are primitive, metamorphic, and igneous classes. The primitive objects have undergone little or no heating, and dominate the outer main belt, the metamorphic objects have been heated sufficiently to exhibit spectral changes, and most of them are in the middle main belt; the igneous objects were formed from a melt, and they are abundant in the inner main belt (Table 3.6, and Fig. 3.12).

Since PCA has been demonstrated as a very powerful tool for asteroid classification as well as for the comparison between asteroids and meteorites (Tholen 1984, Burbine 1991, Britt *et al.* 1992, Gaffey *et al.* 1993a), we used this technique for the classification of the objects in our survey. PCA is a multivariate

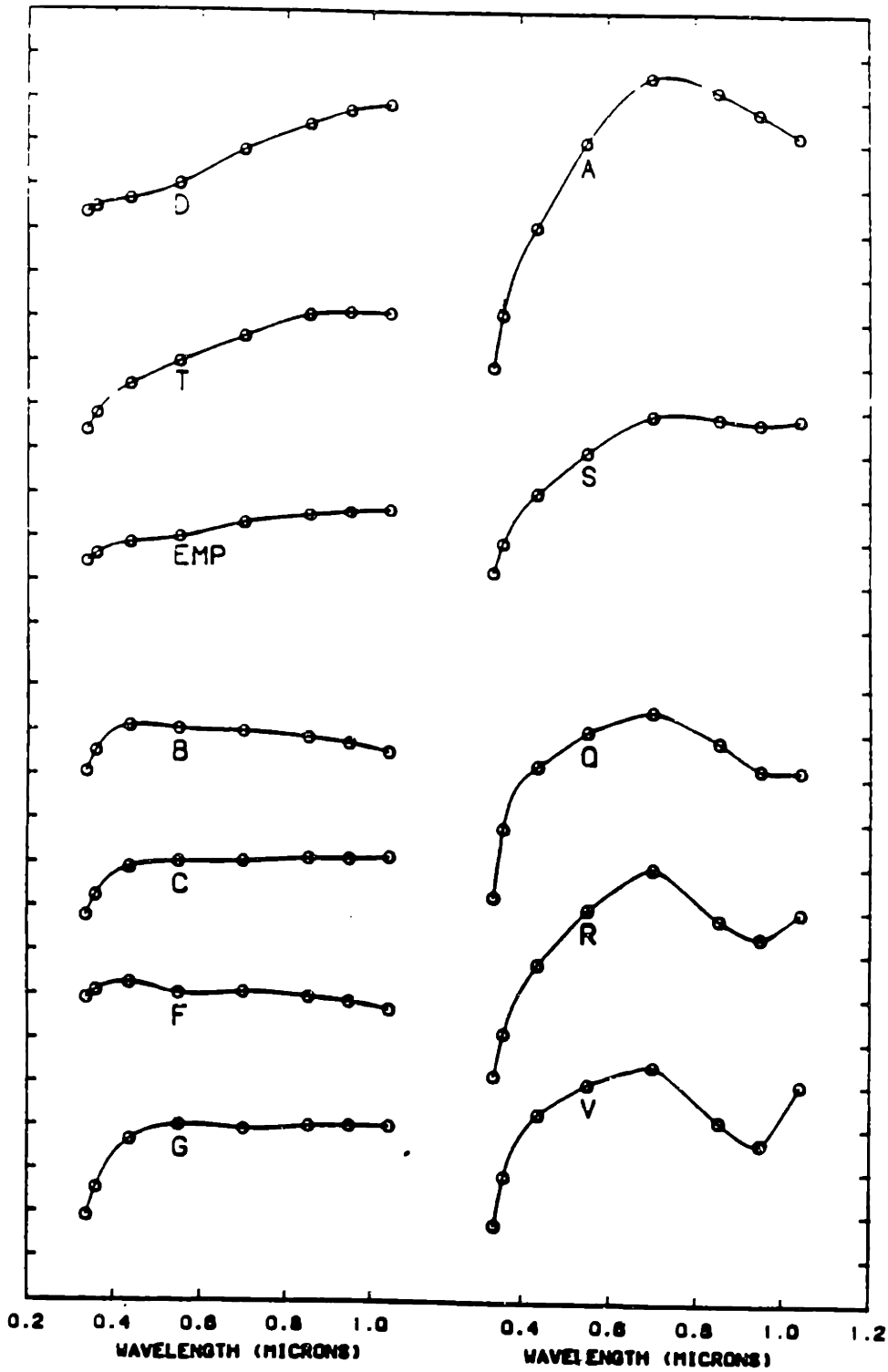

Fig. 3.11. Mean reflectance spectra for the asteroid classes. Tick marks on the ordinate are spaced 0.2 magnitudes apart. (From Tholen 1984, Tholen *et al.* 1989.)

Table 3.4

Asteroid Classes, Albedos, and Spectrum (Tholen *et al.* 1989)

Letter Designation	Albedo	Spectrum
A	moderately high	extremely reddish shortward of 0.7 microns; strong absorption feature longward of 0.7 microns, centered near the 1.05 micron filter
B	moderately low	higher albedo variant of the C class with a tendency toward lower reflectivities at the red end of the spectrum (subclass of the C class)
C	low	ultraviolet absorption feature shortward of 0.4 microns, generally flat to slightly reddish longward of 0.4 microns
D	low	generally featureless spectrum; neutral to slightly reddish shortward of 0.55 microns, very red longward of 0.55 microns; some objects' spectra tend to flatten longward of 0.95 microns
E	high	featureless spectrum; flat to slightly reddish over entire 0.3 to 1.1 micron wavelength range; differs from the spectrally identical M and P classes in albedo only
F	low	featureless spectrum; flat to slightly bluish over entire 0.3 to 1.1 micron wavelength range; differs from the C class in the weakness of the ultraviolet absorption feature (subclass of the C class)
G	low	very strong ultraviolet absorption feature shortward of 0.4 microns, flat longward of 0.4 microns; differs from the C class in the strength of the ultraviolet absorption feature (subclass of the C class)
M	moderate	featureless spectrum; flat to slightly reddish over entire 0.3 to 1.1 micron wavelength range; differs from the spectrally identical E and P classes in albedo only
P	low	featureless spectrum; flat to slightly reddish over entire 0.3 to 1.1 micron wavelength range; differs from the spectrally identical E and M classes in albedo only; spectra are intermediate between C and D classes
Q	moderately high	strong absorption features shortward and longward of 0.7 microns; band center between those of A and V classes (1862 Apollo is the type example)
R	moderately high	strong absorption features shortward and longward of 0.7 microns; band center between those of A and V classes (349 Dembowska is the type example)
S	moderate	moderate to strong absorption feature shortward of 0.7 microns, and moderate to nonexistent absorption feature longward of 0.7 microns
T	low	moderate absorption feature shortward of 0.85 microns, and generally flat longward of 0.85 microns
V	moderately high	strong absorption feature shortward of 0.7 microns and strong absorption feature longward of 0.7 microns, centered near the 0.95 micron filter

I used for inconsistent data (e.g. a low albedo but an A-type spectrum); such a designation would be used only in the case of unconfirmed data; should high-quality data confirm such a combination, then a new asteroid class should be introduced

K this letter has been reserved to represent a class of objects similar to 221 Eos; at this time, no formal definition for this class exists in the taxonomic system described above

U appended to the classifications of those objects that fall far from the cluster center, indicating an unusual spectrum for that class

X in the absence of albedo information, the E, M, and P classes are spectrally degenerate; X is used to represent the spectrum shared by these three classes and should be replaced by E, M, or P once a high-quality albedo becomes available

: indicates noisy data and a classification of lower quality

:: indicates extremely noisy data and a classification of dubious quality

— indicates that physical data do exist but are useless for classification purposes due to excessive noise

Table 3.5

General Mineralogy and Possible Meteorite Analogues of the Asteroid Taxonomic Types

Type	Major Mineral Phases†	Possible Meteorite Analogs‡
V	Pyroxene +/−Feldspar	Eucrites, howardites, diogenites
A	Olivine +/−FeNi metal	Olivine achondrites Pallasites *Olivine-metal partial melt residues*
E	Enstatite (<Fs_1)	Enstatite achondrites (aubrites) Iron-bearing enstatite (Fs_{2-4}) *Fe-bearing Aubrites (Fs_{2-4})*
R	Olivine + Orthopyroxene	*Olivine-pyroxene cumulates* *Olivine-pyroxene partial melt residues*
M	Metal +/−enstatite Hydrated Silicates + organics?	Iron meteorites Enstatite chondrites
S	See Table 3.8b	See Table 3.8b
Q	Olivine + Pyroxene (+ metal)	Ordinary chondrites
C	Iron-bearing hydrated silicates	CI1 & CM2 chondrites *Dehydrated CI1 & CM2 assemblages*
B	Iron-poor hydrated silicates	*Partially dehydrated highly leached CI1-type assemblages*
G	Iron-poor hydrated silicates	*Highly leached CI1-type assemblages*
F	Hydrated silicates + *organics*	*Organic-rich CI1 & CM2 assemblages*
P	*Anhydrous silicates + organics*	Olivine-organic cosmic dust particles
D	*Organics + Anhydrous silicates*	Organic-olivine cosmic dust particles
T	*Troilite (FeS) (+ FeNi metal)*	Troilite-rich iron meteorites
K	Olivine + opaques	CV3/CO3 chondrites
Z	*Organics (+ anhydrous silicates)*	Organic-rich cosmic dust particles

† Mineral species or assemblages in italics are inferred from spectral properties which are not specifically diagnostic.
‡ Analogs in italics have not been found or presently identified in meteorite collections.

From Gaffey *et al.* (1993a).

Table 3.6
Compositional Interpretations of Asteroid Taxonomic Classes

Superclass	Class	Inferred Minerals	Meteorites	Example
Primitive	Z	organics	none	5145
	D	clays, organics	none	1143
	P	clays, organics	none	65
	C	clays, C, organics	CI, CM	31
	K	ol, pyx, carbon	CO, CV	221
Metamorphic	T	?	?	308
	B + F + G	clays, opaques	altered carbonaceous chondrites	10
	Q	pyx, ol, gray NiFe	H, L, LL chondrites	1862
Igneous	V	pyx, ol, plag	eucrites, howardites	4
	R	ol, pyx	ol-rich achondrites	349
	S	pyx, ol, red NiFe	pallasites, irons	6
	A	ol	brachinites	446
	M	NiFe	irons	16
	E	Fe-free pyx	aubrites	64
	(Mars)		SNC meteorites	
	(Moon)		lunar meteorites	

This table is from Bell (personal communication), Bell *et al.* 1989, Britt *et al.* 1992, and Burbine (personal communication). Class Z was proposed by Mueller *et al.* (1992) after the discovery of 5145 Pholus whose extraordinary spectrum matches that of tholin mixtures (Cruikshank *et al* 1991a).

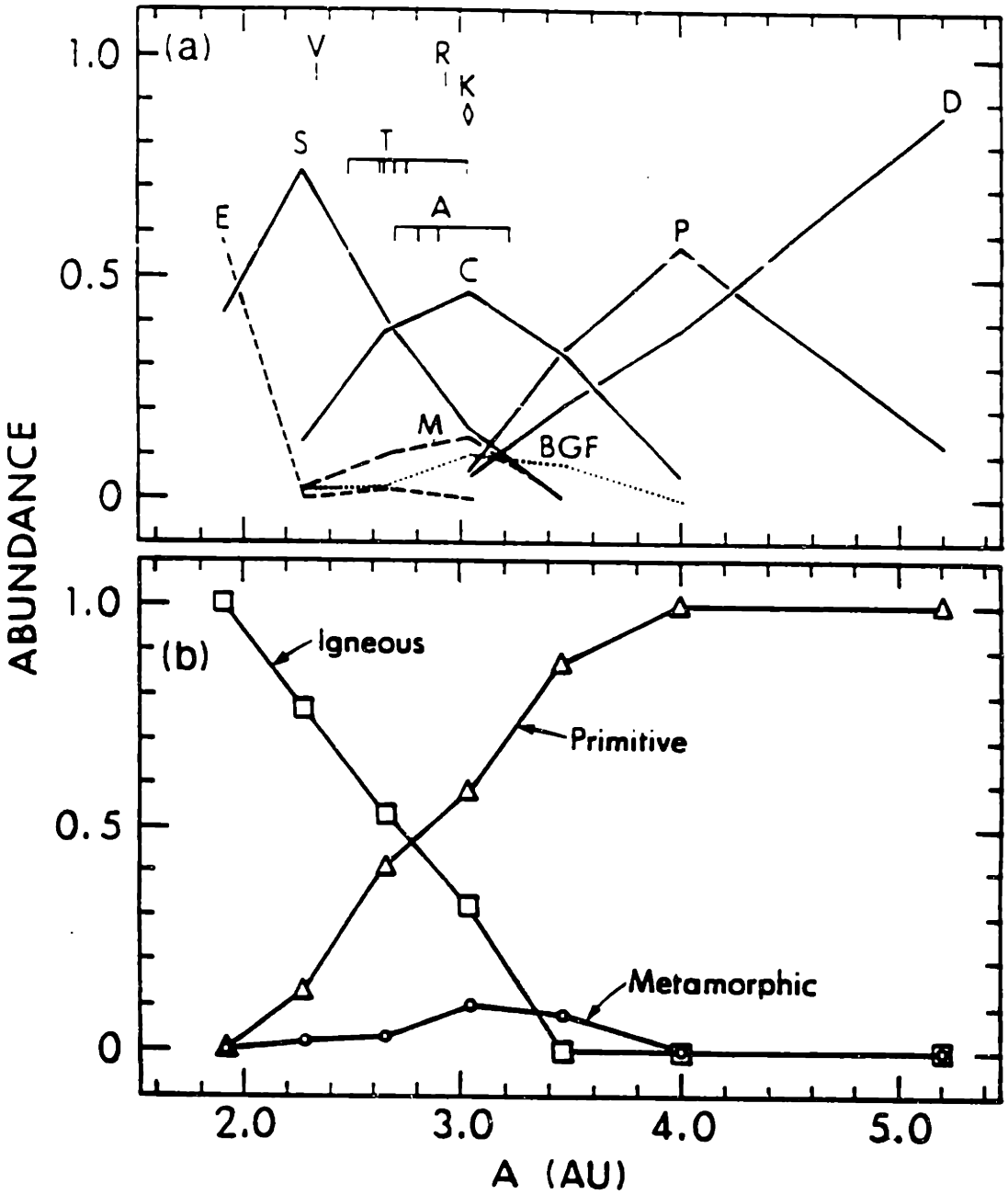

Fig. 3.12. (a) Distribution in the asteroid belt of the taxonomic types of Tholen (1984), plus K class of Bell (1988). (b) Distribution in the asteroid belt of the asteroid superclasses. From Bell (1986a, b), and Bell *et al.* (1989).

analysis technique that transforms a set of correlated variables into a new set of uncorrelated variables called principal components. PCA requires no underlying assumptions. Consider a sample of objects for which two quantities have been measured, x and y. If x and y are correlated, then we may rotate the coordinate system so that one of the two axes coincides with the best-fit line; the other axis remains orthogonal to the first axis. With this *rotation*, the variance along the first axis has been maximized, and the variance along the second axis has been minimized. The first axis is then called the first principal component (PC1) and the second axis is called the second principal component (PC2)(Tholen and Barucci 1989, Tholen 1984). This simple two-dimensional case can be easily generalized to a multi-dimentional data set. The principal components are linear combinations of the original variables and are derived in decreasing order of importance so that the first principal component accounts for the largest possible amount of variance within the data set. The second principal component will account for the second largest amount of the original variance (Chatfield and Collins 1980). PCA is useful for asteroid and meteorite spectra because many of the variables (reflectance at different wavelengths) are highly correlated. Most of the spectral features have very broad bands (such as the ultraviolet and near-infrared absorption bands), so the reflectance at one wavelength is correlated the reflectance at nearby wavelengths (Burbine 1991).

We used the software written by StatSoft™ for the PCA analysis of our spectral data. Our spectra were fitted with high order (7th to 9th) polynomials. Fifty points (variables) were chosen from the polynomial with wavelength coverage ranging from 4800- to 9700-Å (a point for every 100 Å). We also performed PCA using 28 points data set (from 7000- to 9700-Å) to investigate more thoroughly the features around 9000 Å. In order to give some meaningful interpretations for our results, and study possible mineralogical properties for the small asteroids, our PCA population consists of not only SMASS asteroids, but also meteorites (Table 3.7), a subset of previously identified S-class asteroids (Table 3.8a, b, Gaffey *et al.* 1993b, discussed below), and 4 Vesta and 1862 Apollo (using the data from ECAS, Zellner *et al.* 1985), yielding a total of 434 objects. The results are shown in Tables 3.9, 3.10, 3.11, Fig. 3.13a, b, c, Fig. 3.14a, b and Fig. 3.15a, b.

Table 3.9 shows that 87% of the variance distribution information contained in the 50 variables is concentrated on the first and second principal components.

We found the same results as Tholen (1984): the first component represents the ultraviolet absorption feature (slope) and the second represents the near-infrared feature (slope). This conclusion can be verified by examining the correlation coefficients shown in Table 3.10. A high degree of correlation exists among the wavelengths at the blue band. This means that all of the blue band wavelengths contain essentially the same information. Coefficients among the red-band wavelengths show high correlation too. But coefficients between variables involving blue and red wavelengths show much less or no correlation. For example, Two blue bands, 4800 Å and 5200 Å show high degree of correlation. The same is true for two near-infrared bands, 8700 Å and 9200 Å. But almost no correlation can be found for pairs of variables involving one blue and one near-infrared bands. Table 3.11 shows the first four principal component values for 315 asteroids, 80 meteorites, 37 sub S-classes, 4 Vesta and 1862 Apollo.

The distributions in Fig. 3.13a, b are very similar to that of Tholen's (Fig. 3.13c). Therefore, the major class domains, such as D, T, X (E, M, or P), C, S, and A, can be easily determined for the SMASS objects (Table 3.11). Since we have no albedo information about the newly surveyed objects in SMASS, E, M, and P types cannot be separated (symbol X is used to denote these three classes). Because SMASS spectra do not have the same wavelength coverage with respect to ECAS, we have not further classified some of the C types into B's, F's, and G's (Tholen 1984). The boundary objects usually show noisy spectra, and we classified them with the help of Tholen's statistical distribution of some spectral bands (Tholen 1984, Table VIII). These asteroids need to be reobserved in the future. About 20 Vesta-like objects have been detected. We separated them into V and a new group called J types. A complete discussion is given in section 3.6. We also found an unusual object 3628 which shows an ordinary chondrite-like spectrum. This asteroid is analyzed in detail in section 3.7. Asteroid 5145 shows an extraordinary spectrum similar to some organic materials and bears a new class Z (Mueller *et al.* 1992, Binzel 1992, and Davies *et al.* 1993). We did not include 5145 in our PCA. Fig. 3.15c plots the Tholen principal components versus the SMASS principal components for 70 objects observed by both ECAS and SMASS. It's clear that there is some linear correlation between the principal component scores in these two surveys. A few objects show significant difference between SMASS and ECAS measurements. Whether this is due to rotational variation effects or observing errors needs further observational investigations.

Table 3.7

Names and Types of 80 Meteorites Used in the PCA*

#	Meteorite Name	Type	Class	Group
m01	Abee	Chondrite	Enstatite	EH4
m02	Hvittis	Chondrite	Enstatite	EL6
m03	Pillistfer	Chondrite	Enstatite	EL6
m04	Khairpur	Chondrite	Enstatite	EL6
m05	Tieschitz	Chondrite	Ordinary	H3
m06	Ochansk	Chondrite	Ordinary	H4
m07	Castalia	Chondrite	Ordinary	H5
m08	Collescipoli	Chondrite	Ordinary	H5
m09	Pantar	Chondrite	Ordinary	H5
m10	Lancon	Chondrite	Ordinary	H6
m11	Bald Mountain	Chondrite	Ordinary	L4
m12	Cynthiana	Chondrite	Ordinary	L4
m13	Saratov	Chondrite	Ordinary	L4
m14	Homestead	Chondrite	Ordinary	L5
m15	Shelburne	Chondrite	Ordinary	L5
m16	Aumale	Chondrite	Ordinary	L6
m17	Bruderheim	Chondrite	Ordinary	L6
m18	Buschof	Chondrite	Ordinary	L6
m19	Cabeza de Mayo	Chondrite	Ordinary	L6
m20	Colby	Chondrite	Ordinary	L6
m21	Drake Creek	Chondrite	Ordinary	L6
m22	Girgenti	Chondrite	Ordinary	L6
m23	Leedey	Chondrite	Ordinary	L6
m24	Nerft	Chondrite	Ordinary	L6
m25	St. Michel	Chondrite	Ordinary	L6
m26	Tourinnes La Grosse	Chondrite	Ordinary	L6
m27	Zavid	Chondrite	Ordinary	L6
m28	Soko Banja	Chondrite	Ordinary	LL4
m29	Olivenza	Chondrite	Ordinary	LL5
m30	Jelica	Chondrite	Ordinary	LL6
m31	Manbhoom	Chondrite	Ordinary	LL6
m32	Vavilovka	Chondrite	Ordinary	LL6
m33	Paragould	Chondrite	Black	Black LL5
m34	Farmington	Chondrite	Black	Black L5
m35	Sevrukovo	Chondrite	Black	Black L5
m36	Casey County	Iron	Octahedrite	Iron
m37	Butler	Iron	Octahedrite	Iron
m38	Chulafinee	Iron	Octahedrite	Iron
m39	Babb's Mill	Iron	Ataxite	Iron
m40	Veramin	Stony-Iron	Mesosiderite	Stony-Iron
m41	Bereba	Achondrite	Eucrite	Eucrite
m42	Padvarninkai	Achondrite	Eucrite	Eucrite
m43	Sioux County	Achondrite	Eucrite	Eucrite
m44	Jonzac	Achondrite	Eucrite	Eucrite

Table 3.7 (continued)

#	Meteorite Name	Type	Class	Group
m45	Haraiya	Achondrite	Eucrite	Eucrite
m46	Pasamonte	Achondrite	Eucrite	Eucrite
m47	Juvinas	Achondrite	Eucrite	Eucrite
m48	Stannern	Achondrite	Eucrite	Eucrite
m49	Nobleboro	Achondrite	Eucrite	Eucrite
m50	Pavlovka	Achondrite	Howardite	Howardite
m51	Frankfort	Achondrite	Howardite	Howardite
m52	Le Teilleul	Achondrite	Howardite	Howardite
m53	Petersburg	Achondrite	Howardite	Howardite
m54	Johnstown	Achondrite	Diogenite	Diogenite
m55	Roda	Achondrite	Diogenite	Diogenite
m56	Tatahouine	Achondrite	Diogenite	Diogenite
m57	Shalka	Achondrite	Diogenite	Diogenite
m58	Nakhla	Achondrite	Nakhlite	Nakhlite
m59	Chassigny	Achondrite	Chassignite	Chassignite
m60	Orgueil	Chondrite	Carbonaceous	CI
m61	Cold Bokkeveld	Chondrite	Carbonaceous	CM
m62	Cold Bokkeveld	Chondrite	Carbonaceous	CM
m63	Cold Bokkeveld	Chondrite	Carbonaceous	CM
m64	Mighei	Chondrite	Carbonaceous	CM
m65	Murchison	Chondrite	Carbonaceous	CM
m66	Murray	Chondrite	Carbonaceous	CM
m67	Nogoya	Chondrite	Carbonaceous	CM
m68	Kainsaz	Chondrite	Carbonaceous	CO
m69	Ornans	Chondrite	Carbonaceous	CO
m70	Warrenton	Chondrite	Carbonaceous	CO
m71	Warrenton	Chondrite	Carbonaceous	CO
m72	Allende	Chondrite	Carbonaceous	CV
m73	Grosnaja	Chondrite	Carbonaceous	CV
m74	Grosnaja	Chondrite	Carbonaceous	CV
m75	Grosnaja	Chondrite	Carbonaceous	CV
m76	Leoville	Chondrite	Carbonaceous	CV
m77	Mokoia	Chondrite	Carbonaceous	CV
m78	Vigarano	Chondrite	Carbonaceous	CV
m79	Novo Urei	Achondrite	Ureilite	Ureilite
m80	Kakangari	Chondrite	Anomalous	Anomalous

* Spectral data from Gaffey (1976).

Table 3.8a

Summary of the Sub-Classification of S-Type Asteroids[a]

#	Sub S-Type[b]	BII/BI Ratio[b]	BI Center[b]	ANN Type[c]
b0003	S(IV)	0.6	0.928	Sp
b0004	V	2.3	0.933	V
b0006	S(IV)	0.778	0.923	Sp
b0007	S(IV)	0.59	0.96	S
b0011	S(IV)	0.69	0.937	S
b0012	S(II)?	0.22	1.055	So
b0015	S(III)	0.29	0.99	S
b0018	S(V)	1	0.96	S,SoT
b0020	S(VI)	1.45	0.923	Sp
b0025	S(IV)	0.6	0.935	So
b0026	S(II)	0.56	1.027	Sp
b0027	S(IV)	0.47	0.966	S
b0029	S(V)	1.4	0.942	Sp
b0032	S(IV)	1	0.93	Sp
b0033	S(IV)	0.8	0.915	Sp
b0037	S(V)	1.6	0.956	S
b0039	S(II)	0.49	1.029	S
b0040	S(VII)	2	0.928	Sp
b0042	S(I)	0	1.029	So
b0043	S(III)	0.2	1	Sp,S
b0057	S(VII)	2.8	0.92	Sp
b0063	S(II-III)	0.53	1	So
b0067	S(IV)	0.98	0.93	Sp
b0068	S(II)	0.3	1.045	S
b0080	S(IV)	0.6	0.945	So
b0082	S(VI)	1.35	0.927	Sp
b0101	S(V)	1.26	0.955	Sp
b0113	S(I)	0	1.05	So
b0115	S(III-IV)	0.41	0.923	Sp
b0258	S(V)	1	0.968	Sp,SSp
b0264	S(V)	1.15	0.947	Sp
b0354	S(I)	0.1	1.06	So
b0364	S(II)	0.47	1.04	So
b0389	S(V)	1.15	0.95	Sp
b0532	S(III)	0.25	0.975	S
b0584	S(IV)	0.5	0.995	So
b0674	S(VII)	2	0.925	Sp
b1036	S(VI-VII)	1.85	0.92	Sp
b1862	Q			

a: This table also includes objects 4 Vesta (b0004) and 1862 Apollo (b1862).

b: From Gaffey *et al.* (1993), see Table 3.8b. BI--1 μm band, BII--2 μm band.

c: From Howell *et al.* (1992).

Table 3.8b

General Mineralogy and Possible Meteorite Analogues of the S-Asteroid Subtypes

Subtype†	Mineralogy†	Possible Meteorite Analogs†
S(I)	Olivine >>> pyroxene (+/−FeNi metal)‡	Pallasites Pyroxene-poor ureilites Pyroxene-poor brachinites *Olivine-metal partial melt residues#*
S(II)	Olivine >> clinopyroxene (+/−FeNi metal)‡ (0.05 < cpx/(ol+cpx) < 0.20)	Cpx-bearing ureilites Cpx-bearing brachinites *Olivine-Cpx cumulates#* *Cpx-bearing pallasites#* *Highly metamorphosed C-type assemblages#*
S(III)	Olivine > clinopyroxene + orthopyroxene (+/−FeNi metal)‡	Cpx- and opx-bearing ureilites
S(IV)	Olivine + orthopyroxene (+/−FeNi metal)‡ (0.20 < opx/(ol+opx) < 0.50)	Opx-bearing ureilites Lodranites Winonites & IAB irons H,L,LL Chondrites
S(V)	Olivine ~ clinopyroxene (+/−FeNi metal)‡	Lodranites *Cpx-basalt intrusions into H-chondrite matrix#*
S(VI)	Olivine ~ orthopyroxene (+/−FeNi metal)‡	Siderophyres (Steinbach) Lodranites Winonites & IAB irons *Subsolidus-reduced chondrites#* *Anorthosites#*
S(VII)	Pyroxene > olivine (+/−FeNi metal)‡ (Orthopyroxene > clinopyroxene)	Mesosiderites Siderophyres (Steinbach) Lodranites Winonites & IAB irons *Cpx-poor mesosiderites#* *Subsolidus-reduced chondrites#* *Anorthosites#*

† Characterizations from Gaffey *et al.* (1993a, b).

‡ Metal Abundance is poorly constrained and appears to be highly variable.

Assemblages not presently identified in the meteorite collections.

Table 3.9

Variance Distribution among the Components (50 points data)

Component	Percent of Variance
1st	58.7%
2nd	28.6%
3rd	7.4%
4th	3.7%

Table 3.10

Correlation Matrix for the variables (50 points data)*

Wav. (Å)	4800	5200	5700	6200	6700	7200	7700	8200	8700	9200	9700
4800	1	0.93	-0.61	-0.70	-0.63	-0.57	-0.42	-0.13	0.08	0.15	0.16
5200	0.93	1	-0.48	-0.63	-0.55	-0.48	-0.34	-0.04	0.17	0.23	0.23
5700	-0.61	-0.48	1	0.83	0.73	0.67	0.58	0.35	0.14	0.05	0.03
6200	-0.70	-0.63	0.83	1	0.97	0.93	0.86	0.60	0.32	0.21	0.18
6700	-0.63	-0.55	0.73	0.97	1	0.99	0.93	0.66	0.37	0.26	0.25
7200	-0.57	-0.48	0.67	0.93	0.99	1	0.96	0.71	0.42	0.30	0.30
7700	-0.42	-0.34	0.58	0.86	0.93	0.96	1	0.86	0.61	0.50	0.50
8200	-0.13	-0.04	0.35	0.60	0.66	0.71	0.86	1	0.92	0.86	0.84
8700	0.08	0.17	0.14	0.32	0.37	0.42	0.61	0.92	1	0.96	0.96
9200	0.15	0.23	0.05	0.21	0.26	0.30	0.50	0.86	0.96	1	0.99
9700	0.16	0.23	0.03	0.18	0.25	0.30	0.50	0.84	0.96	0.99	1

* Due to the large matrix size (50x50), this table displays the results for only 11 variables (wavelengths from 4800 Å to 9700 Å). But the correlation is still clear. The pair of blue wavelengths show high degree of correlation; so do the pair of red or infrared wavelengths. However, The pair of variables involving one blue and one red wavelengths show almost no correlation.

Table 3.11

Scores on the first four principal Component Axes for Asteroids, Meteorites, and Sub S-classes and Assigned Classes for Asteroids (50 points data)

Objects	PC1	PC2	PC3	PC4	Old	New
Asteroids						
3	-0.83	0.657	-0.64	-0.418	S	
4	6.522	-3.001	3.359	-0.926	V	
6	0.719	-0.55	-0.951	0.213	S	
7	-2.083	0.353	-0.524	-0.759	S	
8	-5.618	-0.425	-0.276	1.116	S	
10	10.664	0.475	0.06	1.273	C	
14	0.397	-0.235	1.379	1.746	S	
18	-3.632	0.645	-1.122	0.339	S	
22	3.087	4.288	1.965	-0.615	M	
25	-4.941	-0.428	-1.402	-0.605	S	
28	-2.367	0.643	-0.784	-0.158	S	
29	-1.395	1.786	-0.553	0.321	S	
32	-2.197	-0.135	-0.451	0.118	S	
36	8.65	3.749	-0.755	0.284	C	
38	8.696	3.632	1.965	1.908	C	
39	-3.126	0.081	0.435	0.444	S	
42	-3.536	0.903	0.514	0.974	S	
43	-0.479	-0.921	-0.28	0.143	S	
53	9.653	4.654	0.324	-0.374	XC	C*
54	8.201	3.976	-0.28	-0.076	C	
55	4.758	3.835	-0.502	0.262	M	
61	-1.571	0.243	-0.608	-0.121	S	
68	-1.456	-0.167	-0.719	0.135	S	
71	0.729	1.259	-1.656	0.956	S	
72	-4.256	3.91	-1.38	0.57	TDG	S*
73	-5.395	0.31	5.333	2.595	S	
82	1.221	-0.13	-0.998	-0.508	S	
86	8.637	2.872	0.004	-0.268	C	
88	11.052	3.514	2.509	-1.047	C	
111	8.344	3.58	-0.529	0.233	C	
116	-0.467	0.518	-0.029	0.307	S	
124	-2.507	-0.012	-0.71	0.217	S	
126	-4.491	-0.159	0.926	0.488	S	
128	5.615	2.917	-0.228	0.401	C	
131	4.44	2.107	-0.065	-0.119	SU	C*
134	9.434	3.269	-0.334	0.305	C	
137	8.191	4.12	-1.194	-0.255	C	
138	-1.191	-0.117	-1.143	-0.017	S	
149	-4.552	-0.414	-0.604	0.294	S	
157	9.202	3.2	1.903	0.518		C
158	-0.459	0.953	1.306	0.132	S	
167	1.684	0.158	1.212	0.209	S	

Table 3.11 (continued)

Objects	PC1	PC2	PC3	PC4	Old	New
169	-6.989	1.376	-1.385	-0.253	S	
185	8.999	2.3	-1.277	0.533	C	
186	-0.343	0.623	-0.949	0.845	S	
196	-4.886	2.111	2.372	0.432	S	
204	-1.501	0.014	-0.054	0.483	S	
211	9.715	3.645	-0.142	0.777	C	
218	-2.238	0.907	1.709	0.773	S	
221	-0.007	1.728	0.859	0.079	S	
230	-2.061	1.179	0.293	-0.299	S	
231	3.9	3.399	-0.099	0.199		X
234	-6.399	3.067	0.447	1.073	S	
235	-4.088	2.985	-2.721	1.006	S	
237	-2.563	-1.083	1.63	-0.187	S	
239	-2.258	3.068	-0.802	0.695		S
243	-2.087	0.695	0.408	0.253	S	
245	-2.88	-0.26	-0.384	-0.169	S	
248	2.496	4.051	1.234	1.21		X
256	2.936	3.827	-0.104	0.049		X
287	-5.947	1.171	0.055	-0.627	S	
289	-8.784	-4.235	-0.58	0.849	A	
290	-3.646	-0.396	-0.215	-0.111		S
291	-2.675	-1.394	6.265	2.705		S
292	-5.206	-0.269	-0.645	0.276		S
297	-4.012	2.342	-0.755	2.434		S
314	7.88	3.1	0.572	-0.142		C
319	3.428	4.504	-0.1	-0.221		X
339	-0.121	2.575	-0.039	-0.156	S	
345	7.384	2.989	-0.844	-0.029	C	
346	-0.646	-0.71	-0.561	0.589	S	
349	2.917	-4.011	0.674	-0.365	R	
350	6.662	4.632	0.414	0.033	C	
354	-7.6	0.313	0.137	0.489	S	
371	-5.893	-2.325	0.525	-1.471	QSV	S*
374	-2.917	0.43	-0.303	-0.078	S	
384	-1.317	0.998	0.11	-0.154	S	
402	-1.743	2.919	-0.251	0.688	S	
416	-5.323	0.813	-1.13	0.14	S	
430	8.949	2.32	-0.744	0.387		C
441	0.843	3.152	-0.703	0.601	M	
446	-11.299	-4.107	-0.09	0.914	A	
456	-3.045	0.687	3.165	0.787		S
467	-0.071	5.95	-0.711	0.521		T
470	-4.774	0.393	-0.173	0.232	S	
471	-0.211	0.285	-0.59	-0.678	S	
474	4.469	3.554	0.663	-0.417		X
477	-2.235	0.716	-0.765	0.068	S	

Table 3.11 (continued)

Objects	PC1	PC2	PC3	PC4	Old	New
480	-2.468	-1.476	2.42	1.307	S	
481	6.47	2.714	-1.332	1.452	C	
495	10.292	2.844	0.938	-0.241		C
509	-1.707	0.274	-0.641	0.083	S	
511	7.164	2.66	1.213	0.646	C	
512	-7.226	-1.051	-0.309	-0.682	S	
518	-0.042	-1.307	-0.641	-0.644		S
519	1.108	-0.25	-1.55	0.682	S	
529	-4.647	1.947	3.679	0.535	S	
541	9.54	3.353	6.156	2.184		C
550	-5.806	0.169	0.709	0.14	S	
563	-4.198	-0.463	-1.925	-0.21	S	
582	-6.459	0.065	-0.195	0.871	S	
599	-3.903	2.968	1.442	1.673	S	
631	-3.529	-0.048	1.876	1.07	S	
639	-1.066	2.749	-0.386	0.239	S	
653	-4.152	3.102	1.209	1.036	S	
675	-3.974	0.08	-0.032	0.547	S	
683	7.359	2.688	0.573	0.374		C
702	7.28	3.119	-0.375	-0.14	C	
720	3.501	0.534	2.263	0.222	S	
722	-7.81	-0.601	1.884	-0.526		S
724	14.295	3.095	-12.893	-4.778		C
732	-6.704	5.605	-4.216	0.717		D
737	-1.42	0.624	-0.01	-0.047	S	
752	5.697	5.038	1.082	0.061		X
774	-2.555	0.116	-0.558	0.54		S
787	-1.562	-1.024	-1.844	-0.261		S
788	9.715	3.198	1.536	0.409		C
803	-1.327	5.773	0.153	0.799		T
808	-0.471	-0.437	0.254	-0.39		S
811	1.172	0.736	3.085	1.019	S	
813	-7.732	0.246	-1.087	0.006		S
851	-3.103	-0.497	1.036	0.563	S	
863	-15.559	-2.714	0.721	-0.097	A	
879	-3.739	0.971	2.889	1.19		S
900	-4.93	3.468	-1.665	0.305		S
915	-7.863	0.009	1.419	-1.452		S
918	-3.743	-1.293	-0.946	0.321		S
951	-5.262	-0.13	-0.934	0.146	S	
1063	0.626	3.035	-1.892	1.091		X
1071	1.136	3.492	0.602	0.75		X
1084	8.364	3.862	2.525	1.4		C
1110	-3.331	0.415	-0.508	-0.134		S
1143	-7.261	7.146	0.279	-0.154	D	
1144	-3.908	4.516	0.212	1.34	D	T*

Table 3.11 (continued)

Objects	PC1	PC2	PC3	PC4	Old	New
1145	-1.111	5.249	0.873	-1.228		T
1165	6.06	3.12	-1.909	-0.317		C
1166	-3.195	0.841	-0.762	0.457		S
1198	-3.686	1.848	-1.413	-0.514		S
1257	10.216	3.94	2.974	-1.512		C
1264	8.226	2.798	-0.199	0.074		C
1273	1.952	-5.378	2.36	-1.425		V
1279	5.236	1.94	0.544	0.603		C
1289	0.791	2.199	-2.528	-1.283	S	
1302	12.071	1.997	3.223	1.44		C
1325	-3.869	0.855	1.966	-0.091		S
1358	9.11	3.133	1.583	0.073		C
1375	-3.193	0.527	0.749	-0.508		S
1379	0.774	1.5	1.63	0.769		S
1393	-8.904	2.805	0.843	-1.001		S
1451	-0.743	-0.676	-0.958	-0.695		S
1463	4.042	3.436	-1.942	0.096		X
1471	-4.869	6.534	-1.871	0.383		D
1478	-11.885	3.743	0.359	-0.752		S
1480	-0.28	0.087	-0.601	-0.397		S
1501	-2.511	-0.065	-1.037	-0.681		S
1518	-8.182	0.389	1.245	-0.35		S
1534	7.207	3.798	-0.752	0.838		C
1577	-5.145	-0.049	1.892	0.086		S
1584	-2.006	-0.224	-0.914	-0.094	S	
1607	-0.877	-0.627	-0.086	-0.471		S
1626	-4.545	-0.738	1.663	0.141		S
1628	4.087	3.632	-1.5	0.26		X
1646	5.982	3.249	0.368	-0.272		C
1651	-5.728	-0.572	0.662	0.311		S
1653	7.778	1.226	0.407	0.072		C
1658	-6.039	1.634	1.287	-0.817	AS	S*
1679	4.315	2.85	-0.356	0.645		X
1697	1.05	5.332	-1.454	0.621		T
1712	4.966	3.934	2.013	1.255		X
1722	-3.374	-0.018	-0.235	-0.434		S
1725	1.749	1.117	1.298	-0.008		S
1743	6.517	1.685	2.898	0.682		C
1749	-5.331	6.395	-1.27	-0.067		D
1772	-7.011	1.475	1.612	0.143		S
1781	0.369	3.341	0.025	0.599		X
1807	-6.156	-0.426	1.257	-0.424		S
1854	-1.821	0.816	-0.374	-0.917		S
1892	-7.607	3.385	0.086	-1.238		S
1906	-5.161	-0.808	2.69	-2.328		V
1907	0.282	0.032	1.01	-0.485		S

Table 3.11 (continued)

Objects	PC1	PC2	PC3	PC4	Old	New
1929	3.051	-6.226	2.857	-1.033		V
1933	-2.712	-4.022	2.808	-0.657		V
1934	-3.934	-0.271	1.776	-1.114		S
1967	-3.209	-0.751	-0.082	-0.522		S
1995	3.36	4.759	1.274	-1.111		X
2011	-2.564	-6.151	0.675	-1.296		J
2014	-1.57	-0.668	1.116	0.601		S
2017	-8.448	0.713	1.051	-0.531		S
2024	-6.467	0.822	-0.091	-1.428		S
2060	8.295	3.226	0.847	0.239	B	
2070	-5.754	-1.847	1.752	1.137		S
2074	-6.83	-1.1	0.002	-1.099		S
2078	1.35	-1.352	-0.113	0.019		S
2091	5.022	2.617	-0.061	0.328		C
2098	1.44	5.1	-0.416	-0.996		T
2105	-6.605	1.217	-3.116	1.088		S
2107	-1.847	-0.053	0.431	-0.364		S
2113	1.081	-5.163	0.698	-2.491		V
2119	-6.991	1.236	0.675	-1.257		S
2128	3.799	3.546	4.628	2.021		X
2130	-5.989	-0.245	-0.35	-0.697		S
2140	4.757	3.221	-0.825	-0.285		X
2143	-6.181	-2.349	-4.773	-4.089		S
2149	-4.759	2.358	1.061	-0.746		S
2159	-6.754	-0.715	0.682	-0.253		S
2174	-9.076	2.39	2.731	-0.85		S
2204	3.882	3.452	-1.605	-0.289		X
2215	-1.927	-0.077	-3.697	-1.947		S
2253	-4.835	0.02	0.48	-0.309		S
2259	7.358	3.556	0.13	0.681		C
2299	-2.713	0.779	1.199	-0.599		S
2327	-12.331	2.34	0.697	0.563		S
2365	-2.221	-0.04	0.37	-0.317		S
2403	0.822	0.469	-1.922	-1.243		S
2420	-2.584	-0.23	-1.678	-0.966		S
2440	-4.661	0.136	-1.643	0.416		S
2442	0.682	-9.927	-1.768	-2.489		J
2444	2.501	2.591	-0.488	1.334		X
2503	9.035	3.153	1.845	-0.631		C
2538	-5.728	1.036	2.306	-0.576		S
2558	-7.137	2.634	0.638	-0.684		S
2590	-1.399	-1.65	1.431	-1.237		V
2599	-3.454	0.418	-0.103	0.657		S
2645	4.369	2.331	-6.353	-2.285		X
2728	9.323	3.625	3.302	0.065		C
2775	-2.834	1.461	-0.057	-1.042		S

Table 3.11 (continued)

Objects	PC1	PC2	PC3	PC4	Old	New
2790	-6.594	0.222	1.534	0.386		S
2908	6.779	3.05	3.257	0.18		C
2920	-8.376	7.134	3.952	1.511		D
2923	6.516	3.767	4.97	1.853		C
2946	8.651	6.638	-0.357	-2.425		C
2965	-3.893	-0.745	1.462	-2.354		S
2966	-1.469	1.283	4.664	0.215		S
3109	3.332	4.095	0.204	-1.172		X
3153	3.826	-3.854	1.515	-2.166		V
3155	-5.874	-7.916	4.022	-2.705		J
3158	1.402	0.638	0.056	-0.661		S
3167	-3.113	1.422	-0.559	0.104		S
3220	-4.458	-0.336	0.872	-0.434		S
3231	9.79	3.39	-1.101	-0.796		C
3268	-0.511	-1.22	1.255	-2.848		V
3285	-10.608	2.224	1.074	-1.081		S
3321	0.241	-1.395	-1.583	-0.47		S
3332	-7.923	-0.009	-0.999	0.709		S
3354	-2.402	1.079	0.997	-1.411		S
3381	3.847	2.756	-0.54	-0.884		X
3431	9.224	3.035	1.196	0.629		C
3494	-1.705	-2.587	-0.018	-2.891		V
3501	-6.984	7.18	-1.597	0.572		D
3523	-1.68	0.463	2.751	0.99		S
3528	-6.192	2.547	3.719	-0.034		S
3559	8.976	3.497	1.367	0.009		C
3578	6.223	3.496	1.463	0.657		C
3586	0.487	1.546	-4.034	-0.22		S
3628	9.85	-2.958	3.077	-2.38		O
3657	0.276	-8.144	2.293	-0.562		J
3665	3.632	4.2	-2.693	-0.786		X
3674	-2.151	-1.116	0.55	0.511		S
3677	-5.899	-0.891	-0.525	0.639		S
3740	2.974	2.858	4.759	1.337		X
3748	-7.744	0.234	5.512	1.029		S
3759	7.335	3.453	-1.916	-0.49		C
3760	-4.962	2.463	-0.987	-1.312		S
3792	-0.909	1.31	2.152	-1.75		S
3869	-1.766	-6.193	4.582	-1.653		J
3915	9.566	3.884	-2.922	-0.75		C
3935	-1.998	1.071	0.055	-1.878		S
3944	-0.498	-3.567	0.883	-2.031		V
3963	-0.983	1.471	0.282	-0.245		S
3968	0.917	-2.902	0.805	-1.941		V
3999	7.887	3.221	-0.13	-0.335		C
4002	0.051	-0.276	-0.959	0.314		S

Table 3.11 (continued)

Objects	PC1	PC2	PC3	PC4	Old	New
4005	-2.975	-6.811	4.441	-2.652		J
4006	2.605	4.696	-1.515	-0.08		X
4025	-9.074	-1.375	0.487	0.808		S
4031	3.618	3.31	0.281	0.498		X
4038	-4.807	-0.331	1.962	-2.82		V
4062	-9.136	-2.354	-0.789	0.524		S
4085	-4.921	0.407	2.221	-0.217		S
4104	-3.547	2.125	2.151	-0.474		S
4145	-6.384	0.651	-0.344	-2.716		S
4147	2.243	-2.129	1.725	-1.714		V
4156	7.68	2.884	-2.18	0.175		C
4159	-6.867	2.24	2.149	-0.482		S
4165	0.913	3.105	-2.25	-0.26		X
4179	0.075	-1.276	-0.627	-0.2		S
4215	-1.039	-5.223	2.94	-2.419		J
4219	13.439	3.777	3.216	0.211		C
4282	7.221	4.112	1.675	-0.289		C
4353	2.031	3.173	0.446	0.263		X
4370	-1.865	0	-0.836	-0.245		S
4373	-0.282	-0.378	-1.602	-1.273		S
4376	-2.925	-1.265	-0.199	-0.706		S
4440	3.011	2.642	-1.028	0.33		X
4510	-1.899	0.885	-0.288	-0.745		S
4546	0.243	-2.461	1.404	-1.488		V
4562	10.189	3.573	2.573	-0.521		C
4606	-6.772	0.444	2.185	-1.789		S
4635	7.017	2	-3.085	-0.53		C
4640	-8.797	1.184	-0.157	-1.213		S
4673	-4.328	1.435	4.21	-0.351		S
4761	-0.394	1.24	-0.517	-0.669		S
4939	-8.095	1.508	1.955	-1.052		S
4948	-7.957	0.514	2.521	-0.788		S
4956	1.918	4.582	-1.257	-1.498		X
5065	7.716	4.972	0.45	-0.893		C
5118	-0.175	-1.184	-1.018	0.039		S
1991VK	-6.562	-0.658	5.867	-0.024		S
1991VL	-1.196	-2.12	1.337	-1.364		V
1991WA	0.324	-0.032	-0.216	-1.71		S
1991XB	2.096	1.755	-0.795	-1.331		S
1992CC1	0.985	1.208	-3.597	-2.372		S
1992NA	8.796	2.55	0.784	0.332		C
1992TC	4.756	2.871	-3.807	-0.64		X
1992UB	5.367	3.233	-3.166	-1.566		X

Table 3.11 (continued)

Objects	PC1	PC2	PC3	PC4
Meteorites				
m01	0.918	4.168	0.494	0.371
m02	-2.363	-0.065	-0.698	2.157
m03	-1.515	0.006	-0.585	2.503
m04	-6.49	-0.395	-0.067	3.046
m05	1.77	-2.156	-0.151	1.672
m06	5.419	-2.015	-0.163	-0.262
m07	-0.394	-4.387	-0.034	1.595
m08	4.787	-2.725	0.799	0.076
m09	1.783	-2.754	-0.038	1.337
m10	4.135	-4.886	0.376	0.944
m11	2.124	-3.158	-0.223	0.976
m12	-0.274	-4.118	0.228	0.266
m13	0.142	-1.991	-0.328	0.936
m14	-3.143	-5.223	-0.009	1.178
m15	-0.806	-7.185	0.535	0.568
m16	5.55	-5.982	0	0.67
m17	6.997	-3.99	0.369	0.083
m18	5.715	-8.526	0.263	0.775
m19	9.225	-7.014	0.461	0.223
m20	4.097	-5.314	0.355	0.842
m21	0.651	-11.593	0.775	0.901
m22	2.247	-8.739	-0.067	1.448
m23	2.4	-5.446	0.467	1.06
m24	3.847	-6.879	0.587	0.597
m25	1.239	-9.943	0.27	0.707
m26	5.413	-7.338	0.252	0.594
m27	5.519	-5.123	0.185	0.387
m28	-0.69	-5.497	-0.228	1.113
m29	2.995	-4.663	0.128	0.247
m30	3.309	-4.166	-0.621	0.989
m31	5.888	-7.993	0.152	1.89
m32	6.08	-5.941	0.354	0.803
m33	1.808	1.664	-1.139	0.301
m34	6.182	-0.413	0.751	0.303
m35	4.467	0.916	-0.348	0.6
m36	-2.941	3.791	-0.861	0.994
m37	-5.339	3.29	-1.231	1.551
m38	-2.168	2.922	-0.781	1.318
m39	0.546	2.049	-0.846	1.033
m40	-12.283	3.224	-0.336	0.612
m41	6.624	-5.844	0.563	-1.548
m42	7.723	-8.878	0.827	-2.266
m43	6.808	-3.243	0.727	-1.98
m44	4.808	-8.865	1.467	-3.451
m45	1.799	-5.389	1.367	-3.244

Table 3.11 (continued)

Objects	PC1	PC2	PC3	PC4
m46	-0.18	-5.824	1.053	-2.776
m47	3.189	-8.755	0.352	-3.393
m48	5.314	-3.004	1.042	-2.952
m49	1.309	-6.806	1.494	-3.01
m50	8.727	-9.112	0.748	-1.959
m51	9.482	-13.71	-0.179	-1.531
m52	6.181	-8.743	1.494	-2.425
m53	3.617	-6.989	0.732	-2.774
m54	5.329	-21.091	-3.875	1.566
m55	9.003	-12.126	-0.032	-1.276
m56	13.541	-18.788	-2.955	1.566
m57	10.553	-10.658	1.223	-2.266
m58	-8.884	-15.326	-3.798	7.753
m59	2.251	-19.496	-0.939	6.923
m60	-8.916	-2.215	-2.482	4.63
m61	1.894	-0.29	-1.777	3.056
m62	9.183	-0.084	-1.794	2.735
m63	10.406	0.119	-1.931	2.781
m64	6.987	1.184	-2.303	2.714
m65	7.357	0.794	-2.303	2.826
m66	3.426	0.672	-1.707	2.494
m67	9.297	0.704	-2.35	3.377
m68	0.532	-0.44	-0.009	1.717
m69	0.843	0.436	-0.454	0.92
m70	1.611	-0.204	-0.672	0.903
m71	2.951	-0.686	0.042	0.785
m72	1.429	0.705	-0.721	1.167
m73	-0.797	-1.101	-1.447	2.703
m74	10.278	0.143	-2.159	1.348
m75	7.685	0.095	-0.839	1.628
m76	-5.838	-2.747	-1.12	3.6
m77	-0.521	1.779	0.315	0.795
m78	0.559	-0.864	-0.792	2.384
m79	1.966	-3.748	-0.445	3.184
m80	-7.212	-4.585	-1.693	4.414
Sub S-classes				
b0003	-1.864	-0.851	-0.41	-0.886
b0004	5.177	-3.816	1.4	-1.23
b0006	-0.637	0.249	0.145	-0.391
b0007	-5.7	-0.741	-0.085	-0.674
b0011	-2.044	-0.919	-2.223	0.066
b0012	-5.809	2.872	-1.599	0.211
b0015	-3.434	0.693	-0.508	0.044
b0018	-3.771	0.99	-0.909	-0.01

Table 3.11 (continued)

Objects	PC1	PC2	PC3	PC4
b0020	-1.087	-0.071	-1.241	-0.294
b0025	-5.636	0.064	-0.658	-0.884
b0026	-4.364	0.884	-3.181	-1.159
b0027	-3.674	-0.715	-4.502	-2.273
b0029	-2.777	1.26	-1.334	-0.687
b0032	-5.396	-0.903	-2.099	-0.999
b0033	-0.592	-0.634	-0.537	1.211
b0037	-2.116	-0.18	-1.455	0.054
b0039	-5.128	0.107	-1.275	-0.215
b0040	-4.711	-0.554	-3.737	-0.958
b0042	-5.08	0.375	-1.909	-0.137
b0043	-1.037	-1.648	-2.449	-1.082
b0057	-4.267	-0.358	-0.203	0.586
b0063	-8.948	-0.574	-2.007	-1.202
b0067	-4.362	-2.042	-0.639	1.845
b0068	-3.017	-1.465	-3.054	0.178
b0080	-4.321	-1.274	-4.392	0.817
b0082	-3.243	-3.05	-4.615	0.208
b0101	-5.128	-0.864	-0.659	1.373
b0113	-3.466	-0.771	-3.232	-0.207
b0115	1.103	-2.808	-2.736	0.467
b0258	-3.026	-0.049	-3.891	-2.262
b0264	-5.457	-0.47	-1.48	-1.503
b0354	-7.665	-1.123	-2.826	-0.319
b0364	-4.055	-1.059	-0.026	1.321
b0389	-1.58	1.861	-1.882	-1.305
b0532	-0.743	-0.866	-4.384	-0.468
b0584	-3.875	-1.48	-2.227	-0.442
b0674	-2.126	-0.536	-6.166	-1.325
b1036	-2.64	-1.307	-2.807	0.393
b1862	1.411	-3.546	-0.777	0.636

"Old" means the asteroid type was defined by Tholen (1984) or from UBV photometry. "New" means the asteroid was a new SMASS target, except for *s meaning the classified types are different from that assigned by ECAS or UBV photometry. New types O and J will be discussed in the following sections.

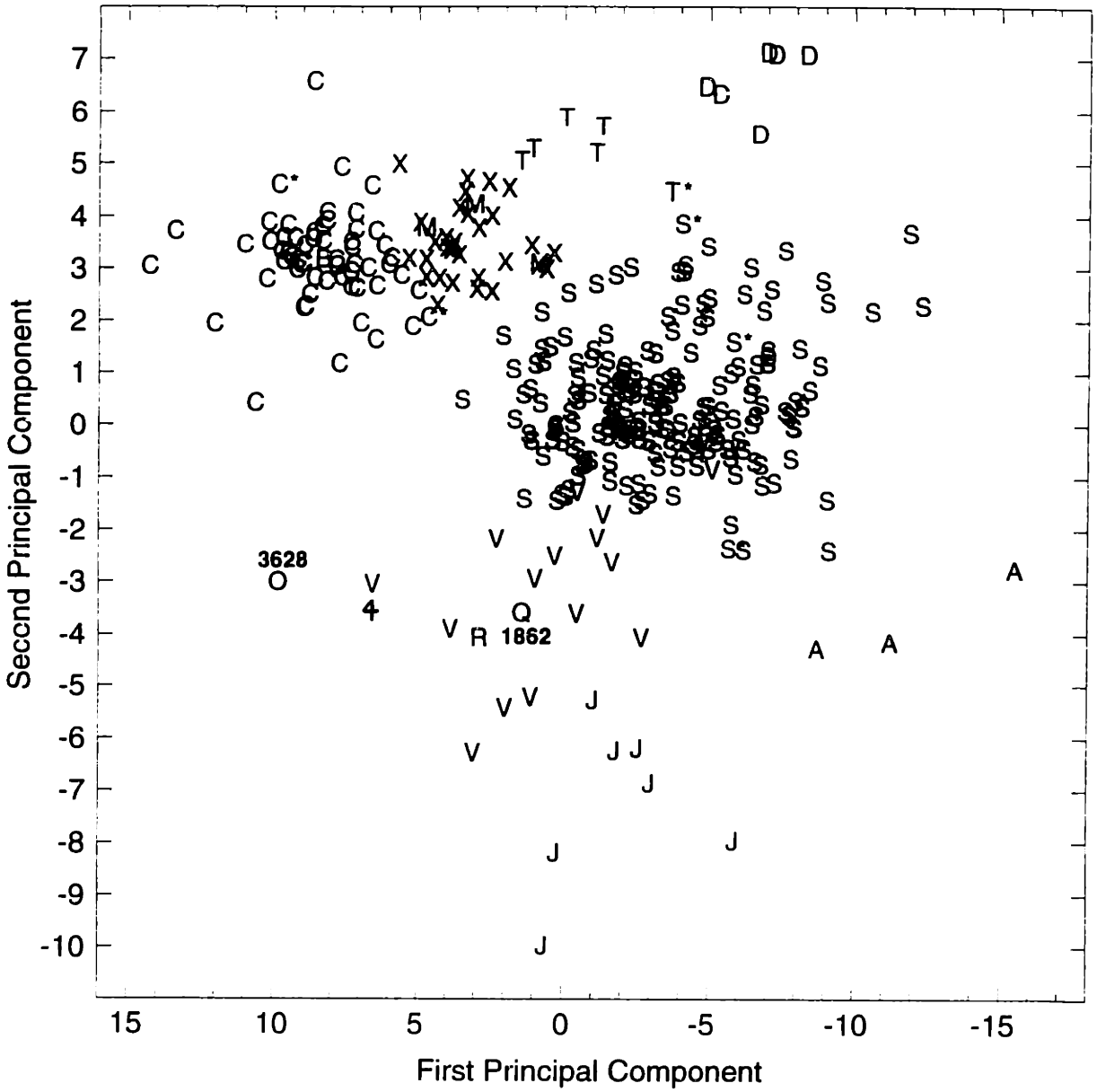

Fig. 3.13a. Domains of various asteroid taxonomic classes in the principal component space (PC1 vs PC2) for 315 objects over 50 wavelength bands (4800-9700 Å). Note three asteroids (1906, 3268, and 4038) showing relatively strong absorption features around 9000 Å (similar to Vesta) are not separated from the S-types. (However, see Fig. 3.13b). * means the classified types are different from that assigned by ECAS, or UBV photometry. Asteroids located on the lower-right region show extremely strong 1 μm absorption features (much lower than Vesta's). We proposed a new class J for these objects. The spectrum and PCA location for asteroid 3628 differs sufficiently from the Q-class (the data for Q-type asteroid 1862 Apollo are from ECAS) leading us to propose a new class: O. See detailed discussions about J and O classes in section 3.6 and 3.7, respectively.

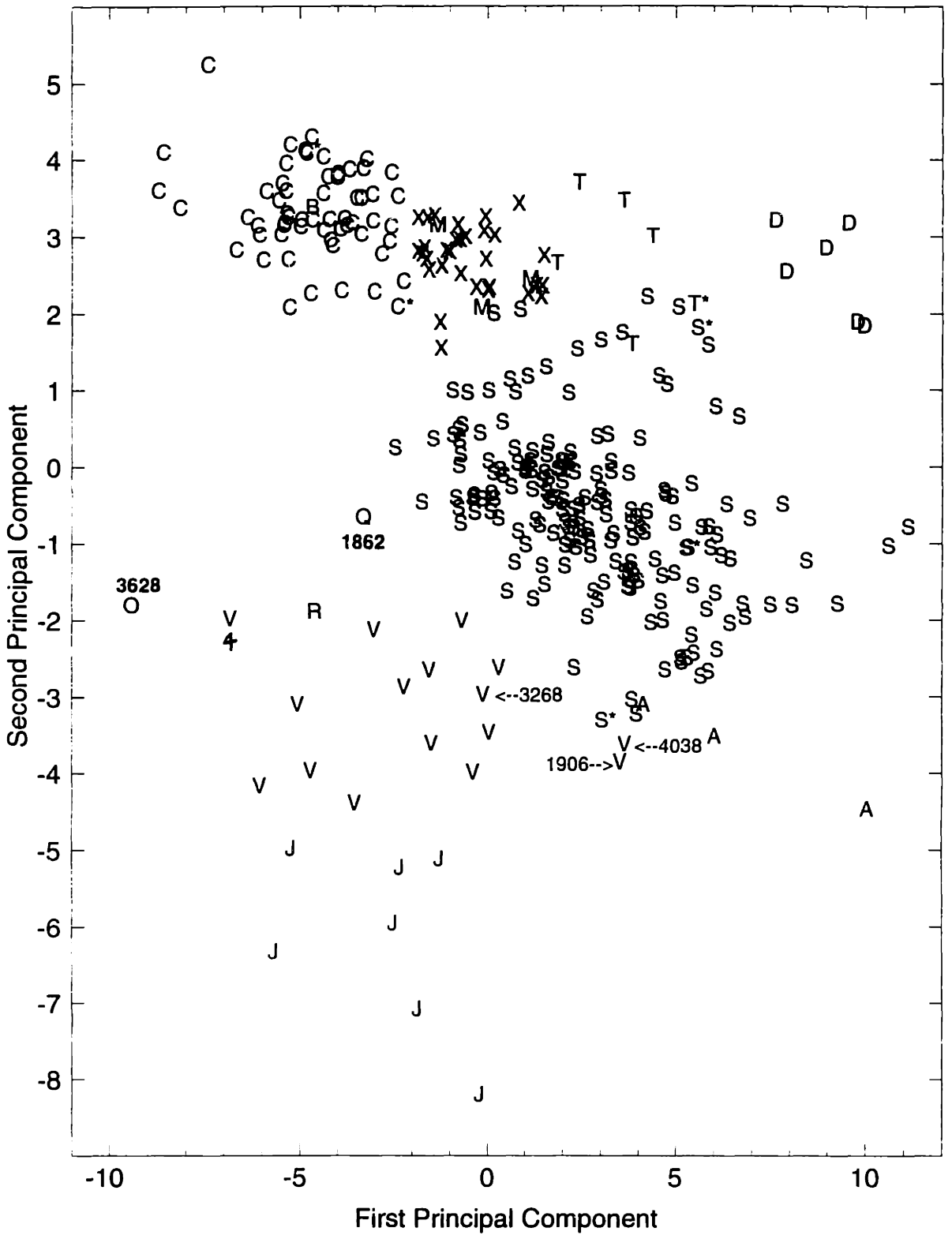

Fig. 3.13b. Domains of various asteroid taxonomic classes in the principal component space for 315 objects over 28 wavelength bands (7000-9700 Å). Note now asteroids 1906, 3268, and 4038 (arrows) are completely separated from the S-types. Therefore, we assigned V types for these asteroids (see Fig. 3.13a).

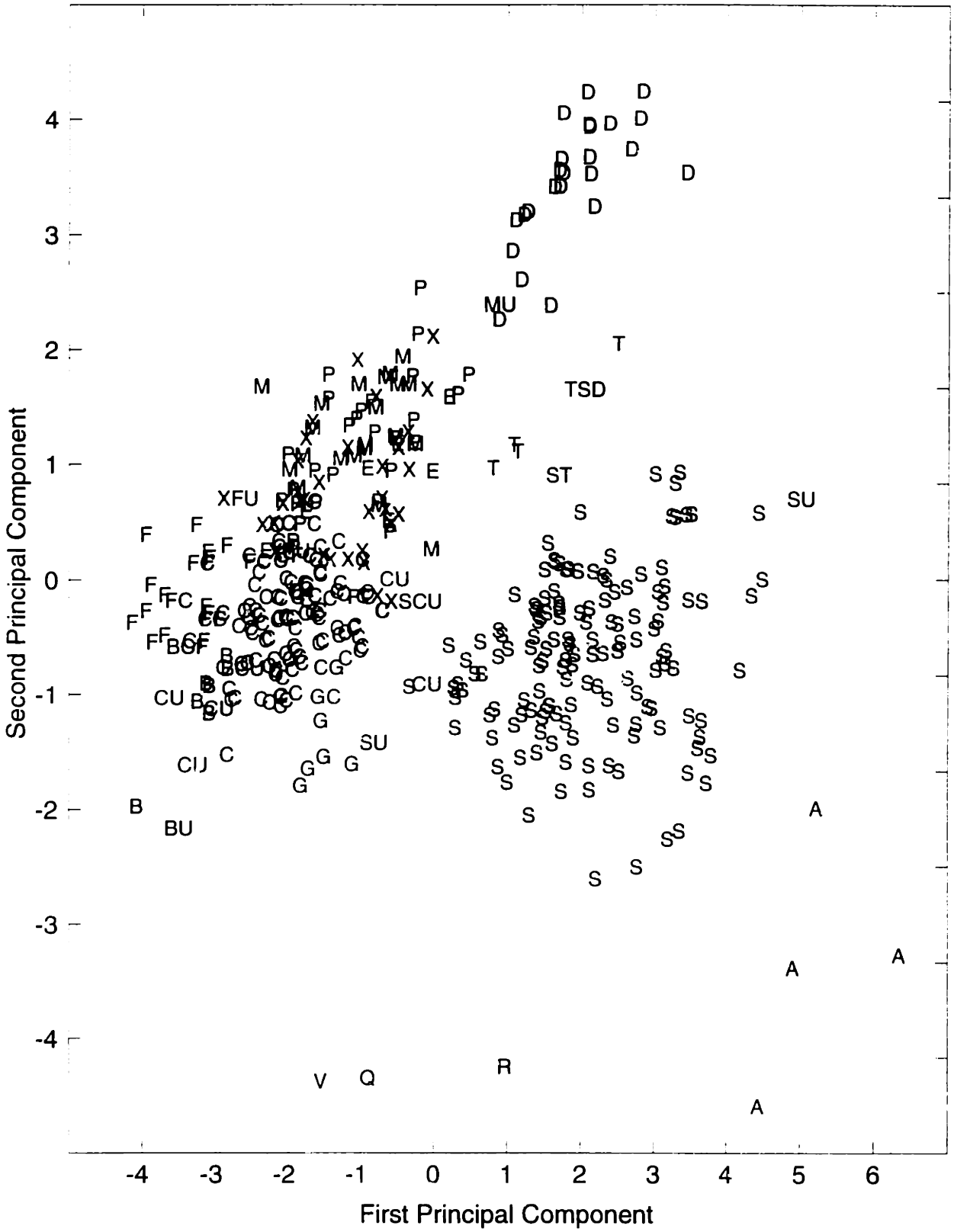

Fig. 3.13c. Domains of asteroid classes from the Eight-Color Asteroid Survey as defined by the principal component analysis performed by Tholen (1984).

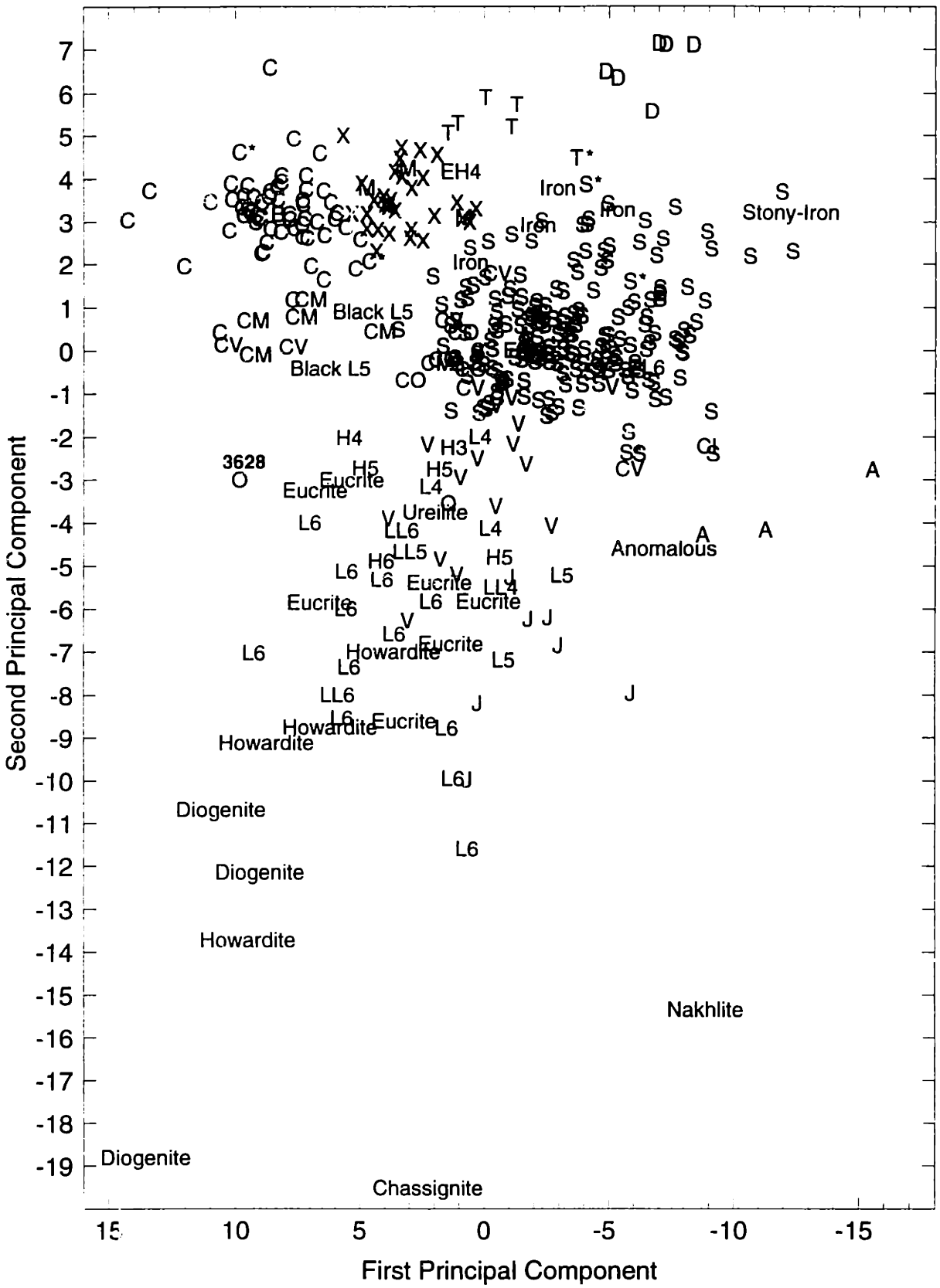

Fig. 3.14a. Domains of 315 asteroid taxonomic classes and 80 meteorite types in the principal component space (50 wavelength band (4800-9700 Å) data).

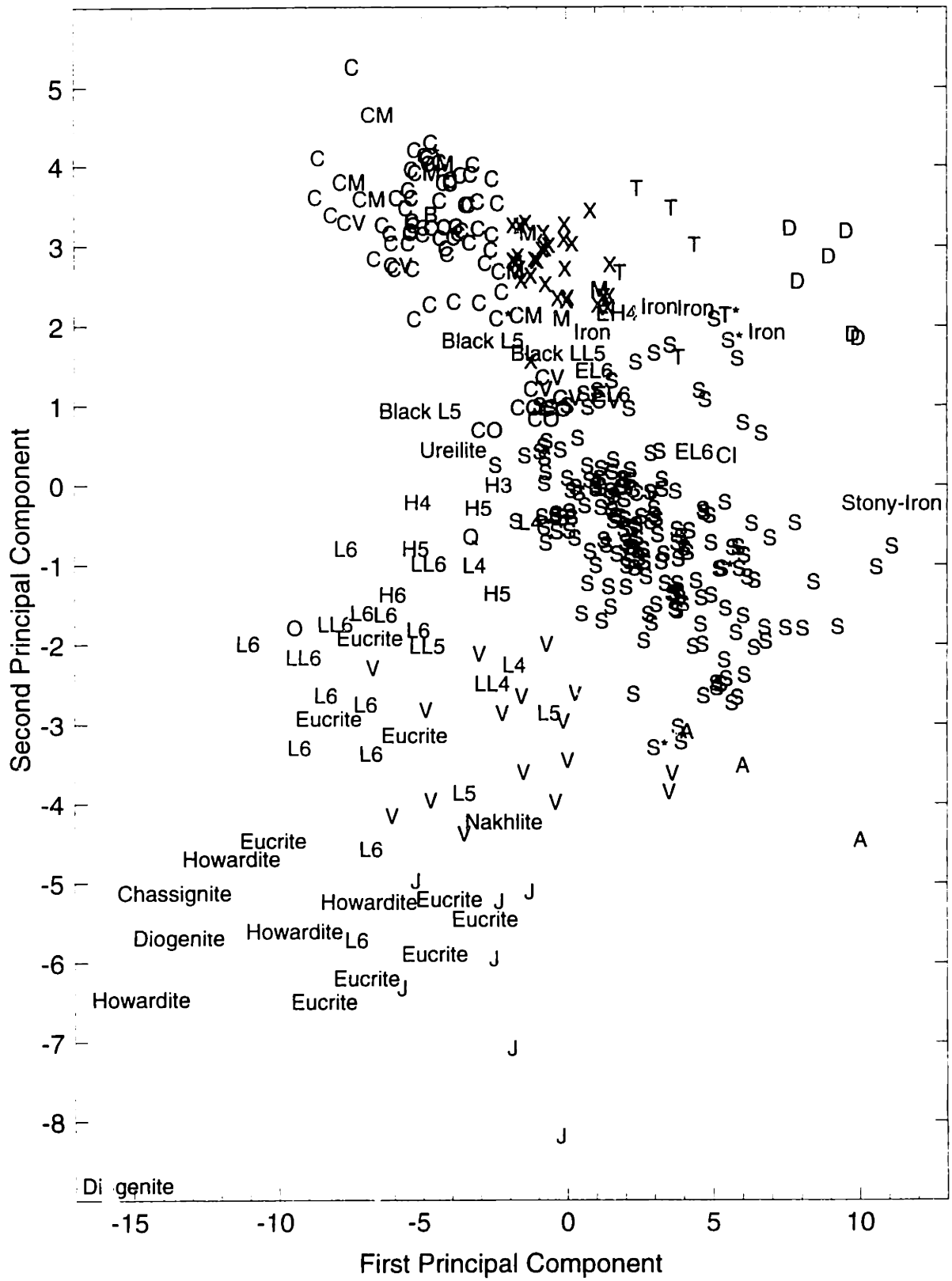

Fig. 3.14b. Domains of 315 asteroid taxonomic classes and 80 meteorite types in the principal component space (28 wavelength band (7000-9700 Å) data).

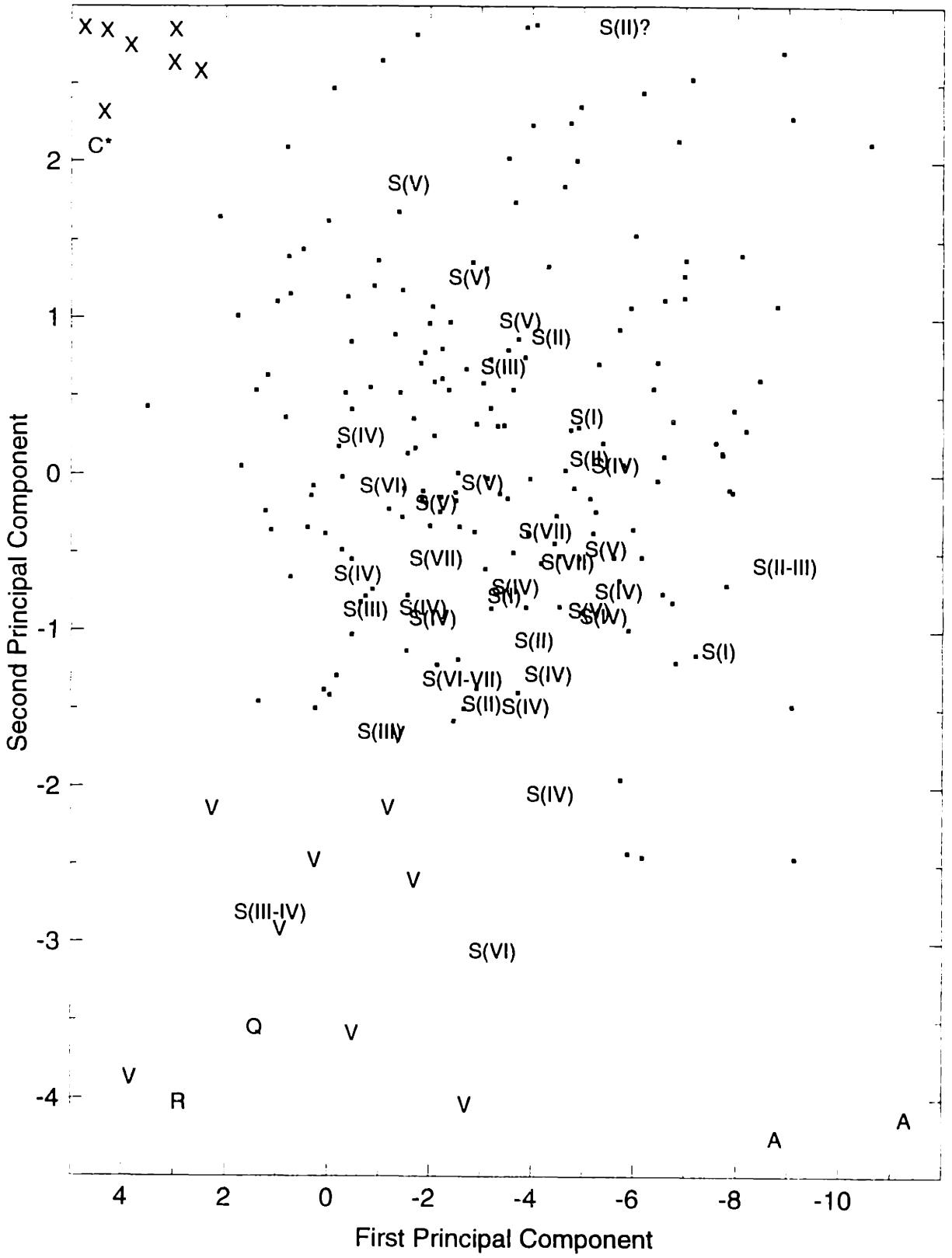

Fig. 3.15a. Domains of SMASS S-classes and Gaffey *et al*'s sub S-types in the principal component space (50 wavelength band data, SMASS S-asteroids are represented as points). See discussions below.

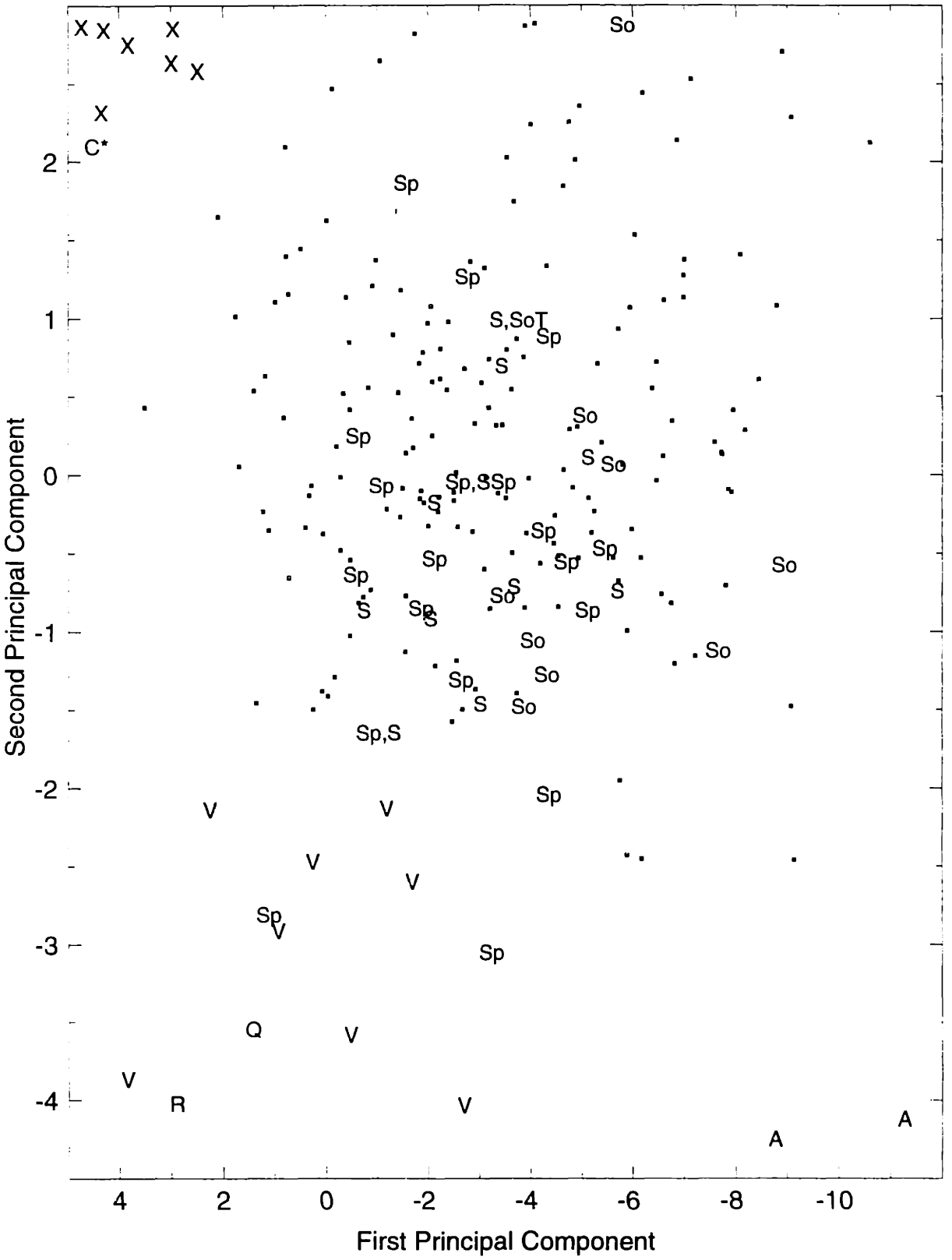

Fig. 3.15b. Domains of SMASS S-classes and Howell *et al*'s sub S-types in the principal component space (50 wavelength band data, SMASS S-asteroids are represented as points). See discussions below.

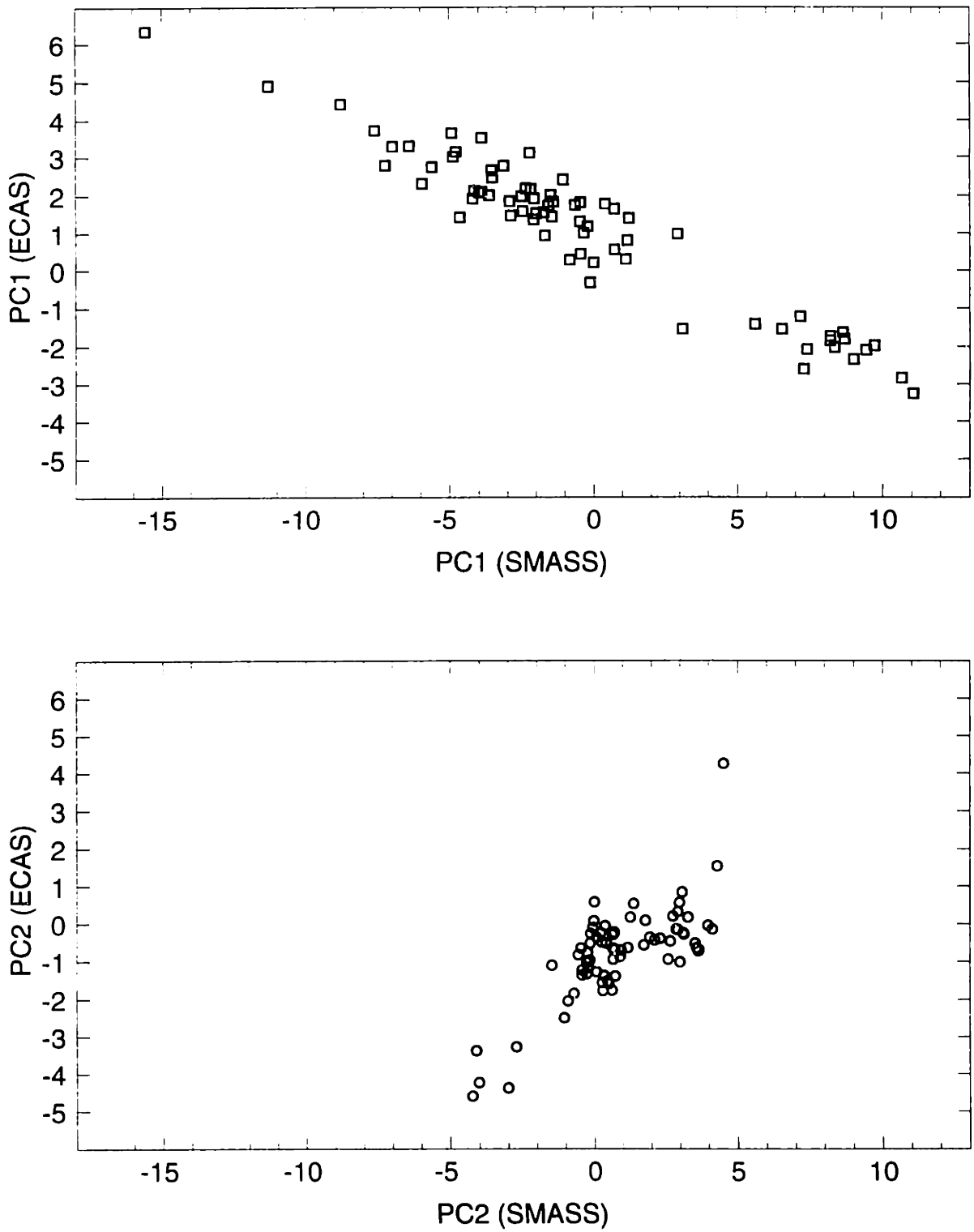

Fig. 3.15c. Comparison between Tholen principal components and SMASS principal components for 70 objects observed by both ECAS and SMASS. **Top** shows the plot of Tholen 1st principal components vs SMASS 1st principal components. **Bottom** shows the plot of Tholen 2nd principal components vs SMASS 2nd principal components.

Gaffey *et al.* (1993b) used the 1 μm (BI) and 2 μm (BII) band 'epth ratios and center positions to separate 7 sub-classes within the S-asteroids (Table 3.8a, b). The sub-types exhibit surface silicate assemblages ranging from pure olivine (dunite) through olivine-pyroxene mixtures to pure pyroxene or pyroxene-feldspar mixtures (basalts). We tried to use our PCA analysis to separate the SMASS S-type asteroids into Gaffey *et al.*'s subclasses. However, Fig. 3.15a shows that Gaffey *et al.*'s subclasses do not separate cleanly in our PC1 vs PC2 plot. Separation does not appear possible through the PCA due to our narrow spectral coverage in the SMASS data. The primary difficulty is the lack of spectral information for the 2 μm band which is very impcrtant for mineralogical analysis.

Howell *et al.* (1992) proposed three classes for the S-asteroid population using Asteroid Neural Network (ANN). The three classes are S_o, S and S_p. S_o for olivine rich, S_p for pyroxene rich, and S for olivine-pyroxene mixture. Fig. 3.15b shows that our PCA cannot classify the SMASS S-asteroids into these sub-classes either. However, examining the spectra of S-asteroids close to the Vesta family members in the principal component space shows that most of these asteroids are pyroxene rich.

We investigated the distributions of minimum band position and depth near 1 μm for the SMASS asteroids except for the Cs, Xs, Ts, and Ds. The results are shown in Fig. 3.16a and b. Since pyroxene can have a strong absorption band around 9400 Å, we believe that the asteroids in the area close to Vesta family members (Fig. 3.16b) are pyroxene-rich objects. Combining Fig. 3.16b with the asteroids' spectra and their positions relative to the Vesta family members in the PCA plot (Fig. 3.13a and b), we can identify pyroxene-rich asteroids in SMASS. Identifying olivine-rich asteroids is difficult because our spectra cannot go beyond 1 μm. But we can still identify a few olivine-rich candidates by using Fig. 3.16b (objects close to A-type asteroids), the spectra, and relative positions to A-type asteroids in the PCA. The results are summarized in Table 3.12. The locations of pyroxene-rich asteroids in the principal component space are shown in Fig. 3.16c. The spectra of 8 candidates for olivine-rich asteroids and their locations in the principal component space are shown in Fig. 3.17a and 3.17b, respectively.

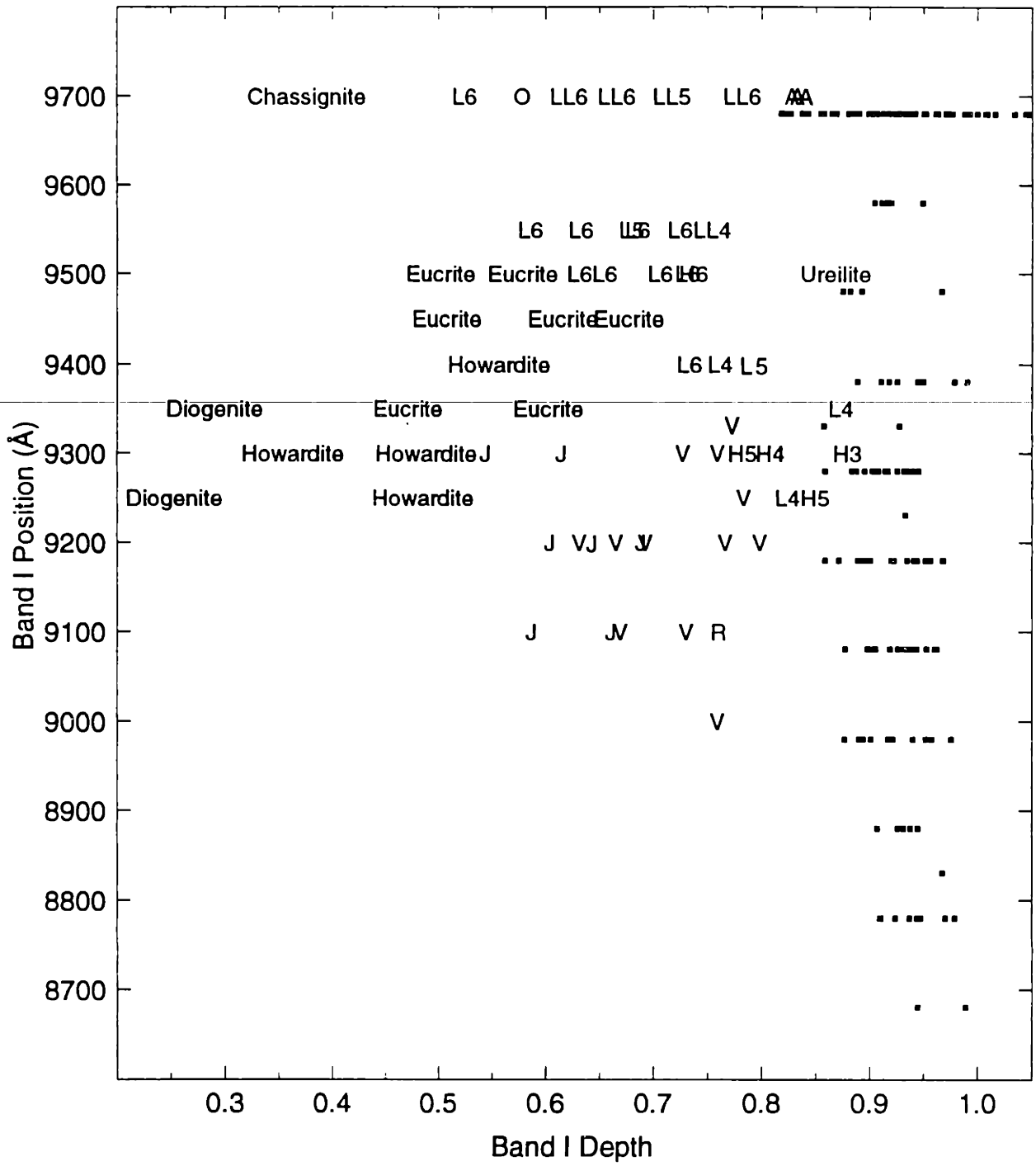

Fig. 3.16a. Band I minimum position vs depth plot for meteorites and SMASS objects showing near-infrared absorption features (S asteroids are represented as points). The depth is the ratio of band I and the maximum around 7500 Å. Objects whose band I minimum position is at 9700 Å or beyond are plotted at 9700 Å in the figure (anything beyond 9700 Å will be treated as falling at 9700 Å). Note the chondrites and achondrites are separated more cleanly than the PCA (Fig. 3.14a, b).

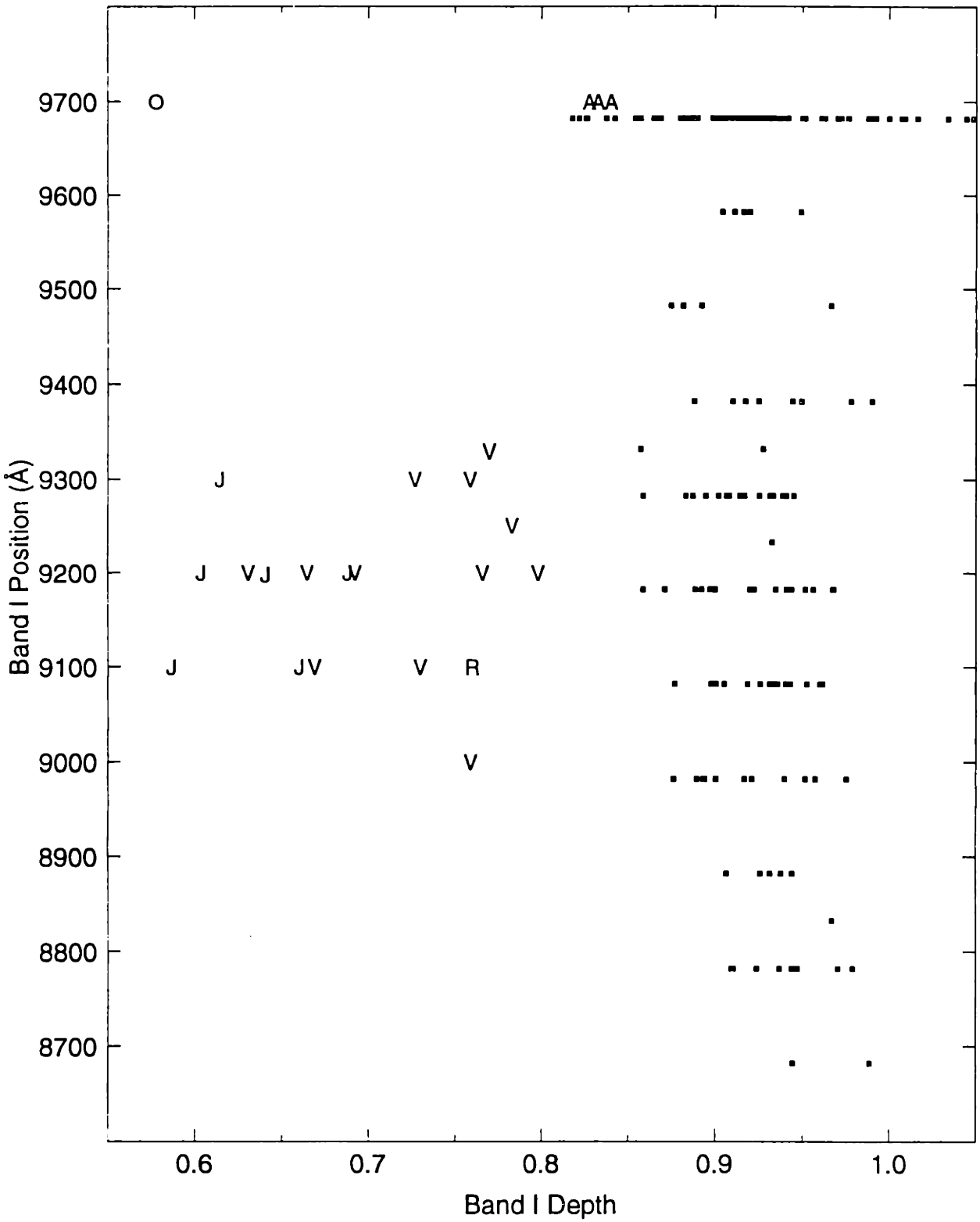

Fig. 3.16b. Band I minimum position vs depth plot for SMASS objects showing near-infrared absorption features (S asteroids are represented as points). The depth is the ratio of band I and the maximum around 7500 Å.

Table 3.12
List of Pyroxene- and Olivine-Rich Asteroids in SMASS

Asteroids	Band I Min*	Band I Depth**	Pyroxene-Rich	Olivine-Rich
3	9300	0.932	yes	
7	9400	0.918	yes	
25	9400	0.910	yes	
28	9200	0.941	yes	
32	9100	0.919	yes	
61	9300	0.917	yes	
73	9300	0.902	yes	
82	9100	0.898	yes	
116	9200	0.935	yes	
124	8900	0.938	yes	
126	9300	0.907	yes	
167	9000	0.917	yes	
237	9200	0.859	yes	
290	9200	0.901	yes	
291	9350	0.857	yes	
292	8800	0.937	yes	
374	9300	0.932	yes	
470	9300	0.945	yes	
477	8800	0.948	yes	
480	9100	0.877	yes	
509	9100	0.933	yes	
518	9000	0.877	yes	
631	9100	0.932	yes	
675	9300	0.941	yes	
737	9200	0.920	yes	
722	>10000	>0.856		yes
774	8800	0.944	yes	
787	8800	0.909	yes	
808	9100	0.898	yes	
915	>10000	>0.869		yes
918	8800	0.911	yes	

Table 3.12 (continued)

Asteroids	Band I Min*	Band I Depth**	Pyroxene-Rich	Olivine-Rich
1110	9300	0.934	yes	
1375	8800	0.924	yes	
1518	>10000	>0.931		yes
1584	9100	0.919	yes	
1626	9200	0.889	yes	
1722	9300	0.908	yes	
1807	>10000	>0.882		yes
2014	9000	0.894	yes	
2078	9200	0.871	yes	
2299	9200	0.893	yes	
2365	9300	0.895	yes	
2599	9100	0.961	yes	
3158	9000	0.921	yes	
3674	9000	0.890	yes	
4002	8900	0.932	yes	
4025	>10000	>0.916		yes
4062	>10000	>0.901		yes
4145	>10000	>0.818		yes
4606	>10000	>0.857		yes

* The wavelength at minimum near-infrared band position.

** The depth ratio of band I and the maximum position around 7500 Å.

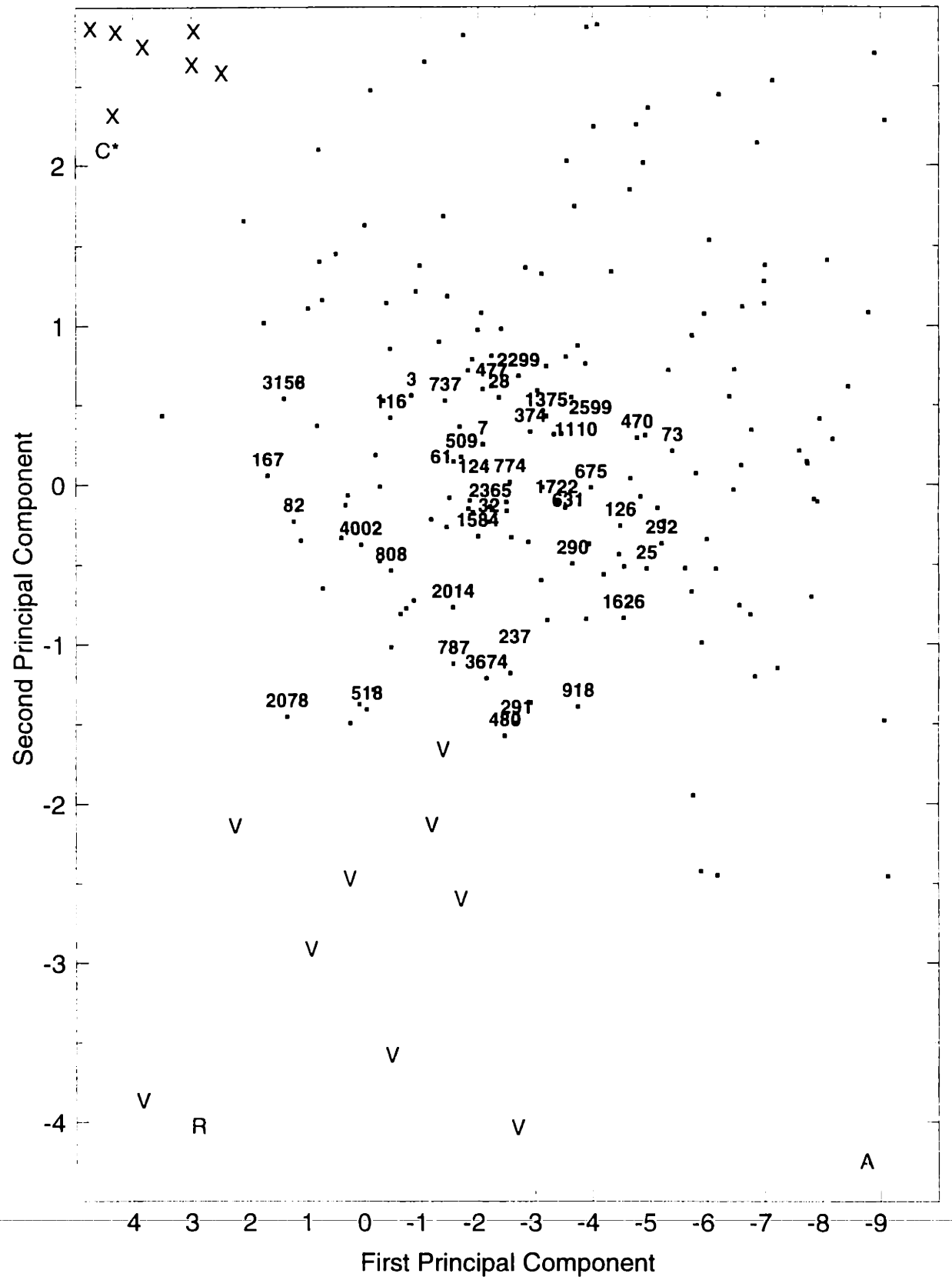

Fig. 3.16c. The locations of identified pyroxene-rich asteroids in the principal component space (S asteroids are represented as points).

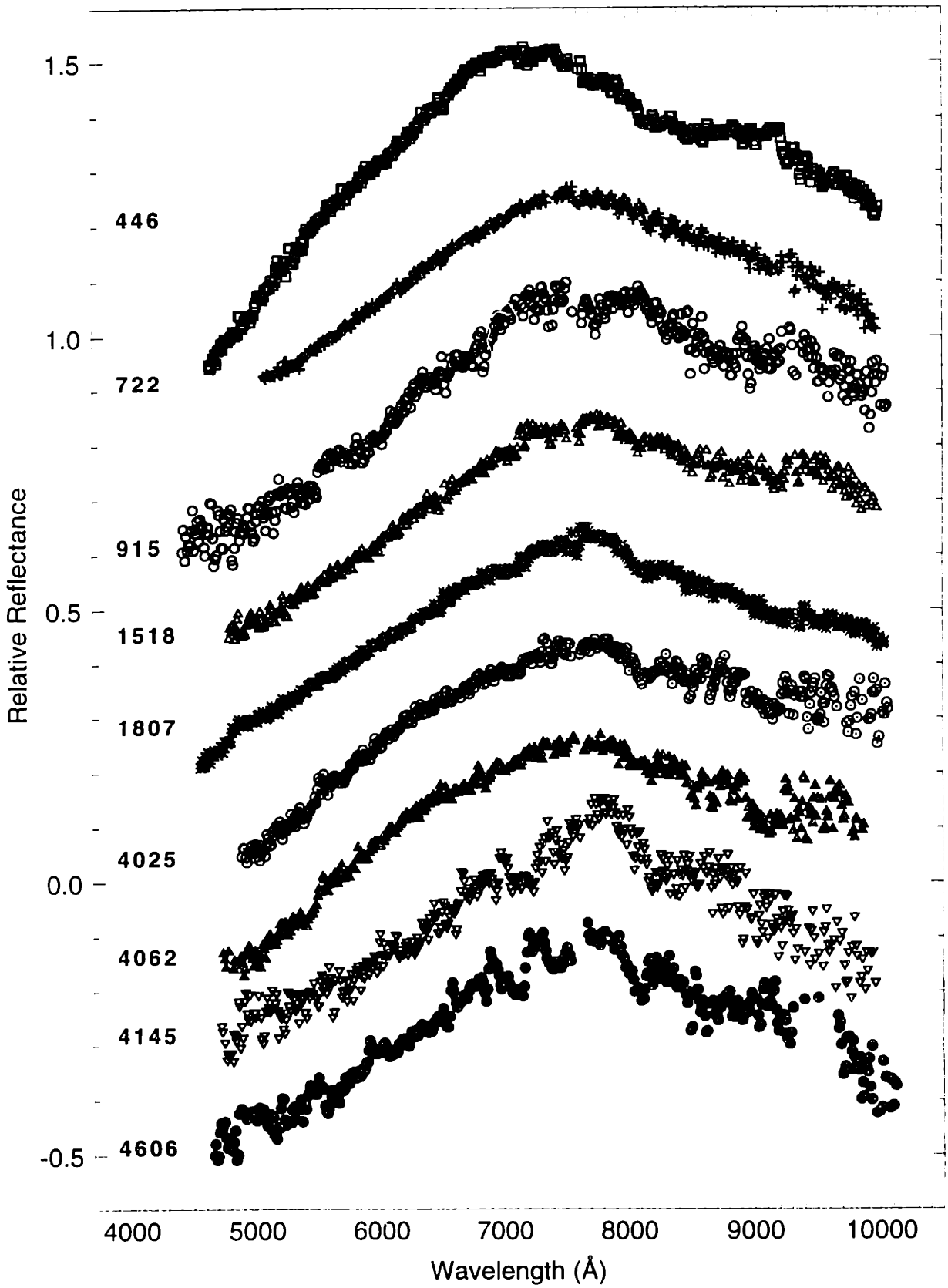

Fig. 3.17a. Spectra of 8 candidates for olivine-rich asteroids and an A-type asteroid 446 Aeternitas. The spectra are offset vertically for clarity.

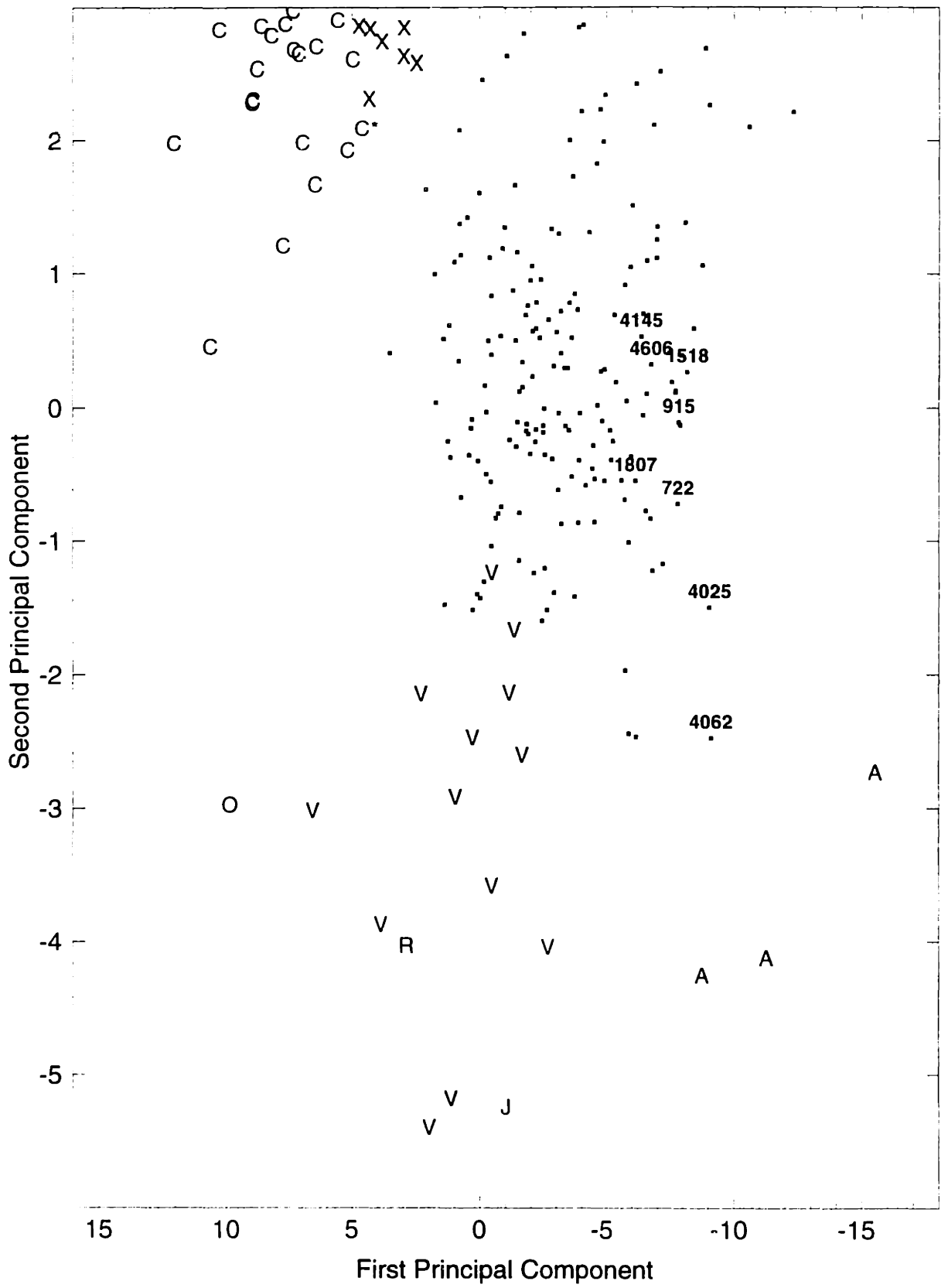

Fig. 3.17b. The locations of identified olivine-rich asteroids in the principal component space (S asteroids are represented as points).

We examined if there was any principal component space dependence for the S-asteroids with different diameters. Principal component plots (Fig. 3.18a), running box plots (Fig. 3.18b, c), and statistical *f*-test (Variance test, 99% confidence level) (Gravetter and Wallnau 1988) revealed that small S asteroids span more principal component space than the large asteroids. The difference is probably due to two reasons: First, more S asteroids close to A-types show up in small sizes (see Fig. 3.17b) and they are located on the low-right side in Fig. 3.13a. Band I position vs depth plot (Fig. 3.19) also shows that olivine seems to be much more abundant among small asteroids. However, we should emphasize that such a conclusion is not secure because of our limited spectral coverage. Second, we also have several small inner main-belt asteroids showing featureless spectra longward of 7000 Å (red to near-infrared). Typical asteroid are 169, 1478, 1892, 2105, 2327 (Fig. 3.20). Their optical spectra are similar to two outer main-belt asteroids: 387 and 980 (Burbine *et al.* 1992). These asteroids are located on the upper-right corner in Fig. 3.13a and their spectra show almost no absorption features near 1 μm. Burbine *et al.* (1992) concluded that such spectra indicate the possible presence of spinel, an aluminum-magnesium oxide mineral commonly present in inclusions in CV3 and CO3 meteorites. These authors also speculated that spinel-bearing asteroids represent material formed in the same nebular zone as the CV3 and CO3 chondrites but either at an earlier time in the nebula when such inclusions might have been a relatively larger fraction of the nebula grain population, or in locations where nebular processes (e.g., settling to the midplane) had concentrated such inclusions. The discovery indicates that possible spinel-bearing objects are common in the asteroid belt. In order to escape the strong electromagnetic induction heating (Scott *et al.* 1989), inner main-belt spinel-bearing objects should exist in smaller sizes.

We found two asteroids, 1279 Uganda and 1653 Yakhontovia showing similar spectra to 44 Nysa (Fig. 3.21). The relatively featureless, high albedo spectrum of 44 Nysa indicates a surface dominated by a nonabsorbing, spectrally neutral phase such as enstatite, forsterite or some other Fe-poor silicates (Gaffey *et al.* 1989). A weak pyroxene band around 9000 Å is shown in the spectra of 44 and 1279. A relatively strong pyroxene band at 9000 Å appears in the spectrum of 1653. The spectra of these three asteroids are consistent with the low Fe and Ca enstatite seen in meteorites (Gaffey *et al.* 1989). Asteroids 1279 and 1653 do not belong to the Nysa family. The surfaces of these three asteroids are probably the

crust or exposed mantle of a differentiated parent body with enstatite chondrite bulk composition (Zellner *et al.* 1977).

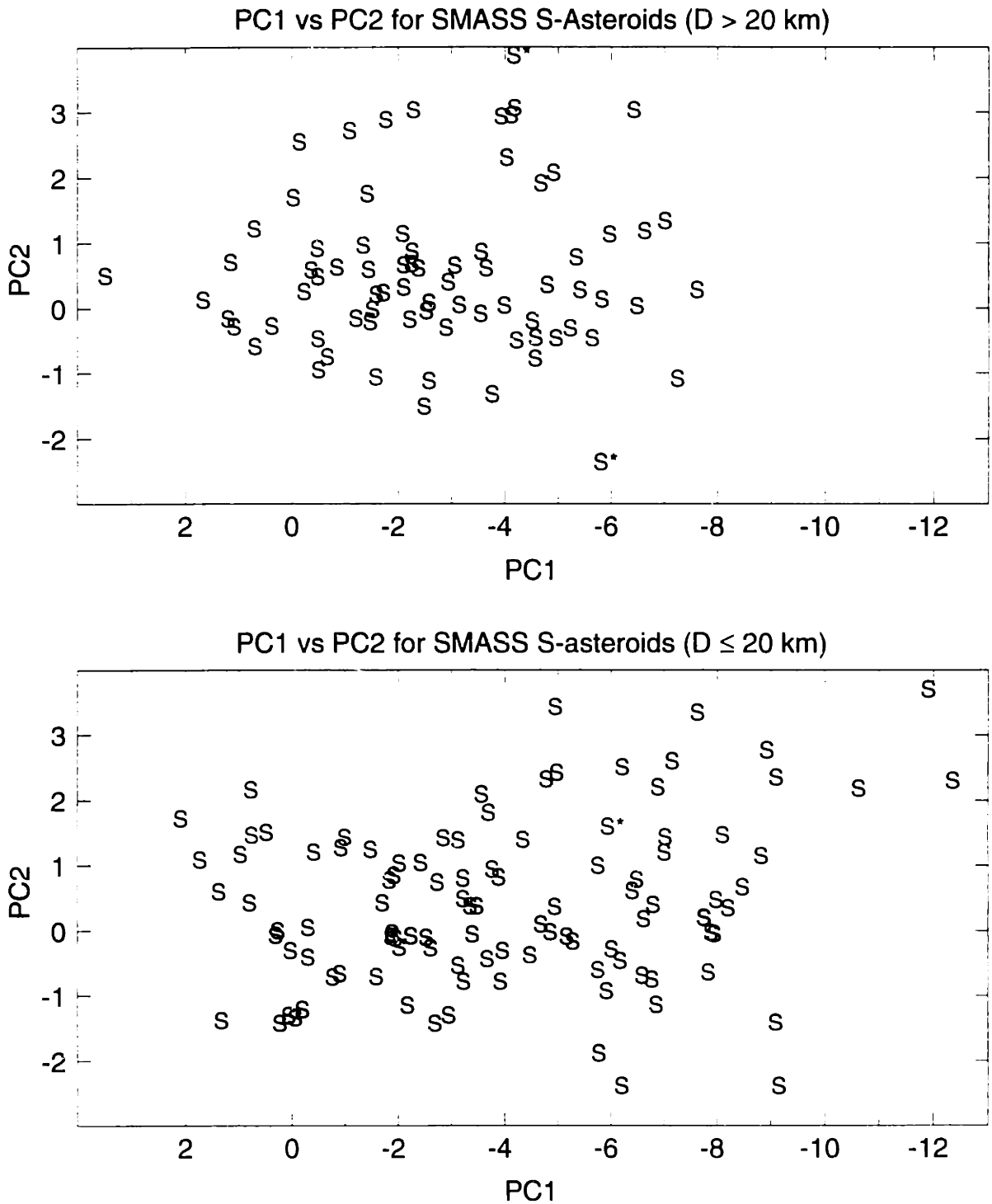

Fig. 3.18a. PC1 vs PC2 plots for SMASS S-asteroids with D greater or less than 20 km. Small objects occupy more principal component space than the larger ones.

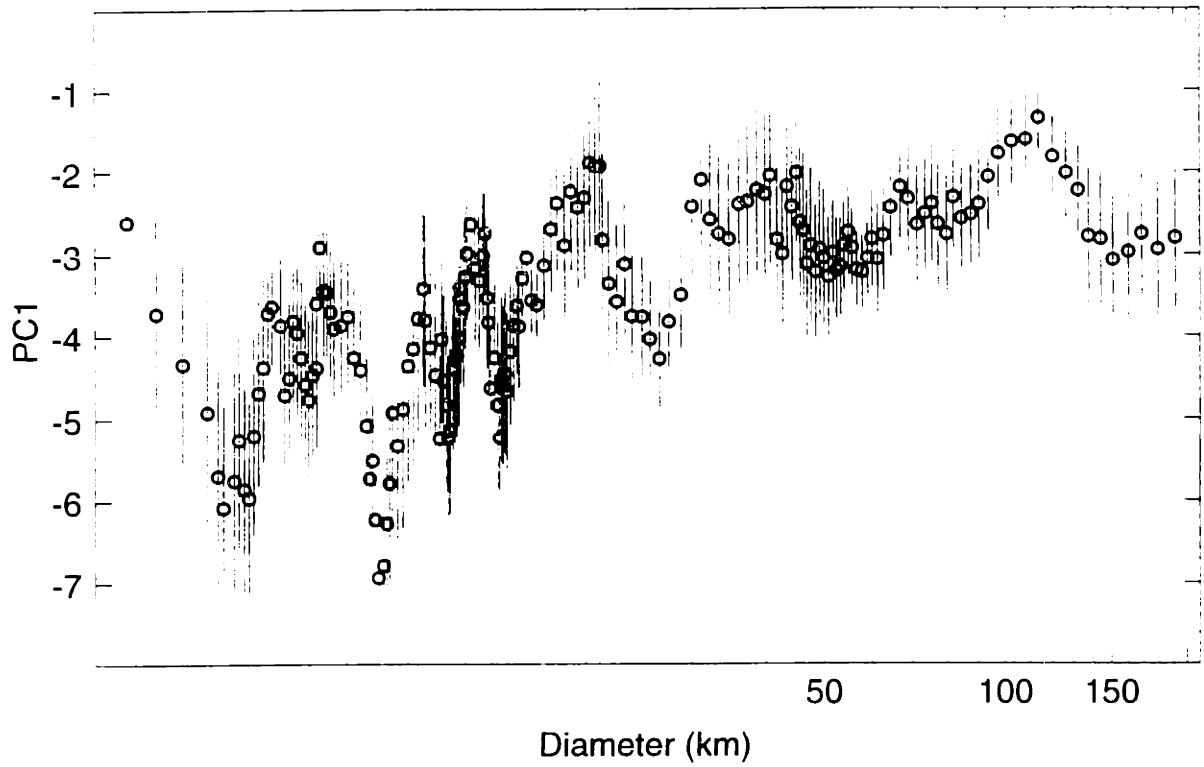

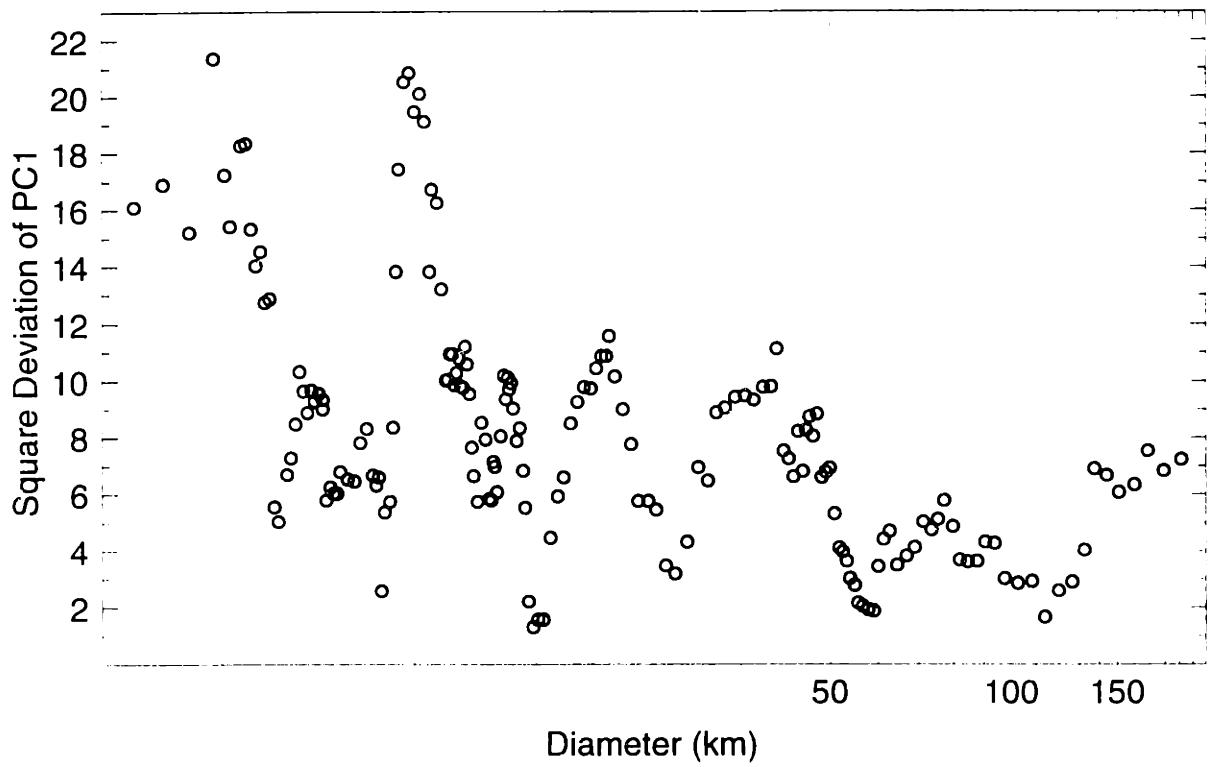

Fig. 3.18b. (**Top**) D vs PC1 running box plot (box size 10) for SMASS S-asteroids (including the error bar--standard deviation of the mean). (**Bottom**) running box plot of D vs square deviation of PC1. Small objects show much more variations than the large objects.

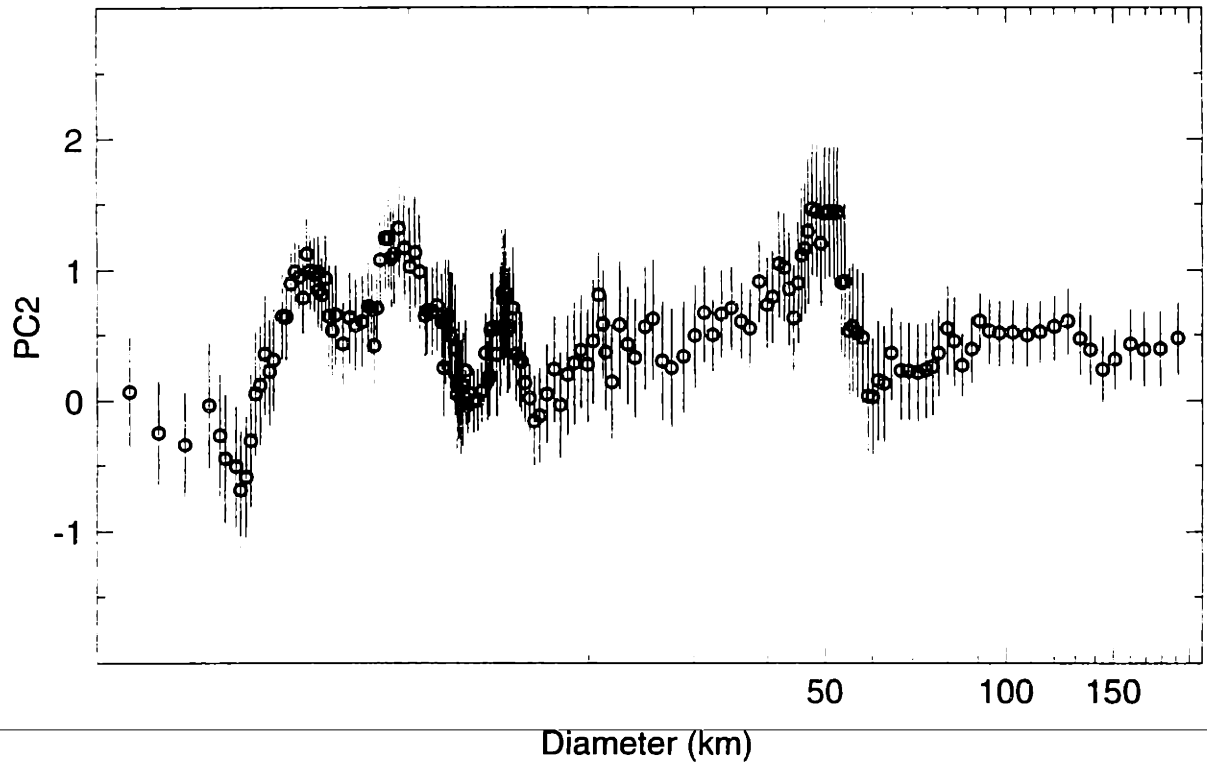

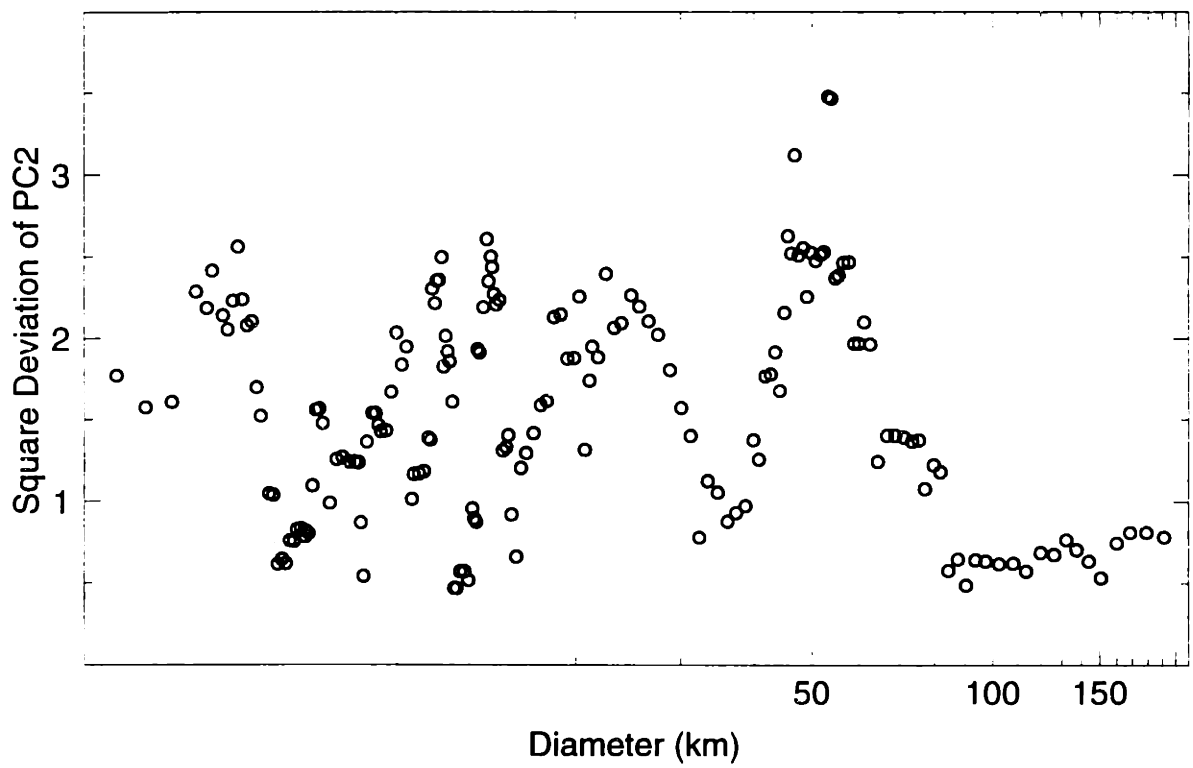

Fig. 3.18c. Fig. 3.18b. (**Top**) D vs PC2 running box plot (box size 10) for SMASS S-asteroids (including the error bar--standard deviation of the mean). (**Bottom**) running box plot of D vs square deviation of PC2. Greater variations appear among small objects.

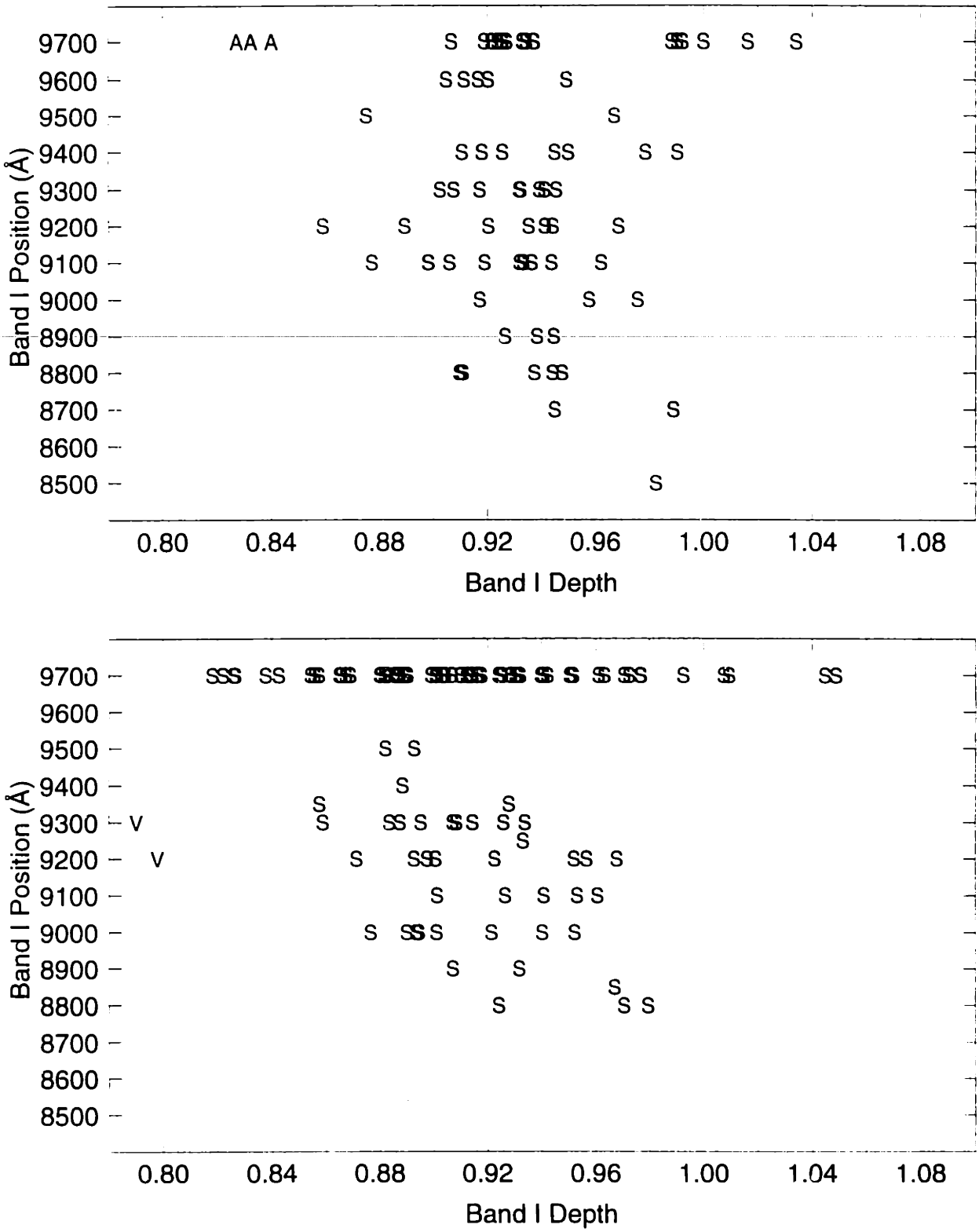

Fig. 3.19. Band I minimum position vs depth plot for large (D > 20 km, **top**) and small (D ≤ 20 km, **bottom**) asteroids. More small asteroids appear on the upper-left (possible olivine-rich objects) and upper-right (possible spinel-bearing objects) regions.

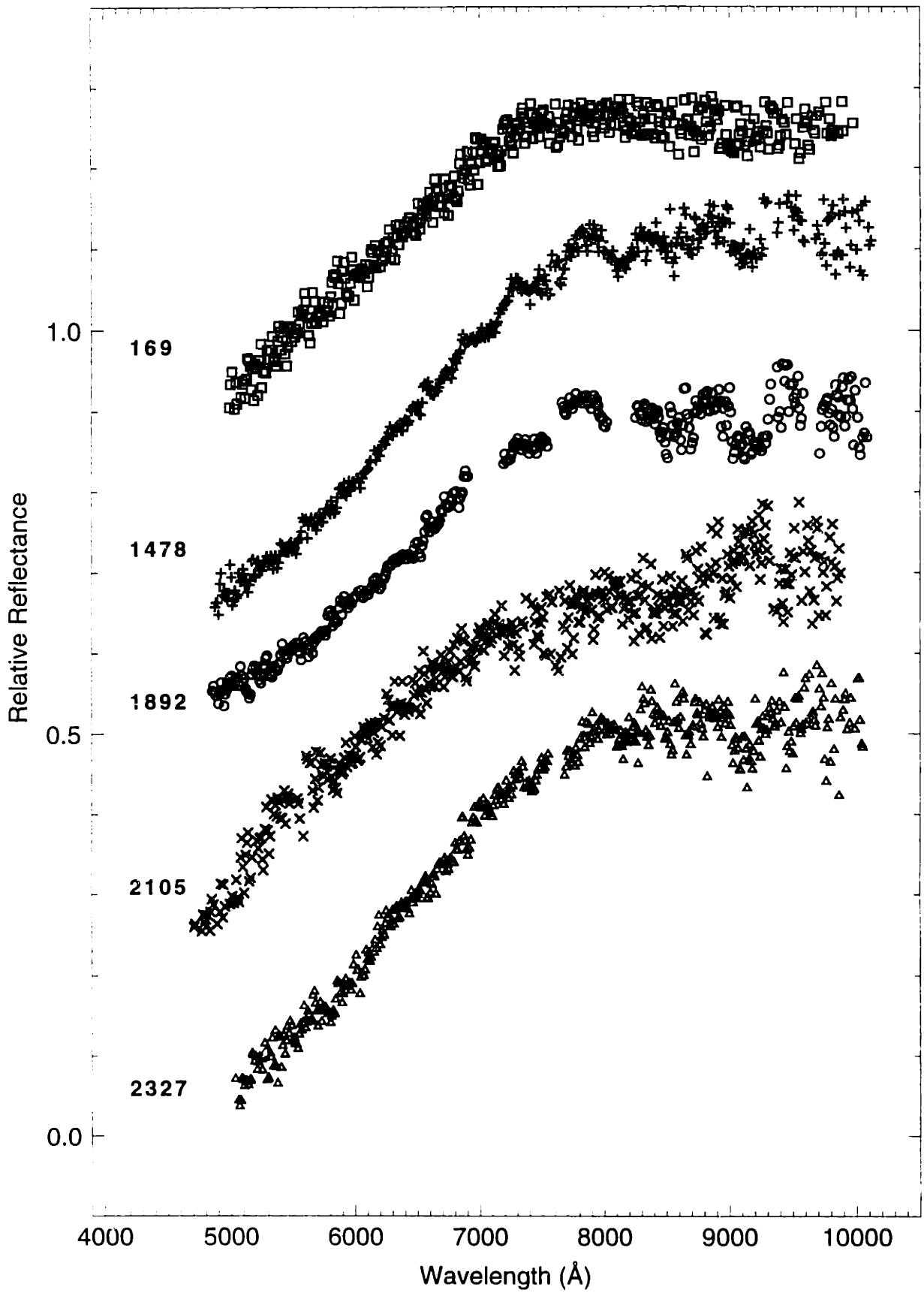

Fig. 3.20. Featureless red to near-infrared spectra for 5 asteroids.

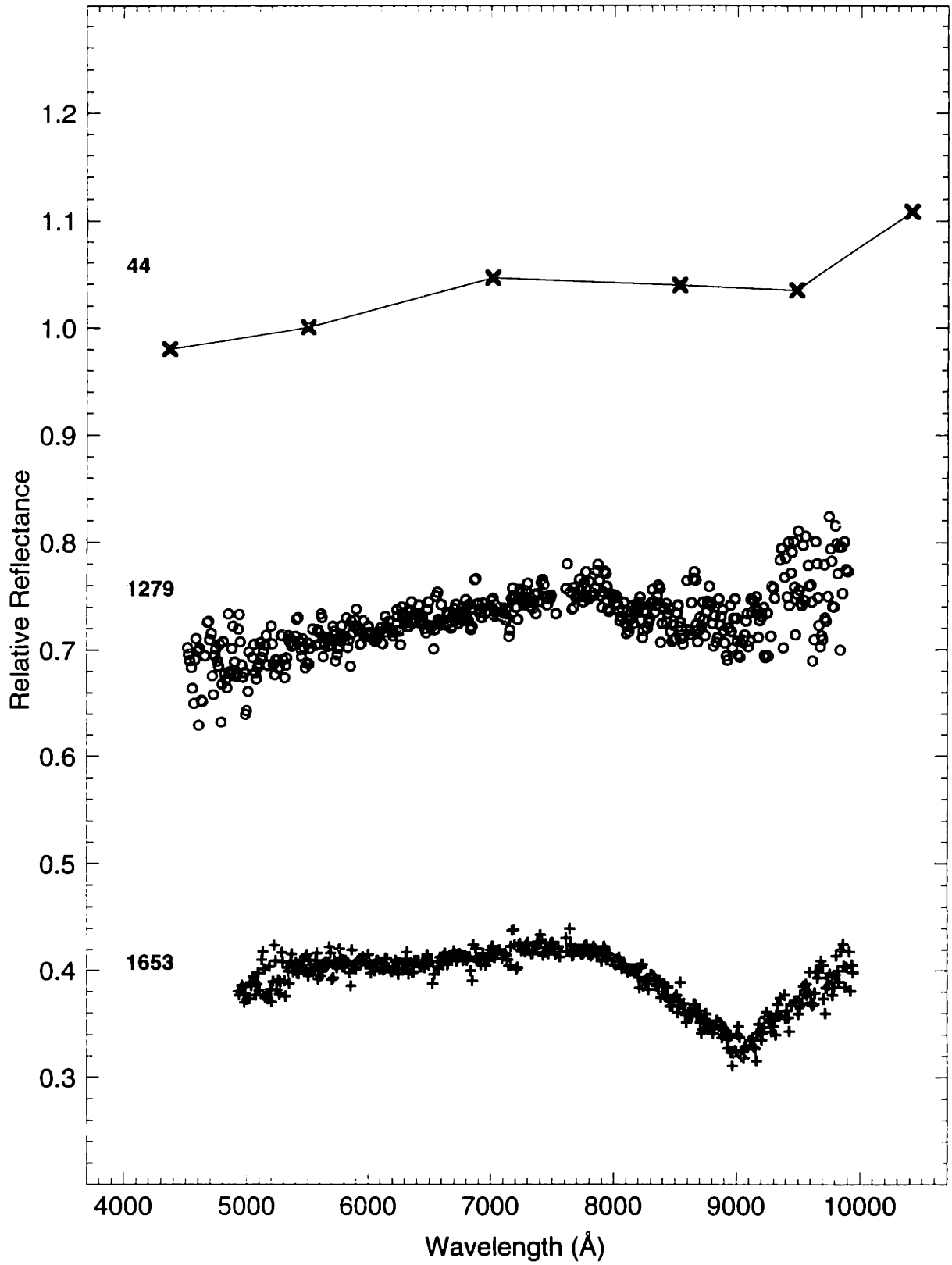

Fig. 3.21. Spectra of asteroids 44, 1279, and 1653. The data for 44 is from ECAS (Zellner *et al.* 1985).

3.4 Analysis and Discussion

SMASS and the Eight-Color Asteroid Survey (ECAS) are the two major asteroid spectroscopic surveys conducted to date. More than 800 total objects have been observed by ECAS and SMASS. Fig. 3.22 shows their number distributions in the solar system. Below 2.7 A.U., SMASS and ECAS have similar distributions. For reasons discussed below, SMASS does not have comparable sampling beyond 2.7 A.U. Fig. 3.23a and b display the type distributions as a function of semi-major axis and diameter for SMASS and ECAS objects. Most of the SMASS objects belong to C and S classes, and the S-class asteroids dominate the inner belt. This is similar to the ECAS results (Tholen 1984). The obvious difference is more small V-types show up in SMASS (see detailed discussions in section 3.6). Fig. 3.24a, b show the type distribution of the combination of these two surveys.

Because our survey was magnitude limited and sought to measure the smallest known asteroids, our sample is biased toward inner main-belt objects. Therefore, the number distribution is not uniform in the main belt. In order to partially avoid this selection effect, we separated the surveyed asteroids into two groups to analyze the relation between type distributions and sizes. Group one has $a \leq 2.7$ A.U. (excluding near-Earth asteroids). Group two includes objects with $a > 2.7$ A.U., but not including Trojan asteroids. Fig. 3.25 and 3.26 show the type distributions for different sizes (note there is a substantial paucity of observed small objects in the outer main belt). It's clearly shown that C types dominate the larger asteroids ($D > 100$ km), and C asteroids are abundant in the outer main belt. S asteroids are much more abundant in the inner main belt and dominate among smaller sizes. However, investigations by Luu and Jewitt (1989) show that albedo bias influences the apparent ratio of the number of S types to the number of C types. The mean albedo of S types (0.19) is four times higher than that of C types (0.05). Both ECAS and SMASS are magnitude-limited surveys (down to 18 magnitudes). The smallest detectable C types are always larger than the smallest detectable S types. Monte Carlo simulations (Luu and Jewitt 1989) show that real S/C number ratio at the 3:1 resonance region is 2-5 times lower than the apparent ratio depending on the power law index of the size distribution of the main-belt asteroids. We used 3 as the correction coefficient and applied this correction for C and S asteroids obtained by ECAS and SMASS. Fig. 3.27 shows the distributions

of C and S asteroids before and after applying for the albedo bias correction. The results indicate that C and S asteroids probably have comparable distributions in the main belt.

Although small asteroids show similar taxonomic distributions to their large counterparts, they show much more diverse spectral features than the larger ones, especially among the S asteroids. Fig. 3.28 shows an example of the spectral diversity observed in SMASS. Spectra from red-featureless to extremely strong pyroxene absorption band have all been revealed in the plot. Such diverse features indicate that small asteroids may have more versatile compositions than the larger objects in the main belt. Small asteroids are likely the collisional breakups of large differentiated and undifferentiated parent bodies. They may represent distinct units of the large parent bodies. In addition, small asteroids have been less affected by regolith processes. Therefore, they may contain more complete compositional information than the larger objects.

In our PCA, meteorite spectral data (Gaffey 1976) have also been included. Fig. 3.14a, b show the asteroids and meteorites in our PCA space. The results are similar to Britt *et al.*'s (1992). The meteorites show much more variant spectra than the asteroids. Due to different data set and classification criteria, we cannot separate all of the meteorite classes in our PCA, especially, the achondrites and ordinary chondrites. But minimum band position and depth analysis (Fig. 3.16a) shows that chondrites and achondrites can be separated. This indicates that our PCA has not effectively used the information around 1 μm because of noise and wavelength cutoff at 9700 Å. As noted by Britt *et al* (1992), the principal components of meteorite spectra are offset from those of the asteroid population. The same offset of carbonaceous chondrites and irons from their most frequently suggested asteroid analogues: Cs and Ms (one of the Xs), is particularly notable. We found no direct meteorite analogues for the A, D, and T type asteroids. The reason for the mismatch is still in debate. Detailed discussions about the relations between basaltic achondrites and Vesta family will be given in section 3.6.

Small A-type asteroids (dunite or pure olivine), showing an extremely reddish feature shortward of 7000 Å and strong absorption feature longward of 7000 Å, have not yet been detected in SMASS. Our observational results indicate that A-types are very rare among kilometer-sized asteroids. However, we believe

olivine-rich asteroids are not uncommon in smaller sizes, at least with respect to the larger asteroids. The S types in the low-right region of our principal component space (Fig. 3.13a, b, Fig. 3.15a, b, and Fig. 3.17b) are probably olivine-rich objects. These asteroids are located on the region close to the A-type asteroids in the minimum band position vs depth plot (Fig. 3.16b). Spectra of 8 objects in these regions are shown in Fig. 3.17a. The spectra of these asteroids include a strong ultraviolet absorption feature, slightly weaker than the A-types (due to particle size effects?), and an absorption band centered beyond 1 μm. These features are different from the spectra of pyroxenes. The results from SMASS indicate that if dunites do exist in the main belt, their sizes should be smaller than that Bell *et al.* (1989) predicted, probably below 1 km in diameter. Another alternative for the lack of observable dunites in SMASS is that most of the olivine mantle materials may exist in the S asteroid population, and have been mixed with other minerals such as the pyroxenes, which dominates the pyroxene-olivine-mixture spectra (Fig. 3.29, Burns 1989) as we see in the spectra of the SMASS objects. Partial differentiation may make up of mineral mixture instead of segregation (Gaffey *et al.* 1993b, Burbine and Burns personal communication).

Fig. 3.30a and b plot the type distribution of SMASS asteroid in the semi-major axis vs the eccentricity and sine inclination spaces. Some asteroid families such as Phocaea, Maria(#4), and Vesta can be easily identified. The following section will briefly discuss the observational results of several asteroid families.

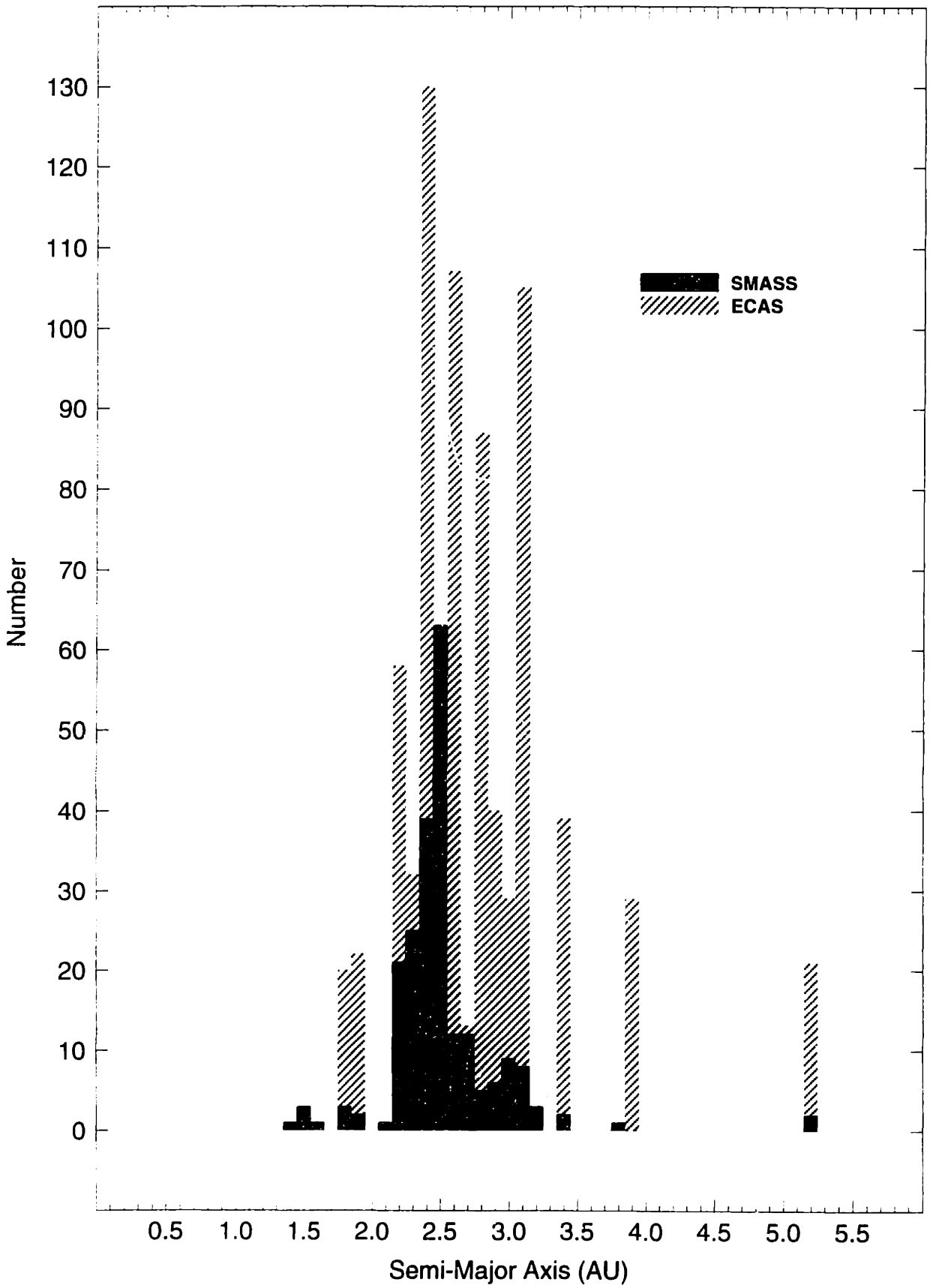

Fig. 3.22. Distribution of SMASS and ECAS Asteroids.

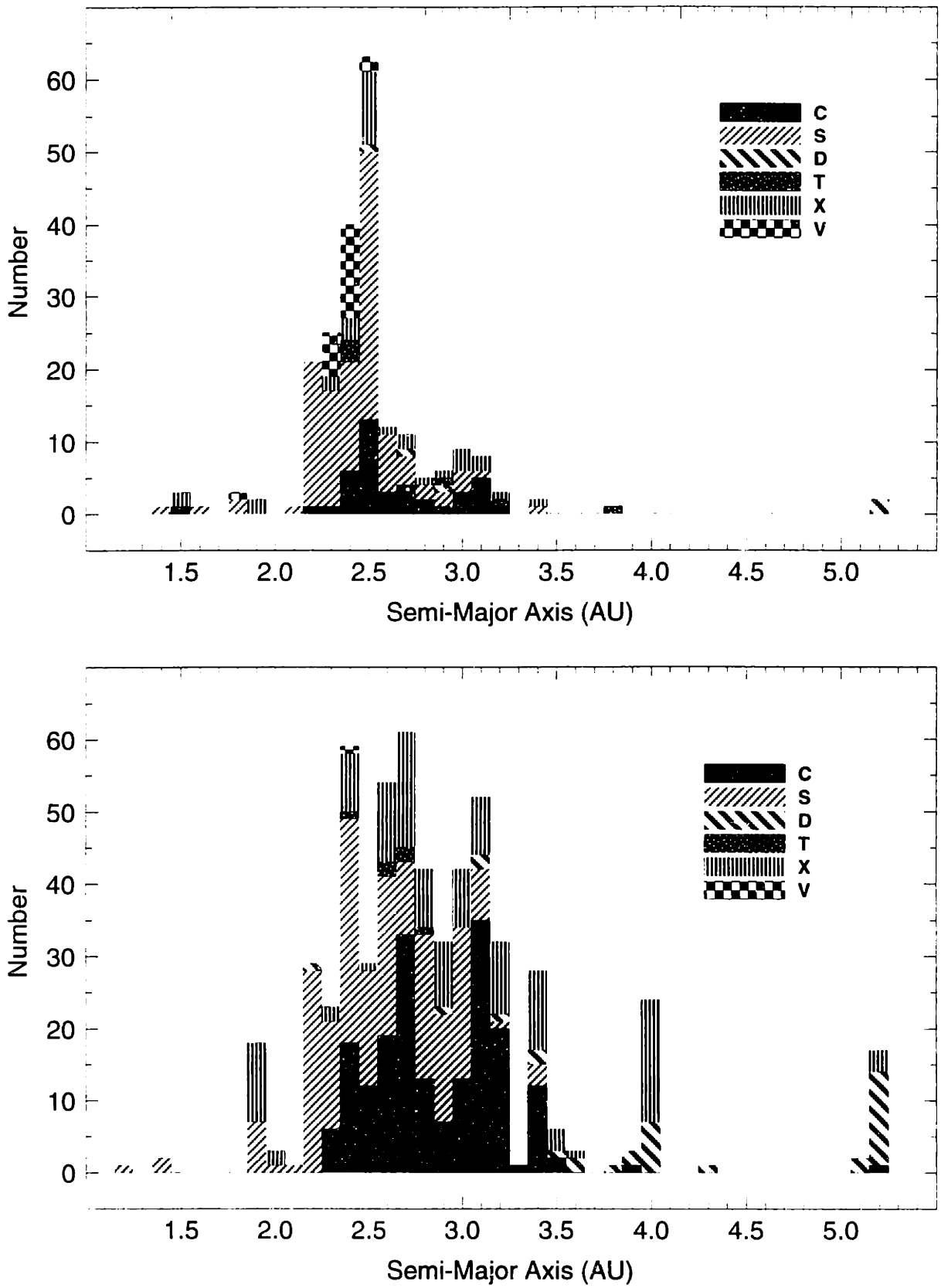

Fig. 3.23a. Heliocentric distribution of the taxonomic classes of SMASS new objects (**top**) and ECAS objects (**bottom**).

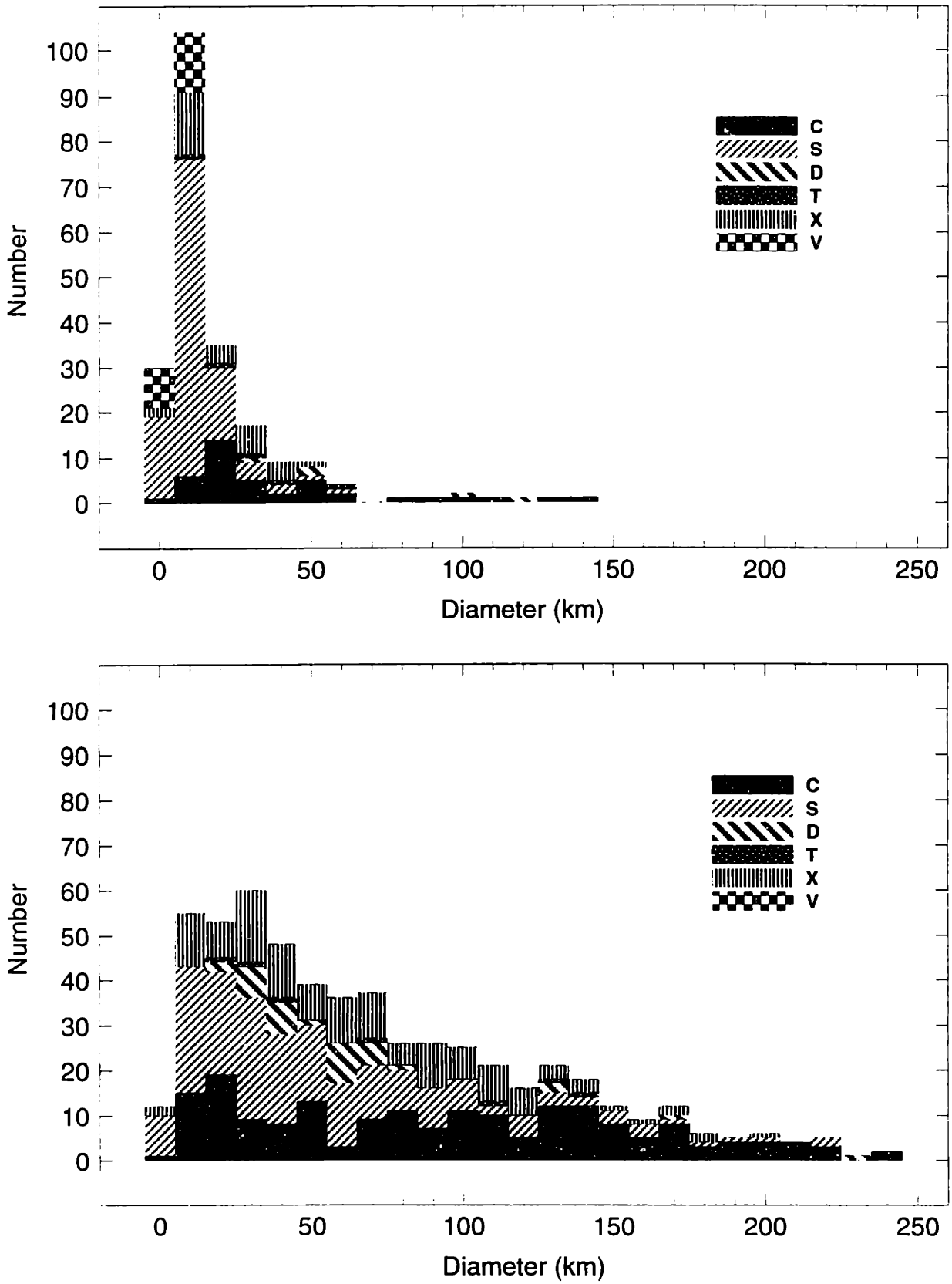

Fig. 3.23b. Size distribution of the taxonomic classes of SMASS new objects (**top**) and ECAS objects (**bottom**).

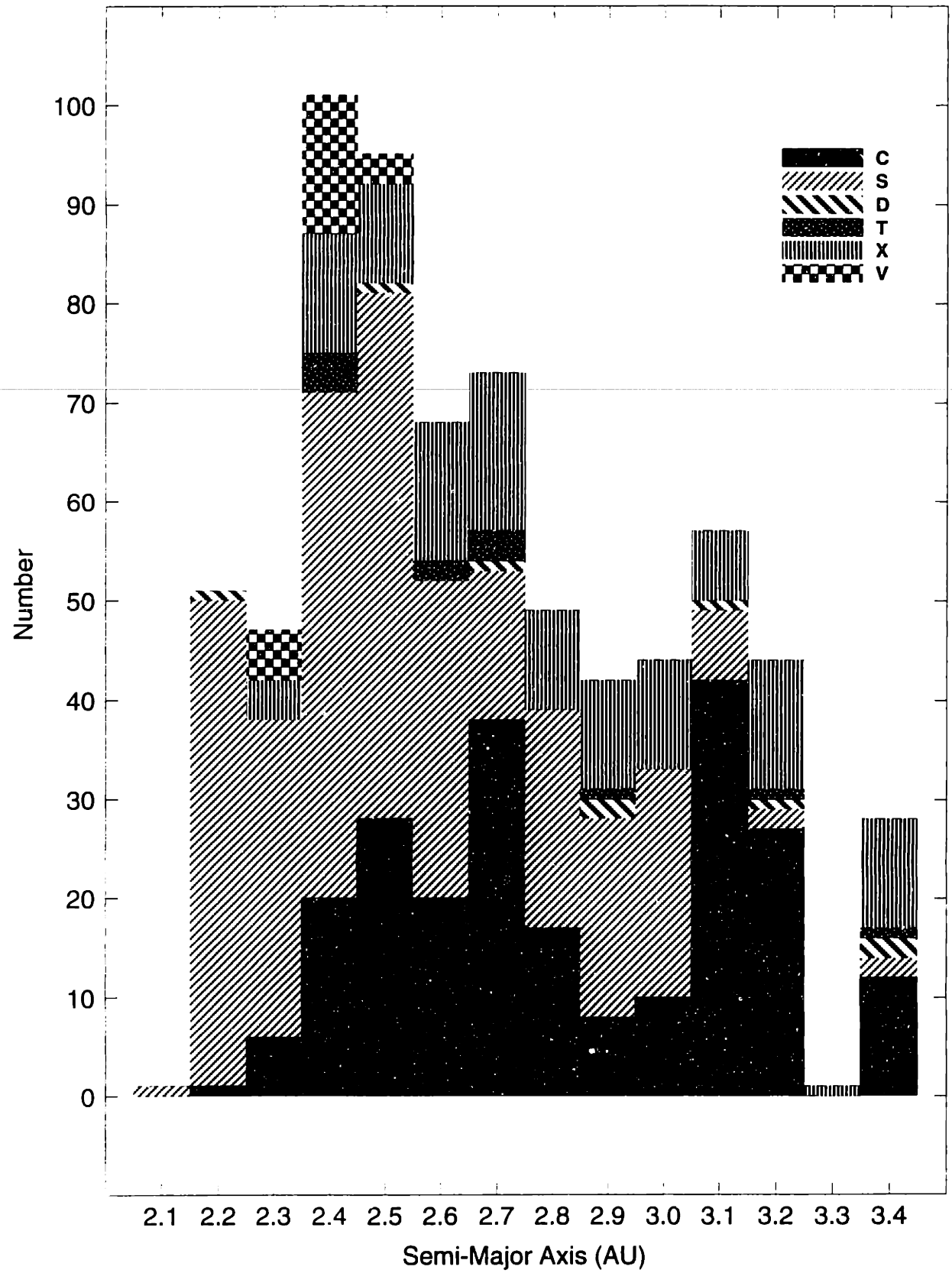

Fig. 3.24a. Heliocentric distribution of the taxonomic classes of 800 asteroids surveyed by SMASS and ECAS.

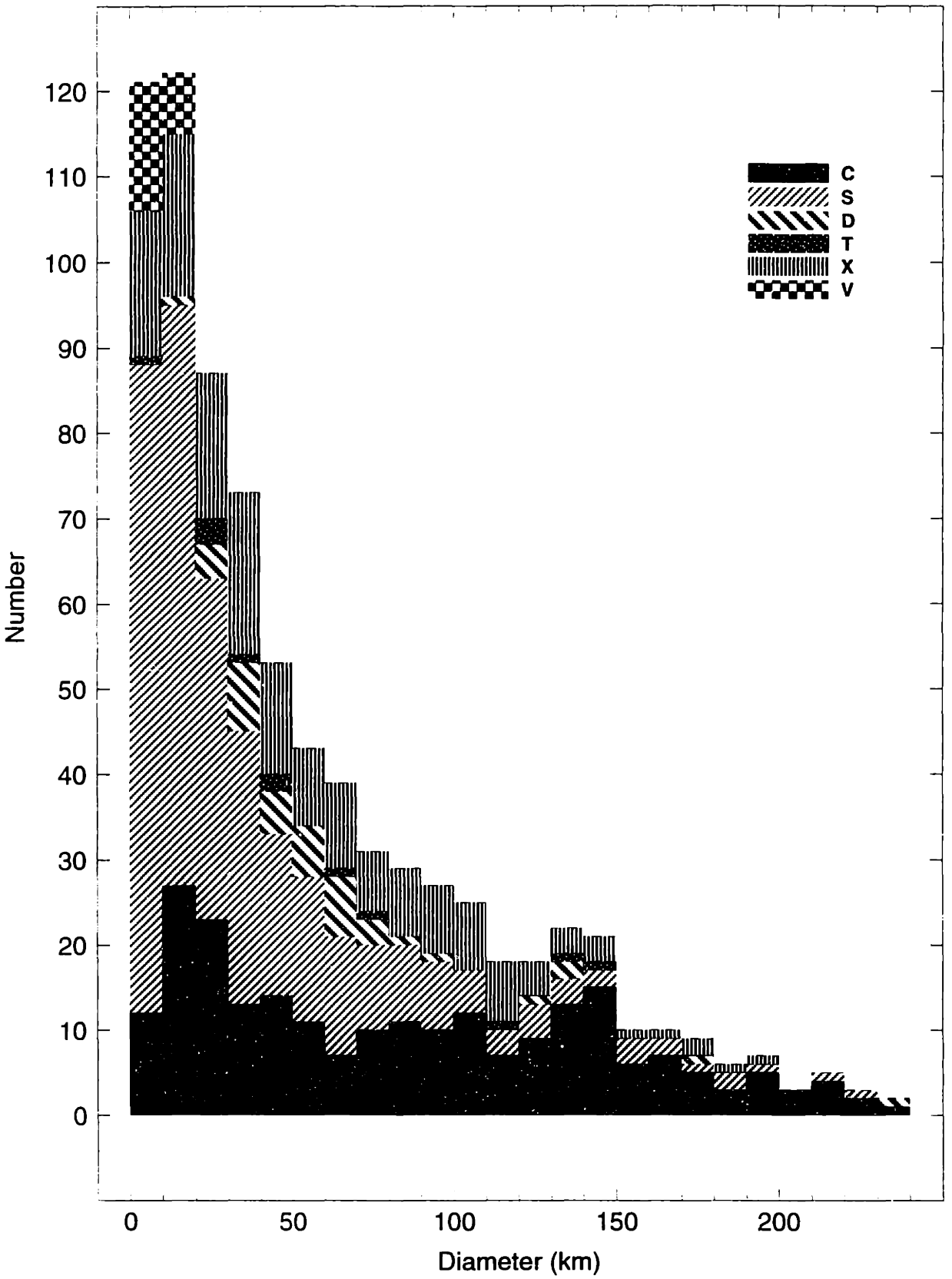

Fig. 3.24b. Size distribution of the taxonomic classes of 800 asteroids surveyed by SMASS and ECAS.

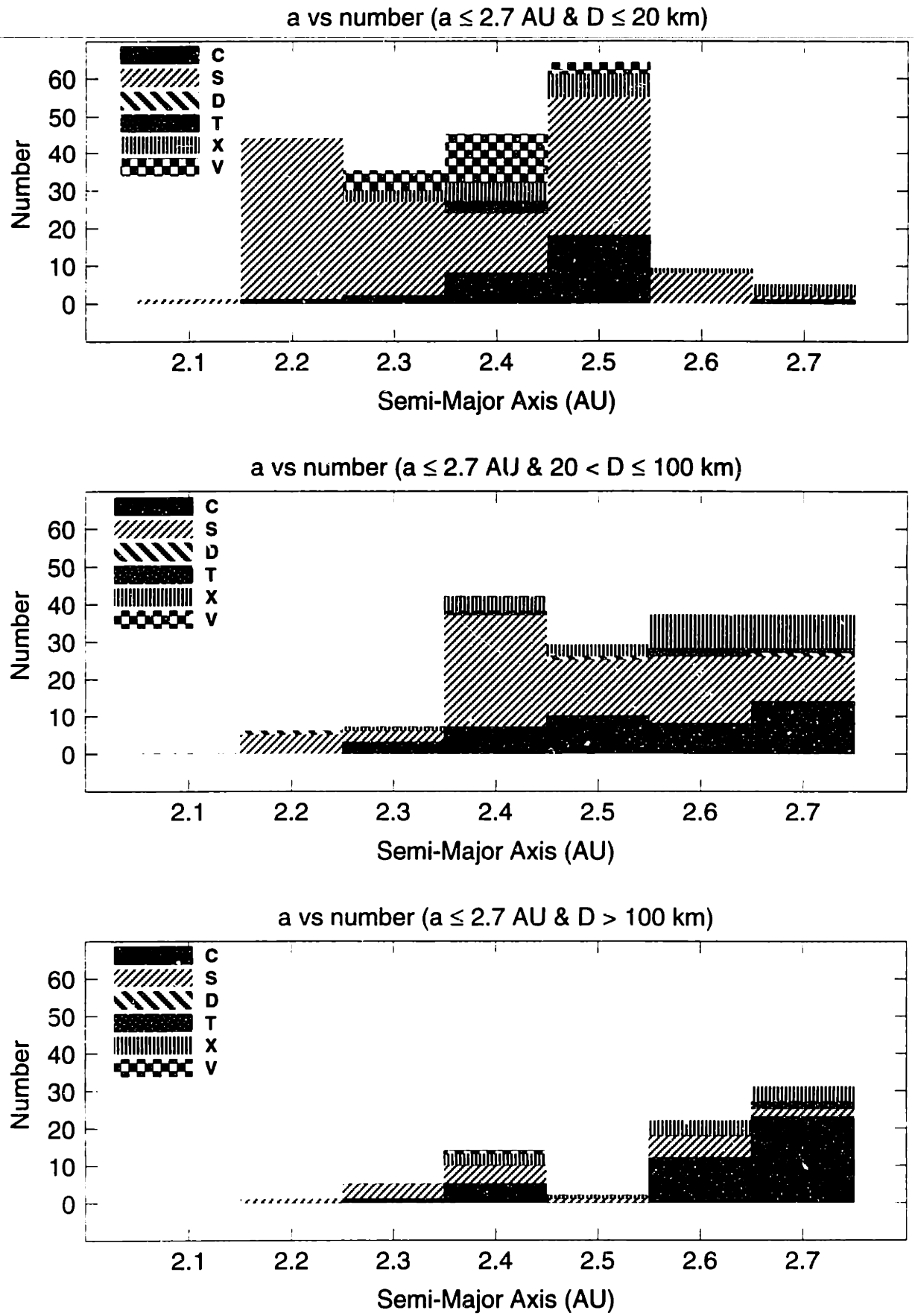

Fig. 3.25. Type distribution for 3 different size groups in the inner belt.

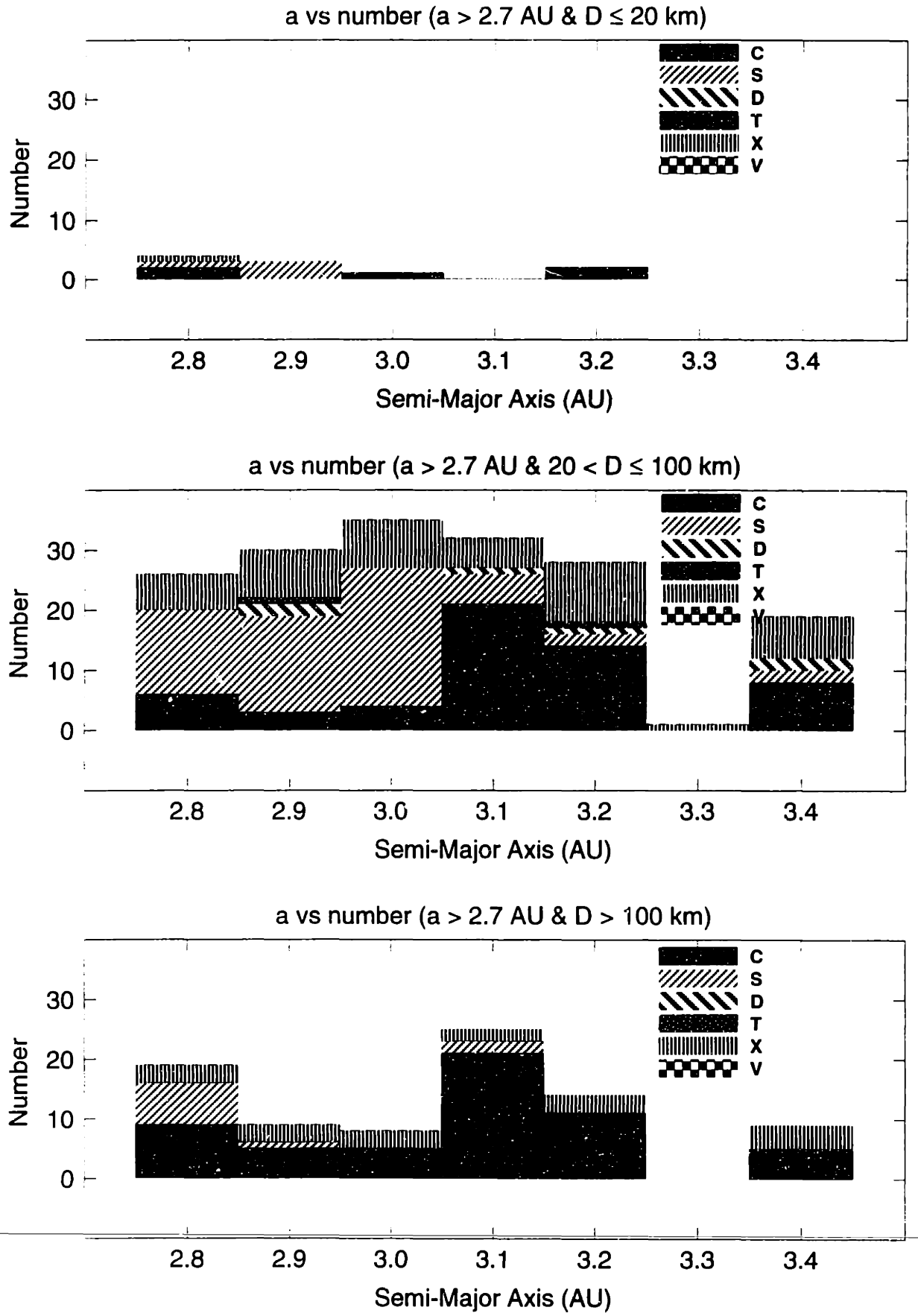

Fig. 3.26. Type distribution for 3 different size groups in the outer belt.

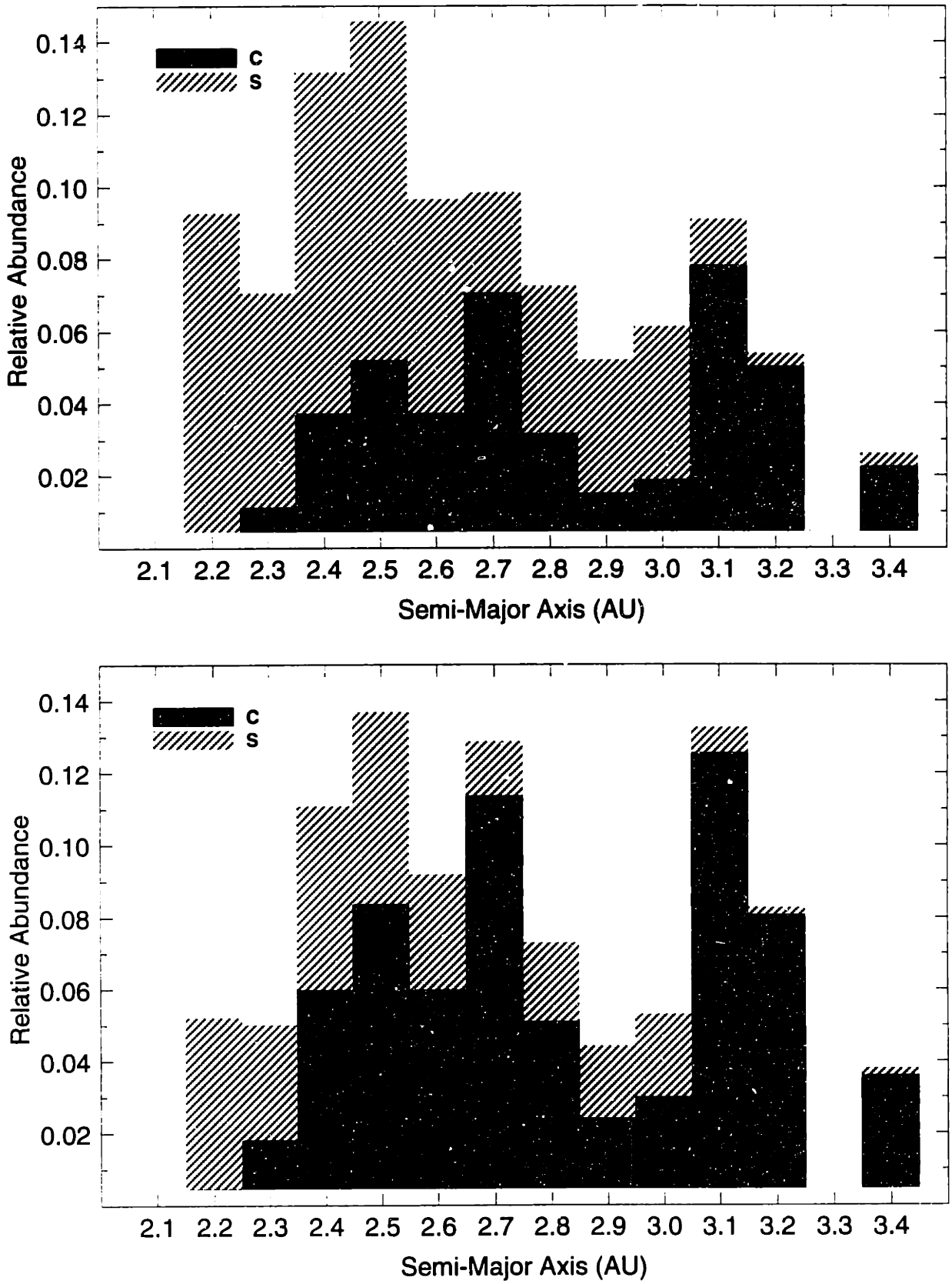

Fig. 3.27. Histogram of C- and S-type distributions before (**top**) and after (**bottom**) albedo bias correction.

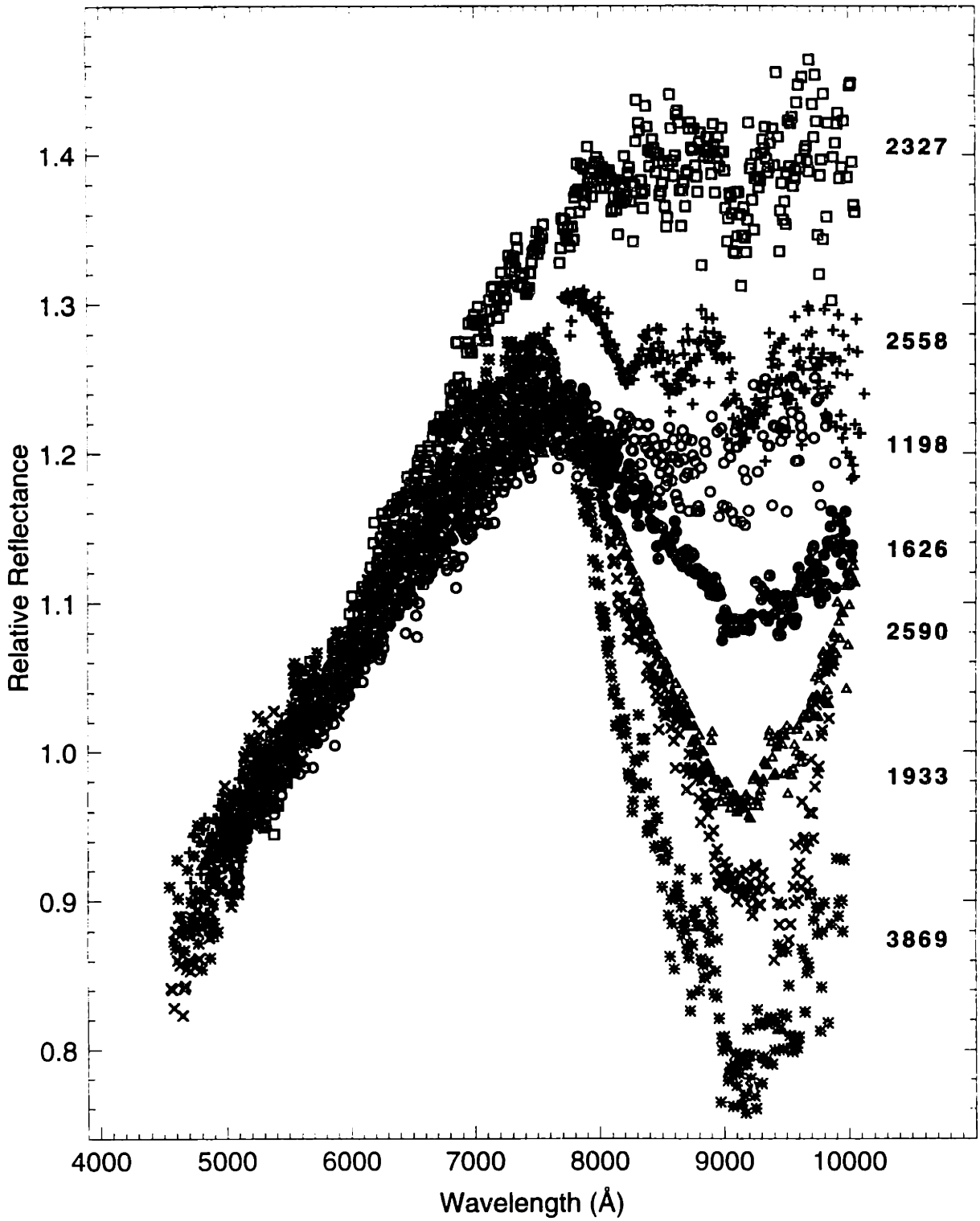

Fig. 3.28. An example of diverse spectral features observed in the SMASS. This plot shows the large range of variations for absorption features within the pyroxene 1 μm band. These variations range from no absorption (top, no pyroxene at all?) to extremely strong absorption (bottom). The diameter range for these samples is 3 to 12 km.

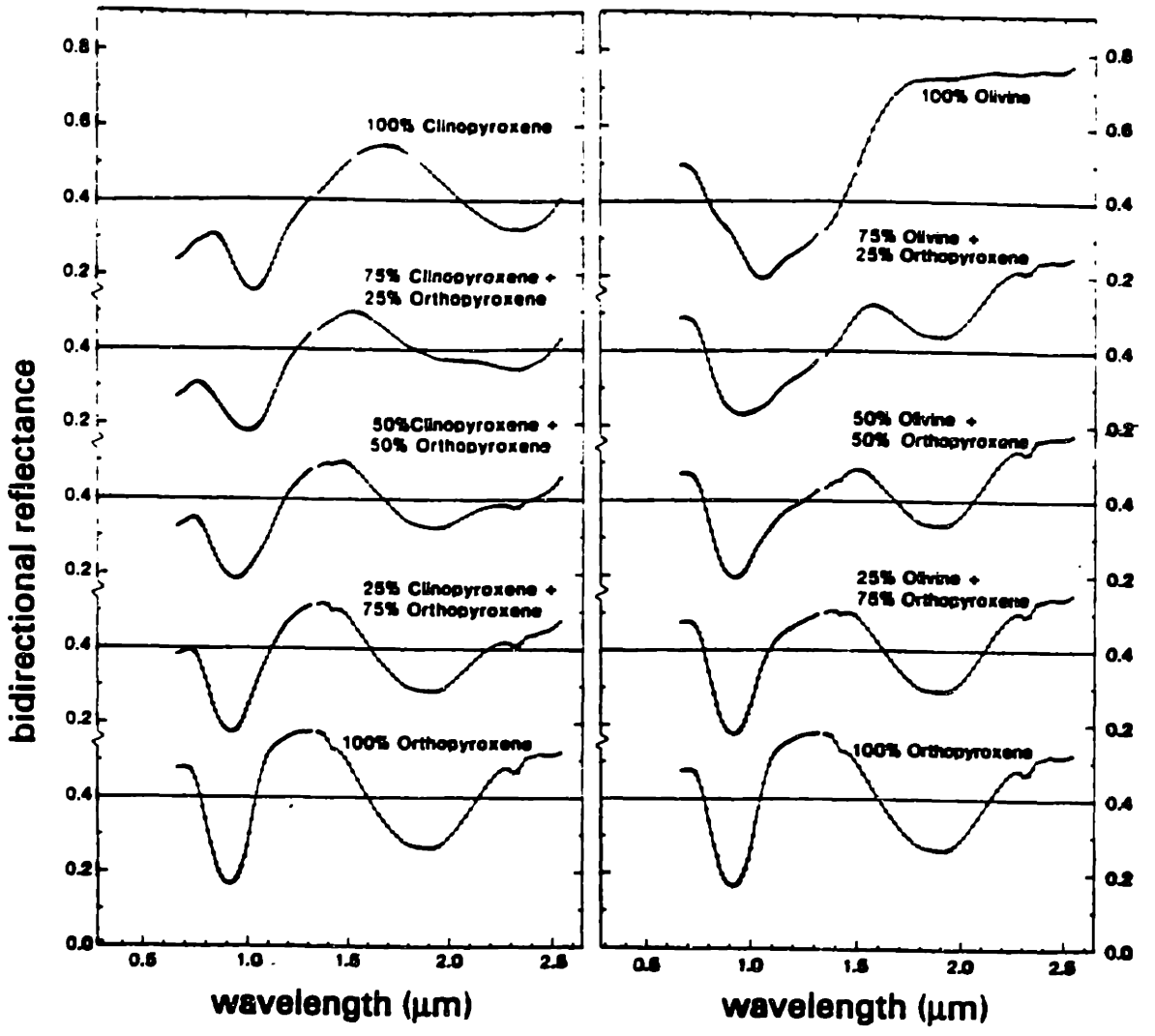

Fig. 3.29. Reflectance spectra of mixed-mineral assemblages (Burns 1989). Left: orthopyroxene-clinopyroxene mixtures; Right: orthopyroxene-olivine mixtures. Pyroxene dominates the mineral-mixture spectra and olivine causes the broadening of the 1 µm pyroxene band.

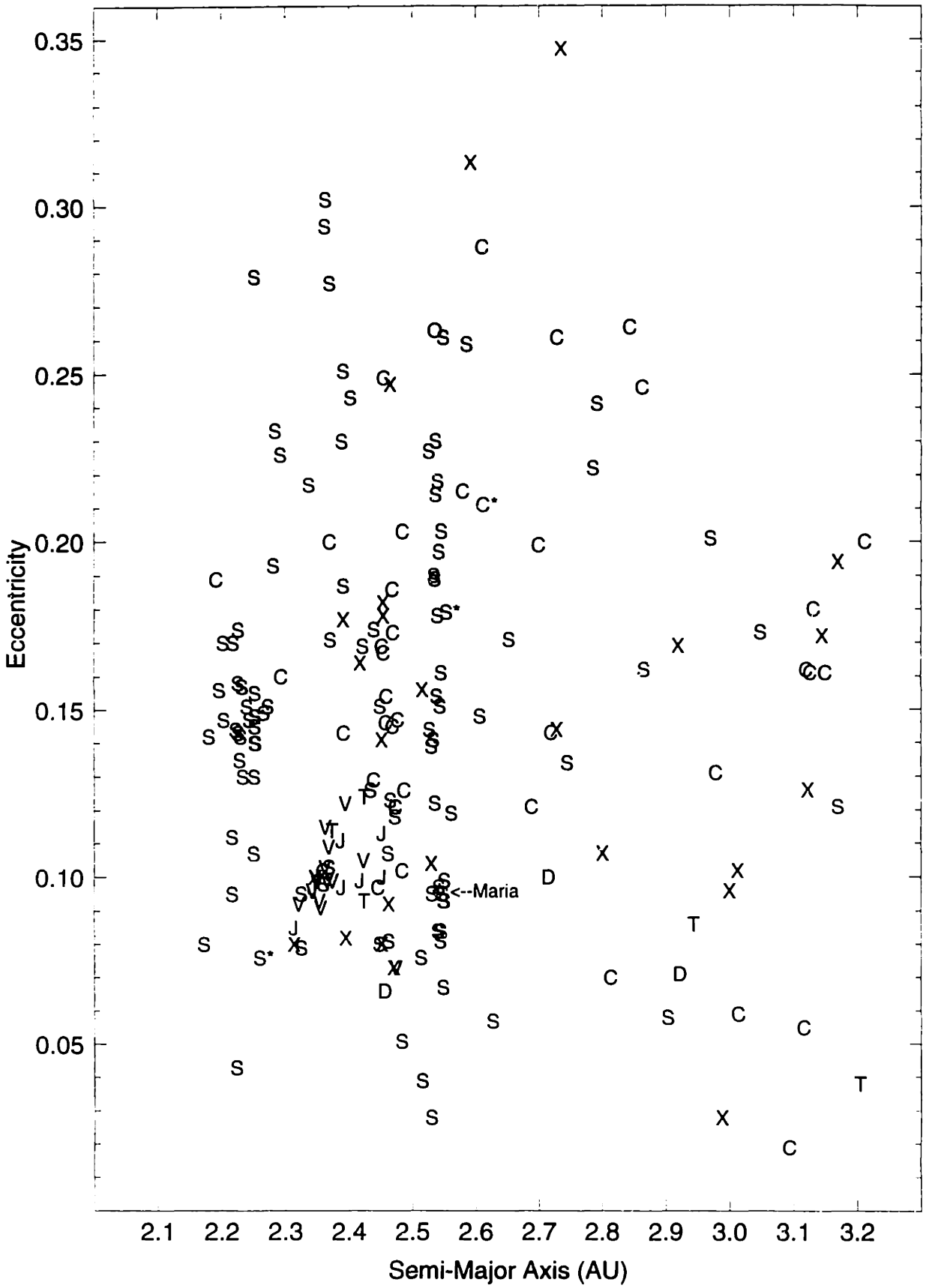

Fig. 3.30a. Semi-major axis (*a*) vs eccentricity (*e*) plot for SMASS new objects.

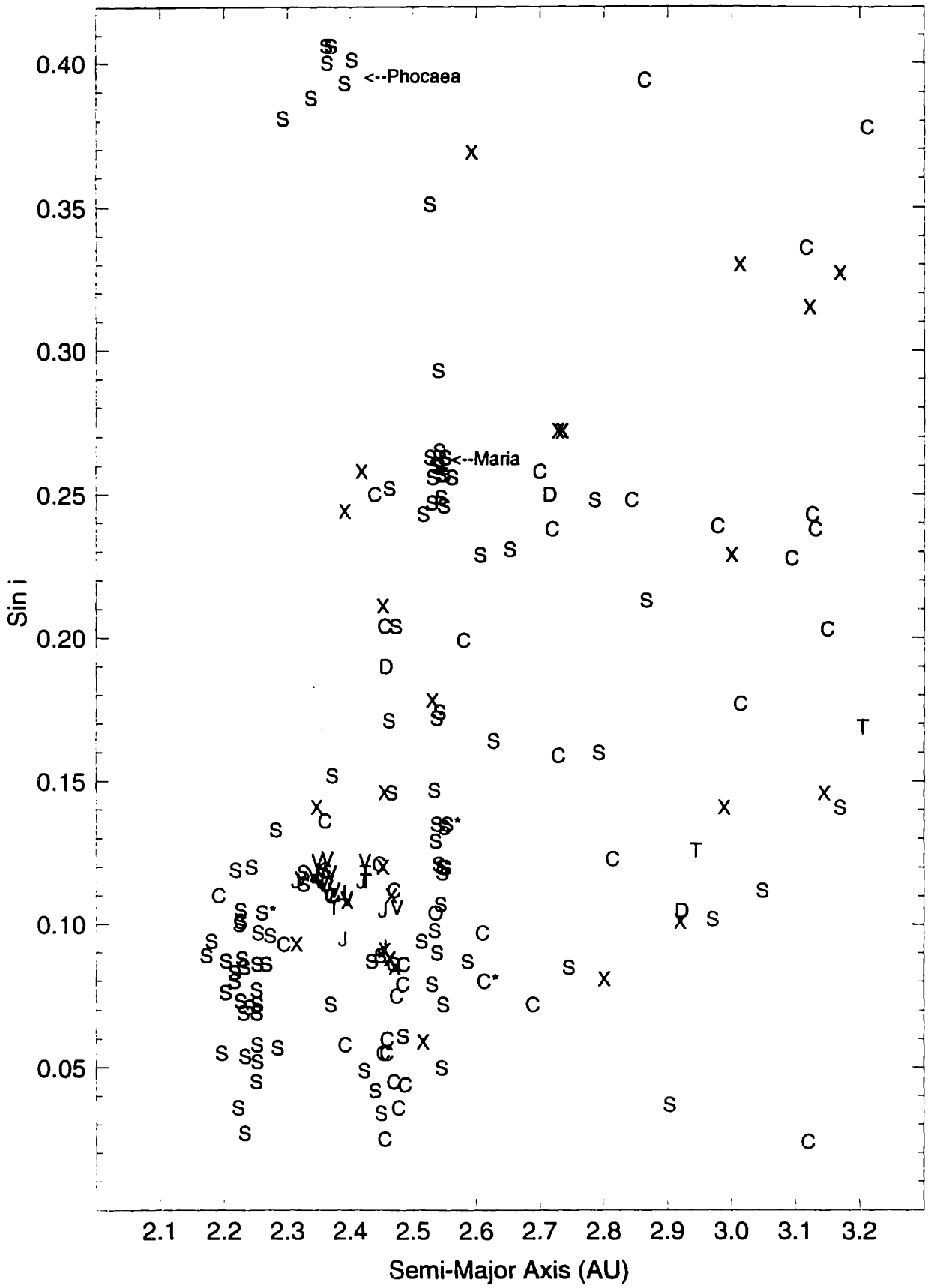

Fig. 3.30b. Semi-major axis (*a*) vs inclination (sin *i*) plot for SMASS new objects.

3.5 Observational Results for Several Asteroid Families

It is widely accepted that asteroid families formed through the collisional disruption of a larger parent body (Chapman *et al.* 1989). The family members share the same parent body's composition and formation age. A fair number of family members were observed in SMASS. Table 3.13 reconstitutes and summarizes the taxonomic results for 12 families for which there are four or more SMASS observed members. The results in Table 3.13 clearly indicate that most families show taxonomic homogeneity. A few families, such as #67 Laetitia family, have a great variety of taxonomic compositions. Asteroid 1 Ceres (C-type) is probably a member in the Laetitia family. If #67 Laetitia is a true family association, it implies that there was strong differentiation within the parent body. Although the true distribution of taxonomic types among the near-Earth population is masked by observational bias due to their small sizes and special orbits (Luu and Jewitt 1990, McFadden *et al.* 1989), our SMASS shows that near-Earth asteroid population is diverse in terms of surface compositions. Among 9 observed asteroids, 5 S, 2 X, 1 C, and 1 V-type asteroids were discovered. The two asteroids (4031 and 4440) in the Hungaria family are probably E types, as indicated by Gaffey *et al.* (1992). Observation of 5 new objects in #24 Nysa family strongly indicates that all of the family members, except 44 Nysa, are C types, or perhaps F types (a subset of C type). This family is in the inner main belt, usually dominated by S asteroids. Interestingly, the largest object in this family, 44 Nysa, is an E-type asteroid. There is some separation between 44 Nysa and the rest of the family. If indeed, 44 Nysa is one of the family members, the juxtaposition of the C or F fragments and the largest known E is surprising (Williams 1992). Family #165 and #196 are associated with the Vesta family (#169), and will be discussed in the next section.

Table 3.13

Observational Results for 12 Asteroid Families or Groups

	Near-Earth								
Asteroid	4179	1991VK	1991VL	1991WA	1991XB	1992CC1	1992NA	1992TC	1992UB
Type	S	S	V:	S	S	S	C	X	X
	Mars Crossing								
Asteroid	512	1198	2074	2078	2204	2253	3674		
Type	S	S	S	S	X	S	X		

Table 3.13 (continued)

Phocaea

Asteroid	25	290	1584	1626	1934	2014	2105	2965	3792	4761	4956
Type	S	S	S	S	S	S	S	S	S	S	X:

Eos (#2)

Asteroid	221	339	529	639	653	2091
Type	S	S	S	S	S	C:

Koronis (#3)

Asteroid	158	167	243	263	720	811	1289	1635	1725
Type	S	S	S	S	S	S	S	S	S

Maria (#4)

Asteroid	879	2420	3158	3167	3332	4159
Type	S	S	S	S	S	S

Nysa (#24)

Asteroid	44	2728	2923	3963	3999	4219	4562
Type	E	C	C	S	C	C	C

Laetitia (#67)

Asteroid	39	374	441	446
Type	S	S	M	A

Ausonia (#165)

Asteroid	1273	1697	1929	2011	3944
Type	V	T	V	J	V

Vesta (#169)

Asteroid	4	1906	3268	3494	4038	4147	4215
Type	V	V	V	V	V	V	J

Tinchen (#196)

Asteroid	1933	2024	2590	3155	3657	3968	4546
Type	V	S	V	J	V	V	V

Flora (#189)

Asteroid	8	951	1451	1651
Type	S	S	S	S

The family definitions are from Williams (1992) and personal communication.

: Indicates a noisy spectrum and/or a classification of dubious quality.

We now examine several families with at least 6 observed members to investigate the compositional diversity within each family. Fig. 3.31 shows the spectra of #3 Koronis family. This family has been carefully studied by Binzel (1988) and Binzel *et al.* (1993b). Asteroids 158 and 1289 have spectra which are essentially identical to that of 243 Ida. However, the other six members show spectra that are substantially different. Asteroids 167, 263, 720, 811, 1635, and 1725 show deeper band depths at 9000 Å. Fig. 3.32 shows the heliocentric distribution of the Koronis family and depicts the locations of Ida and the other observed family members. It is interesting to note that the three asteroids that are most spectrally similar, 158, 243, and 1289 are all adjacent to one another. The six asteroids which are farthest from 243 Ida, 167, 263, 720, 811, 1635, and 1725 show the greatest spectral differences. The observed spectral variations suggest that there is a compositional gradient within the family. However, such a conclusion must be considered tentative because of the small sample size of only 9 objects.

Fig 3.33 and 3.34 show the spectra and heliocentric distribution of 10 objects in the Phocaea group. All are classified as S types from our PCA. Most of the asteroids display similar spectral features, except 2105, 1934, and 2965. Asteroid 2105 shows a featureless spectrum longward of 7000 Å and is located at the edge of this family. Asteroids 1934 and 2965 are probably olivine-rich objects (Binzel and Xu 1990). Fig. 3.35 and 3.36 show the spectra and distribution of 6 members in the Eos family. Asteroids 221 Eos and 653 Berenike were defined as K class by Bell (1988). The Eos family seems to have a great variety of compositions. Asteroids 339, 639, and 2091 show almost no pyroxene 1 μm band absorption features. But a strong pyroxene or perhaps olivine absorption band is revealed in the spectrum of 529 Preziosa. Fig. 3.37 and 3.38 show the spectra and distribution of 6 asteroids in the Maria family. All 6 members are S-types. The spectra indicate that this family has uniform composition. Fig. 3.39 shows the spectra of 5 members in the Nysa family. Fig. 3.40 shows the spectra of 9 near-Earth asteroids, and their locations in the principal component space, respectively. As noted by Britt *et al.* (1992), we found that near-Earth asteroids are closer to the ordinary chondrites than other S or C classes in the principal component space (Fig. 3.41).

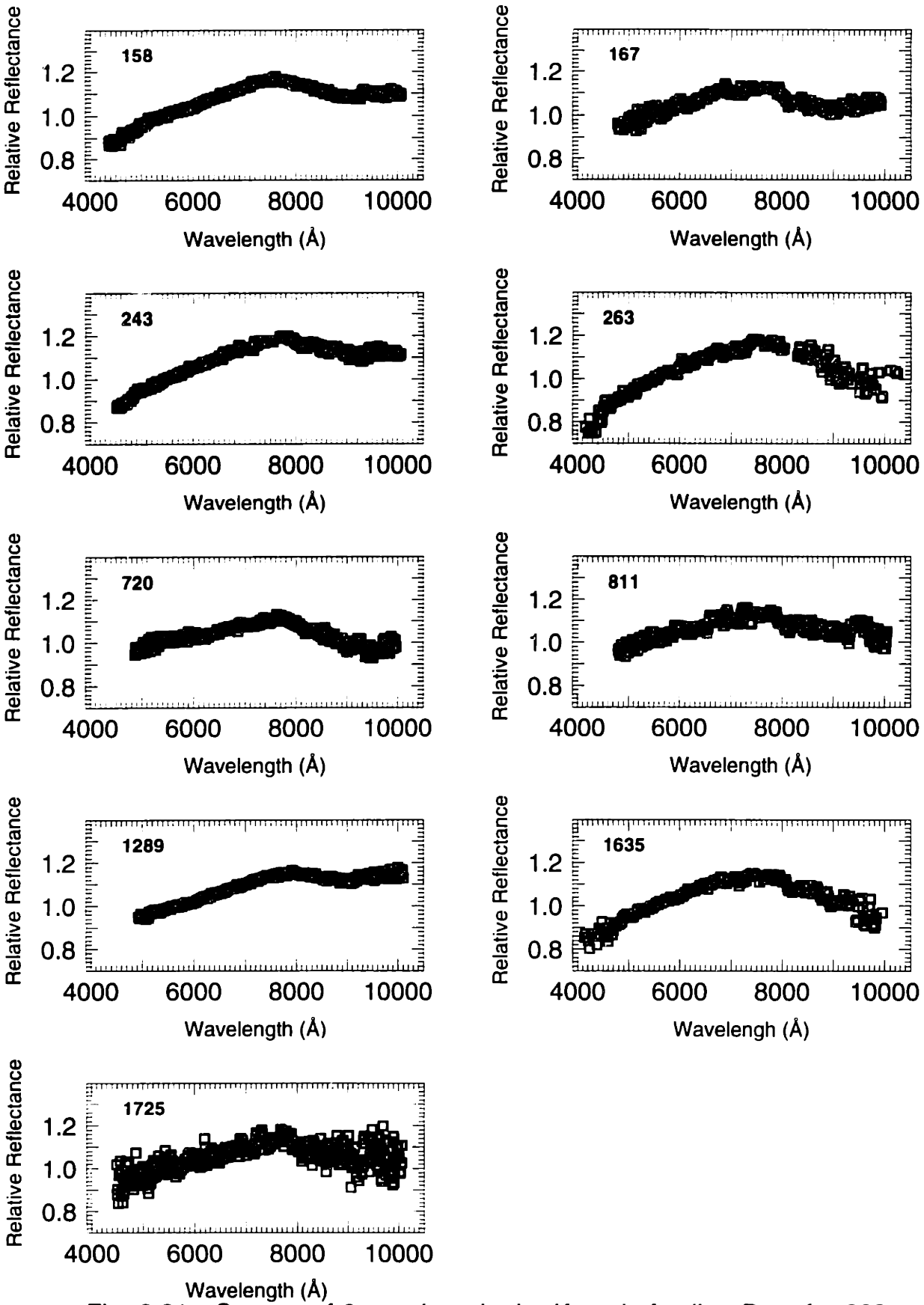

Fig. 3.31. Spectra of 9 members in the Koronis family. Data for 263, and 1635 were obtained by Binzel and Bus in September 1993.

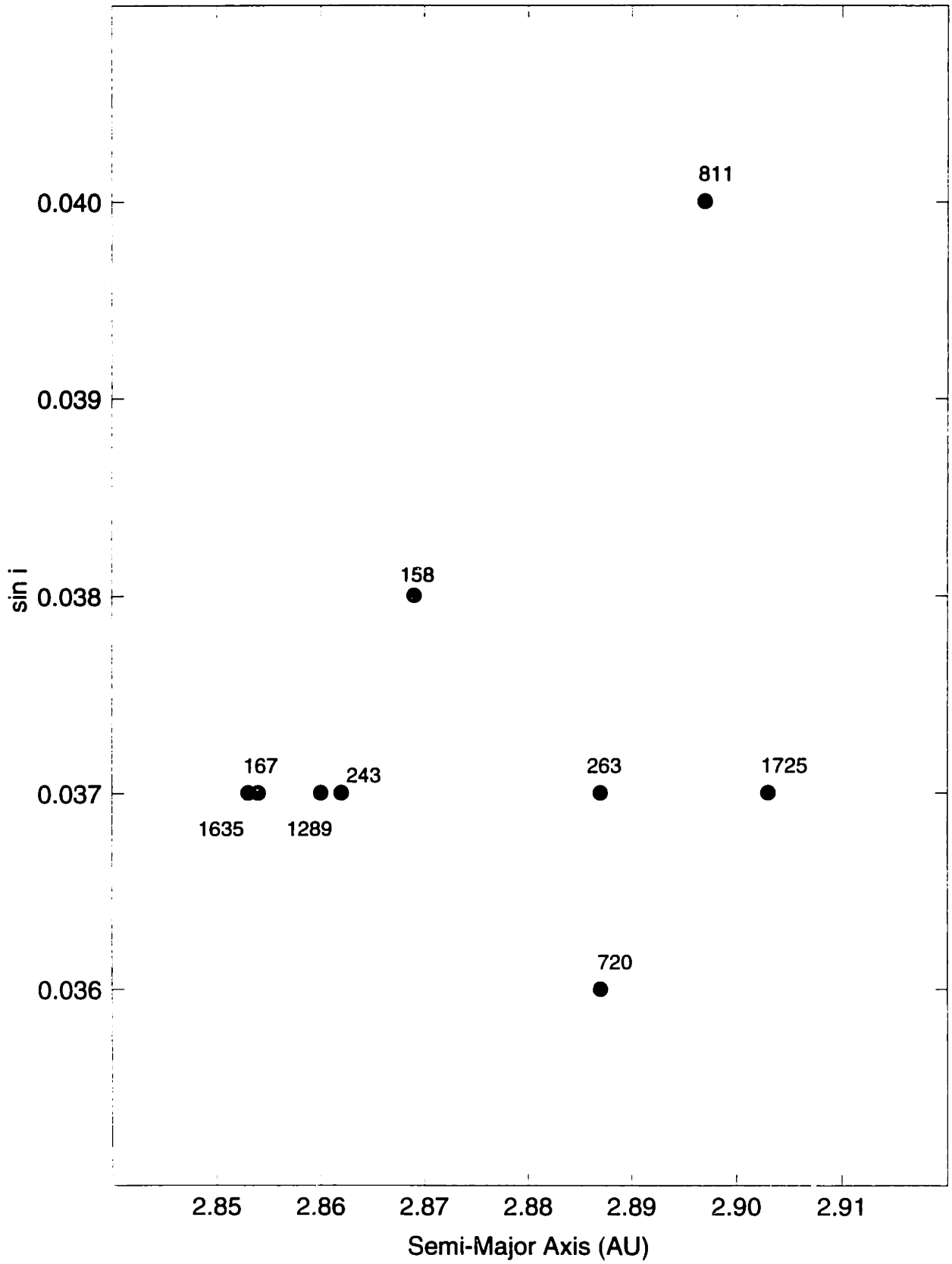

Fig. 3.32. Heliocentric distribution of 9 observed asteroids in the Koronis family.

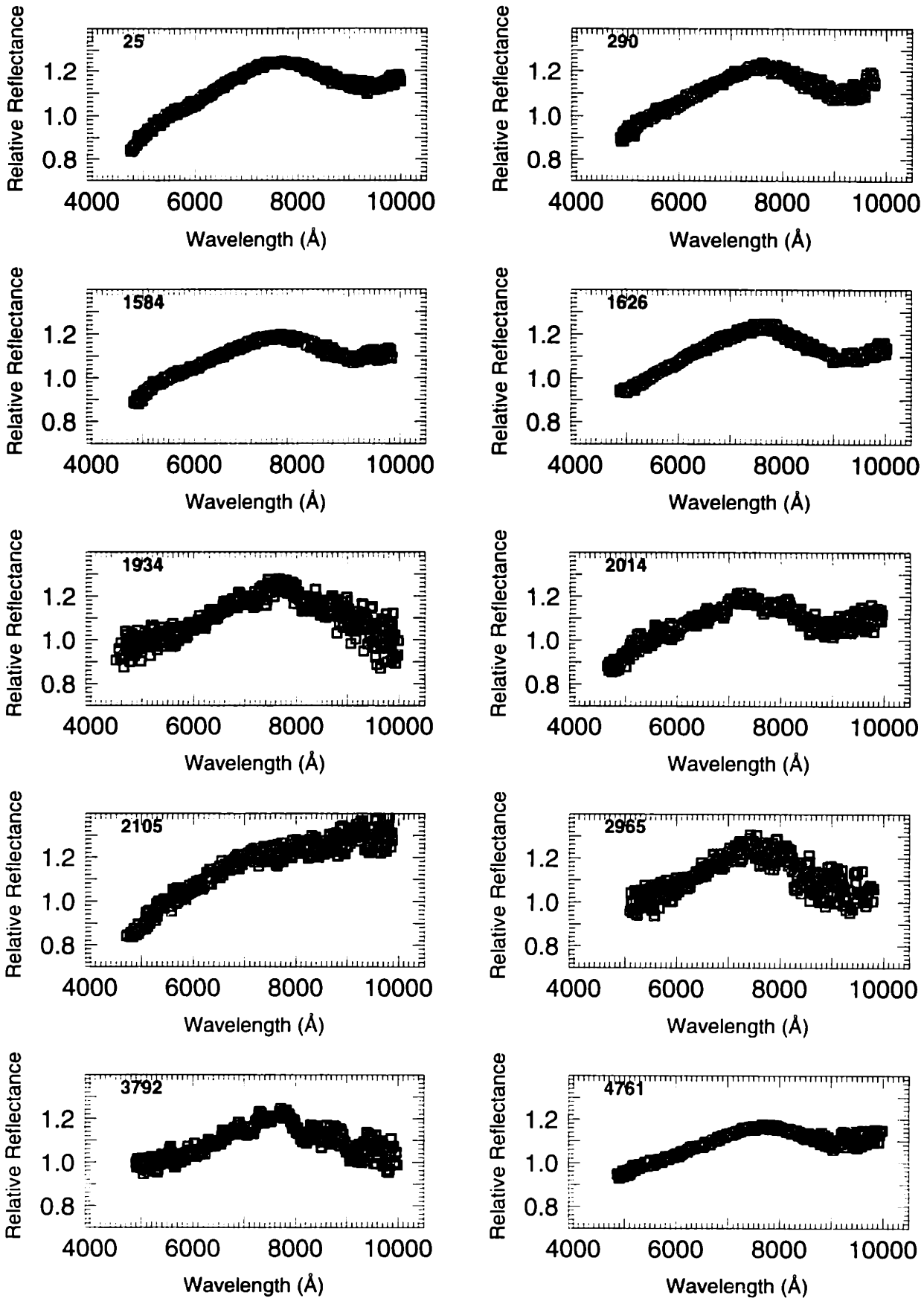

Fig. 3.33. Spectra of 10 members in the Phocaea group.

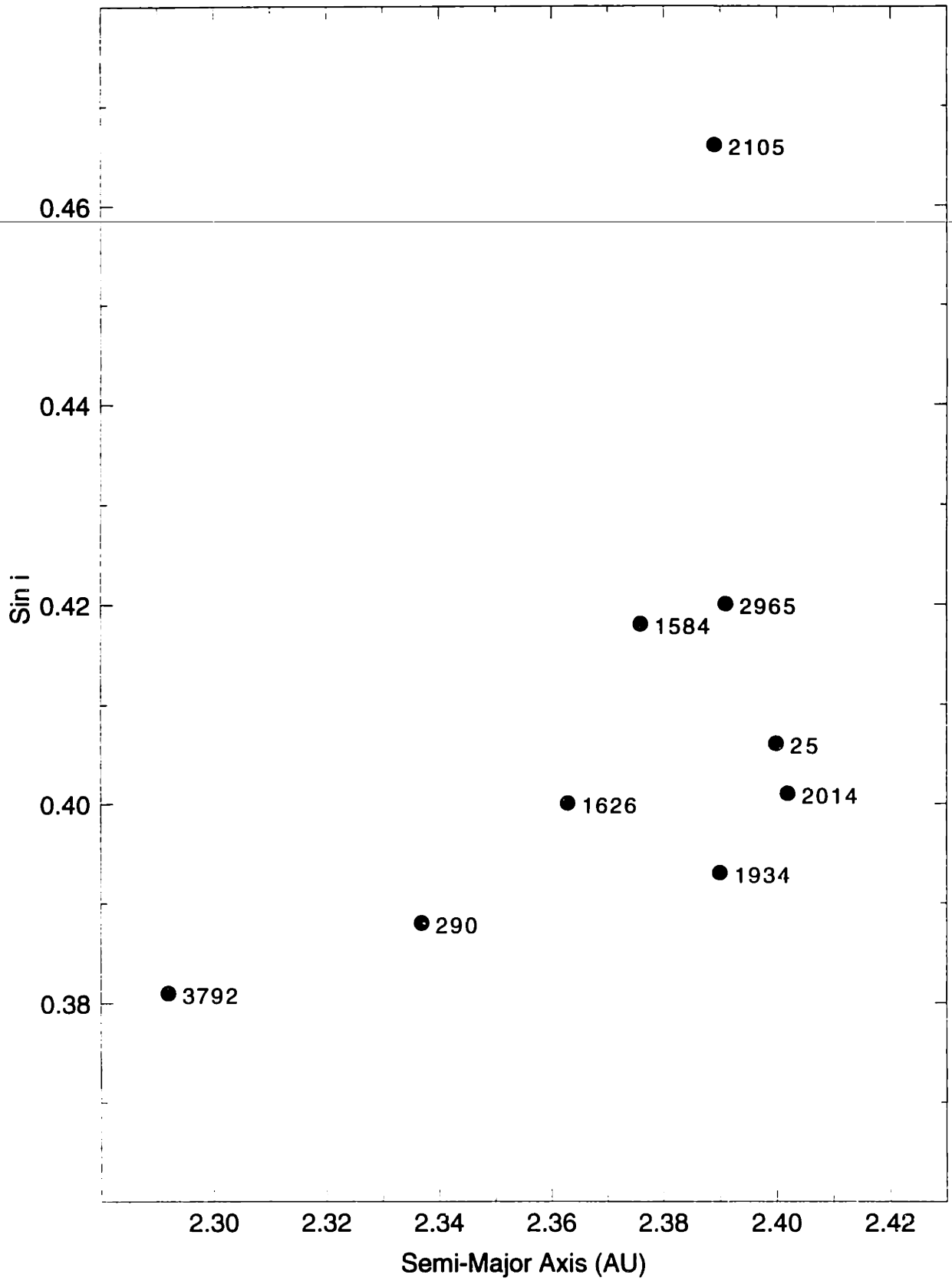

Fig. 3.34. Heliocentric distribution of 9 observed asteroids in the Phocaea group (element information for 4761 not available).

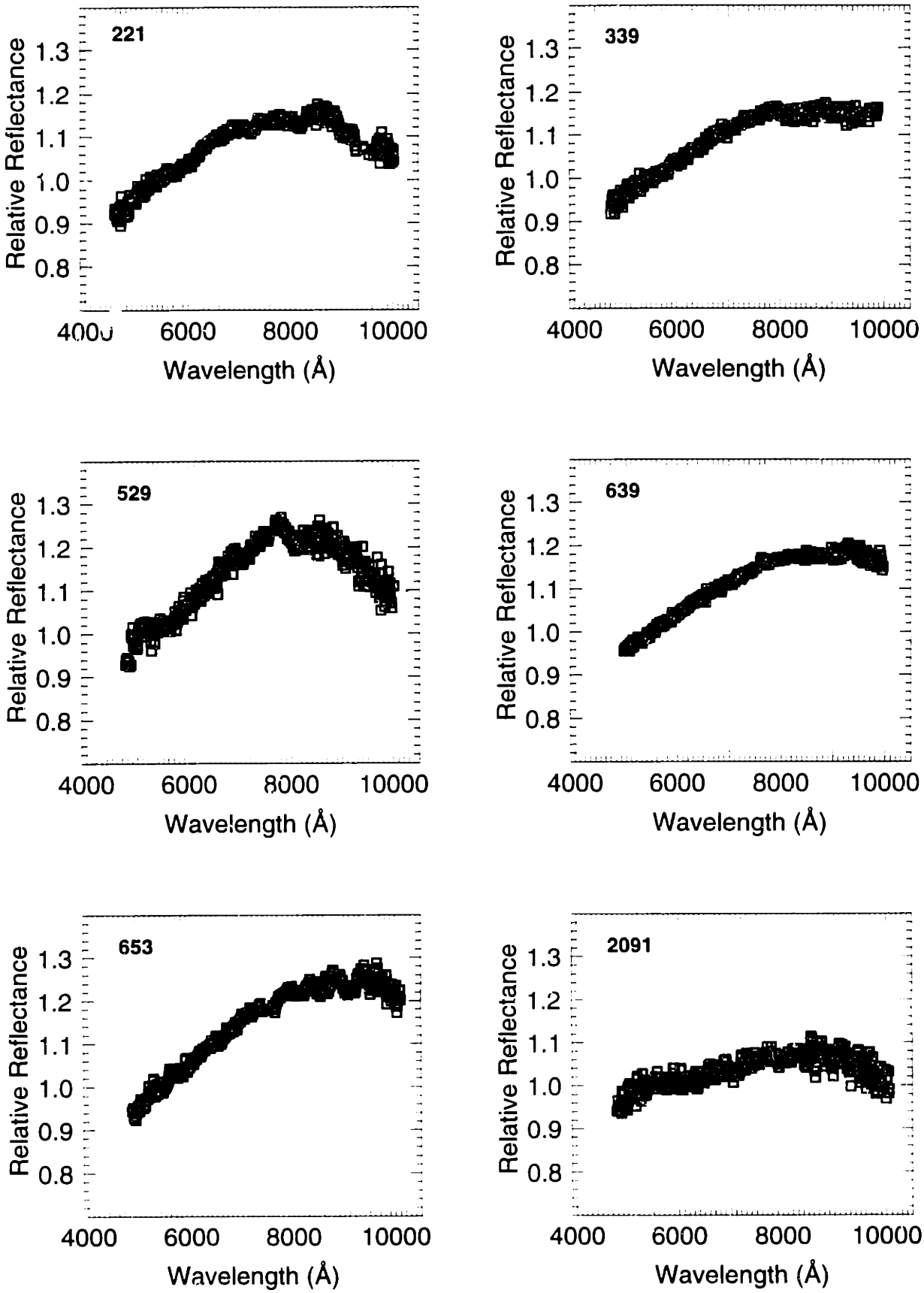

Fig. 3.35. Spectra of 6 members in the Eos family.

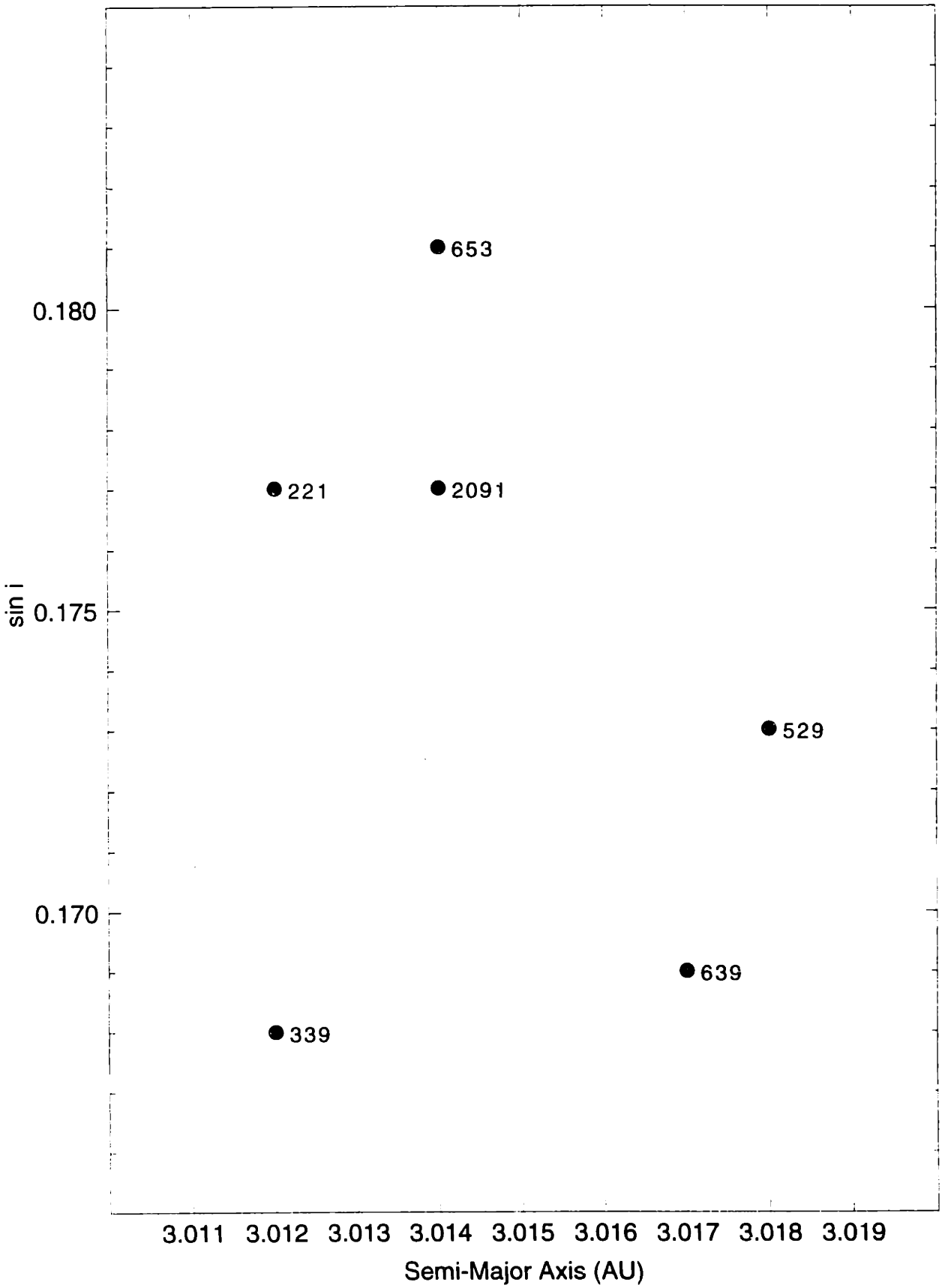

Fig. 3.36. Heliocentric distribution of 6 observed asteroids in the Eos family.

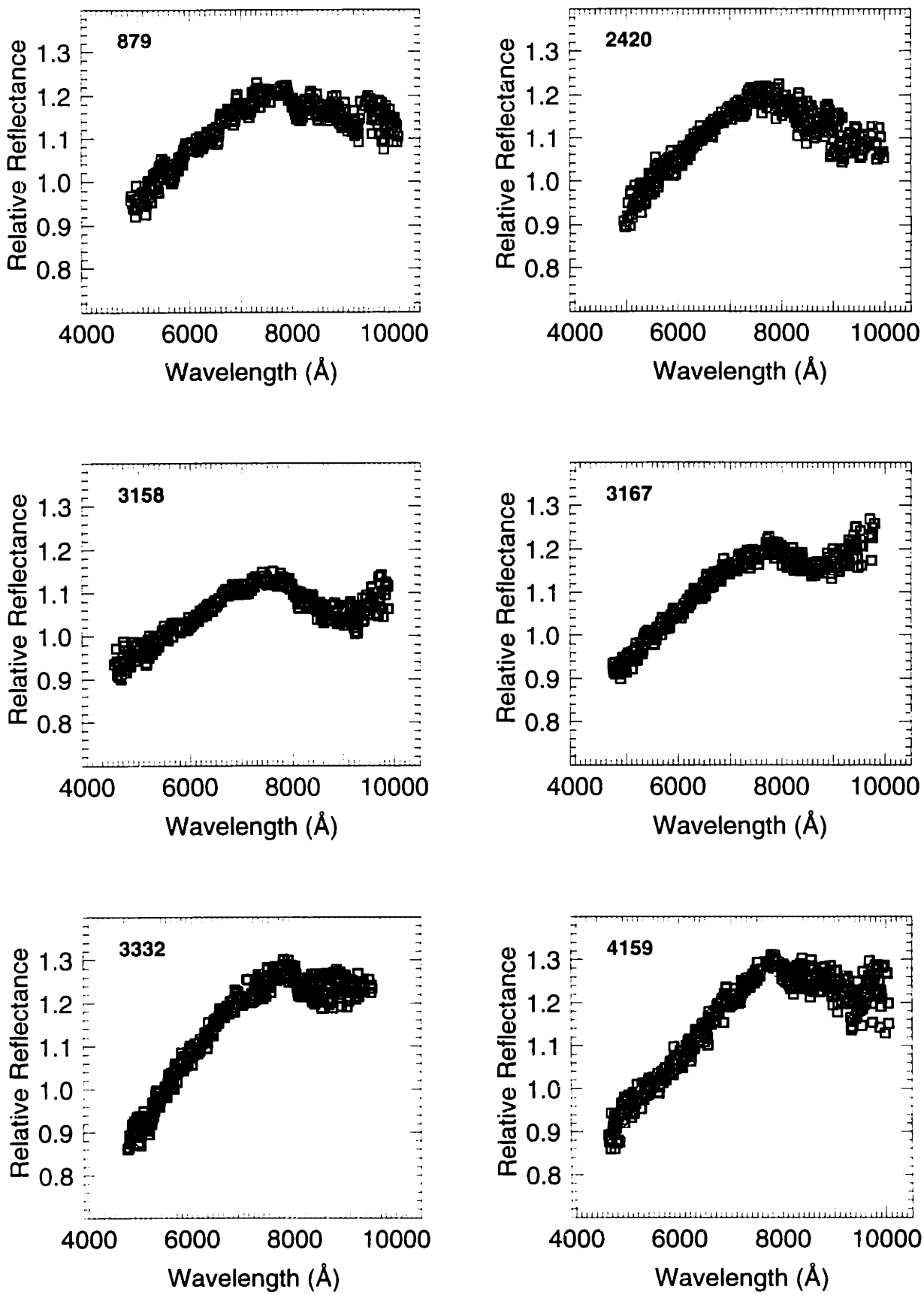

Fig. 3.37. Spectra of 6 members in the Maria family.

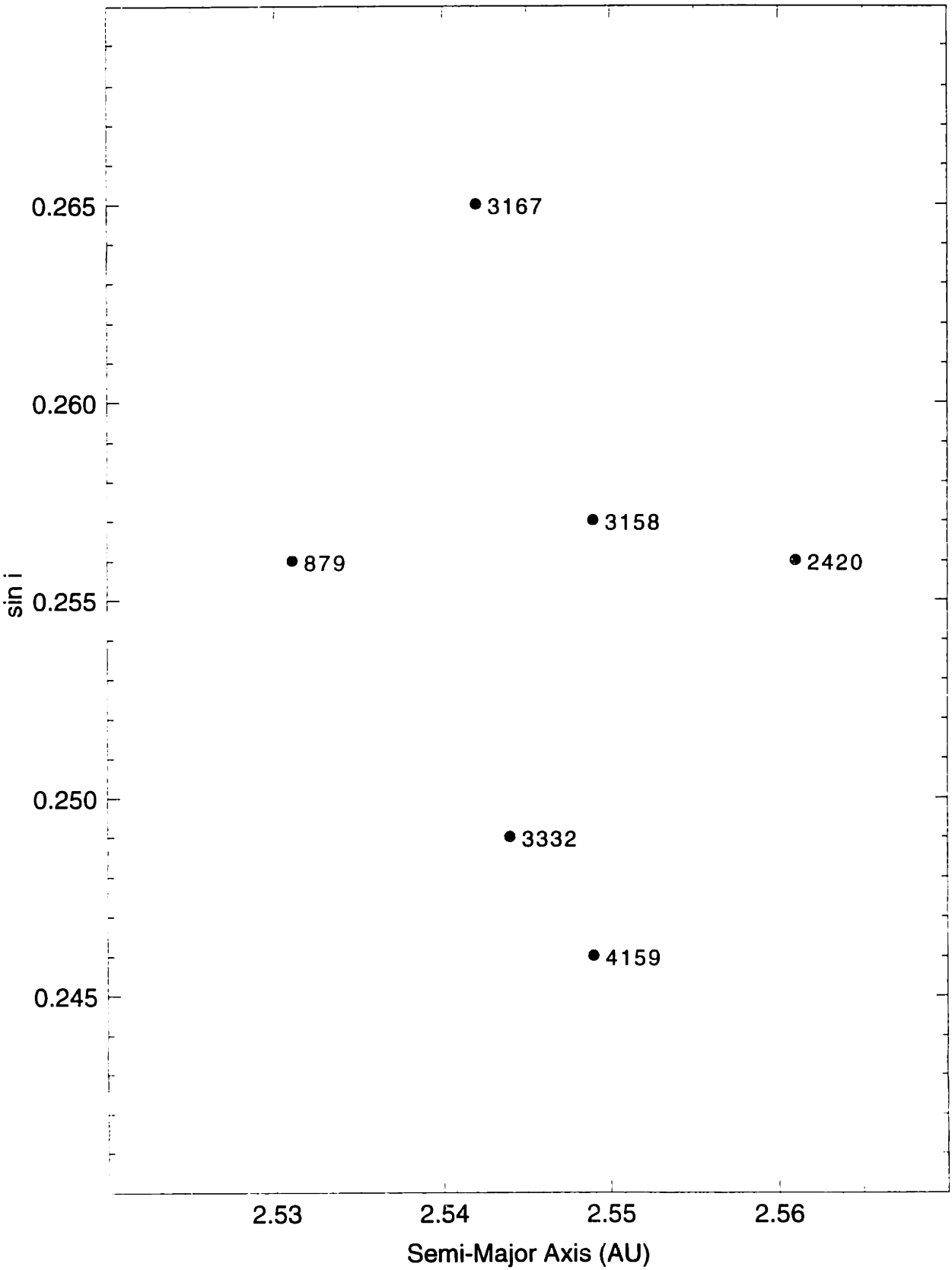

Fig. 3.38. Heliocentric distribution of 6 observed asteroids in the Maria family.

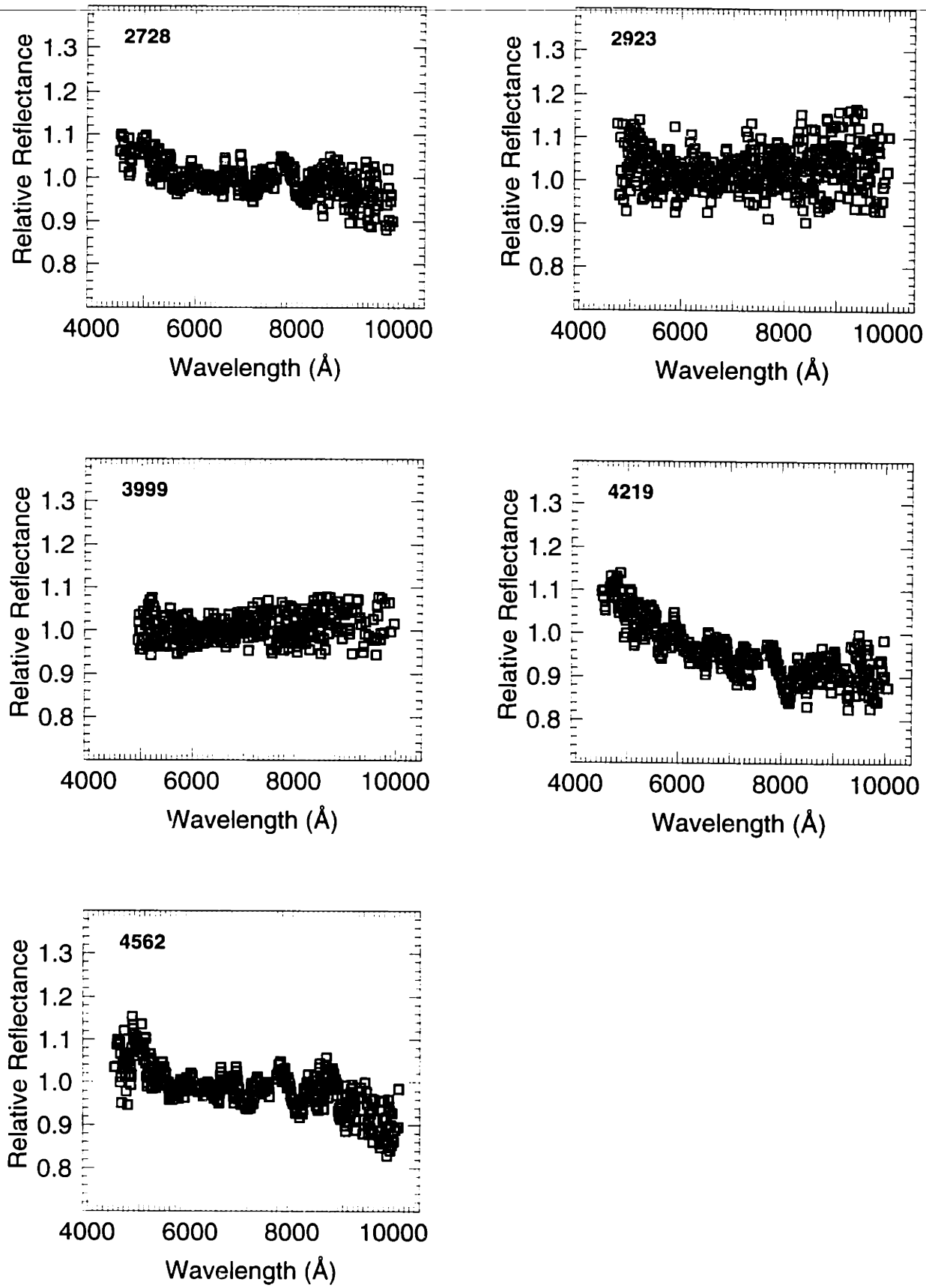

Fig. 3.39. Spectra of 5 members in the Nysa family.

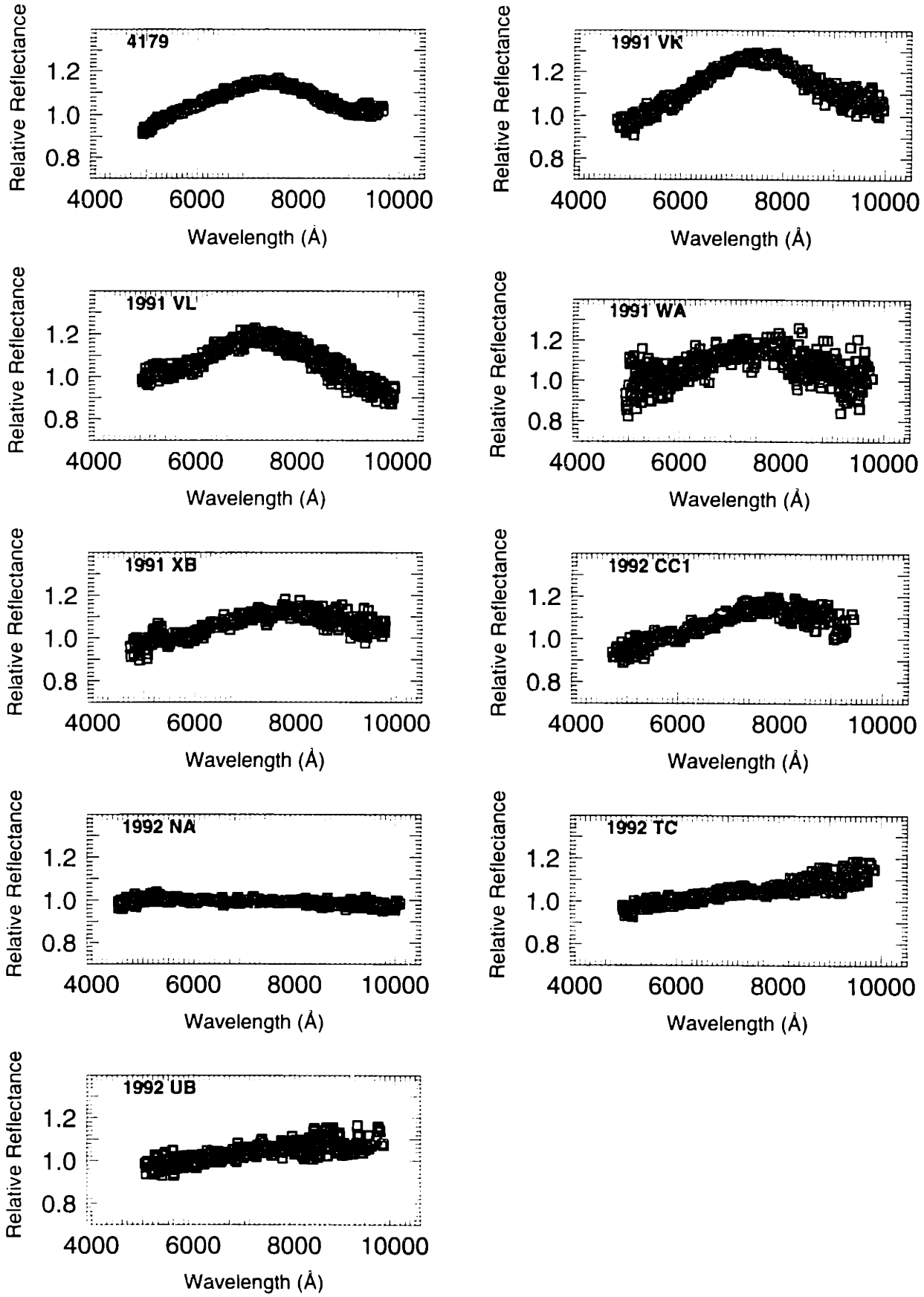

Fig. 3.40. Spectra of 9 near-Earth asteroids.

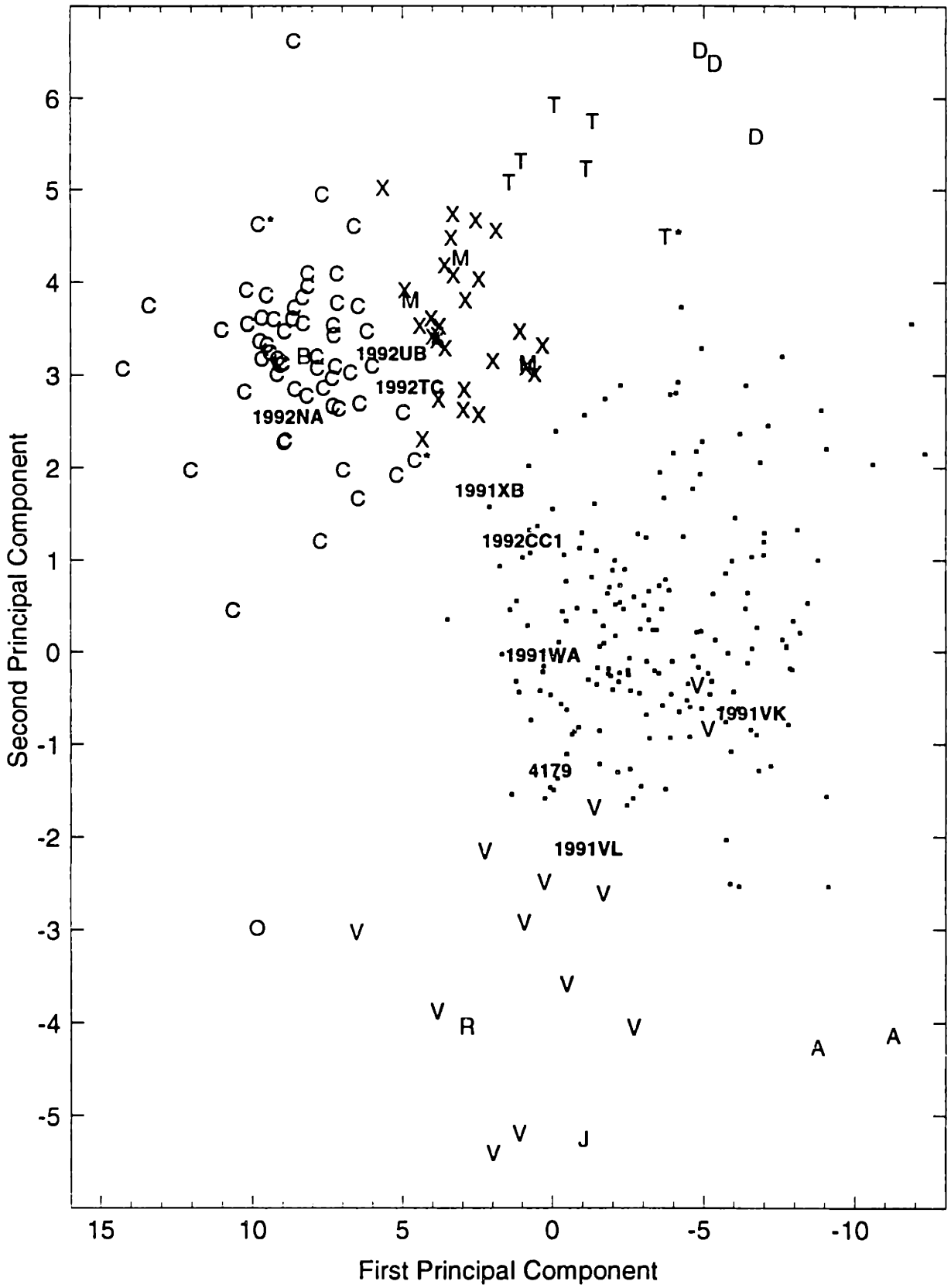

Fig. 3.41. The locations of 9 near-Earth asteroids in the principal component space (315 SMASS objects).

3.6 Chips Off of Vesta: Evidence for the Parent Body of Basaltic Achondrites

About 6% of the meteorites falling to Earth have an igneous composition indicative of an origin in lava flows or basaltic intrusions on other planetary bodies. Although a few individual basaltic achondrite meteorites are now generally recognized to have been derived from the Moon and Mars, there remains a debate over the parent body for most of these meteorites: the eucrites, diogenites, and howardites (McSween 1985). Compositionally, the eucrites have the characteristics of surface basalts, the diogenites are plutonic, and the howardites are polymict breccias consisting of eucrite and diogenite fragments.

Asteroid 4 Vesta has been at the center of the debate over the howardite-eucrite-diogenite (HED) parent body. Vesta's optical spectrum, first measured by McCord *et al.* (1970), contains a strong absorption band due to pyroxene centered near 9000 Å. On the basis of comparison with laboratory spectra of basaltic achondrites and Apollo 11 lunar samples, McCord *et al.* concluded that Vesta's surface is basaltic. Subsequent researchers (Larson and Fink 1975) have interpreted that Vesta has a differentiated basaltic crust composed of a Mg-rich and Ca-poor clinopyroxene pigeonite. Drake (1979) argued that Vesta must be the source for the basaltic achondrite meteorites. Vesta's spectrum and apparent basaltic achondrite composition is unique among all other large main-belt asteroids, over 600 of which had been investigated (Zellner *et al.* 1985) before the SMASS program started. However, apparent dynamical difficulties in delivering fragments from Vesta to the Earth have precluded any general consensus toward this conclusion (Wetherill 1987). Vesta is far from dynamically favored meteorite source regions, the 3:1 Jovian and the ν_6 secular resonances, where asteroid orbits can dynamically evolve into Earth-crossing trajectories (Wisdom 1985, Wetherill 1988). Obtaining meteorite samples from Vesta requires a seemingly implausible first step in which large (kilometer-sized) fragments must be ejected with sufficient velocities to reach a resonance (Greenberg and Chapman 1983, Wetherill 1985, Greenberg and Nolan 1989).

Our SMASS results reveal observational evidence that large (multikilometer) fragments have been ejected from Vesta with significant velocities, implying that substantial meteoroid parent body samples from Vesta can reach the resonances. In SMASS, we obtained spectra of 16 out of ~30 asteroids that have

been proposed to be linked to Vesta as a dynamical family (Zappalà *et al.* 1990, Williams 1989, 1992, and personal communication) and more than 100 other small main-belt asteroids in the region nearby Vesta (Fig. 3.42, Tables 3.14 and 3.15). Thirteen of the observed Vesta family members and eight of the other small main-belt asteroids sampled display basaltic achondrite spectra, characterized most notably by a strong pyroxene absorption band near 9000 Å (Fig. 3.43 and 3.44). Those in Fig. 3.43 are similar to Vesta, showing the spectral characteristics of eucrite meteorites with absorption band centers near 9400 Å. Given that Vesta's spectrum is distinct among main-belt asteroids and the close dynamical relation of these small asteroids, they are almost certainly fragments excavated from Vesta's crust. The only significant differences they show from Vesta's spectrum are steeper slopes shortward of 7500 Å, possibly attributable to slight variations in Fe content, surface opacity, or grain sizes. Particle size effects either from solid rock surfaces or particulate surface material might also produce the observed differences in band depths and spectral slopes. Such slope variations are readily seen within the class of eucrite meteorites (Gaffey 1976).

The spectra in Fig. 3.44, however, show more extreme basaltic achondrite features: they peak more sharply at a shorter wavelength and show a much deeper and less broad 9000 Å absorption band which is centered at a shorter wavelength than for eucrites. These characteristics are suggestive of diogenite basaltic achondrite meteorites. A positive relation to diogenites, however, must await additional spectroscopic measurements between 1.0 and 1.5 μm. At these wavelengths, diogenites are distinguished from eucrites by their lack of a weak feldspar absorption band. Because these spectra (Fig. 3.44) are visibly distinguishable from Vesta's overall spectrum and fall far from Vesta when translated into principal component space, we propose that these asteroids represent a new taxonomic class which we denote by the letter J (mnemonic for the Johnstown diogenite meteorite). Diogenites are plutonic rocks with coarse grain sizes formed during crystal accumulation in a subsurface magma chamber within a body having a eucritic surface, perhaps forming at substantial depths (Grove and Bartels 1992). Large impacts could subsequently excavate diogenite samples. Gaffey (1983) found at least one pyroxene-rich region on Vesta which he interpreted as having a diogenite composition resulting from impact excavation.

Table 3.14

Summary of Vesta-Family Observations

Asteroid		Observation Dates (UT)	N*
4	Vesta	91/10/31	3
		91/12/07	1
		92/03/14	1
1273	Helma	93/01/21	2
1646	Rosseland	92/11/26	2
		92/11/27	2
1906	Naef	91/12/07	3
		91/12/08	4
		91/12/14	3
		91/12/15	6
1929	Kollaa	92/11/27	2
1933	Tinchen	92/09/06	2
		92/09/07	3
2011	Veteraniya	92/11/29	1
		92/11/30	1
		92/12/01	1
2024	McLaughlin	93/01/21	2
2113	Ehrdni	93/01/21	3
2442	Corbett	92/11/30	1
		92/12/01	1
2590	Mourao	92/11/26	3
3153	Lincoln	92/11/28	1
		92/12/01	1
3155	Lee	91/10/28	4
		91/10/29	4
3268	De Sanctis	92/03/11	2
3494	1980 XW	93/01/21	2
3657	1978 ST6	92/09/06	2
		92/09/07	4
3869	Norton	92/03/11	3
		92/03/12	3
3944	Halliday	92/11/28	1
		92/11/29	2
		92/12/01	1
3968	Koptelov	92/09/05	3
		92/09/06	3
4005	1972 TC2	91/12/07	2
		91/12/08	6
4038	Kristina	91/10/29	4
4147	Lennon	92/09/05	3
		92/09/06	3
4215	1987 VE1	93/01/21	2
4510	Shawna	93/01/21	1
4546	Franck	92/11/28	2

* The number of independent spectral images for each night.

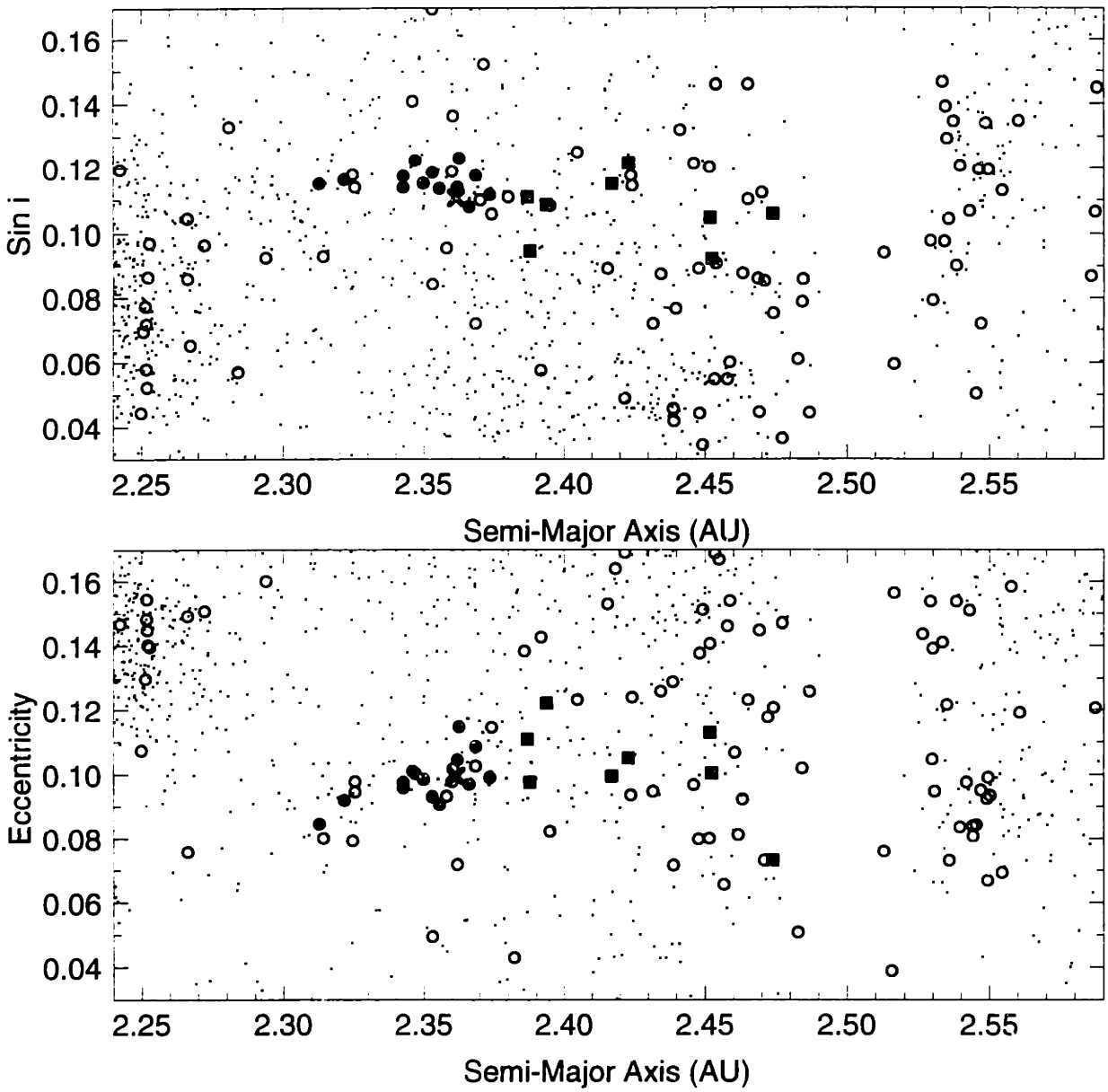

Fig. 3.42. Distribution of asteroids in proper orbital element space (Milani and Knezevic 1992) in the inner main belt for **(top)** semi-major axis versus sin i (inclination) and **(bottom)** semi-major axis versus eccentricity. Vesta's position is denoted by **×**. The symbol • indicates the positions for the thirteen predicted Vesta family asteroids that we have observed to display basaltic achondrite spectra. Positions for asteroids that we have also observed, but which do not have spectral properties like basaltic achondrites are denoted by o. Eight additional discovered basaltic achondrite asteroids, depicted by ■, bridge the region between Vesta and the 3:1 resonance Kirkwood gap (evidenced by the paucity of asteroids at 2.50 AU, right). Note that these latter objects are found only within limited ranges of inclination and eccentricity which encompass Vesta.

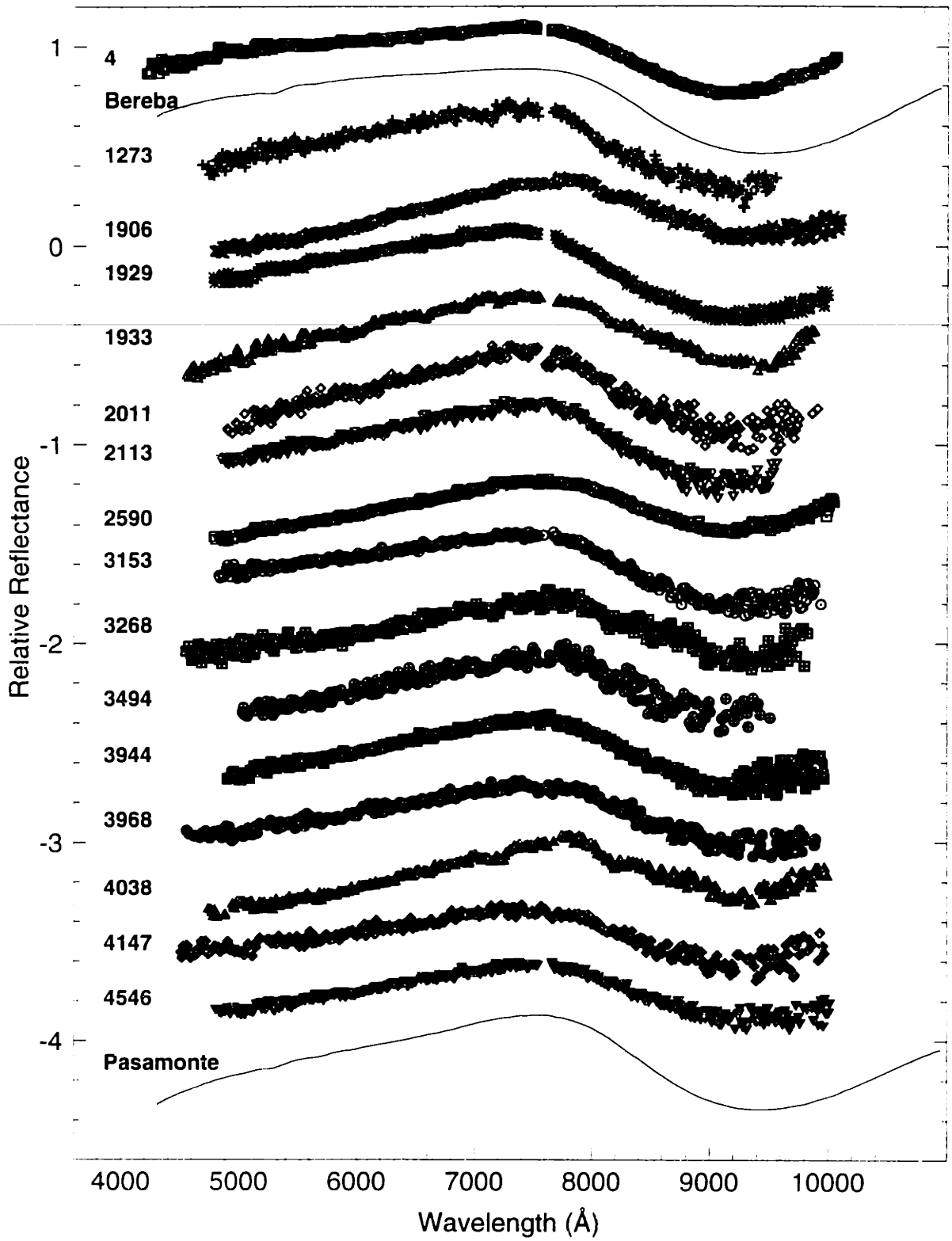

Fig. 3.43. Spectra for fifteen of the asteroids (D=4-8 km) that display a deep absorption band near 9000 Å, characteristic of basaltic achondrites. A spectrum of Vesta itself, obtained with the same instrumentation is included for comparison. Spectral characteristics for all of these asteroids fall within the range measured for eucrites, where measurements for Bereba and Pasamonte (solid lines, Gaffey 1976) are included for comparison. Spectra have been offset vertically for clarity.

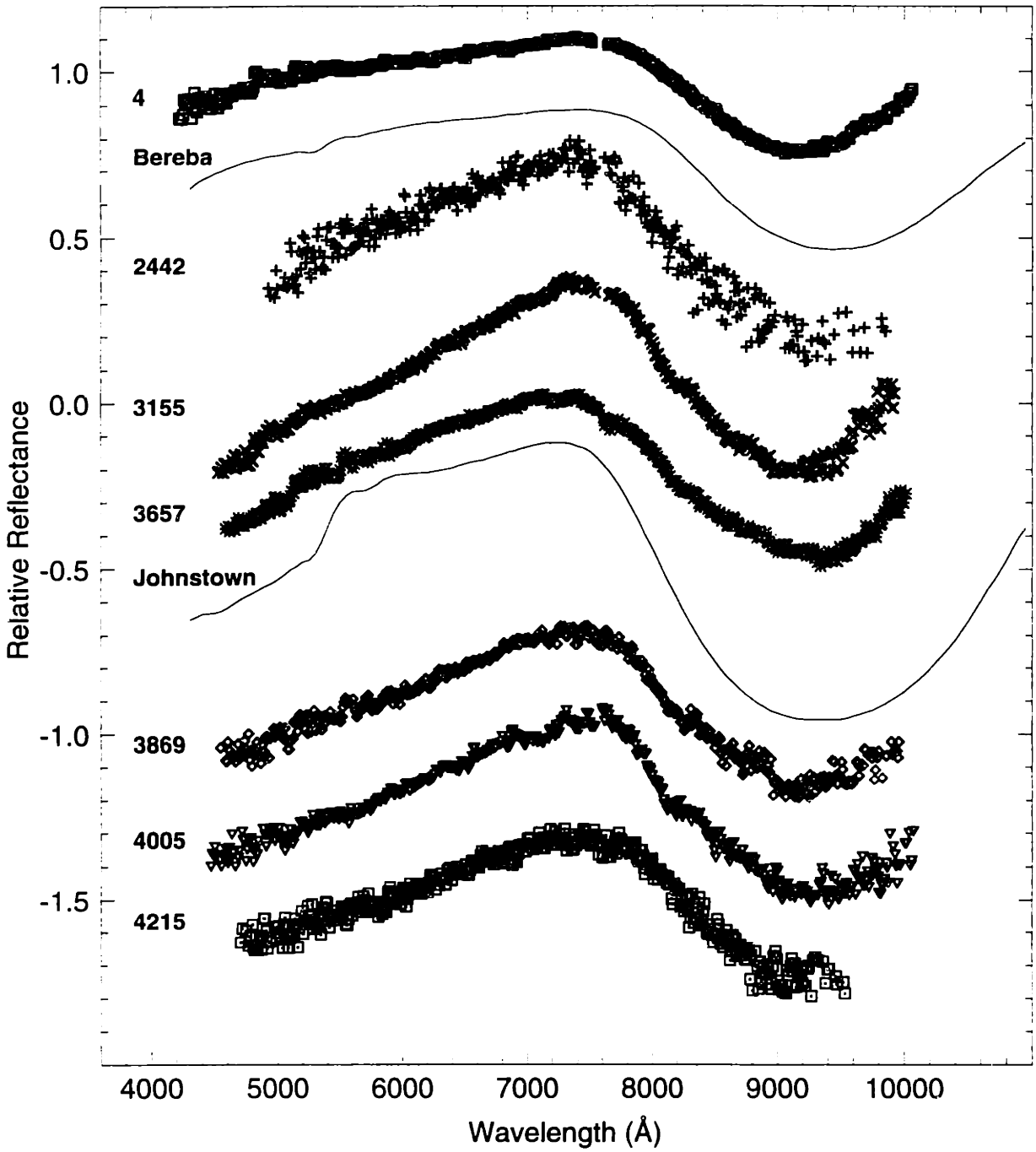

Fig. 3.44. Spectra for six additional basaltic achondrite main-belt asteroids (D=6-10 km). Vesta and the Bereba eucrite meteorite are included for comparison. Compared with eucrite spectra, these asteroids show steeper slopes below 7500 Å, sharper peaks, and deeper 9000 Å absorption bands centered at a shorter wavelength. Their spectral properties are more analogous to the diogenite class of basaltic achondrite meteorites. A spectrum of the Johnstown diogenite meteorite (Gaffey 1976) is included for comparison. A new taxonomic class *J* is proposed for diogenite-analog asteroids. All spectra have been offset vertically for clarity.

Could large fragments, such as these basaltic achondrite asteroids be excavated from Vesta? We explicitly examine impacts as the likely excavation process. For a fragment of mass m to escape a parent body's surface, its total kinetic energy E upon ejection must be greater than or equal to the potential energy needed to escape, E_{esc}. We denote $E_a = E - E_{esc}$ as the additional kinetic energy of the fragment beyond E_{esc}. Thus

$$\frac{1}{2}mv^2_{eject} = \frac{1}{2}mv^2_{esc} + \frac{1}{2}mv^2_a \qquad (3.6.1)$$

where v_{eject} is the ejection velocity of the fragment, v_{esc} is the surface escape velocity for the parent body, and v_a is the scalar value for the additional velocity. For Vesta we assume that the mean diameter is 520 km (Dunham 1991) and the mean density is 3.5 g cm^{-3} to compute v_{esc} = 365 m/s. To compute v_a, which allows a fragment to achieve an independent heliocentric orbit, we first assume the parent body has a circular orbit. The orbital velocity can be written as $v_{orb} = \sqrt{(GM/a)}$, and for a small velocity change

$$\Delta v = -\frac{1}{2}(GM)^{\frac{1}{2}} a^{-\frac{3}{2}} \Delta a \qquad (3.6.2)$$

where Δa is the change in semi-major axis of the fragment's orbit with respect to the parent body and M is the solar mass. The planar tangential component of the fragment's additional velocity is given by $v_a = -\Delta v$, where for positive values of v_a (in the direction of the parent body's orbital velocity) the semi-major axis increases and v_{orb} decreases. The radial and out of plane components serve to change the fragment's orbital eccentricity (e) and inclination (i). For a parent body in an eccentric orbit, Δe and Δi for a fragment's orbit are highly sensitive to the parent body's position at the time of ejection. Because Vesta has a modest orbital eccentricity (Milani and Knezevic 1992), and because e and i are subject to secular perturbations, we cannot reliably use these orbital elements to compute specific values for v_a. Thus, $v_a = |\Delta v|$ represents our only reliable value for the magnitude of any specific fragment's additional velocity. However it also represents a minimum for v_a, being based on only the planar tangential component. We choose to account for the existence of all three vector components by assuming them to be equal and obtain $v_a = \sqrt{3}|\Delta v|$ for the three-dimensional resultant, where ejection velocities based on this assumed isotropy should give a reliable average for a

sample of fragments (Table 3.15). Individual ejection velocities for the isotropic and minimum velocity cases are thus estimated by:

$$v^2_{eject} = v^2_{esc} + \frac{3}{4} GM\, a^{-3} (\Delta a)^2$$

$$v^2_{min} = v^2_{esc} + \frac{1}{4} GM\, a^{-3} (\Delta a)^2 \qquad (3.6.3)$$

The largest fragments excavated from a target body during an impact event are most likely spalls originating from the surface near the impact point (Melosh 1984). We can relate the total volume of the spall fragments (V_{sp}) to the diameter of the impacting projectile (d) by:

$$\frac{V_{sp}}{d^3} = \frac{0.8\, \pi\, T}{\rho_T\, C_L\, v} \left[1 - \left(\frac{2\, v_{eject}}{v} \right)^{\frac{1}{3}} \right] \qquad (3.6.4)$$

where T is the dynamic tensile strength of the target (taken to be 10^8 Pa), ρ_T is density of the target (assumed 3.5 g cm^{-3}), C_L is the wave propagation speed in the target (assumed 6 km/s), and v is the projectile impact velocity (Melosh 1985).

We estimate v following the methods described by Namiki and Binzel (1991). From a bias-free set of 536 known asteroids larger than 30 km in diameter whose orbits currently cross that of Vesta, we determined the distribution of relative encounter velocities and collisional probabilities using the equations in (Wetherill 1967). The mean encounter velocity is found to be 5.24 km/s and the mean collisional probability is 5.90×10^{-18} km^{-2} yr^{-1} (Fig. 3.45). We estimate V_{sp} from the basaltic achondrite asteroid diameters (Table 3.15), and find their total volume is equivalent to that of a sphere 8 km in radius. For their mean value, V_{eject} = 450 m/s, our solution of Eq. (3.6.4) implies that an impactor 130 km in diameter is required to produce this volume of spall fragments. If the remainder of the ~30 predicted family members are also spall fragments from Vesta, then we estimate that a 160 km impactor is required.

The sizes of the largest observed fragments and their ejection velocities can also be used as a constraint for impact dynamics models. For current models (Melosh 1984), the estimated maximum thickness of spall fragments (z_{sp}) is

$$z_{sp} = \frac{T\,d}{\rho_T\, C_L\, v_{eject}}. \qquad (3.6.5)$$

We test this relation using z_{sp} = 8 km as a boundary condition and 500 m/s as a representative velocity based on the six largest fragments (Table 3.15) and find that Eq. (3.6.5) unrealistically requires an impactor diameter larger than Vesta itself! If we allow that these Vesta fragments could be considerably elongated such that the spall thickness represents the smallest tri-axial dimension (a speculation not based on lightcurve information), a spall thickness of 2 to 3 km might be reasonable. For values of z_{sp} in this size range and an ejection velocity of 500 m/s, we find a required impactor diameter of 200 to 300 km.

How do these impactor sizes compare with the largest that Vesta can withstand? To investigate Vesta's survival, we use dimensionless pi-scaling (Melosh 1989). Following (Tonks and Melosh 1992) to establish a disruption criterion that the excavated volume equals the total volume of the target, Vesta could survive the impact of a projectile 240 km across, and therefore likely survive the impact events suggested by spallation models.

The circumstantial evidence linking the 13 Vesta family basaltic achondrite asteroids to Vesta itself appears to be overwhelming. Their mean orbital velocities are all within 200 m/s of Vesta and their spectral properties are distinctive and uniquely match Vesta (Gaffey 1983). These observations thus establish confirmed members of the previously proposed Vesta family (Zappalà *et al.* 1990, Williams 1989, 1992).

Are the eight other basaltic achondrite asteroids that bridge the region between Vesta and the 3:1 resonance (Fig. 3.42, Table 3.15) also genetically related to Vesta? The observations lead us to argue in favor of such a link for three reasons. First, they are spectrally indistinguishable from the confirmed Vesta family members and Vesta itself. Second, all of their orbits cross that of Vesta. Third, these additional basaltic achondrite fragments are found to be coplanar with Vesta (i.e. they have nearly equal orbital inclinations) and also have very similar orbital eccentricities (Fig. 3.42). This latter argument establishes a strong dynamical

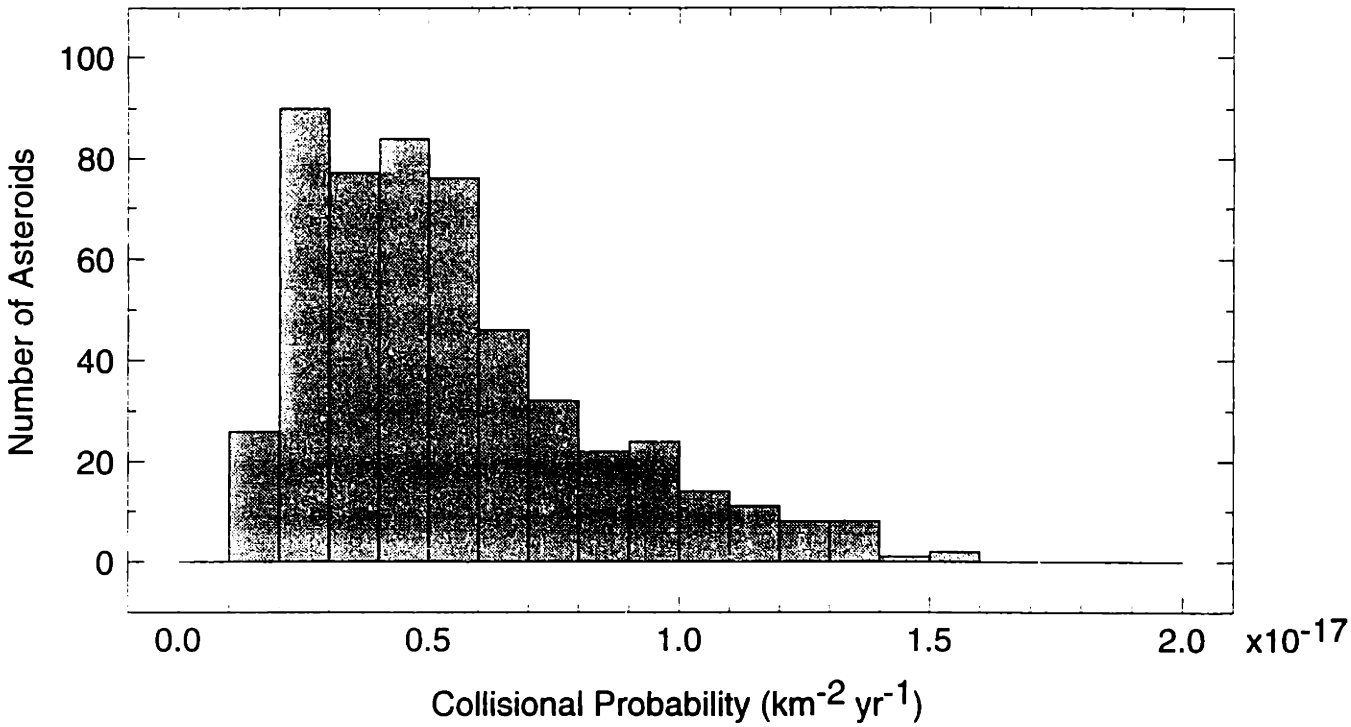

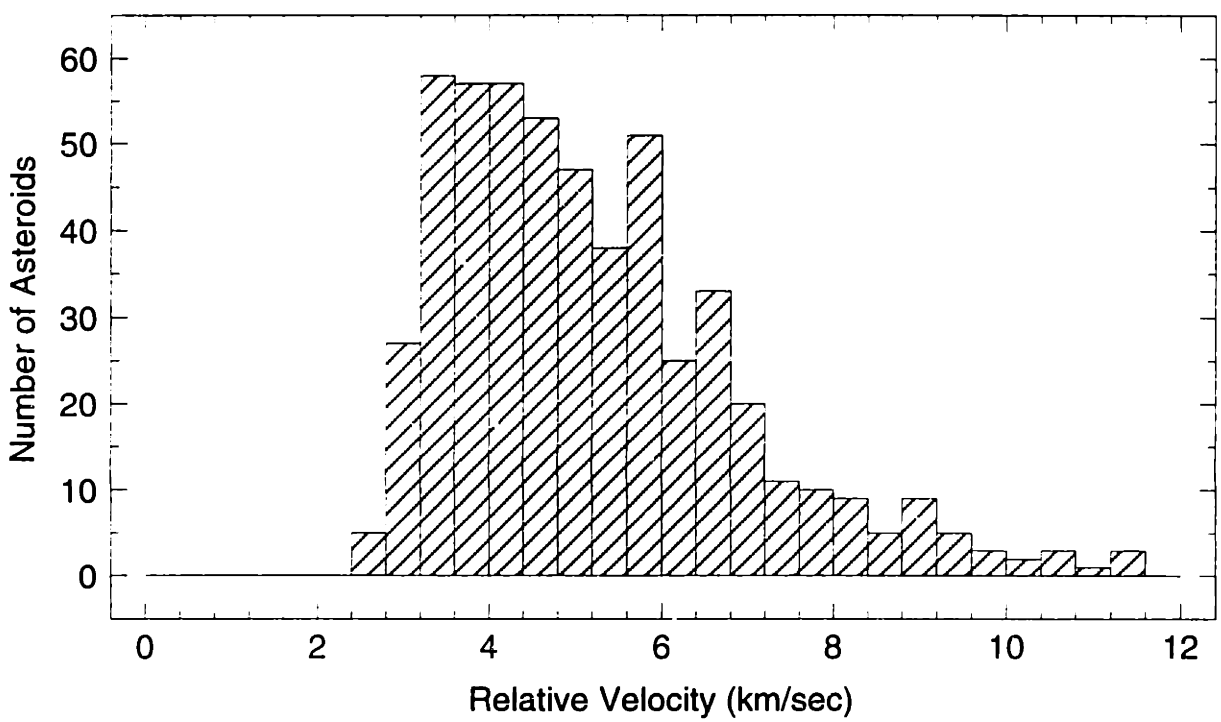

Fig. 3.45. Distributions of **(top)** intrinsic collisional probabilities and **(bottom)** relative encounter velocities for 536 numbered asteroids (diameters $\geq$ 30 km) whose orbits intersect Vesta's, computed using the methods of Namiki and Binzel (1991). Their mean collisional probability is 5.90 x 10^{-18} km^{-2} yr^{-1} and mean relative velocity is 5.24 km/s.

Table 3.15

Summary of Dynamical and Physical Properties for Observed Vesta Family Members and Near-Resonance Asteroids*

Asteroid		D (km)	Proper Elements a	e	sin i	Families		Class	V_a (m/s)	V_{eject} (m/s)	V_{min} (m/s)
Observed Vesta Family Members											
4	Vesta	520	2.36154	0.0994	0.1106	Z31	W169	V			
1646	Rosseland	26	2.3603	0.1015	0.1363		W169	C			
1906	Naef	6	2.37362	0.099	0.1116	Z31	W169	V	86	375	368
1929	Kollaa	8	2.3626	0.1147	0.123		W165	V	8	365	365
1933	Tinchen	6	2.35296	0.0933	0.1169	Z35	W196	V	61	370	367
2024	McLaughlin	8	2.3254	0.0945	0.1139	Z35	W196	S			
2590	Mourao	6	2.3425	0.0958	0.1174	Z35	W196	V	135	389	373
3155	Lee	7	2.34263	0.0974	0.1165	Z35	W196	J	134	389	373
3268	De Sanctis	5	2.3468	0.1002	0.1223	Z35	W169	V	105	380	370
3494	1980 XW	6	2.34972	0.0985	0.1152	Z31	W169	V	49	375	368
3657	1978 ST6	7	2.31262	0.0882	0.1146		W196	J	348	504	417
3944	Halliday	5	2.3684	0.1085	0.1177		W165	V	49	368	366
3968	Koptelov	7	2.32151	0.0928	0.118	Z35	W196	V	284	463	400
4038	Kristina	4	2.36618	0.0987	0.1102	Z31	W169	V	33	366	365
4147	Lennon	6	2.36197	0.1027	0.1141	Z31	W169	V	3	365	365
4510	Shawna	8	2.36	0.0977	0.1189	Z31	W169	S			
4546	Franck	4	2.3556	0.0905	0.1136	Z31	W196	V	42	367	366
Basaltic Achondrites Discovered Between Vesta and the 3:1 Resonance											
1273	Helma	6	2.3937	0.1222	0.1085			V	229	431	388
2011	Veteraniya	6	2.38695	0.1108	0.1109			J**	181	407	380
2113	Ehrdni	5	2.4738	0.0731	0.1057			V	798	877	588
2442	Corbett	6	2.38767	0.0974	0.0945			J	186	410	380
3153	Lincoln	5	2.4229	0.1049	0.1216			V	436	569	443
3869	Norton	5	2.45247	0.1002	0.0921			J	646	742	522
4005	1979 TC2	7	2.45195	0.1128	0.1045			J	642	739	520
4215	1987 VE1	10	2.4171	0.0993	0.1151			J	395	538	430
3:1 Resonance			2.5						984	1049	675
ν6 Resonance			2.18						1290	1341	829

* Basaltic achondrite asteroids are classified as V or J (new class proposed here) based on their eucrite-like or diogenite-like spectra. Their diameters are based on absolute magnitudes (H) and an assumed albedo of 0.38, the IRAS measured value for Vesta. Vesta's diameter is based on occultation results (Dunham 1991). Proper elements are from Milani and Knezevic (1992). Separate columns list the predicted family identifications (Zappalà *et al.* 1990, Williams 1989, 1992). Z31 and W169 denote the Vesta family. Z35 and W196 denote the Tinchen family, predicted to be related to Vesta. W165 refers to the Ausonia family (Williams 1989, 1992). Three predicted Vesta-related asteroids, 1646, 2024, and 4510, have compositional classes unlike Vesta and are likely interlopers. Velocity estimates (derived in the text) are given for probable Vesta fragments. The last entries give velocities necessary for fragments from Vesta to reach the 3:1 and ν6 resonances.

** Asteroid 2011 has a pyroxene absorption band depth (around 9000 Å) between V and J types. This asteroid was classified as a J-type from the PCA.

constraint in that for an object launched from a parent body with a velocity v_{eject}, the changes in eccentricity and inclination scale proportional to v_{eject} / v_{orb} and $\tan^{-1} (v_{eject} / v_{orb})$, respectively. For Vesta's heliocentric orbital velocity equal to 19.4 km/s, the maximum inferred ejection velocity of 0.88 km/s (if optimally directed) would change e or sin(i) values by about 0.05 from those of Vesta itself. For all eight asteroids, these elements are within 0.03 of Vesta's values.

How likely is it that the orbital element similarities between Vesta and the near-resonance basaltic achondrites are due to random chance? Over the semi-major axis range of 2.38 to 2.50 AU, we have sampled 50 asteroids. For the case of sin(i), 22 are within ±0.03 of Vesta thereby making a 44% probability (22/50) that any one basaltic achondrite would fall in this range. The probability for all eight discovered basaltic achondrites to fall within this range of Vesta is therefore 0.44^8, equal to 0.2%. For the case of eccentricity, the analogous individual and group probabilities are 48% and 0.3%. The combined random probability for the observed coincidence in both orbital elements is thus only 0.06%.

The conclusions that the family and near-resonance basaltic achondrite asteroids are derived from Vesta pose a challenge for impact mechanics models to demonstrate that fragments 4-10 km across can be produced with ejection velocities of at least 500 m/s. Current spallation models seem to require nearly-catastrophic impacts into Vesta to generate such fragment sizes and velocities. Such impacts are unlikely to have occurred if Vesta's observed eucritic crust is relatively thin, as the spectral signature of this crust could not have been retained in the face of a consequent disorganized reaccumulation (Davis *et al.* 1985). If Vesta's eucritic crust has substantial thickness (Grove and Bartels 1992), the constraint against it having experienced a nearly-catastrophic impact is less severe. The largest observed eucritic fragment (10 km), sets a lower limit on the crustal thickness. Possible resolution to this problem may come from spallation models that allow for a target to be previously fractured or to be inhomogeneous with a lower density crust overlaying a higher density mantle. Such a model may allow thicker spall fragments to be produced from modest impacts.

Crater studies of the moon and terrestrial planets also suggest evidence for the ability of impacts to produce large ejecta units with high velocities. For the 93 km lunar crater Copernicus, several large secondary craters are inferred to have

been formed by 1 to 2 km fragments ejected at 500 m/s (Vickery 1986). Secondary craters related to the 225 km crater Mozart on Mercury were likely formed from 2 to 4 km fragments ejected at similar velocities (Vickery 1987). For these secondary crater progenitors, it remains an open question whether they were coherent intact fragments or clumps of ejecta. Analogously for the discovered basaltic achondrite asteroids, it is uncertain whether they are intact fragments or rubble pile accumulations. The latter could form from proximate material having nearly identical ejection velocities which is able to re-accrete through self-gravity into bodies whose ultimate sizes are substantially greater than that of the largest intact fragment.

Finally, the discovery of basaltic achondrite asteroids spanning the region between Vesta and the 3:1 resonance provides a trail of evidence for a dynamical link between Vesta and basaltic achondrite meteorites. Equation 5 suggests that the sizes of spalled fragments are inversely proportional to their ejection velocities. Based on the 590 m/s mean ejection velocity for the eight 5 to 10 km near-resonance fragments, many more numerous meteoroid parent body fragments (0.1 to >1 km) could be ejected from Vesta with velocities exceeding the 700 to 1,000 m/s necessary to fall within the 3:1 resonance. Velocities 200 to 300 m/s higher could allow Vesta fragments to reach the ν_6 resonance. These scaling arguments make it plausible that the three known 1-4 km V-type near-Earth asteroids (Cruikshank *et al.* 1991b) are derived from Vesta. Injection of such large fragments to the resonances for subsequent delivery to the inner solar system is a critical step towards yielding a measurable sample of meteorites (Greenberg and Chapman 1983, Wetherill 1985, Greenberg and Nolan 1989).

3.7 Evidence for the Existence of A Main-Belt Ordinary Chondrite Asteroid

More than 80 percent of the meteorites falling to Earth are stone-like assemblages of olivine and pyroxene which are classified as ordinary chondrites (McSween 1987). They represent samples of the primitive solar nebula that have undergone only modest thermal evolution over the age of the solar system. Even though most meteorites are believed to be derived from the asteroid belt, two decades of remote sensing observations of main-belt asteroids have not previously revealed one whose visible and near-infrared reflectance spectrum matches that of ordinary chondrites as measured in the laboratory. Two theories have been proposed and are currently under debate. One hypothesis for the mismatch in the abundance of ordinary chondrite meteorites and detected asteroid source bodies is that "space weathering" processes alter ordinary chondrite asteroid surfaces, disguising their measured spectra (e.g., Wetherill and Chapman 1988, Britt and Pieters 1993, Pieters and McFadden 1994, Gaffey *et al.* 1993a). A second alternative is that ordinary chondrite asteroid source bodies exist at sizes below the limits of previous remote sensing surveys (Gaffey 1984, Gaffey *et al.* 1989, Bell *et al.* 1989, Fanale *et al.* 1992, Clark 1993). Small ordinary chondrites could escape from heating or be preserved as an unheated core inside a differentiated body. Subsequent collisions could bring their sizes even smaller.

Our SMASS program has yielded the discovery of one main-belt asteroid whose spectrum is similar to ordinary chondrite meteorites (Binzel *et al.* 1993a). A summary of observations for this asteroid, 3628 Boznemcová, is presented in Table 3.16. The reduction of observations obtained during December 1991 revealed its spectrum to be unlike that observed for any other main-belt asteroid, characterized by a flat slope shortward of 0.8 μm and a deep, broad absorption band extending out beyond 1 μm (Fig. 3.46). The 1 μm absorption band is much deeper than that of common S-class asteroids and pure olivine A-class asteroids and broader than that of pyroxene-rich basaltic achondrite (V-class) asteroids. Although repeated exposures on a single night consistently showed the same features, a confident interpretation of such a unique asteroid spectrum required additional confirming observations.

Asteroid 3628 was extensively re-observed during its next apparition in early 1993. Visible wavelength spectra obtained through multiple CCD exposures on

two nights in January confirmed the previously observed features. To define better the characteristics of the absorption band beyond 1 μm, we used the University of Massachusetts NICMOS3 camera (NICMASS) (Skrutskie *et al.* 1993) at the Michigan-Dartmouth-MIT Observatory to obtain flux measurements using J and H filters centered at 1.26- and 1.64-μm, respectively. We achieved a calibration between these infrared data and the visible spectrum through simultaneous visible wavelength measurements at the University of Texas McDonald Observatory (McD) using a CCD detector and an R filter centered at 0.67 μm (Binzel *et al.* 1993a). The results of these simultaneous measurements are summarized in Table 3.17, where the intrinsic colors for the asteroid (within the astronomical magnitude system) are derived by subtracting out the solar colors. For transformation of the asteroid magnitude measurements to relative reflectance (Fig. 3.46), we use the relation:

$$I_2 = I_1 \; 10^{0.4(m_1-m_2)} \qquad (3.7.1)$$

where (m_1-m_2) successively corresponds to the tabulated (R-J) and (R-H) reflectance. We establish $I_1 = 1.047$ for the R filter, where this value corresponds to the mean relative reflectance at 0.67 μm as measured from the visible spectrum.

Table 3.16

Visible and Near-Infrared Observations of Asteroid 3628 Boznemcová

Observation Date (UT)	Telescope	Wavelengths (μm)
91/12/08	MDM 2.4-m	0.5 - 1.0
93/01/21	MDM 2.4-m	0.5 - 1.0
93/01/22	MDM 2.4-m	0.5 - 1.0
93/03/05	MDM 1.3-m	1.26, 1.64
93/03/07*	MDM 1.3-m	1.26, 1.64
93/03/07*	McDonald 0.7-m	0.67

* Denotes simultaneous observations.

Table 3.17

Results for Simultaneous Visible and Near-Infrared Observations of Asteroid 3628

	R	R - J	R - H
Asteroid Measurements (mag.)	17.72 ± 0.11	0.68 ± 0.17	1.26 ± 0.19
Adopted Solar Colors (mag.)*		0.806	1.096
Asteroid Reflectance (mag.)		-0.13 ± 0.17	0.16 ± 0 .19

* From Campins *et al.* (1985), Bessel and Brett (1988).

While the spectrum of asteroid 3628 differs from that previously seen for any other main-belt asteroid, Fig. 3.46 reveals its closest similarity is with that of the near-Earth asteroid 1862 Apollo, previously identified as a potential inner solar system source body for ordinary chondrite meteorites (McFadden *et al.* 1985). Mineralogically, the deep absorption band observed near 1 μm can arise from the presence of olivine, pyroxene, and to a lesser extent feldspar, which are commonly found in meteorites (Gaffey *et al.* 1989). From a database of laboratory spectra of meteorites (Gaffey 1976), we find that the spectral features of asteroid 3628 are most consistent with the properties measured for ordinary chondrites (Fig. 3.46). Although we would not necessarily expect a perfect spectral fit between an object measured in space and our collection of meteorite materials, the differences must be carefully examined. Below 0.5 μm, the asteroid data mismatch the presented c dinary chondrite spectra by about 1-σ. If the difference is real, it could arise from minor variations in Fe content, grain size and/or surface opacity differences. Over the range 0.5- to 1.0-μm, the data fit well within the range measured for ordinary chondrite samples (Gaffey 1976), where only a subset are presented in the figure. The depth of the asteroid spectrum near 1 μm is most consistent with LL6 chondrites (6 is the most re-crystallized metamorphic grade), but because the depth is sensitive to both surface particle size and composition, we consider it to be consistent with L6 chondrites as well. H6 meteorites appear to display a 1 μm absorption band narrower than indicated by the asteroid measurements, making this association less likely. At 1.26 μm, the asteroid measurement falls close to both L6 and LL6 chondrites and remains within 1-σ of H6 chondrites. At 1.64 μm the asteroid measurement uncertainty is large and all ordinary chondrite types are consistent within the 1-σ error. Based on the above analysis and the location of

3628 in the principal component space (Fig. 3.13a), we have proposed a new taxonomic class "O" for this asteroid (Table 3.11).

Fig. 3.47 reveals that the orbital location of asteroid 3628 is in accord with predictions for ordinary chondrite source bodies based on orbital evolution models and meteorite fall time statistics (Wetherill 1987). Specifically, it is proximate to the Kirkwood gap at the 3:1 Jovian resonance, a major transfer zone for asteroid material to the inner solar system (Wisdom 1985). The high orbital eccentricity of the asteroid could increase the efficiency with which it could contribute meteoritic material to the inner solar system. The long-term stability of its orbit, in the vicinity of the resonance, has yet to be determined.

If the ordinary chondrite interpretation of 3628 Boznemcová's spectrum is correct, what constraints can the SMASS survey statistics place on the abundance of main-belt ordinary chondrite asteroids? As a first step, we derive a value of 7 km for the asteroid's estimated diameter (Binzel *et al.* 1993a). Fig. 3.47 shows the estimated diameters for other SMASS asteroids observed in the vicinity of the 3:1 resonance, where 70 of them are smaller than 20 km. Asteroid 3628 is one of the smallest surveyed, being one of ~20 having an estimated diameter less than 10 km. Although only limited inference can be made from a sample of one, it appears that ordinary chondrite material represents no more than a few percent of the asteroids within the size range surveyed so far.

Can the inferred composition for asteroid 3628 be used to discriminate between the proposed alternatives for explaining the apparent mismatch in the abundance of ordinary chondrite meteorites and asteroid source bodies? No. Although the size of the asteroid is consistent with the "small source body" alternative, it can also be argued that the small size does not rule out space weathering because the collisional lifetime for a 7 km asteroid may be less than 10^8 year (Namiki and Binzel 1991). If asteroid 3628 is a young collisional fragment, it is possible that space weathering processes have had insufficient time to alter its surface.

The apparent spectral match between a main-belt asteroid and ordinary chondrite meteorites, however, does illuminate a path toward resolving the ordinary chondrite paradox since it demonstrates that such material may be

detected with current instrumentation. For the small source body alternative, asteroids having ordinary chondrite spectral properties should become more numerous as we push surveys to smaller sizes. For the space weathering alternative, a spectrally disguised ordinary chondrite mineralogy is considered possible for a subset of S-class asteroids (Table 3.8b, Gaffey *et al.* 1993b). Confirmation of this hypothesis could arise if small ordinary chondrite asteroids are found to be preferentially clustered in the vicinity of some of these larger parent bodies, where the small asteroids could be fresh "unweathered" fragments excavated by collisions in a manner similar to what is observed for the Vesta family (see section 3.6 and Binzel and Xu 1993). In addition to 1862 Apollo and 3628 Boznemcová, a Mars-crossing asteroid 2078 Nanking and a near-Earth asteroid 1993 VW (Binzel and Bus, personal communication) were also found to be good candidates for ordinary chondrites. The spectrum of 2078 Nanking (see the appendix) is similar to that of H-chondrites. Nanking was classified as an S-type asteroid from our PCA.

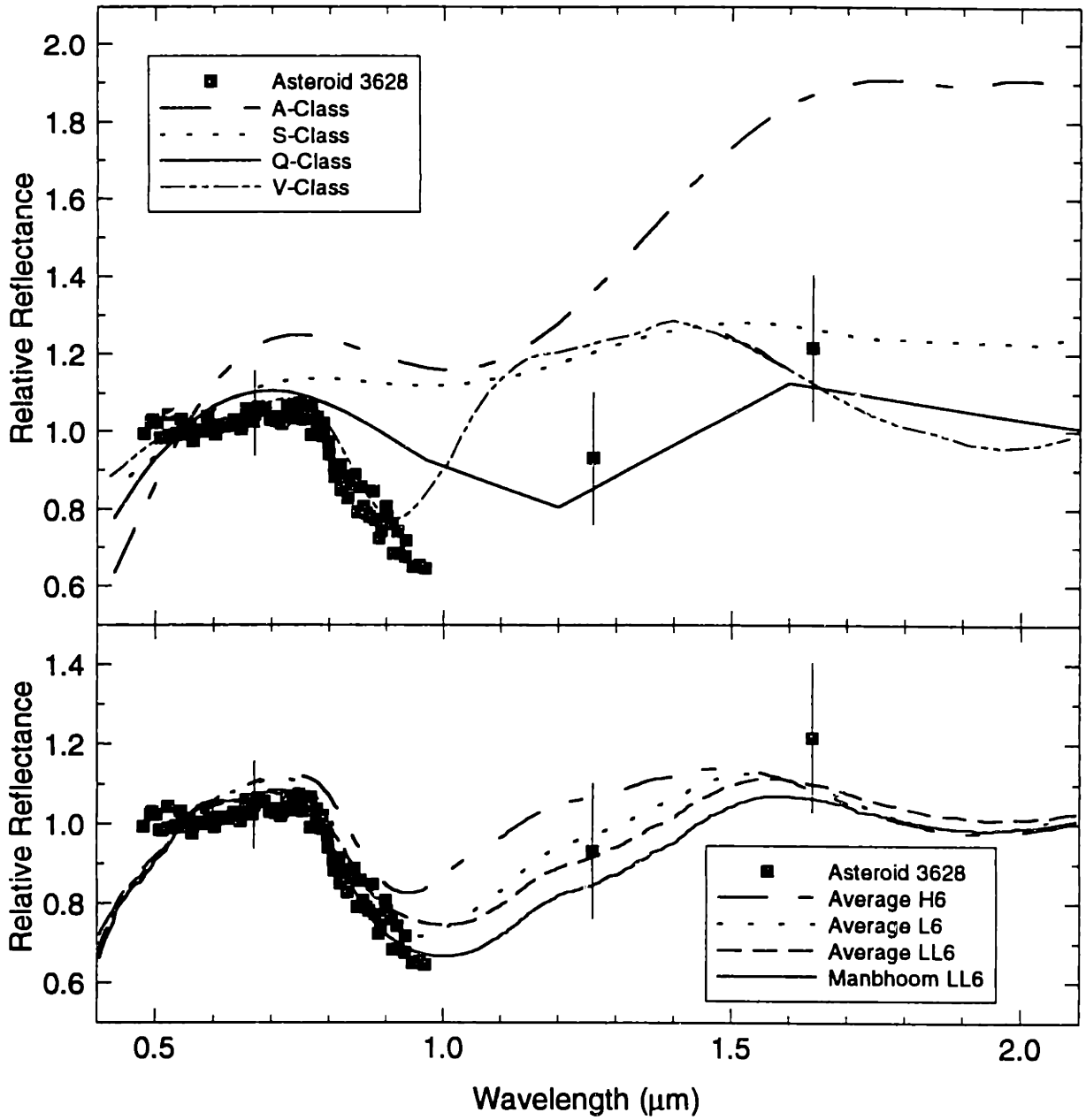

Fig. 3.46. Visible and near-infrared reflectance spectrum of asteroid 3628 (■) compared with (**top**) spectra of other asteroids and (**bottom**) spectra of ordinary chondrite meteorites. Error bars are affixed to the points denoting simultaneous measurements at 0.67-, 1.26-, and 1.64-μm. The absorption band is most similar to that for the Q-class, corresponding to the near-Earth asteroid 1862 Apollo. In comparison with laboratory spectra of meteorites (**bottom**), the asteroid measurements are most consistent with L6 and LL6 ordinary chondrites. Comparison asteroid data for the A-class (246 Asporina), S-class (3 Juno), V-class (4 Vesta), and Q-class are from (McFadden *et al.* 1985, Cruikshank and Hartmann 1984, Bell *et al.* 1988). The meteorite data are from (Gaffey 1976).

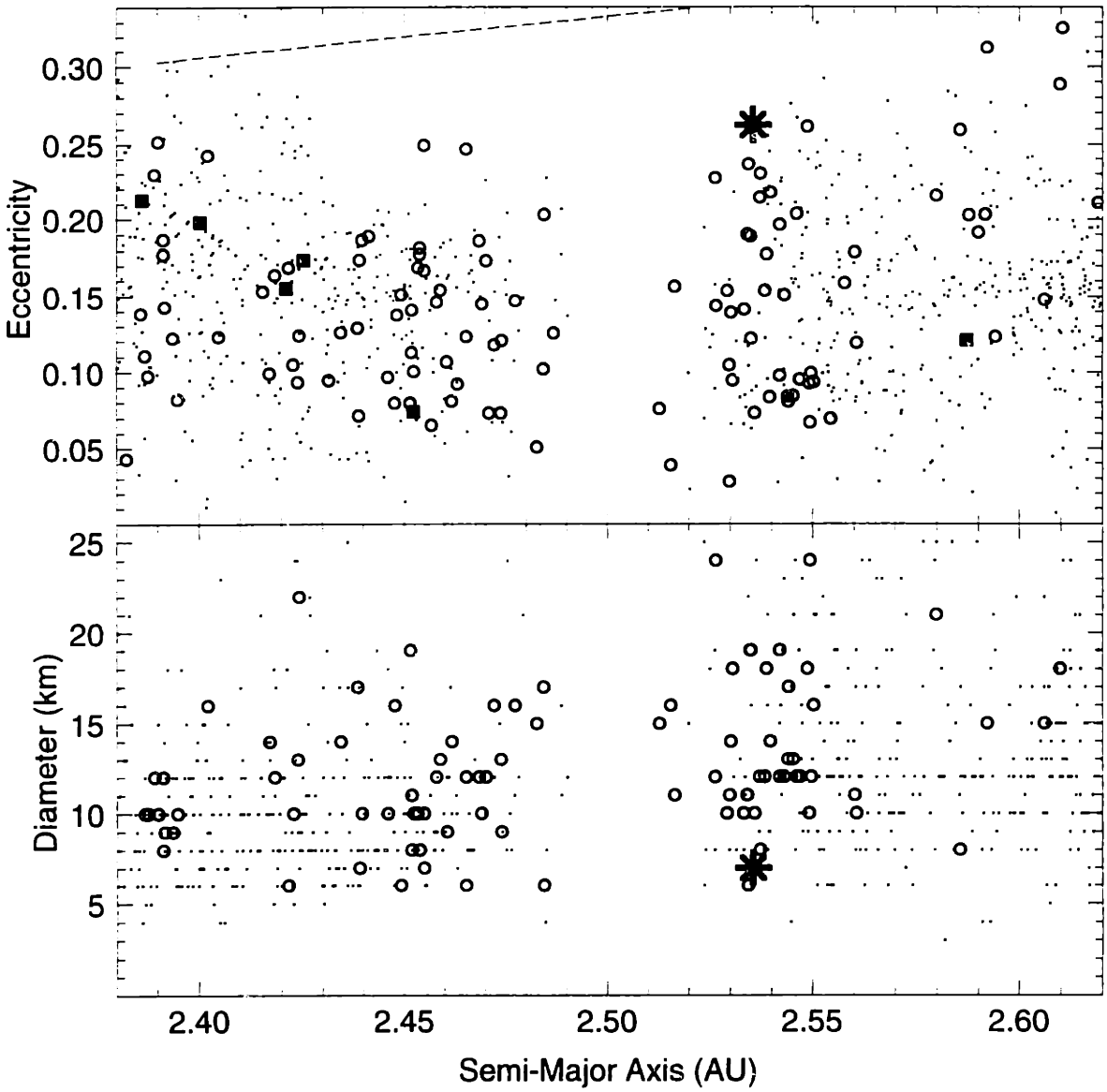

Fig. 3.47. Distributions of (**top**) asteroid orbital eccentricities and (**bottom**) asteroid diameters versus distance from the Sun in the vicinity of the 3:1 Jovian resonance Kirkwood gap (2.50 AU), a predicted meteorite source region. The location of asteroid 3628 is depicted by (✱) at 2.54 AU and all other asteroids spectroscopically surveyed by the SMASS program are depicted by (o). A subset of asteroids within the taxonomic S-class may have ordinary chondrite mineralogies, if their spectral characteristics are disguised by "space weathering" processes (Gaffey *et al.* 1993b). Their orbital locations are indicated by (■). Proper orbital elements (Milani and Knezevic 1992) have been used to depict the asteroid locations. The high orbital eccentricity of asteroid 3628 places it near a Mars-crossing orbit (dashed line at top). The asteroid's orbital inclination is modest, having a value $\sin i = 0.2625$.

4. Summary and Future Work

4.1 Summary

This is the first systematic photometric and spectroscopic survey of kilometer-sized asteroids. Rotational rates and lightcurves have been measured for more than 30 asteroids with average diameters less than 5 km. Three of these objects were new discoveries made during the course of the photometric survey. Low resolution spectra of more than 300 asteroids were obtained, with wavelength coverage ranging from 4000- to 10000-Å. More than half of the objects in the spectroscopic survey have diameters less than 20 km. Several asteroid families have also been investigated. Results from the CCD photometric and spectroscopic survey lead to the following conclusions:

1. Small asteroids show increasing rotational rates with decreasing size.

Small asteroids have a mean rotational frequency substantially faster than that of larger main-belt asteroids. It is clear that rotational rates increase with decreasing diameters. We detected the second shortest rotational period currently known, 2.35 hr, suggesting a density of ≥ 2 g cm^{-3} for an unstressed interior. The lack of substantially faster rotational periods as predicted from the collisional models could indicate that small asteroids have weak or fractured interiors. Their strength cannot withstand higher rotational rates. All lightcurves were investigated for nonperiodic variations due to free precession, possibly observable for some small asteroids. Although such motion could not be ruled out in all cases, no conclusive detection of free procession was made.

2. Asteroid fragments have nearly constant mean shapes over many orders of mass.

The lightcurve amplitudes of small and large asteroids are similar, which implies that there is no significant size dependence on the shapes of collisional fragments over the range of 1 to 50 km. Therefore, collisional fragmentation is probably the only process to determine their shapes. The SMALS result is consistent with laboratory investigations.

3. Our observational results are fully consistent with a main-belt origin for most near-Earth asteroids.

A statistical study revealed that near-Earth asteroids show comparable spin rates and shapes with their similar-sized main-belt counterparts, but are substantially different from the properties of cometary nuclei. If the existing sample is representative of the comet population, our analysis of the asteroid and comet samples constrains the fraction of comets to between 0 and 40 percent of the total near-Earth asteroid population. Thus we estimate 60 to 100% of the near-Earth asteroid population is derived from the main belt.

4. Ordinary chondrites do exist in the main belt.

The survey discovered an ordinary chondrite object for the first time among the main-belt asteroids. SMASS demonstrates that ordinary chondrite materials do exist in the main belt and can be detected with current instrumentation. The discovery may provide a breakthrough for the long standing meteorite-asteroid paradox. However, the paucity of ordinary chondrites in the main belt remains an unresolved problem. We cannot rule out either of the two hypotheses currently under debate.

5. Vesta is established as the source for the basaltic achondrite meteorites.

We found more than 20 asteroids showing basaltic achondrite spectral properties. Among them, 13 have orbits that are similar to Vesta's and were previously predicated to be dynamically associated with Vesta. Eight bridge the orbital space between Vesta and 3:1 resonance, a proposed source region for meteorites. These asteroids are probably multikilometer-sized fragments excavated from Vesta through impacts. The sizes, ejection velocities of 500 m/s, and the proximity of these fragments to the 3:1 resonance establish Vesta as a dynamically viable source for eucrite, diogenite, and howardite meteorites.

6. Our spectroscopic survey has begun to reveal a more complete picture of the asteroid compositions down to small sizes. Small asteroids show similar taxonomic distributions but more diverse spectral properties than the large asteroids.

The observed small asteroid population was successfully classified by a new principal component analysis. Our statistical results show that the majority of the small main-belt asteroids belong to C and S classes, similar to the distribution of large asteroids. However, the small asteroids show much more diverse spectral features than the larger ones, from featureless possible spinel-bearing, through

ordinary chondrite, achondrite-like, to olivine-rich asteroids. Such diversity indicates that small asteroids may have a greater variety of compositions. We have not detected any kilometer-sized A-type asteroid. However, olivine-rich objects could exist among some of the S asteroids, which show olivine-rich spectral features. Although the initial investigation from the spectroscopic survey revealed that members in most of the observed families show uniform taxonomic distributions, some compositional gradients or inhomogeneities seem to exist within most families.

4.2 Future Work

The SMALS and SMASS have improved our understanding of the physical and compositional properties of small asteroids in the solar system. However, additional observational and theoretical investigations are still necessary to attack further several problems which have been mentioned in the former chapters.

Asteroid 3628 was discovered to reveal a reflectance spectrum similar to ordinary chondrite meteorites. This asteroid is located in the vicinity of the 3:1 Jovian resonance--a predicted meteorite source region. However, with only one ordinary chondrite object identified, it certainly cannot discriminate between two hypotheses for explaining the mismatch in the abundance of ordinary chondrite meteorites and asteroid source bodies. Confirmation can be made if more and more small ordinary chondrite asteroids are discovered and their distribution is determined. Observing a sufficient number of small asteroids, especially in the 3:1 resonance region, is urgently necessary (e.g., Binzel *et al.* 1993a).

Complete understanding of the mineralogical properties of the small asteroids requires infrared data, especially the spectral features around the 2 μm band. Infrared investigations of these small asteroids will help us understand better about the mineralogical properties of the small asteroids and the dunite shortage problem. We have too few spectral data on the small outer main-belt asteroids (Fig. 3.29). Therefore, more future observations should be concentrated on the outer main belt region.

Both SMASS and other spectroscopic studies of the near-Earth asteroids (e.g., McFadden *et al.* 1989) show that a great majority of the near-Earth objects belong to the S-class (possible meteoritic analogues are stony-irons or achondrites). Such mineralogical compositions seem to be a mismatch with both meteorites and main-belt asteroids. Investigations by Luu and Jewitt (1989) concluded that this mismatch is due to a selection effect because the S asteroids are significantly brighter than most of the other common types. Few previous observations have concentrated on the near-Earth asteroid population. Therefore, an extensive new observational survey of the increasingly known population is needed to increase our complete understanding of the near-Earth mineralogical properties.

Collisions play a major role in the physical evolution of the asteroids and may particularly influence the rotational state of the smallest asteroids. Off-center collisions can misalign the principal body axis from the rotational axis so that free precession occurs. The survey found that there are some objects that are candidates for non-periodic behavior. These asteroids are 4432, 1981 EA12, and 1981 EJ9. Investigations by Harris (1993) show that near-Earth asteroid 4179 and some other objects, including 3288, 3102, 1689, 1220, 887, 288, are very likely candidates for free precession. Measurement of free precession would place important constraints on asteroid collision frequencies and internal properties. A rigorous, systematic, and enduring observational survey is necessary to confirm the occurrence of free precession.

Spectroscopic observations of more small asteroid family members are necessary for helping us understand both dynamical and chemical evolution of the families. Our initial investigation of the Koronis family suggests the existence of a compositional gradient in the family. At present, the observed number of members in the family is too small to make a firm conclusion.

Finally, the small sample of cometary nuclei rotational rates may have selection effects on the comparison between comets and near-Earth asteroids. Photometric observations of cometary nuclei are needed to increase our knowledge of their physical properties.

References

Adams, J. B. 1974. Visible and Near-Infrared Diffuse Reflectance Spectra of Pyroxenes as Applied to Remote Sensing of Solid Objects in the Solar System. *JGR* **79**, 4829-4836.

Adams, J. B. 1975. Interpretation of Visible and Near-Infrared Diffuse Reflectance Spectra of Pyroxenes and Other Rock-Forming Minerals. In *Infrared and Raman Spectroscopy of Lunar and Terrestrial Minerals* (C. Karr Ed.), pp. 91-116. Academic Press, New York.

Barucci, M. A., M. T. Capria, A. Coradini, and M. Fulchignoni 1987. Classification of Asteroids using G-Mode Analysis. *Icarus* **72**, 304-324.

Bell, J. F. 1986a. Mineralogical Evolution of the Asteroid Belt (abstract). *Meteoritics* **21**, 333-334

Bell, J. F. 1986b. Mineralogical Evolution of Meteorite Parent Bodies (abstract). *Lunar Planet Sci.* **18**, 985-986.

Bell, J. F. 1988. A Probable Asteroidal Parent Body for the CV or CO Chondrites (abstract). *Meteoritics* **23**, 256-257.

Bell, J. F., P. D. Owensby, B R. Hawke, and M. J. Gaffey 1988. The 52-Color Asteroid Survey: Final Results and Interpretation (abstract). *Lunar Plant. Sci.* **19**, 57-58.

Bell, J. F., D. R. Davis, W. K. Hartmann, and M. J. Gaffey 1989. Asteroids: The Big Picture. In *Asteroids II* (R. P. Binzel, T. Gehrels, and M. S. Matthews, Eds.), pp. 921-945. Univ. of Arizona Press, Tucson.

Belton, M. J. S. 1991. Characterization of the Rotation of Cometary Nuclei. In *Comets in the Post-Halley Era* (Newburn, R. L., Jr. *et al.*, Eds.), Vol. **2**, 691-721. Kluwer Academic Publishers. The Netherlands.

Bessel, M. S., and M. J. Brett 1988. JHKLM Photometry: Standard Systems,

Passbands, and Intrinsic Colors. *Publ. Astron. Soc. Pac.* **100**, 1134-1151.

Binzel, R. P. 1984. The Rotation of Small Asteroids. *Icarus* **57**, 294-306

Binzel, R. P. 1986. *Collisional Evolution in the Asteroid Belt: An Observational and Numerical Study.* Ph.D. Thesis. Univ. of Texas at Austin.

Binzel, R. P. 1987. A Photoelectric Survey of 130 Asteroids. *Icarus* **72**, 135-208.

Binzel, R. P. 1988. Collisional Evolution in the Eos and Koronis Asteroid Families: Observational and Numerical Results. *Icarus* **73**, 303-313.

Binzel, R. P. 1989. An Overview of the Asteroids. In *Asteroids II* (R. P. Binzel, T. Gehrels, M. S. Matthews, Eds.), pp. 3-18. Univ. of Arizona Press, Tucson.

Binzel, R. P. 1992. The Optical Spectrum of 5145 Pholus. *Icarus* **99**, 238-240.

Binzel, R. P. and J. D. Mulholland 1983. A Photoelectric Lightcurve Survey of Small Main Belt Asteroids. *Icarus* **56**, 519-533.

Binzel, R. P., T. Gehrels, and M. S. Matthews (Eds.) 1989a. *Asteroids II.* Univ. of Arizona Press, Tucson.

Binzel, R. P., P. Farinella, V. Zappalà, and A. Cellino 1989b. Asteroid Rotation Rates: Distributions and Statistics. In *Asteroids II* (R. P. Binzel, T. Gehrels, M. S. Matthews, Eds.), pp. 416-441. Univ. of Arizona Press, Tucson.

Binzel, R. P., and S. Xu 1990. Asteroid 2965 Surikov: A Piece of the Missing Mantle? *BAAS* **22**, 1115-1116.

Binzel, R. P., and L. M. Sauter 1992. Trojan, Hilda, and Cybele Asteroids: New Lightcurve Observations and Analysis. *Icarus* **95**, 222-238.

Binzel, R. P., S. Xu, S. J. Bus, and E. Bowell 1992a. Small Main-Belt Asteroid Lightcurve Survey. *Icarus* **99**, 225-237.

Binzel, R. P., S. Xu, S. J. Bus, and E. Bowell 1992b. Origins for the Near-Earth Asteroids. *Science* **257**, 779-782.

Binzel, R. P., S. Xu 1992. Chips Off of Asteroid 4 Vesta: Evidence for the Parent Body of Basaltic Achondrite Meteorites. *Science* **260**, 186-191.

Binzel, R. P., S. Xu, S. J. Bus, M. F. Skrutskie, M. R. Meyer, P. Knezek, E. S. Barker 1993a. Discovery of A Main-Belt Asteroid Resembling Ordinary Chondrite Meteorites. *Science* **262**, 1541-1543.

Binzel, R. P., S. Xu, S. J. Bus 1993b. Spectral Variations Within the Koronis Family: Possible Implications for the Surface Colors of Asteroid 243 Ida. *Icarus* **106**, 608-611.

Binzel, R. P., S. Xu, T. H. Burbine, and S. J. Bus 1994. Small Main-Belt Asteroid Spectroscopic Survey. In Preparation.

Bowell, E., B. Hapke, D. Domingue, K. Lumme, J. Peltoniemi, and A. W. Harris 1989. Application of Photometric Models to Asteroids. In *Asteroids II* (R. P. Binzel, T. Gehrels, M. S. Matthews, Eds.), pp. 524-556. Univ. of Arizona Press, Tucson.

Britt, D. T., and C. M. Pieters 1993. Darkening in Black and Gas-Rich Ordinary Chondrites: The Spectral Effects of Opaque Morphology and Distribution. Geoc. Cosm. Acta. In press.

Britt, D. T., D. J. Tholen, J. F. Bell, and C. M. Pieters 1992. Comparison of Asteroid and Meteorite Spectra: Classification by Principal Component Analysis. *Icarus* **99**, 153-166.

Burbine, T. H., Jr. 1991. Principal Component Analysis of Asteroid and Meteorite Spectra from 0.3 to 2.5 μm. M.S. Thesis. Univ. of Pittsburgh.

Burbine, T. H., M. J. Gaffey, and J. F. Bell 1992. S Asteroids 387 Aquitania and 980 Anacostia: Possible Fragments of the Breakup of A Spinel-Rich Parent Body with CO3/CV3 Affinities. *Meteoritics* **27**, 424-434.

Burns, J. A. 1971. The Alignment of Asteroid Rotation. In *Physical Studies of Minor Planets* (T. Gehrels, Ed.), pp. 257-262. NASA SP-267.

Burns, J. A. and V. S. Safronov 1973. Asteroid Nutation Angles. *Mon. Not. Roy. Astron. Soc.* **165**, 403-411.

Burns, R. G. 1970. *Mineralogical Applications of Crystal Field Theory.* Cambridge Univ. Press. New York.

Burns, R. G. 1989. Spectral Mineralogy of Terrestrial Planets: Scanning Their Surfaces Remotely. *Mineralogical Magazine* **53**, pp. 135-151.

Burns, R. G. 1993. *Mineralogical Applications of Crystal Field Theory*, 2nd Edition. Cambridge Univ. Press. New York.

Bus, S. J., E. Bowell, E. M. Shoemaker, and C. T. Kowal 1986. Photographic Recovery of UCAS Asteroids. *Bul. Amer. Astron. Soc.* **18**, 793.

Campins, H., G H. Rieke, and M. J. Lebofsky 1985. Absolute Calibration of photometry at 1 through 5 μm. *A. J.* **90**, 896-899.

Chapman, C. R., P. Paolicchi, V. Zappalà, R. P. Binzel, and J. F. Bell 1989. Asteroid Families: Physical Properties and Evolution. In *Asteroids II* (R. P. Binzel, T. Gehrels, M. S. Matthews, Eds.), pp. 386-415. Univ. of Arizona Press, Tucson.

Chatfield, C., and A. J. Collins 1980. *Introduction to Multivariate Analysis.* Chapman and Hall. New York.

Clark, B. E. 1993. *Spectral Reflectance Studies and Optical Surface Alteration in the Search for Links between Meteorites and Asteroids.* Ph.D. Thesis. University of Hawaii, Honolulu.

Cloutis, E., M. J. Gaffey, T. L. Jackowski, and K. L. Reed 1986. Calibrations of Phase Abundance, Composition, and Particle Size Distribution for Olivine-Orthopyroxene Mixtures from Reflectance Spectra. *JGR* **91**, 11641-11653.

Cochran, A. L., and T. G. Barnes, III 1981. Spectrophotometry With A Self-Scanned Silicon Photodiode Array: I. Instrumentation and Reductions. *Ap. J. Suppl.* **45**, 73-81.

Cruikshank, D. P., W. K. Hartmann 1984. The Meteorite-Asteroid Connection: Two Olivine-Rich Asteroids. *Science* **223**, 281-283.

Cruikshank, D. P., L. J. Allamandola, W. K. Hartmann, D. J. Tholen, R. H. Brown, C. N. Matthews, and J. F. Bell 1991a. Solid C≡N Bearing Material on Outer Solar System Bodies. *Icarus* **94**, 345-353.

Cruikshank, D. P., D. J. Tholen, W. K. Hartmann, J. F. Bell, and R. H. Brown 1991b. Three basaltic Earth-Approaching Asteroids and the Source of the Basaltic Meteorites. *Icarus 89*, 1-13.

Cunningham, C. 1985. *Asteroids: The Next Frontier.* Willmann-Bell, Inc. Richmond, Virginia.

Davies, J. K., M. V. Sykes, and D. P. Cruikshank 1993. Near-Infrared Photometry and Spectroscopy of the Unusual Minor Planet 5145 Pholus (1992 AD). *Icarus* **102**, 166-169.

Davis, D. R., C. R. Chapman, S. J. Weidenschilling, and R. Greenberg 1985. Collisional History of Asteroids: Evidence From Vesta and the Hirayama Families. *Icarus* **62**, 30-53.

Davis, D. R., P. Farinella, P. Paolicchi, S. J. Weidenschilling, and R. P. Binzel. 1989. Asteroid Collisional History: Effects on Sizes and Spins. In *Asteroids II* (R. P. Binzel, T. Gehrels, M. S. Matthews, Eds.), pp. 805-826. Univ. of Arizona Press, Tucson.

Drake, M. J. 1979. Geochemical Evolution of the Eucrite Parent Body: Possible Nature and Evolution of Asteroid 4 Vesta? In *Asteroids* (T. Gehrels, Ed.), pp. 765-782. Univ. of Arizona Press, Tucson.

Dunham, D. W. 1991. *Occultation Newsl.* **5**, 93.

Fanale, F. P., B. E. Clark, and J. F. Bell 1992. A Spectral Analysis of Ordinary Chondrites, S-Type Asteroids and Their Component Minerals: Genetic Implications. *JGR* **97**, 20863-20874.

Fujiwara, A., P. Cerroni, D. Davis, E. Ryan, M. Di Martino, K. Holsapple, and K. Housen 1989. Experiments and Scaling Laws for Catastrophic Collisions. In *Asteroids II* (R. P. Binzel, T. Gehrels, M. S. Matthews, Eds.), pp. 240-265. Univ. of Arizona Press, Tucson.

Fyfe, W. S. 1964. *Geochemistry of Solids.* Mcgraw-Hill. New York.

Gaffey, M. J. 1976. Spectral Reflectance Characteristics of the meteorite Classes. *JGR* **81**, 905-920.

Gaffey, M. J. 1983. The Asteroid (4) Vesta: Rotational Spectral Variations, Surface Material Heterogeneity, and implications for the origin of the Basaltic Achondrites. *Lunar Plant. Sci. Conf.* **14**, 231-232.

Gaffey, M. J. 1984. Rotational Spectral Variations of Asteroid (8) Flora: Implications for the Nature of S-Type Asteroids and for the Parent Bodies of the Ordinary Chondrites. *Icarus* **60**, 83-114.

Gaffey, M. J., J. F. Bell, and D. P. Cruikshank 1989. Reflectance Spectroscopy and Asteroid Surface Mineralogy. In *Asteroids II* (R. P. Binzel, T. Gehrels, M. S. Matthews, Eds.), pp. 98-127. Univ. of Arizona Press, Tucson.

Gaffey, M. J., K. L. Reed, and M. S. kelley 1992. Relationship of E-type Apollo Asteroid 3103 (1982 BB) to the Enstatite Achondrite Meteorites and the Hungaria Asteroids. *Icarus* **100**, 95-109.

Gaffey, M.J., T. H. Burbine, and R. P. Binzel 1993a. Asteroid Spectroscopy: Progress and Perspectives. *Meteoritics* **28**, 161-187.

Gaffey, M. J., J. F. Bell, R. H. Brown, T. H. Burbine, J. L. Piatek, K. L. Reed, and D. A. Chaky 1993b. Mineralogic Variations within the S-Type Asteroid Class. *Icarus* **106**, 573-602.

Gehrels, T. (Ed.) 1979. *Asteroids.* Univ. of Arizona Press, Tucson.

Gibbons, J. D. 1985. *Nonparametric Statistical Inference*, 2nd Edition. Marcel Dekker. New York.

Gradie, J., C. R. Chapman, and E. F. Tedesco 1989. Distribution of Taxonomic Classes and the Compositional Structure of the Asteroid Belt. In *Asteroids II* (R. P. Binzel, T. Gehrels, M. S. Matthews, Eds.), pp. 316-335. Univ. of Arizona Press, Tucson.

Gravetter, F. J., and L. B. Wallnau 1988. *Statistics for the Behavioral Sciences.* West Publishing Company, St. Paul.

Greenberg, R., and C. R. Chapman 1983. Asteroids and Meteorites: Parent Bodies and Delived Samples. *Icarus* **55**, 455-481.

Greenberg, R., and M. C. Nolan 1989. Delivery of Asteroids and Meteorites to the Inner Solar System. In *Asteroids II* (R. P. Binzel, T. Gehrels, M. S. Matthews, Eds.), pp. 778-804. Univ. of Arizona Press, Tucson.

Grove, T. L., and K. S. Bartels 1992. *Proc. Lunar Plant. Soc.* **22**, 437.

Harris, A. W. 1994. Tumbling Asteroids. *Icarus* **107**, 209-211.

Hartmann, W. K. 1992. *Moons and Planets.* Wadsworth Publishing Company. Belmont, California.

Howell, E. S., E. Merenyi, and L. A. Lebofsky 1994. Classification of Asteroid Spectra Using A Neural Network. *JGR* in press.

Jewitt, D. C., and K. J. Meech 1988. Optical Properties of Cometary Nuclei and A Preliminary Comparison with Asteroids. *Ap. J.* **328**, 974-986.

Jewitt, D. C. 1991. Cometary Photometry. In *Comets in the Post-Halley Era* (Newburn, R. L., Jr. *et al.*, Eds.), Vol. **1**, 19-65. Kluwer Academic Publishers. The Netherlands.

Klein, C., and C. S. Hurlbut, Jr. 1993. Manual of Mineralogy, 21st edition. John Wiley and Sons, New York.

Landolt, A. U. 1983. UBVRI Photometric Standard Stars Around the Celestial Equator. *Astron. J.* **88**, 439-460.

Larson, H. P., and U. Fink 1975. Infrared Spectral Observations of Asteroid 4 Vesta. *Icarus* **26**, 420-427.

Lipschutz, M. E., M. J. Gaffey, and P. Pellas 1989. Meteoritic Parent Bodies: Nature, Number, Size and Relation to Present-Day Asteroids. In *Asteroids II* (R. P. Binzel, T. Gehrels, and M. S. Matthews, Eds.), pp. 740-777. Univ. of Arizona Press, Tucson.

Luu, J. X., and D. C. Jewitt 1989. On the Relative Numbers of C Types and S Types Among Near-Earth Asteroids. *A. J.* **98**, 1905-1911.

Luu, J. X., and D. C. Jewitt 1990. Charge-Coupled Device Spectra of asteroids. I. Near-Earth and 3:1 Resonance Asteroids. *A. J.* **99**, 1985-2011.

McCord, T. B., J. B. Adams, and T. V. Johnson 1970. Asteroid Vesta: Spectral Reflectivity and Compositional Implications. *Science* **168**, 1445-1447.

McFadden, L. A., M. J. Gaffey, and T. B. McCord 1985. Near-Earth Asteroids: Possible Sources from Reflectance Spectroscopy. *Science* **229**, 160-163.

McFadden, L. A., D. J. Tholen, G. J. Veeder 1989. Physical Properties of Aten, Apollo and Amor Asteroids. In *Asteroids II* (R. P. Binzel, T. Gehrels, and M. S. Matthews, Eds.), PP. 442-467. Univ. of Arizona Press, Tucson.

McSween, H. Y. 1985. SNC Meteorites: Clues to Martian Petrologic Evolution? *Rev. Geophys.* **23**, 391-416.

McSween, H. Y. 1987. Meteorites and their Source Bodies. Cambridge Univ. Press, New York.

Melosh, H. J. 1984. Impact Ejection, Spallation, and the Origin of Meteorites. *Icarus* **59**, 234-260.

Melosh, H. J. 1985. Ejection of Rock Fragments from Planetary Bodies. *Geology* **13**, 144-148.

Melosh, H. J. 1989. *Impact Cratering: A Geological Process.* Oxford Univ. Press, New York.

Milani, A., and Z. Knezevic 1992. Asteroid Proper Elements and Secular Resonances. *Icarus* **98**, 211-232.

Mueller, B. E. A., D. J. Tholen, W. K. Hartmann, and D. P. Cruikshank 1992. Extraordinary Colors of Asteroidal Object (5145) 1992 AD. *Icarus* **97**, 150-154.

Namiki, N., and R. P. Binzel 1991. 951 Gaspra: A Pre-Galileo Estimate of Its Surface Evolution. *Geophys. Res. Lett.* **18**, 1155-1158.

Pieters, C. M., and L. A. McFadden 1994. Meteorite and Asteroid Reflectance Spectroscopy: Clues to the Early Solar System Processes. In *Ann. Rev. Earth Planet. Sci.* In press. Annual Reviews Inc., Palo Alto, California.

Sawyer, S. R. 1991. A High Resolution CCD Spectroscopic Survey of Low Albedo Main Belt Asteroids. Ph.D. Thesis. Univ. of Texas at Austin.

Scott, E. R. D., G. J. Taylor, H. E. Newsom, F. Herbert, M. Zolensky, and J. F. Kerridge 1989. Chemical, Thermal, and Impact Processing of Asteroids. In *Asteroids II* (R. P. Binzel, T. Gehrels, and M. S. Matthews, Eds.), pp. 701-739. Univ. of Arizona Press, Tucson.

Shoemaker, E. M., J. G. Williams, E. F. Helin, and R. F. Wolfe 1979. Earth-Crossing Asteroids: Orbital Classes, Collision Rates With Earth, and Origin. In *Asteroids* (T. Gehrels, Ed.), pp. 253-282. Univ. of Arizona Press, Tucson.

Shoemaker, E. M. 1983. Asteroid and Comet Bombardment of the Earth. *Ann. Rev. Earth Planet. Sci.* **11**, 461-494.

Shoemaker, E. M., and R. F. Wolfe 1986. Mass Extinctions, Crater Ages and Comet Showers. In *The Galaxy and the Solar System* (R. Smoluchowski, J. N. Bahcall, and M. S. Matthews, Eds.), pp. 338-386. Univ. of Arizona Press, Tucson.

Siegel, S. 1956. *Nonparametric Statistics for the Behavioral Sciences.* McGraw-Hill, New York.

Stellingwerf, R. F. 1978. Period Determination Using Phase Dispersion Minimization. *Astrophys. J.* **224**, 953-960.

Tedesco, E. F., J. G. Williams, D. L. Matson, G. J. Veeder, J. C. Gradie, and L. A. Lebofsky 1989. A Three-Parameter Asteroid Taxonomy. *A. J.* **97**, 580-606.

Tholen, D. J. 1984. Asteroid Taxonomy from Cluster Analysis Photometry. Ph.D. Thesis. Univ. of Arizona. Tucson.

Tholen, D. J., and M. A. Barucci 1989. Asteroid Taxonomy. In *Asteroids II* (R. P. Binzel, T. Gehrels, and M. S. Matthews, Eds.), pp. 298-315. Univ. of Arizona Press, Tucson.

Toriks, W. B., H. J. Melosh 1992. Core Formation by Giant Impact. *Icarus* **100**, 326-346

Vickery, A. M. 1986. Size-Velocity Distribution of Large Ejecta Fragments. *Icarus* **67**, 224-236.

Vickery, A. M. 1987. Variation in Ejecta Size with Ejection Velocity. *Geophys. Res. Lett.* **14**, 726-729.

Vilas, F., and L. A. McFadden 1992. CCD Reflectance Spectra of Selected Asteroids. I. Presentation and Data Analysis Considerations. *Icarus* **100**, 85-94.

Walsh, J. E. 1965. Handbook of Nonparametric Statistics (Vol. II). Van Nostrand, Princeton, New Jersey.

Weidenschilling, S. J. 1981. How Fast Can An Asteroid Spin? *Icarus* **46**, 124-126.

Weissman, P. R., M. F. A'Hearn, L. A. McFadden, and H. Rickman 1989. Evolution of Comets Into Asteroids. In *Asteroids II* (R. P. Binzel, T. Gehrels, and M. S. Matthews, Eds.), pp. 880-920. Univ. of Arizona Press, Tucson.

Wetherill, G. W. 1967. Collisions in the Asteroid belt. *J.G.R.* **72**, 2429-2444.

Wetherill, G. W. 1975. Late Heavy Bombardment of the Moon and Terrestrial Planets. *Proc. Lunar Sci. Conf.* **6**, 1539-1561.

Wetherill, G. W. 1985. Asteroidal Source of Ordinary Chondrites. *Meteoritics* **20**, 1-22.

Wetherill, G. W. 1987. Dynamical relations Between Asteroids, meteorites and Apollo-Amor Objects. *Phil. Trans. R. Soc. Lond. A* **323**, 323-337.

Wetherill, G. W. 1988. Where Do the Apollo Objects Come From? *Icarus* **76**, 1-18.

Wetherill, G. W. 1989. Origin of the Asteroid Belt. In *Asteroids II* (R. P. Binzel, T. Gehrels, and M. S. Matthews, Eds.), pp. 661-680. Univ. of Arizona Press, Tucson.

Wetherill, G. W., and C. R. Chapman 1988. Asteroids and Meteorites. In *Meteorites and the Early Solar System* (J. F. Kerridge, and M. S. Matthews, Eds.), pp. 35-67. Univ. of Arizona Press, Tucson.

Williams, J. G. 1989. Asteroid Family Identifications and Proper Elements. In *Asteroids II* (R. P. Binzel, T. Gehrels, and M. S. Matthews, Eds.), pp. 1034-1072. Univ. of Arizona Press, Tucson.

Williams, J. G. 1992. Asteroid Families--An Initial Search. *Icarus* **96**, 251-280.

Wisdom, J. 1982. The Origin of the Kirkwood Gaps, A Mapping for Asteroidal

Motion Near the 3/1 Commonsurability. *A. J.* **87**, 577-593.

Wisdom, J. 1983. Chaotic Behavior and the Origin of the 3/1 Kirkwood Gap. *Icarus* **56**, 51-74.

Wisdom, J. 1985. Meteorites May Follow A Chaotic Route to Earth. *Nature* **315**, 731-733.

Wisniewski, W. Z. 1991. Physical Study of Small Asteroids. I. Lightcurves and Taxonomy of 10 Asteroids. *Icarus* **90**, 117-122.

Xu, S., R. P. Binzel, T. H. Burbine, and S. J. Bus 1993. Small Main-Belt Asteroid Spectroscopic Survey. *BAAS* **25**, 1135.

Zappalà, V., A. Cellino, A. M. Barucci, M. Fulchignoni, and D. F. Lupishko 1990. An Analysis of the Amplitude-Phase Relationship Among Asteroids. *Astron. Astrophys.* **231**, 548-560.

Zappalà, V., A. Cellino, P. Farinella, and Z. Knezevic 1990. Asteroid Families. I. Identification by Hierarchical Clustering and Reliability Assessment. *A. J.* **100**, 2030-2046.

Zellner, B., M. Leake, D. Morrison, and J. G. Williams 1977. The E asteroids and the Origin of the Enstatite Achondrites. *Geochim. Cosmochim. Acta* **41**, 1759-1767.

Zellner, B., D. J. Tholen, and E. F. Tedesco 1985. The Eight-Color Asteroid Survey: Results for 589 Minor Planets. *Icarus* **61**, 355-416.

Appendix

Composite Lightcurves of 33 Asteroids Obtained by SMALS (1987-1991)
(Presented in the Order of Table 2.2)
and
Spectra of 316 Asteroids Obtained by SMASS (1991-1993)
(Presented in the order of Table 3.1, ECAS data (**X**) are also presented if available)

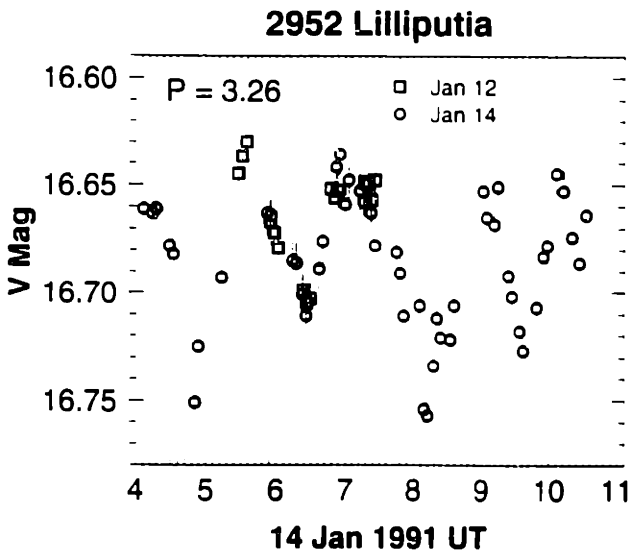
2952 Lilliputia
P = 3.26
Jan 12
Jan 14
V Mag
16.60
16.65
16.70
16.75
4 5 6 7 8 9 10 11
14 Jan 1991 UT

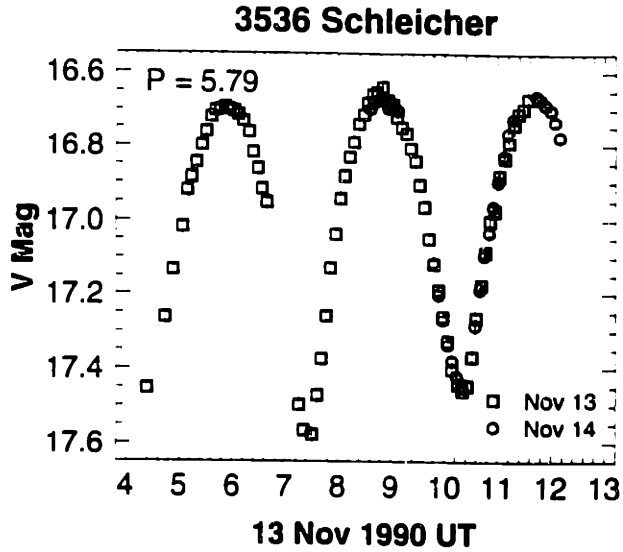
3536 Schleicher
P = 5.79
Nov 13
Nov 14
V Mag
16.6
16.8
17.0
17.2
17.4
17.6
4 5 6 7 8 9 10 11 12 13
13 Nov 1990 UT

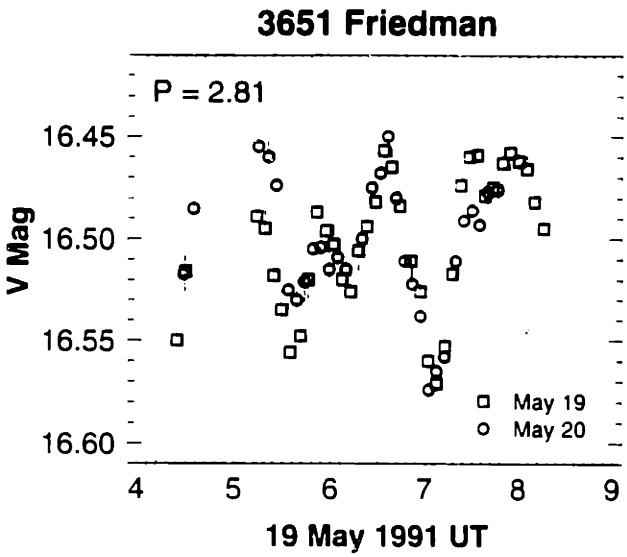
3651 Friedman
P = 2.81
May 19
May 20
V Mag
16.45
16.50
16.55
16.60
4 5 6 7 8 9
19 May 1991 UT

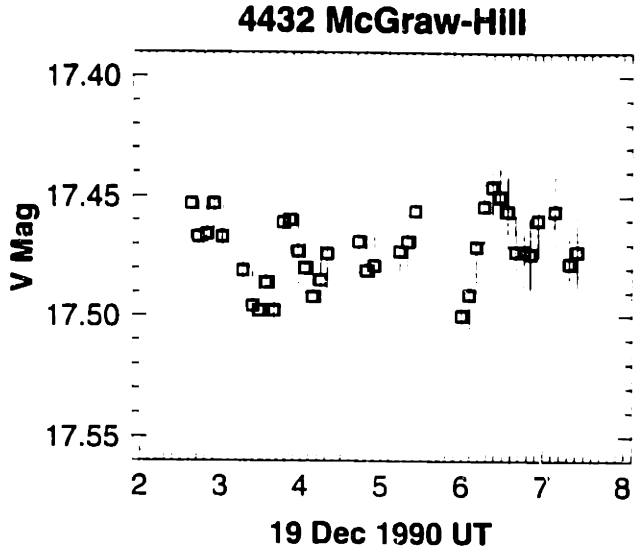
4432 McGraw-Hill
V Mag
17.40
17.45
17.50
17.55
2 3 4 5 6 7 8
19 Dec 1990 UT

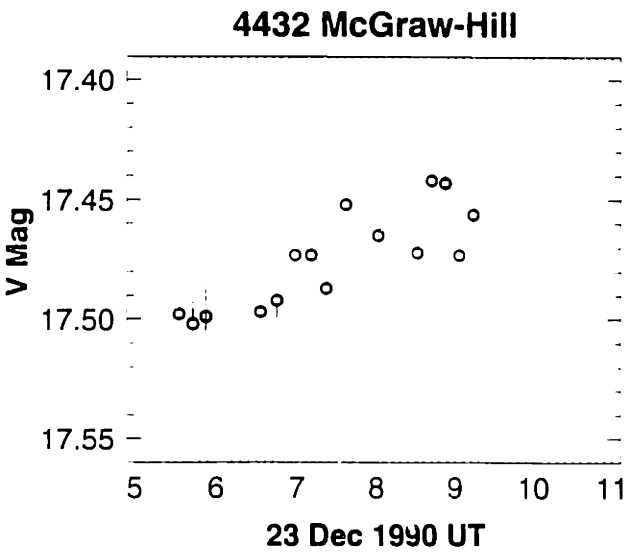
4432 McGraw-Hill
V Mag
17.40
17.45
17.50
17.55
5 6 7 8 9 10 11
23 Dec 1990 UT

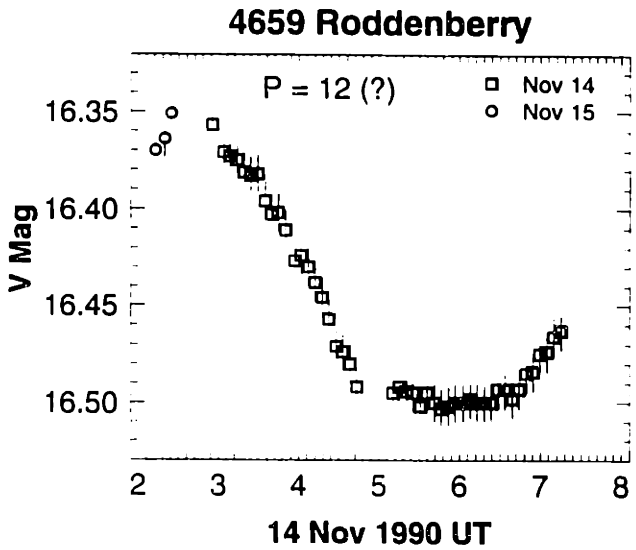
4659 Roddenberry
P = 12 (?)
Nov 14
Nov 15
V Mag
16.35
16.40
16.45
16.50
2 3 4 5 6 7 8
14 Nov 1990 UT

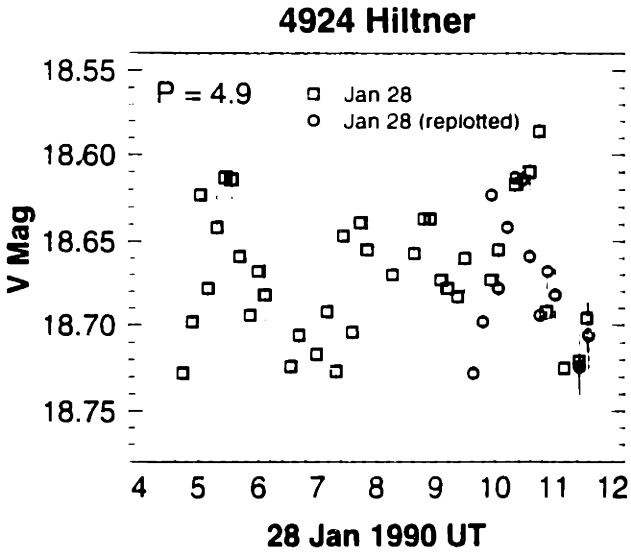
4924 Hiltner
P = 4.9
Jan 28
Jan 28 (replotted)
V Mag
18.55
18.60
18.65
18.70
18.75
4 5 6 7 8 9 10 11 12
28 Jan 1990 UT

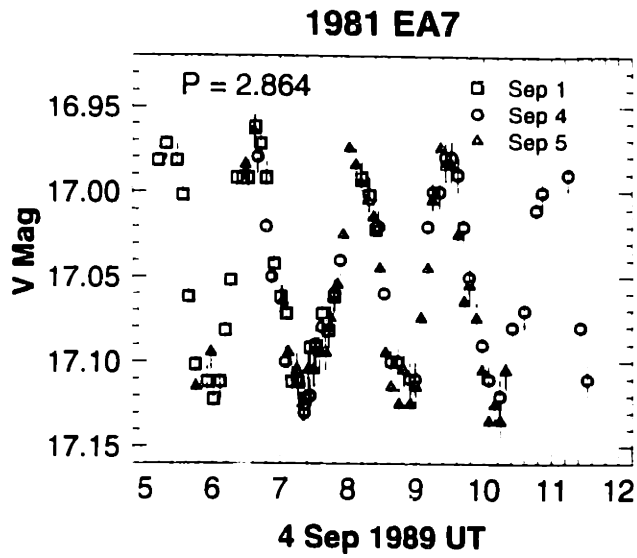
1981 EA7
P = 2.864
Sep 1
Sep 4
Sep 5
V Mag
16.95
17.00
17.05
17.10
17.15
5 6 7 8 9 10 11 12
4 Sep 1989 UT

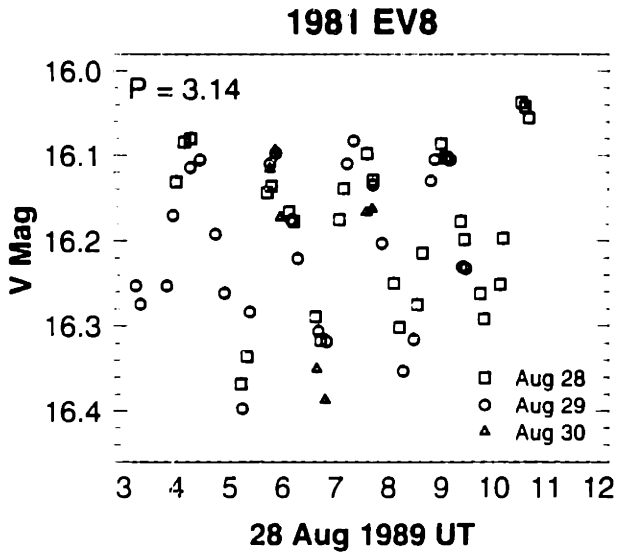
1981 EV8
P = 3.14
Aug 28
Aug 29
Aug 30
V Mag
16.0
16.1
16.2
16.3
16.4
3 4 5 6 7 8 9 10 11 12
28 Aug 1989 UT

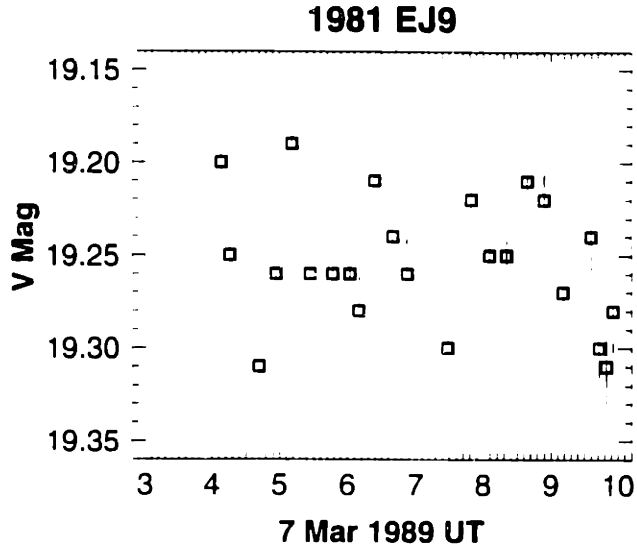
1981 EJ9
V Mag
19.15
19.20
19.25
19.30
19.35
3 4 5 6 7 8 9 10
7 Mar 1989 UT

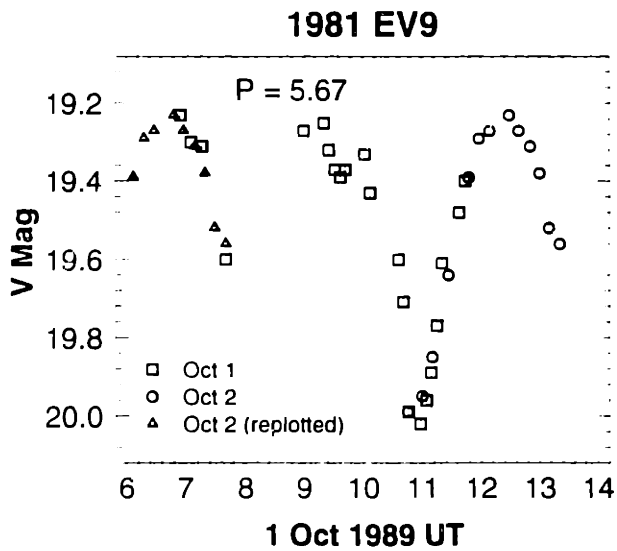
1981 EV9
P = 5.67
Oct 1
Oct 2
Oct 2 (replotted)
V Mag
19.2
19.4
19.6
19.8
20.0
6 7 8 9 10 11 12 13 14
1 Oct 1989 UT

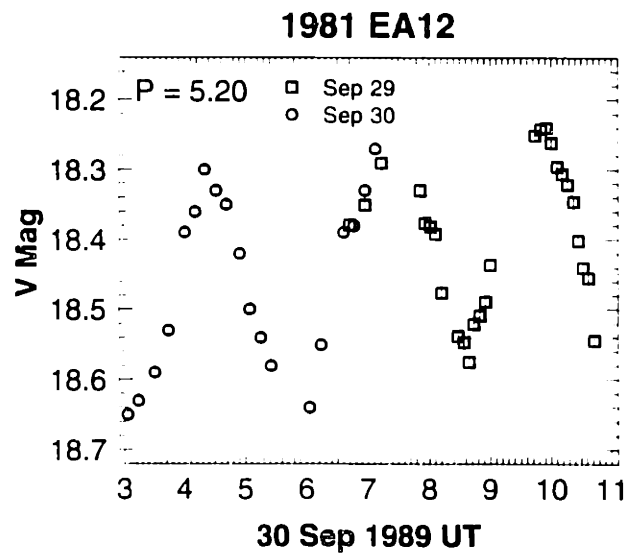
1981 EA12
P = 5.20
Sep 29
Sep 30
V Mag
18.2
18.3
18.4
18.5
18.6
18.7
3 4 5 6 7 8 9 10 11
30 Sep 1989 UT

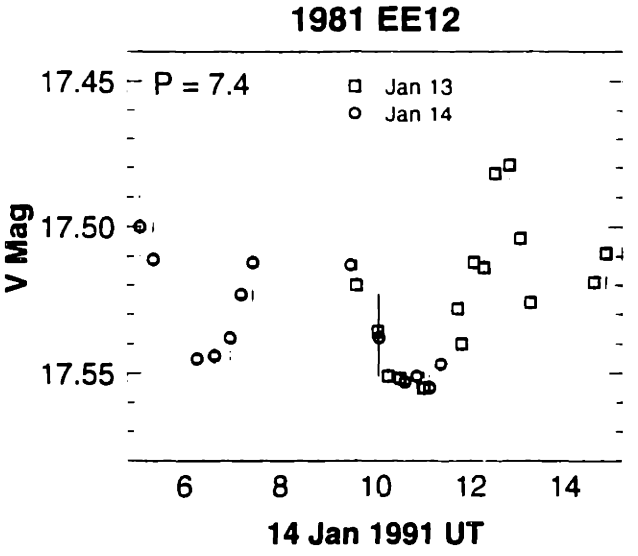
1981 EE12
P = 7.4
Jan 13
Jan 14
V Mag
17.45
17.50
17.55
6
8
10
12
14
14 Jan 1991 UT

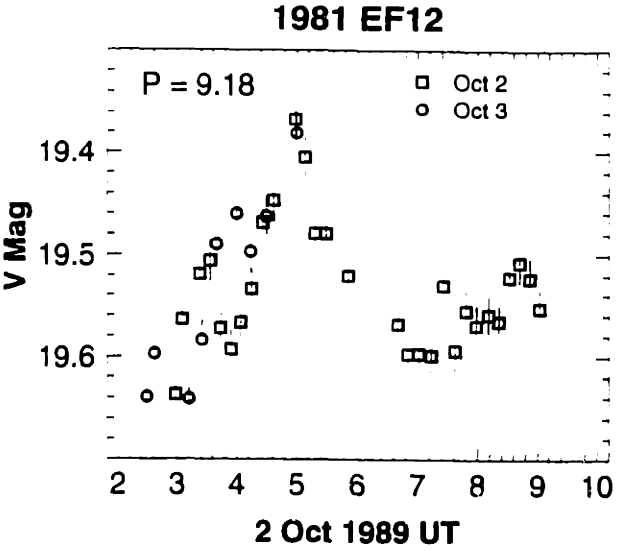
1981 EF12
P = 9.18
Oct 2
Oct 3
V Mag
19.4
19.5
19.6
2
3
4
5
6
7
8
9
10
2 Oct 1989 UT

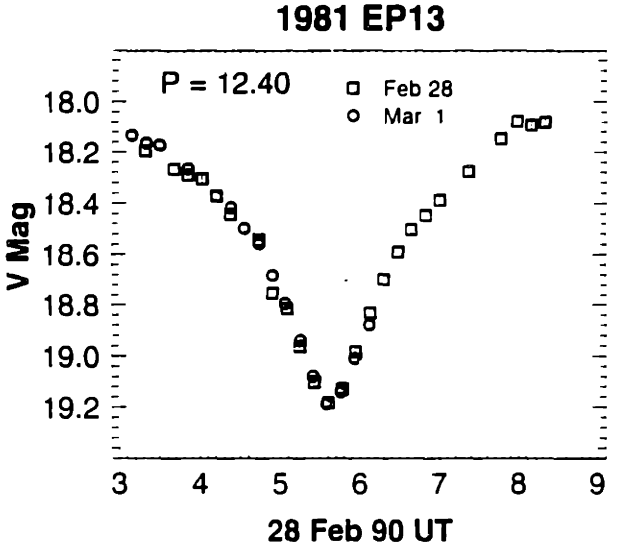
1981 EP13
P = 12.40
Feb 28
Mar 1
V Mag
18.0
18.2
18.4
18.6
18.8
19.0
19.2
3
4
5
6
7
8
9
28 Feb 90 UT

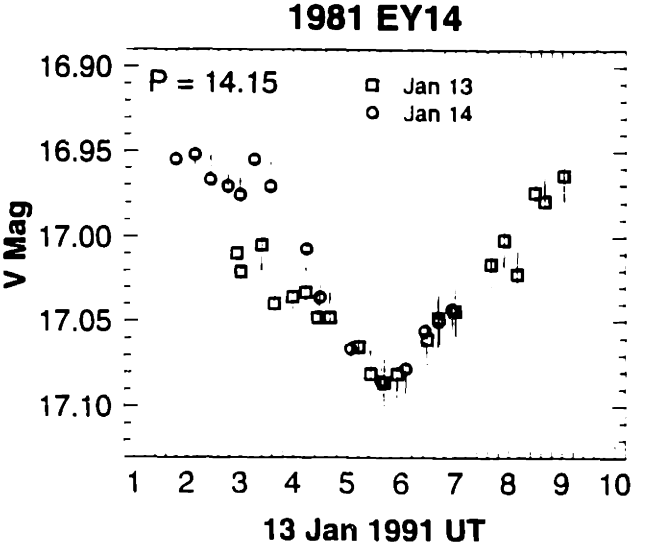
1981 EY14
P = 14.15
Jan 13
Jan 14
V Mag
16.90
16.95
17.00
17.05
17.10
1
2
3
4
5
6
7
8
9
10
13 Jan 1991 UT

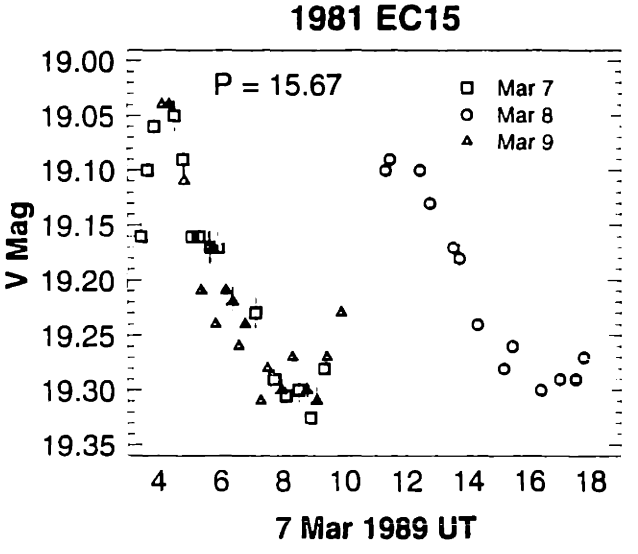
1981 EC15
P = 15.67
Mar 7
Mar 8
Mar 9
V Mag
19.00
19.05
19.10
19.15
19.20
19.25
19.30
19.35
4
6
8
10
12
14
16
18
7 Mar 1989 UT

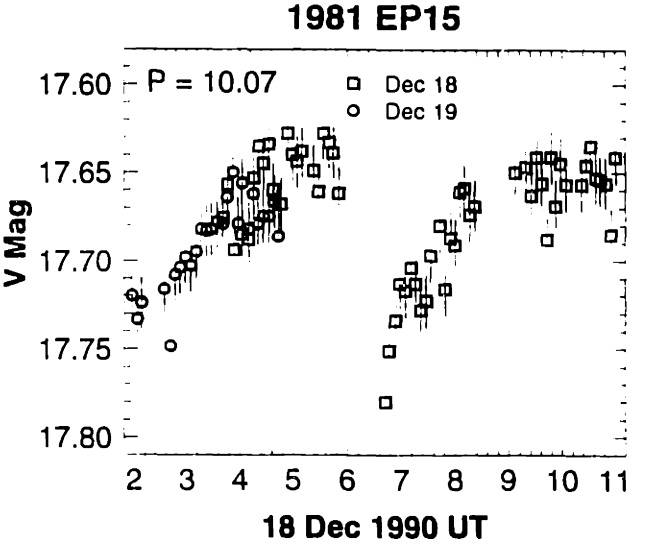
1981 EP15
P = 10.07
Dec 18
Dec 19
V Mag
17.60
17.65
17.70
17.75
17.80
2
3
4
5
6
7
8
9
10
11
18 Dec 1990 UT

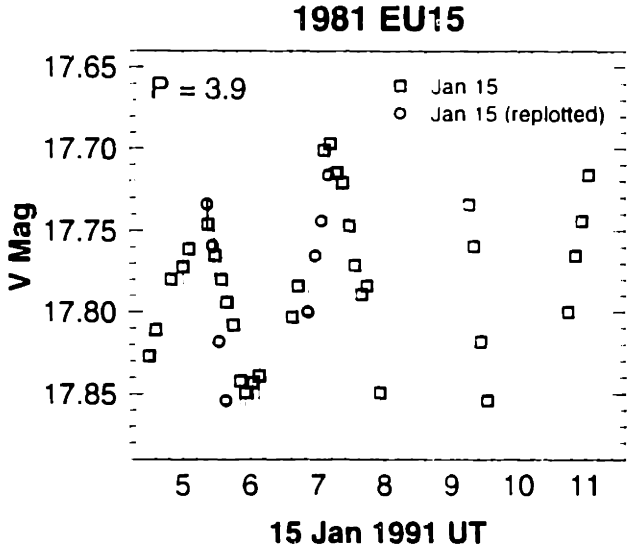
1981 EU15
P = 3.9
Jan 15
Jan 15 (replotted)
V Mag
17.65
17.70
17.75
17.80
17.85
5 6 7 8 9 10 11
15 Jan 1991 UT

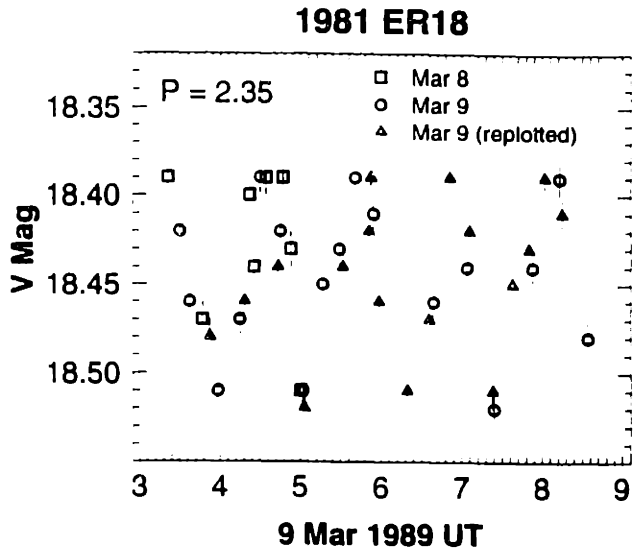
1981 ER18
P = 2.35
Mar 8
Mar 9
Mar 9 (replotted)
V Mag
18.35
18.40
18.45
18.50
3 4 5 6 7 8 9
9 Mar 1989 UT

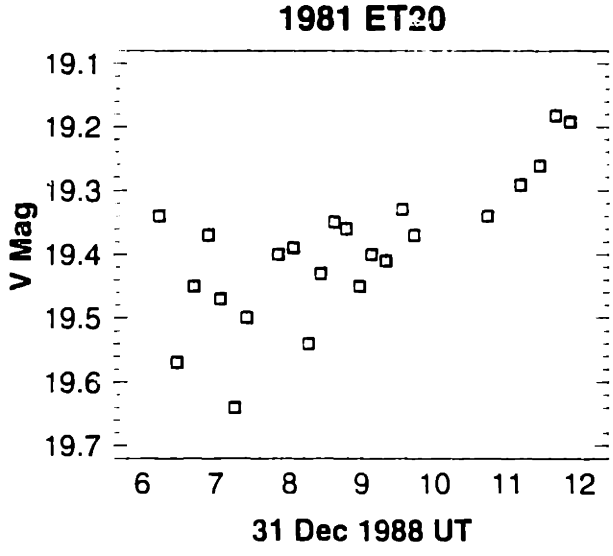
1981 ET20
V Mag
19.1
19.2
19.3
19.4
19.5
19.6
19.7
6 7 8 9 10 11 12
31 Dec 1988 UT

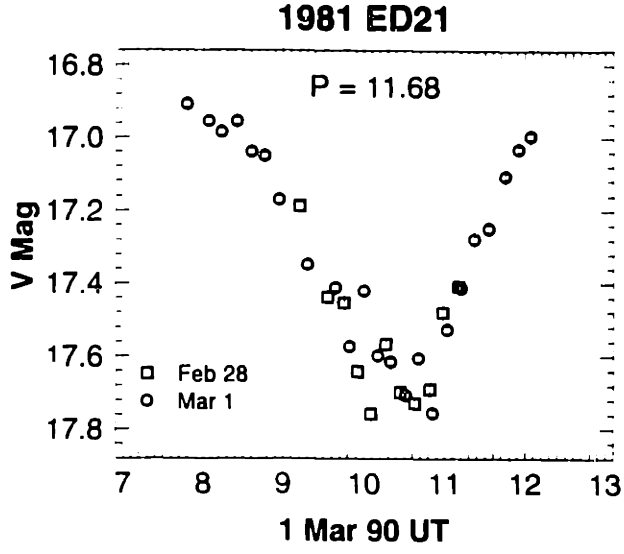
1981 ED21
P = 11.68
Feb 28
Mar 1
V Mag
16.8
17.0
17.2
17.4
17.6
17.8
7 8 9 10 11 12 13
1 Mar 90 UT

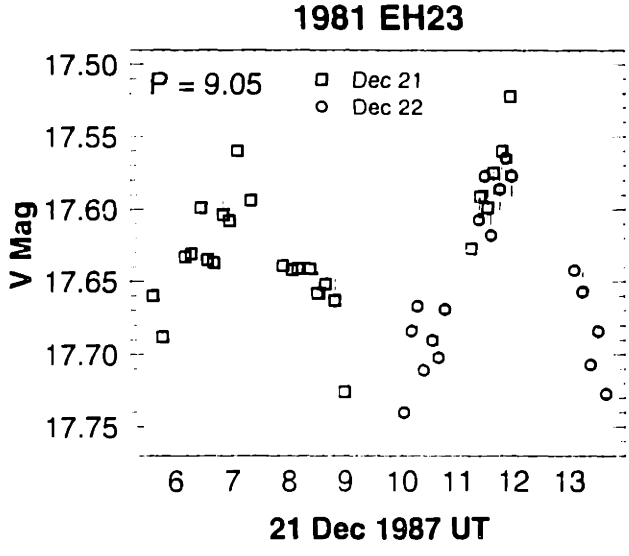
1981 EH23
P = 9.05
Dec 21
Dec 22
V Mag
17.50
17.55
17.60
17.65
17.70
17.75
6 7 8 9 10 11 12 13
21 Dec 1987 UT

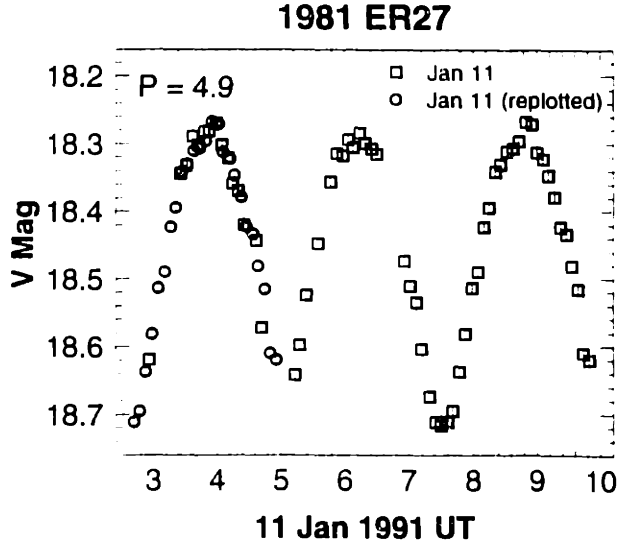
1981 ER27
P = 4.9
Jan 11
Jan 11 (replotted)
V Mag
18.2
18.3
18.4
18.5
18.6
18.7
3 4 5 6 7 8 9 10
11 Jan 1991 UT

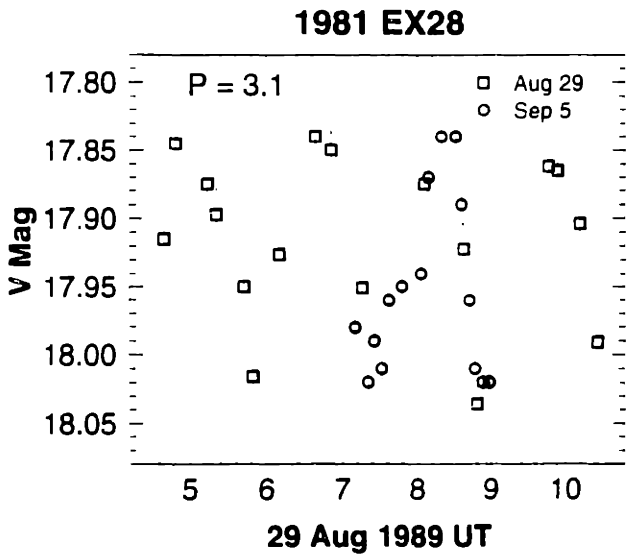
1981 EX28
P = 3.1
Aug 29
Sep 5
V Mag
17.80
17.85
17.90
17.95
18.00
18.05
5
6
7
8
9
10
29 Aug 1989 UT

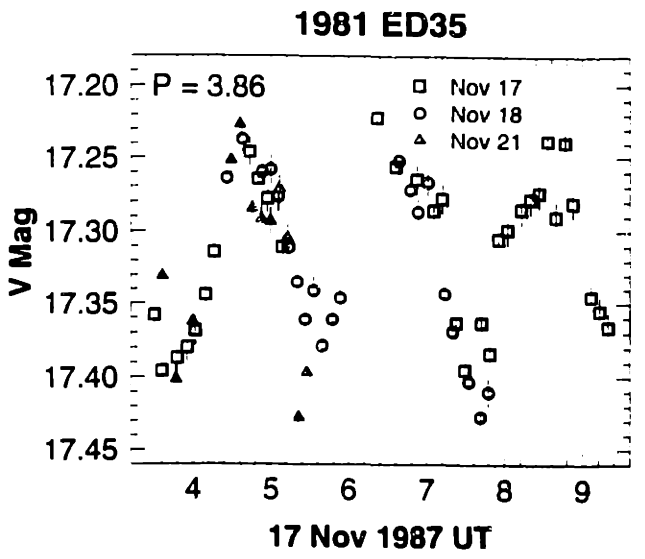
1981 ED35
P = 3.86
Nov 17
Nov 18
Nov 21
V Mag
17.20
17.25
17.30
17.35
17.40
17.45
4
5
6
7
8
9
17 Nov 1987 UT

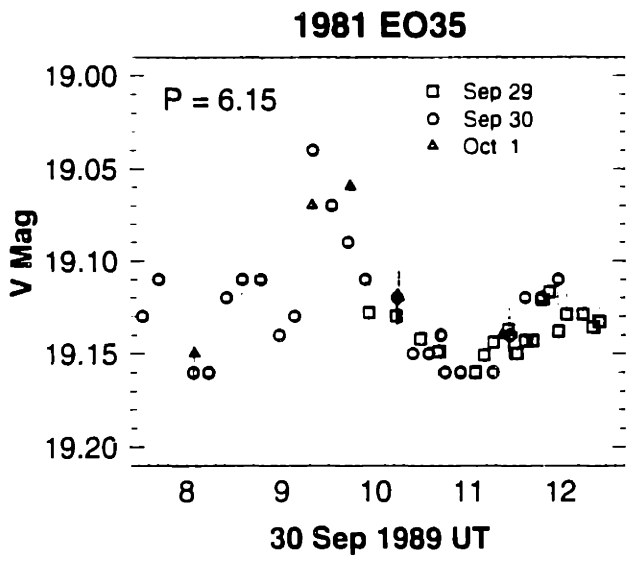
1981 EO35
P = 6.15
Sep 29
Sep 30
Oct 1
V Mag
19.00
19.05
19.10
19.15
19.20
8
9
10
11
12
30 Sep 1989 UT

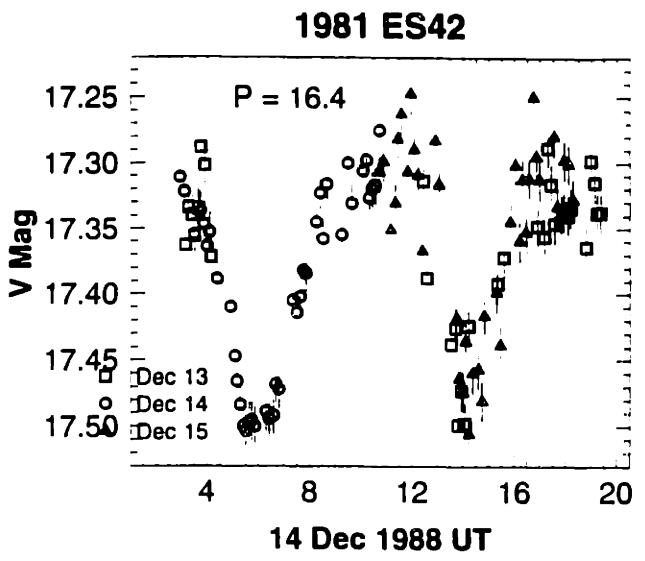
1981 ES42
P = 16.4
Dec 13
Dec 14
Dec 15
V Mag
17.25
17.30
17.35
17.40
17.45
17.50
4
8
12
16
20
14 Dec 1988 UT

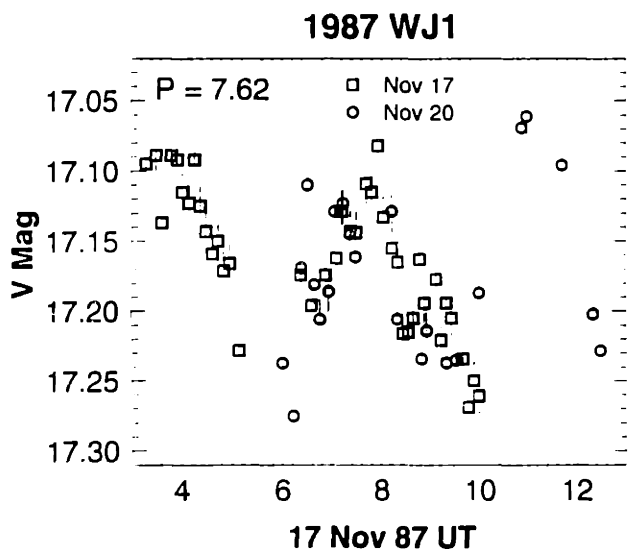
1987 WJ1
P = 7.62
Nov 17
Nov 20
V Mag
17.05
17.10
17.15
17.20
17.25
17.30
4
6
8
10
12
17 Nov 87 UT

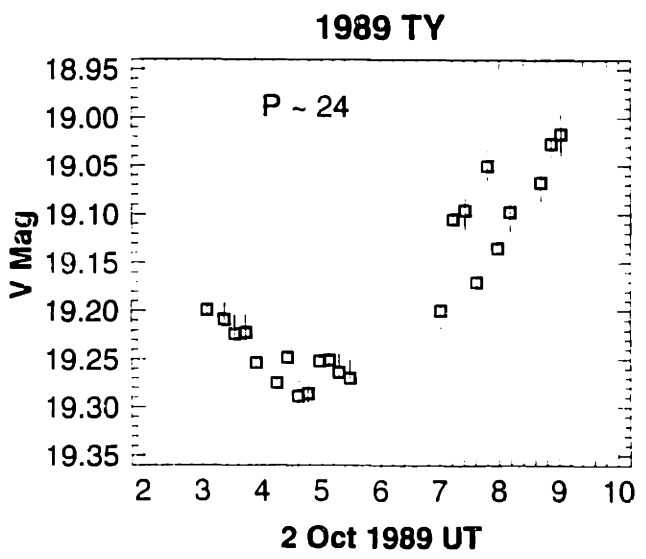
1989 TY
P ~ 24
V Mag
18.95
19.00
19.05
19.10
19.15
19.20
19.25
19.30
19.35
2
3
4
5
6
7
8
9
10
2 Oct 1989 UT

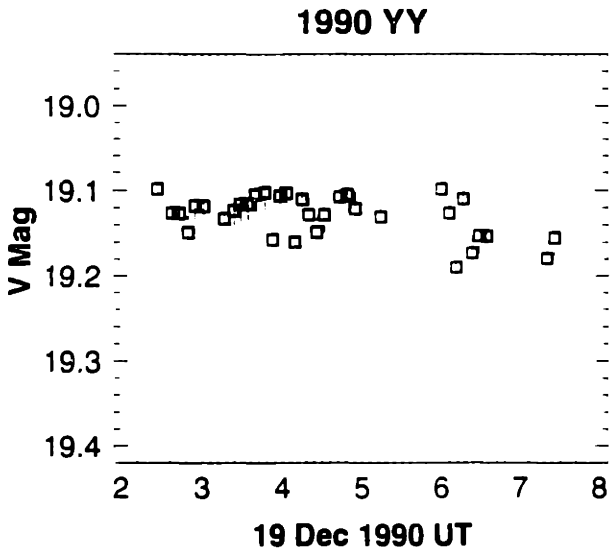
1990 YY
V Mag
19.0
19.1
19.2
19.3
19.4
2
3
4
5
6
7
8
19 Dec 1990 UT

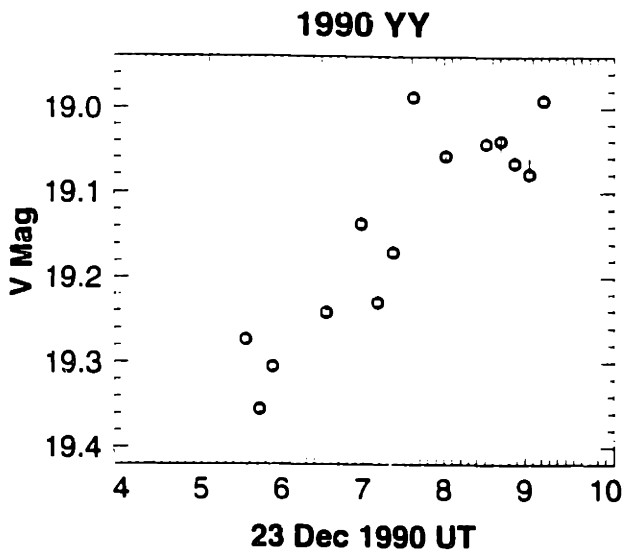
1990 YY
V Mag
19.0
19.1
19.2
19.3
19.4
4
5
6
7
8
9
10
23 Dec 1990 UT

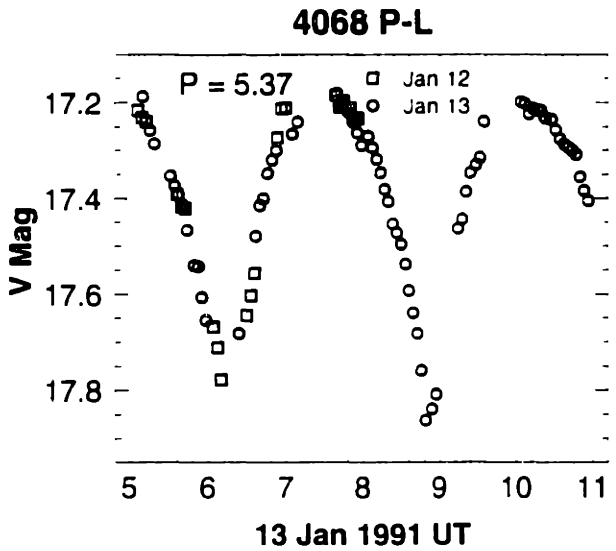
4068 P-L
P = 5.37
Jan 12
Jan 13
V Mag
17.2
17.4
17.6
17.8
5
6
7
8
9
10
11
13 Jan 1991 UT

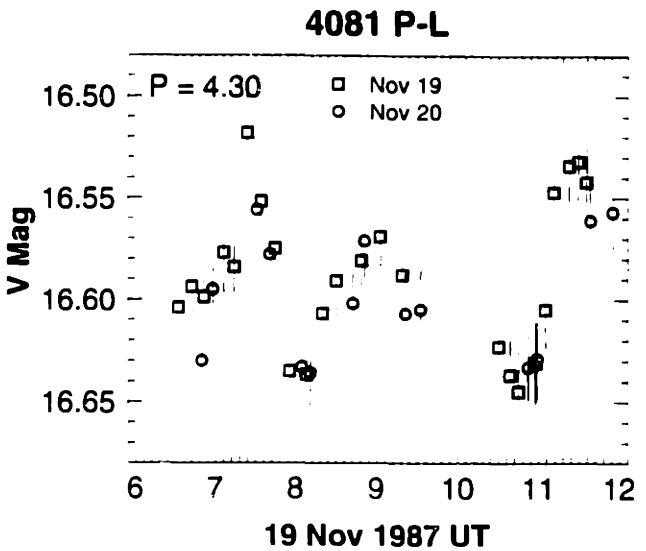
4081 P-L
P = 4.30
Nov 19
Nov 20
V Mag
16.50
16.55
16.60
16.65
6
7
8
9
10
11
12
19 Nov 1987 UT

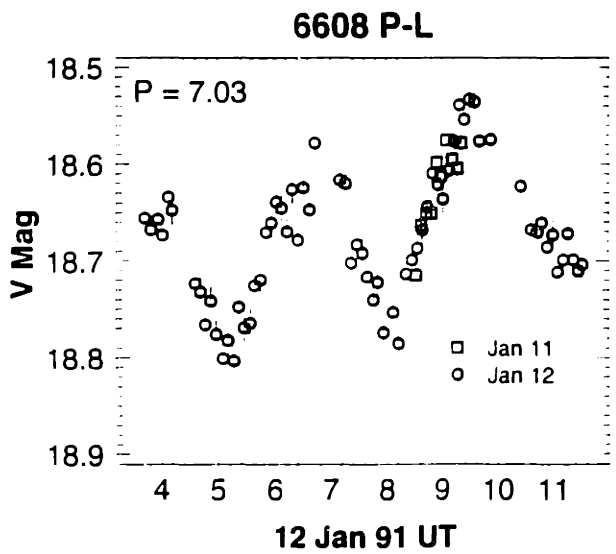
6608 P-L
P = 7.03
Jan 11
Jan 12
V Mag
18.5
18.6
18.7
18.8
18.9
4
5
6
7
8
9
10
11
12 Jan 91 UT

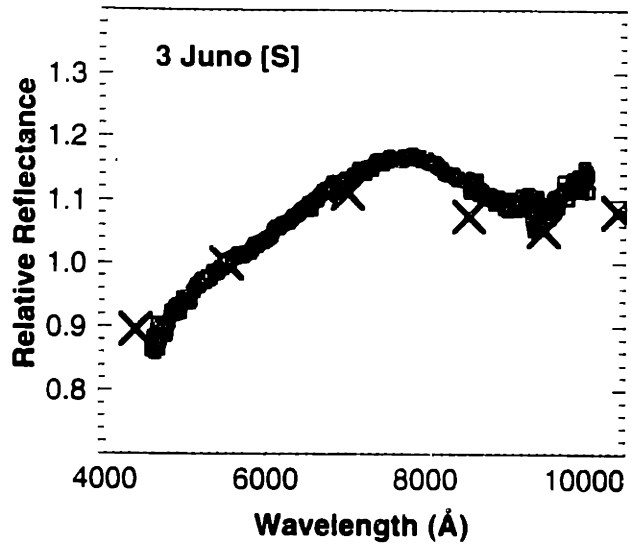
3 Juno [S]
Relative Reflectance
1.3
1.2
1.1
1.0
0.9
0.8
4000
6000
8000
10000
Wavelength (Å)

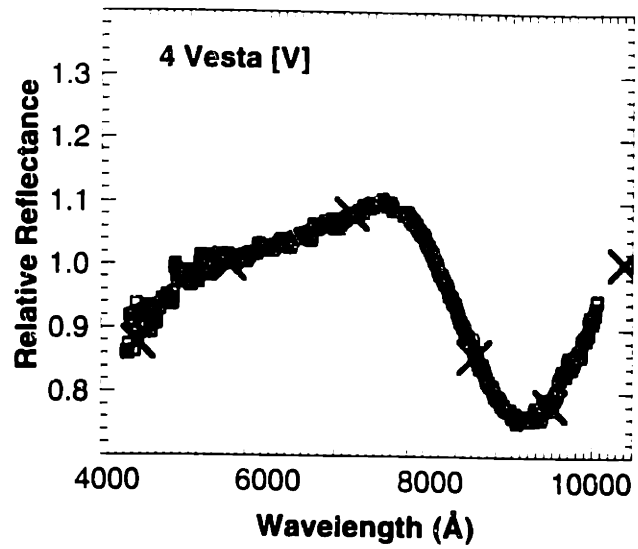
4 Vesta [V]
Relative Reflectance
1.3
1.2
1.1
1.0
0.9
0.8
4000
6000
8000
10000
Wavelength (Å)

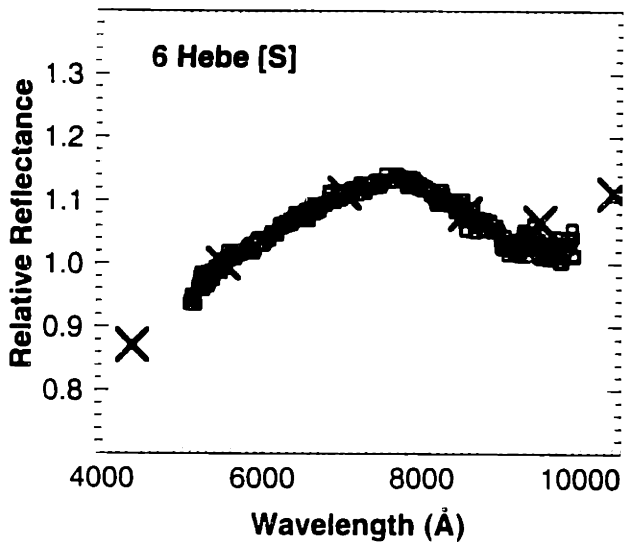
6 Hebe [S]
Relative Reflectance
1.3
1.2
1.1
1.0
0.9
0.8
4000
6000
8000
10000
Wavelength (Å)

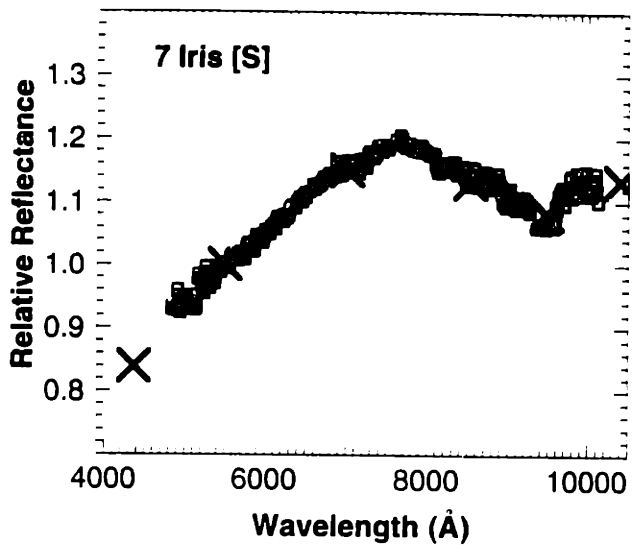
7 Iris [S]
Relative Reflectance
1.3
1.2
1.1
1.0
0.9
0.8
4000
6000
8000
10000
Wavelength (Å)

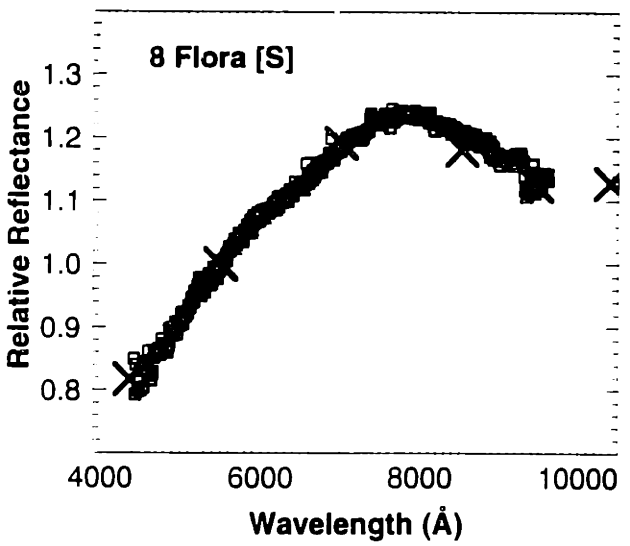
8 Flora [S]
Relative Reflectance
1.3
1.2
1.1
1.0
0.9
0.8
4000
6000
8000
10000
Wavelength (Å)

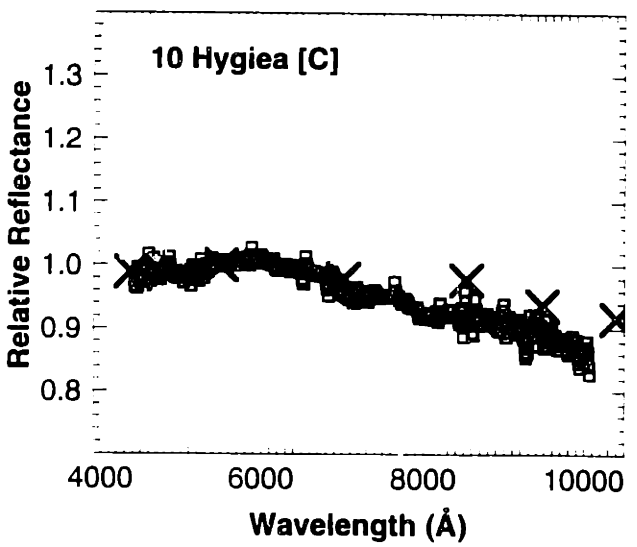
10 Hygiea [C]
Relative Reflectance
1.3
1.2
1.1
1.0
0.9
0.8
4000
6000
8000
10000
Wavelength (Å)

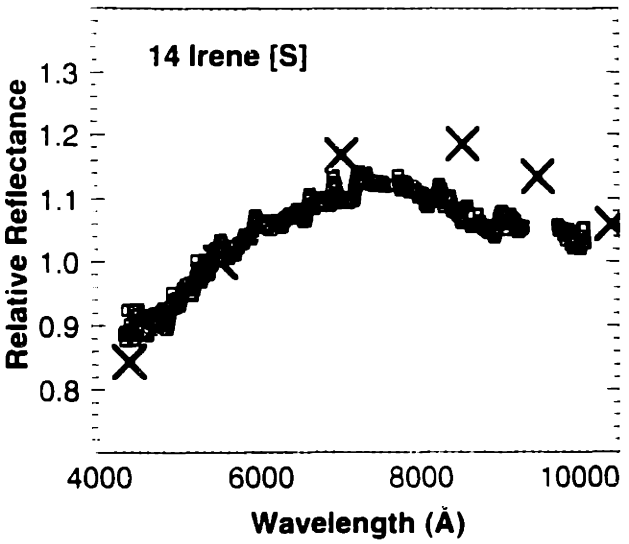
14 Irene [S]
Relative Reflectance
1.3
1.2
1.1
1.0
0.9
0.8
4000
6000
8000
10000
Wavelength (Å)

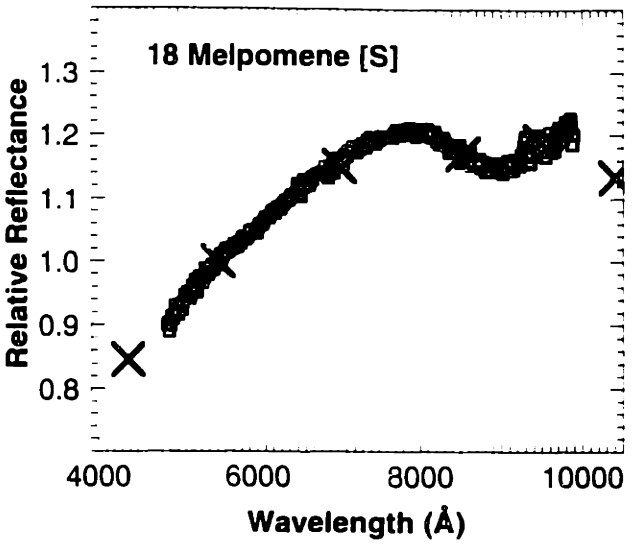
18 Melpomene [S]
Relative Reflectance
1.3
1.2
1.1
1.0
0.9
0.8
4000
6000
8000
10000
Wavelength (Å)

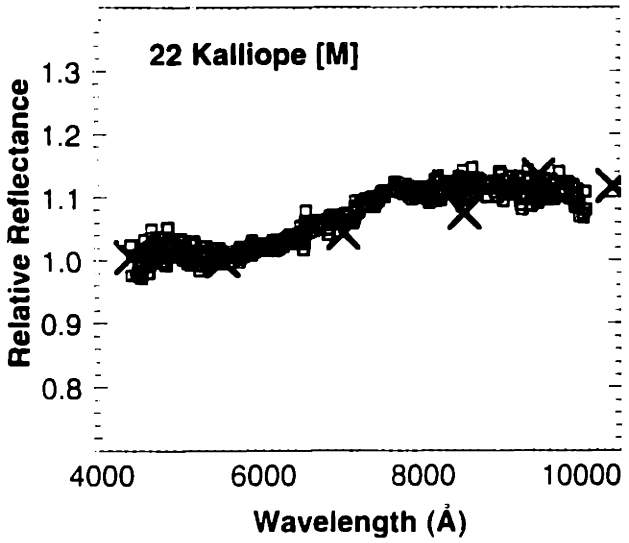
22 Kalliope [M]
Relative Reflectance
1.3
1.2
1.1
1.0
0.9
0.8
4000
6000
8000
10000
Wavelength (Å)

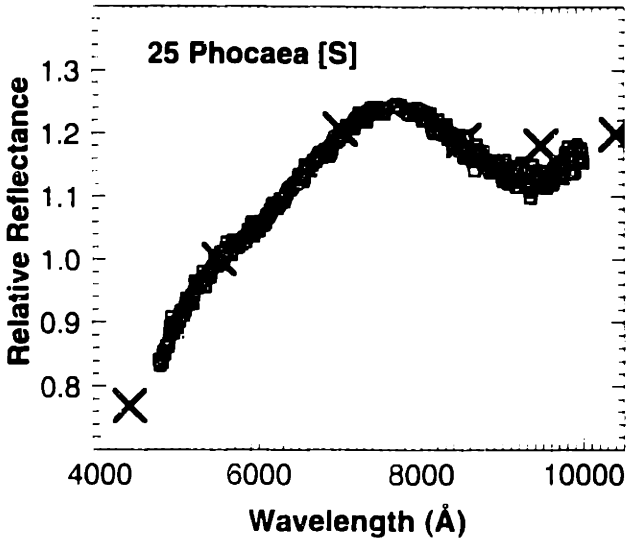
25 Phocaea [S]
Relative Reflectance
1.3
1.2
1.1
1.0
0.9
0.8
4000
6000
8000
10000
Wavelength (Å)

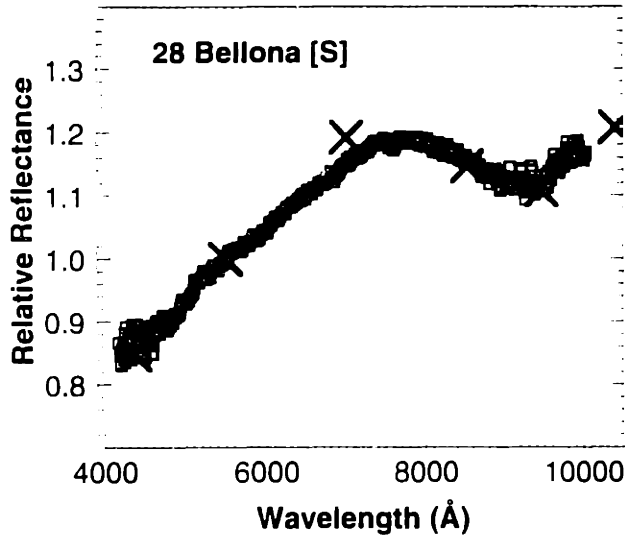
28 Bellona [S]
Relative Reflectance
1.3
1.2
1.1
1.0
0.9
0.8
4000
6000
8000
10000
Wavelength (Å)

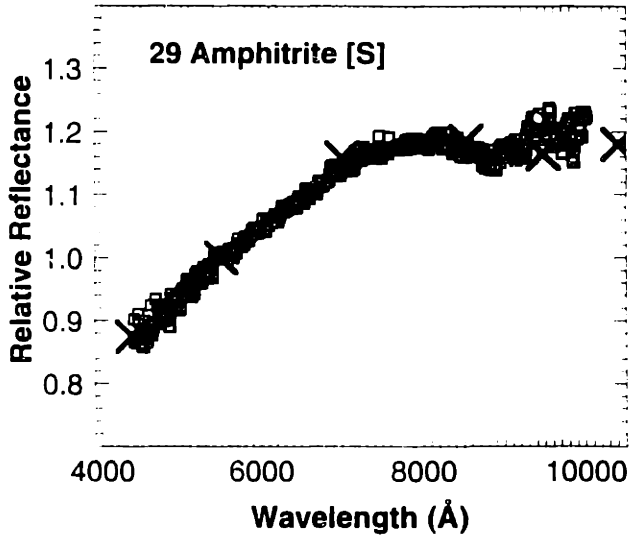
29 Amphitrite [S]
Relative Reflectance
1.3
1.2
1.1
1.0
0.9
0.8
4000
6000
8000
10000
Wavelength (Å)

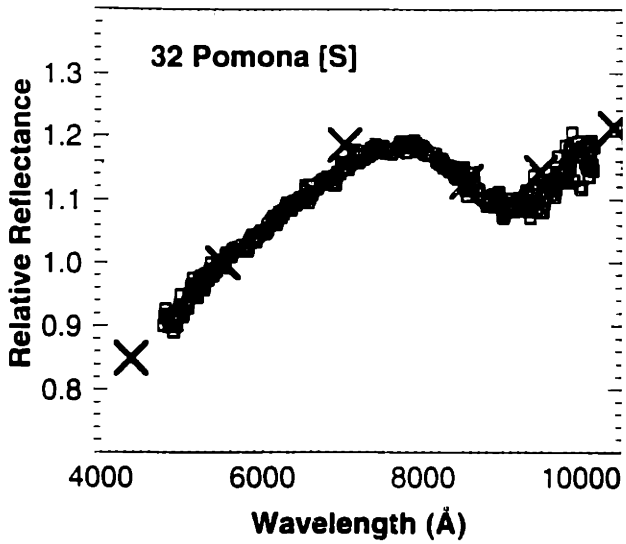
32 Pomona [S]
Relative Reflectance
1.3
1.2
1.1
1.0
0.9
0.8
4000
6000
8000
10000
Wavelength (Å)

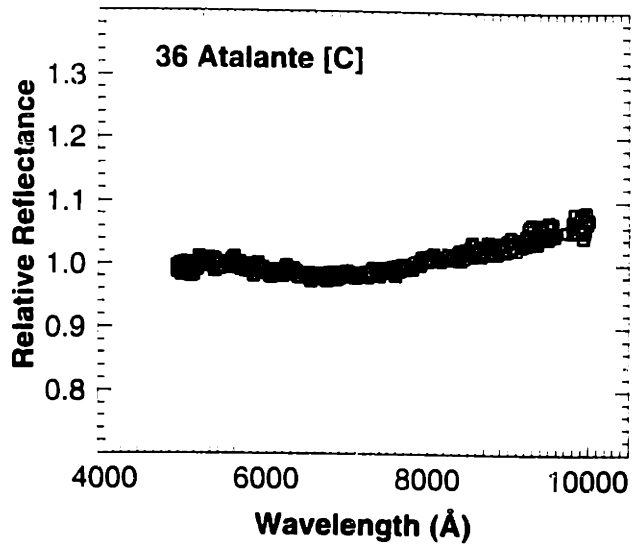
36 Atalante [C]
Relative Reflectance
1.3
1.2
1.1
1.0
0.9
0.8
4000
6000
8000
10000
Wavelength (Å)

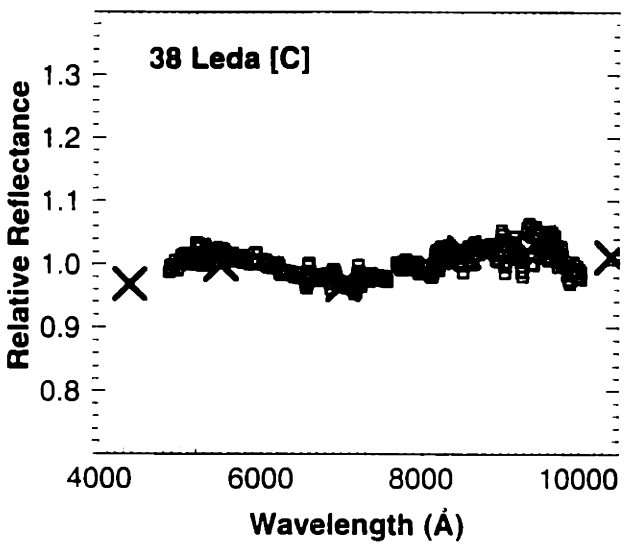
38 Leda [C]
Relative Reflectance
1.3
1.2
1.1
1.0
0.9
0.8
4000
6000
8000
10000
Wavelength (Å)

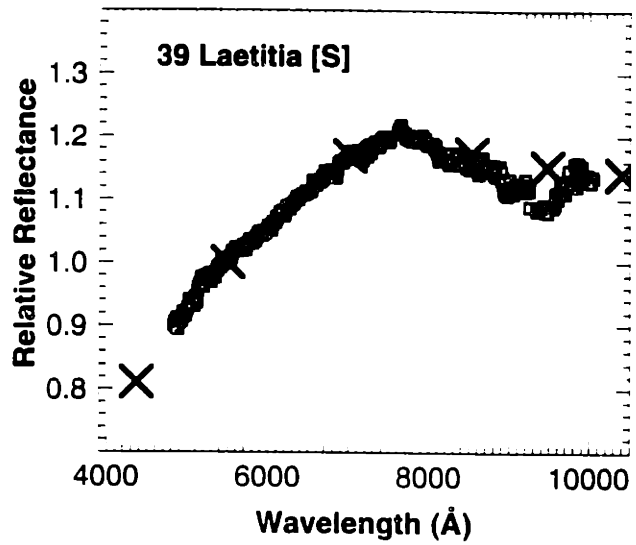
39 Laetitia [S]
Relative Reflectance
1.3
1.2
1.1
1.0
0.9
0.8
4000
6000
8000
10000
Wavelength (Å)

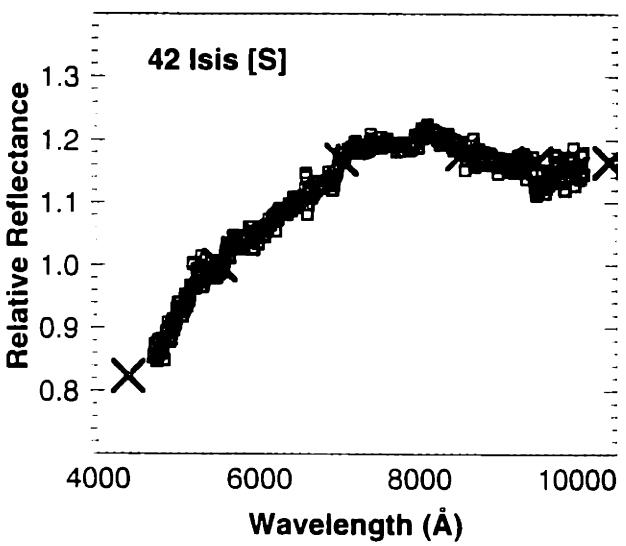
42 Isis [S]
Relative Reflectance
1.3
1.2
1.1
1.0
0.9
0.8
4000
6000
8000
10000
Wavelength (Å)

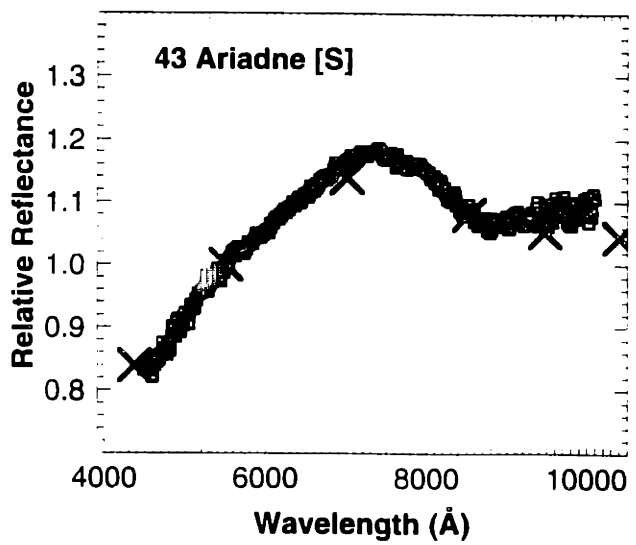
43 Ariadne [S]
Relative Reflectance
1.3
1.2
1.1
1.0
0.9
0.8
4000
6000
8000
10000
Wavelength (Å)

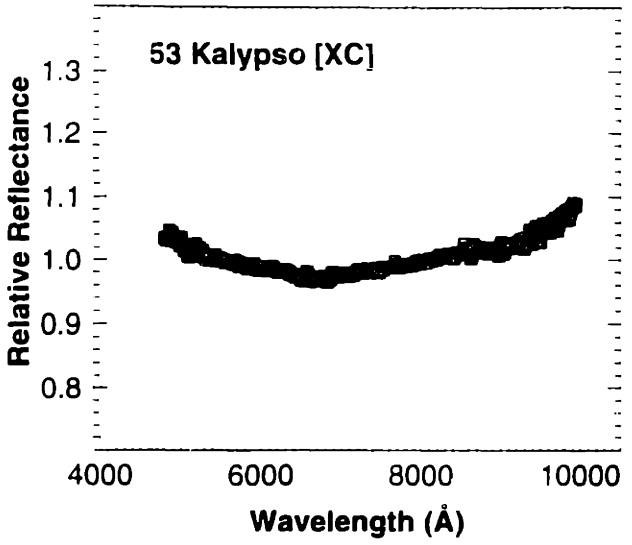
53 Kalypso [XC]
Relative Reflectance
1.3
1.2
1.1
1.0
0.9
0.8
4000
6000
8000
10000
Wavelength (Å)

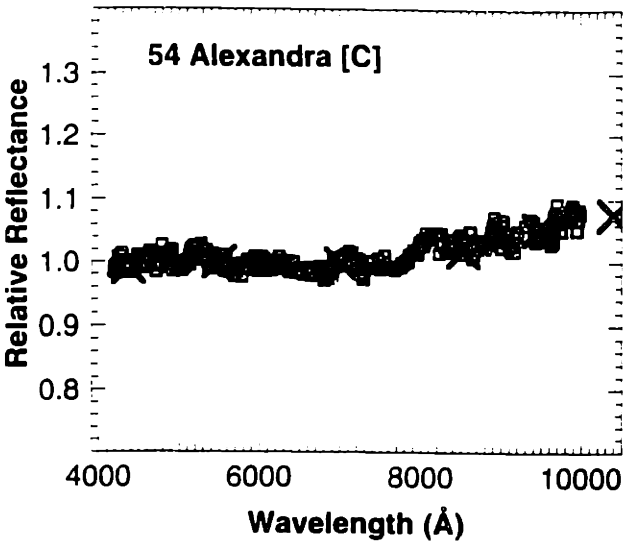
54 Alexandra [C]
Relative Reflectance
1.3
1.2
1.1
1.0
0.9
0.8
4000
6000
8000
10000
Wavelength (Å)

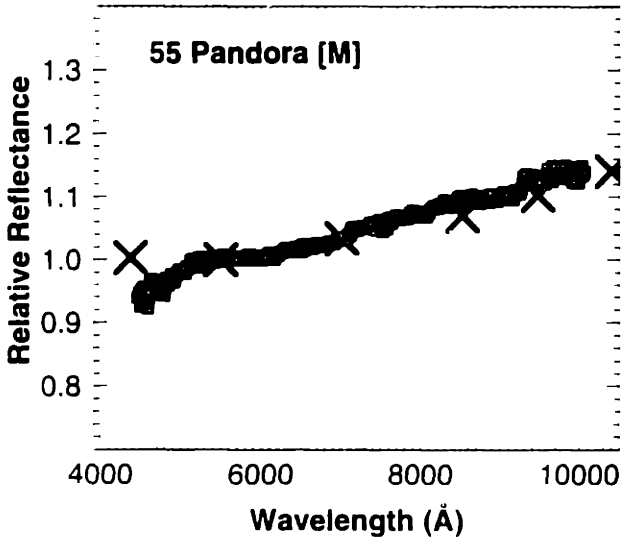
55 Pandora [M]
Relative Reflectance
1.3
1.2
1.1
1.0
0.9
0.8
4000
6000
8000
10000
Wavelength (Å)

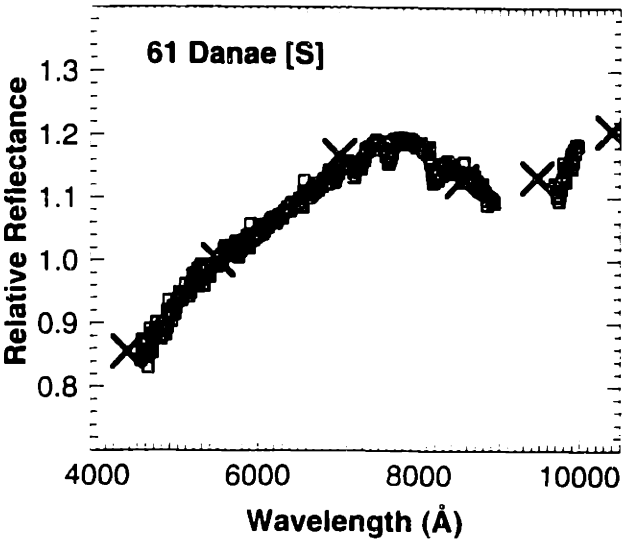
61 Danae [S]
Relative Reflectance
1.3
1.2
1.1
1.0
0.9
0.8
4000
6000
8000
10000
Wavelength (Å)

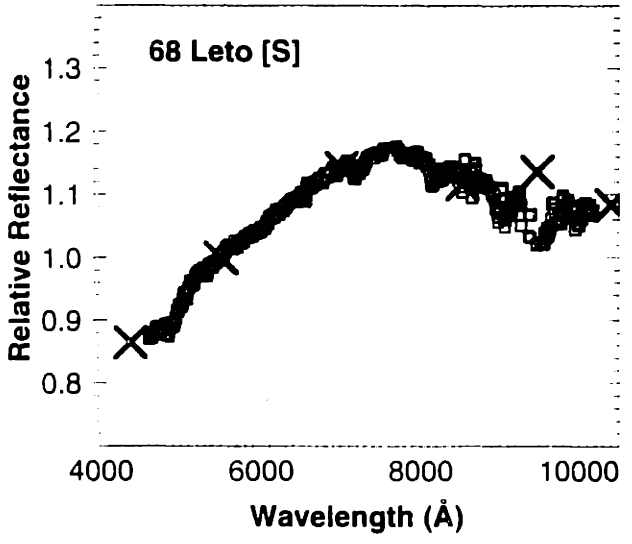
68 Leto [S]
Relative Reflectance
1.3
1.2
1.1
1.0
0.9
0.8
4000
6000
8000
10000
Wavelength (Å)

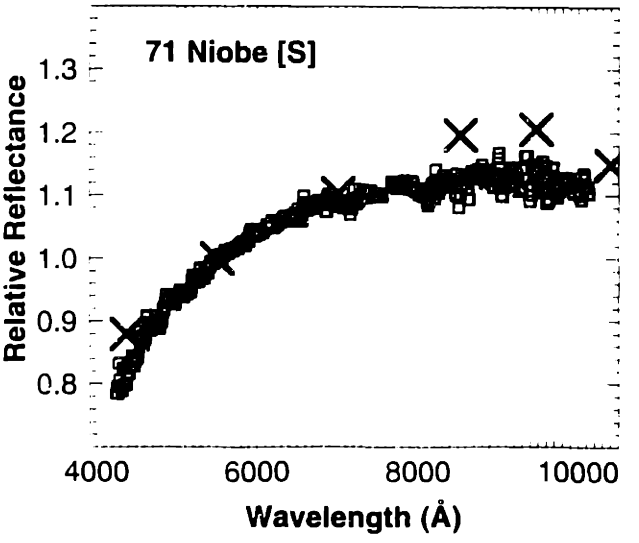
71 Niobe [S]
Relative Reflectance
1.3
1.2
1.1
1.0
0.9
0.8
4000
6000
8000
10000
Wavelength (Å)

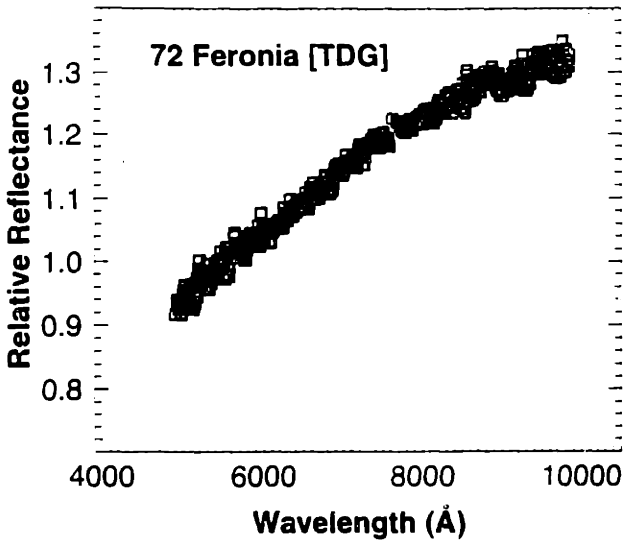
72 Feronia [TDG]
Relative Reflectance
1.3
1.2
1.1
1.0
0.9
0.8
4000
6000
8000
10000
Wavelength (Å)

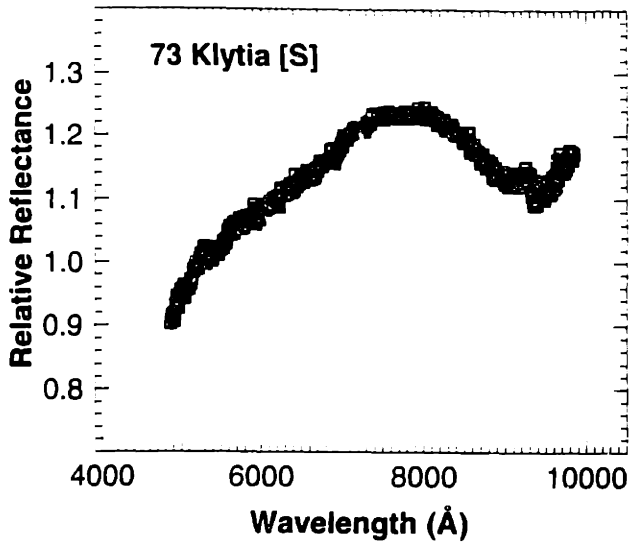
73 Klytia [S]
Relative Reflectance
1.3
1.2
1.1
1.0
0.9
0.8
4000
6000
8000
10000
Wavelength (Å)

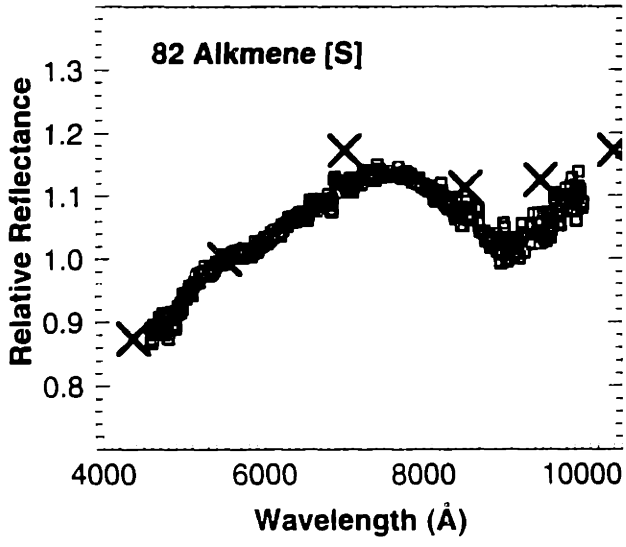
82 Alkmene [S]
Relative Reflectance
1.3
1.2
1.1
1.0
0.9
0.8
4000
6000
8000
10000
Wavelength (Å)

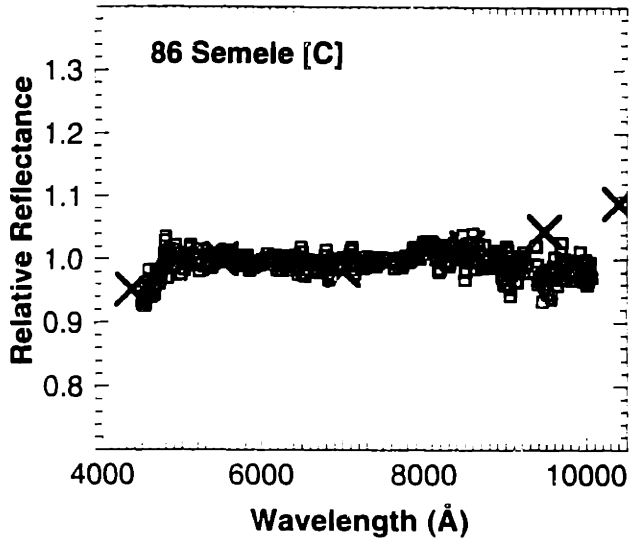
86 Semele [C]
Relative Reflectance
1.3
1.2
1.1
1.0
0.9
0.8
4000
6000
8000
10000
Wavelength (Å)

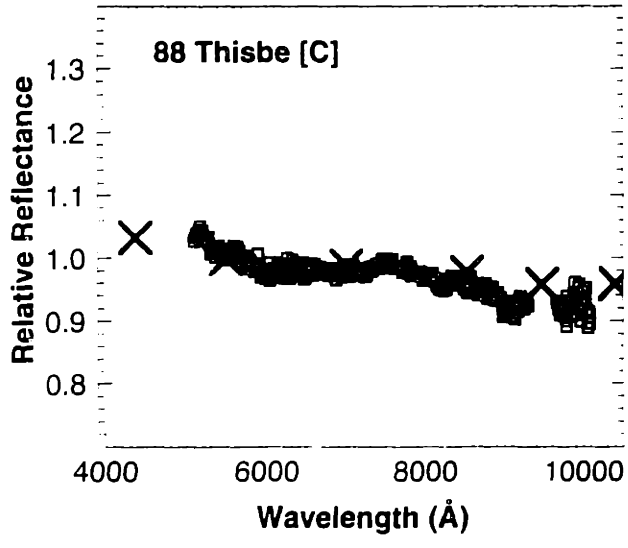
88 Thisbe [C]
Relative Reflectance
1.3
1.2
1.1
1.0
0.9
0.8
4000
6000
8000
10000
Wavelength (Å)

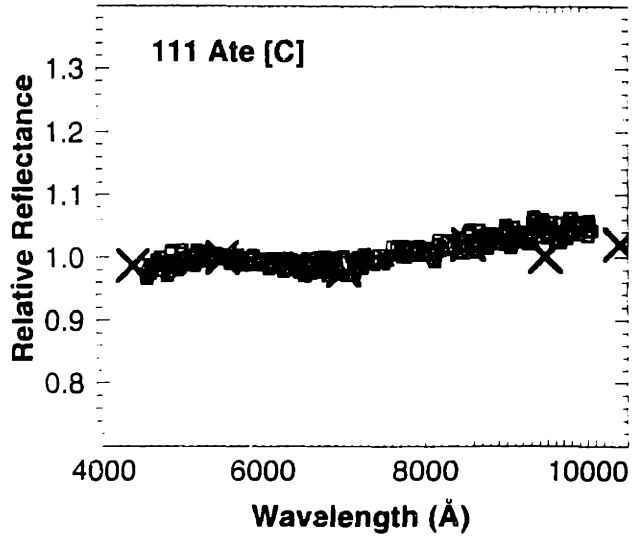
111 Ate [C]
Relative Reflectance
1.3
1.2
1.1
1.0
0.9
0.8
4000
6000
8000
10000
Wavelength (Å)

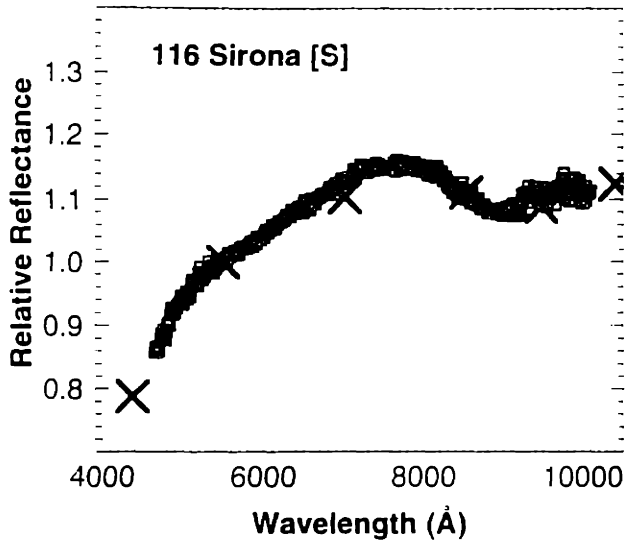
116 Sirona [S]
Relative Reflectance
1.3
1.2
1.1
1.0
0.9
0.8
4000
6000
8000
10000
Wavelength (Å)

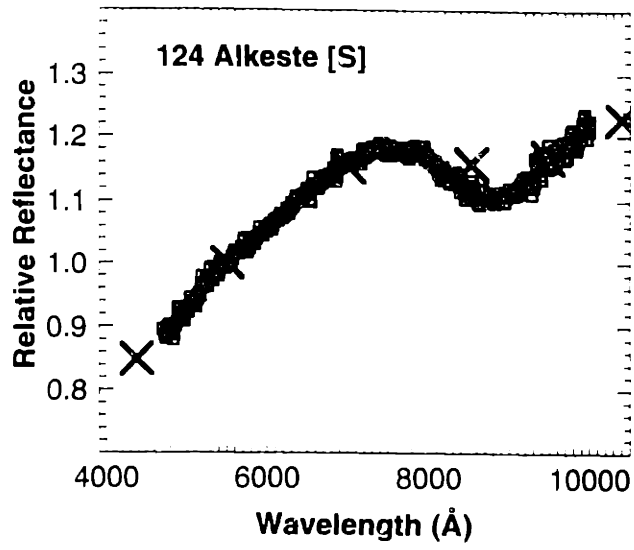
124 Alkeste [S]
Relative Reflectance
1.3
1.2
1.1
1.0
0.9
0.8
4000
6000
8000
10000
Wavelength (Å)

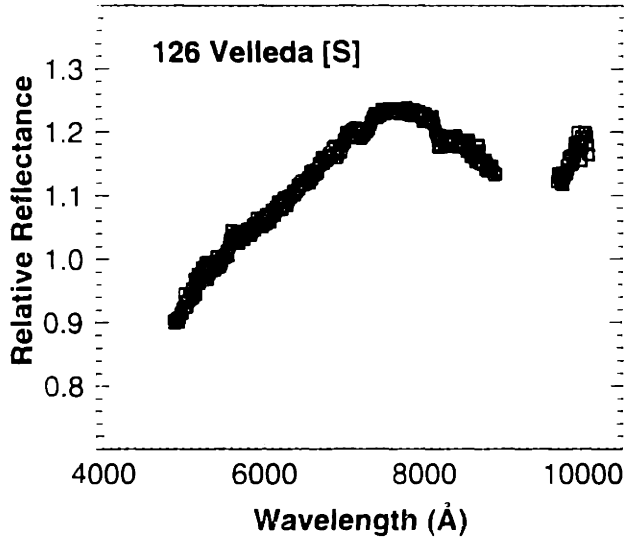
126 Velleda [S]
Relative Reflectance
1.3
1.2
1.1
1.0
0.9
0.8
4000
6000
8000
10000
Wavelength (Å)

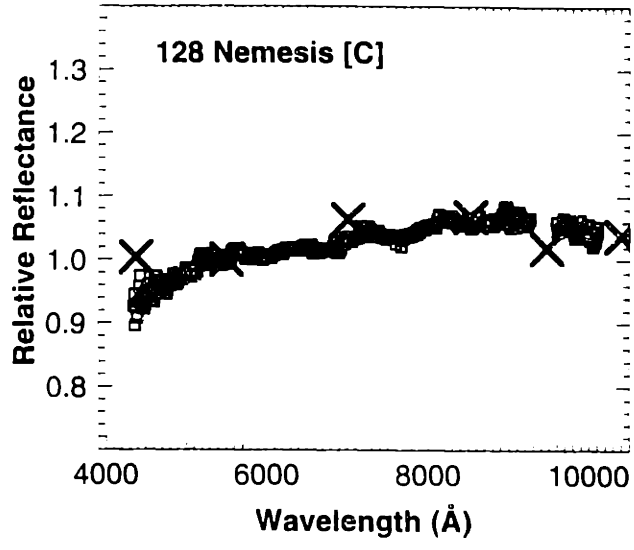
128 Nemesis [C]
Relative Reflectance
1.3
1.2
1.1
1.0
0.9
0.8
4000
6000
8000
10000
Wavelength (Å)

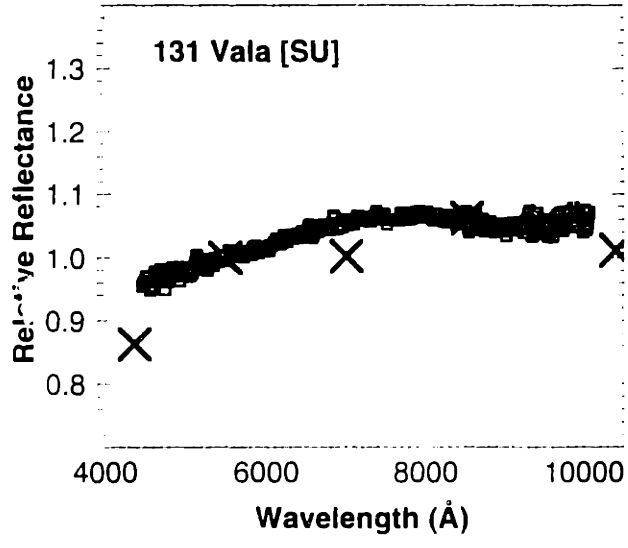
131 Vala [SU]
1.3
1.2
1.1
1.0
0.9
0.8
4000
6000
8000
10000
Wavelength (Å)

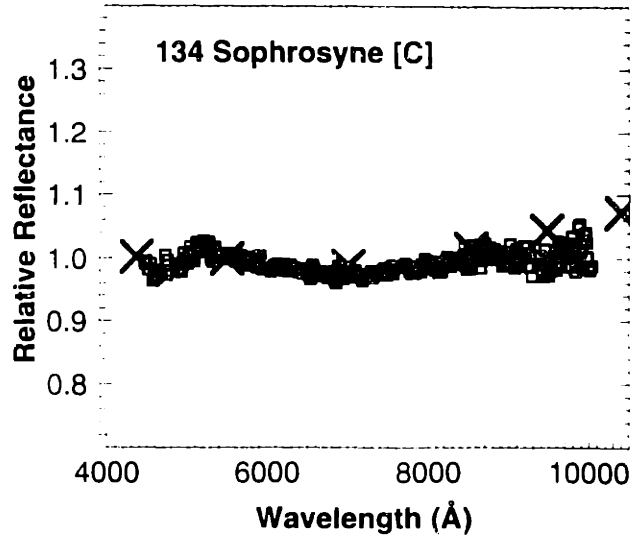
134 Sophrosyne [C]
Relative Reflectance
1.3
1.2
1.1
1.0
0.9
0.8
4000
6000
8000
10000
Wavelength (Å)

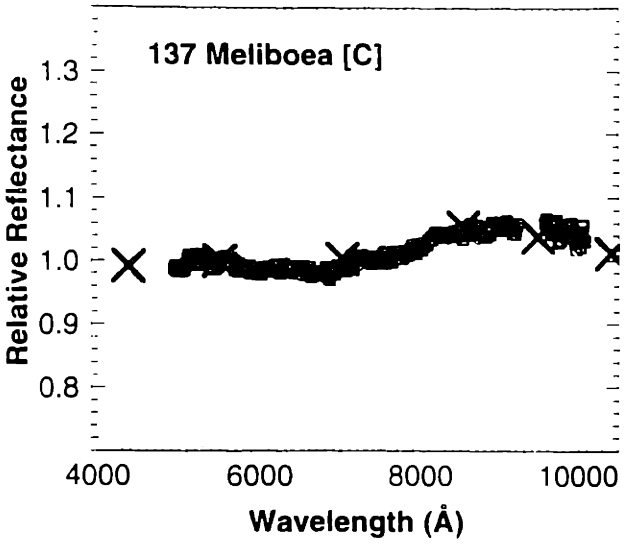
137 Meliboea [C]
Relative Reflectance
1.3
1.2
1.1
1.0
0.9
0.8
4000
6000
8000
10000
Wavelength (Å)

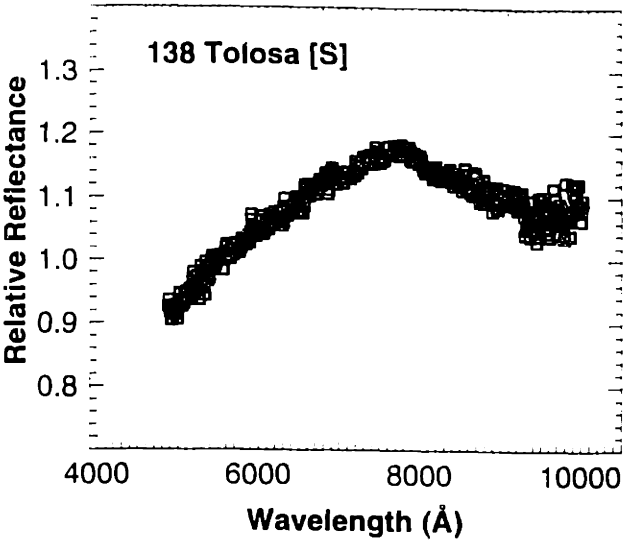
138 Tolosa [S]
Relative Reflectance
1.3
1.2
1.1
1.0
0.9
0.8
4000
6000
8000
10000
Wavelength (Å)

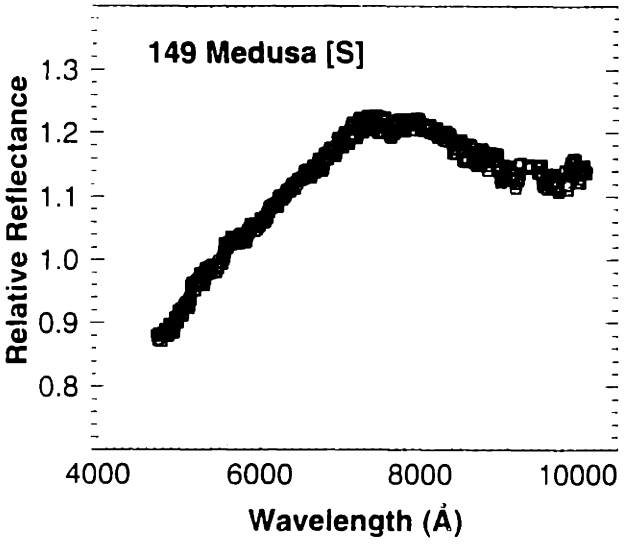
149 Medusa [S]
Relative Reflectance
1.3
1.2
1.1
1.0
0.9
0.8
4000
6000
8000
10000
Wavelength (Å)

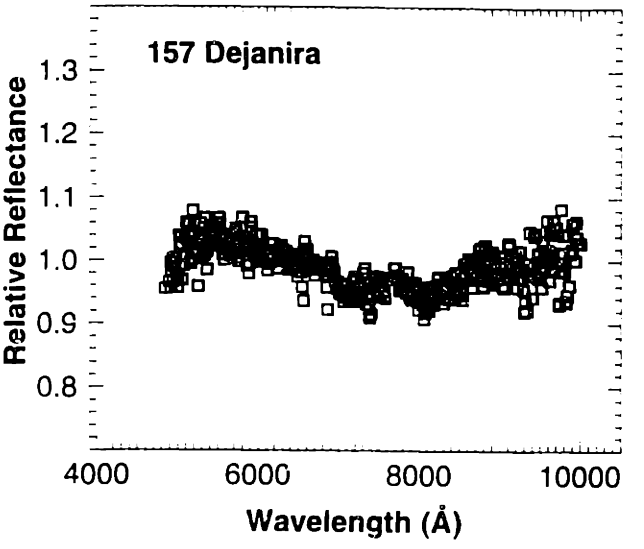
157 Dejanira
Relative Reflectance
1.3
1.2
1.1
1.0
0.9
0.8
4000
6000
8000
10000
Wavelength (Å)

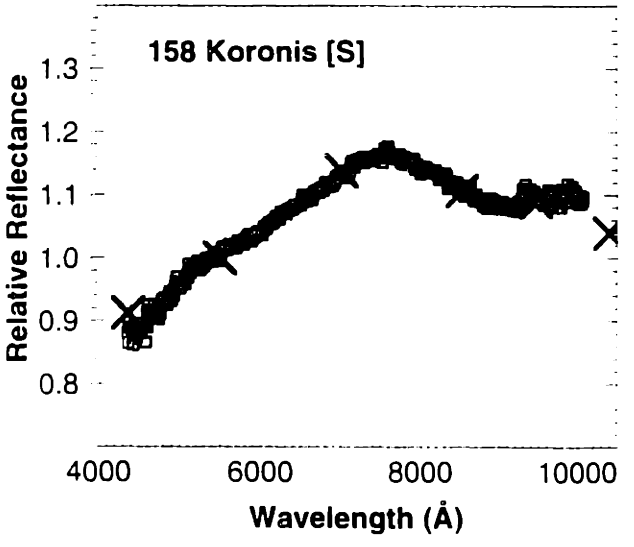
158 Koronis [S]
Relative Reflectance
1.3
1.2
1.1
1.0
0.9
0.8
4000
6000
8000
10000
Wavelength (Å)

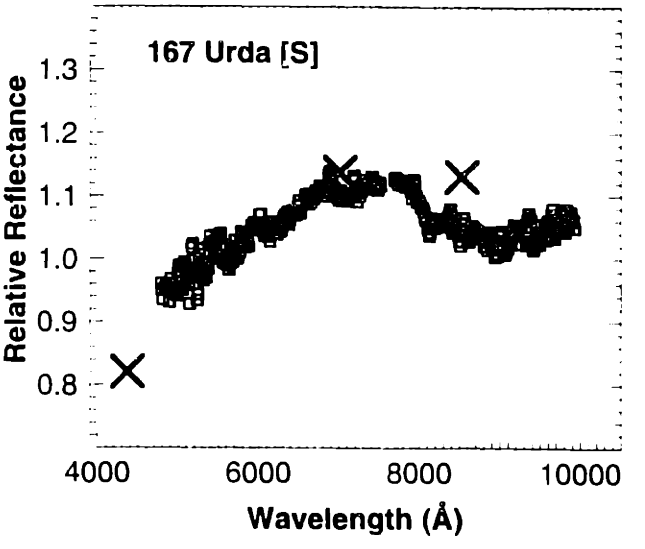
167 Urda [S]
Relative Reflectance
1.3
1.2
1.1
1.0
0.9
0.8
4000
6000
8000
10000
Wavelength (Å)

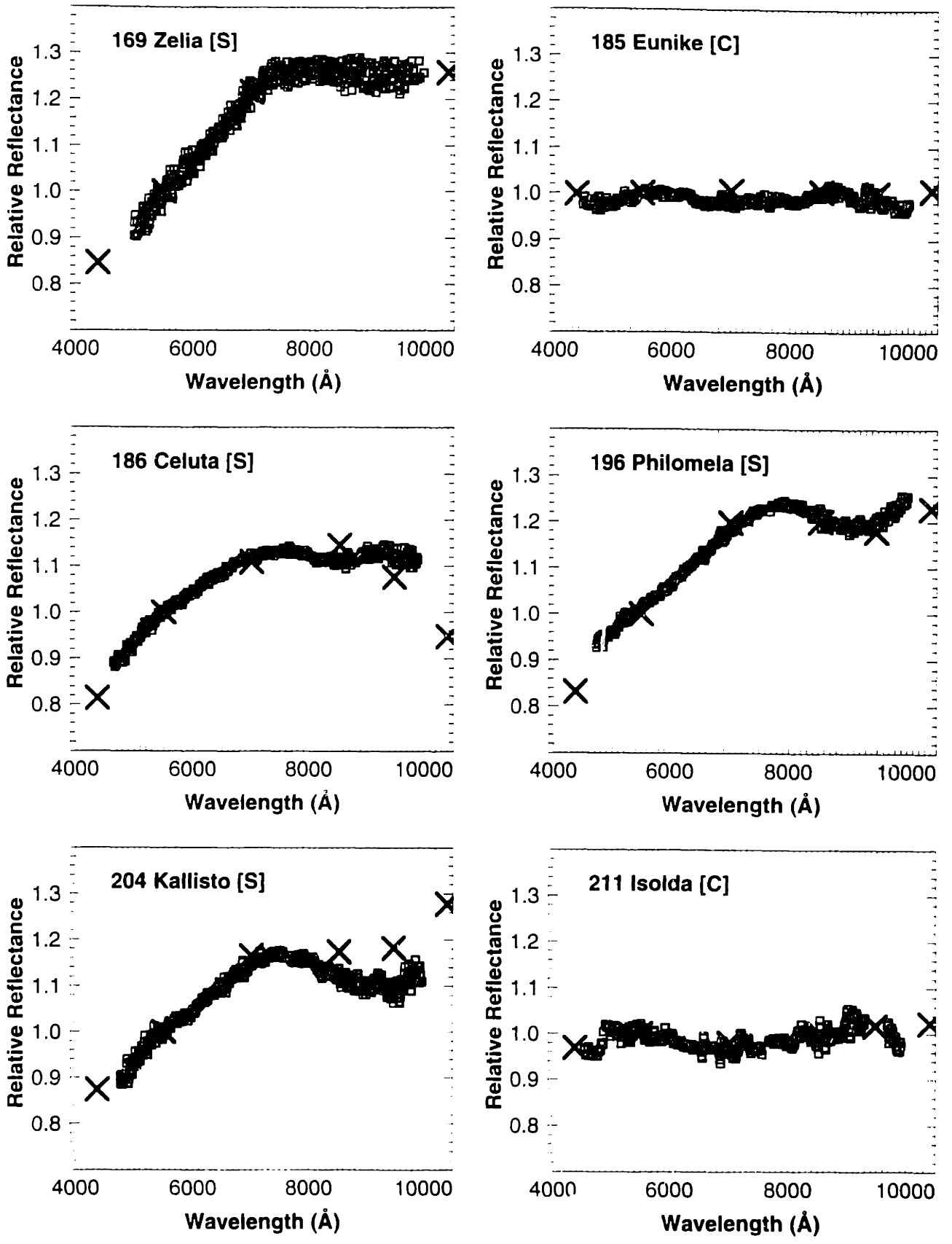
169 Zelia [S]
185 Eunike [C]
186 Celuta [S]
196 Philomela [S]
204 Kallisto [S]
211 Isolda [C]
Relative Reflectance
Wavelength (Å)
0.8
0.9
1.0
1.1
1.2
1.3
4000
6000
8000
10000

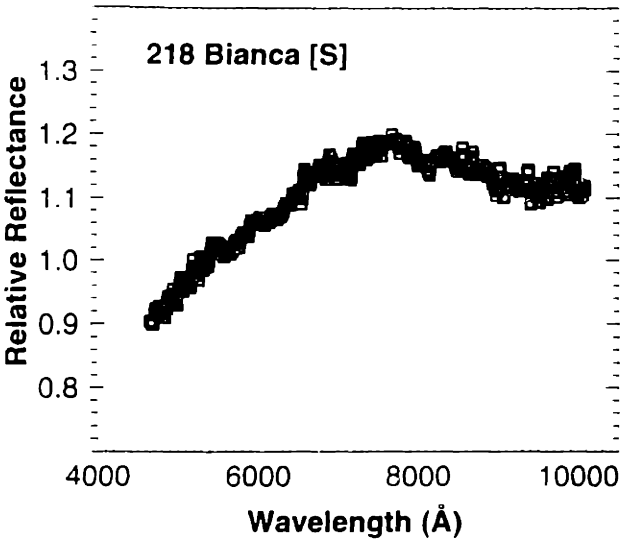
218 Bianca [S]
Relative Reflectance
1.3
1.2
1.1
1.0
0.9
0.8
4000
6000
8000
10000
Wavelength (Å)

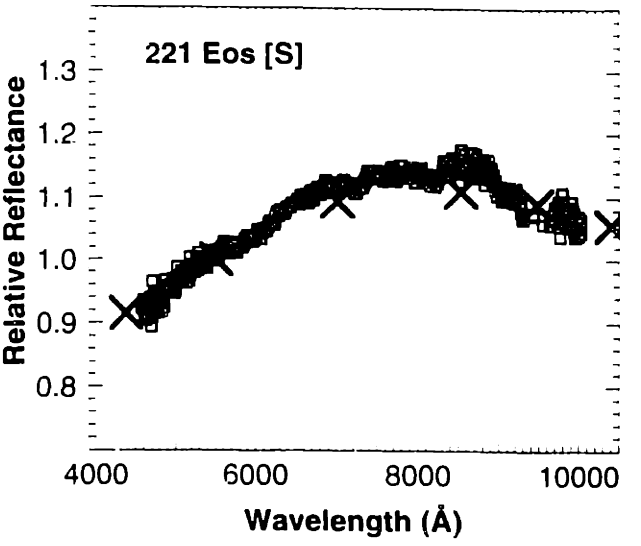
221 Eos [S]
Relative Reflectance
1.3
1.2
1.1
1.0
0.9
0.8
4000
6000
8000
10000
Wavelength (Å)

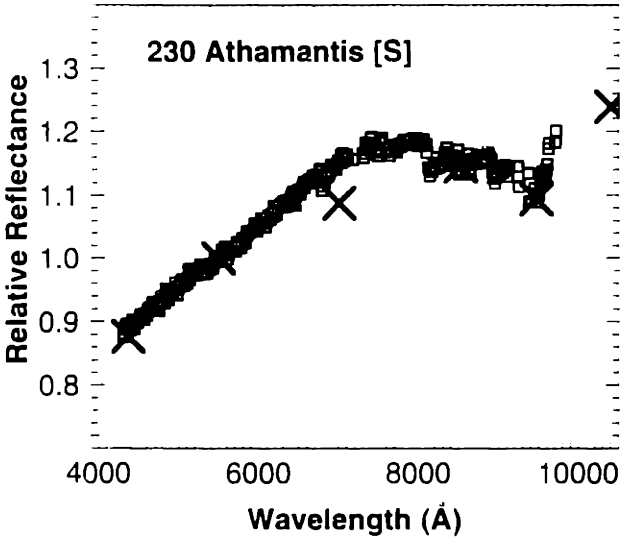
230 Athamantis [S]
Relative Reflectance
1.3
1.2
1.1
1.0
0.9
0.8
4000
6000
8000
10000
Wavelength (Å)

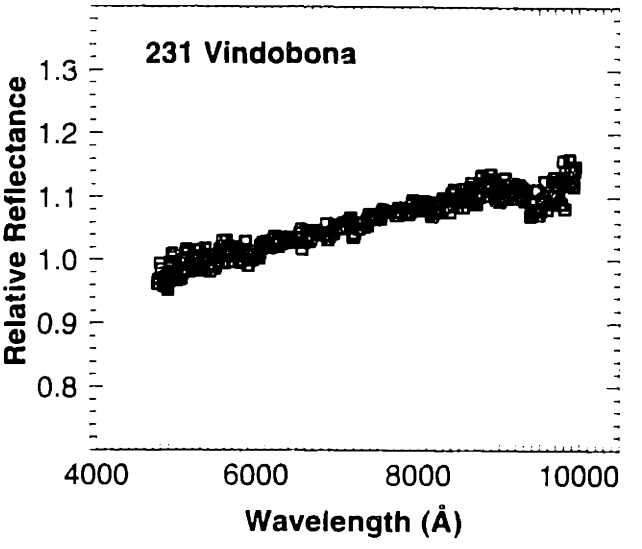
231 Vindobona
Relative Reflectance
1.3
1.2
1.1
1.0
0.9
0.8
4000
6000
8000
10000
Wavelength (Å)

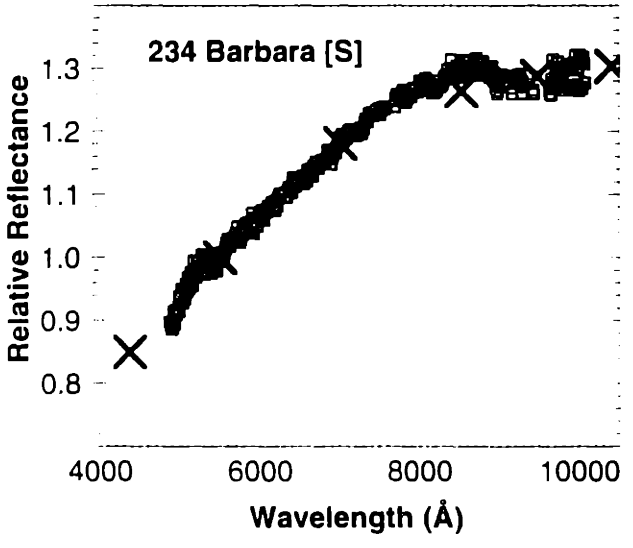
234 Barbara [S]
Relative Reflectance
1.3
1.2
1.1
1.0
0.9
0.8
4000
6000
8000
10000
Wavelength (Å)

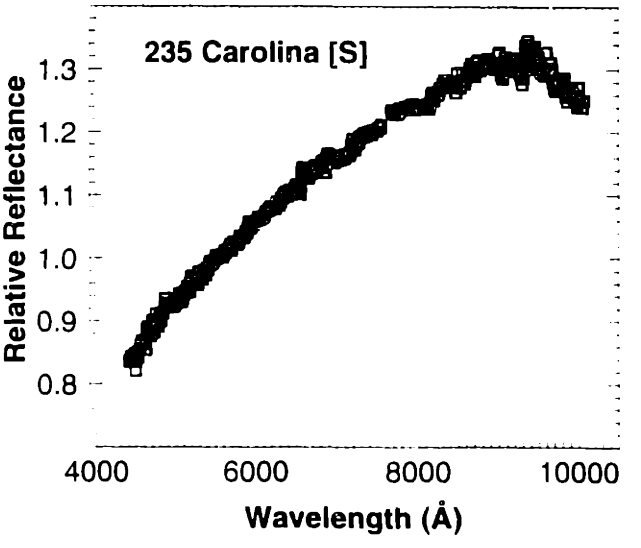
235 Carolina [S]
Relative Reflectance
1.3
1.2
1.1
1.0
0.9
0.8
4000
6000
8000
10000
Wavelength (Å)

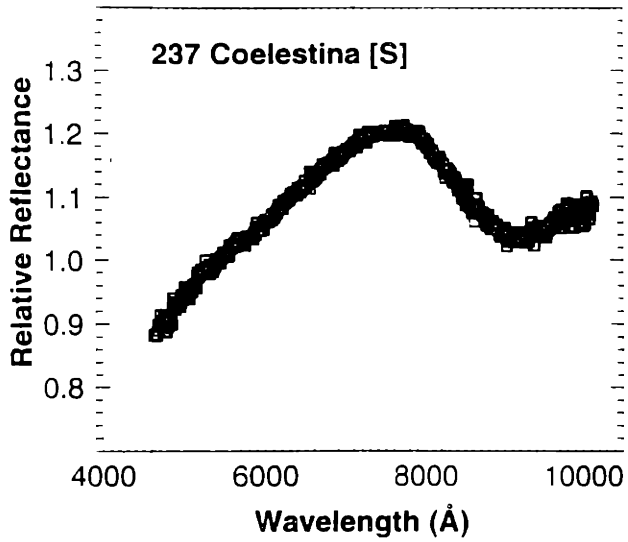
237 Coelestina [S]
Relative Reflectance
1.3
1.2
1.1
1.0
0.9
0.8
4000
6000
8000
10000
Wavelength (Å)

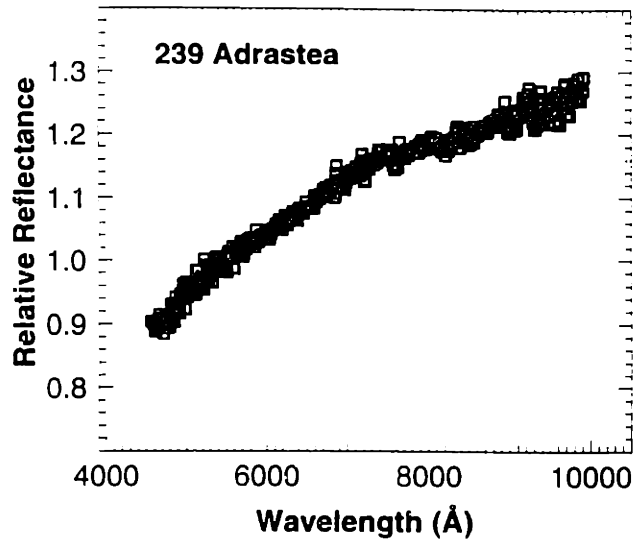
239 Adrastea
Relative Reflectance
1.3
1.2
1.1
1.0
0.9
0.8
4000
6000
8000
10000
Wavelength (Å)

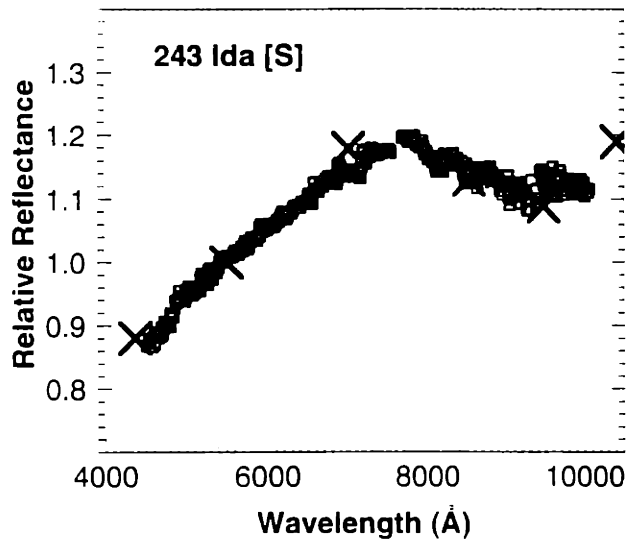
243 Ida [S]
Relative Reflectance
1.3
1.2
1.1
1.0
0.9
0.8
4000
6000
8000
10000
Wavelength (Å)

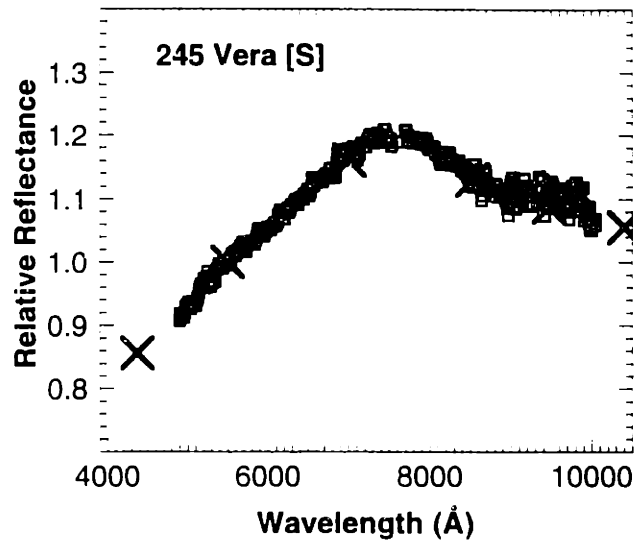
245 Vera [S]
Relative Reflectance
1.3
1.2
1.1
1.0
0.9
0.8
4000
6000
8000
10000
Wavelength (Å)

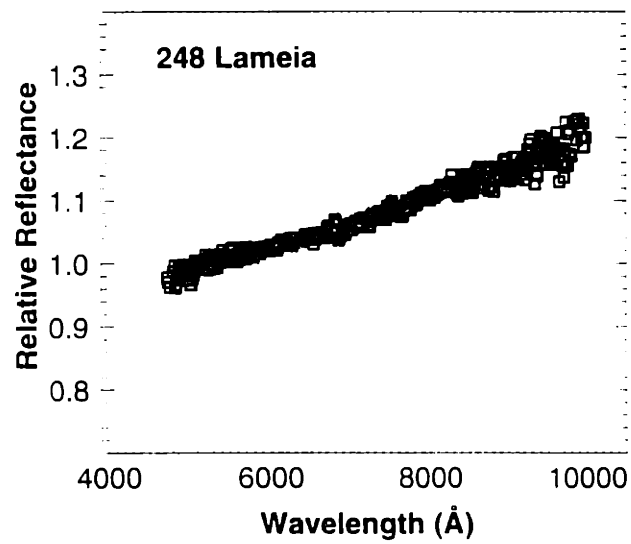
248 Lameia
Relative Reflectance
1.3
1.2
1.1
1.0
0.9
0.8
4000
6000
8000
10000
Wavelength (Å)

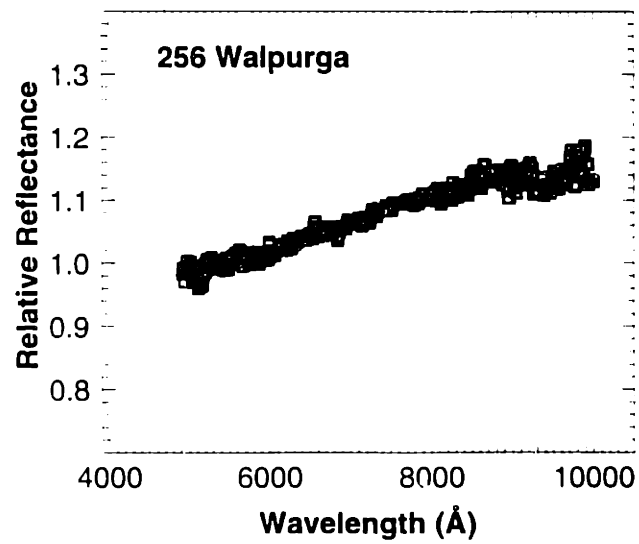
256 Walpurga
Relative Reflectance
1.3
1.2
1.1
1.0
0.9
0.8
4000
6000
8000
10000
Wavelength (Å)

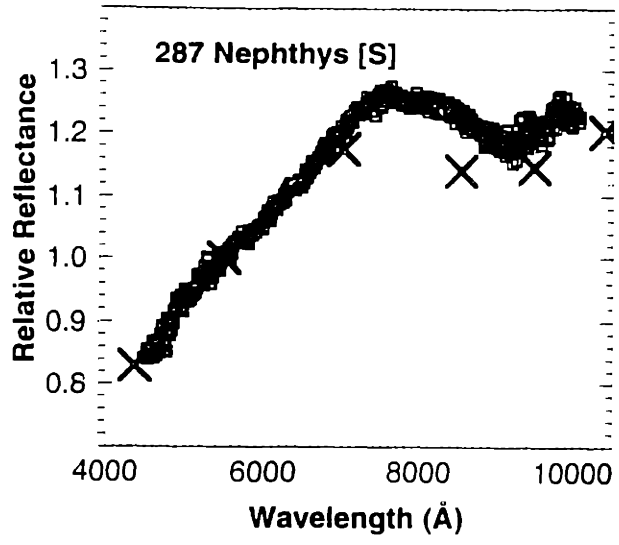
287 Nephthys [S]
Relative Reflectance
1.3
1.2
1.1
1.0
0.9
0.8
4000
6000
8000
10000
Wavelength (Å)

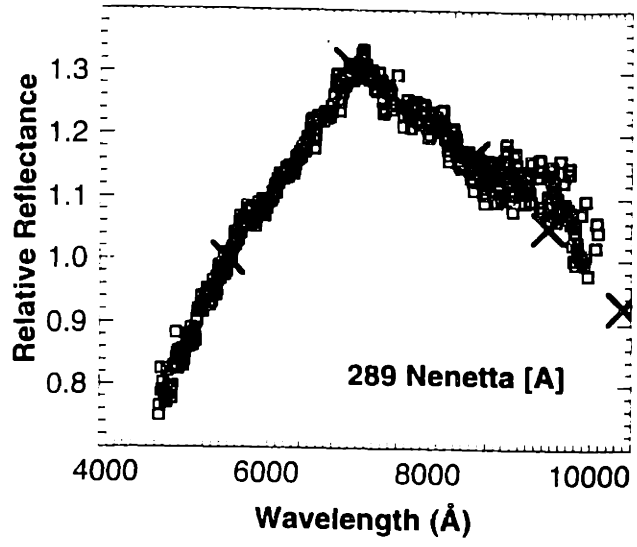
289 Nenetta [A]
Relative Reflectance
1.3
1.2
1.1
1.0
0.9
0.8
4000
6000
8000
10000
Wavelength (Å)

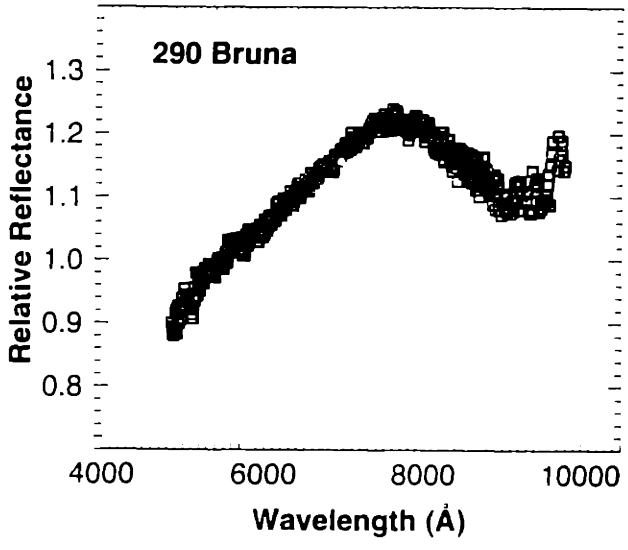
290 Bruna
Relative Reflectance
1.3
1.2
1.1
1.0
0.9
0.8
4000
6000
8000
10000
Wavelength (Å)

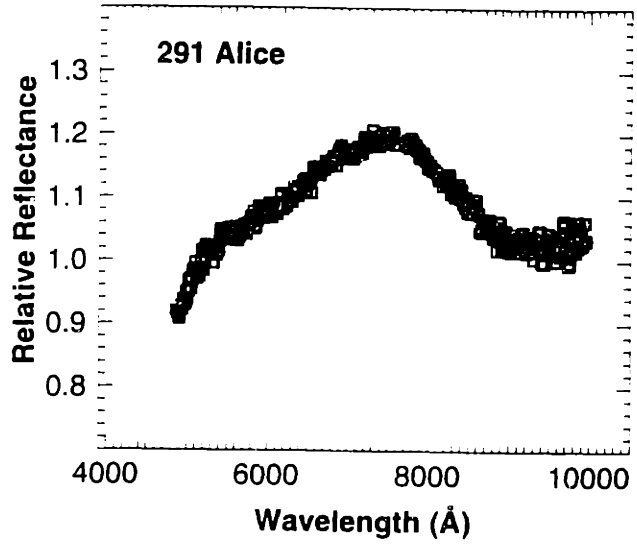
291 Alice
Relative Reflectance
1.3
1.2
1.1
1.0
0.9
0.8
4000
6000
8000
10000
Wavelength (Å)

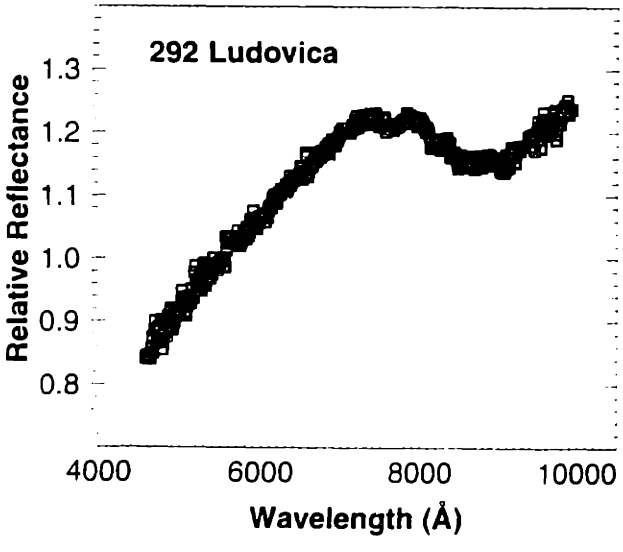
292 Ludovica
Relative Reflectance
1.3
1.2
1.1
1.0
0.9
0.8
4000
6000
8000
10000
Wavelength (Å)

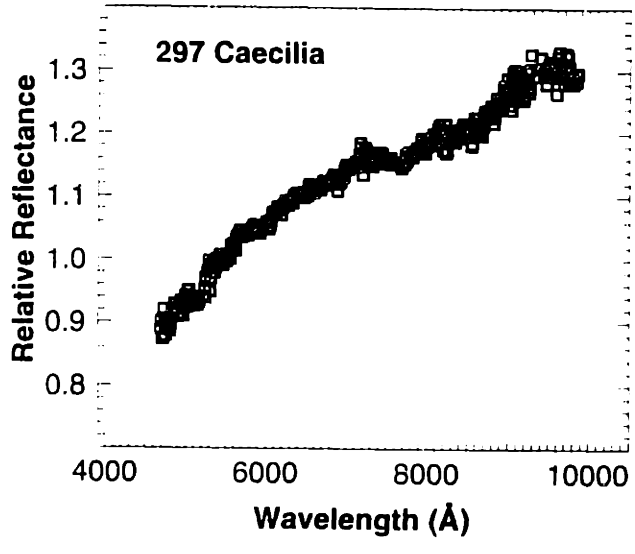
297 Caecilia
Relative Reflectance
1.3
1.2
1.1
1.0
0.9
0.8
4000
6000
8000
10000
Wavelength (Å)

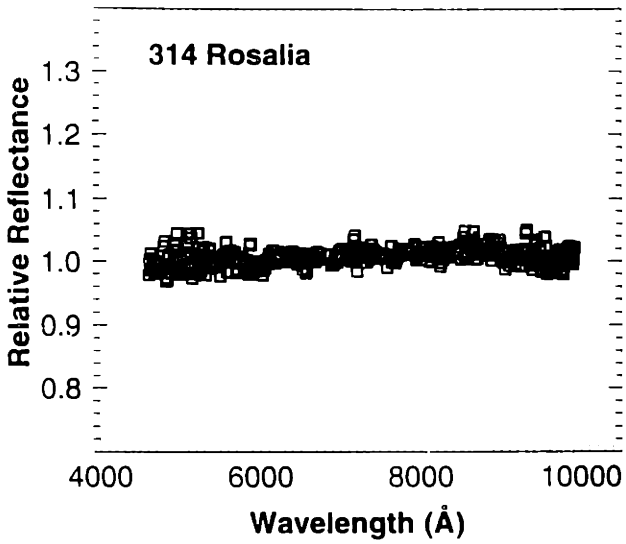
314 Rosalia
Relative Reflectance
1.3
1.2
1.1
1.0
0.9
0.8
4000
6000
8000
10000
Wavelength (Å)

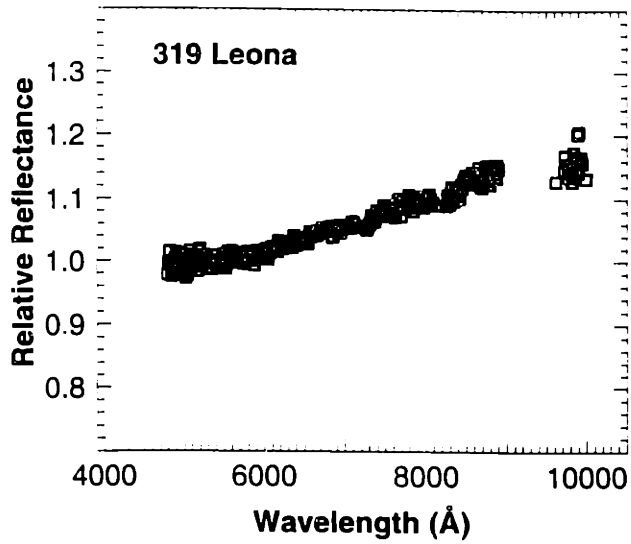
319 Leona
Relative Reflectance
1.3
1.2
1.1
1.0
0.9
0.8
4000
6000
8000
10000
Wavelength (Å)

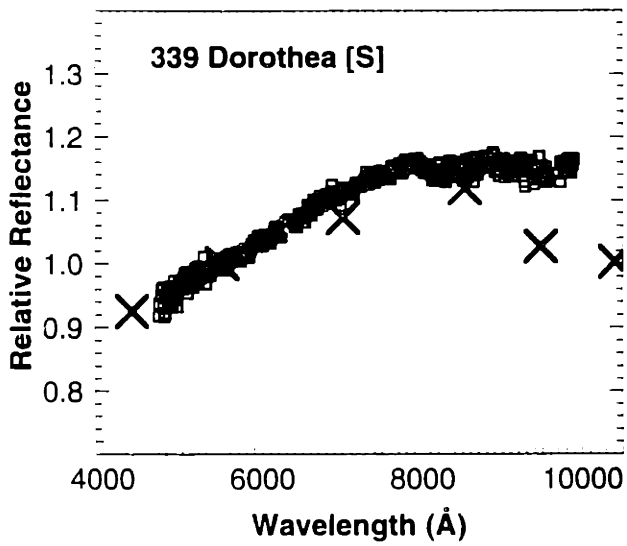
339 Dorothea [S]
Relative Reflectance
1.3
1.2
1.1
1.0
0.9
0.8
4000
6000
8000
10000
Wavelength (Å)

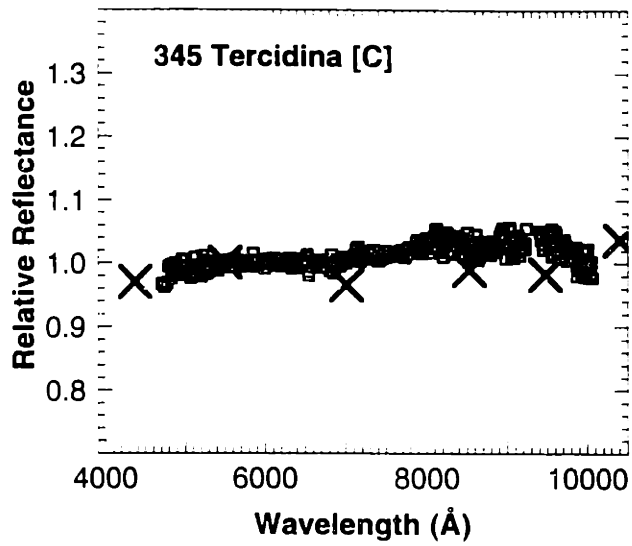
345 Tercidina [C]
Relative Reflectance
1.3
1.2
1.1
1.0
0.9
0.8
4000
6000
8000
10000
Wavelength (Å)

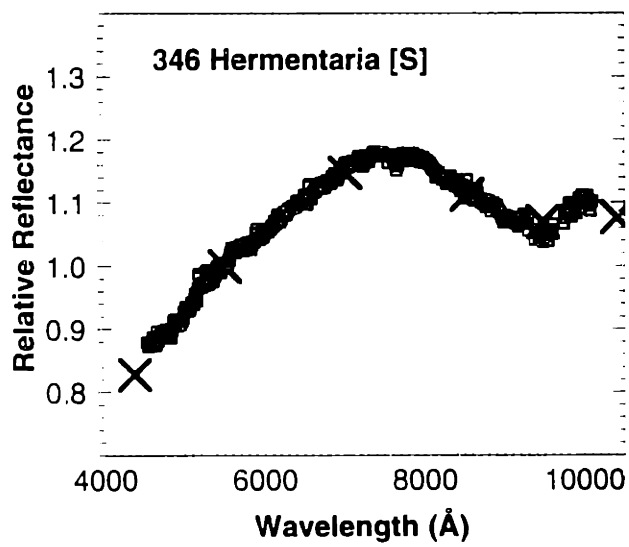
346 Hermentaria [S]
Relative Reflectance
1.3
1.2
1.1
1.0
0.9
0.8
4000
6000
8000
10000
Wavelength (Å)

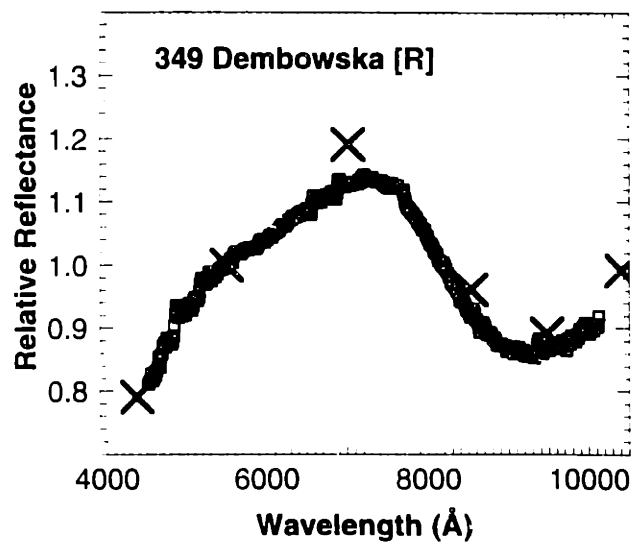
349 Dembowska [R]
Relative Reflectance
1.3
1.2
1.1
1.0
0.9
0.8
4000
6000
8000
10000
Wavelength (Å)

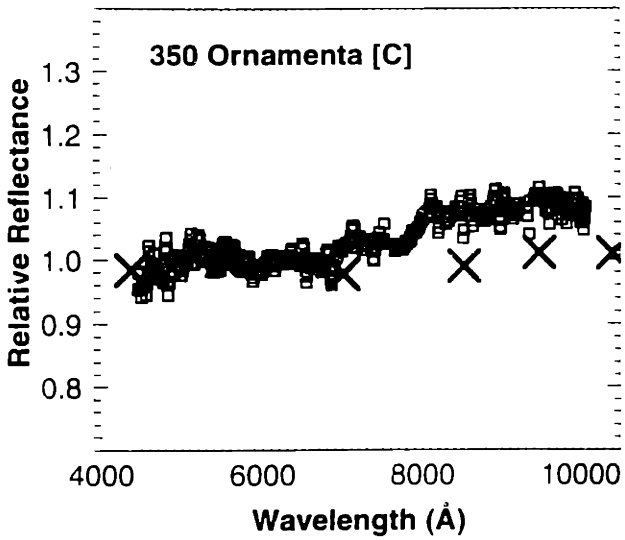
350 Ornamenta [C]
Relative Reflectance
1.3
1.2
1.1
1.0
0.9
0.8
4000
6000
8000
10000
Wavelength (Å)

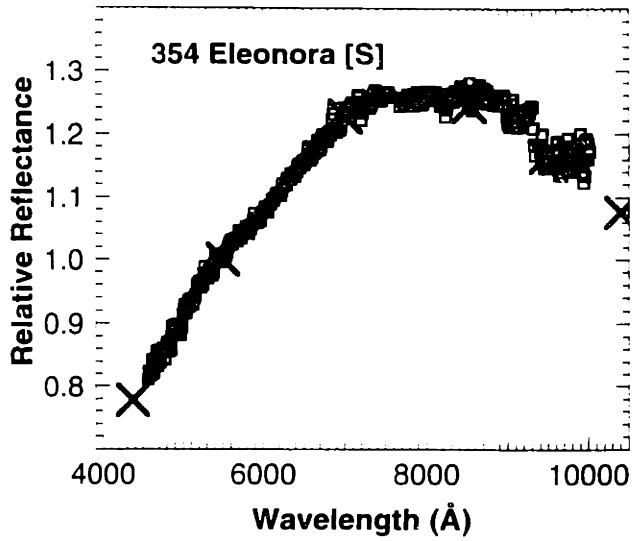
354 Eleonora [S]
Relative Reflectance
1.3
1.2
1.1
1.0
0.9
0.8
4000
6000
8000
10000
Wavelength (Å)

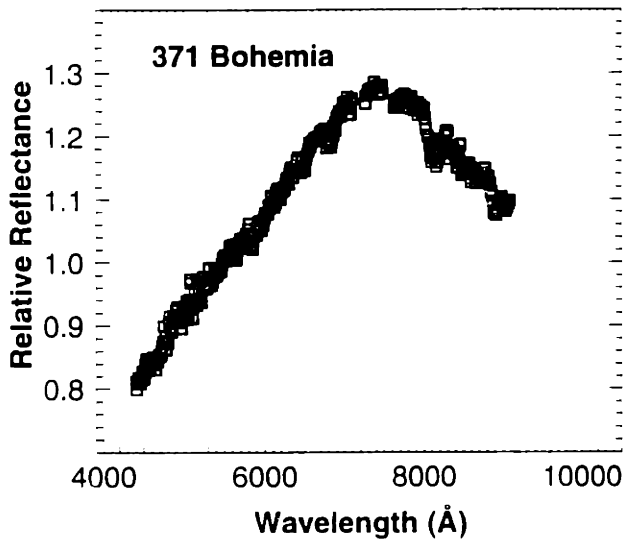
371 Bohemia
Relative Reflectance
1.3
1.2
1.1
1.0
0.9
0.8
4000
6000
8000
10000
Wavelength (Å)

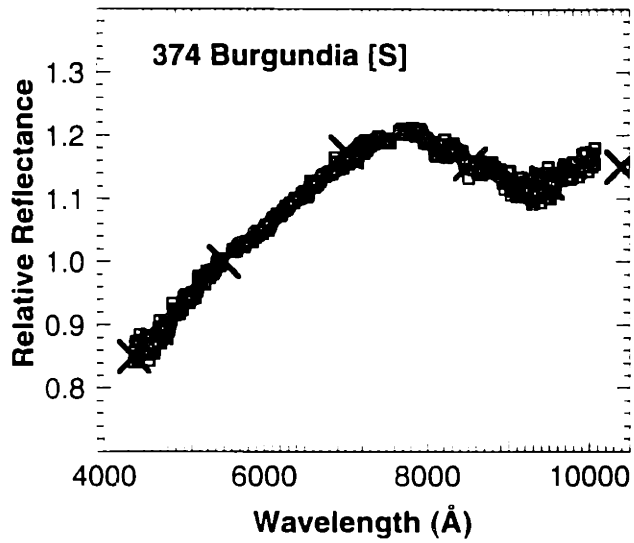
374 Burgundia [S]
Relative Reflectance
1.3
1.2
1.1
1.0
0.9
0.8
4000
6000
8000
10000
Wavelength (Å)

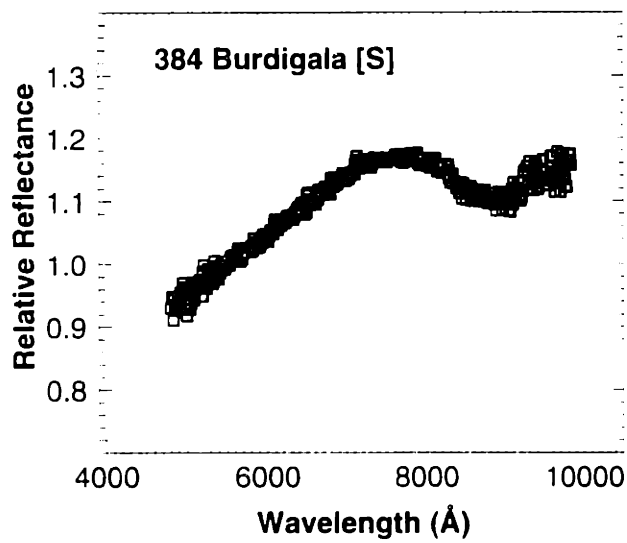
384 Burdigala [S]
Relative Reflectance
1.3
1.2
1.1
1.0
0.9
0.8
4000
6000
8000
10000
Wavelength (Å)

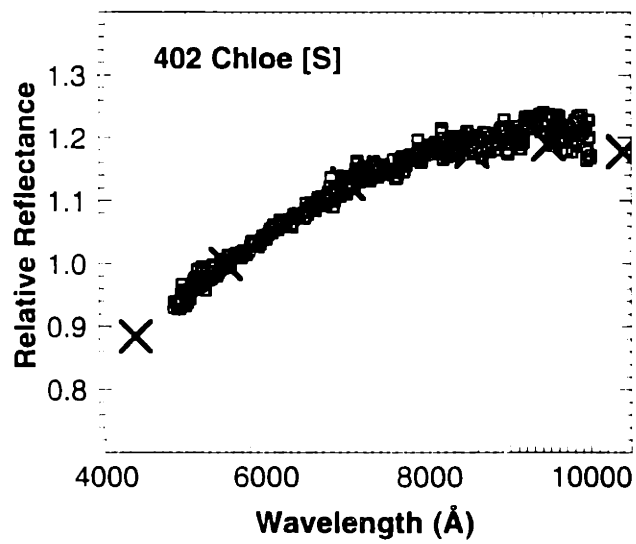
402 Chloe [S]
Relative Reflectance
1.3
1.2
1.1
1.0
0.9
0.8
4000
6000
8000
10000
Wavelength (Å)

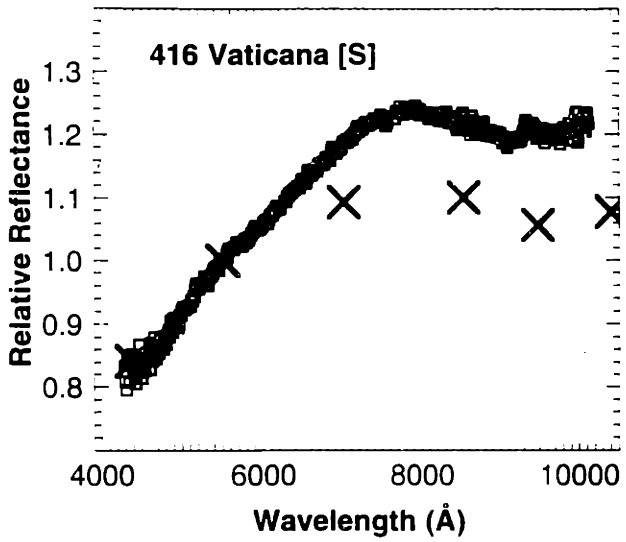
416 Vaticana [S]
Relative Reflectance
1.3
1.2
1.1
1.0
0.9
0.8
4000
6000
8000
10000
Wavelength (Å)

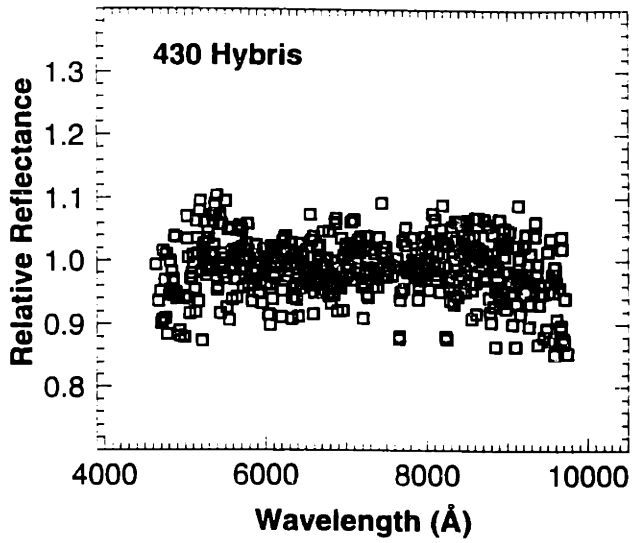
430 Hybris
Relative Reflectance
1.3
1.2
1.1
1.0
0.9
0.8
4000
6000
8000
10000
Wavelength (Å)

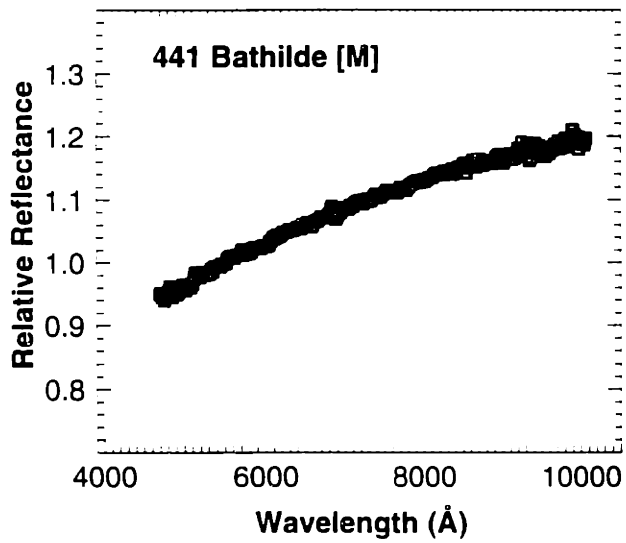
441 Bathilde [M]
Relative Reflectance
1.3
1.2
1.1
1.0
0.9
0.8
4000
6000
8000
10000
Wavelength (Å)

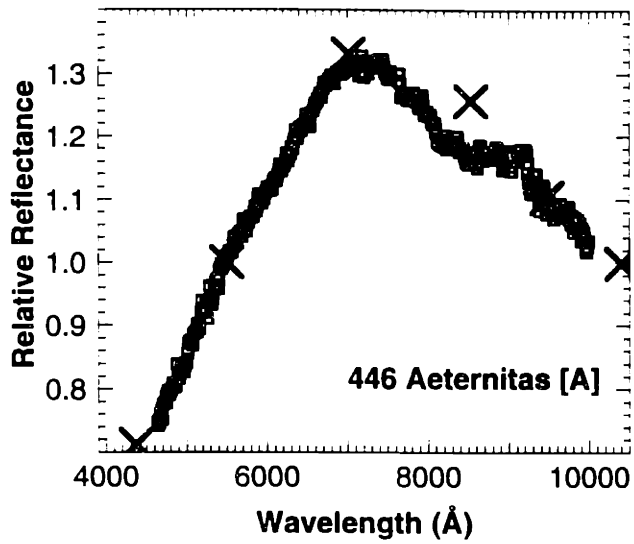
446 Aeternitas [A]
Relative Reflectance
1.3
1.2
1.1
1.0
0.9
0.8
4000
6000
8000
10000
Wavelength (Å)

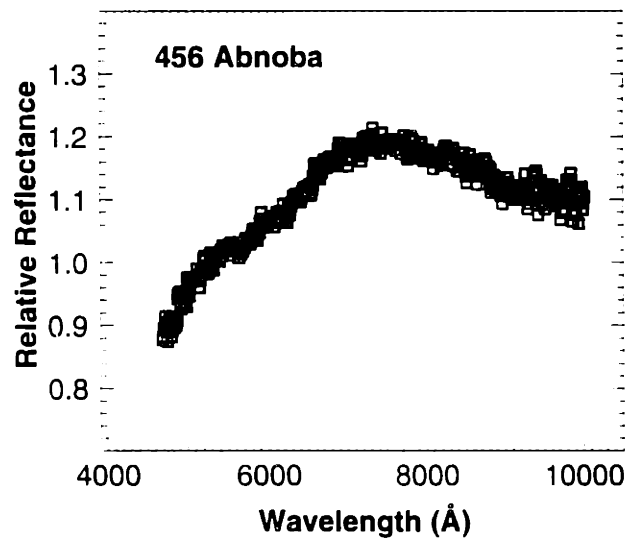
456 Abnoba
Relative Reflectance
1.3
1.2
1.1
1.0
0.9
0.8
4000
6000
8000
10000
Wavelength (Å)

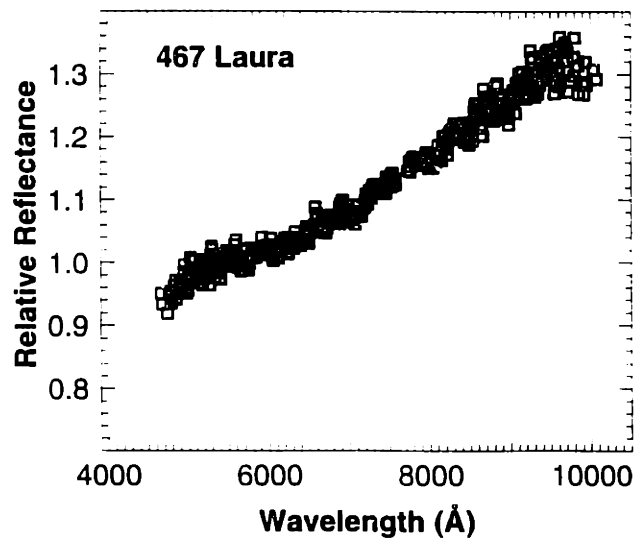
467 Laura
Relative Reflectance
1.3
1.2
1.1
1.0
0.9
0.8
4000
6000
8000
10000
Wavelength (Å)

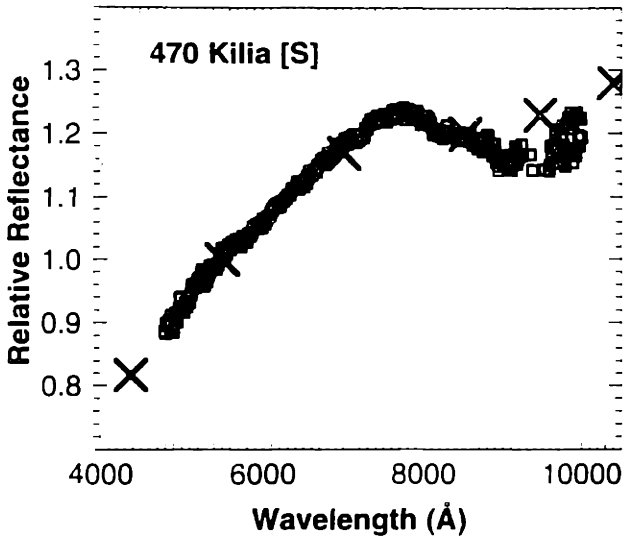
470 Kilia [S]
Relative Reflectance
1.3
1.2
1.1
1.0
0.9
0.8
4000
6000
8000
10000
Wavelength (Å)

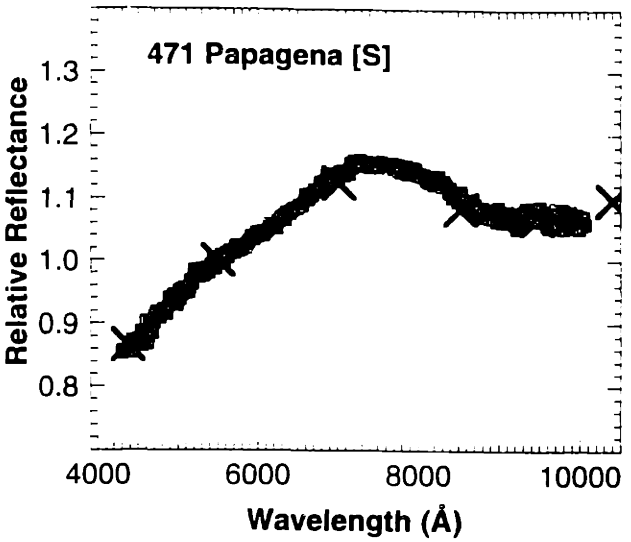
471 Papagena [S]
Relative Reflectance
1.3
1.2
1.1
1.0
0.9
0.8
4000
6000
8000
10000
Wavelength (Å)

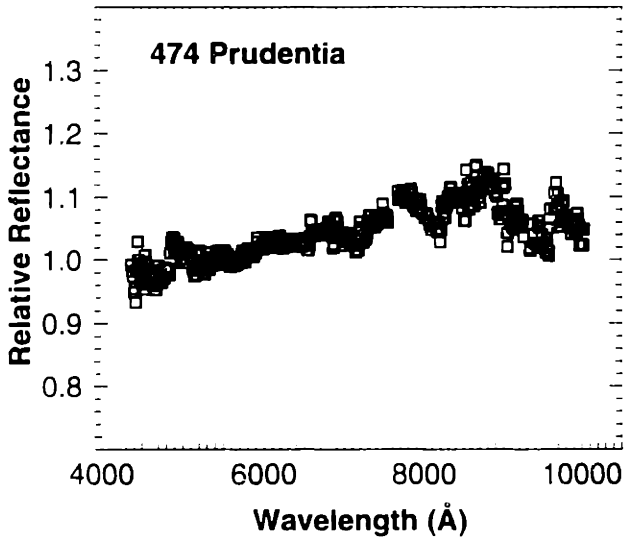
474 Prudentia
Relative Reflectance
1.3
1.2
1.1
1.0
0.9
0.8
4000
6000
8000
10000
Wavelength (Å)

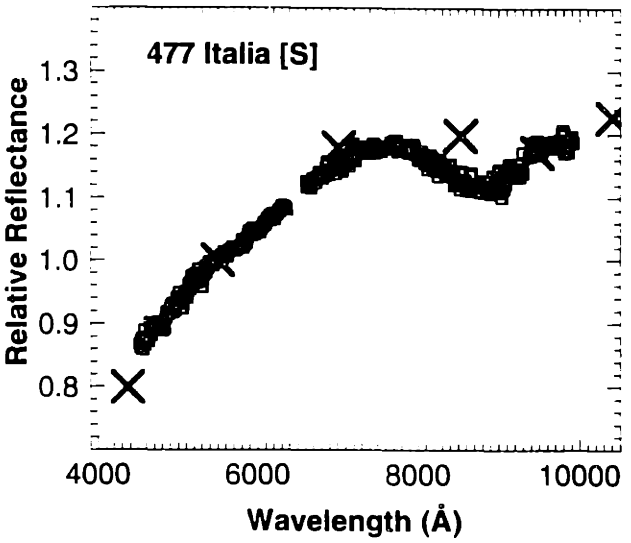
477 Italia [S]
Relative Reflectance
1.3
1.2
1.1
1.0
0.9
0.8
4000
6000
8000
10000
Wavelength (Å)

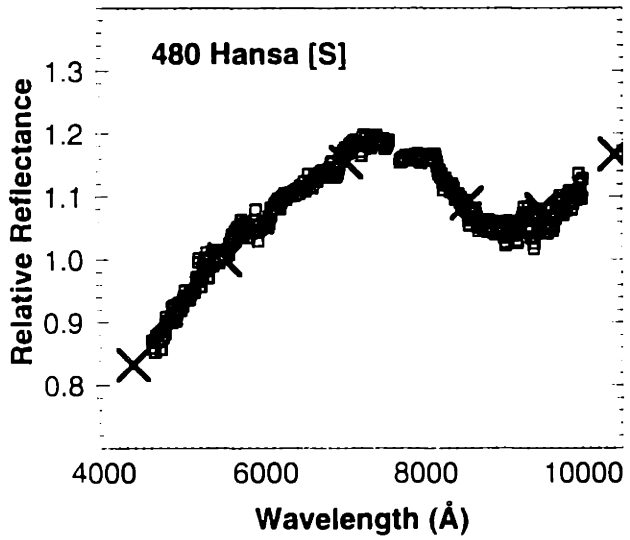
480 Hansa [S]
Relative Reflectance
1.3
1.2
1.1
1.0
0.9
0.8
4000
6000
8000
10000
Wavelength (Å)

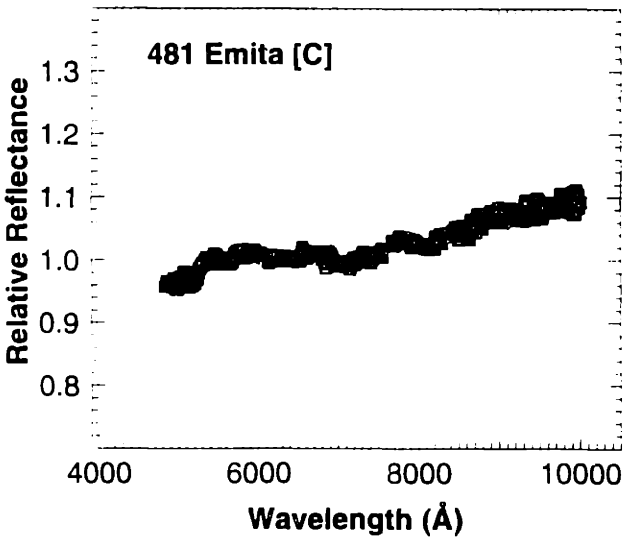
481 Emita [C]
Relative Reflectance
1.3
1.2
1.1
1.0
0.9
0.8
4000
6000
8000
10000
Wavelength (Å)

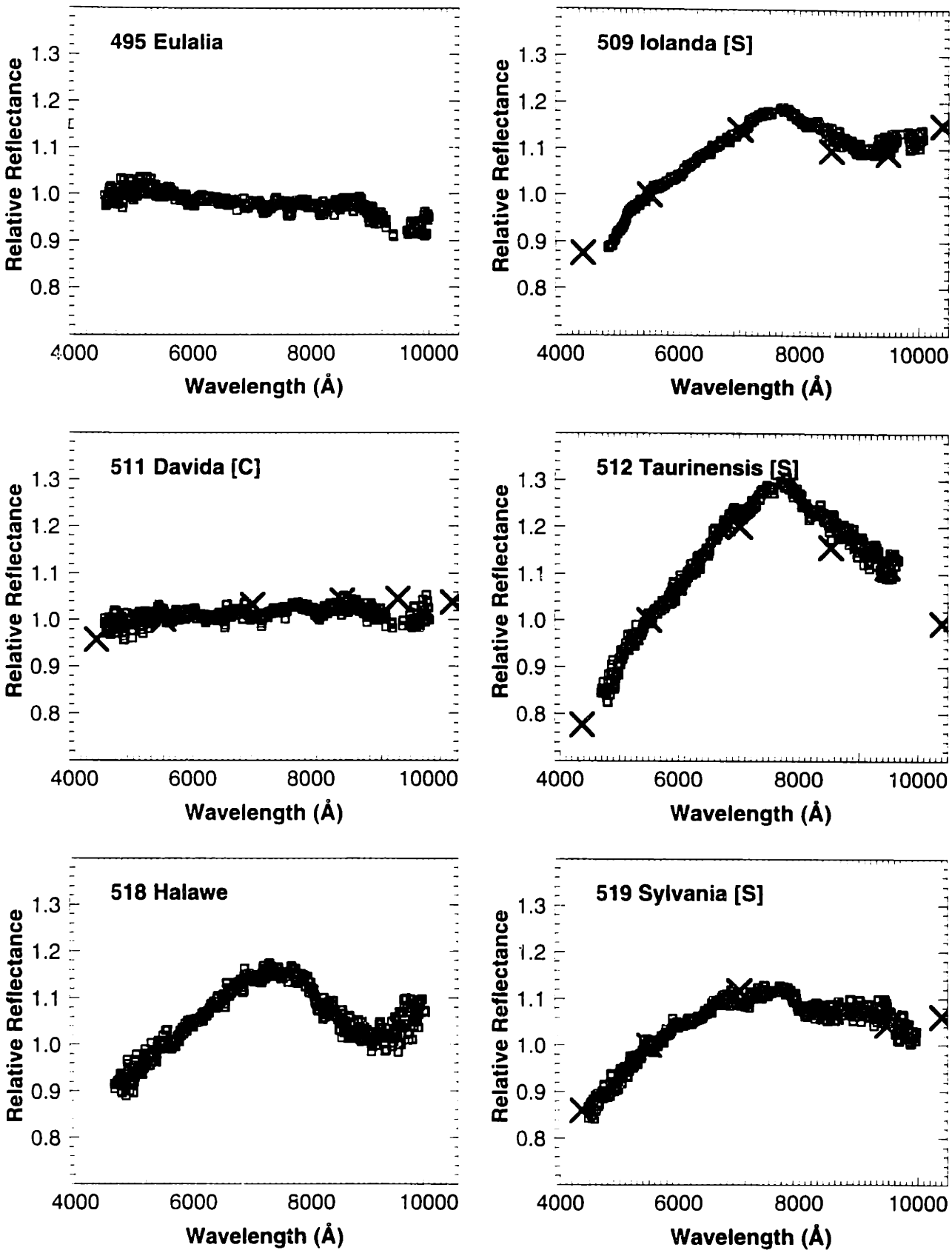
495 Eulalia
509 Iolanda [S]
511 Davida [C]
512 Taurinensis [S]
518 Halawe
519 Sylvania [S]
Relative Reflectance
Wavelength (Å)
0.8
0.9
1.0
1.1
1.2
1.3
4000
6000
8000
10000

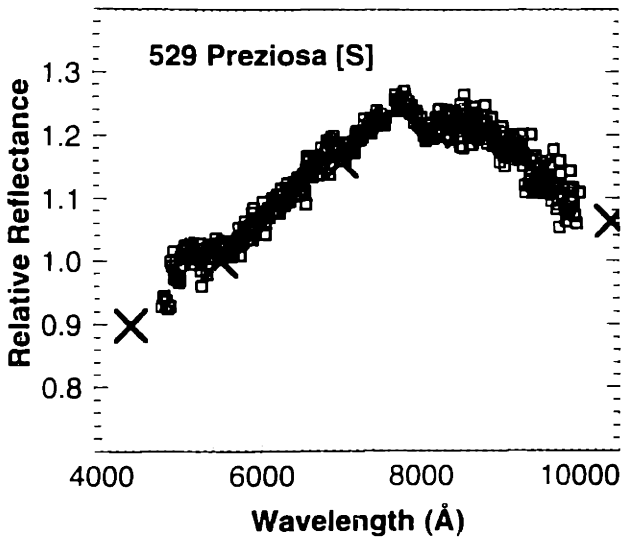
529 Preziosa [S]
Relative Reflectance
1.3
1.2
1.1
1.0
0.9
0.8
4000
6000
8000
10000
Wavelength (Å)

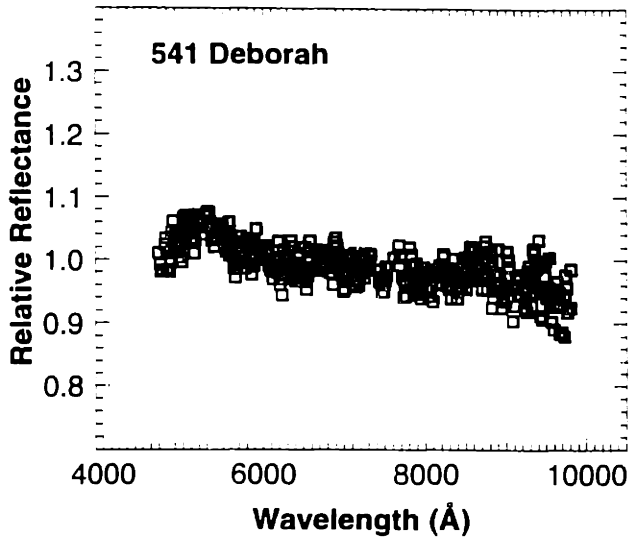
541 Deborah
Relative Reflectance
1.3
1.2
1.1
1.0
0.9
0.8
4000
6000
8000
10000
Wavelength (Å)

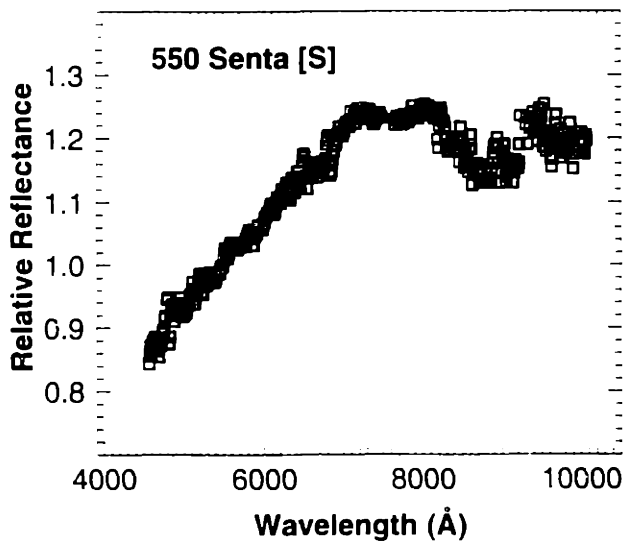
550 Senta [S]
Relative Reflectance
1.3
1.2
1.1
1.0
0.9
0.8
4000
6000
8000
10000
Wavelength (Å)

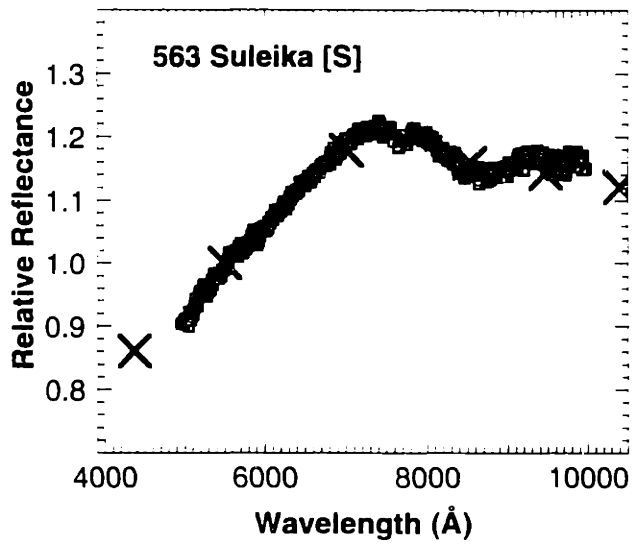
563 Suleika [S]
Relative Reflectance
1.3
1.2
1.1
1.0
0.9
0.8
4000
6000
8000
10000
Wavelength (Å)

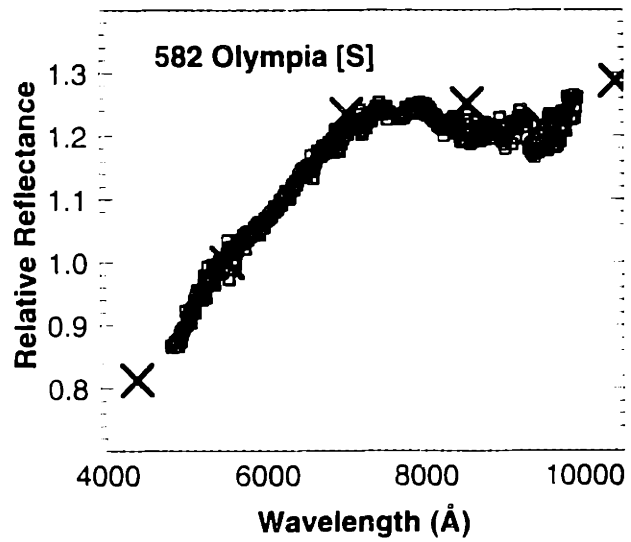
582 Olympia [S]
Relative Reflectance
1.3
1.2
1.1
1.0
0.9
0.8
4000
6000
8000
10000
Wavelength (Å)

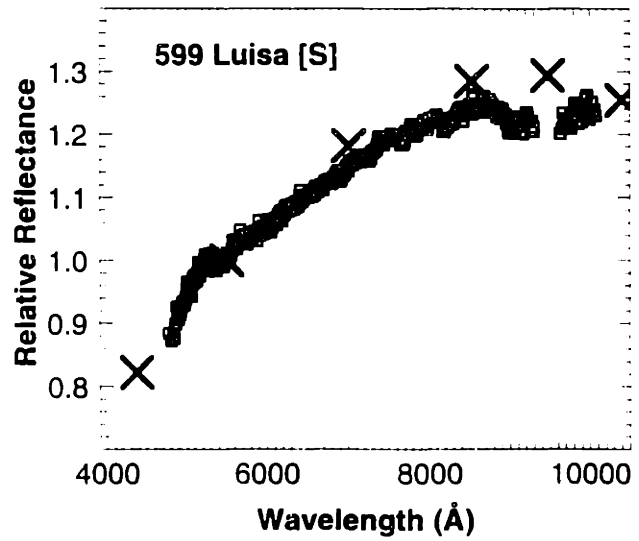
599 Luisa [S]
Relative Reflectance
1.3
1.2
1.1
1.0
0.9
0.8
4000
6000
8000
10000
Wavelength (Å)

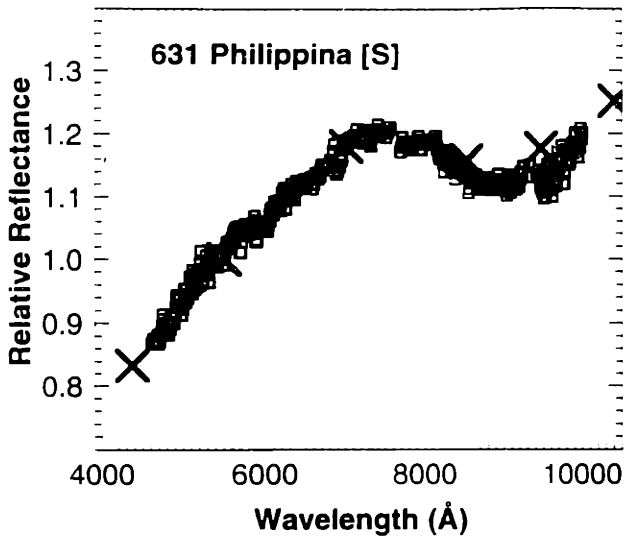
631 Philippina [S]
Relative Reflectance
1.3
1.2
1.1
1.0
0.9
0.8
4000
6000
8000
10000
Wavelength (Å)

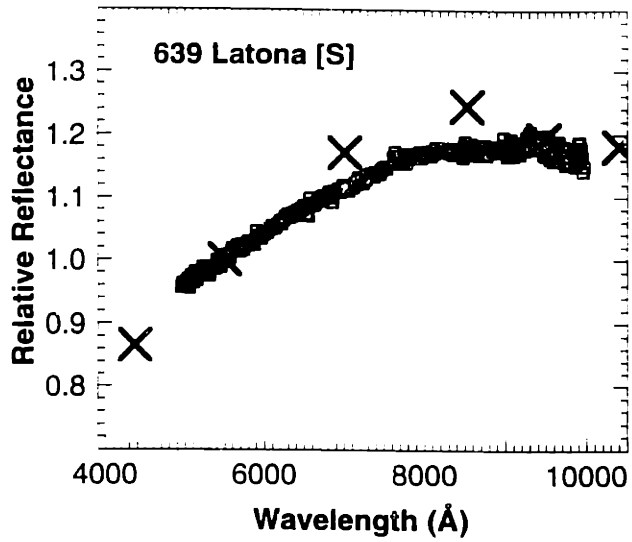
639 Latona [S]
Relative Reflectance
1.3
1.2
1.1
1.0
0.9
0.8
4000
6000
8000
10000
Wavelength (Å)

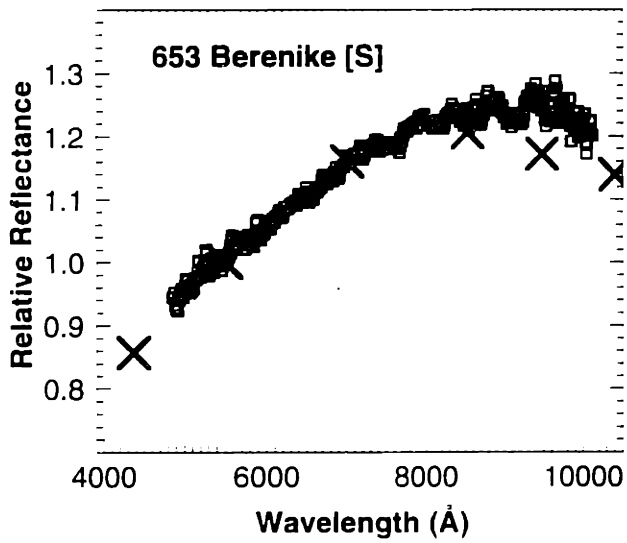
653 Berenike [S]
Relative Reflectance
1.3
1.2
1.1
1.0
0.9
0.8
4000
6000
8000
10000
Wavelength (Å)

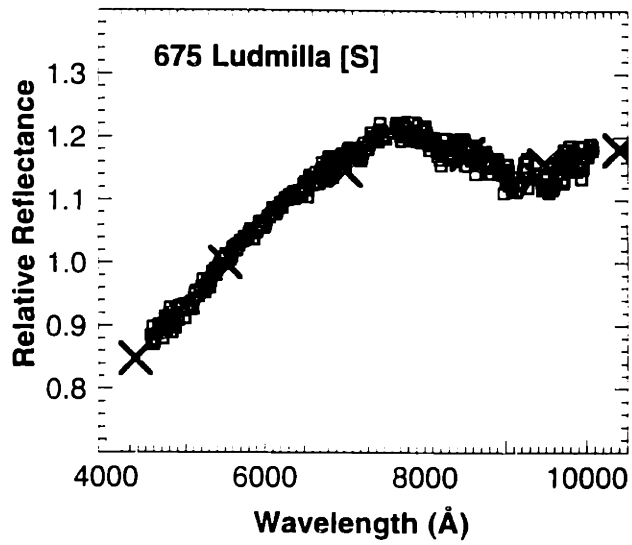
675 Ludmilla [S]
Relative Reflectance
1.3
1.2
1.1
1.0
0.9
0.8
4000
6000
8000
10000
Wavelength (Å)

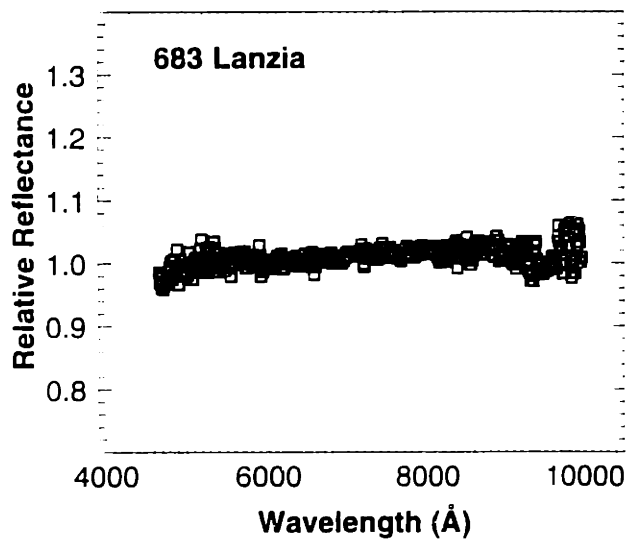
683 Lanzia
Relative Reflectance
1.3
1.2
1.1
1.0
0.9
0.8
4000
6000
8000
10000
Wavelength (Å)

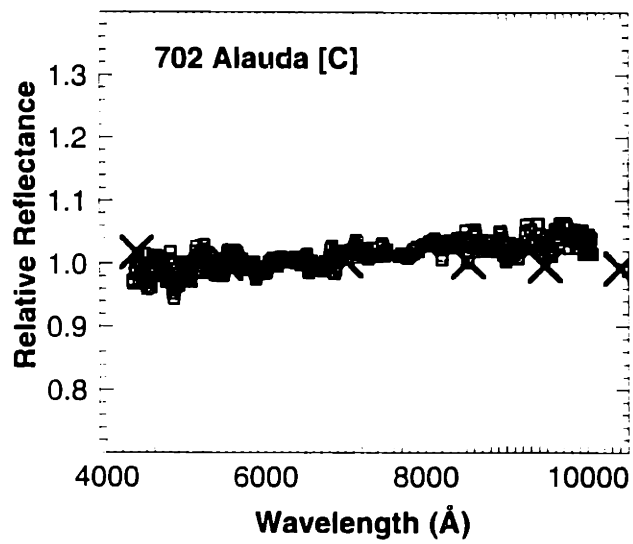
702 Alauda [C]
Relative Reflectance
1.3
1.2
1.1
1.0
0.9
0.8
4000
6000
8000
10000
Wavelength (Å)

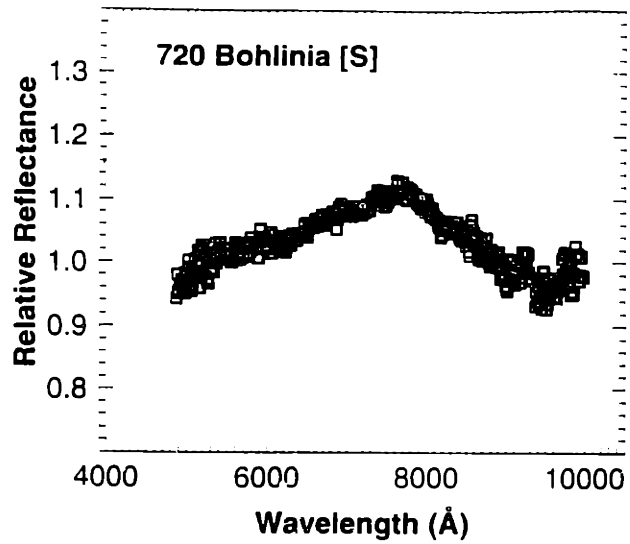
720 Bohlinia [S]
Relative Reflectance
1.3
1.2
1.1
1.0
0.9
0.8
4000
6000
8000
10000
Wavelength (Å)

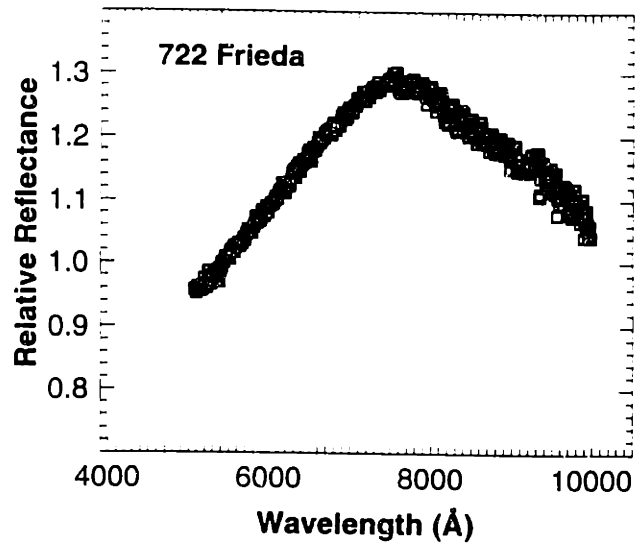
722 Frieda
Relative Reflectance
1.3
1.2
1.1
1.0
0.9
0.8
4000
6000
8000
10000
Wavelength (Å)

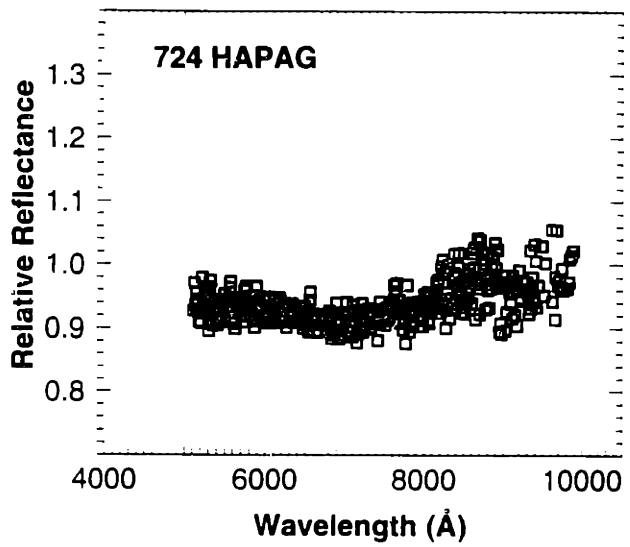
724 HAPAG
Relative Reflectance
1.3
1.2
1.1
1.0
0.9
0.8
4000
6000
8000
10000
Wavelength (Å)

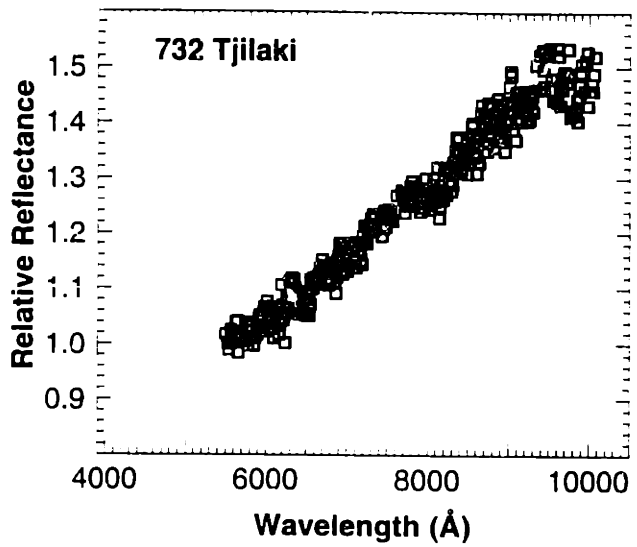
732 Tjilaki
Relative Reflectance
1.5
1.4
1.3
1.2
1.1
1.0
0.9
4000
6000
8000
10000
Wavelength (Å)

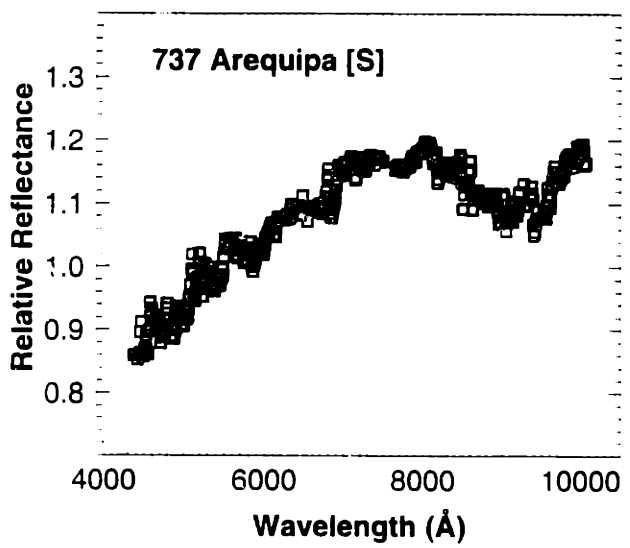
737 Arequipa [S]
Relative Reflectance
1.3
1.2
1.1
1.0
0.9
0.8
4000
6000
8000
10000
Wavelength (Å)

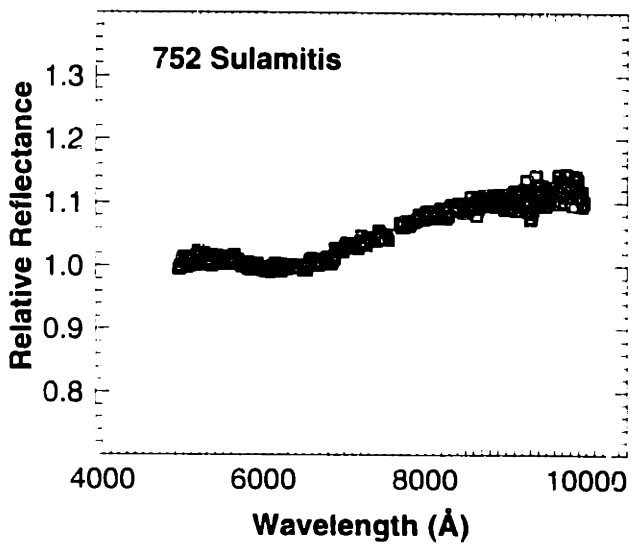
752 Sulamitis
Relative Reflectance
1.3
1.2
1.1
1.0
0.9
0.8
4000
6000
8000
10000
Wavelength (Å)

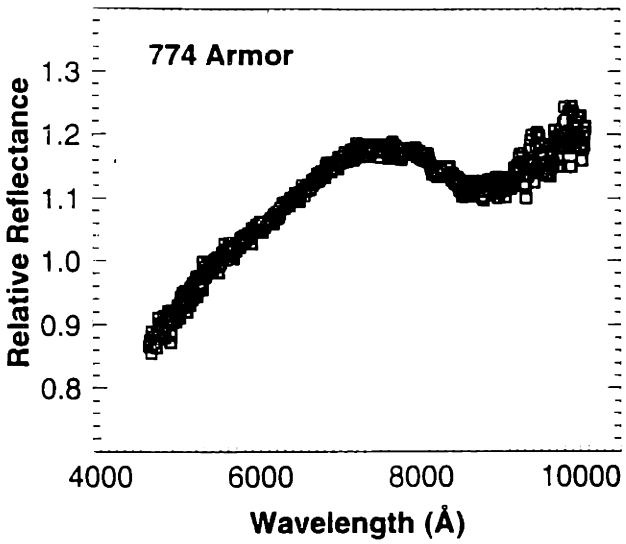
774 Armor
Relative Reflectance
1.3
1.2
1.1
1.0
0.9
0.8
4000
6000
8000
10000
Wavelength (Å)

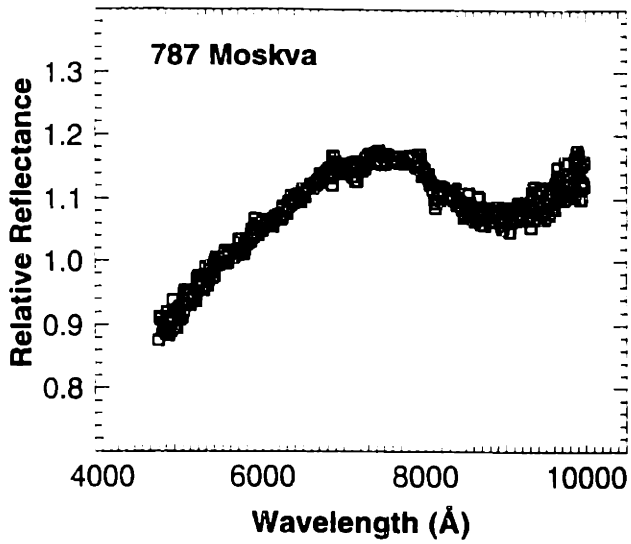
787 Moskva
Relative Reflectance
1.3
1.2
1.1
1.0
0.9
0.8
4000
6000
8000
10000
Wavelength (Å)

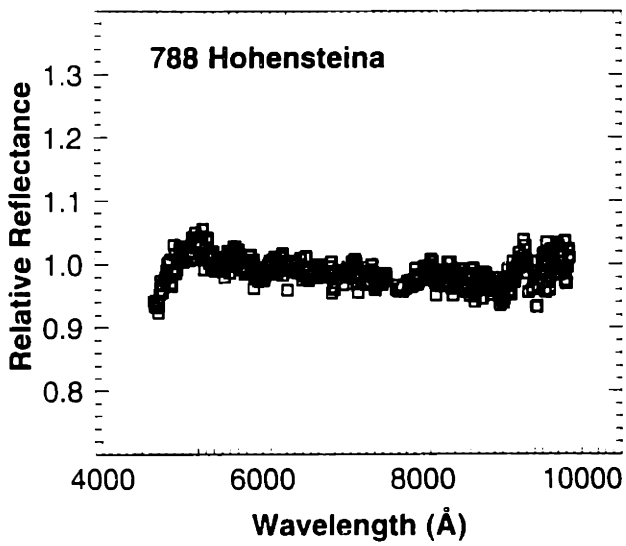
788 Hohensteina
Relative Reflectance
1.3
1.2
1.1
1.0
0.9
0.8
4000
6000
8000
10000
Wavelength (Å)

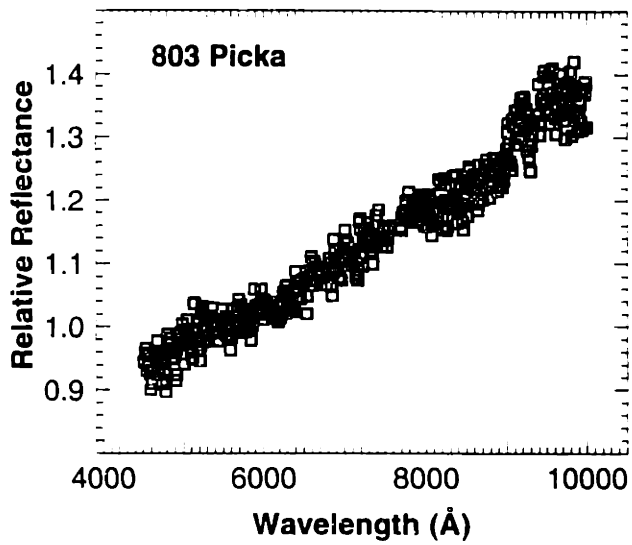
803 Picka
Relative Reflectance
1.4
1.3
1.2
1.1
1.0
0.9
4000
6000
8000
10000
Wavelength (Å)

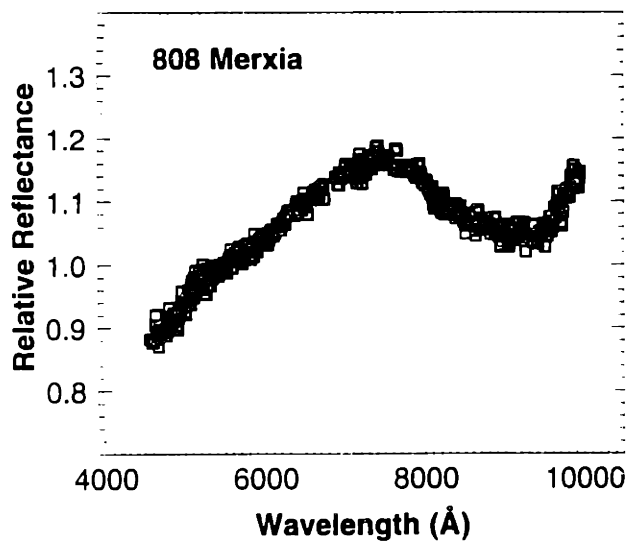
808 Merxia
Relative Reflectance
1.3
1.2
1.1
1.0
0.9
0.8
4000
6000
8000
10000
Wavelength (Å)

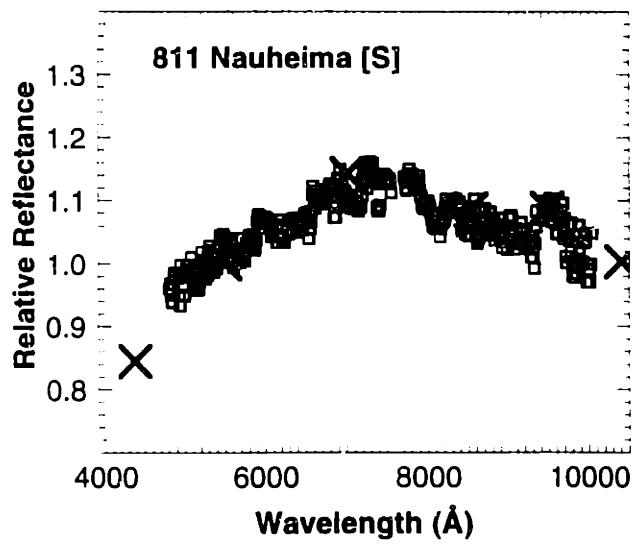
811 Nauheima [S]
Relative Reflectance
1.3
1.2
1.1
1.0
0.9
0.8
4000
6000
8000
10000
Wavelength (Å)

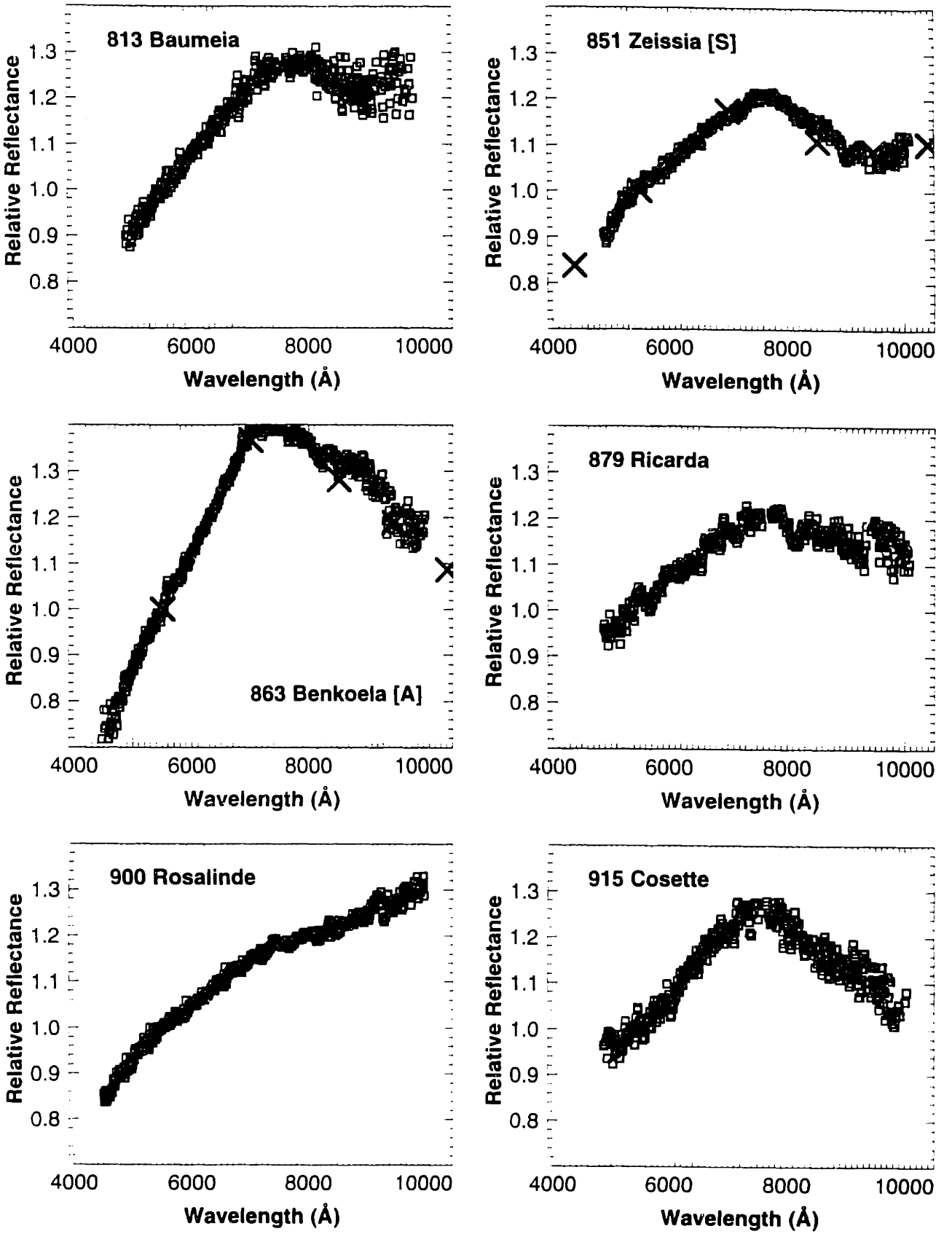
813 Baumeia
851 Zeissia [S]
863 Benkoela [A]
879 Ricarda
900 Rosalinde
915 Cosette
Relative Reflectance
Wavelength (Å)
0.8
0.9
1.0
1.1
1.2
1.3
4000
6000
8000
10000

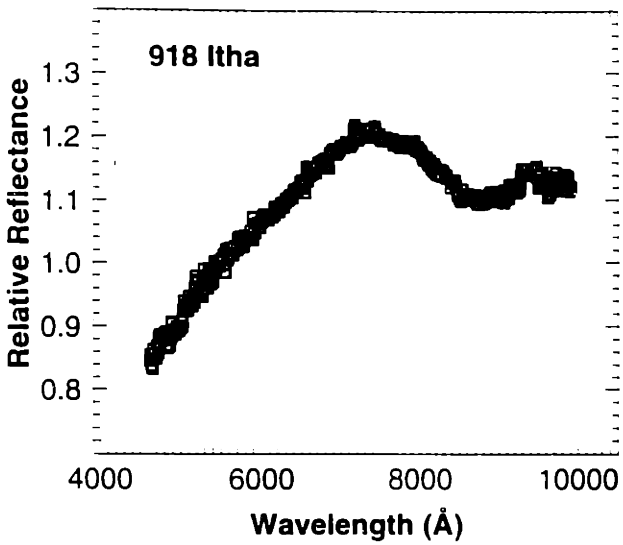
918 Itha
Relative Reflectance
1.3
1.2
1.1
1.0
0.9
0.8
4000
6000
8000
10000
Wavelength (Å)

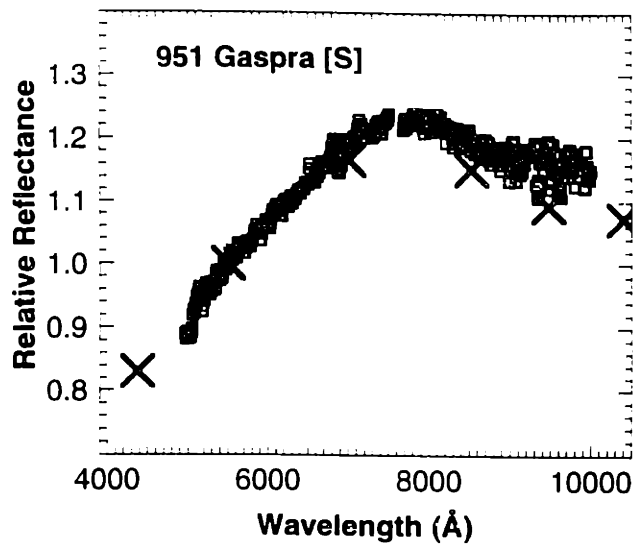
951 Gaspra [S]
Relative Reflectance
1.3
1.2
1.1
1.0
0.9
0.8
4000
6000
8000
10000
Wavelength (Å)

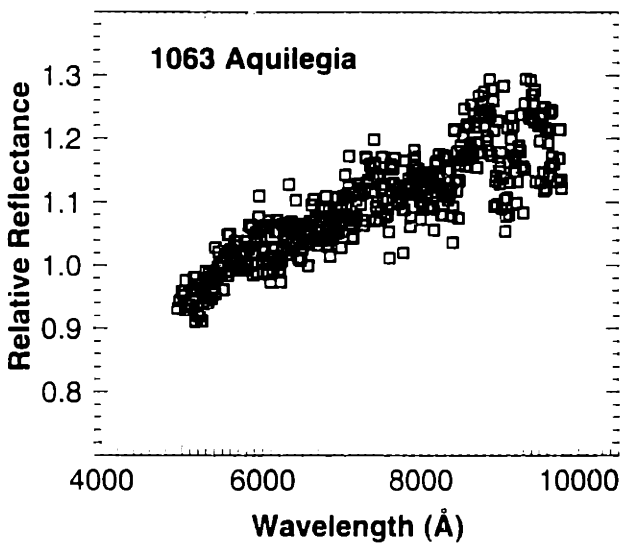
1063 Aquilegia
Relative Reflectance
1.3
1.2
1.1
1.0
0.9
0.8
4000
6000
8000
10000
Wavelength (Å)

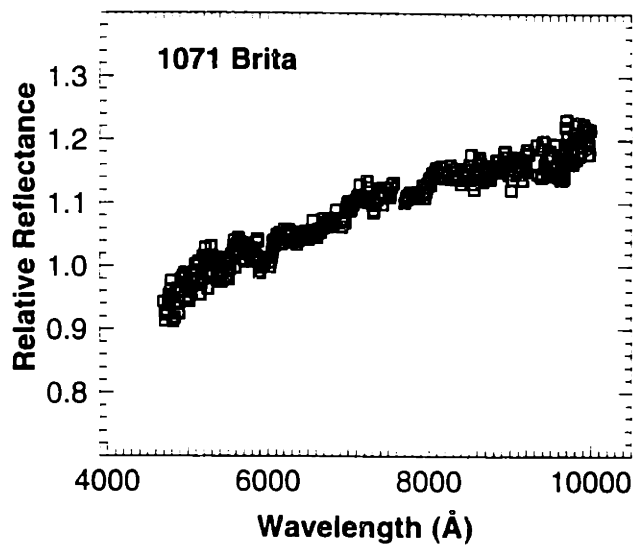
1071 Brita
Relative Reflectance
1.3
1.2
1.1
1.0
0.9
0.8
4000
6000
8000
10000
Wavelength (Å)

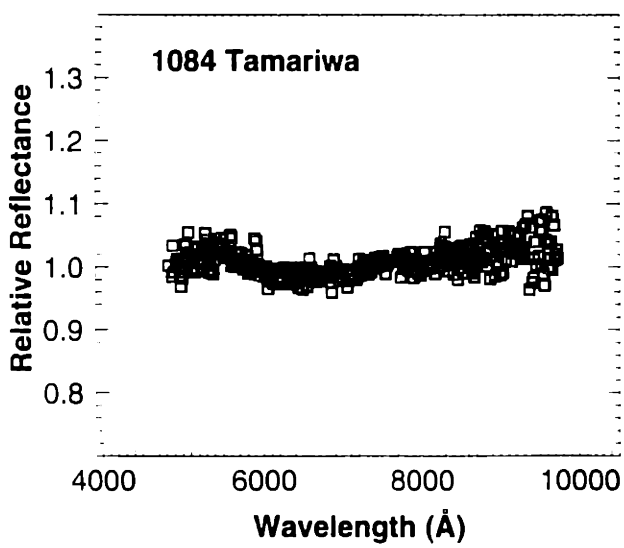
1084 Tamariwa
Relative Reflectance
1.3
1.2
1.1
1.0
0.9
0.8
4000
6000
8000
10000
Wavelength (Å)

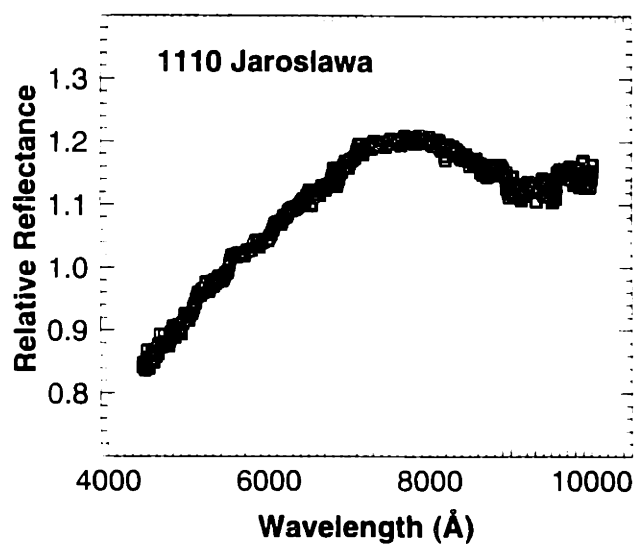
1110 Jaroslawa
Relative Reflectance
1.3
1.2
1.1
1.0
0.9
0.8
4000
6000
8000
10000
Wavelength (Å)

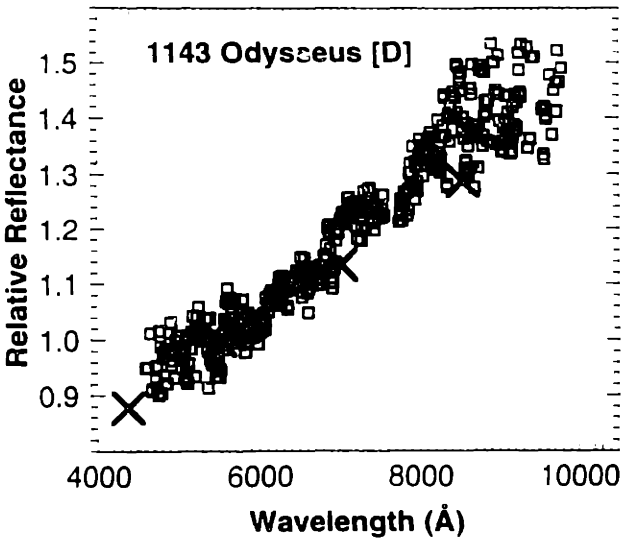
1143 Odysseus [D]
Relative Reflectance
Wavelength (Å)

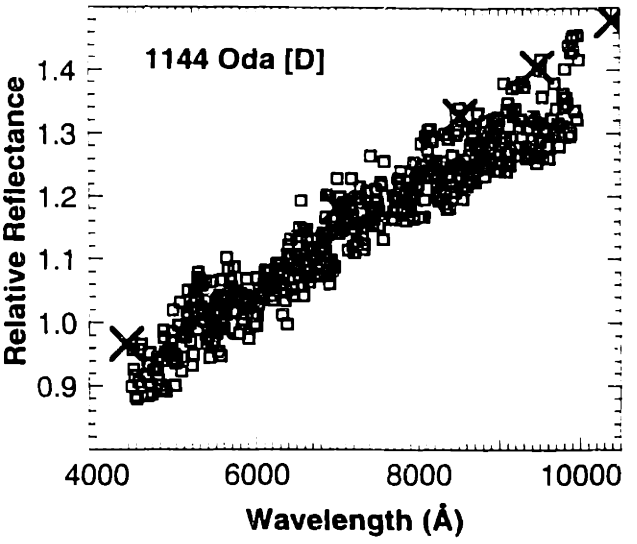
1144 Oda [D]
Relative Reflectance
Wavelength (Å)

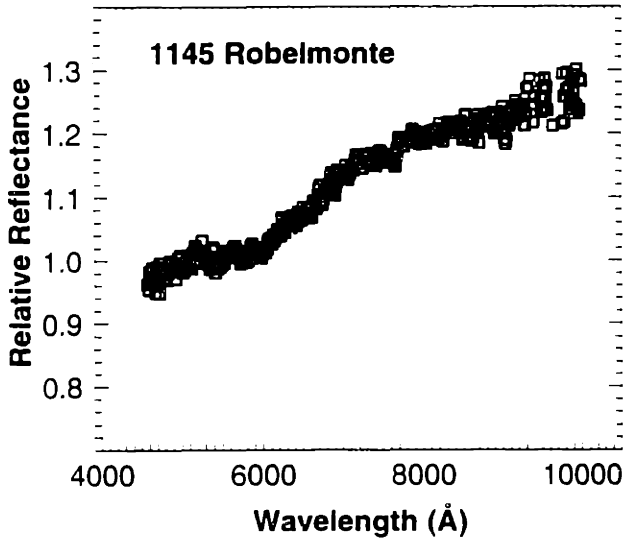
1145 Robelmonte
Relative Reflectance
Wavelength (Å)

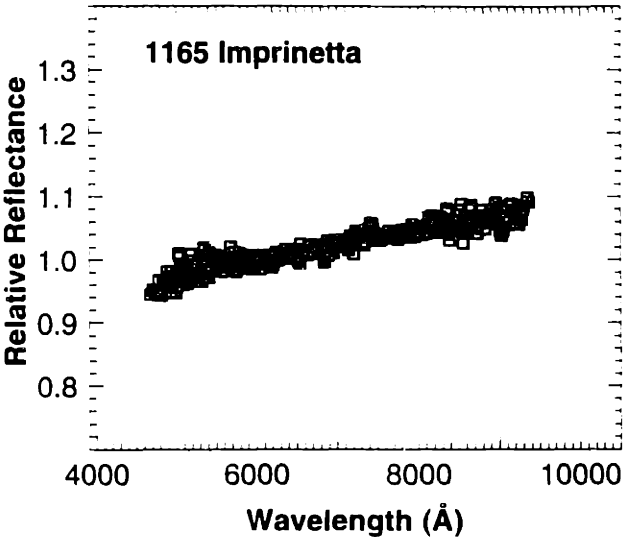
1165 Imprinetta
Relative Reflectance
Wavelength (Å)

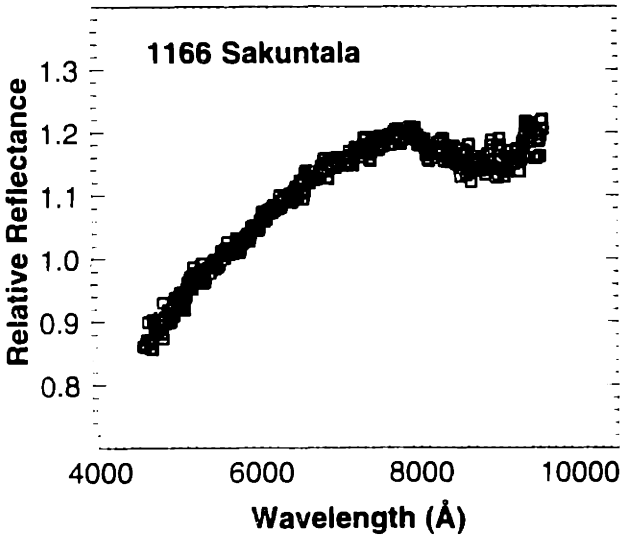
1166 Sakuntala
Relative Reflectance
Wavelength (Å)

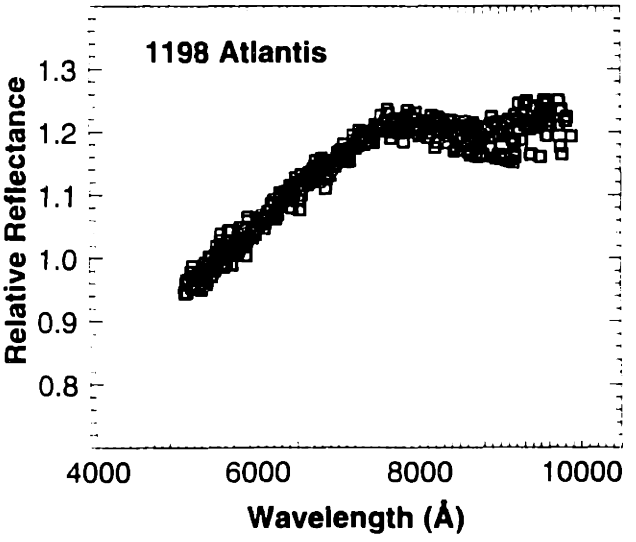
1198 Atlantis
Relative Reflectance
Wavelength (Å)

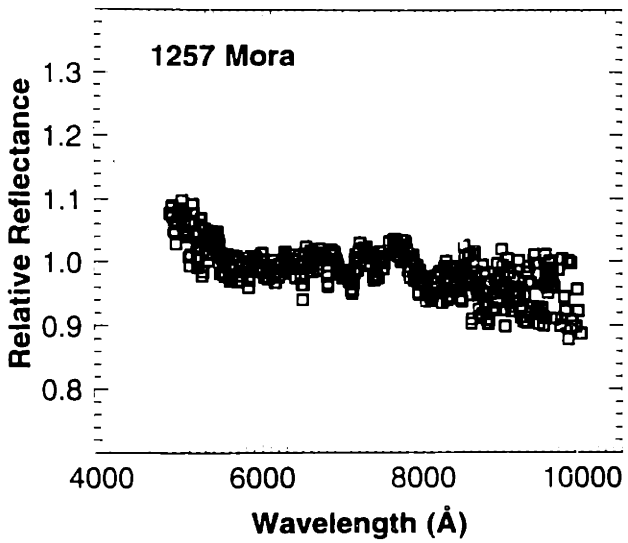
1257 Mora
Relative Reflectance
1.3
1.2
1.1
1.0
0.9
0.8
4000
6000
8000
10000
Wavelength (Å)

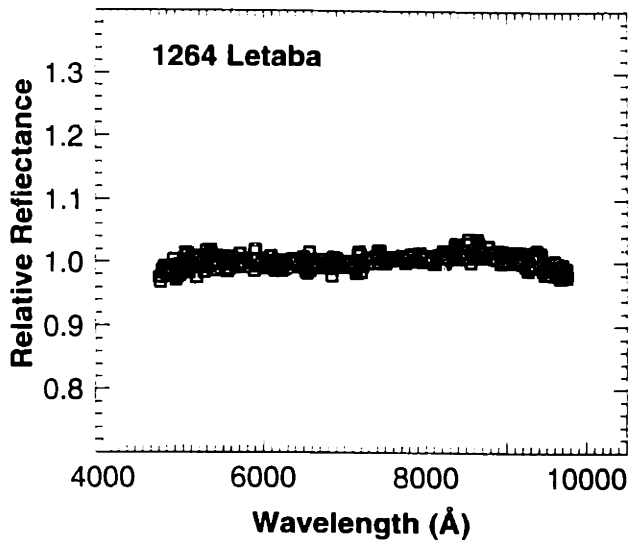
1264 Letaba
Relative Reflectance
1.3
1.2
1.1
1.0
0.9
0.8
4000
6000
8000
10000
Wavelength (Å)

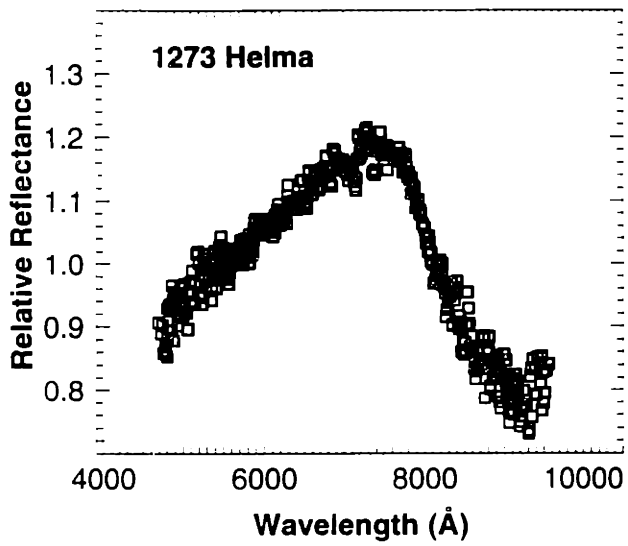
1273 Helma
Relative Reflectance
1.3
1.2
1.1
1.0
0.9
0.8
4000
6000
8000
10000
Wavelength (Å)

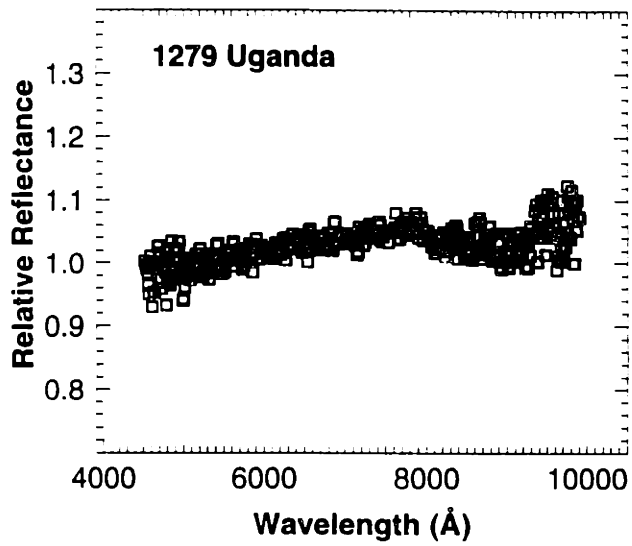
1279 Uganda
Relative Reflectance
1.3
1.2
1.1
1.0
0.9
0.8
4000
6000
8000
10000
Wavelength (Å)

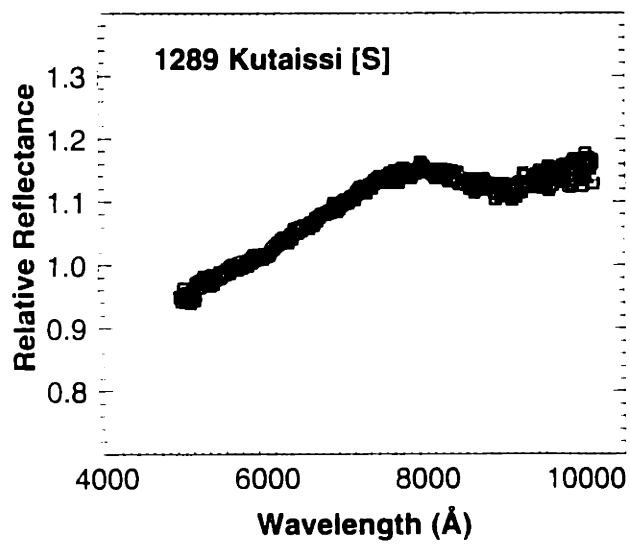
1289 Kutaissi [S]
Relative Reflectance
1.3
1.2
1.1
1.0
0.9
0.8
4000
6000
8000
10000
Wavelength (Å)

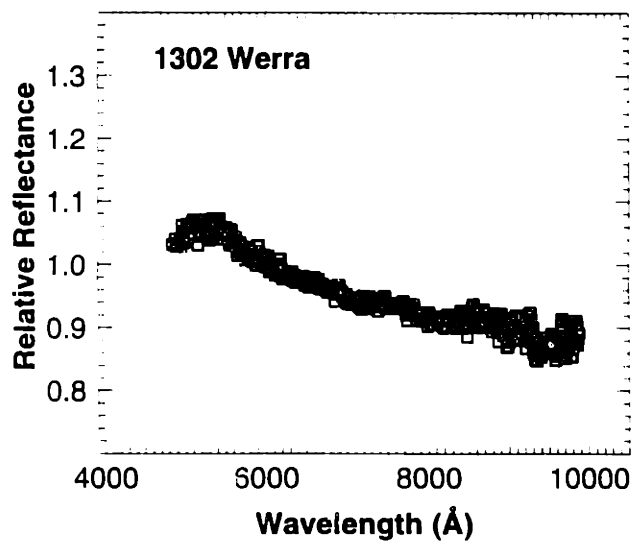
1302 Werra
Relative Reflectance
1.3
1.2
1.1
1.0
0.9
0.8
4000
6000
8000
10000
Wavelength (Å)

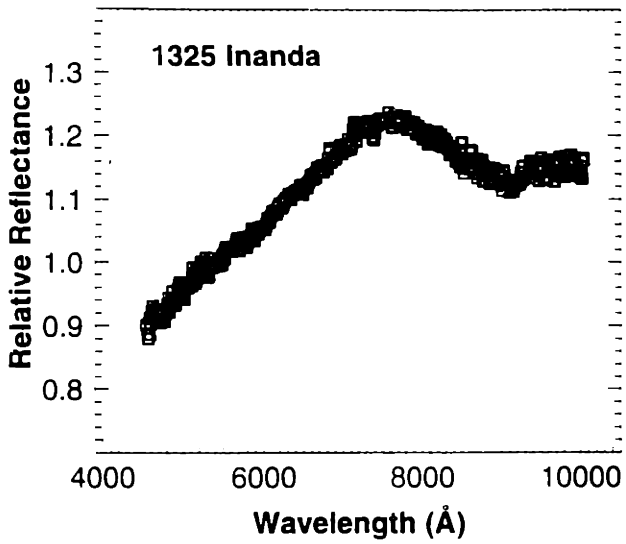
1325 Inanda
Relative Reflectance
1.3
1.2
1.1
1.0
0.9
0.8
4000
6000
8000
10000
Wavelength (Å)

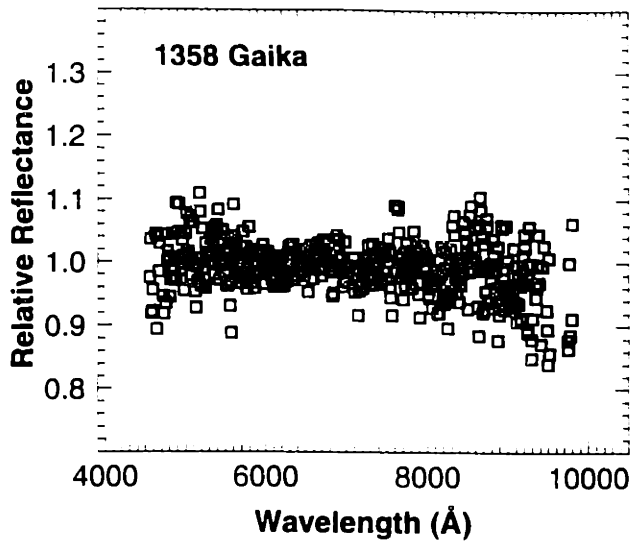
1358 Gaika
Relative Reflectance
1.3
1.2
1.1
1.0
0.9
0.8
4000
6000
8000
10000
Wavelength (Å)

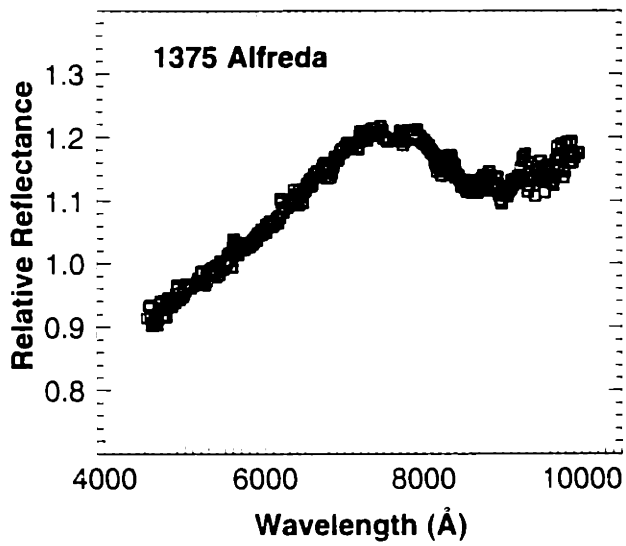
1375 Alfreda
Relative Reflectance
1.3
1.2
1.1
1.0
0.9
0.8
4000
6000
8000
10000
Wavelength (Å)

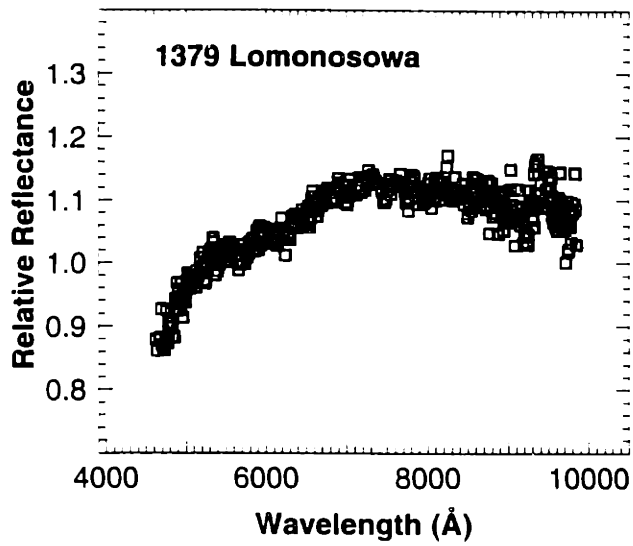
1379 Lomonosowa
Relative Reflectance
1.3
1.2
1.1
1.0
0.9
0.8
4000
6000
8000
10000
Wavelength (Å)

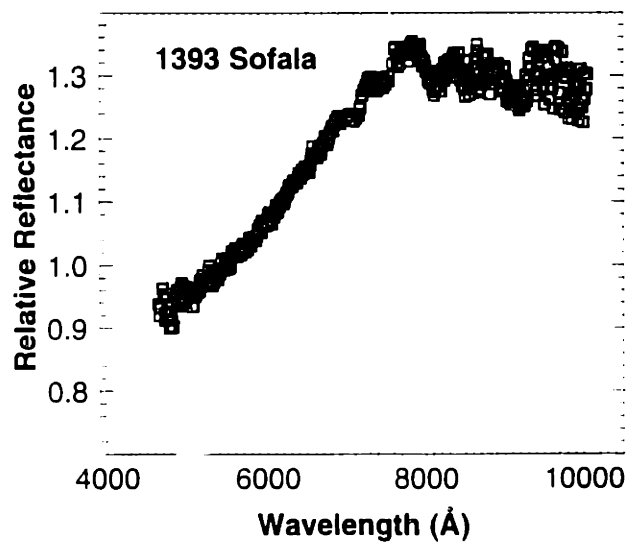
1393 Sofala
Relative Reflectance
1.3
1.2
1.1
1.0
0.9
0.8
4000
6000
8000
10000
Wavelength (Å)

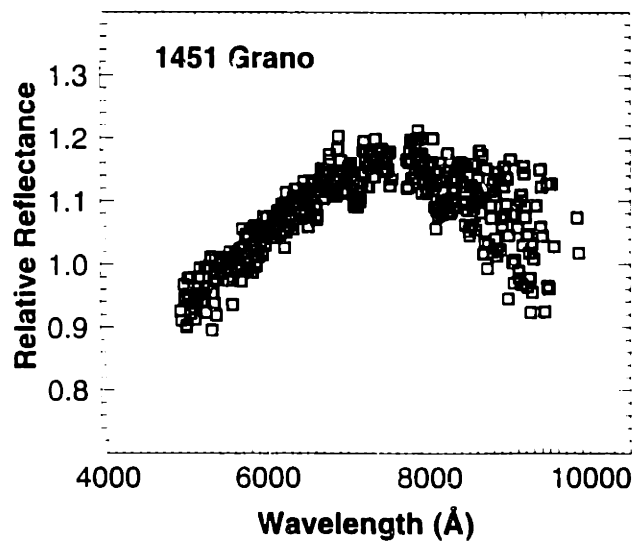
1451 Grano
Relative Reflectance
1.3
1.2
1.1
1.0
0.9
0.8
4000
6000
8000
10000
Wavelength (Å)

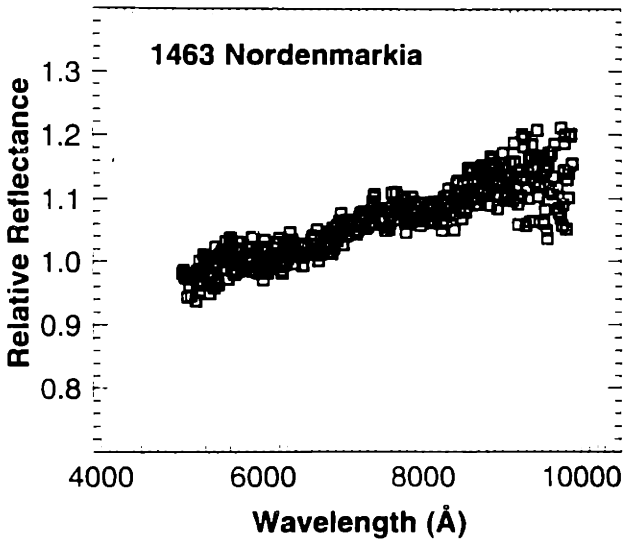
1463 Nordenmarkia
Relative Reflectance
1.3
1.2
1.1
1.0
0.9
0.8
4000
6000
8000
10000
Wavelength (Å)

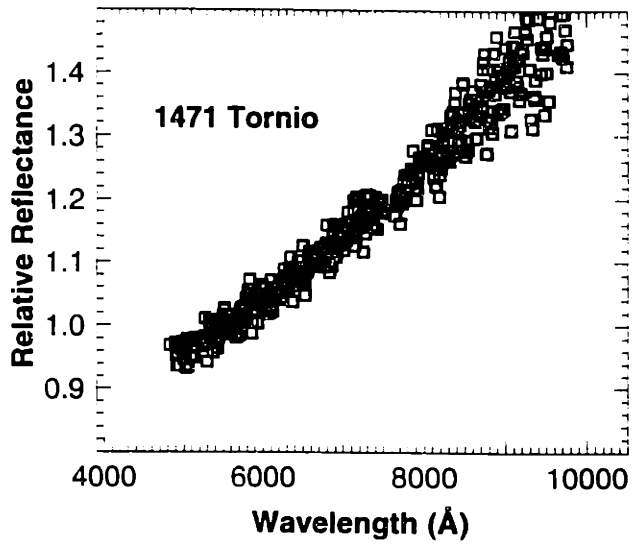
1471 Tornio
Relative Reflectance
1.4
1.3
1.2
1.1
1.0
0.9
4000
6000
8000
10000
Wavelength (Å)

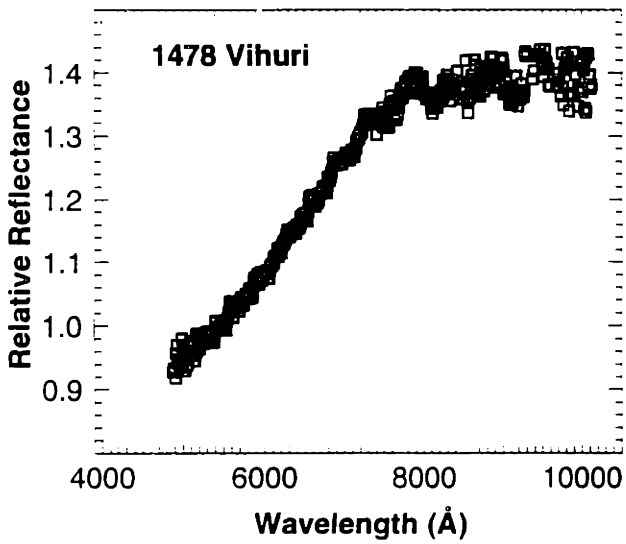
1478 Vihuri
Relative Reflectance
1.4
1.3
1.2
1.1
1.0
0.9
4000
6000
8000
10000
Wavelength (Å)

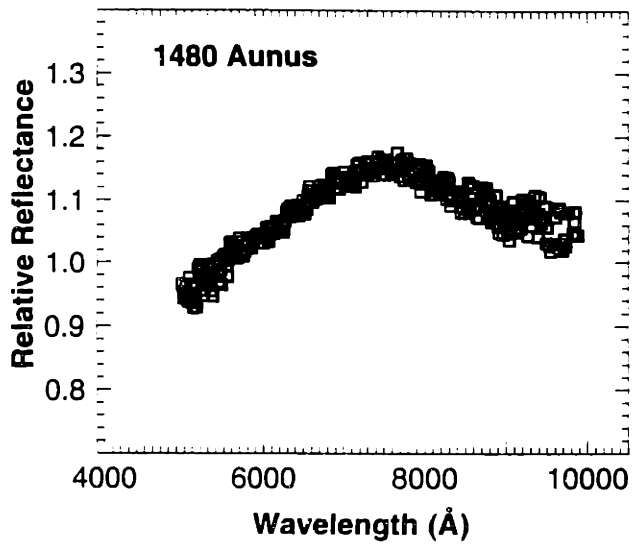
1480 Aunus
Relative Reflectance
1.3
1.2
1.1
1.0
0.9
0.8
4000
6000
8000
10000
Wavelength (Å)

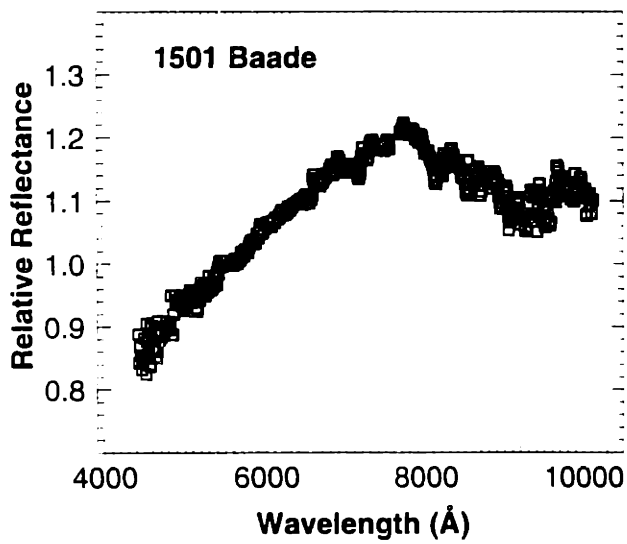
1501 Baade
Relative Reflectance
1.3
1.2
1.1
1.0
0.9
0.8
4000
6000
8000
10000
Wavelength (Å)

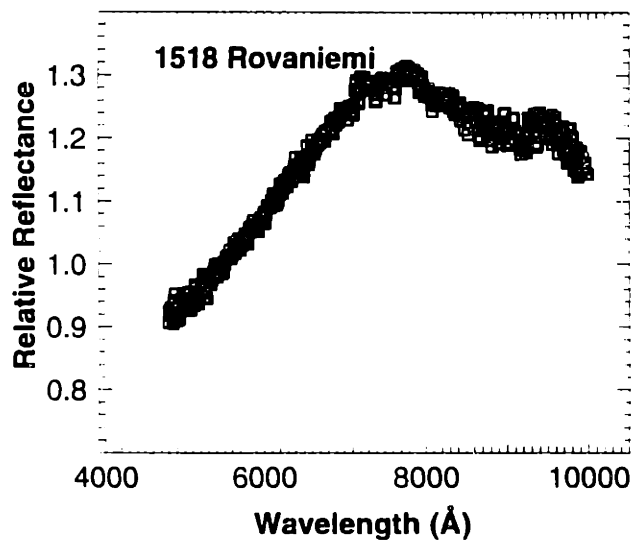
1518 Rovaniemi
Relative Reflectance
1.3
1.2
1.1
1.0
0.9
0.8
4000
6000
8000
10000
Wavelength (Å)

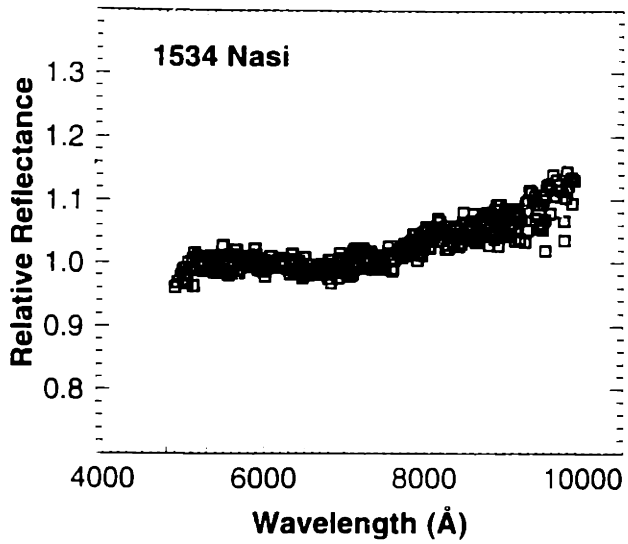
1534 Nasi
Relative Reflectance
1.3
1.2
1.1
1.0
0.9
0.8
4000
6000
8000
10000
Wavelength (Å)

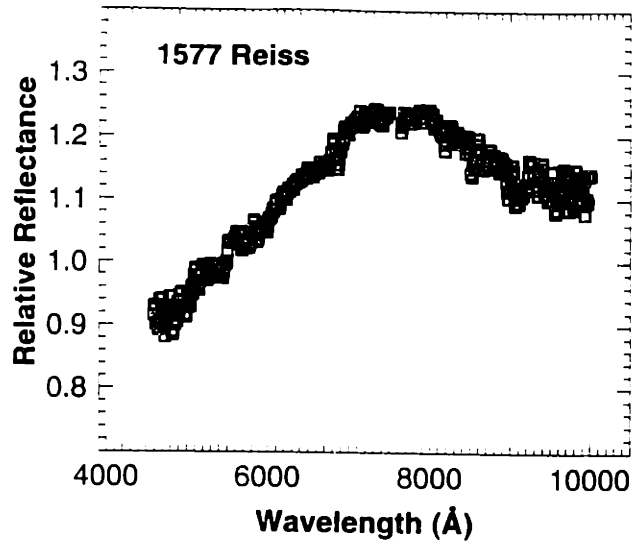
1577 Reiss
Relative Reflectance
1.3
1.2
1.1
1.0
0.9
0.8
4000
6000
8000
10000
Wavelength (Å)

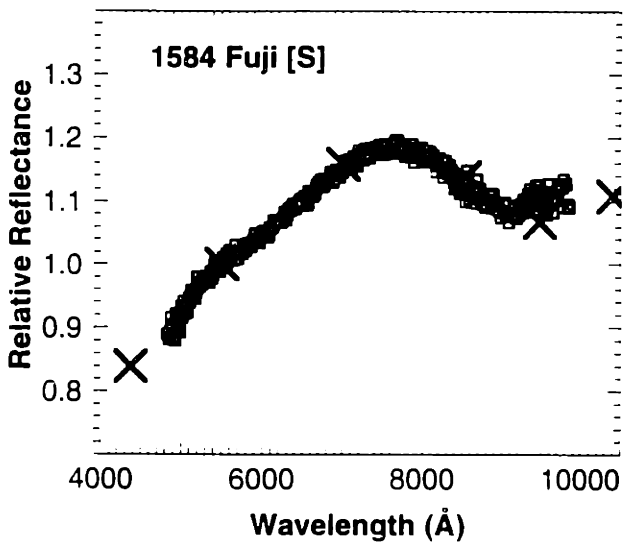
1584 Fuji [S]
Relative Reflectance
1.3
1.2
1.1
1.0
0.9
0.8
4000
6000
8000
10000
Wavelength (Å)

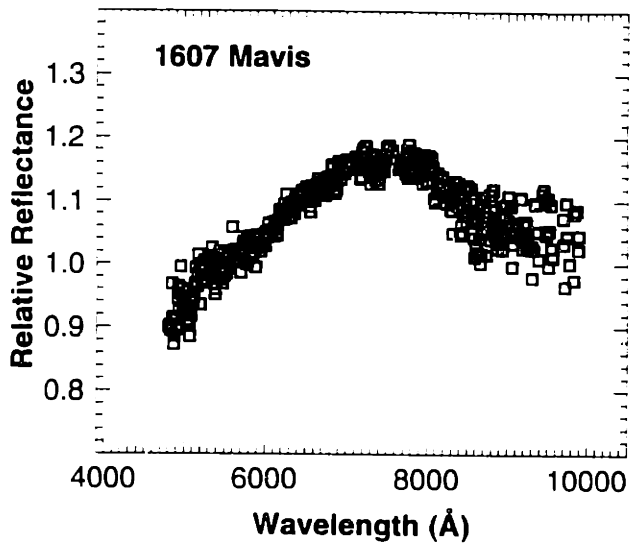
1607 Mavis
Relative Reflectance
1.3
1.2
1.1
1.0
0.9
0.8
4000
6000
8000
10000
Wavelength (Å)

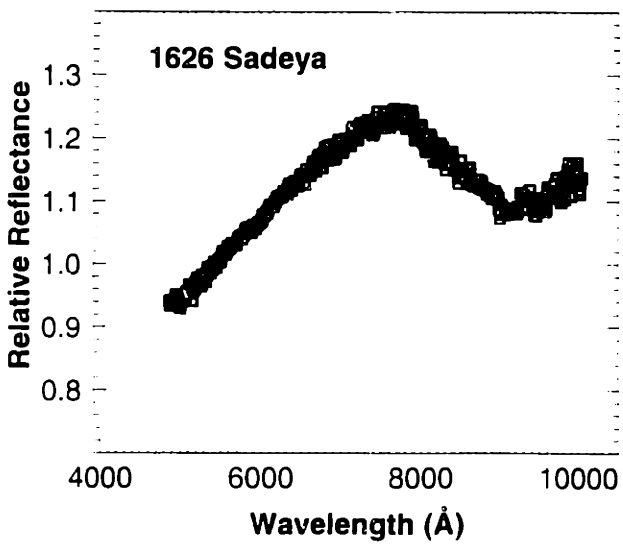
1626 Sadeya
Relative Reflectance
1.3
1.2
1.1
1.0
0.9
0.8
4000
6000
8000
10000
Wavelength (Å)

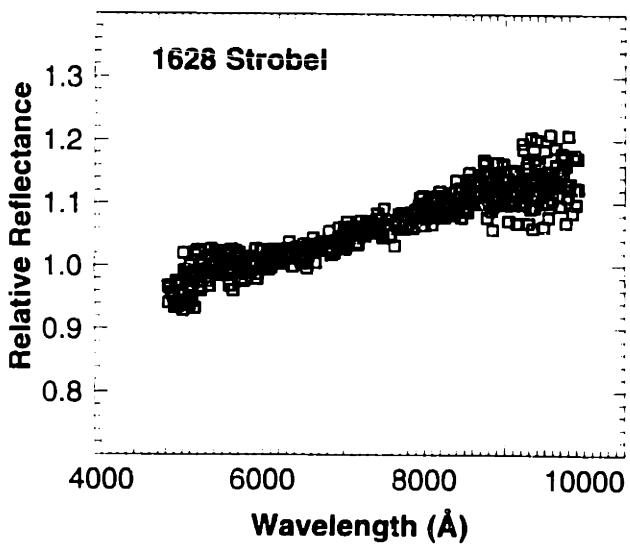
1628 Strobel
Relative Reflectance
1.3
1.2
1.1
1.0
0.9
0.8
4000
6000
8000
10000
Wavelength (Å)

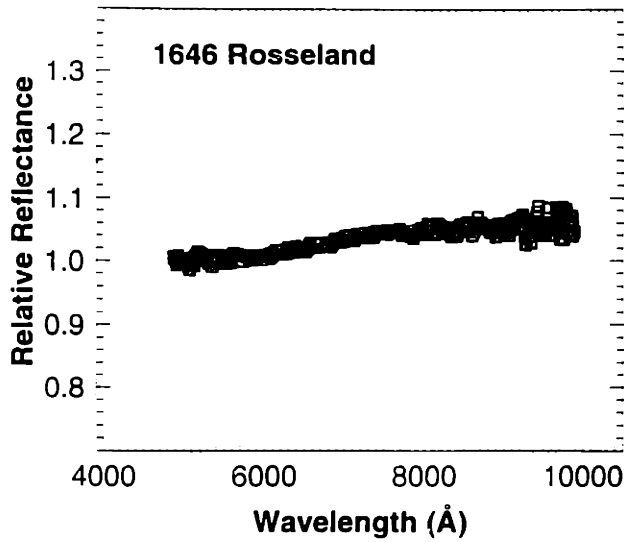
1646 Rosseland
Relative Reflectance
1.3
1.2
1.1
1.0
0.9
0.8
4000
6000
8000
10000
Wavelength (Å)

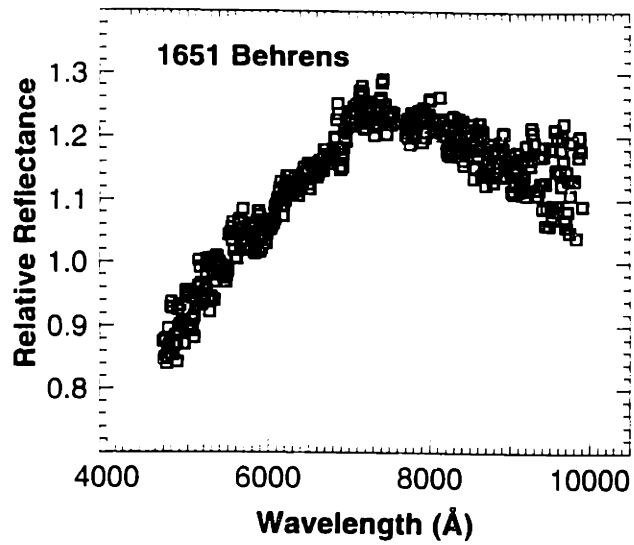
1651 Behrens
Relative Reflectance
1.3
1.2
1.1
1.0
0.9
0.8
4000
6000
8000
10000
Wavelength (Å)

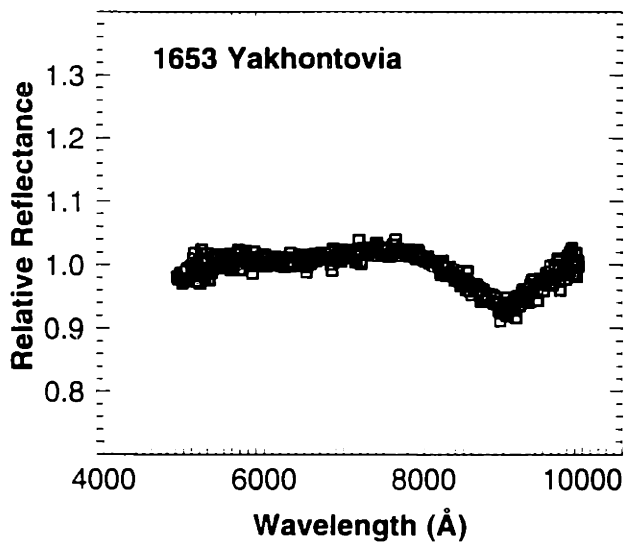
1653 Yakhontovia
Relative Reflectance
1.3
1.2
1.1
1.0
0.9
0.8
4000
6000
8000
10000
Wavelength (Å)

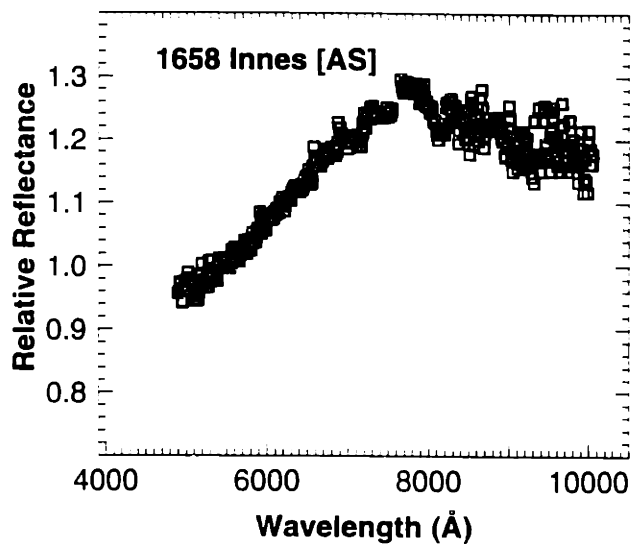
1658 Innes [AS]
Relative Reflectance
1.3
1.2
1.1
1.0
0.9
0.8
4000
6000
8000
10000
Wavelength (Å)

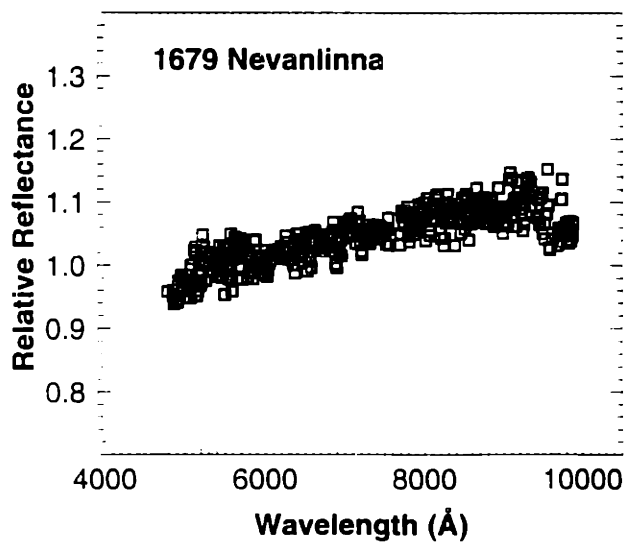
1679 Nevanlinna
Relative Reflectance
1.3
1.2
1.1
1.0
0.9
0.8
4000
6000
8000
10000
Wavelength (Å)

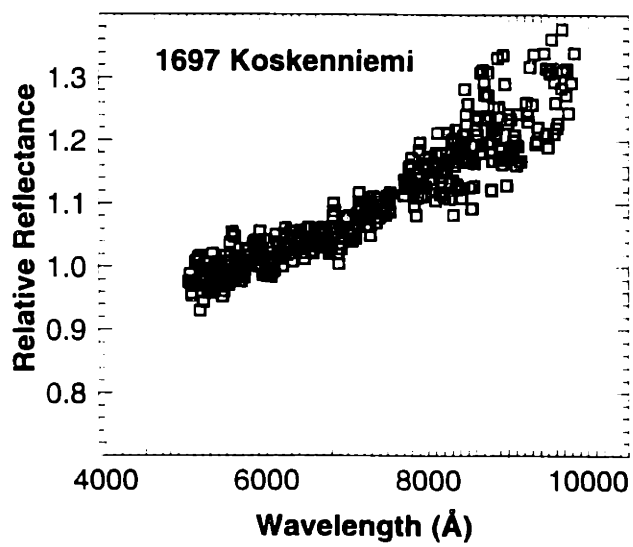
1697 Koskenniemi
Relative Reflectance
1.3
1.2
1.1
1.0
0.9
0.8
4000
6000
8000
10000
Wavelength (Å)

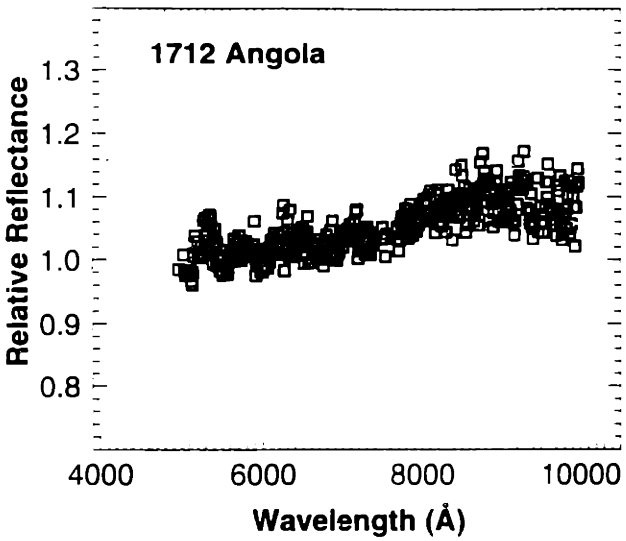
1712 Angola
Relative Reflectance
1.3
1.2
1.1
1.0
0.9
0.8
4000
6000
8000
10000
Wavelength (Å)

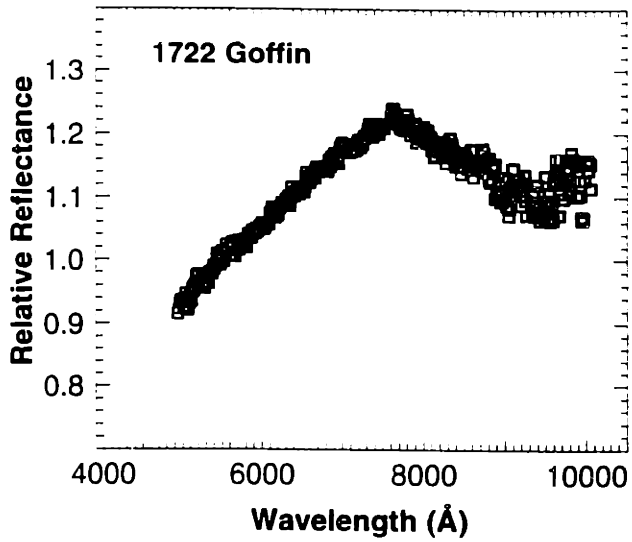
1722 Goffin
Relative Reflectance
1.3
1.2
1.1
1.0
0.9
0.8
4000
6000
8000
10000
Wavelength (Å)

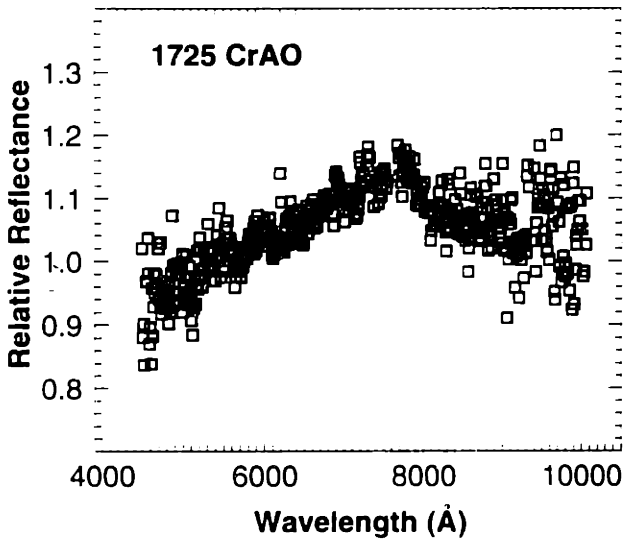
1725 CrAO
Relative Reflectance
1.3
1.2
1.1
1.0
0.9
0.8
4000
6000
8000
10000
Wavelength (Å)

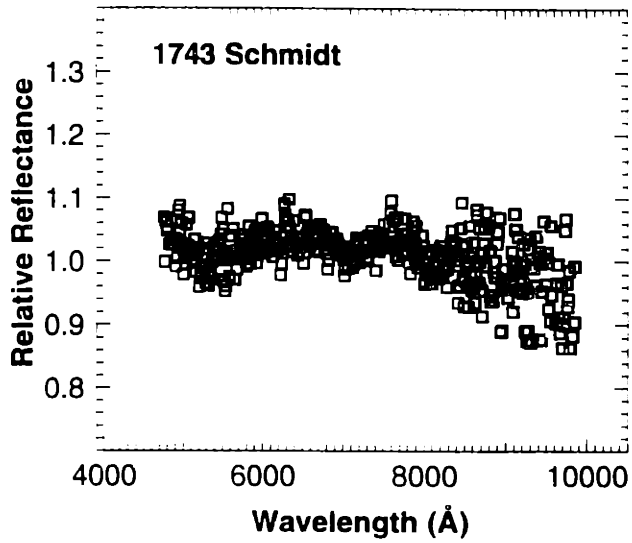
1743 Schmidt
Relative Reflectance
1.3
1.2
1.1
1.0
0.9
0.8
4000
6000
8000
10000
Wavelength (Å)

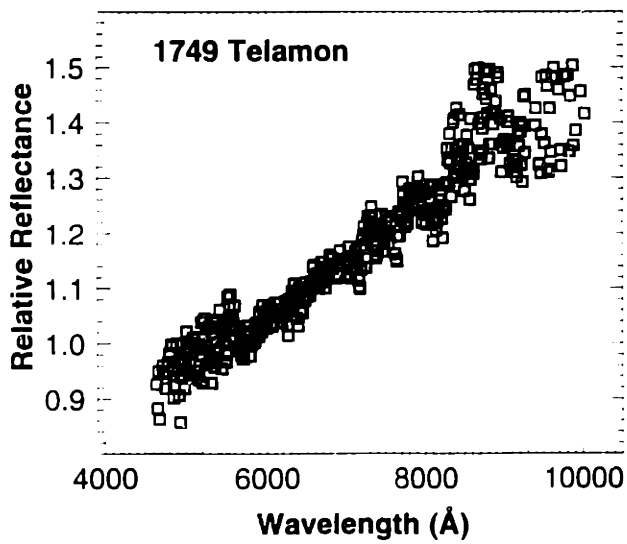
1749 Telamon
Relative Reflectance
1.5
1.4
1.3
1.2
1.1
1.0
0.9
4000
6000
8000
10000
Wavelength (Å)

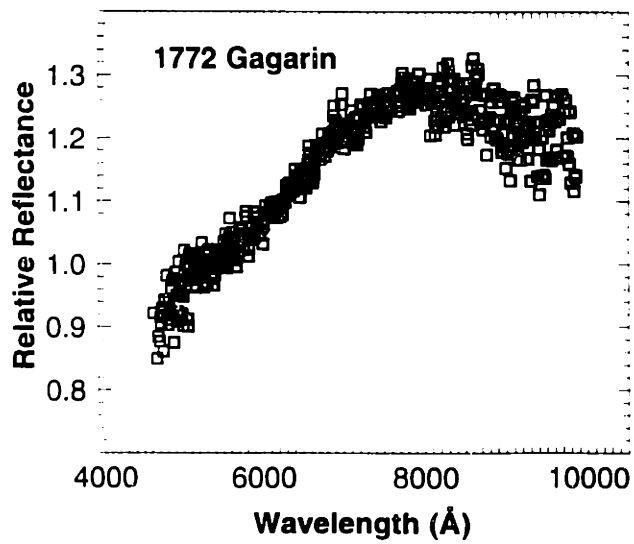
1772 Gagarin
Relative Reflectance
1.3
1.2
1.1
1.0
0.9
0.8
4000
6000
8000
10000
Wavelength (Å)

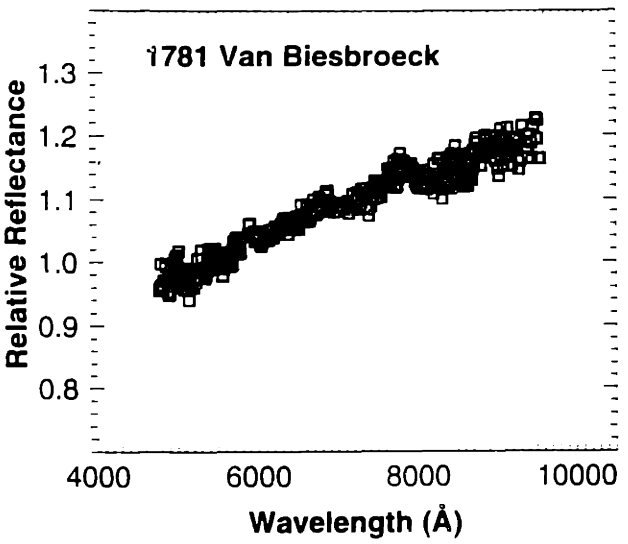
1781 Van Biesbroeck
Relative Reflectance
1.3
1.2
1.1
1.0
0.9
0.8
4000
6000
8000
10000
Wavelength (Å)

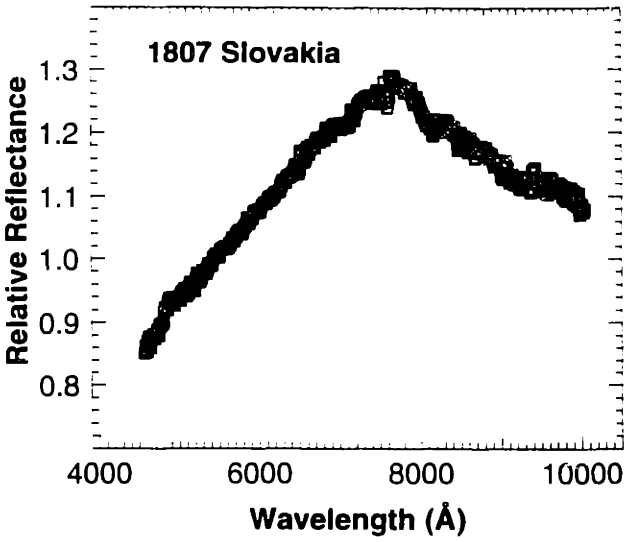
1807 Slovakia
Relative Reflectance
1.3
1.2
1.1
1.0
0.9
0.8
4000
6000
8000
10000
Wavelength (Å)

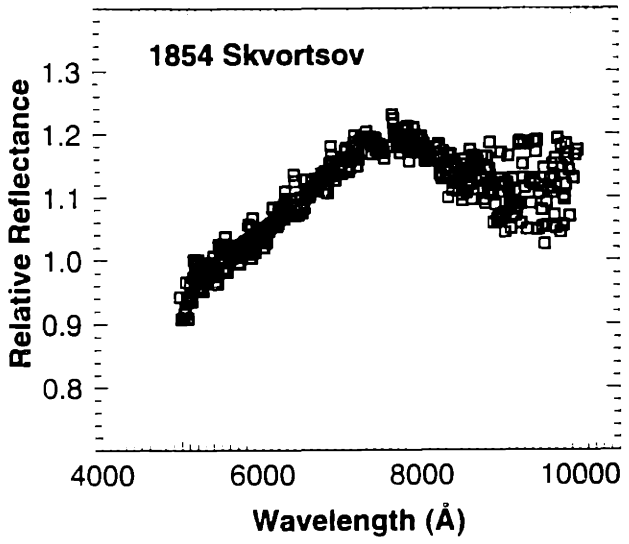
1854 Skvortsov
Relative Reflectance
1.3
1.2
1.1
1.0
0.9
0.8
4000
6000
8000
10000
Wavelength (Å)

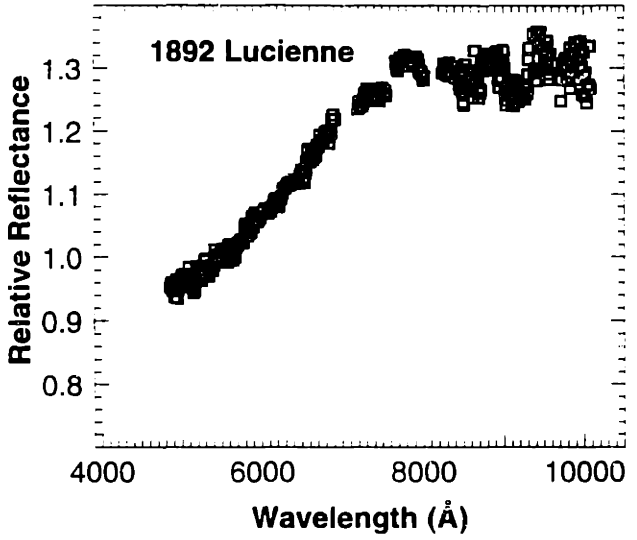
1892 Lucienne
Relative Reflectance
1.3
1.2
1.1
1.0
0.9
0.8
4000
6000
8000
10000
Wavelength (Å)

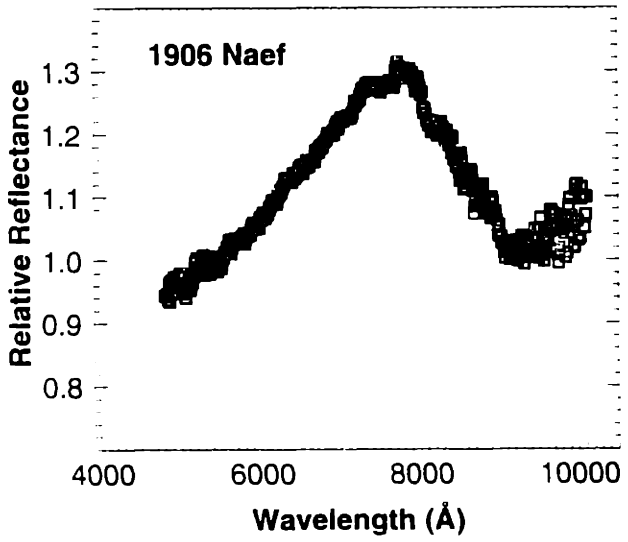
1906 Naef
Relative Reflectance
1.3
1.2
1.1
1.0
0.9
0.8
4000
6000
8000
10000
Wavelength (Å)

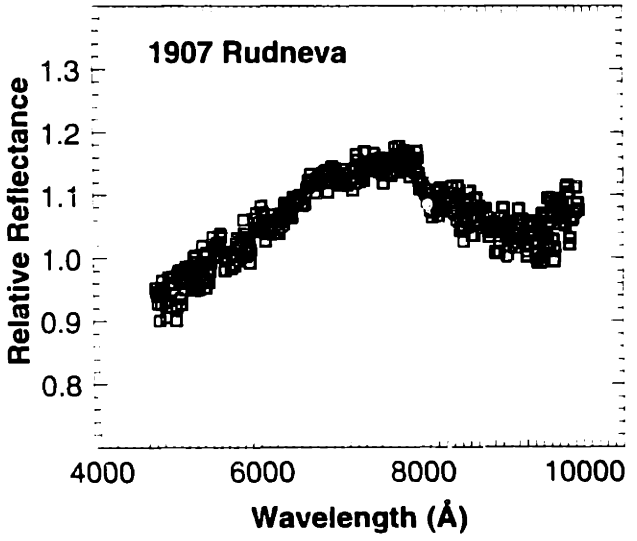
1907 Rudneva
Relative Reflectance
1.3
1.2
1.1
1.0
0.9
0.8
4000
6000
8000
10000
Wavelength (Å)

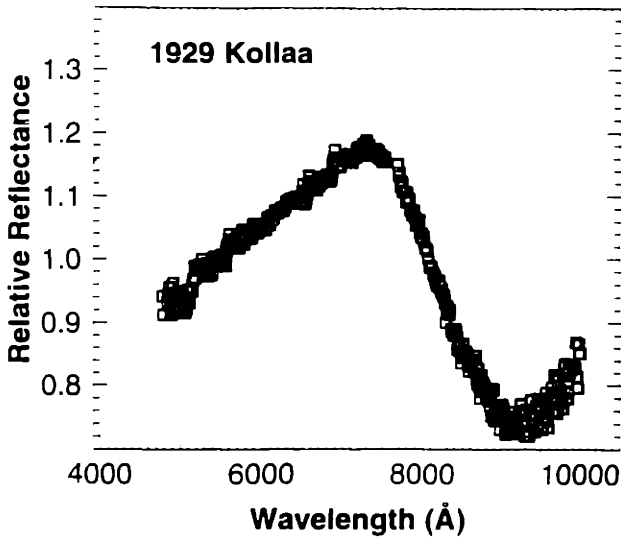
1929 Kollaa
Relative Reflectance
1.3
1.2
1.1
1.0
0.9
0.8
4000
6000
8000
10000
Wavelength (Å)

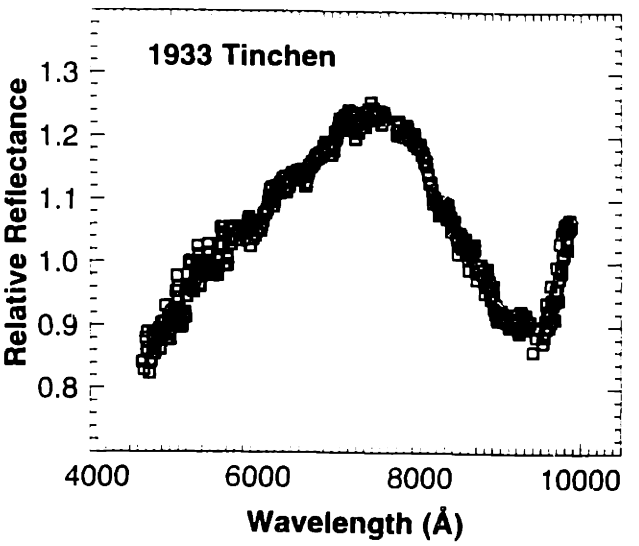
1933 Tinchen
Relative Reflectance
1.3
1.2
1.1
1.0
0.9
0.8
4000
6000
8000
10000
Wavelength (Å)

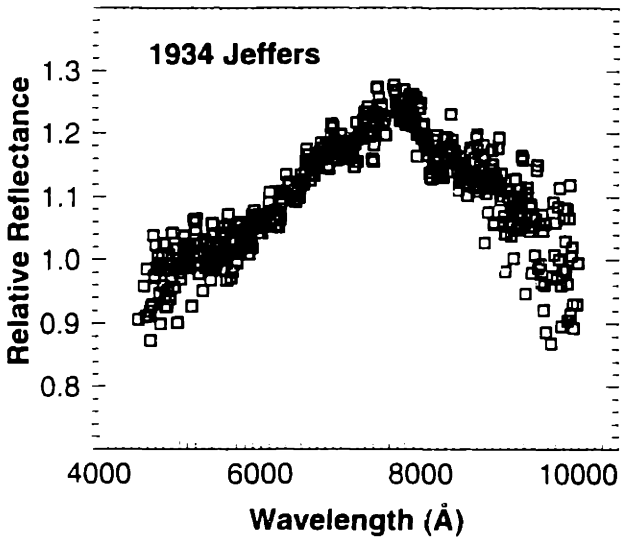
1934 Jeffers
Relative Reflectance
1.3
1.2
1.1
1.0
0.9
0.8
4000
6000
8000
10000
Wavelength (Å)

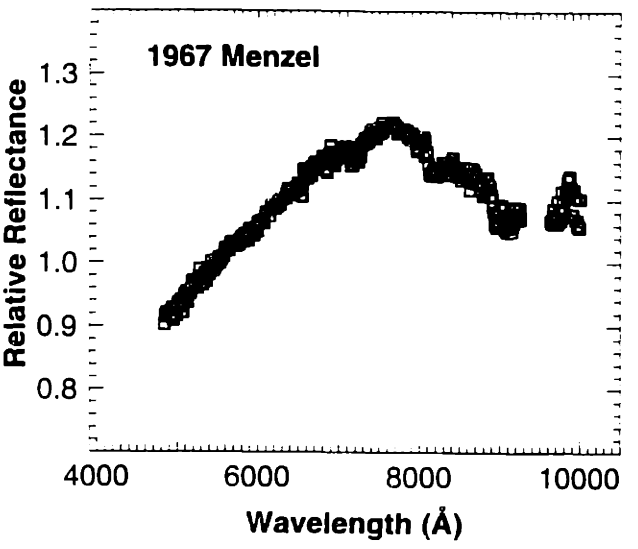
1967 Menzel
Relative Reflectance
1.3
1.2
1.1
1.0
0.9
0.8
4000
6000
8000
10000
Wavelength (Å)

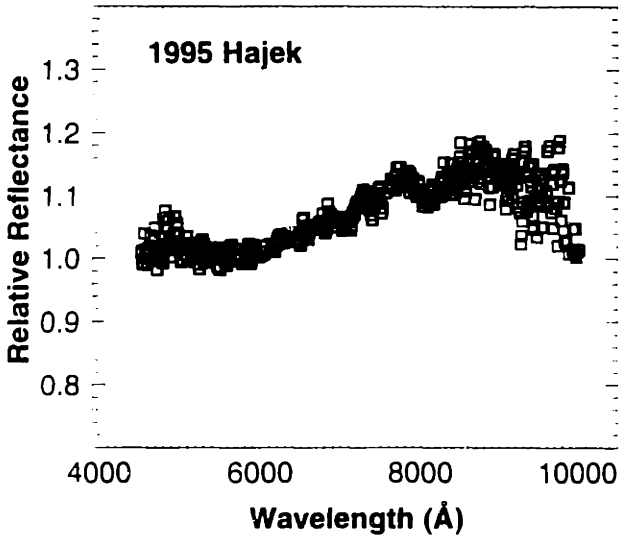
1995 Hajek
Relative Reflectance
1.3
1.2
1.1
1.0
0.9
0.8
4000
6000
8000
10000
Wavelength (Å)

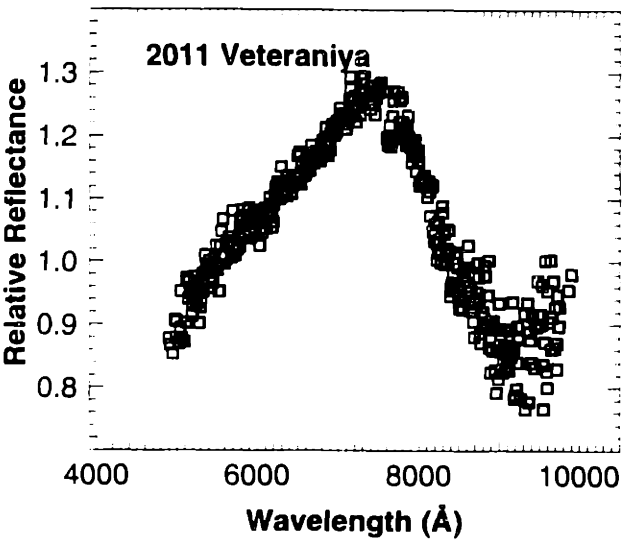
2011 Veteraniya
Relative Reflectance
1.3
1.2
1.1
1.0
0.9
0.8
4000
6000
8000
10000
Wavelength (Å)

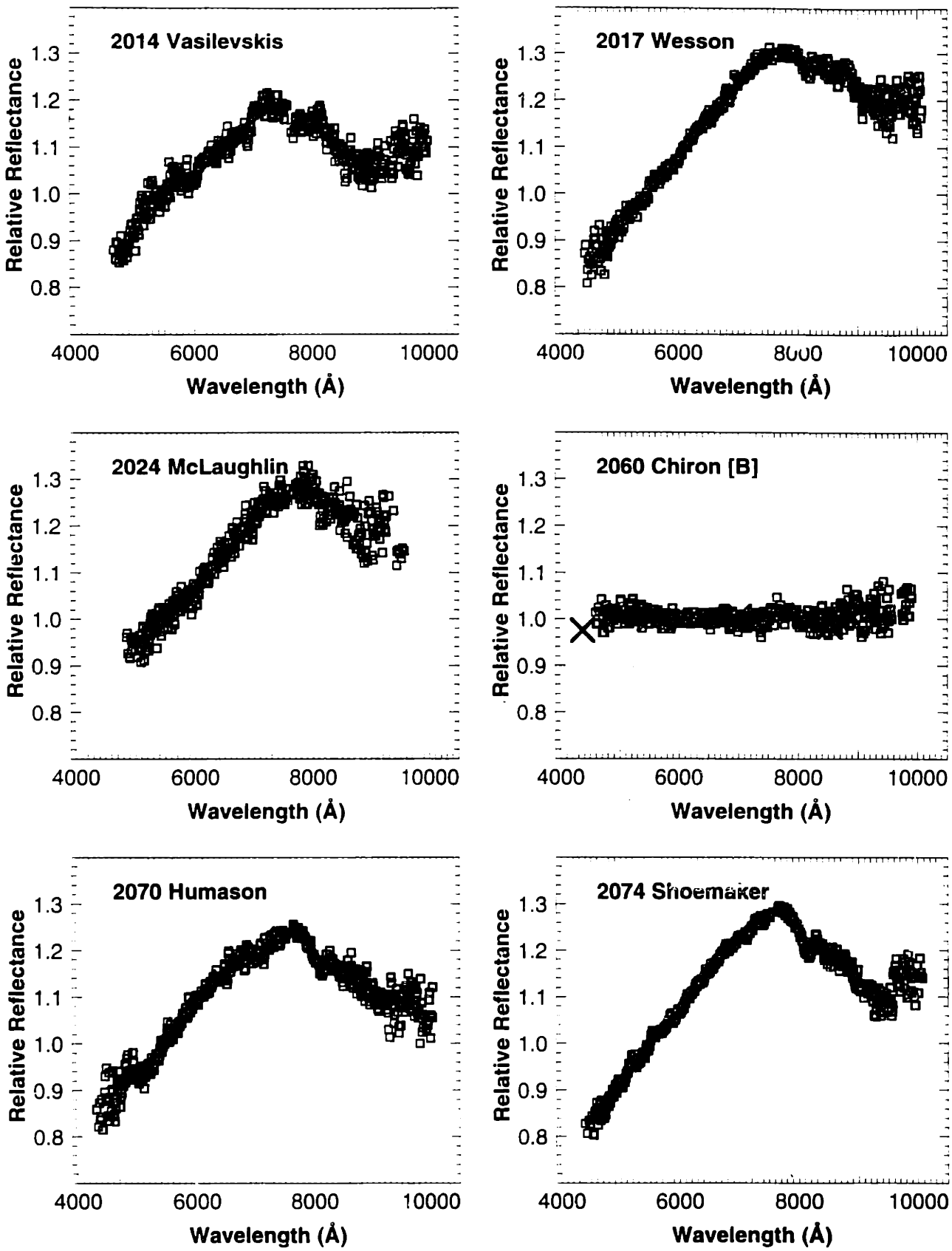
2014 Vasilevskis
2017 Wesson
2024 McLaughlin
2060 Chiron [B]
2070 Humason
2074 Shoemaker
Relative Reflectance
Wavelength (Å)
0.8
0.9
1.0
1.1
1.2
1.3
4000
6000
8000
10000

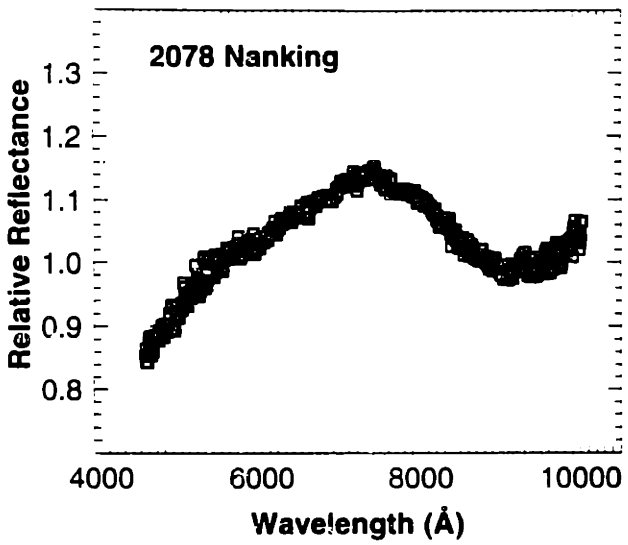
2078 Nanking
Relative Reflectance
1.3
1.2
1.1
1.0
0.9
0.8
4000
6000
8000
10000
Wavelength (Å)

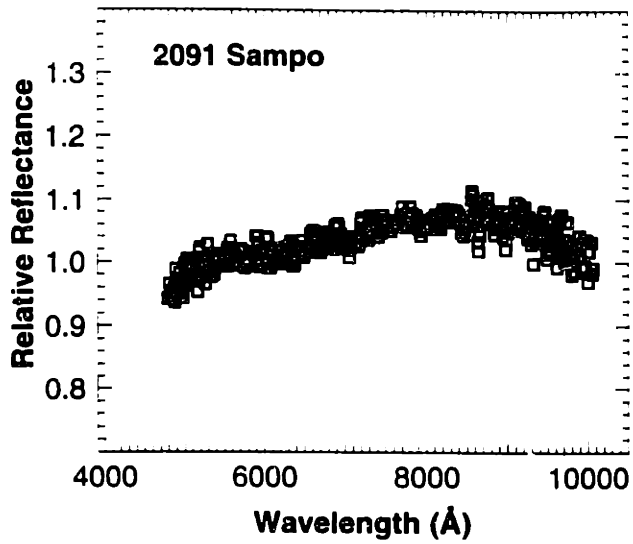
2091 Sampo
Relative Reflectance
1.3
1.2
1.1
1.0
0.9
0.8
4000
6000
8000
10000
Wavelength (Å)

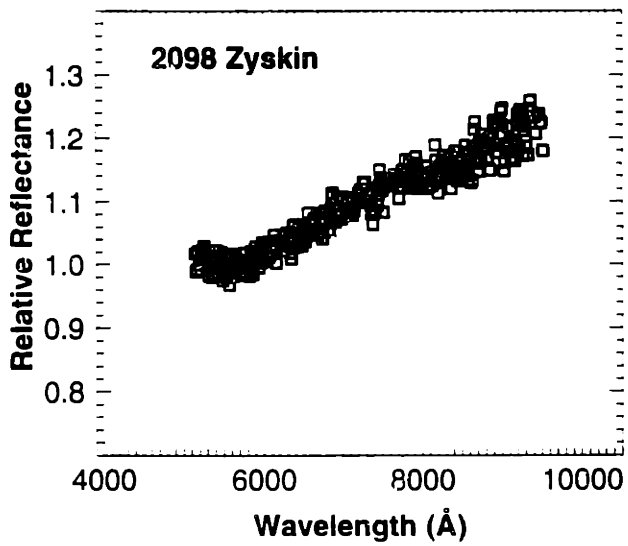
2098 Zyskin
Relative Reflectance
1.3
1.2
1.1
1.0
0.9
0.8
4000
6000
8000
10000
Wavelength (Å)

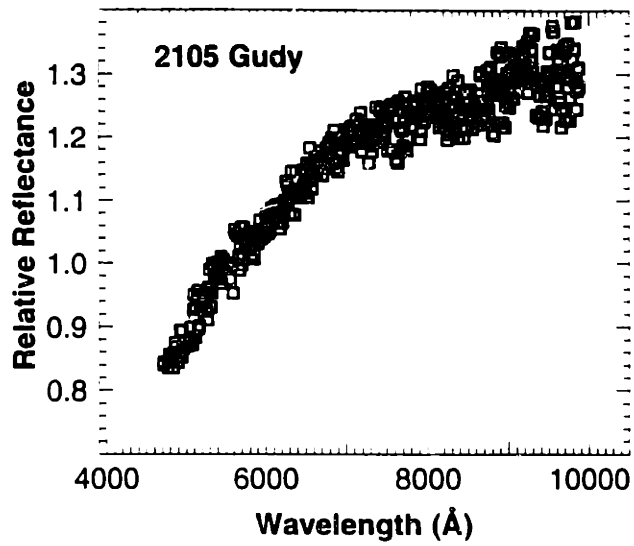
2105 Gudy
Relative Reflectance
1.3
1.2
1.1
1.0
0.9
0.8
4000
6000
8000
10000
Wavelength (Å)

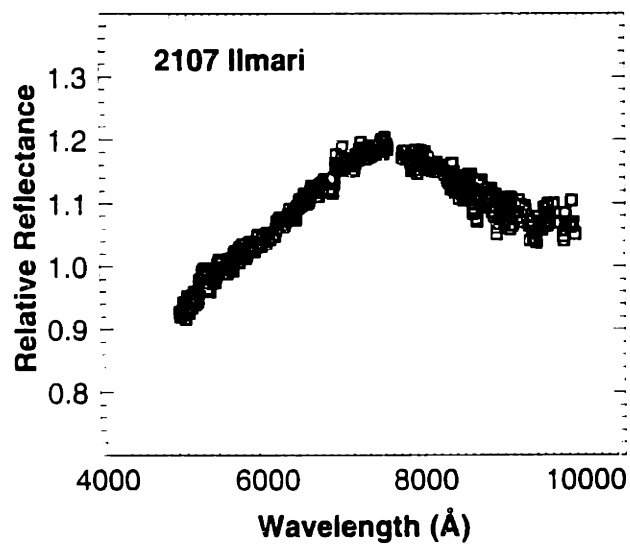
2107 Ilmari
Relative Reflectance
1.3
1.2
1.1
1.0
0.9
0.8
4000
6000
8000
10000
Wavelength (Å)

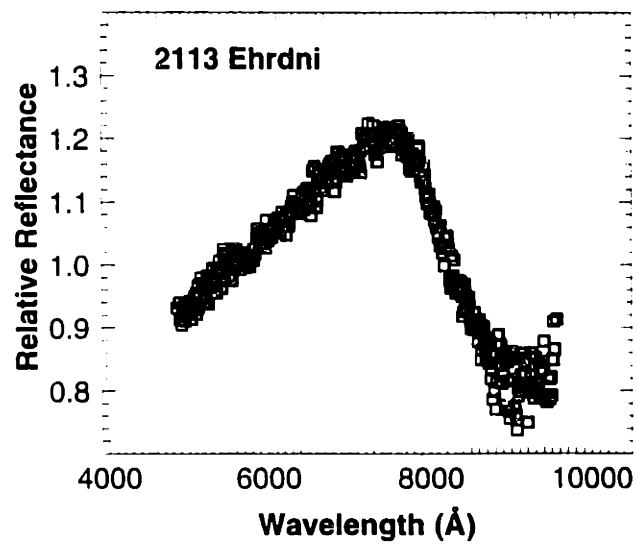
2113 Ehrdni
Relative Reflectance
1.3
1.2
1.1
1.0
0.9
0.8
4000
6000
8000
10000
Wavelength (Å)

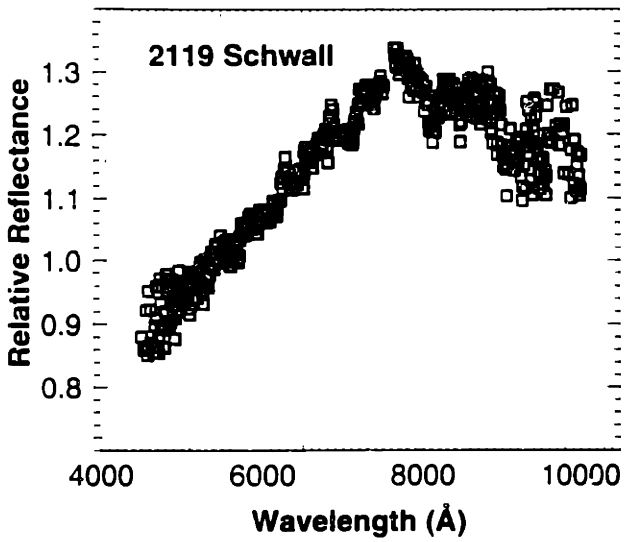
2119 Schwall
Relative Reflectance
1.3
1.2
1.1
1.0
0.9
0.8
4000
6000
8000
10000
Wavelength (Å)

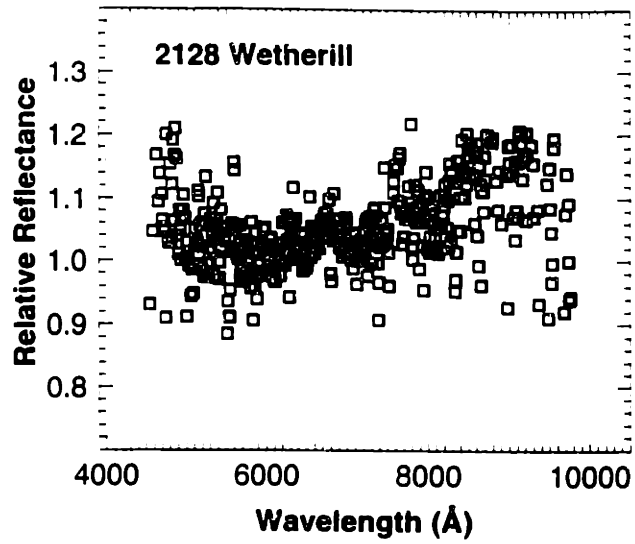
2128 Wetherill
Relative Reflectance
1.3
1.2
1.1
1.0
0.9
0.8
4000
6000
8000
10000
Wavelength (Å)

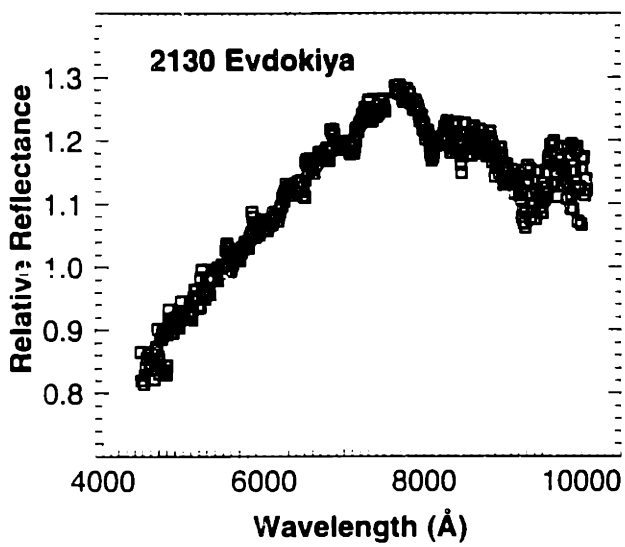
2130 Evdokiya
Relative Reflectance
1.3
1.2
1.1
1.0
0.9
0.8
4000
6000
8000
10000
Wavelength (Å)

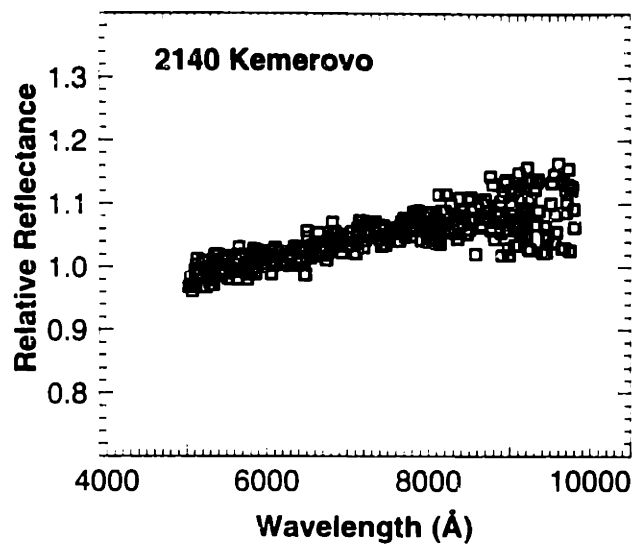
2140 Kemerovo
Relative Reflectance
1.3
1.2
1.1
1.0
0.9
0.8
4000
6000
8000
10000
Wavelength (Å)

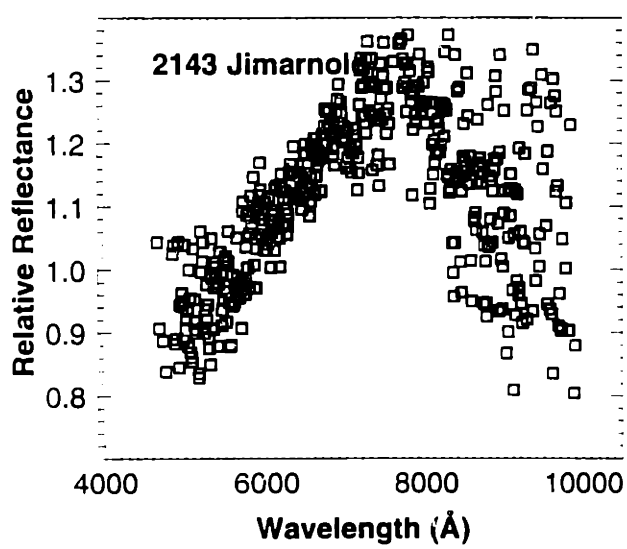
2143 Jimarnol
Relative Reflectance
1.3
1.2
1.1
1.0
0.9
0.8
4000
6000
8000
10000
Wavelength (Å)

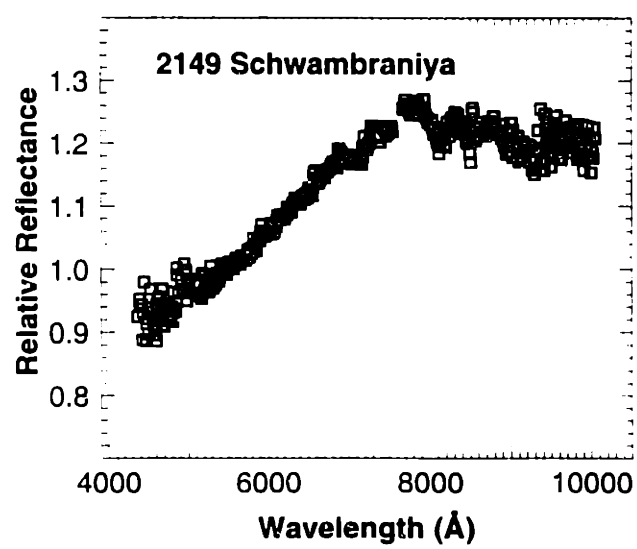
2149 Schwambraniya
Relative Reflectance
1.3
1.2
1.1
1.0
0.9
0.8
4000
6000
8000
10000
Wavelength (Å)

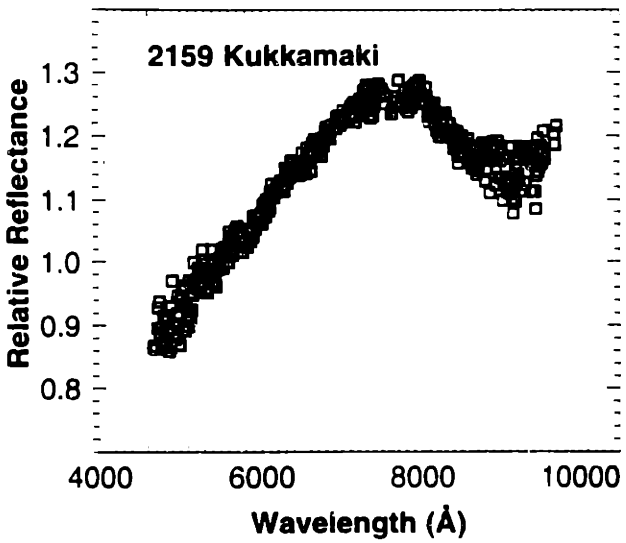
2159 Kukkamaki
Relative Reflectance
1.3
1.2
1.1
1.0
0.9
0.8
4000
6000
8000
10000
Wavelength (Å)

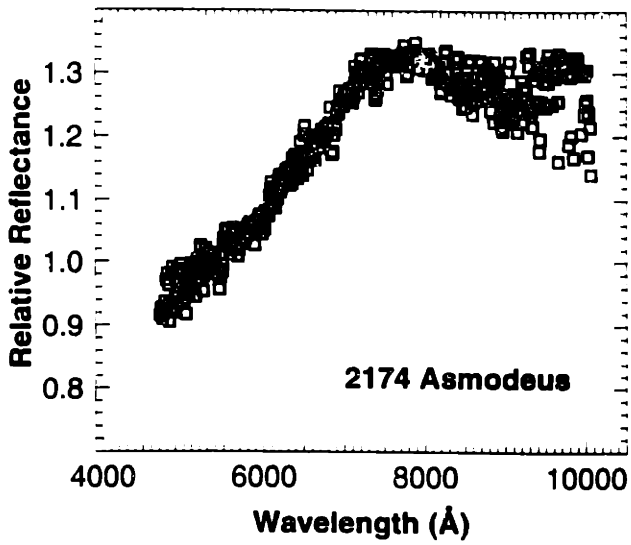
2174 Asmodeus
Relative Reflectance
1.3
1.2
1.1
1.0
0.9
0.8
4000
6000
8000
10000
Wavelength (Å)

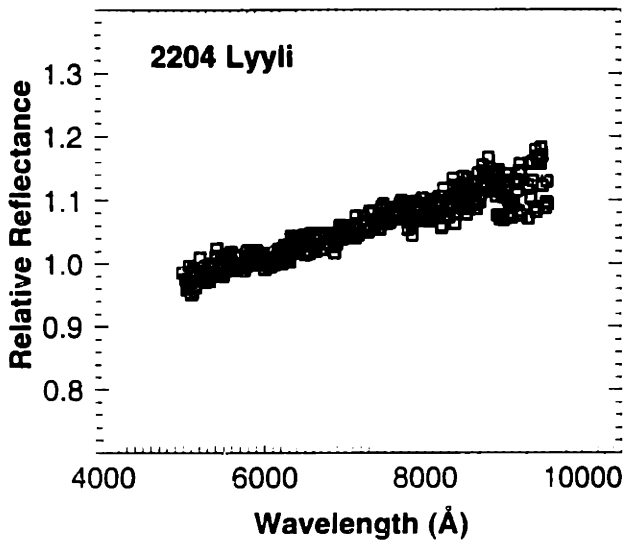
2204 Lyyli
Relative Reflectance
1.3
1.2
1.1
1.0
0.9
0.8
4000
6000
8000
10000
Wavelength (Å)

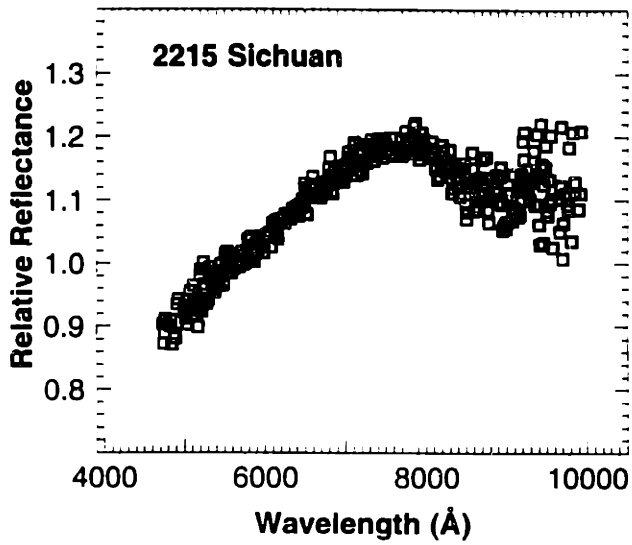
2215 Sichuan
Relative Reflectance
1.3
1.2
1.1
1.0
0.9
0.8
4000
6000
8000
10000
Wavelength (Å)

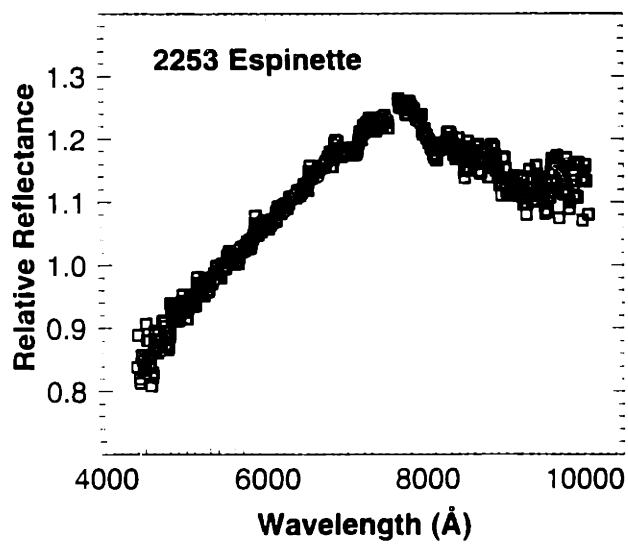
2253 Espinette
Relative Reflectance
1.3
1.2
1.1
1.0
0.9
0.8
4000
6000
8000
10000
Wavelength (Å)

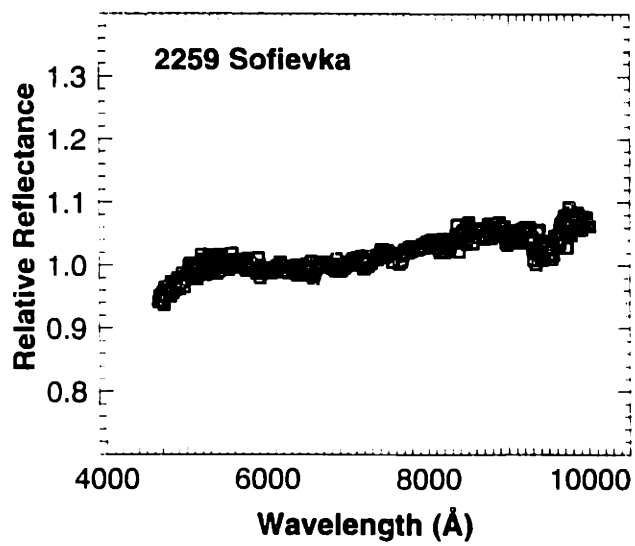
2259 Sofievka
Relative Reflectance
1.3
1.2
1.1
1.0
0.9
0.8
4000
6000
8000
10000
Wavelength (Å)

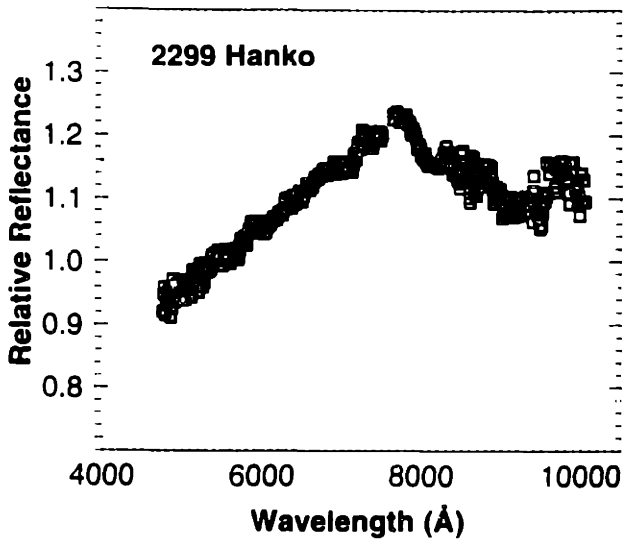
2299 Hanko
Relative Reflectance
1.3
1.2
1.1
1.0
0.9
0.8
4000
6000
8000
10000
Wavelength (Å)

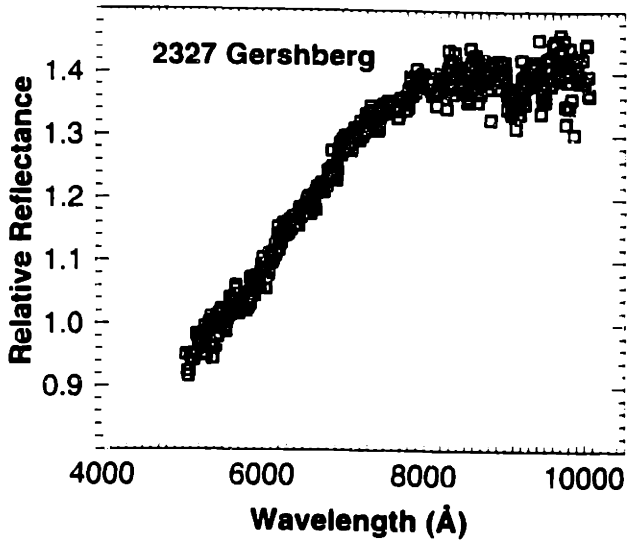
2327 Gershberg
Relative Reflectance
1.4
1.3
1.2
1.1
1.0
0.9
4000
6000
8000
10000
Wavelength (Å)

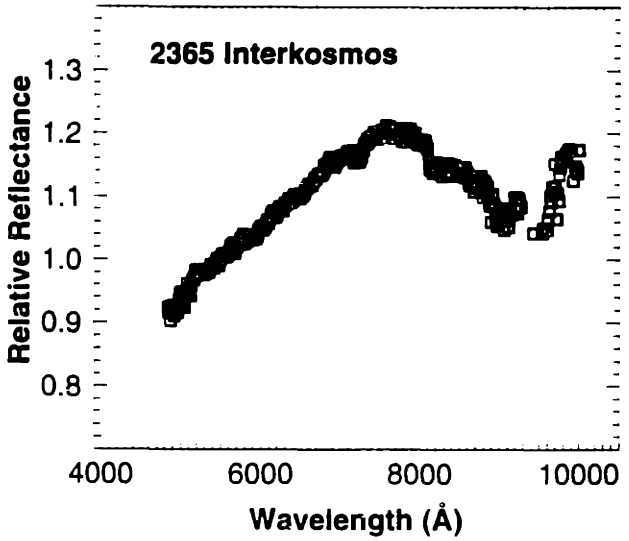
2365 Interkosmos
Relative Reflectance
1.3
1.2
1.1
1.0
0.9
0.8
4000
6000
8000
10000
Wavelength (Å)

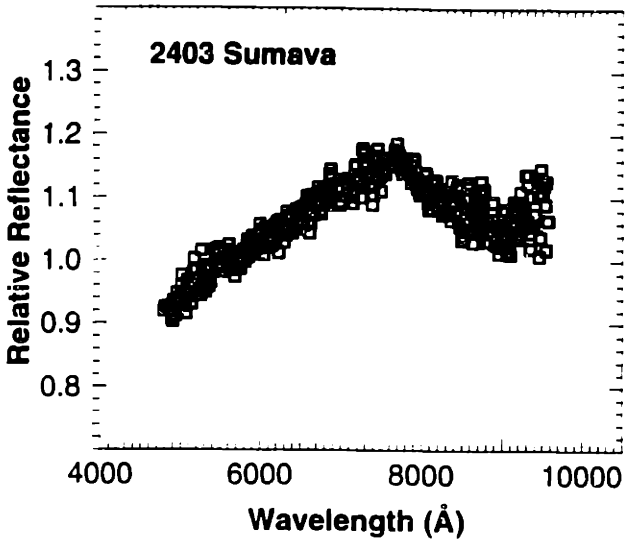
2403 Sumava
Relative Reflectance
1.3
1.2
1.1
1.0
0.9
0.8
4000
6000
8000
10000
Wavelength (Å)

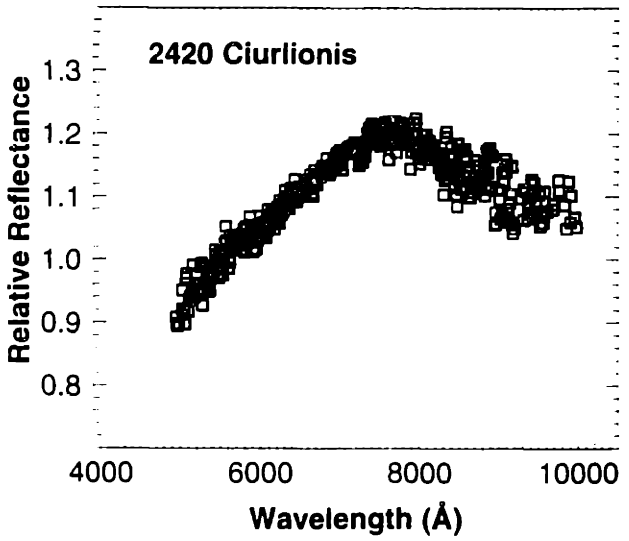
2420 Ciurlionis
Relative Reflectance
1.3
1.2
1.1
1.0
0.9
0.8
4000
6000
8000
10000
Wavelength (Å)

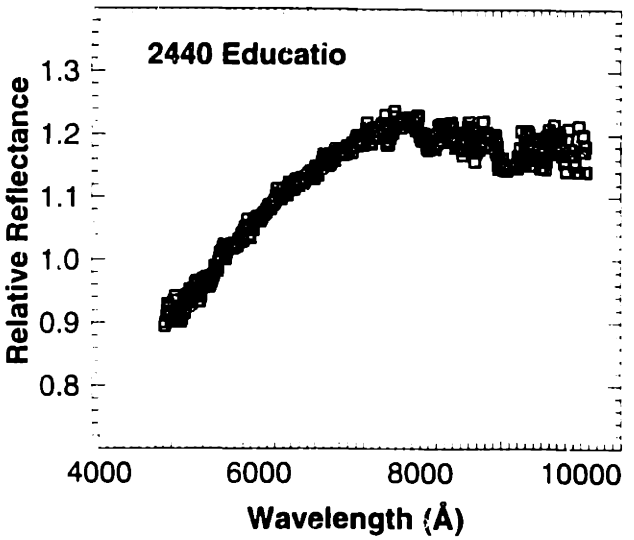
2440 Educatio
Relative Reflectance
1.3
1.2
1.1
1.0
0.9
0.8
4000
6000
8000
10000
Wavelength (Å)

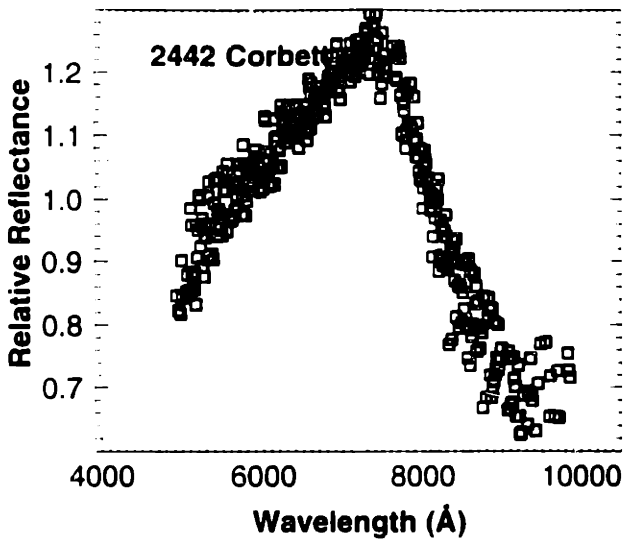
2442 Corbett
Relative Reflectance
1.2
1.1
1.0
0.9
0.8
0.7
4000
6000
8000
10000
Wavelength (Å)

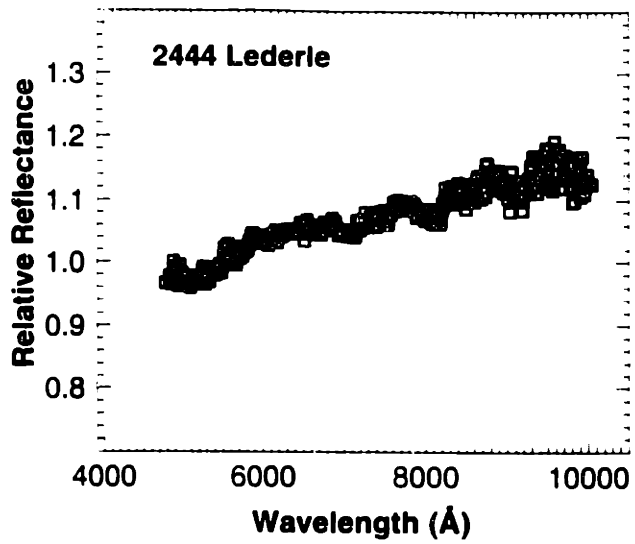
2444 Lederle
Relative Reflectance
1.3
1.2
1.1
1.0
0.9
0.8
4000
6000
8000
10000
Wavelength (Å)

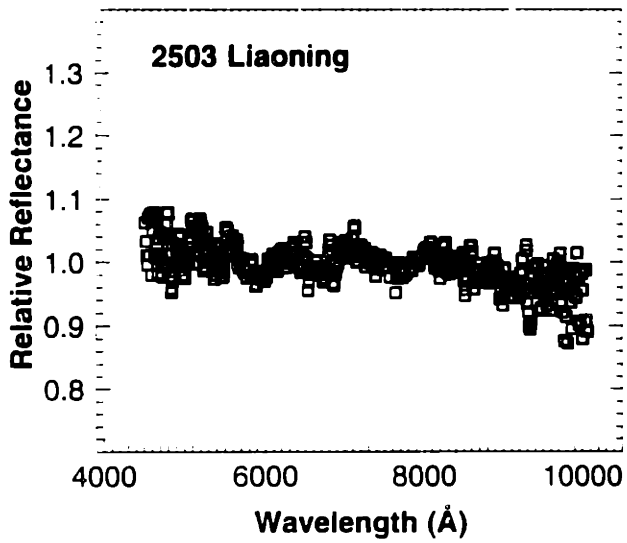
2503 Liaoning
Relative Reflectance
1.3
1.2
1.1
1.0
0.9
0.8
4000
6000
8000
10000
Wavelength (Å)

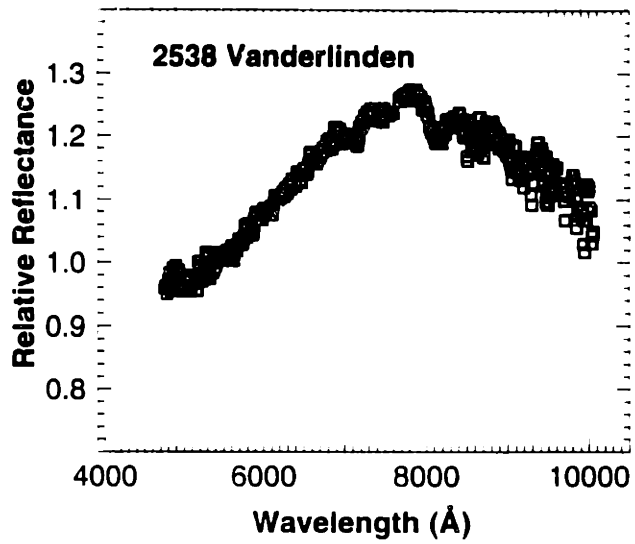
2538 Vanderlinden
Relative Reflectance
1.3
1.2
1.1
1.0
0.9
0.8
4000
6000
8000
10000
Wavelength (Å)

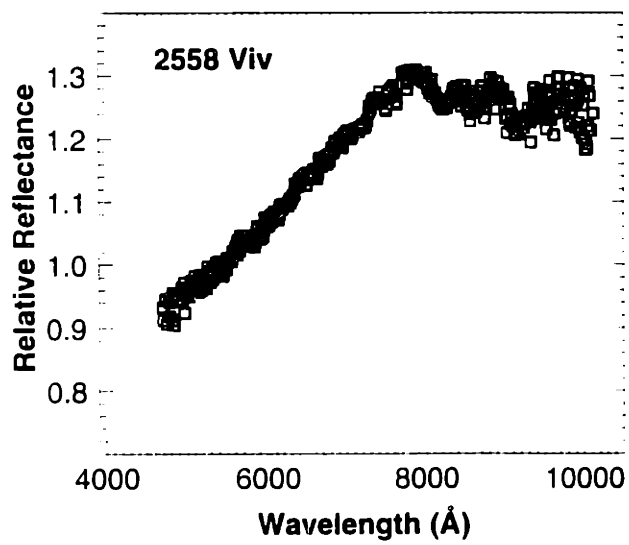
2558 Viv
Relative Reflectance
1.3
1.2
1.1
1.0
0.9
0.8
4000
6000
8000
10000
Wavelength (Å)

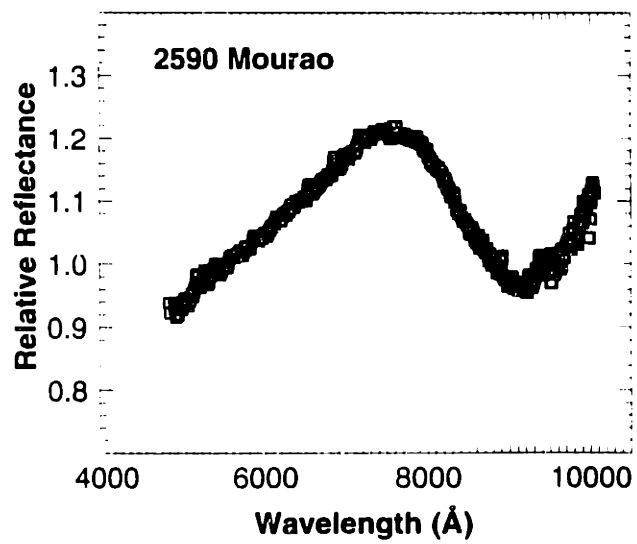
2590 Mourao
Relative Reflectance
1.3
1.2
1.1
1.0
0.9
0.8
4000
6000
8000
10000
Wavelength (Å)

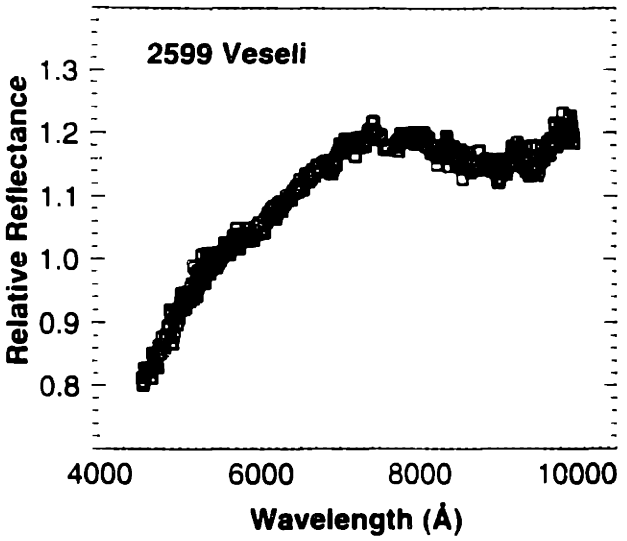
2599 Veseli
Relative Reflectance
1.3
1.2
1.1
1.0
0.9
0.8
4000
6000
8000
10000
Wavelength (Å)

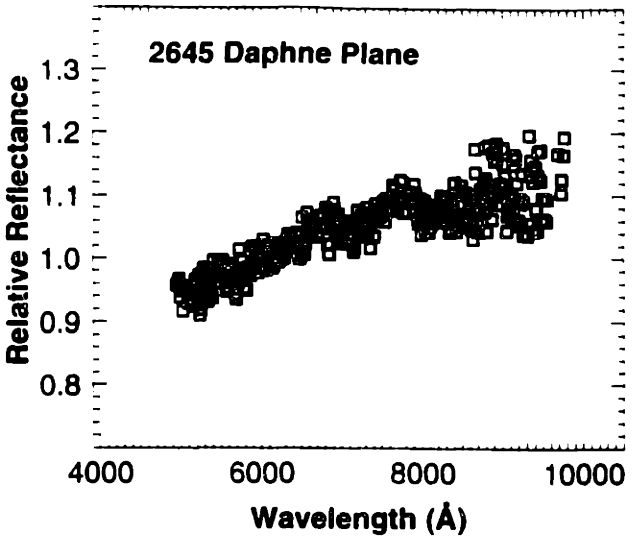
2645 Daphne Plane
Relative Reflectance
1.3
1.2
1.1
1.0
0.9
0.8
4000
6000
8000
10000
Wavelength (Å)

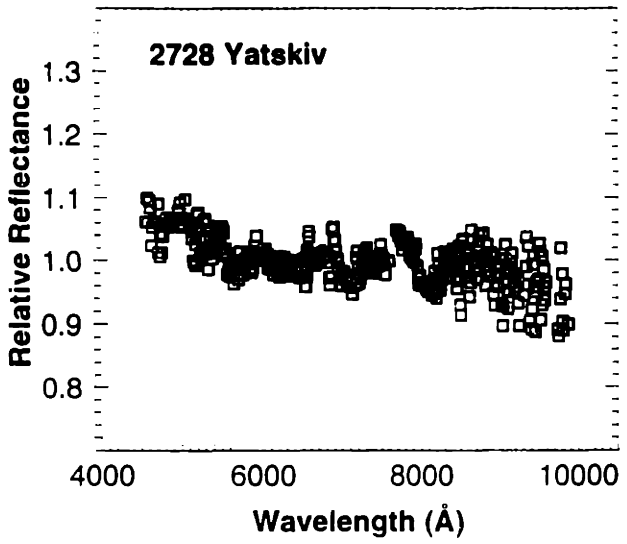
2728 Yatskiv
Relative Reflectance
1.3
1.2
1.1
1.0
0.9
0.8
4000
6000
8000
10000
Wavelength (Å)

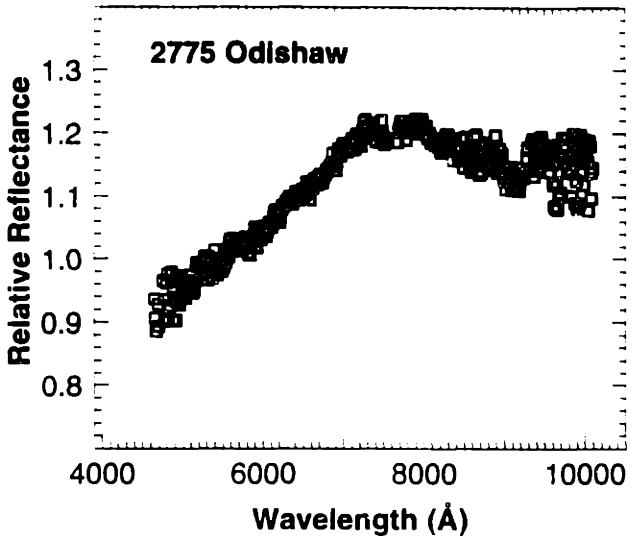
2775 Odishaw
Relative Reflectance
1.3
1.2
1.1
1.0
0.9
0.8
4000
6000
8000
10000
Wavelength (Å)

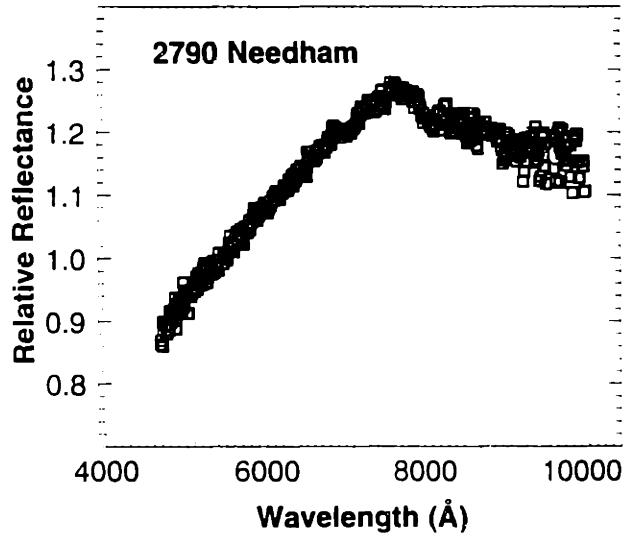
2790 Needham
Relative Reflectance
1.3
1.2
1.1
1.0
0.9
0.8
4000
6000
8000
10000
Wavelength (Å)

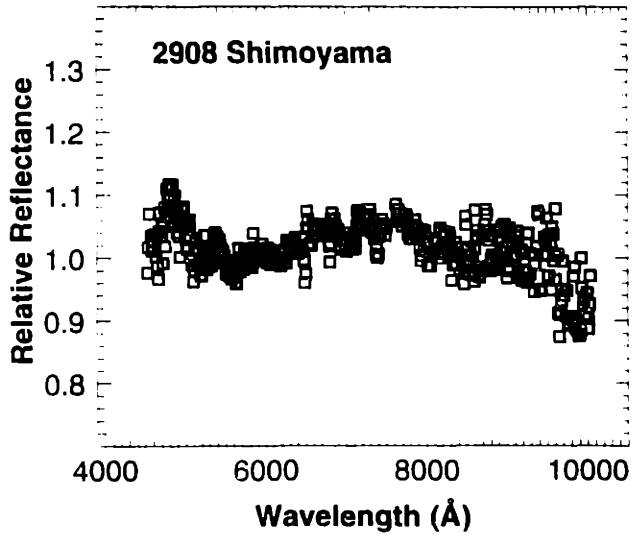
2908 Shimoyama
Relative Reflectance
1.3
1.2
1.1
1.0
0.9
0.8
4000
6000
8000
10000
Wavelength (Å)

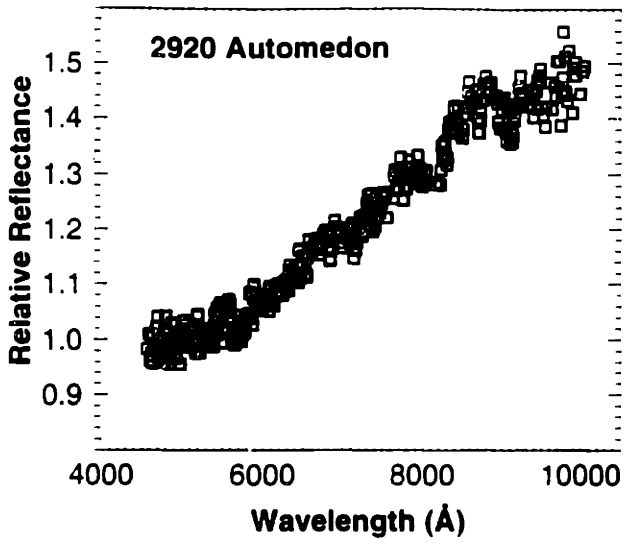
2920 Automedon
Relative Reflectance
1.5
1.4
1.3
1.2
1.1
1.0
0.9
4000
6000
8000
10000
Wavelength (Å)

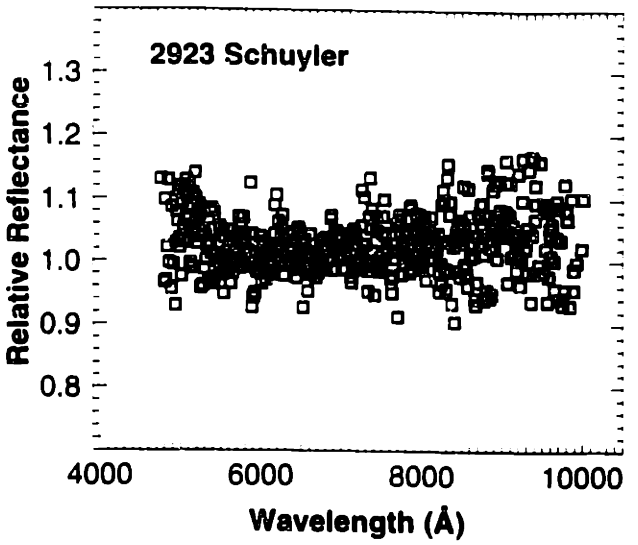
2923 Schuyler
Relative Reflectance
1.3
1.2
1.1
1.0
0.9
0.8
4000
6000
8000
10000
Wavelength (Å)

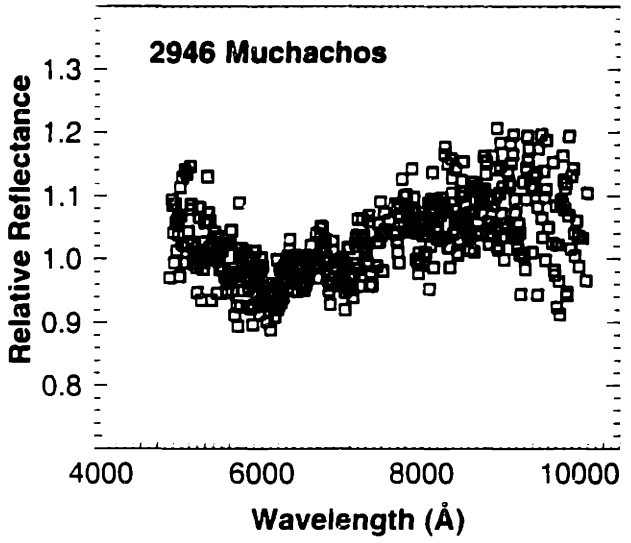
2946 Muchachos
Relative Reflectance
1.3
1.2
1.1
1.0
0.9
0.8
4000
6000
8000
10000
Wavelength (Å)

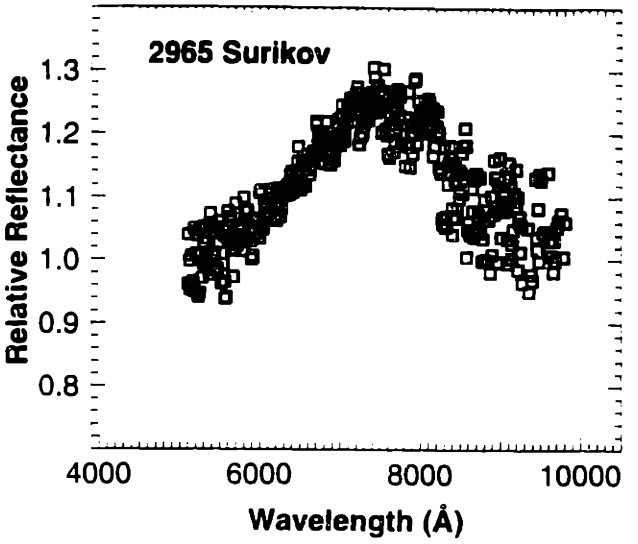
2965 Surikov
Relative Reflectance
1.3
1.2
1.1
1.0
0.9
0.8
4000
6000
8000
10000
Wavelength (Å)

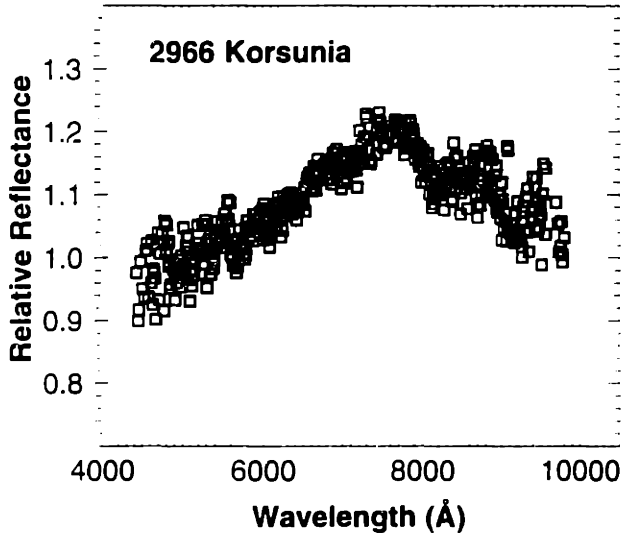
2966 Korsunia
Relative Reflectance
1.3
1.2
1.1
1.0
0.9
0.8
4000
6000
8000
10000
Wavelength (Å)

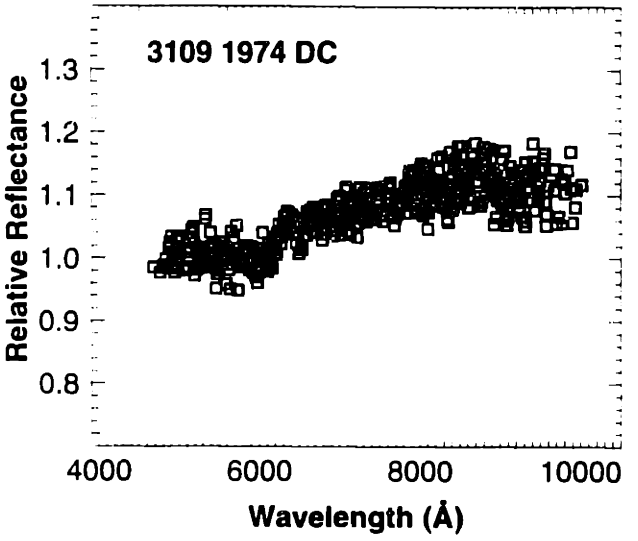
3109 1974 DC
Relative Reflectance
1.3
1.2
1.1
1.0
0.9
0.8
4000
6000
8000
10000
Wavelength (Å)

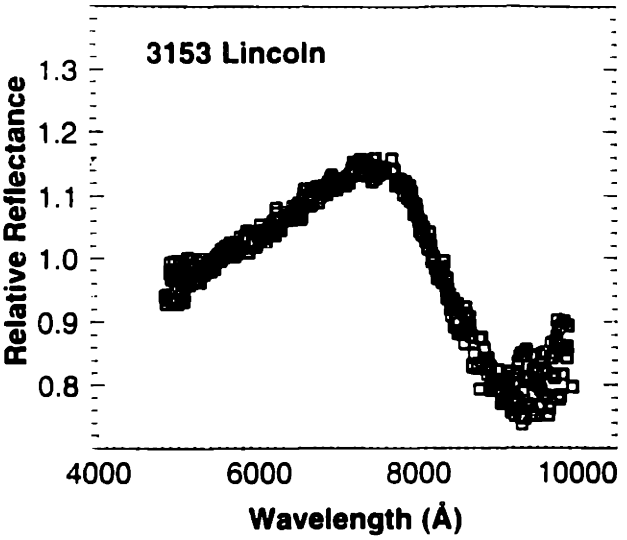
3153 Lincoln
Relative Reflectance
1.3
1.2
1.1
1.0
0.9
0.8
4000
6000
8000
10000
Wavelength (Å)

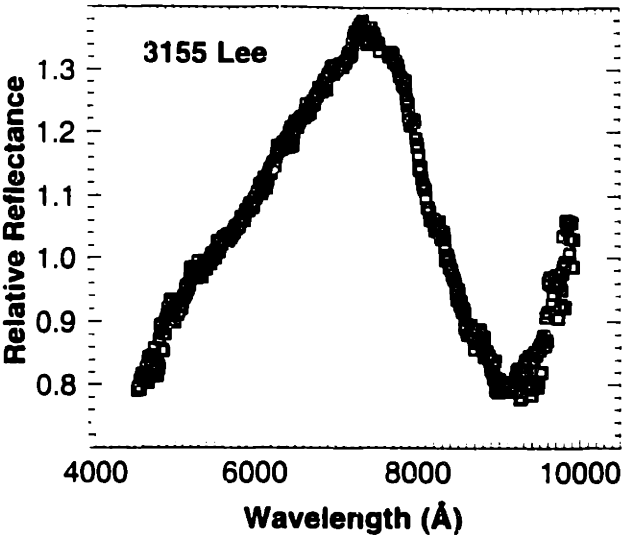
3155 Lee
Relative Reflectance
1.3
1.2
1.1
1.0
0.9
0.8
4000
6000
8000
10000
Wavelength (Å)

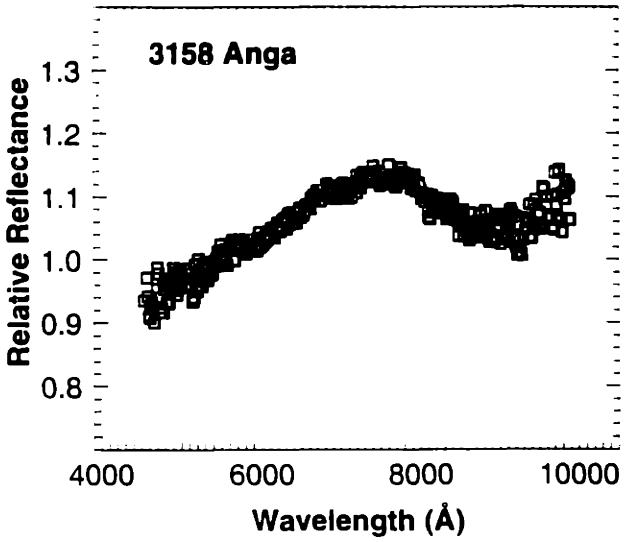
3158 Anga
Relative Reflectance
1.3
1.2
1.1
1.0
0.9
0.8
4000
6000
8000
10000
Wavelength (Å)

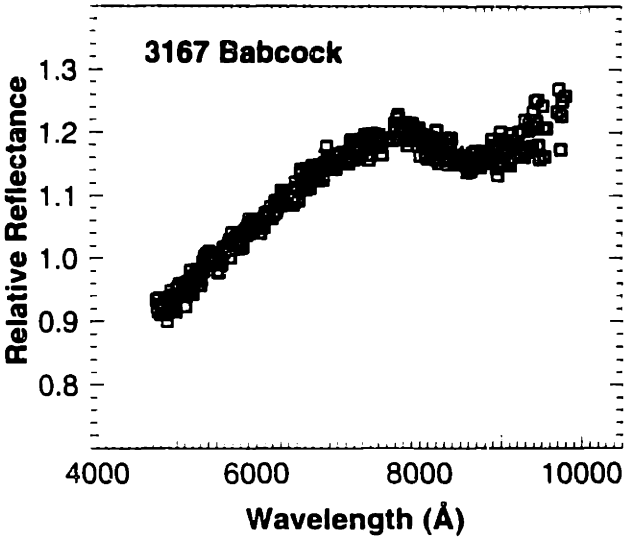
3167 Babcock
Relative Reflectance
1.3
1.2
1.1
1.0
0.9
0.8
4000
6000
8000
10000
Wavelength (Å)

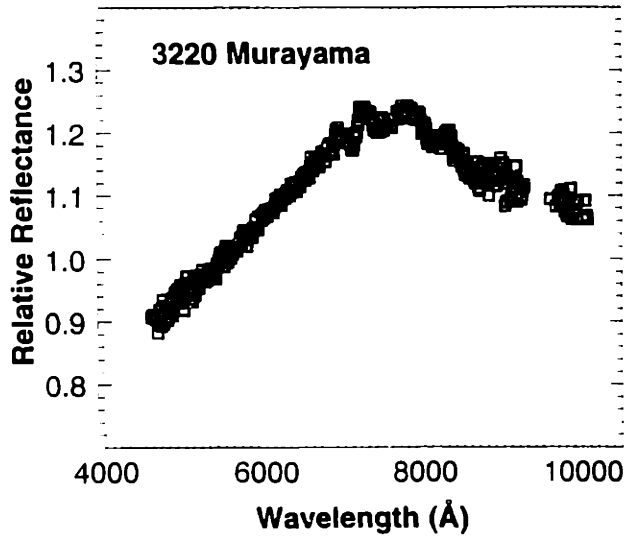
3220 Murayama
Relative Reflectance
1.3
1.2
1.1
1.0
0.9
0.8
4000
6000
8000
10000
Wavelength (Å)

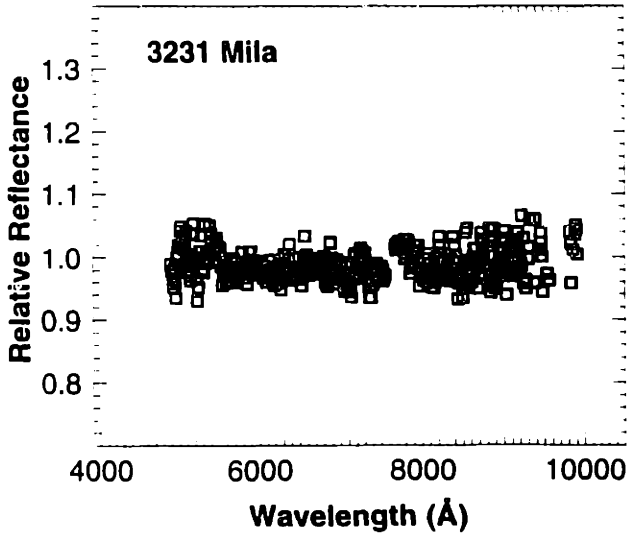
3231 Mila
Relative Reflectance
1.3
1.2
1.1
1.0
0.9
0.8
4000
6000
8000
10000
Wavelength (Å)

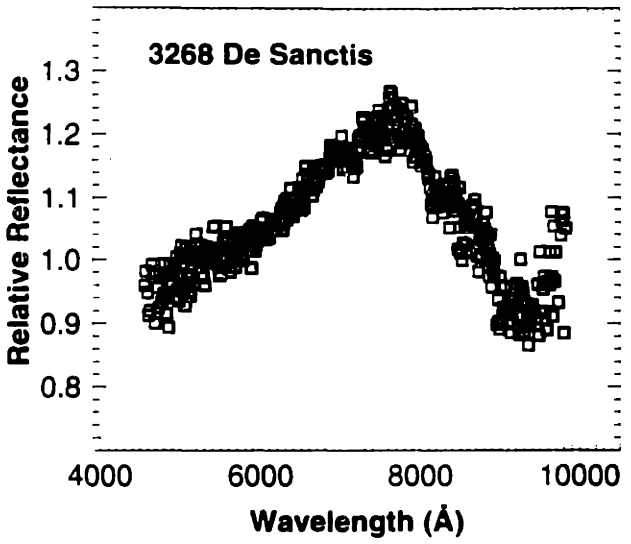
3268 De Sanctis
Relative Reflectance
1.3
1.2
1.1
1.0
0.9
0.8
4000
6000
8000
10000
Wavelength (Å)

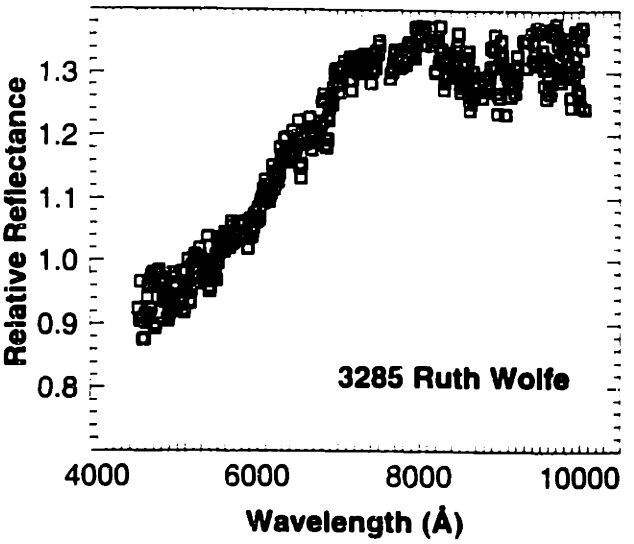
3285 Ruth Wolfe
Relative Reflectance
1.3
1.2
1.1
1.0
0.9
0.8
4000
6000
8000
10000
Wavelength (Å)

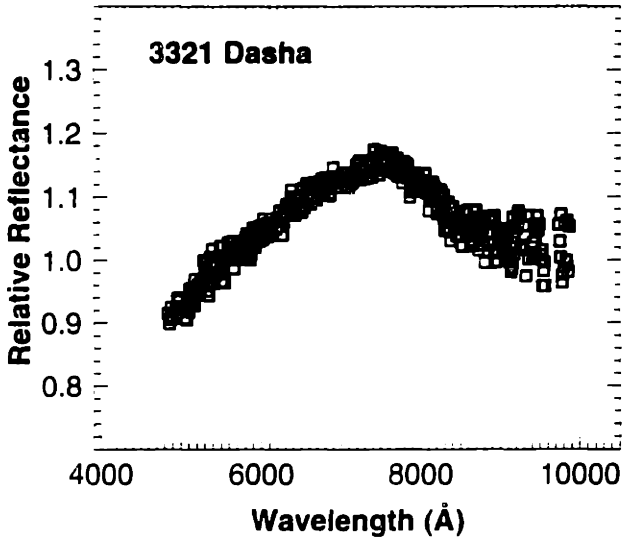
3321 Dasha
Relative Reflectance
1.3
1.2
1.1
1.0
0.9
0.8
4000
6000
8000
10000
Wavelength (Å)

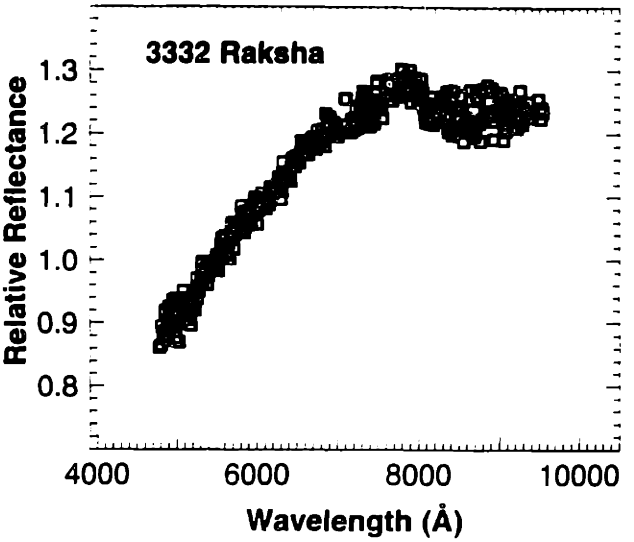
3332 Raksha
Relative Reflectance
1.3
1.2
1.1
1.0
0.9
0.8
4000
6000
8000
10000
Wavelength (Å)

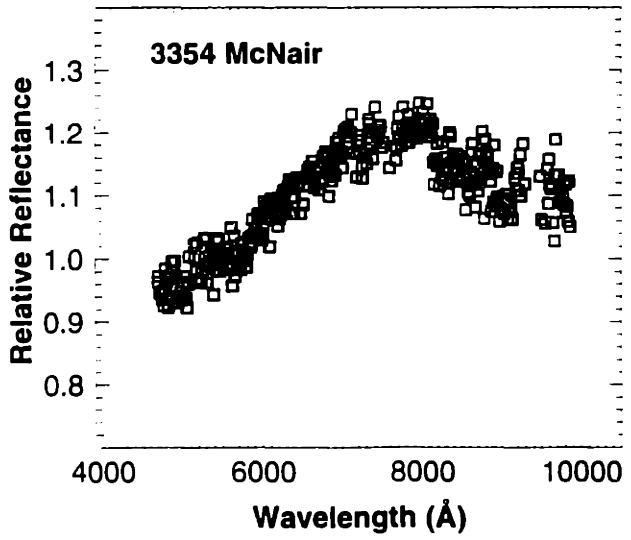
3354 McNair
Relative Reflectance
1.3
1.2
1.1
1.0
0.9
0.8
4000
6000
8000
10000
Wavelength (Å)

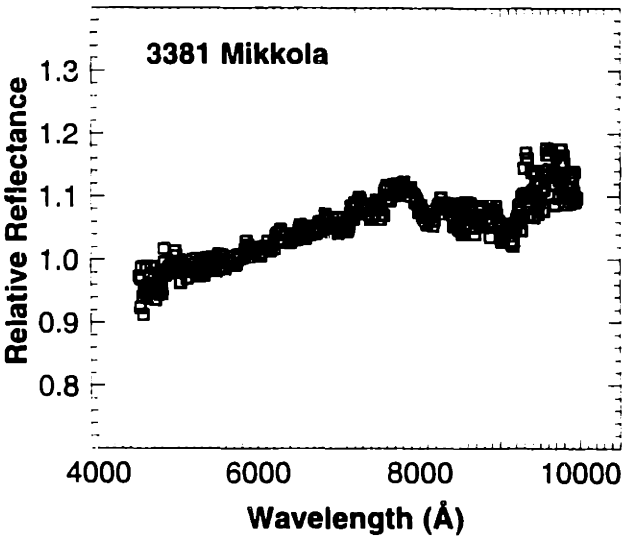
3381 Mikkola
Relative Reflectance
1.3
1.2
1.1
1.0
0.9
0.8
4000
6000
8000
10000
Wavelength (Å)

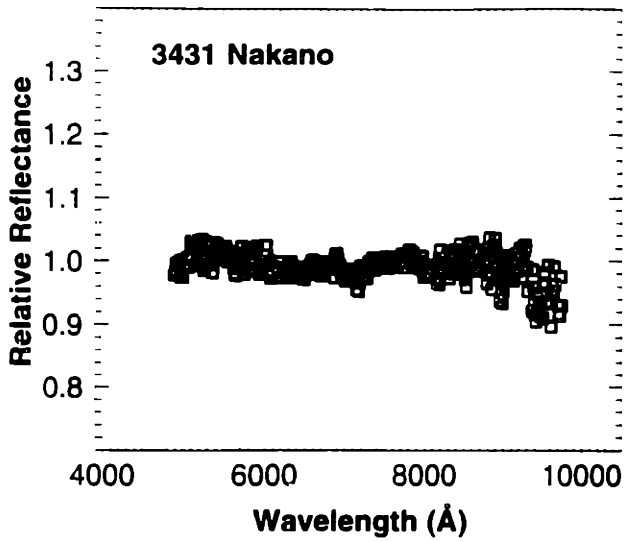
3431 Nakano
Relative Reflectance
1.3
1.2
1.1
1.0
0.9
0.8
4000
6000
8000
10000
Wavelength (Å)

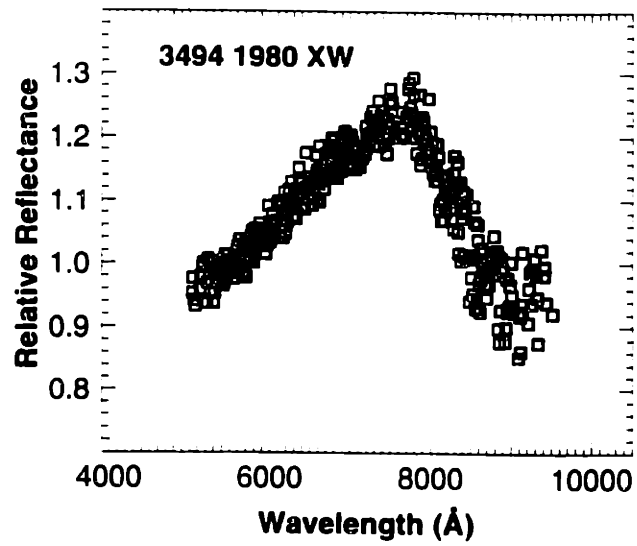
3494 1980 XW
Relative Reflectance
1.3
1.2
1.1
1.0
0.9
0.8
4000
6000
8000
10000
Wavelength (Å)

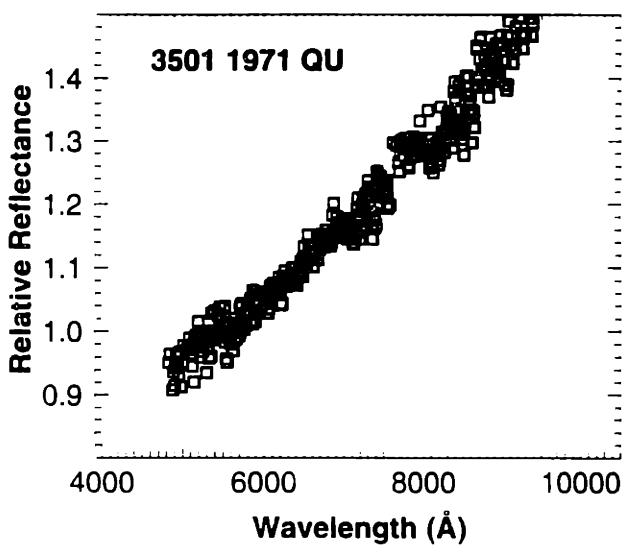
3501 1971 QU
Relative Reflectance
1.4
1.3
1.2
1.1
1.0
0.9
4000
6000
8000
10000
Wavelength (Å)

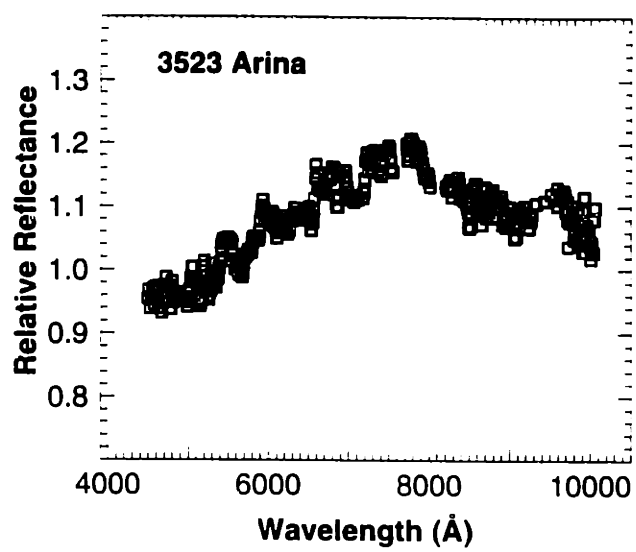
3523 Arina
Relative Reflectance
1.3
1.2
1.1
1.0
0.9
0.8
4000
6000
8000
10000
Wavelength (Å)

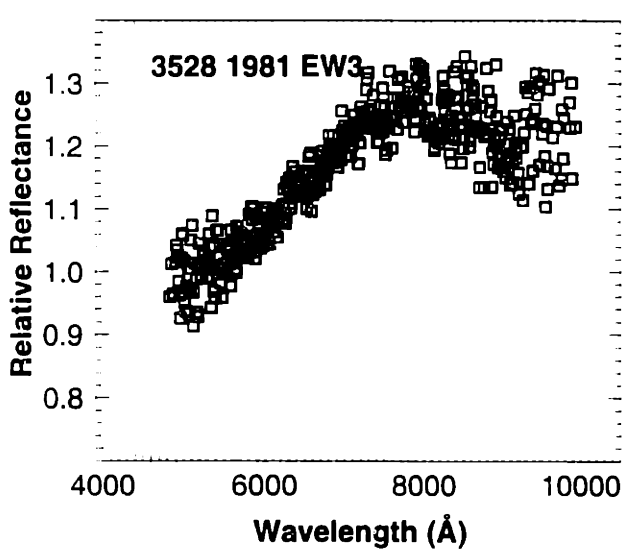
3528 1981 EW3
Relative Reflectance
1.3
1.2
1.1
1.0
0.9
0.8
4000
6000
8000
10000
Wavelength (Å)

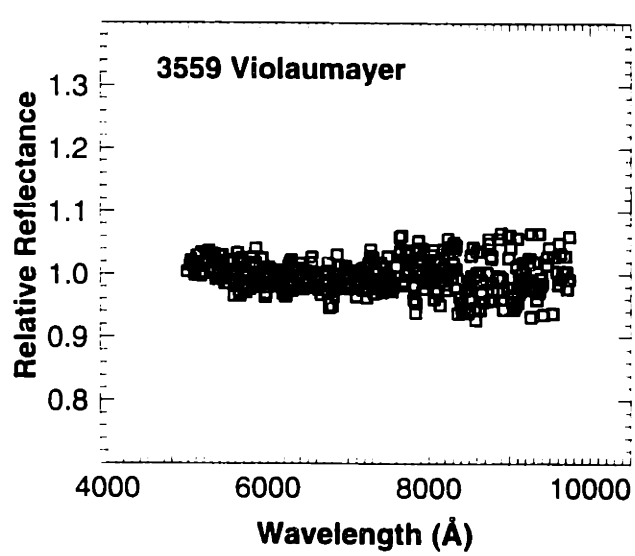
3559 Violaumayer
Relative Reflectance
1.3
1.2
1.1
1.0
0.9
0.8
4000
6000
8000
10000
Wavelength (Å)

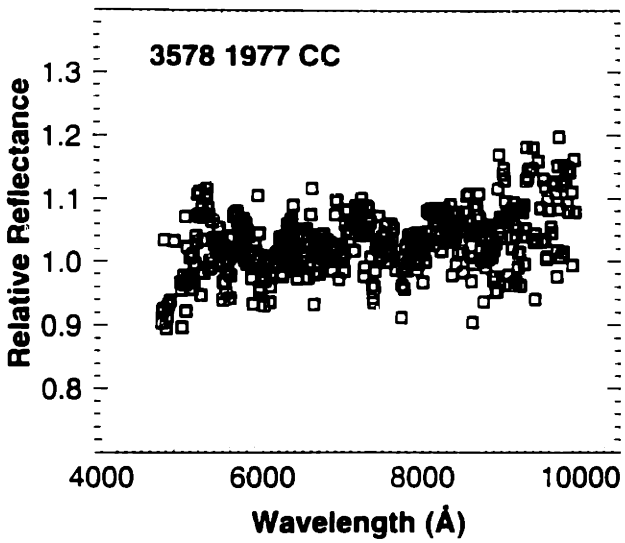
3578 1977 CC
Relative Reflectance
1.3
1.2
1.1
1.0
0.9
0.8
4000
6000
8000
10000
Wavelength (Å)

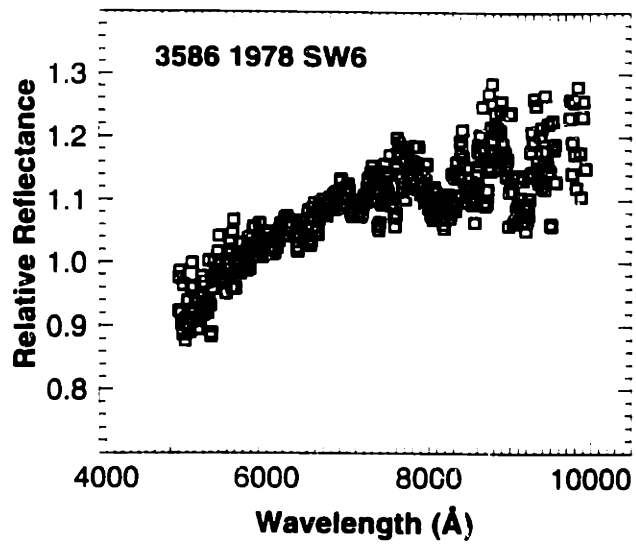
3586 1978 SW6
Relative Reflectance
1.3
1.2
1.1
1.0
0.9
0.8
4000
6000
8000
10000
Wavelength (Å)

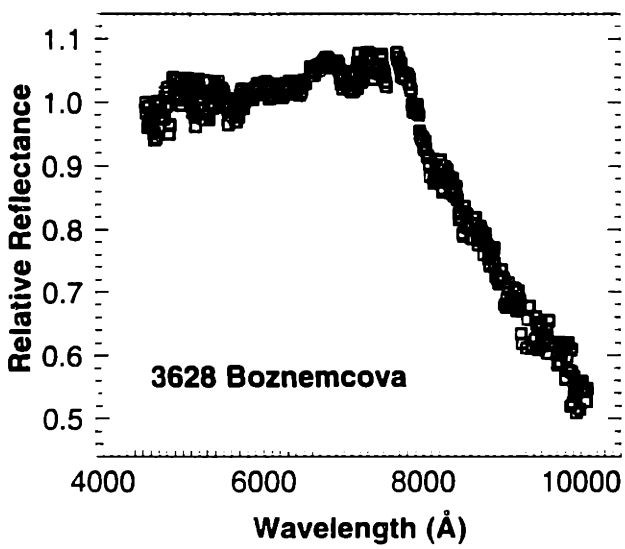
3628 Boznemcova
Relative Reflectance
1.1
1.0
0.9
0.8
0.7
0.6
0.5
4000
6000
8000
10000
Wavelength (Å)

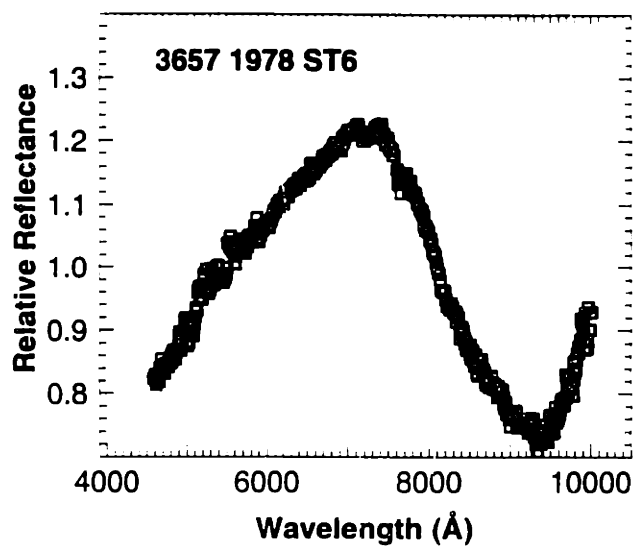
3657 1978 ST6
Relative Reflectance
1.3
1.2
1.1
1.0
0.9
0.8
4000
6000
8000
10000
Wavelength (Å)

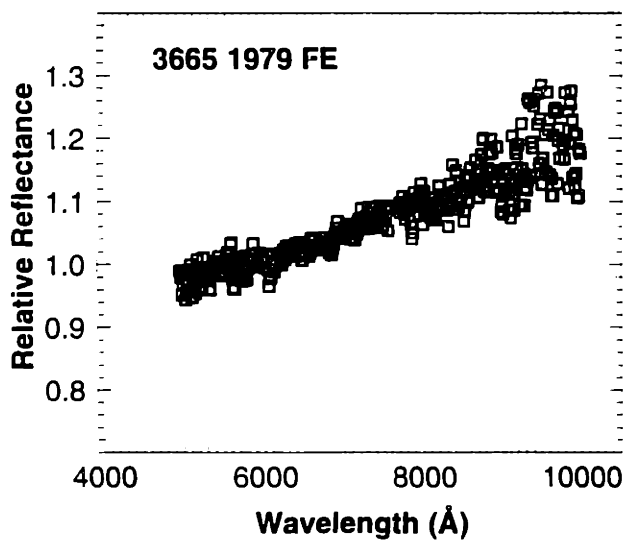
3665 1979 FE
Relative Reflectance
1.3
1.2
1.1
1.0
0.9
0.8
4000
6000
8000
10000
Wavelength (Å)

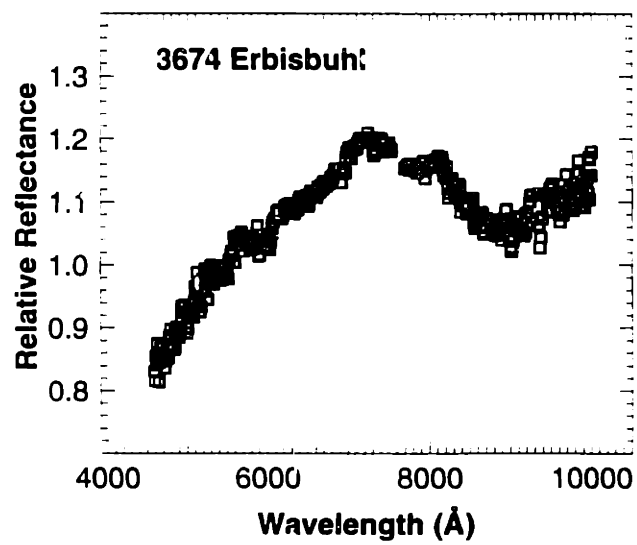
3674 Erbisbuhl
Relative Reflectance
1.3
1.2
1.1
1.0
0.9
0.8
4000
6000
8000
10000
Wavelength (Å)

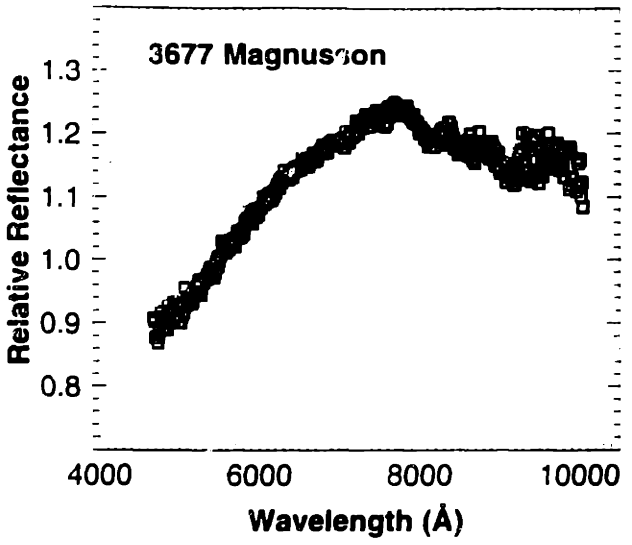
3677 Magnusson
Relative Reflectance
1.3
1.2
1.1
1.0
0.9
0.8
4000
6000
8000
10000
Wavelength (Å)

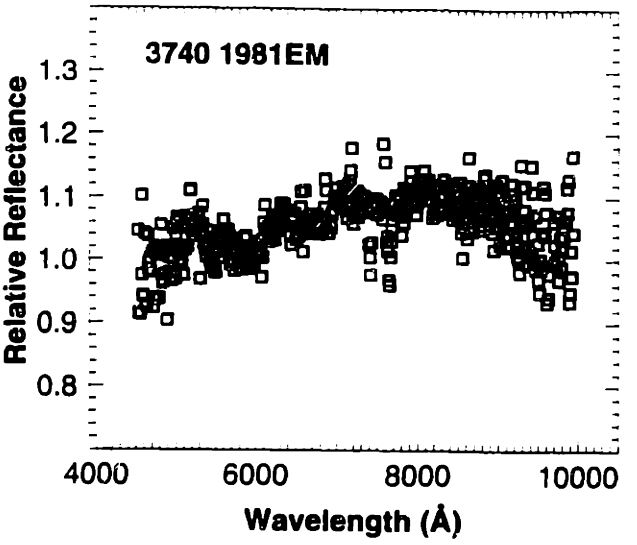
3740 1981EM
Relative Reflectance
1.3
1.2
1.1
1.0
0.9
0.8
4000
6000
8000
10000
Wavelength (Å)

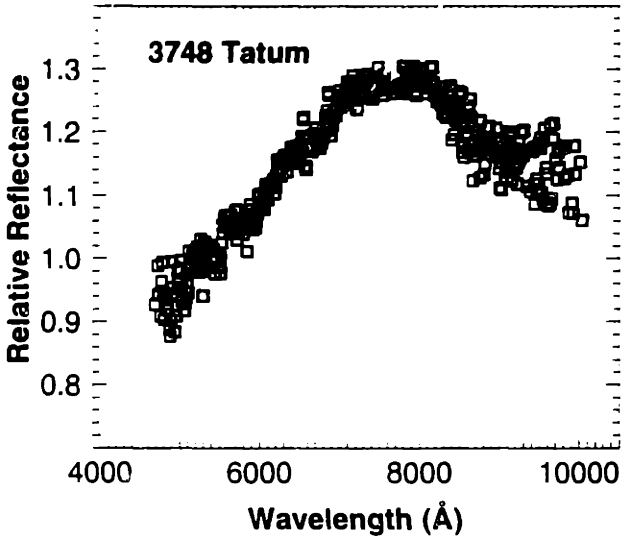
3748 Tatum
Relative Reflectance
1.3
1.2
1.1
1.0
0.9
0.8
4000
6000
8000
10000
Wavelength (Å)

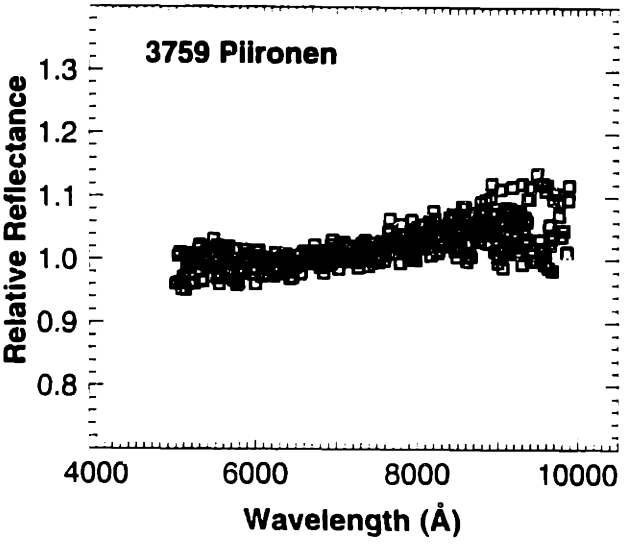
3759 Piironen
Relative Reflectance
1.3
1.2
1.1
1.0
0.9
0.8
4000
6000
8000
10000
Wavelength (Å)

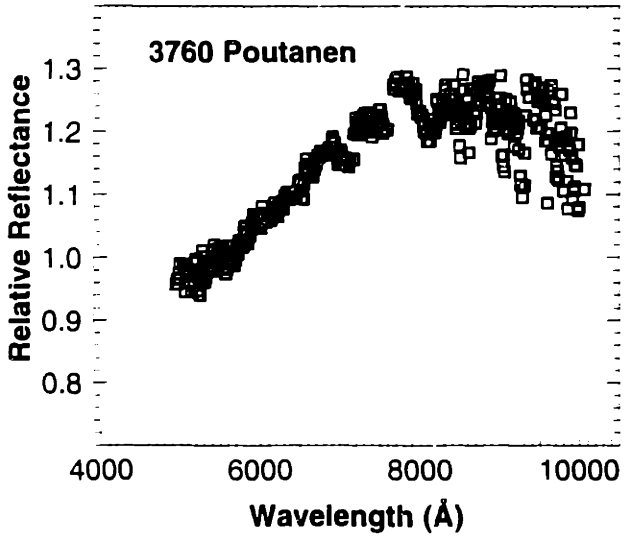
3760 Poutanen
Relative Reflectance
1.3
1.2
1.1
1.0
0.9
0.8
4000
6000
8000
10000
Wavelength (Å)

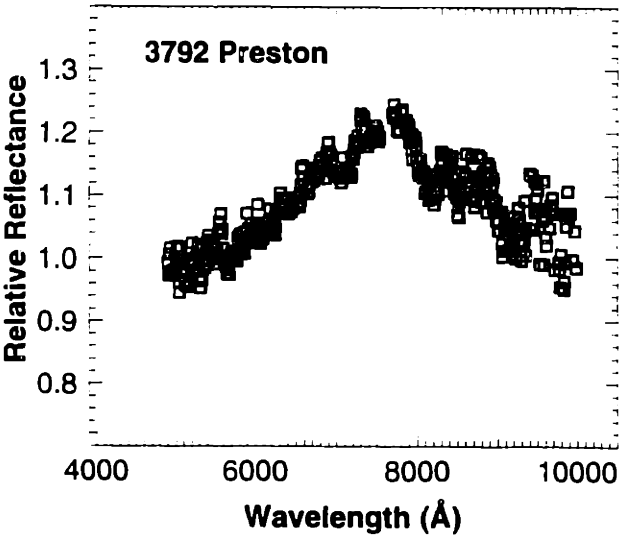
3792 Preston
Relative Reflectance
1.3
1.2
1.1
1.0
0.9
0.8
4000
6000
8000
10000
Wavelength (Å)

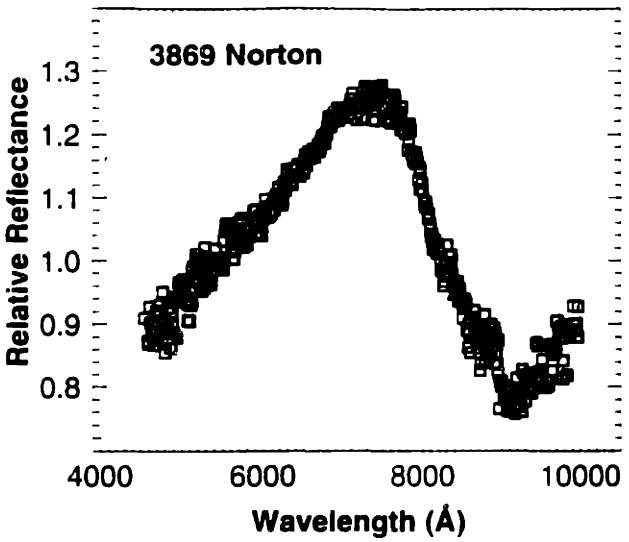
3869 Norton
Relative Reflectance
1.3
1.2
1.1
1.0
0.9
0.8
4000
6000
8000
10000
Wavelength (Å)

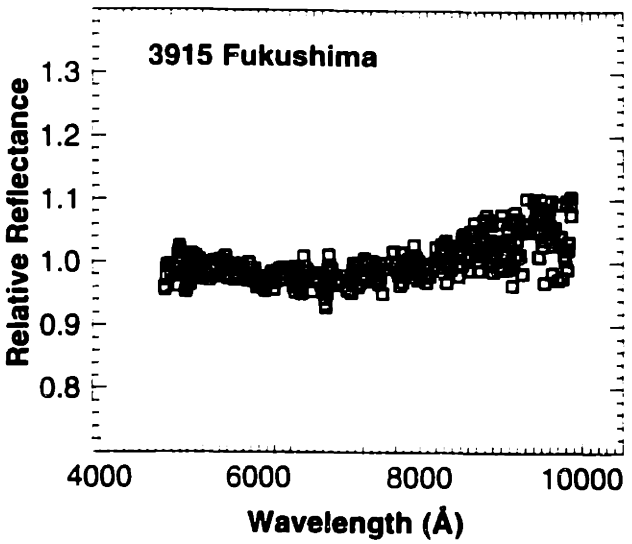
3915 Fukushima
Relative Reflectance
1.3
1.2
1.1
1.0
0.9
0.8
4000
6000
8000
10000
Wavelength (Å)

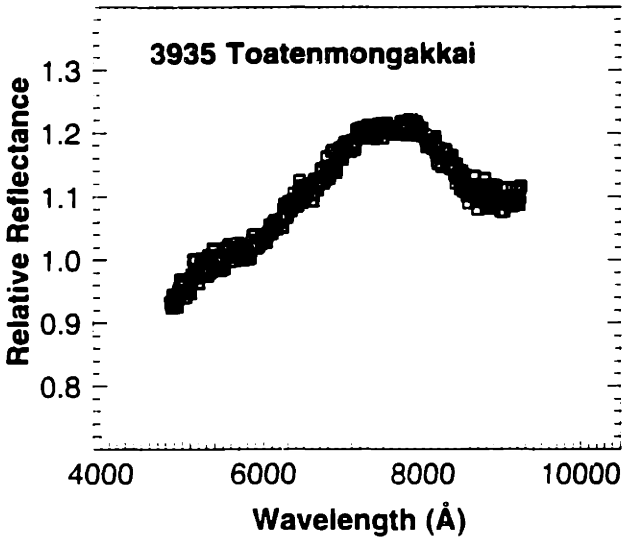
3935 Toatenmongakkai
Relative Reflectance
1.3
1.2
1.1
1.0
0.9
0.8
4000
6000
8000
10000
Wavelength (Å)

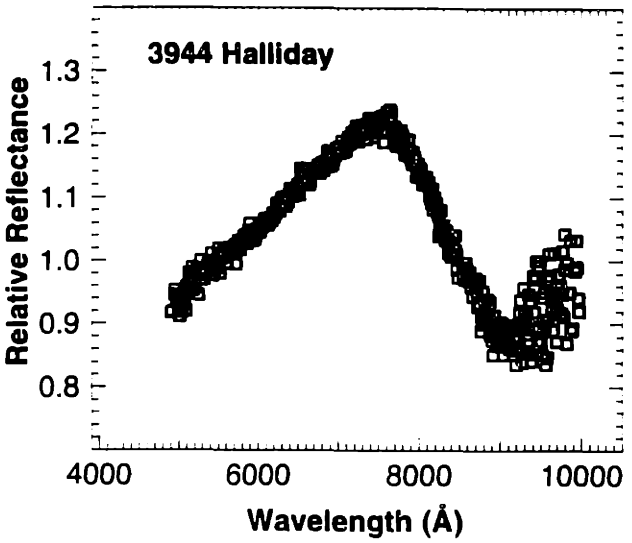
3944 Halliday
Relative Reflectance
1.3
1.2
1.1
1.0
0.9
0.8
4000
6000
8000
10000
Wavelength (Å)

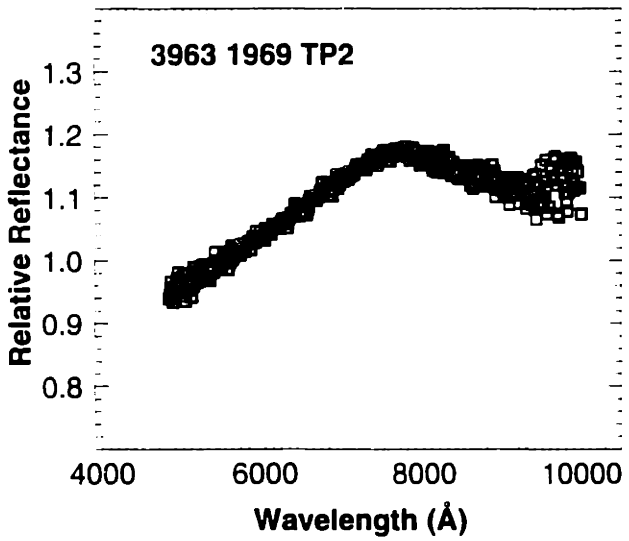
3963 1969 TP2
Relative Reflectance
1.3
1.2
1.1
1.0
0.9
0.8
4000
6000
8000
10000
Wavelength (Å)

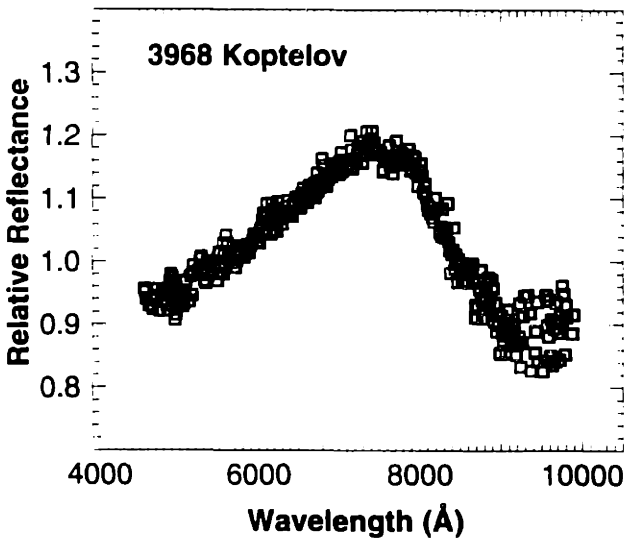
3968 Koptelov
Relative Reflectance
1.3
1.2
1.1
1.0
0.9
0.8
4000
6000
8000
10000
Wavelength (Å)

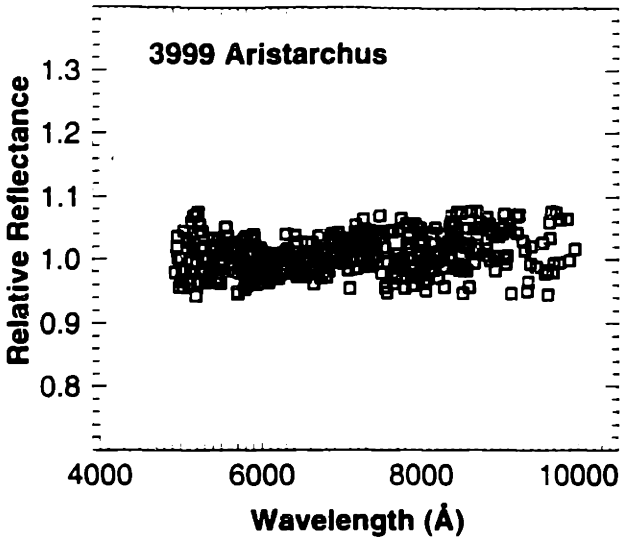
3999 Aristarchus
Relative Reflectance
1.3
1.2
1.1
1.0
0.9
0.8
4000
6000
8000
10000
Wavelength (Å)

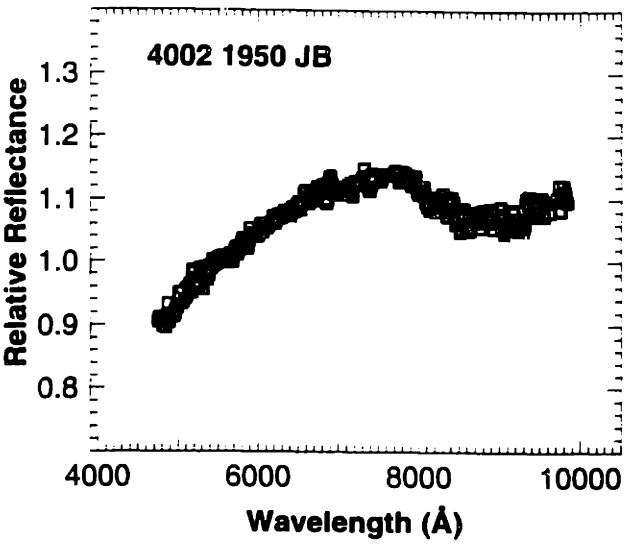
4002 1950 JB
Relative Reflectance
1.3
1.2
1.1
1.0
0.9
0.8
4000
6000
8000
10000
Wavelength (Å)

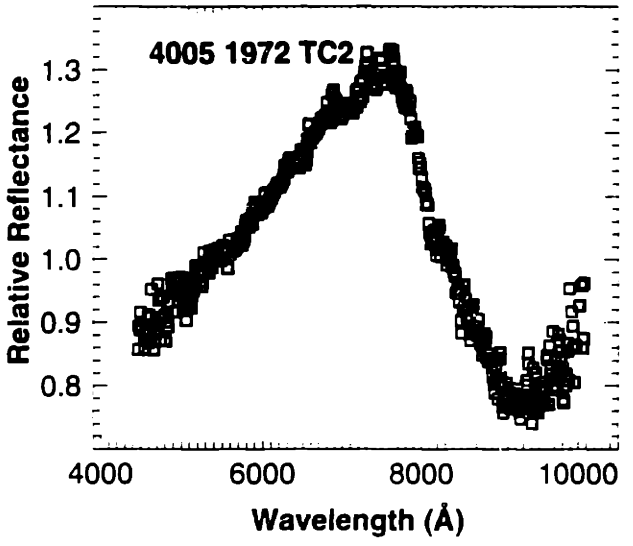
4005 1972 TC2
Relative Reflectance
1.3
1.2
1.1
1.0
0.9
0.8
4000
6000
8000
10000
Wavelength (Å)

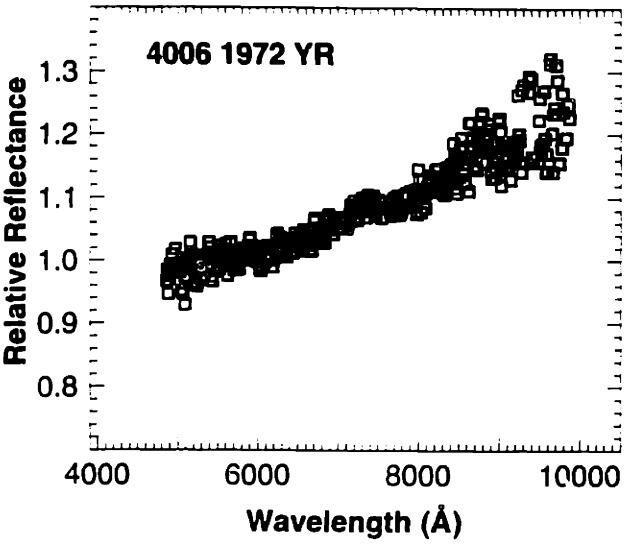
4006 1972 YR
Relative Reflectance
1.3
1.2
1.1
1.0
0.9
0.8
4000
6000
8000
10000
Wavelength (Å)

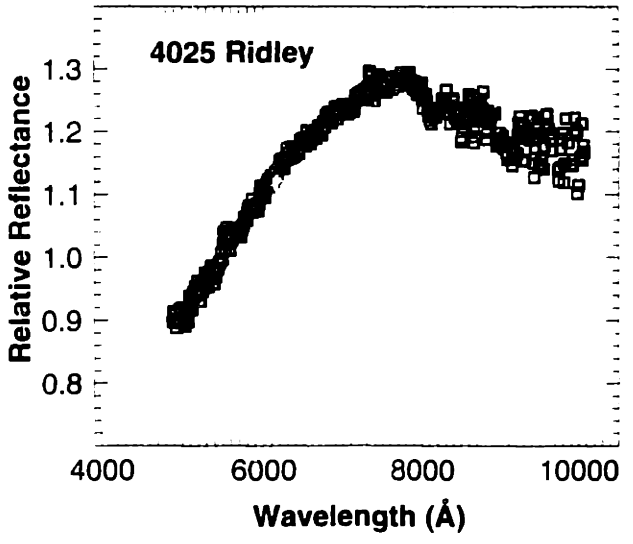
4025 Ridley
Relative Reflectance
1.3
1.2
1.1
1.0
0.9
0.8
4000
6000
8000
10000
Wavelength (Å)

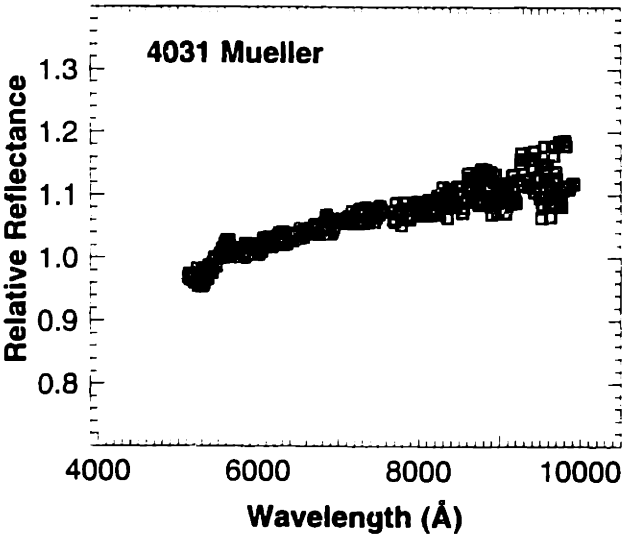
4031 Mueller
Relative Reflectance
1.3
1.2
1.1
1.0
0.9
0.8
4000
6000
8000
10000
Wavelength (Å)

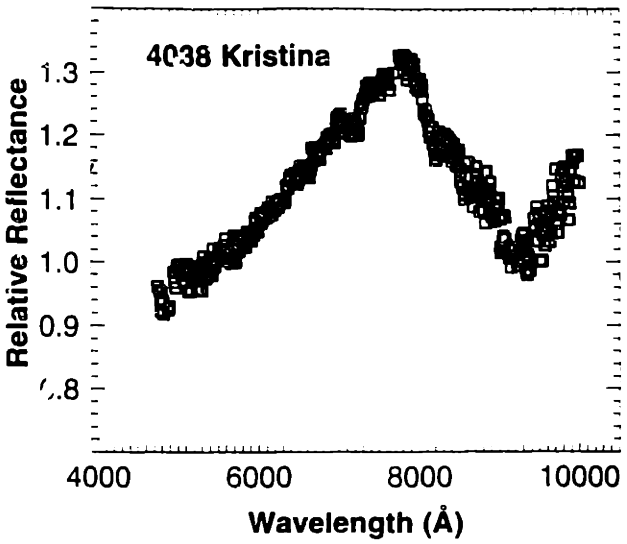
4038 Kristina
Relative Reflectance
1.3
1.2
1.1
1.0
0.9
0.8
4000
6000
8000
10000
Wavelength (Å)

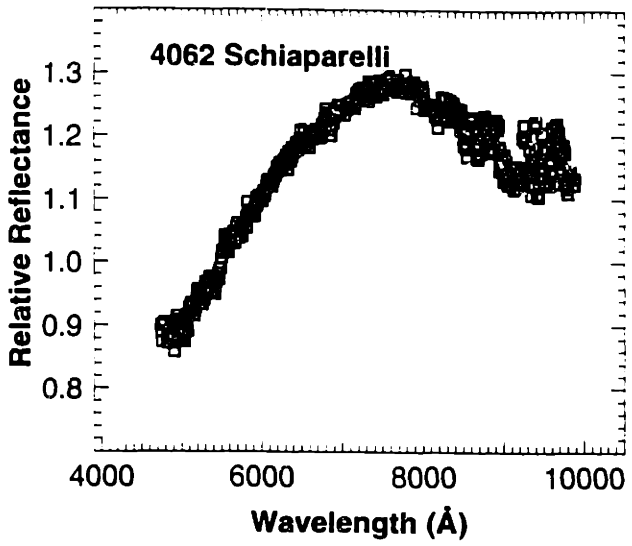
4062 Schiaparelli
Relative Reflectance
1.3
1.2
1.1
1.0
0.9
0.8
4000
6000
8000
10000
Wavelength (Å)

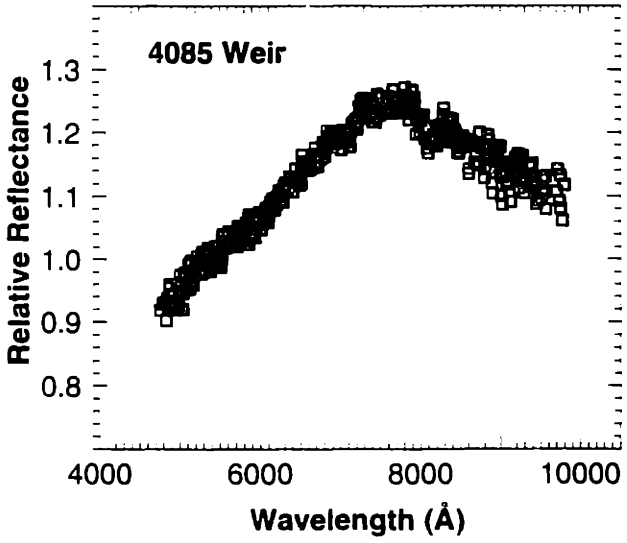
4085 Weir
Relative Reflectance
1.3
1.2
1.1
1.0
0.9
0.8
4000
6000
8000
10000
Wavelength (Å)

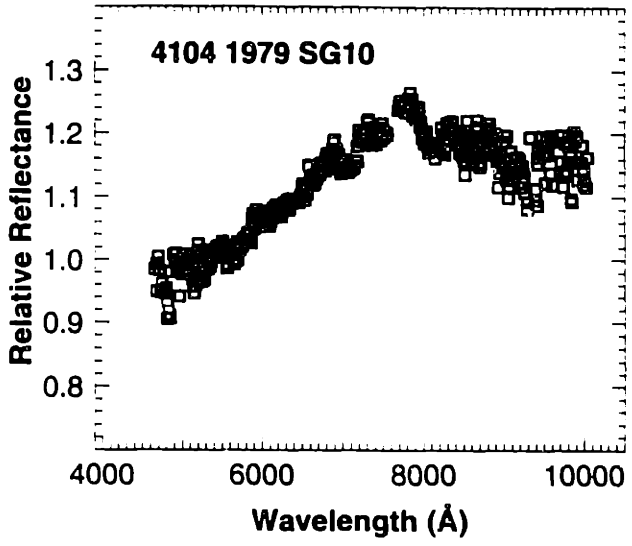
4104 1979 SG10
Relative Reflectance
1.3
1.2
1.1
1.0
0.9
0.8
4000
6000
8000
10000
Wavelength (Å)

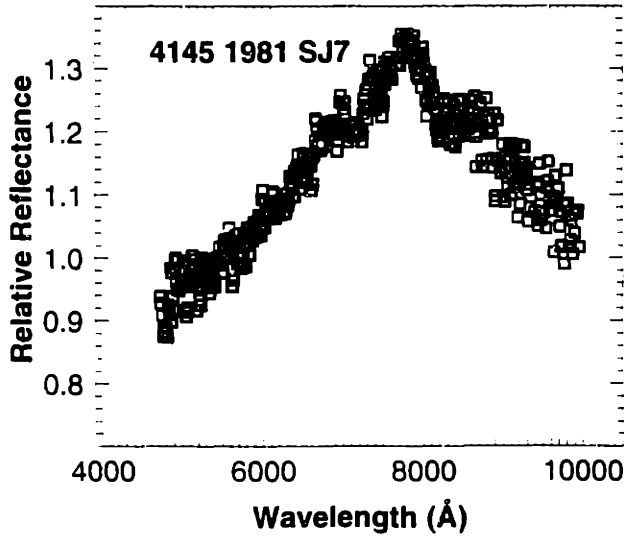
4145 1981 SJ7
Relative Reflectance
1.3
1.2
1.1
1.0
0.9
0.8
4000
6000
8000
10000
Wavelength (Å)

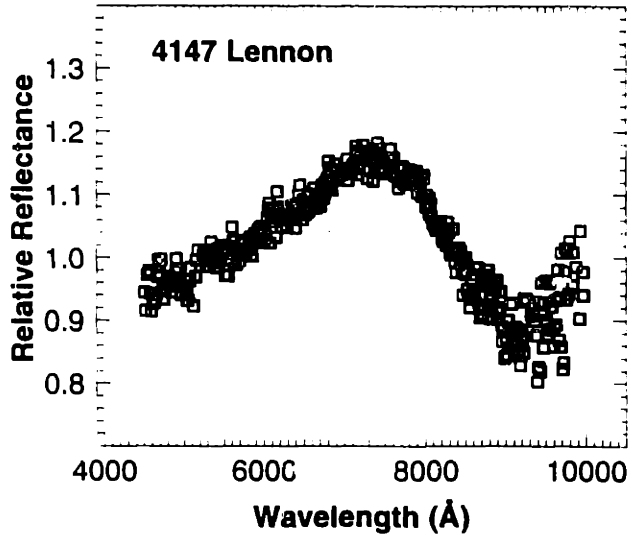
4147 Lennon
Relative Reflectance
1.3
1.2
1.1
1.0
0.9
0.8
4000
6000
8000
10000
Wavelength (Å)

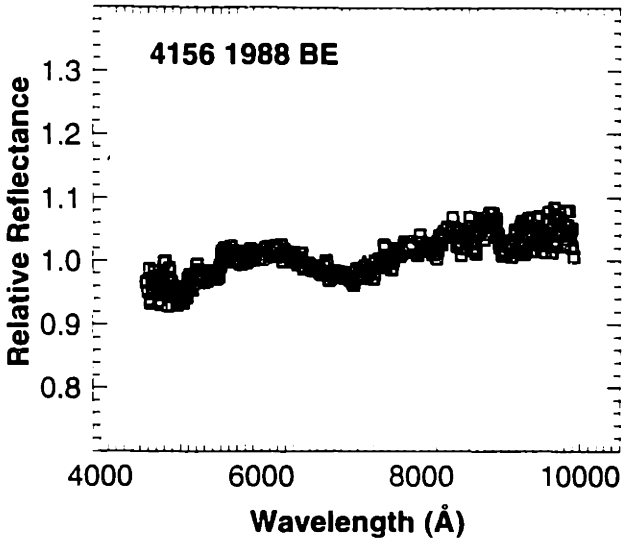
4156 1988 BE
Relative Reflectance
1.3
1.2
1.1
1.0
0.9
0.8
4000
6000
8000
10000
Wavelength (Å)

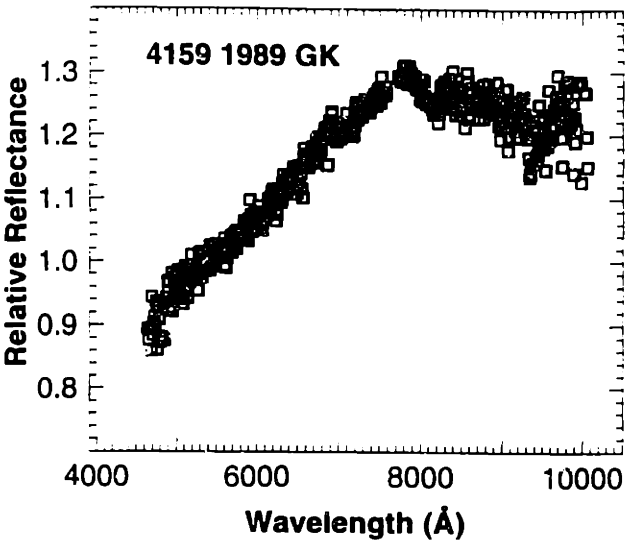
4159 1989 GK
Relative Reflectance
1.3
1.2
1.1
1.0
0.9
0.8
4000
6000
8000
10000
Wavelength (Å)

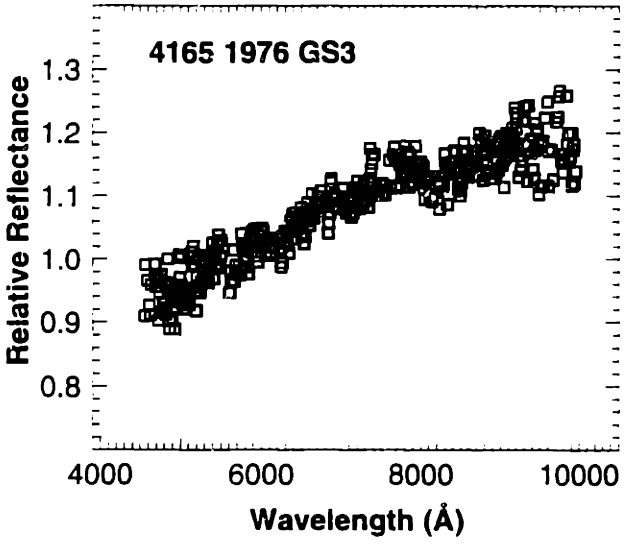
4165 1976 GS3
Relative Reflectance
1.3
1.2
1.1
1.0
0.9
0.8
4000
6000
8000
10000
Wavelength (Å)

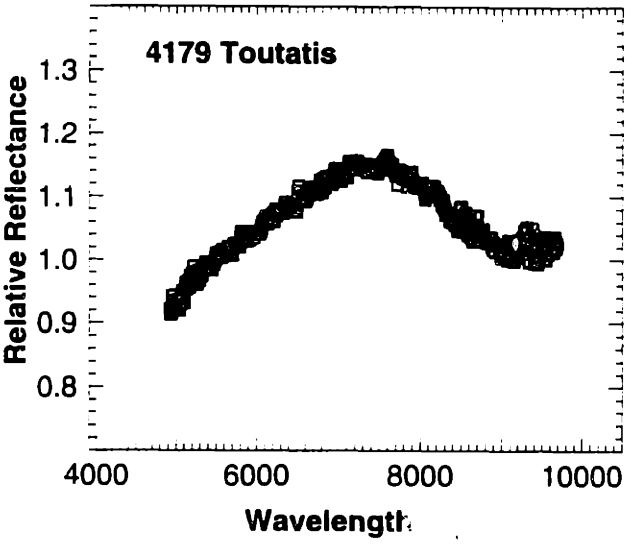
4179 Toutatis
Relative Reflectance
1.3
1.2
1.1
1.0
0.9
0.8
4000
6000
8000
10000
Wavelength

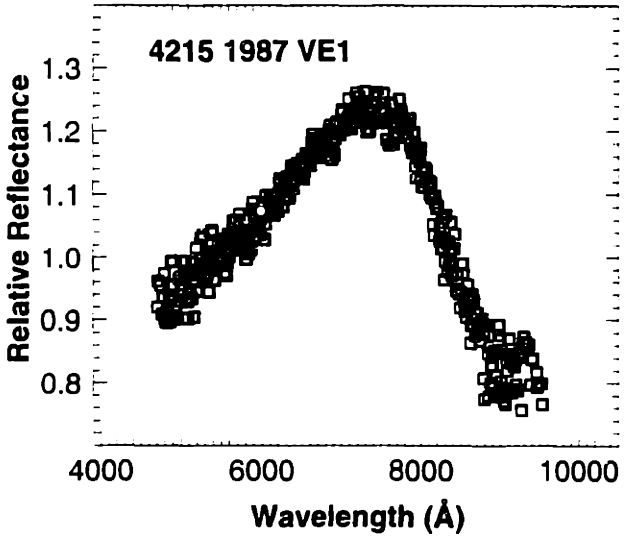
4215 1987 VE1
Relative Reflectance
1.3
1.2
1.1
1.0
0.9
0.8
4000
6000
8000
10000
Wavelength (Å)

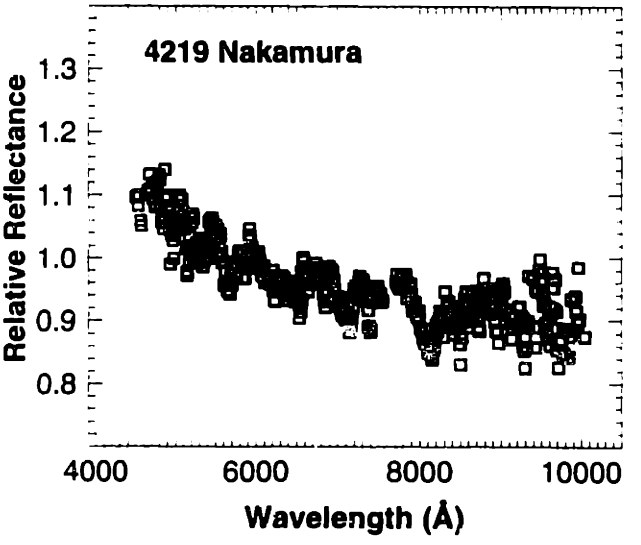
4219 Nakamura
Relative Reflectance
1.3
1.2
1.1
1.0
0.9
0.8
4000
6000
8000
10000
Wavelength (Å)

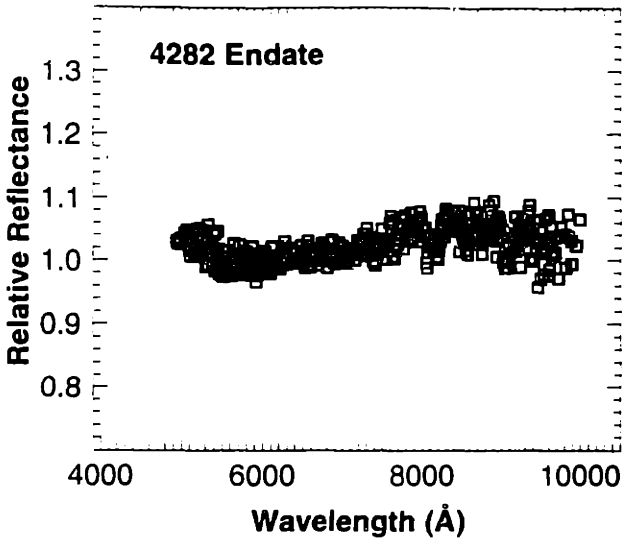
4282 Endate
Relative Reflectance
1.3
1.2
1.1
1.0
0.9
0.8
4000
6000
8000
10000
Wavelength (Å)

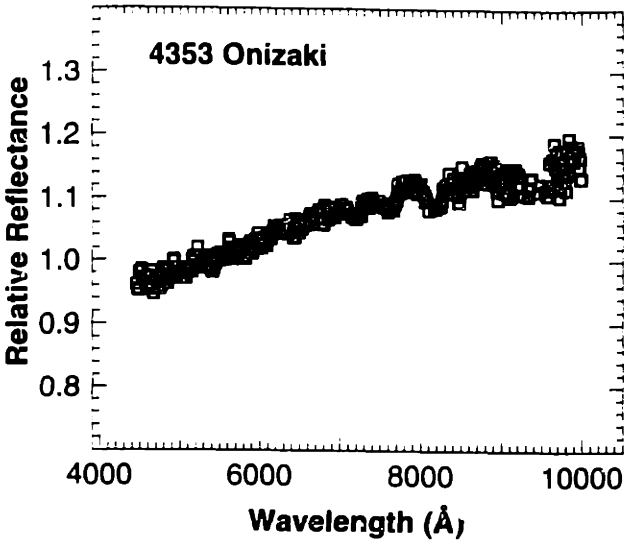
4353 Onizaki
Relative Reflectance
1.3
1.2
1.1
1.0
0.9
0.8
4000
6000
8000
10000
Wavelength (Å)

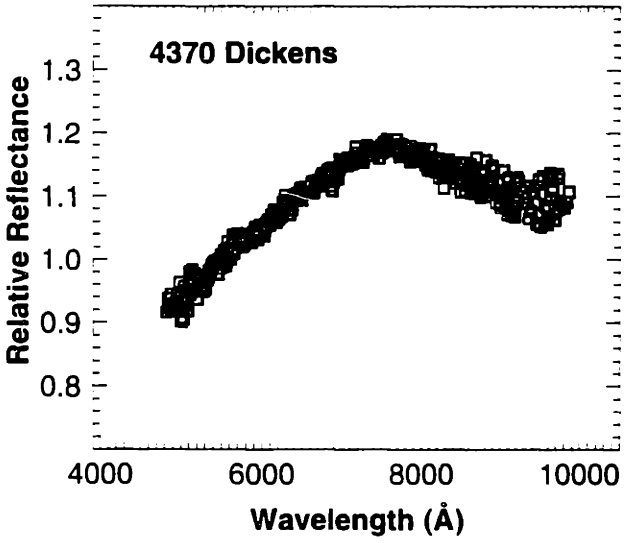
4370 Dickens
Relative Reflectance
1.3
1.2
1.1
1.0
0.9
0.8
4000
6000
8000
10000
Wavelength (Å)

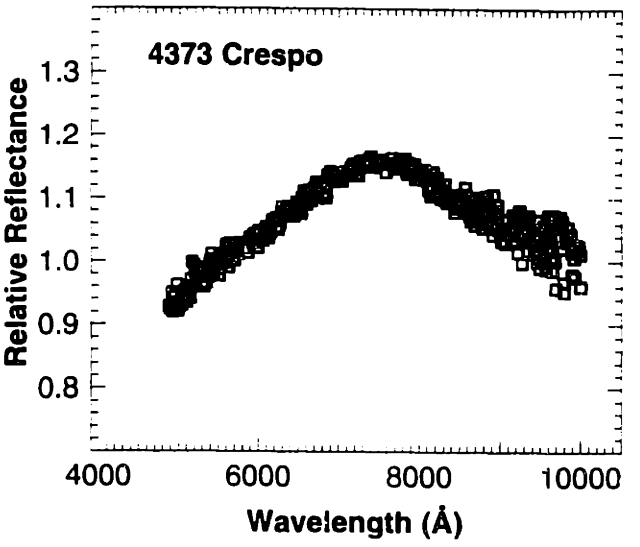
4373 Crespo
Relative Reflectance
1.3
1.2
1.1
1.0
0.9
0.8
4000
6000
8000
10000
Wavelength (Å)

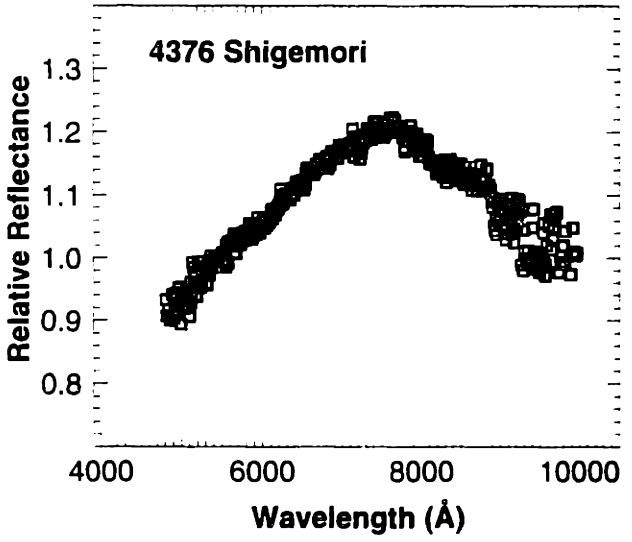
4376 Shigemori
Relative Reflectance
1.3
1.2
1.1
1.0
0.9
0.8
4000
6000
8000
10000
Wavelength (Å)

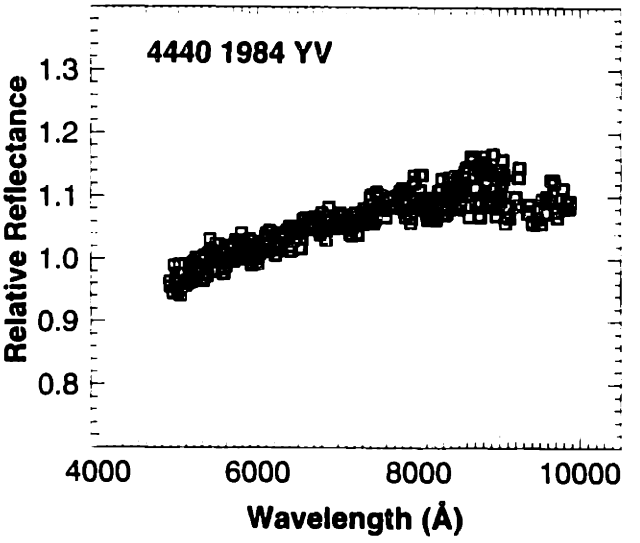
4440 1984 YV
Relative Reflectance
1.3
1.2
1.1
1.0
0.9
0.8
4000
6000
8000
10000
Wavelength (Å)

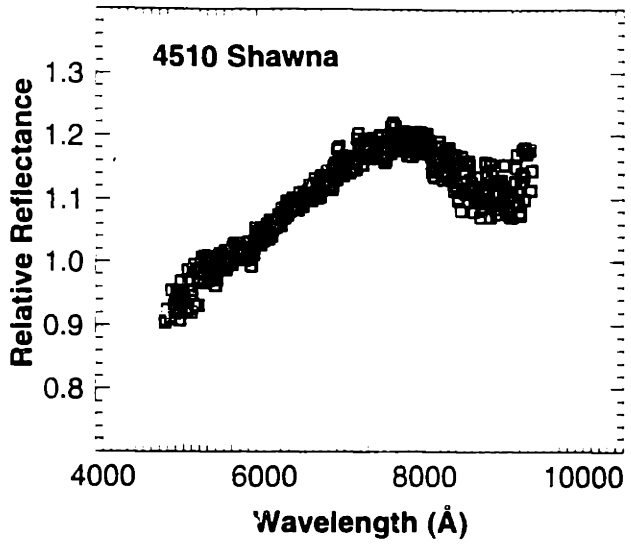
4510 Shawna
Relative Reflectance
1.3
1.2
1.1
1.0
0.9
0.8
4000
6000
8000
10000
Wavelength (Å)

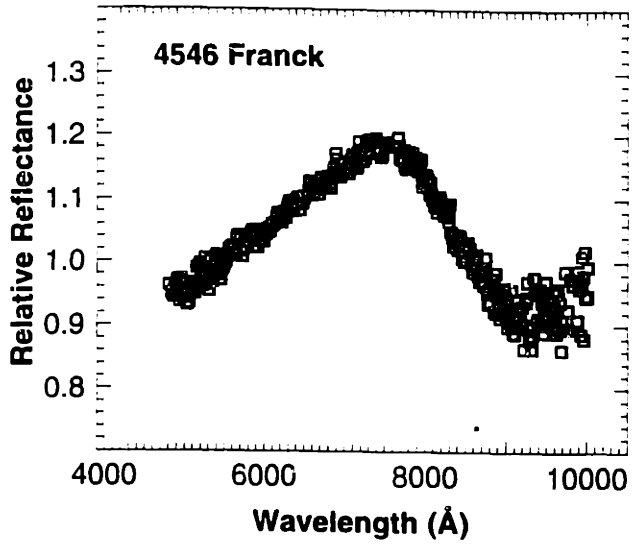
4546 Franck
Relative Reflectance
1.3
1.2
1.1
1.0
0.9
0.8
4000
6000
8000
10000
Wavelength (Å)

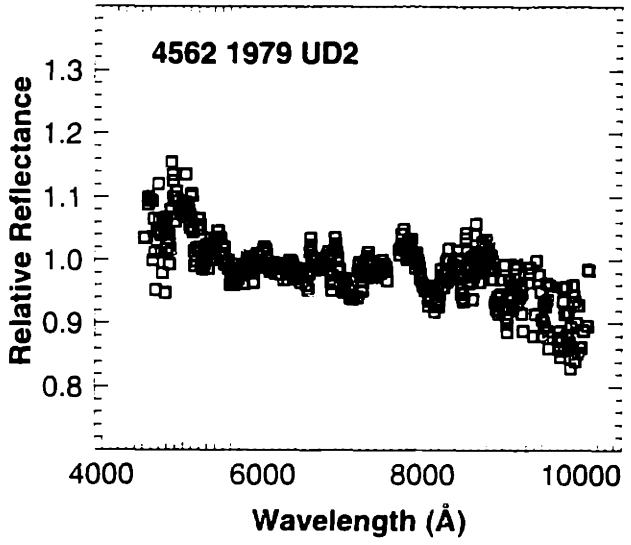
4562 1979 UD2
Relative Reflectance
1.3
1.2
1.1
1.0
0.9
0.8
4000
6000
8000
10000
Wavelength (Å)

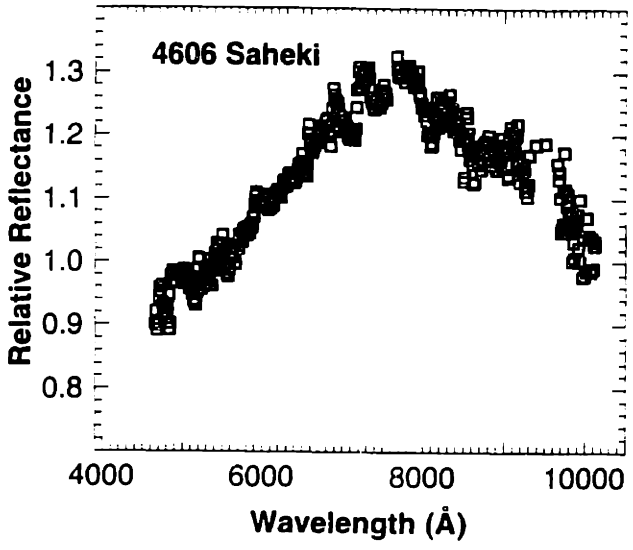
4606 Saheki
Relative Reflectance
1.3
1.2
1.1
1.0
0.9
0.8
4000
6000
8000
10000
Wavelength (Å)

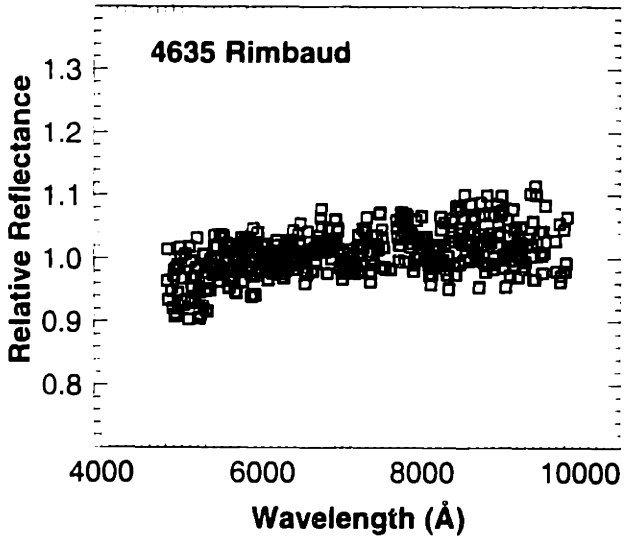
4635 Rimbaud
Relative Reflectance
1.3
1.2
1.1
1.0
0.9
0.8
4000
6000
8000
10000
Wavelength (Å)

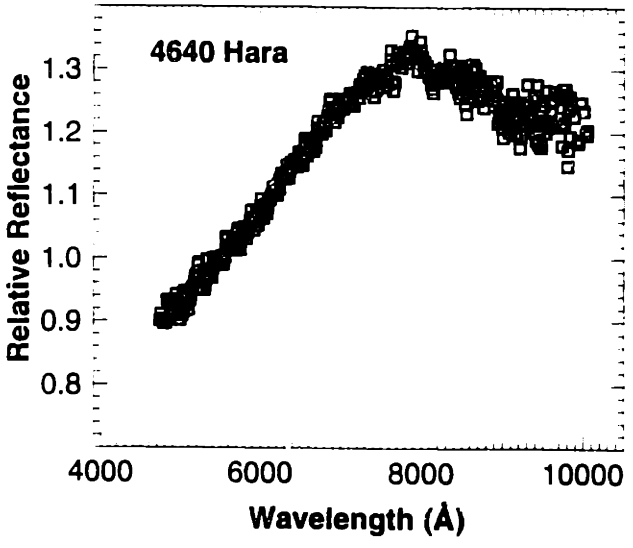
4640 Hara
Relative Reflectance
1.3
1.2
1.1
1.0
0.9
0.8
4000
6000
8000
10000
Wavelength (Å)

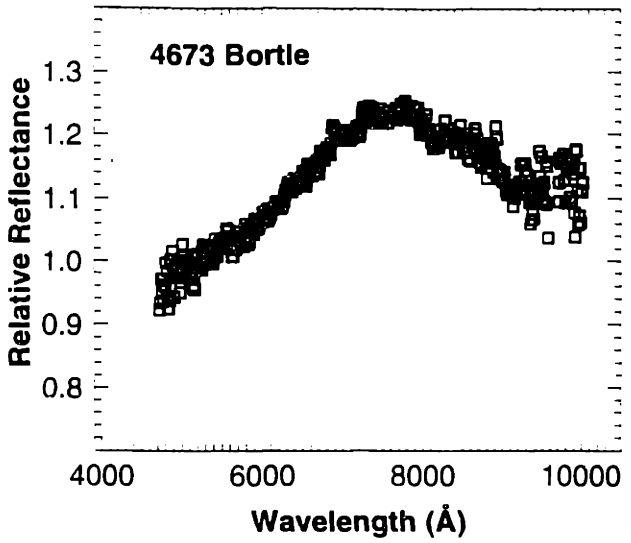
4673 Bortle
Relative Reflectance
1.3
1.2
1.1
1.0
0.9
0.8
4000
6000
8000
10000
Wavelength (Å)

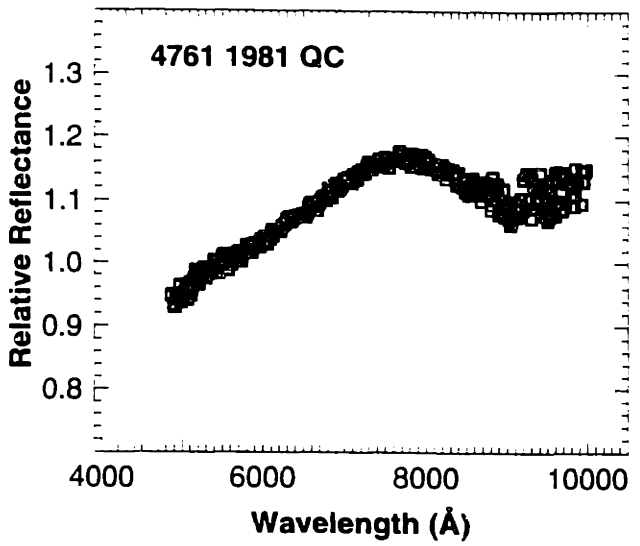
4761 1981 QC
Relative Reflectance
1.3
1.2
1.1
1.0
0.9
0.8
4000
6000
8000
10000
Wavelength (Å)

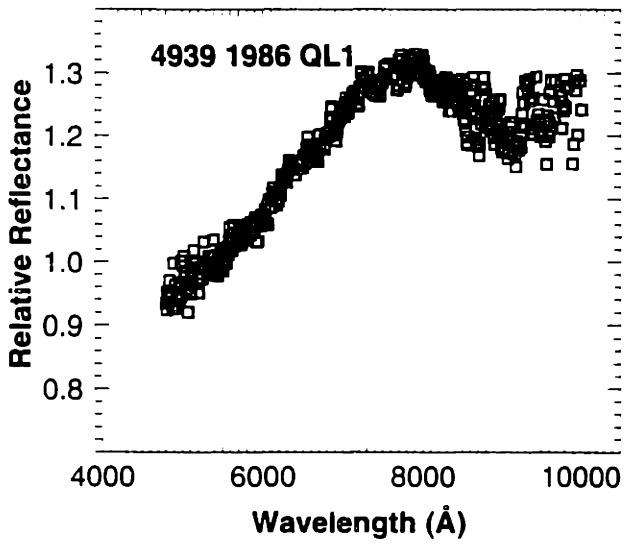
4939 1986 QL1
Relative Reflectance
1.3
1.2
1.1
1.0
0.9
0.8
4000
6000
8000
10000
Wavelength (Å)

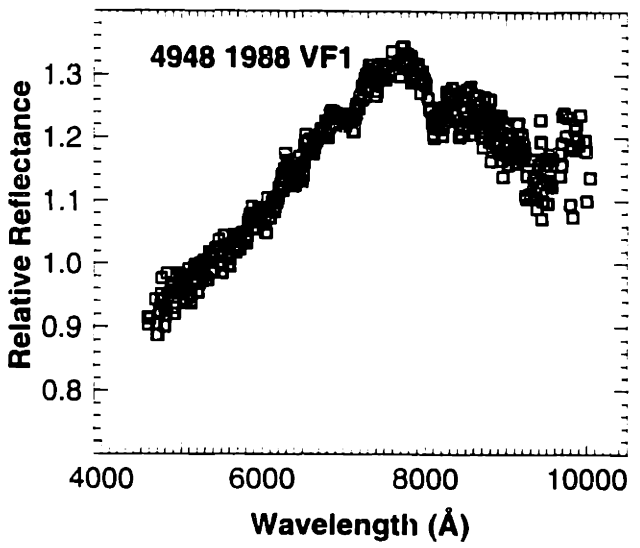
4948 1988 VF1
Relative Reflectance
1.3
1.2
1.1
1.0
0.9
0.8
4000
6000
8000
10000
Wavelength (Å)

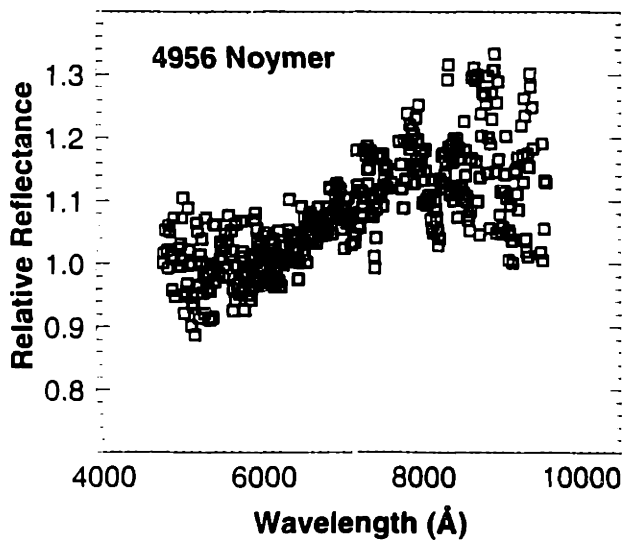
4956 Noymer
Relative Reflectance
1.3
1.2
1.1
1.0
0.9
0.8
4000
6000
8000
10000
Wavelength (Å)

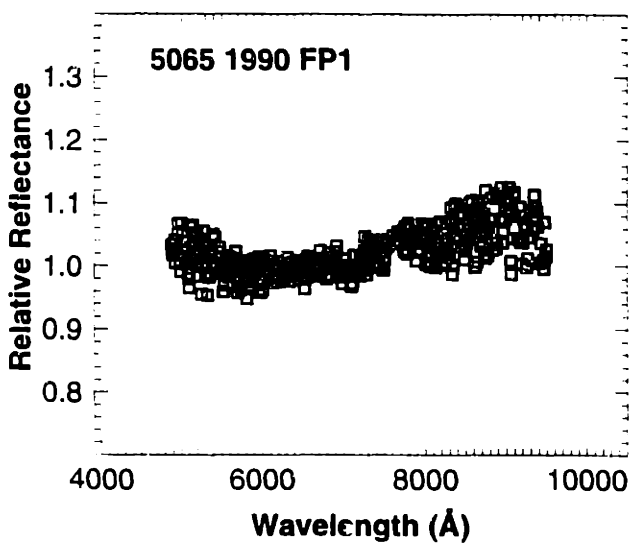
5065 1990 FP1
Relative Reflectance
1.3
1.2
1.1
1.0
0.9
0.8
4000
6000
8000
10000
Wavelength (Å)

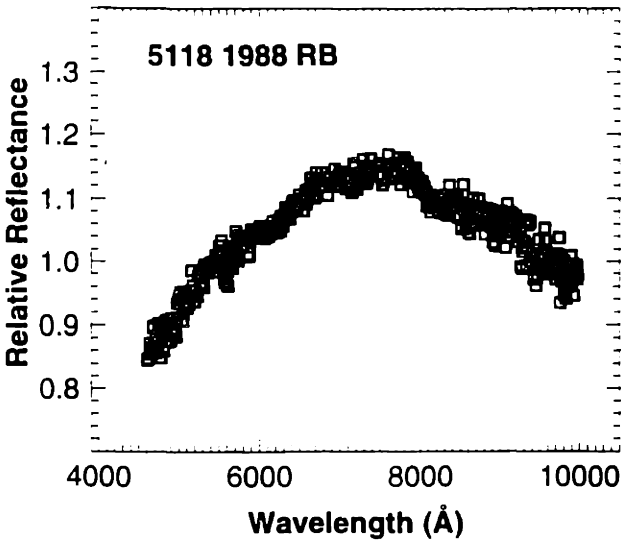
5118 1988 RB
Relative Reflectance
1.3
1.2
1.1
1.0
0.9
0.8
4000
6000
8000
10000
Wavelength (Å)

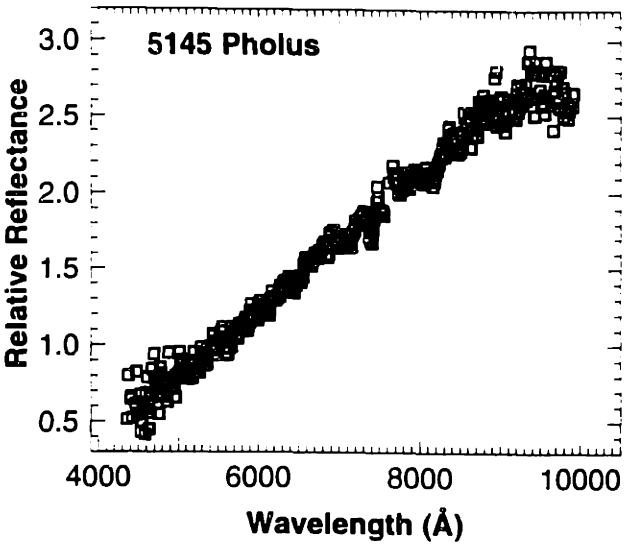
5145 Pholus
Relative Reflectance
3.0
2.5
2.0
1.5
1.0
0.5
4000
6000
8000
10000
Wavelength (Å)

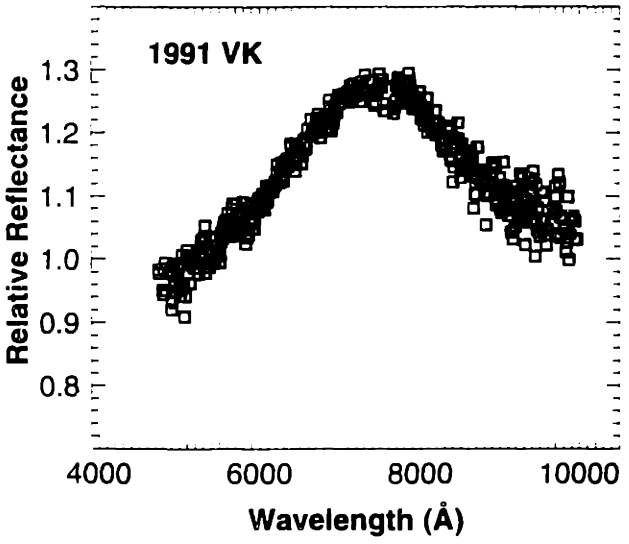
1991 VK
Relative Reflectance
1.3
1.2
1.1
1.0
0.9
0.8
4000
6000
8000
10000
Wavelength (Å)

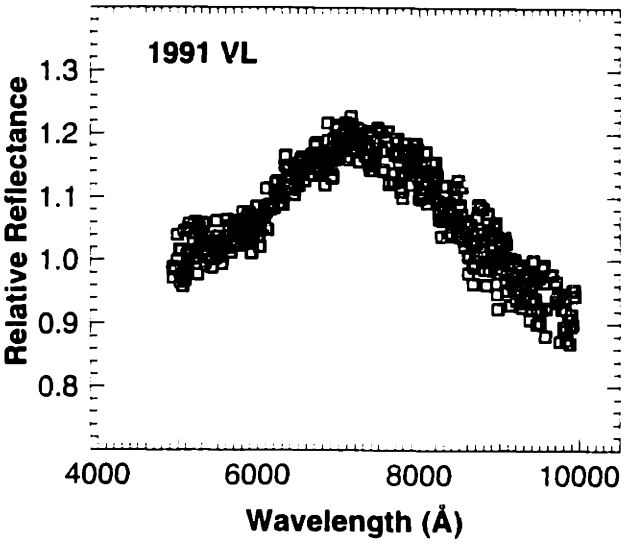
1991 VL
Relative Reflectance
1.3
1.2
1.1
1.0
0.9
0.8
4000
6000
8000
10000
Wavelength (Å)

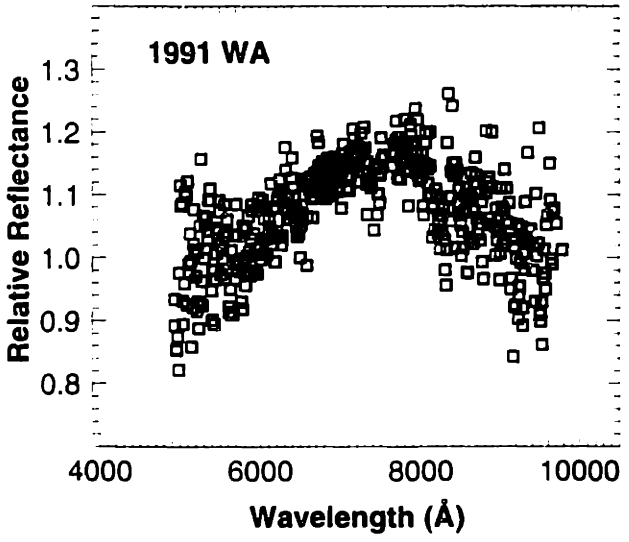
1991 WA
Relative Reflectance
1.3
1.2
1.1
1.0
0.9
0.8
4000
6000
8000
10000
Wavelength (Å)

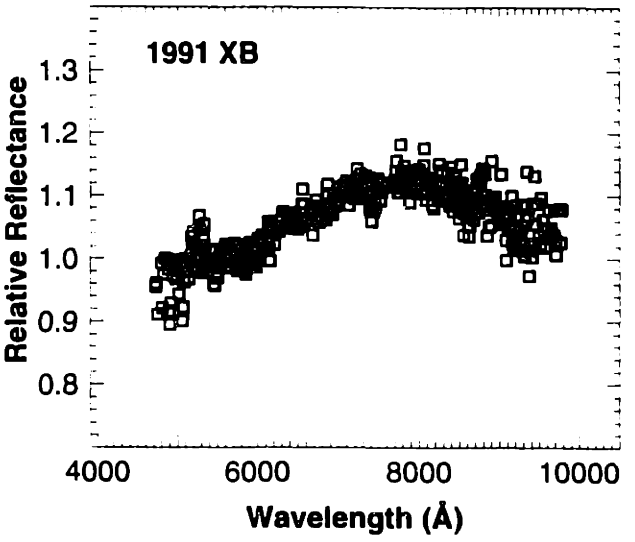
1991 XB
Relative Reflectance
1.3
1.2
1.1
1.0
0.9
0.8
4000
6000
8000
10000
Wavelength (Å)

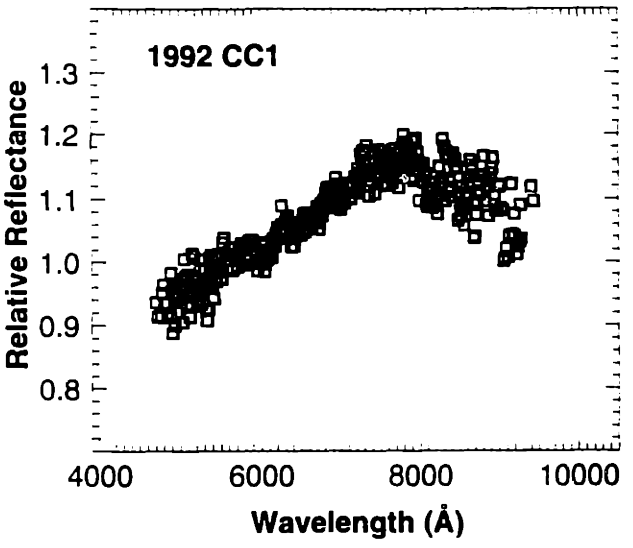
1992 CC1
Relative Reflectance
1.3
1.2
1.1
1.0
0.9
0.8
4000
6000
8000
10000
Wavelength (Å)

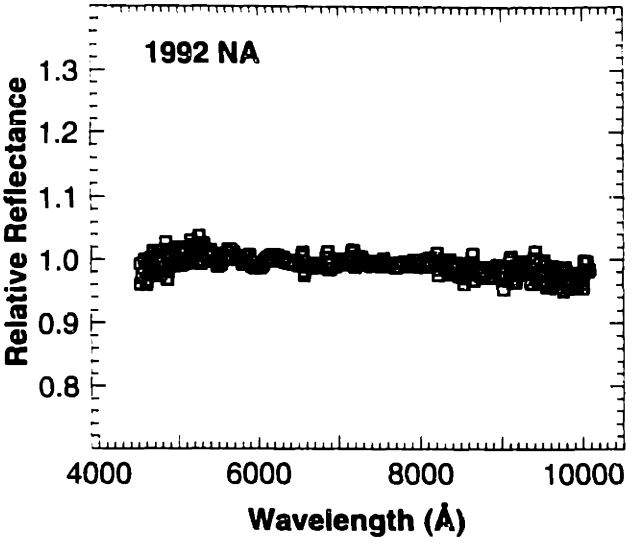
1992 NA
Relative Reflectance
1.3
1.2
1.1
1.0
0.9
0.8
4000
6000
8000
10000
Wavelength (Å)

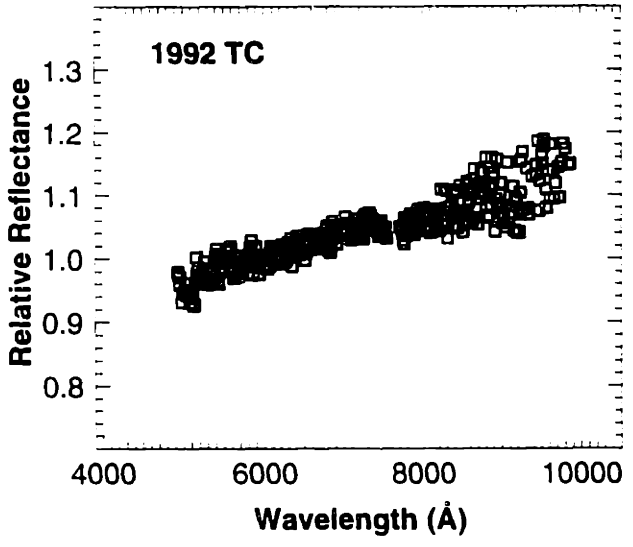
1992 TC
Relative Reflectance
1.3
1.2
1.1
1.0
0.9
0.8
4000
6000
8000
10000
Wavelength (Å)

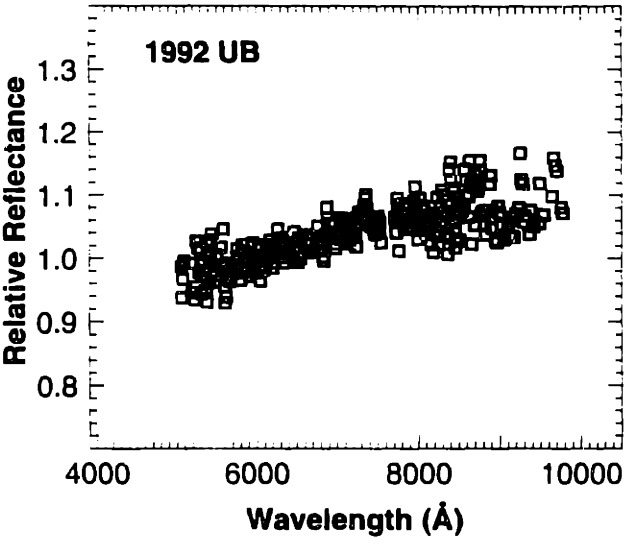
1992 UB
Relative Reflectance
1.3
1.2
1.1
1.0
0.9
0.8
4000
6000
8000
10000
Wavelength (Å)